NORTHWESTERN UNIVERSITY

Engineering Responses of Soft Materials

A DISSERTATION

SUBMITTED TO THE GRADUATE SCHOOL
IN PARTIAL FULFILLMENT OF THE REQUIREMENTS

for the degree

DOCTOR OF PHILOSOPHY

Field of Applied Physics

By

Hang Yuan (袁航)

EVANSTON, ILLINOIS

June 2022

ABSTRACT

Engineering Responses of Soft Materials

Hang Yuan (袁航)

Engineering responses of soft materials at hierarchical time and length scales is of great interest to both fundamental science and technological applications. In recent years, the hybridization between emerging soft condense matters and conventional hard condense matters keeps enriching the materials library of humankind and opens another largely-uncharted venue for innovating the design of soft materials with controlled responses, which has great potential future applications compatible with living systems. This work demonstrates some preliminary efforts of engineering soft materials at different scales to achieve controlled responses to various external stimuli, and ultimately lead to the desired properties and functionalities. Utilizing a combination of experimental, computational and theoretical approaches, this work focuses on deciphering the fundamental mechanisms behind each observed phenomena and developing theoretical frameworks for better assisting the design of responsive soft materials. With deepening understanding of those materials, increasing number of natural/synthetic soft materials are expected to be engineered in the future for the continual development of technology.

Acknowledgements

I am grateful to have met so many wonderful people through my graduate study. First of all, I would like to express my sincere gratitude to my advisor Prof. Monica Olvera de la Cruz. She has been guiding, supporting and encouraging me from the first day I joined the group. I appreciate her trust and providing me great freedom to explore a diverse range of interesting research problems. I was truly fortunate to work with her in my graduate study, where I received both professional scholarly mentorship and warmhearted personal advice. Furthermore, I also want to thank my committee members, Prof. Samuel Stupp, Prof. Michelle Driscoll and Prof. Petia Vlahovska, for taking time to review this thesis and their expert knowledge are crucial for accomplishing works presented in this thesis.

It's an enjoyable experience to work in a friendly and supportive research group and I am indebted to many past and present members of Olvera de la Cruz group. My simulation techniques benefited a lot from Dr. Trung Nguyen, Prof. Baofu Qiao and Dr. Felipe Jimenez Angeles. I want to thank Dr. Shuangping Liu, Dr. Yaohua Li, Dr. Yihao Liang and Dr. Siyu Li who helped me in many ways and Dr. Debarshee Bagchi and Dr. Leticia Lopez for being my nice officemates. Besides, I was also appreciative to have amazing cohorts in the research group and Applied Physics Graduate Program and many friends met along the journey.

I was fortunate to work with many brilliant collaborators. I worked closely with Dr. Chuang Li and Dr. Garrett C. Lau in Prof. Stupp's group at Northwestern University

and also Dr. Shuangping Liu and Aaveg Aggarwal from my own group to design hydrogel robots. I enjoyed playing around hydrogel robots in Prof. Stupp's lab. After that, I had an opportunity to work on magnetic colloidal particles with Dr. Michael Wang in Prof. Paul M. Chaikin's group at New York University. And their great physics questions initiated my interests in microhydrodynamics (particularly the Stokesian Dynamics). In roughly the same period, I also collaborated with Zhengyan Zhang and Dr. Dou Yong in Prof. Kyle J. M. Bishop's group at Columbia University, which introduced me to the systems of Quincke particles. It was a pleasurable experience to gradually unveil the mechanisms of Quincke oscillators through our many remote meetings and email communications. During the COVID-19 pandemic, I was also lucky to know Dr. Bo Zhang in Dr. Alexey Snezhko's group at Argonne National Laboratory, where I got the chance to combine my experiences with Quincke particles and Stokesian Dynamics, which fostered my interests of collective behaviors in active matters.

I also want to thank my parents for providing unconditional supports throughout all these years and giving me complete freedom for making independent decisions.

My research works involved a large portion of computational study and many of them were built upon various open-source packages. I would like to particularly thank those anonymous contributors in open-source communities who generously shared their code in public. My research works would take much longer time without their contributions.

Finally, I would like to acknowledge the Center for Bio-Inspired Energy Science (CBES) and Center for Computation & Theory of Soft Materials (CCTSM) for providing funding supports and computational resources throughout my Ph.D. career.

Dedication

To the memory of five years (2017 - 2022).

Table of Contents

List of Abbreviations

AOT: sodium bis(2-ethylhexyl) sulfosuccinate. 74, 113, 114, 116, 123, 228

MCH^+: protonated merocyanine. 134, 150–153, 174–176, 185

NaAOT: dioctyl sulfosuccinate sodium salt. 83–85

Ni: nickel. 134, 145, 153–156, 172–174, 176, 177

SP: spiropyran. 134, 150–153, 161, 174–176

A-B: Adams-Bashforth. 240

ABAQUS: Abaqus FEA. 108

B-L: Beer–Lambert. 151

BD: Brownian Dynamics. 195, 241, 243

BLAS: Basic Linear Algebra Subprograms. 238

C-G: Cauchy-Green. 140, 146–148, 156, 158, 162, 163

C-P: Car–Parrinello. 41, 42

CBES: Center for Bio-Inspired Energy Science. 5

CCTSM: Center for Computation & Theory of Soft Materials. 5

CCW: counter-clockwise. 247–253

CMC: critical micelle concentration. 84, 113, 114

COMSOL: COMSOL Multiphysics. 108, 111, 160–163, 167, 168, 172

CSP: Curie's Symmetry Principle. 266

CUDA: Compute Unified Device Architecture. 237, 297

CW: clockwise. 247, 249, 251, 252

DC: direct current. 35, 71, 245, 247, 248, 253

DMA: Dynamic Mechanical Analysis. 172, 175

DOF: degrees of freedom. 37, 193–195, 257

DPD: Dissipative Particle Dynamics. 70, 195

EDL: electric double layer. 72

EI: electrostatic interactions. 229, 230, 241, 242, 253–255

EOM: equations of motion. 142–144, 163–167, 233–235, 240, 241, 296

F-H: Flory–Huggins. 152, 153

F-P: Fokker-Planck. 233

FDM: Finite Difference Method. 240

FDT: Fluctuation-Dissipation Theorem. 233, 297

FEM: Finite Element Method. 108, 111, 112, 168, 169, 172, 299

FEniCSx: FEniCSx. 108, 168

FvK: Föppl-von Kármán. 43, 51, 52, 57, 58, 61, 62, 66, 67, 69

G-L: Green-Lagrange. 140, 163

GBT: Gauss-Bonnet Theorem. 56

GMRES: Generalized Minimal Residual Method. 239

GPU: graphics processing unit. 236, 244, 297

HI: hydrodynamic interactions. 194, 226, 230, 243, 253–255, 259, 260, 262, 264, 265, 299

HOOMD: Highly Optimized Object-oriented Molecular Dynamics. 243

i.i.d.: independent and identically distributed. 233, 235

I/O: Input/Output. 244

L-J: Lennard-Jones. 53, 63, 65

LAMMPS: Large-scale Atomic/Molecular Massively Parallel Simulator. 53–55, 243

LAPACK: Linear Algebra Package. 238

LBM: Lattice Boltzmann Method. 70, 195, 298

LCEs: liquid crystal elastomers. 188

LRT: Lorentz Reciprocal Theorem. 206, 209–211, 281–283, 294, 374–379, 387

M-W: Maxwell-Wagner. 75, 96, 99

MD: Molecular Dynamics. 41, 42, 299

MPCD: Multi-particle Collision Dynamics. 70, 195

N-H: Neo-Hookean. 147, 149, 173

N-P: Nernst-Planck. 71, 76, 80, 86, 116

N-S: Navier-Stokes. 71, 76, 78, 196, 197

Numba: a just-in-time compiler for Python. 237

ODE: ordinary differential equations. 92, 119, 240, 241

OpenCL: Open Computing Language. 237

ORR: Onsager reciprocal relations. 266, 267

P-K: Piola-Kirchhoff. 141, 142, 158–160, 163, 166, 168

PD: Polar Decomposition. 140

PDE: partial differential equations. 92, 108, 111, 161

Pe: Péclet number. 84

PNP: Poisson-Nernst-Planck. 116, 126

PPPM: Particle-Particle Particle-Mesh. 54, 242

PyCUDA: Pythonic access to CUDA parallel computation API. 237

R-K: Runge-Kutta. 241

Re: Reynolds number. 69, 72, 73, 89, 197, 233

RFD: Random Finite Difference. 240

RPY: Rotne-Prager-Yamakawa. 218, 223, 229, 234, 286, 290, 349, 355

S-E: Stokes-Einstein. 114

SANS: Small-angle neutron scattering. 113

SAS: Symbolic Algebra System. 167, 297

SAXS: Small-angle X-ray scattering. 135, 137

SD: Stokesian Dynamics. 5, 37, 38, 70, 195, 196, 203, 224, 225, 235, 253, 257, 260, 261, 265, 294–297, 299, 343

SNOPT: Sparse Nonlinear OPTimizer. 172

SQUID: superconducting quantum interference device. 135, 172

St: Strouhal number. 197

SymPy: A Python library for symbolic mathematics. 297

T-M: Taylor-Melcher. 73, 76

Taichi: A parallel programming language originated in computer graphics.. 237

TRS: time reversal symmetry. 38, 211, 259–261, 265, 267, 294

List of Symbols

N_A**:** Avogadro constant. 152, 300

$\mathcal{O}$**:** big O asymptotic notation. 194, 203, 234, 235, 239

k_B**:** Boltzmann constant. 81, 113, 147, 152, 233

ρ_f**:** free charge density. 77

q_s**:** free surface charge density. 77, 92, 94, 96, 102, 109

e**:** elementary charge. 80, 113

σ**:** electric conductivity. 77, 80

κ**:** bending rigidity. 43

K**:** bulk modulus. 144, 147, 172, 174, 176

M**:** magnetic modulus. 48, 50, 69

ν**:** Poisson's ratio. 43

G**:** shear modulus. 144, 147, 172, 174, 176

γ**:** stiffness parameter. 149, 172, 174, 176

k**:** stretching constant. 42, 45, 54

Y**:** Young's modulus. 43

$:$ **:** double contraction. 143, 159

d^c**:** cutoff distance. 213, 224, 225, 238

$\mathcal{W}_{el}$**:** elastic strain energy density. 144, 146, 148, 149, 153, 156, 157, 163

$\delta\mathcal{W}$**:** virtual work. 143

ϵ_0**:** absolute electric permittivity of vacuum. 77, 113

ϵ_r**:** relative electric permittivity. 77

K**:** equilibrium constant of a chemical reaction. 84

$\mathbf{J}_e$**:** electric currents. 85, 90, 91, 110, 117, 120

$\mathbf{J}_s$**:** surface flux. 109

$\mathbf{J}$**:** total flux of transport process. 80

$\mathbf{f}$**:** volumetric force vector. 78, 143, 196–198, 269

$\mathbf{f}_e$**:** interfacial electric force vector. 78, 96

$\mathbf{F}_e$**:** total electric force vector. 96

$\mathbf{F}$**:** total force vector. 90, 198, 229, 270, 279

$\mathcal{F}^{-1}$**:** inverse Fourier transformation. 271

ϕ**:** volume fraction. 152, 153

f**:** frequency. 162

ω**:** angular frequency. 150

ξ**:** friction coefficient. 81

δ**:** gap distance. 106, 216

$\mathcal{W}$**:** standard Gaussian noise. 233

$\boldsymbol{\nabla}$**:** gradient operator. 111, 139

$\boldsymbol{\nabla}_s$**:** surface gradient operator. 81

$\mathcal{H}$**:** Hamiltonian. 42, 50

$\boldsymbol{I}$**:** identity tensor. 78, 90, 139

I**:** light intensity. 150

δ_{ij}**:** Kronecker delta. 200, 267, 370, 382

δ_{ijkl}**:** fourth-rank deviatoric traceless unit tensor. 209, 371

ℓ_0**:** equilibrium length. 42, 45, 48, 54

L_c**:** characteristic length scale. 77, 196

Λ**:** Lagrange multiplier. 53, 64

∇^{-2}**:** inverse Laplace operator. 276

λ_B**:** Bjerrum length. 113

λ_D**:** Debye length. 85, 93, 120, 126

ε_{ij}**:** right-hand 2D Levi-Civita symbol. 268

ε_{ijk}**:** right-hand 3D Levi-Civita symbol. 201, 267, 370, 382

$\mathbf{B}$**:** magnetic flux density. 136, 154–156, 161, 172, 176, 177, 267

φ_m**:** magnetic scalar potential. 154, 162

$\mathbf{H}$**:** magnetic field strength. 154, 156

$\mathbf{H}_b$**:** background magnetic field strength. 154, 162, 169

$\mathbf{M}$**:** magnetization. 156, 172, 177

$\mathbf{M}_0$**:** residual magnetization. 154, 169, 172

μ**:** mobility coefficient. 80, 114, 117

$\mathcal{M}_\infty$**:** far-field grand mobility tensor. 207, 224, 225, 238, 239

$\mathcal{M}$**:** full grand mobility tensor. 212, 224, 225, 229, 233, 239, 294–296

$\boldsymbol{M}_{UF}$**:** mobility tensor connecting force and translational velocity. 90, 101, 236

$\boldsymbol{M}_{UT}$**:** mobility tensor connecting torque and translational velocity. 90, 101

$\boldsymbol{M}_{\Omega F}$**:** mobility tensor connecting force and angular velocity. 90, 101

$\boldsymbol{M}_{\Omega T}$**:** mobility tensor connecting torque and angular velocity. 90, 101

μ_0**:** absolute magnetic permeability of vacuum. 44, 77, 154

μ_r**:** relative magnetic permeability. 77, 154

$\hat{\mathbf{n}}_{12}$**:** unit normal vector, pointing from medium 1 to medium 2. 81, 94

$\hat{\mathbf{n}}$**:** unit outer normal vector. 47, 109

N**:** number of particles. 113, 370, 381

$\hbar$**:** reduced Planck constant. 151

$\mathbf{x}$**:** position in the deformed configuration. 139

$\mathbf{X}$**:** position in the reference configuration. 139

$\mathbf{r}$**:** position vector. 44, 88, 165, 198, 228, 270

$\hat{\mathbf{r}}$**:** unit position vector. 94, 215

p**:** pressure. 79, 170, 196, 197, 266

$\boldsymbol{Q}$**:** electric quadrupole moment. 93, 105

a^h**:** hydrodynamic radius. 81, 113

a**:** particle radius. 88, 94, 106, 109, 120, 126, 197, 203, 370, 381

k_-: backward reaction rate constant. 83, 114, 119, 150

k_+: forward reaction rate constant. 83, 114, 150

τ_{mw}^P: Maxwell-Wagner relaxation time of dipole moments. 96, 99, 124, 227

τ_{mw}^Q: Maxwell-Wagner relaxation time of quadrupole moments. 96

$\mathcal{R}_\delta^\infty$: far-field grand resistance tensor. 224, 225, 239

$\mathcal{R}_\delta$: near-field grand resistance tensor. 213, 224, 225, 238, 239

$\boldsymbol{R}$: rotation tensor. 140

$\mathbb{E}$: the set of all edges. 42

$\mathbb{N}$: the set of natural numbers. 274

$\mathbb{R}$: the set of real numbers. 109, 146, 148

$\mathbb{V}$: the set of all vertices. 44, 49

r: source/sink of chemical reactions. 80, 83, 115

$\boldsymbol{C}$: Cauchy-Green strain tensor. 140, 141, 146, 148, 156, 158, 162

$\boldsymbol{\epsilon}$: Green-Lagrange strain tensor. 140, 141, 163

$\boldsymbol{\sigma}$: Cauchy stress tensor. 78, 141–143, 177, 196, 198

$\boldsymbol{\sigma}^e$: electric stress tensor. 96

$\boldsymbol{P}$: first Piola-Kirchhoff stress tensor. 141, 142, 163

$\boldsymbol{S}$: second Piola-Kirchhoff stress tensor. 141, 142

$\boldsymbol{U}$: stretch tensor. 140

T: temperature. 81, 113, 147, 152, 233

τ_c: characteristic time scale. 196

Δt: time step. 241

List of Tables

List of Figures

CHAPTER 1

Introduction

"Physics is about questioning, studying, probing nature."

There is an old saying by the prominent Chinese philosopher Xun Zi (荀子) in his classic essay "*On Learning*" (劝学篇) — " We humans are not born any more superior than animals. We have become superior because we learn and we learned how to make use of materials (君子生非异也，善假于物也)." The word, materials (物), in the original quote actually refers to any tangible tools humans leveraged in a much broader context. However, the quote still offers insight and wisdom even if we restrict the meaning of it to the materials from a modern scientific perspective. The world we live in already has a myriad of natural materials; meanwhile, scientists and engineers are still keep creating innumerable artificial materials. Being fortunate to have such a repository of diverse materials, it is an eternal theme of science to learn about materials and make use of those materials for continual innovations of technology.

Our understanding of any unknown materials start with probing its responses caused by an external disturbance. For example, the British physicist Robert Hooke discovered the famous Hooke's law [**1**] in the 1670s, which states that the extension of a spring is proportional to the force ($\mathbf{F} = -k\Delta\mathbf{x}$). Here, we understand the property of an elastic spring by simply pulling the spring and measuring the resulted restoring forces. Similarly,

the Irish English physicist George Gabriel Stokes derived the well-known Stokes' law [**2**] in 1850s, which states that the resistive force acting on a sphere moving through a viscous fluid is proportional to its velocity ($\mathbf{F} = 6\pi\mu a\mathbf{U}$). In this example, the property of a viscous fluid is studied by perturbing the viscous fluid via a moving sphere and measuring the corresponding drag forces from the surrounding fluid. Looking back the history of science, countless fundamental principles of materials, such as the Fick's law [**3**], the Ohm's law [**4**], the Fourier's law [**5**], etc., have been discovered and they all can be viewed in this perspective.

After hundreds of years of development in science, scientists are able to study more and more complex materials with accumulated knowledge [**6**, **7**]. Nowadays, the relationship between material responses and external perturbations are not necessarily linear anymore. However, the philosophy guiding the material researches remain essentially the same: we understand the materials by probing its responses to external perturbations. Among all those materials studied in the past a few decades, the "hard condense matters", which generally deals with materials with structural rigidity, such as crystalline solids, glasses, metals, insulators, and semiconductors, etc., are rather extensively studied due to the success of quantum mechanics and relatively clearly-identified order in those systems. On the other hand, the "soft condense matters" is a relatively young and emerging field with many uncharted problems, where systems under study generally lack of a clearly-defined order and do not involve any quantum effects. Many soft materials, such as liquid crystals, gels, foams, polymers, granular matter, emulsions and biological tissues, etc., have lots of industrial applications and have been integrated into our daily life.

Compared with hard condense matters, soft condense matters usually involve more building blocks and are studied in larger length and time scales. More importantly, the "soft" nature of soft materials enables easy hybriding with conventional hard condense matters. This yields a large class of unexplored soft materials responsive to mechanical forces [**8**,**9**], chemicals [**10**,**11**], electric fields [**12**,**13**], magnetic fields [**14**,**15**], light [**16**,**17**], heat [**18**–**20**] and so on. Such "active" soft materials provide a vast design space for controlling over its responses via external stimuli [**21**–**25**]. But meanwhile, couplings between multiple response mechanisms are usually inevitably introduced. Even for a material responsive to only a single external stimulus, the response of its active components is commonly coupled with the response of the embedding passive medium. These couplings make the active soft materials a more complex system to understand comprehensively. However, "Standing on the shoulders of giants", it's time for a more mature science to understand the behaviors of more complex systems, such as the unique properties of those novel active soft materials.

Understanding the properties of the soft materials is only the first step. To make use of materials for the benefits of humankind, the ultimate goal is to engineer the responses of soft materials for desired functionalities. This takes one step further than just probing the responses of materials. If probing the responses of materials provides us some preliminary pictures of material properties, engineering responses requires a certain level of abstraction of probed results to obtain a more thorough understanding of the fundamental mechanisms. With a proper theoretical description of mechanisms and if we are fortunate enough, we can engineer soft materials to generate specific responses under the influence of external stimuli for targeted functions.

To make the above statement more clear, this work centers around the theme — *engineering responses of soft materials* — and attempts to address this topic with a few concrete active soft material systems primarily from theoretical and computational perspectives. This work is composed of two major parts. The first part of this work focuses on the individual behaviors of three different soft materials at different length and time scales. It aims to give a flavor of the diversity of active soft materials and demonstrates how to learn the responses of soft materials to external stimuli at an individual level with appropriate methodologies. In the second part, this work attempts to understand the collective responses of soft materials. It advances individual studies and is crucial for designing desired functions from an assembly of soft materials. For readers do not have a shared background, I have tried my best to write each chapter in a pedagogical and self-containing manner. However, occasionally there are some cross-references between chapters (such as Chap. 3 and Chap. 5, Chap. 5 and Chap. 6, etc.) in order to elucidate their underlying connections for a better understanding and also avoid unnecessary repetitions. In the following, brief overviews of each chapter's content and the organization of chapters are summarized:

Part 1: Individual Behaviors. In the first part of this work, each chapter presents a concrete example of engineering responses of soft materials. Three different soft material systems are selected and their individual behaviors in response to external stimuli, such as electric/magnetic fields and light, are systematically studied via theoretical and numeric methodologies at hierarchical scales, ranging from microscopic scale, to mesoscopic scale and to macroscopic scale. Three chapters in the first part are arranged

with the order of increasing length and time scales. Chapter 2 studies the morphological changes of nanometer-sized magnetoelastic shells under the influence of an external magnetic field; Chapter 3 studies the oscillatory motions of micron-sized colloidal particles driven by a direct current (DC) electric field ; Chapter 4 studies the robotic functionalities of millimeter-sized hydrogel-metal hybrids with dual response to both light and magnetic fields.

Chapter 2: Magnetoelastic Shells. Elastic crystalline membranes exhibit a buckling transition from sphere to polyhedron. However, their morphologies are restricted to convex polyhedra and are difficult to externally control. In this chapter, morphological changes of closed crystalline membranes of super-paramagnetic particles are systematically investigated. The competition of magnetic dipole-dipole interactions with the elasticity of this magnetoelastic membrane leads to concave morphologies. We found that the symmetry of the buckled membrane decreases as the magnetic field strength increases. This gives the ability to switch the membrane morphology between convex and concave shapes with specific symmetry and provides promising applications for membrane shape control in the design of actuatable micro-containers for targeted delivery systems.

Chapter 3: Quincke Oscillators. Dielectric particles in weakly conducting fluids rotate spontaneously when subject to strong DC electric fields. Such Quincke rotation near a plane electrode leads to particle translation that enables physical models of active matter. In this chapter, we show that Quincke rollers can also exhibit oscillatory dynamics, whereby particles move back and forth about a fixed location. We explain how oscillations

arise for micron-scale particles commensurate with the thickness of a field-induced boundary layer in the nonpolar electrolyte. This work enables the design of colloidal oscillators.

Chapter 4: Hydrogel Robots. An enormous challenge for science is the design of soft matter in which internal fuels or an external energy input can generate locomotion and shape transformations observed in living organisms. Such materials could assist in productive functions that may range from robotics to smart management of chemical reactions and communication with cells. In this context, hydrated matter that can function in aqueous media would be of great interest. We report here on the design of hydrogels containing a scaffold of high aspect-ratio ferromagnetic nanowires with nematic order dispersed in a polymer network that change shape in response to light and experience torques in rotating magnetic fields. The synergistic response enables fast walking motion of macroscopic objects in water on either flat or inclined surfaces and also guides delivery of cargo through rolling motion and light-driven shape changes. The theoretical description of the response to the external energy input allowed us to program specific trajectories of hydrogel objects that were verified experimentally.

Part 2: Collective Behaviors. In the second part of this work, the focus of study shifts from individual behaviors to collective behaviors of soft materials in response to external stimuli. From a single object to a collection of objects, the interactions between constituent objects of the system make the phenomena observed more diverse and also more complex. As a starting point, colloidal particles engineered to be responsive to electric/magnetic fields serve as ideal synthetic systems for studying the collective behaviors

of out-of-equilibrium systems. Chapter 5 focuses on the collective motions of colloidal particles immersed in a passive fluid, whose mobility is coupled with its internal degrees of freedom (DOF) (if any). Quincke particles is a good examples of such active colloidal particles. With the understanding of individual behaviors of Quincke particles established in Chapter 3, a model based on the Stokesian Dynamics (SD), supplemented with the dynamic equations governing its internal DOF, is developed to describe a population of Quincke particles. Chapter 6 also studies the collective motions of active colloidal particles but focuses more on the effect of surrounding "active fluid". Ferromagnetic colloidal particles driven by a rotating magnetic field induce active flows which modify the collective motions of particles. The concept of odd viscosity is introduced into the Stokesian Dynamics (SD) and a parallel SD framework compatible with odd viscosity is developed to understand the collective behaviors of a population of magnetic spinners.

Chapter 5: Collective Behaviors of Quincke Particles. Spontaneous emergence of correlated states such as flocks and vortices are prime examples of remarkable collective dynamics and self-organization observed in active matter. The formation of globally correlated polar states in geometrically confined systems proceeds through the emergence of a macroscopic steadily rotating vortex that spontaneously selects a clockwise or counterclockwise global chiral state. Here, we reveal that a global vortex formed by colloidal rollers exhibits polar state reversal, and a subsequent formation of the collective states upon re-energizing the system is not random. We combine experiments and simulations to elucidate how a combination of hydrodynamic and electrostatic interactions leads to hidden asymmetries in the local particle positional order reflecting the chiral state of the

system. These asymmetries can be exploited to systematically command subsequent polar states of active liquid through temporal control of the activity.

Chapter 6: Collective Behaviors of Magnetic Spinners. Unlike common passive fluids, a new type of viscosity, odd viscosity, emerges in active fluids with broken time reversal symmetry (TRS), such as those fluids consist of active spinning particles. In recent theories and experiments, the odd viscosity have drawn increasing interests for understanding the non-equilibrium behaviors of active materials. However, the physical effects of odd viscosity are still elusive and only backed by very limited experimental measurements. Here, we study the sedimentation of a collection of driven magnetic colloidal particles. By measuring the steady state particle density profile, interesting broadening density profiles are observed with increasing spinning frequency, which cannot be reproduced with a traditional Stokesian Dynamics simulation. In order to elucidate the fundamental mechanism resulting the observed phenomenon, an extended SD framework with odd viscosity is developed, which attempts to confirm the physical role of odd viscosity in such active systems.

Part 1

Individual Behaviors

CHAPTER 2

Magnetoelastic Shells*

2.1. Introduction

Polyhedra are of great interest to scientists, mathematicians and engineers. They emerge spontaneously in many fields of science. For example, single crystals take various polyhedra shapes, fullerenes adopt beautiful truncated icosahedron shapes [**27**], and bacterial micro-compartments are observed in multiple regular and irregular polyhedral shapes [**28**].

Soft homogeneous elastic membranes, including hallow capsules [**29**–**31**], viral capsids [**32**, **33**], elastic biological membranes [**34**, **35**] and crystalline vesicles [**36**–**38**], can buckle under many conditions. Deformable capsules under pressure changes take on irregular shapes [**39**–**42**]. On the other hand, self-assembled crystalline membranes, like the shells of viruses, generally buckle into shapes with icosahedral symmetry [**43**]. These icosahedral membrane shapes have been explained by homogeneous elasticity theory [**32**, **44**]. Furthermore, membranes with heterogeneous elasticity have been demonstrated to form various regular and irregular polyhedral shapes [**45**]. Such polyhedral morphologies are formed by the competition between stretching energy and bending energy. Although it is possible to engineer membrane morphologies by arranging defects in closed membrane topologies [**46**], these morphologies cannot go beyond polyhedra.

*This chapter is primarily based on the published work [**26**] of Hang Yuan and Monica Olvera de la Cruz†, **Crystalline membrane morphology beyond polyhedra**, *Phys. Rev. E*, Vol. 100, p. 012610, 2019, with modified notations and extended details to comply with the structure of this work.

Here, we explore the possibility to create new closed shell morphologies, other than polyhedra, in a controllable manner. For this purpose, we consider elastic membranes of super-paramagnetic particles because of the exceptional penetration of magnetic fields and bio-compatibility. This provides opportunities to design magnetically responsive nanocarriers for targeted delivery systems in therapeutic applications [**47**–**52**]. Magnetoelastic materials form rich morphologies [**53**, **54**] and can accomplish multimodal locomotion [**55**, **56**] as well as deformations that generate forces between surfaces [**57**] when directed by magnetic fields. The versatility of magnetoelastic filaments, which consist of super-paramagnetic particles connected by elastic linkers, has also been demonstrated experimentally [**58**–**63**] and numerically [**64**–**66**].

Compared to magnetoelastic filaments and open membranes, closed magnetoelastic membranes, which have additional topological constraints, are found here to generate specific symmetries due to the interplay between nonlinear elasticity and magnetic dipole-dipole interactions. In this chapter, a discretized model of magnetoelastic membranes is developed and numerically simulated with the Car–Parrinello (C-P) Molecular Dynamics (MD) simulations [**67**] to find the minimum energy configurations of magnetoelastic membranes under the influence of an external magnetic field [Sec. 2.2]. Following that, the equilibrium morphologies of the closed magnetoelastic membranes with external magnetic fields are systematically investigated for cases with and without the volume constraint [Sec. 2.3]. And the whole chapter concludes with a brief discussion and possible future works [Sec. 2.4].

2.2. Discretized model of magnetoelastic membranes

Unlike the traditional MD, the C-P MD approach relies on the Hamiltonian of the system $\mathcal{H}$ and obtains its force fields by taking derivatives of the overall Hamiltonian with respect to particles' position. Following the idea of the C-P MD, the effective Hamiltonian describing the magnetoelastic membranes at the discretization limit is developed first. Then, the corresponding interactions derived from the Hamiltonian of the magnetoelastic membranes are elaborated and implemented into traditional MD simulations.

2.2.1. Hamiltonian of elastic membranes

As dictated by Euler's polyhedron formula [**68**], we start by triangulating a spherical shell with twelve isolated 5-fold disclinations. The disclinations are positioned on the vertices of an inscribed icosahedron [Fig. 2.1] to minimize the interactions between them [**69**], as proposed by Caspar and Klug [**70**].

The elastic component of the Hamiltonian of a magnetoelastic membrane, following the discretization scheme of Nelson et al. [**44**], is written as

$$\mathcal{H}_e = \sum_{e\in\mathbb{E}} \frac{1}{2} k \left(|\mathbf{r}_1^e - \mathbf{r}_2^e| - \ell_0\right)^2 + \sum_{e\in\mathbb{E}} \frac{1}{2} \tilde{\kappa} \left|\mathbf{n}_1^e - \mathbf{n}_2^e\right|^2 \tag{2.1}$$

where k is microscopic stretching constant and $\tilde{\kappa}$ is microscopic bending rigidity. The sum is over all e elements of $\mathbb{E}$, which is the set of all edges; $\mathbf{r}_1^e$ and $\mathbf{r}_2^e$ are two vertices of the edge e; and $\mathbf{n}_1^e$ and $\mathbf{n}_2^e$ are normal vectors of the two adjacent triangles of the edge e; and ℓ_0 is the equilibrium length. Note that the corresponding continuum limit of the above

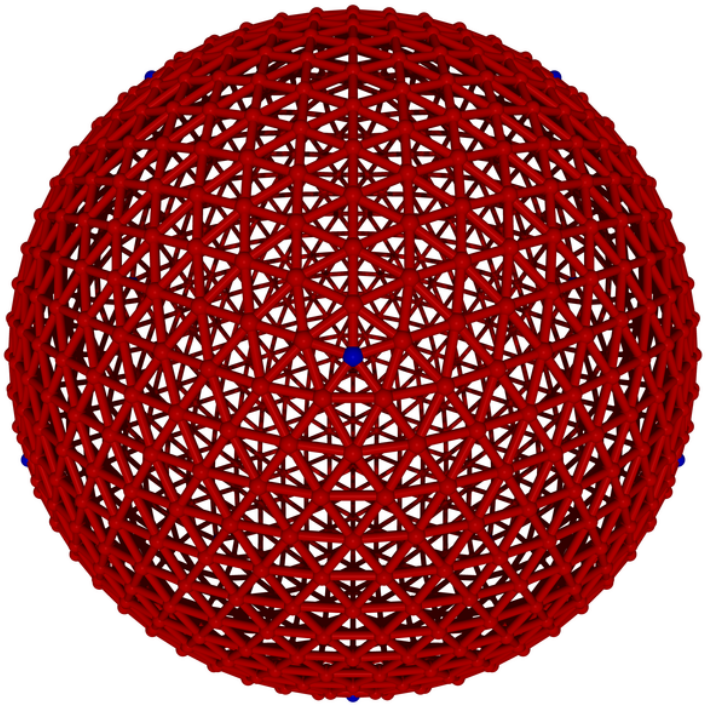

Figure 2.1. Mesh configuration of the spherical shell according to Caspar and Klug construction, which is characterized by two integers h and k [**70**]. Above figure shows the example of $(6, 6)$ structure and it has 1082 vertices, 3240 edges and 2160 faces. Blue vertices correspond to the locations of 5-fold disclinations and there are 12 disclinations in total which are located on vertices of an inscribed icosahedron.

discretized Hamiltonian is mesh dependent [**71**]. With the above described triangulation of a spherical shell, it has been shown that in the continuum limit [**44**, **72**] Young's modulus $Y = \frac{2k}{\sqrt{3}}$, Poisson's ratio $\nu = \frac{1}{3}$ and bending rigidity $\kappa = \frac{\tilde{\kappa}}{\sqrt{3}}$ [see Sec. 2.2.3.2].

Incompressible homogeneous isotropic linear elastic membranes ($\nu = 1/3$) of radius R can be described by two elastic parameters Y and κ. Then, a single dimensionless parameter, $\gamma = \frac{YR^2}{\kappa}$, called the Föppl-von Kármán (FvK) parameter [**73**], completely determines the buckling transition of such systems. Nelson et al. [**32**] have shown that homogeneous elastic membranes undergo a spontaneous buckling transition from sphere

to icosahedron when $\gamma > \gamma^* = 154$, where 154 is the value of γ^* for a flat disk.

2.2.2. Magnetic dipole-dipole interactions

In our study, we place a small super-paramagnetic particle (which does not have a permanent magnetization and the induced magnetization aligns with the external fields) at each vertex. An external magnetic field induces a magnetic dipole on each vertex. Therefore, an additional term for magnetic dipole-dipole interactions is added into the Hamiltonian of the system:

$$\mathcal{H}_m = -\frac{\mu_0}{4\pi} \sum_{\mathbf{r}_i, \mathbf{r}_j \in \mathbb{V}, i \neq j} \frac{1}{|\mathbf{r}_{ij}|^3} \left[3 \left(\boldsymbol{\mu}_i \cdot \hat{\mathbf{r}}_{ij} \right) \left(\boldsymbol{\mu}_j \cdot \hat{\mathbf{r}}_{ij} \right) - \boldsymbol{\mu}_i \cdot \boldsymbol{\mu}_j \right] \tag{2.2}$$

where μ_0 is the absolute magnetic permeability in vacuum, $\boldsymbol{\mu}_i$ is the magnetic dipole moment at vertex i, $\mathbb{V}$ is the set of all vertices, $\mathbf{r}_i$ is the position vector of vertex i, $\mathbf{r}_{ij} = \mathbf{r}_j - \mathbf{r}_i$ and $\hat{\mathbf{r}}_{ij} = \mathbf{r}_{ij} / |\mathbf{r}_{ij}|$ and the sum is over $i \neq j$.

2.2.2.1. nearest neighbor approximation. As the magnetic dipole-dipole interaction is long-range and anisotropic, the exact expression shown in Eqn. 2.2 is difficult for theoretical analysis. In order to get more physical insights, a simplified form, which considers only nearest neighbor interactions, is helpful for extracting another important dimensionless parameter.

For simplicity, we further assume the magnetic filed strength is strong enough that the induced magnetic dipole of each super-paramagnetic particles always aligns with the external magnetic field. And we only consider the case where a magnetoelastic membrane

is composed of the same type of super-paramagnetic particles. Then, the induced magnetic dipole moments of each super-paramagnetic particles are the same, i.e. $\boldsymbol{\mu}_i = \boldsymbol{\mu} = \mu\hat{\mathbf{m}}$, where $\boldsymbol{\mu}$ is the magnetic dipole moment of each super-paramagnetic particles, $\mu = |\boldsymbol{\mu}|$ and $\hat{\mathbf{m}}$ is the direction of the external magnetic field.

Then, the original magnetic dipole-dipole interaction [Eqn. 2.2] can be simplified by including only nearest neighbor interactions:

$$\begin{aligned}
\mathcal{H}_m &\approx -\frac{\mu_0}{4\pi} \sum_{\mathbf{r}_i,\mathbf{r}_j\in\mathbf{V},i\neq j} \frac{1}{|\mathbf{r}_{ij}|^3} \left[3\left(\boldsymbol{\mu}\cdot\hat{\mathbf{r}}_{ij}\right)^2 - \mu^2\right] \\
&\approx -\frac{\mu_0}{4\pi} \sum_{\mathbf{r}_i\in\mathbf{V}} \sum_{\mathbf{r}_j\in\text{neighbors of i}} \frac{1}{|\mathbf{r}_{ij}|^3} \left[3\left(\boldsymbol{\mu}\cdot\hat{\mathbf{r}}_{ij}\right)^2 - \mu^2\right] \\
&= \frac{\mu_0\mu^2}{4\pi} \sum_{\mathbf{r}_i\in\mathbf{V}} \sum_{\mathbf{r}_j\in\text{neighbors of i}} \frac{1}{|\mathbf{r}_{ij}|^3} \left[1 - 3\left(\hat{\mathbf{m}}\cdot\hat{\mathbf{r}}_{ij}\right)^2\right]
\end{aligned} \tag{2.3}$$

2.2.2.2. inextensible limit. Furthermore, we assume the membrane is inextensible, which means that the stretching constant k is large enough and thus all edge lengths are close to the equilibrium length ℓ_0. With this assumption, all vertices are roughly equally distant and there are only two types of vertices: vertices with five neighbors (five-fold disclinations) and vertices with six neighbors. Then, the magnetic energy associated with each vertex type can be calculated accordingly:

(1) Hexagonal vertex

In this case, the vertices have six neighbors which locate on vertices of a regular hexagon. Assuming the equilibrium length ℓ_0 is small enough that locally all six neighbors are roughly in the same plane. By choosing z-axis as the normal direction of this regular hexagon (moving frame), locations of six neighbors can be parametrized as $\mathbf{r}_j = \ell_0\hat{\mathbf{r}}_j = \ell_0\left(\cos\frac{j\pi}{3}, \sin\frac{j\pi}{3}, 0\right), j = 0, \cdots, 5$ and the direction

of the external magnetic field in this coordinate system can be expressed as $\hat{\mathbf{m}} = (r_t^i \cos\theta_t^i, r_t^i \sin\theta_t^i, m_n^i)$, where r_t^i is the magnitude of in-plane component of $\hat{\mathbf{m}}$ at vertex i, θ_t^i is the corresponding polar angle in the plane and m_n^i is the magnitude of out-of-plane component of $\hat{\mathbf{m}}$ at vertex i. Note that the components of $\hat{\mathbf{m}}$ in the chosen coordinate system depend on the location of vertex i. Then, the magnetic energy associated with each hexagonal vertex is

$$\begin{aligned}
\epsilon_{\text{hex}}^i &= \frac{\mu_0\mu^2}{4\pi} \sum_{j\in\text{neighbors of i}} \frac{1}{|\mathbf{r}_{ij}|^3} \left[1 - 3\left(\hat{\mathbf{m}}\cdot\hat{\mathbf{r}}_{ij}\right)^2\right] \\
&\approx \frac{\mu_0\mu^2}{4\pi} \sum_{j=0}^{5} \frac{1}{\ell_0^3} \left[1 - 3r_t^{i2}\cos^2\left(\theta_t^i - \frac{j\pi}{3}\right)\right] \\
&= \frac{\mu_0\mu^2}{4\pi}\frac{6}{l_0^3}\left[1 - \frac{3}{2}r_t^{i2}\right]
\end{aligned} \tag{2.4}$$

(2) Pentagonal vertex

By similarly choosing the coordinate system, the locations of neighbor vertices in the pentagonal case can be written as $\mathbf{r}_j = \ell_0\hat{\mathbf{r}}_j = \ell_0\left(\cos\frac{2j\pi}{5}, \sin\frac{2j\pi}{5}, 0\right), j = 0, \cdots, 4$. The magnetic energy associated with each of the disclination vertices is:

$$\begin{aligned}
\epsilon_{\text{pen}}^i &= \frac{\mu_0\mu^2}{4\pi} \sum_{j\in\text{neighbors of i}} \frac{1}{|\mathbf{r}_{ij}|^3} \left[1 - 3\left(\hat{\mathbf{m}}\cdot\hat{\mathbf{r}}_{ij}\right)^2\right] \\
&\approx \frac{\mu_0\mu^2}{4\pi} \sum_{j=0}^{4} \frac{1}{l_0^3} \left[1 - 3r_t^{i2}\cos^2\left(\theta_t^i - \frac{2j\pi}{5}\right)\right] \\
&= \frac{\mu_0\mu^2}{4\pi}\frac{5}{l_0^3}\left[1 - \frac{3}{2}r_t^{i2}\right]
\end{aligned} \tag{2.5}$$

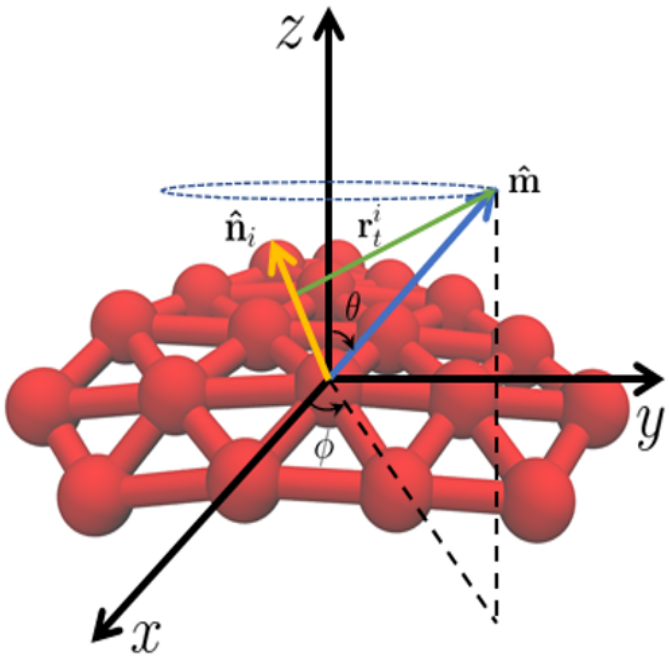

Figure 2.2. A schematic drawing of the local coordinate system defined for a patch of magnetoelastic membranes. $\hat{\mathbf{m}} = (\sin\theta\cos\phi, \sin\theta\sin\phi, \cos\theta)$ represents the direction of a precessing magnetic field around the z-axis, where θ and ϕ are the polar and azimuthal angles, respectively; $\hat{\mathbf{n}}_i$ denotes the unit outer normal vector of i-th vertex and $\mathbf{r}_t^i$ is the corresponding in-plane components of $\hat{\mathbf{m}}$ at the position of i-th vertex, i.e. $\mathbf{r}_t^i = \hat{\mathbf{m}} - (\hat{\mathbf{m}}\cdot\hat{\mathbf{n}}_i)\hat{\mathbf{n}}_i$

.

2.2.2.3. fast precessing limit. Without loss of generality, we consider a precessing external magnetic field around the z-direction as shown in Fig. 2.2. Then, the direction of the external magnetic field is $\hat{\mathbf{m}} = (\sin\theta\cos\phi, \sin\theta\sin\phi, \cos\theta)$ and the unit normal vector of i-th vertex is $\hat{\mathbf{n}}_i = (n_x^i, n_y^i, n_z^i)$ in the lab coordinate system. Then, the magnitude of in-plane components of $\hat{\mathbf{m}}$ at each vertex i is:

$$
\begin{aligned}
r_t^{i2} &= [\hat{\mathbf{m}} - (\hat{\mathbf{m}}\cdot\hat{\mathbf{n}}_i)\hat{\mathbf{n}}_i]^2 = 1 - (\hat{\mathbf{m}}\cdot\hat{\mathbf{n}}_i)^2 \\
&= 1 - \left(\sin\theta\cos\phi n_x^i + \sin\theta\sin\phi n_y^i + \cos\theta n_z^i\right)^2
\end{aligned}
\tag{2.6}
$$

For a fast precessing external magnetic field, i.e. the time scale of elastic deformation is much larger than the period of precessing, $\hat{\mathbf{n}}_i$ is approximately time-independent during periods of precessing. Then,

$$\begin{aligned}\left\langle r_t^{i\,2}\right\rangle &= 1-\frac{1}{2}\sin^2\theta\left(n_x^{i\,2}+n_y^{i\,2}\right)+\cos^2\theta n_z^{i\,2}\\ &= 1-\frac{1}{2}\left[\sin^2\theta-\left(1-3\cos^2\theta\right)n_z^{i\,2}\right]\end{aligned} \tag{2.7}$$

where $\langle\cdot\rangle$ indicates time average over periods of precessing and we can define that

$$\tilde{M}=\frac{\mu_0\mu^2}{4\pi}\frac{1}{l_0^3}\left[1-\frac{3}{2}\left\langle r_t^{i\,2}\right\rangle\right]=\frac{1}{4}\frac{\mu_0}{4\pi}\frac{(3\mu)^2}{l_0^3}\left(\cos^2\theta-\frac{1}{3}\right)\left(n_z^{i\,2}-\frac{1}{3}\right) \tag{2.8}$$

Therefore, the total magnetic energy of the membrane with the nearest neighbor approximation in the inextensible and fast-precessing limit is:

$$\mathcal{H}_m\approx\left(\sum_{\mathbf{r}_i\in\mathbf{V}^{hex}}6+\sum_{\mathbf{r}_i\in\mathbf{V}^{pen}}5\right)\tilde{M}(\mu,\theta)\left(n_z^{i\,2}-\frac{1}{3}\right) \tag{2.9}$$

2.2.2.4. continuum limit. We can bring the above discretization limit expression into the continuum limit by associating each vertex with its Voronoi cell area. The area of a regular hexagon with edge length ℓ_0 is $\frac{3\sqrt{3}}{2}\ell_0^2$ and the corresponding Voronoi cell area of hexagonal vertex is $\frac{\sqrt{3}}{2}\ell_0^2$. Then, the magnetic energy density in the continuum limit is:

$$\epsilon_M=\frac{\epsilon_{\text{hex}}}{\frac{\sqrt{3}}{2}\ell_0^2}=\frac{1}{2}M(\mu,\theta)\left(n_z^2-\frac{1}{3}\right) \tag{2.10}$$

where the magnetic modulus M is defined as

$$M(\mu,\theta)=2\sqrt{3}\frac{\mu_0}{4\pi\ell_0}\left(\frac{3\mu}{\ell_0^2}\right)^2\left(\cos^2\theta-\frac{1}{3}\right) \tag{2.11}$$

The above magnetic modulus changes its sign around $\theta^* = \arccos\left(\sqrt{\frac{1}{3}}\right) \approx 54.7°$, which enables interesting behaviors controlled by precessing angle θ [**57**, **62**, **64**]. And also be aware that it has an addition factor of $2\sqrt{3}$ comparing with the result derived for a square mesh [**74**]. Finally, the total magnetic energy in the continuum limit can be simply expressed as a surface integral of the magnetic energy density:

$$\mathcal{H}_m \approx \oint \frac{1}{2} M \left(n_z^2 - \frac{1}{3}\right) \mathrm{d}S \tag{2.12}$$

If only a static magnetic field along z-axis is applied, corresponding results can be obtained by simply letting $\theta = 0$, i.e.

$$M(\mu, \theta = 0) = 2\sqrt{3} \frac{\mu_0}{4\pi l_0} \left(\frac{3\mu}{l_0^2}\right)^2 \frac{2}{3} \tag{2.13}$$

2.2.2.5. approximate magnetic energy expression. To sum up, with nearest neighbor approximation in the inextensible limit, the exact magnetic energy [Eqn. 2.2] under a static magnetic field can be simplified as

$$\mathcal{H}_m \approx \left(\sum_{\mathbf{r}_i \in \mathbb{V}^{\mathrm{hex}}} 6 + \sum_{\mathbf{r}_i \in \mathbb{V}^{\mathrm{pen}}} 5 \right) \left({n_z^i}^2 - \frac{1}{3} \right) \tilde{M} \tag{2.14}$$

where $\tilde{M} = \frac{1}{4} \frac{\mu_0}{4\pi} \frac{(3\mu)^2}{l_0^3} \frac{2}{3}$, μ is the induced magnetic dipole moment which assumes only one type of super-paramagnetic particles, $\mathbb{V}^{\mathrm{hex}}$ is the set of vertices with 6 neighbors, $\mathbb{V}^{\mathrm{pen}}$ is the set of vertices with 5 neighbors and n_z^i is the z component of normal vector of i-th vertex.

$\tilde{M}$ gives the characteristic energy scale for each nearest neighbor pair of magnetic dipole-dipole interactions in the discretization limit. Similar to the case of elastic membranes, a

magnetic modulus can be defined in the continuum limit as $M = 8\sqrt{3}\frac{\tilde{M}}{\ell_0^2}$, and a dimensionless parameter, $\Gamma = \frac{MR^2}{\kappa}$, called magnetoelastic parameter [**74**] , can be similarly defined. The magnetoelastic parameter Γ characterizes the relative strength between magnetic energy and bending energy.

2.2.3. Hamiltonian of magnetoelastic membranes

Therefore, the magnetoelastic membrane has one additional energy competition from magnetic dipole-dipole interactions, which is tunable via an external magnetic field. The total magnetoelastic energy of the membrane $\mathcal{H}_{em}$ is the sum of elastic and magnetic energies:

(2.15)

$$\begin{aligned}\mathcal{H}_{em} &= \sum_{e\in\mathbb{E}} \frac{1}{2} k \left(|\mathbf{r}_1^e - \mathbf{r}_2^e| - \ell_0\right)^2 + \sum_{e\in\mathbb{E}} \frac{1}{2}\tilde{\kappa} \left|\mathbf{n}_1^e - \mathbf{n}_2^e\right|^2 \\ &\quad - \frac{\mu_0}{4\pi} \sum_{\mathbf{r}_i,\mathbf{r}_j\in\mathbb{V}, i\neq j} \frac{1}{|\mathbf{r}_{ij}|^3} \left[3\left(\boldsymbol{\mu}_i \cdot \hat{\mathbf{r}}_{ij}\right)\left(\boldsymbol{\mu}_j \cdot \hat{\mathbf{r}}_{ij}\right) - \boldsymbol{\mu}_i \cdot \boldsymbol{\mu}_j\right] \\ &\approx \sum_{e\in\mathbb{E}} \frac{1}{2} k \left(|\mathbf{r}_1^e - \mathbf{r}_2^e| - \ell_0\right)^2 + \sum_{e\in\mathbb{E}} \frac{1}{2}\tilde{\kappa} \left|\mathbf{n}_1^e - \mathbf{n}_2^e\right|^2 + \left(\sum_{\mathbf{r}_i\in\mathbb{V}^{\mathrm{hex}}} 6 + \sum_{\mathbf{r}_i\in\mathbb{V}^{\mathrm{pen}}} 5\right) \tilde{M}\left(n_z^{i\,2} - \frac{1}{3}\right)\end{aligned}$$

2.2.3.1. nondimensionalization. By choosing the unit energy as $\tilde{\kappa}$ and the unit length as R (radius of the initial spherical shell), the above expression can be cast into a dimensionless form:

(2.16)
$$\begin{aligned}\tilde{\mathcal{H}}_{em} &= \sum_{e\in\mathbb{E}} \frac{1}{2}\frac{kR^2}{\tilde{\kappa}} \left(\left|\tilde{\mathbf{r}}_1^e - \tilde{\mathbf{r}}_2^e\right| - \tilde{\ell}_0\right)^2 + \sum_{e\in\mathbb{E}} \frac{1}{2}\left|\mathbf{n}_1^e - \mathbf{n}_2^e\right|^2 \\ &+ \left(\sum_{\mathbf{r}_i\in\mathbb{V}^{\text{hex}}} 6 + \sum_{\mathbf{r}_i\in\mathbb{V}^{\text{pen}}} 5\right) \frac{\tilde{M}}{\tilde{\kappa}} \left(n_z^{i\,2} - \frac{1}{3}\right) \\ &= \sum_{e\in\mathbb{E}} \frac{1}{2}\tilde{\gamma} \left(\left|\tilde{\mathbf{r}}_1^e - \tilde{\mathbf{r}}_2^e\right| - \tilde{\ell}_0\right)^2 + \sum_{e\in\mathbb{E}} \frac{1}{2}\left|\mathbf{n}_1^e - \mathbf{n}_2^e\right|^2 + \left(\sum_{\mathbf{r}_i\in\mathbb{V}^{\text{hex}}} 6 + \sum_{\mathbf{r}_i\in\mathbb{V}^{\text{pen}}} 5\right) \tilde{\Gamma} \left(n_z^{i\,2} - \frac{1}{3}\right)\end{aligned}$$

In the process of nondimensionalization, two dimensionless parameters naturally emerge:

(2.17)
$$\tilde{\gamma} = \frac{kR^2}{\tilde{\kappa}}, \quad \tilde{\Gamma} = \frac{\tilde{M}}{\tilde{\kappa}}$$

where $\tilde{\gamma}$ is the "microscopic Föppl-von Kármán (FvK) parameter", which gives characteristic relative strength between stretching interaction and bending interaction at the discretization limit; $\tilde{\Gamma}$ is the "microscopic magnetoelastic parameter", which gives characteristic relative strength between magnetic dipole-dipole interaction and bending interaction at the discretization limit.

2.2.3.2. relationship between discretization and continuum limit. We can also bring the system into the continuum limit, which gives two more familiar dimensionless parameters mentioned before:

(2.18)
$$\gamma = \frac{YR^2}{\kappa}, \quad \Gamma = \frac{MR^2}{\kappa}$$

where γ is the Föppl-von Kármán (FvK) parameter, which gives characteristic relative strength between stretching interaction and bending interaction; Γ is the magnetoelastic parameter, which gives characteristic relative strength between magnetic dipole-dipole interaction and bending interaction. Also note that $\Gamma \propto M \propto \mu^2$ and induced magnetic dipole moment μ is proportional to the strength of external magnetic field, which means that Γ can be directly controlled by an external magnetic field. Correspondences between parameters in the discretization limit and the continuum limit [**44**, **72**] are listed below:

$$Y = \frac{2k}{\sqrt{3}}, \kappa = \frac{\tilde{\kappa}}{\sqrt{3}}, M = \frac{8\sqrt{3}}{l_0^2}\tilde{M} \tag{2.19}$$

note that those pre-factors are topology dependent [**72**] and above values are derived for spherical geometry.

2.2.3.3. dimensionless magnetoelastic energy. Finally, the dimensionless form of total magnetoelastic energy can be written as:

$$\tilde{\mathcal{H}}_{em}\left[\{\mathbf{r}_i\}; \gamma, \Gamma\right] = \frac{\mathcal{H}_{em}}{\kappa} = \tilde{\mathcal{H}}_e\left[\{\mathbf{r}_i\}; \gamma\right] + \tilde{\mathcal{H}}_m\left[\{\mathbf{r}_i\}; \Gamma\right] \tag{2.20}$$

where tilde indicates dimensionless quantities and note that $\tilde{\mathcal{H}}_e$ and $\tilde{\mathcal{H}}_m$ depend linearly on γ and Γ [Eqn. 2.18] respectively.

2.2.4. Volume constraint

Besides magnetic and elastic contributions, a volume constraint [**75**] is also imposed on the membranes to account for internal pressure. This internal pressure is necessary when

the membrane is not penetrable, which is modeled as:

$$\mathcal{H}_v = \Lambda \left(\sum_k \Omega_k - V_{\text{ref}} \right)^2 \tag{2.21}$$

where Ω_k [Eqn. 2.22] is the signed volume of the tetrahedron extended by k-th triangle on the membrane, V_{ref} is the reference volume of the membrane and Λ is the Lagrange multiplier which characterizes the system pressure. V_{ref} is set as volume of the icosahedron after buckling and Λ is set to a large enough value such that the membrane has additional rigidity from due to the volume constraint. The volume constraint is used to capture the effect from the environment surrounding the magnetoelastic membrane and eliminate possible crumpled states [**76**]. Corresponding cases without the volume constraint are also explored, and their morphologies generally do not differ significantly from the cases with the volume constraint. Some crumpled states and collapsed states are observed in high field strength limit for the cases without the volume constraint [Fig. 2.7].

2.2.4.1. simulation details. The simulations are performed in LAMMPS [**77**]. All interactions in the Hamiltonian of the system can be mapped to commonly available interactions in LAMMPS. More specifically, stretching interactions [Eqn. 2.1] are modeled as harmonic bond interactions, bending interactions [Eqn. 2.1] are modeled as harmonic dihedral interactions, and magnetic dipole-dipole interactions [Eqn. 2.2] are modeled as electric dipole-dipole interactions (both electric and magnetic dipole-dipole interactions are equivalent in reduced units). Shifted L-J interactions are included to account for finite size effect of the super-paramagnetic particles and also to increase the stability of the collapsed state simulation. The cutoff of the L-J interactions is set as 0.6 of equilibrium

length ℓ_0. The equilibrium length ℓ_0 is set as the average bond length of the initial mesh.

Each vertex is represented as a point dipole in the simulations. The computation of the long range magnetic dipole-dipole interactions is calculated without a cutoff by using the long range solver PPPM/dipole [**78**] in LAMMPS. Because of properties of super-paramagnetic particles, directions of each dipole are always aligned with the external magnetic field. Besides, only translational degrees of freedom are updated in each time step. Rotational degrees of freedom of each vertex are ignored because super-paramagnetic particles don't have permanent magnetization which decouples magnetics and elasticity.

Initial mesh of the membrane is constructed with the scheme proposed by Caspar and Klug [**70**]and the connectivity of the membrane is preserved during simulations. Different mesh choices (different h,k numbers) are tested to ensure that the observed phenomena are not mesh dependent. All simulations mentioned in this work are performed with mesh $(6, 6)$, which has 1082 vertices, 3240 edges and 2160 faces. We use reduced units for all simulations; the unit energy is $\tilde{\kappa}$ and the unit length is R (radius of initial mesh). By choosing a different stretching constant for harmonic bond interactions(k) and the induced magnetic dipole moment (μ), all possible dimensionless parameters pair (γ, Γ) can be constructed accordingly.

Kinetic energy is also assigned to each vertex to give a fictitious temperature of the system. The simulations start at high temperature and are gradually annealed to find the minimum energy configuration of the system. This annealing process is repeated several

times to ensure that the system is not trapped in local minima.

2.2.4.2. implementation of the volume constraint. The volume constraint is added when the membrane is not penetrable, which is implemented as a fix package of LAMMPS. Additional potential energy from the volume constraint is modeled as shown in Eqn. 2.21. Then, taking derivatives of the above potential with respect to each vertex's position gives the constraint forces due to the volume constraint. For example, consider a triangle consists of three vertices: $\mathbf{r}_1, \mathbf{r}_2, \mathbf{r}_3$. The signed volume of the tetrahedron extended by this triangle is:

$$\Omega_k = \frac{1}{6}\mathbf{r}_1 \cdot \mathbf{r}_2 \times \mathbf{r}_3 \tag{2.22}$$

Taking derivatives of Ω_k with respect to $\mathbf{r}_1$ is

$$\boldsymbol{\nabla}\Omega_k|_{\mathbf{r}_1} = \frac{1}{6}(-y_3z_2 + y_2z_3, x_3z_2 - x_2z_3, -x_3y_2 + x_2y_3) \tag{2.23}$$

Other cases are cyclic permutations of the above result. Note that the interaction from the volume constraint is not pair-like interaction and total constraint force of vertex i is:

$$f^{(i)}_{\text{constraint}} = 2\Lambda \sum_{k \in \text{neighbors of i}} \boldsymbol{\nabla}\Omega_k|_{\mathbf{r}_i} \tag{2.24}$$

2.2.4.3. Computation of curvatures. Computation of curvatures generally requires a surface is differentiable [**79**]. However, in the discretization limit, the surface is composed of flat triangles and is a piece-wise constant surface, which has only C^0 continuity. Then, computation of curvatures on the triangulated surface needs additional cares.

The method used in this work to compute the curvatures of the magnetoelastic membranes follows the work of Meyer et al. [**80**], which is introduced in the context of computer graphics. By associating each vertex with its corresponding Voronoi cell, the mean curvature vector $\mathbf{K}$ and the Gaussian curvature κ_G are calculated by following formulae:

$$\mathbf{K}(\mathbf{r}_i) = \frac{1}{2A(\mathbf{r}_i)} \sum_{j \in \text{neighbors of i}} (\cot \alpha_{ij} + \cot \beta_{ij}) (\mathbf{r}_i - \mathbf{r}_j) \tag{2.25}$$

$$\kappa_G(\mathbf{r}_i) = \left(2\pi - \sum_{j \in \text{external angles}} \theta_j \right) / A(\mathbf{r}_i) \tag{2.26}$$

where α_{ij} and β_{ij} are two angles opposite to the edge defined by vertices $\mathbf{r}_i$ and $\mathbf{r}_j$. $A(\mathbf{r}_i)$ is the area of Voronoi cell of vertex i:

$$A(\mathbf{r}_i) = \frac{1}{8} \sum_{j \in \text{neighbors of i}} (\cot \alpha_{ij} + \cot \beta_{ij}) |\mathbf{r}_i - \mathbf{r}_j|^2 \tag{2.27}$$

and θ_j are the external angles of the Voronoi cell around vertex i. Note that when triangles are obtuse, $A(\mathbf{r}_i)$ needs to be modified [**80**] to make sure that Voronoi cells are non-overlapping, which in turn makes sure that the sum of Gaussian curvature fulfills the Gauss-Bonnet Theorem (GBT) [**79**]. By comparing the direction of mean curvature vector $\mathbf{K}$ with the exterior normal direction of the membrane, a sign can be associated with the mean curvature value to distinguish convex and concave regions of the membrane [see Fig. 2.5].

2.3. Morphologies of magnetoelastic membranes

2.3.1. Magnetoelastic membranes with volume constraint

A collection of possible morphologies of magnetoelastic membranes obtained by systematically varying the two dimensionless parameters, the Föppl-von Kármán parameter γ and the magnetoelastic parameter Γ, are shown in Fig. 2.3. Without magnetic dipole-dipole interactions (Γ=0), when $\gamma < \gamma^*$, the homogeneous elastic crystalline membrane tends to stay spherical [Fig. 2.3a] and when $\gamma > \gamma^*$ it buckles into an icosahedron [Fig. 2.3b] as expected in the conventional homogeneous elastic crystalline membranes [**32**].

At moderate strengths of the magnetic dipole-dipole interaction, as shown in the second row of Fig. 2.3, the structures deform since the magnetic dipoles prefer to line up and stay closer to each other to minimize the magnetic energy. When the membrane is relatively soft ($\gamma < \gamma^*$), the membrane tends to elongate along the direction of the external magnetic field. However, this is opposed by elastic interactions since elasticity prefers the membrane to stay spherical, resulting in an ellipsoid like membrane morphology as shown in Fig. 2.3c.

When the membrane is relatively stiff ($\gamma > \gamma^*$), the membrane undergoes an elastically driven buckling transition. The interplay between nonlinear elasticity and magnetic dipole-dipole interactions distorts the icosahedron. The flat regions of the icosahedron bend inward to reduce the distance between magnetic dipoles and disclinations pair up, resulting in a star-like morphology with six ridges as shown in Fig. 2.3d. Unlike the

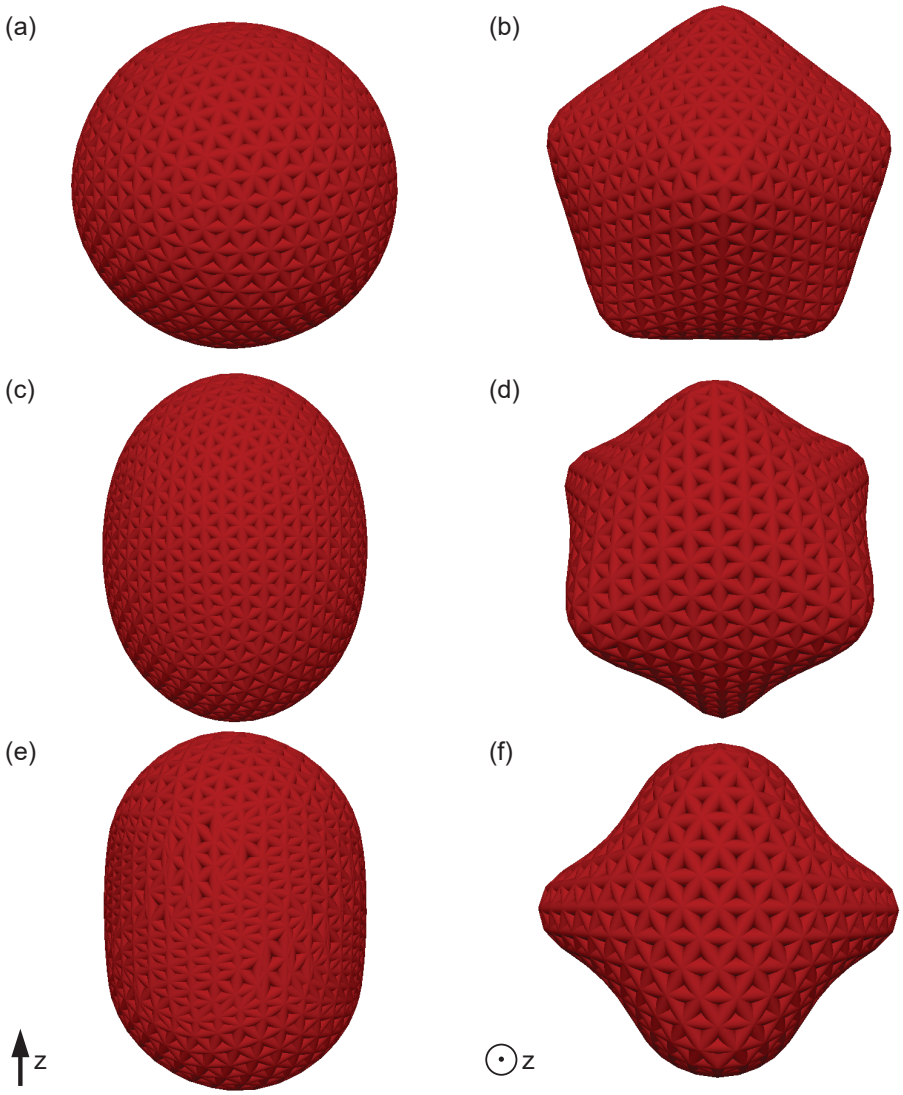

Figure 2.3. A collection of representative minimum energy morphologies of closed magnetoelastic membranes with different parameters pair (γ, Γ): Föppl-von Kármán (FvK) parameter γ and magnetoelastic parameter Γ; γ increases from left to right and Γ increases from top to bottom. (a) spherical shape (100,0); (b) icosahedral shape (1000,0); (c) ellipsoidal shape (100,25); (d) star shape with six ridges (1000,100); (e) cylindrical shape (100,50); (f) star shape with four ridges (1000,200). Note that first column is shown from y-direction and second column is shown from z-direction to give better illustration of morphologies. Arrows indicate the direction of the external magnetic field.

conventional convex polyhedral morphologies of the purely elastic membranes, the magnetoelastic membranes develop concave regions.

Then, consider the case of strong magnetic dipole-dipole interactions, as shown in the third row of Fig. 2.3. The elastic energy becomes comparable with the magnetic energy until the membrane is highly deformed. In this regime, the competition between magnetic energy and elastic energy results in another new family of morphologies.

When the membrane is easily deformed ($\gamma < \gamma^*$), magnetic dipole-dipole interactions tend to elongate the membrane further along the direction of the external magnetic field in this high field strength regime. However, the elastic energy can no longer hold the membrane in a spherical or ellipsoidal shape. The membrane forms a cylindrical shape, as shown in Fig. 2.3e, to minimize the magnetic energy. Although the bending energy is high along edges of two end caps of the cylinder, the total energy decreases by lining up vertices on the side surface of the cylinder.

When the membrane is relatively rigid ($\gamma > \gamma^*$), the elastic energy tries to preserve the total surface area of the membrane since stretching is much more expensive than bending in this case. Meanwhile, the magnetic dipole-dipole interaction tries to reduce the total volume of the membrane to minimize the magnetic energy. This competition, combined with the nonlinearity introduced by the twelve disclinations, results in a star-like morphology with four ridges as shown in Fig. 2.3f.

After showing representative membrane morphologies with the volume constraint in Fig. 2.3. A more detailed diagram of membrane morphologies can be constructed [Fig.

2.4]. Simulations with different dimensionless parameters (γ, Γ) are represented by blue cross symbols in Fig. 2.4. Colors are obtained by the linear interpretation based on simulation data points, which represent the magnetic energy contributions. The magnetic energy contribution χ_m is defined as:

$$\chi_m = \frac{|\mathcal{H}_m|}{|\mathcal{H}_m| + \mathcal{H}_e}$$

where $\mathcal{H}_m$ and $\mathcal{H}_e$ are the total magnetic energy and elastic energy respectively. Based on the magnetic energy contributions, two red contour lines ($\sim 30\%$ and $\sim 60\%$) are drawn to indicate estimated magnetically induced membrane morphologies transition points. Combining with the elastic buckling transition point $\gamma^* \sim 154$ (blue vertical dash line), the phase space of the system is roughly divided into regions which correspond to different possible membrane morphologies. Below the elastic buckling transition point ($\gamma < \gamma^*$), the membrane morphologies change from spherical shapes (region A), to ellipsoidal shapes (region C) and to cylindrical shapes (region E) with increasing magnetoelastic parameter Γ. Above the elastic buckling transition point ($\gamma > \gamma^*$), membrane morphologies change from icosahedral shapes (region B), to star shapes with six ridges (region D) and to star shapes with four ridges (region F) with increasing magnetoelastic parameter Γ. Blank regions correspond to an extremely strong magnetic field strength limit, where membrane morphologies are generally two-fold symmetric or collapsed.

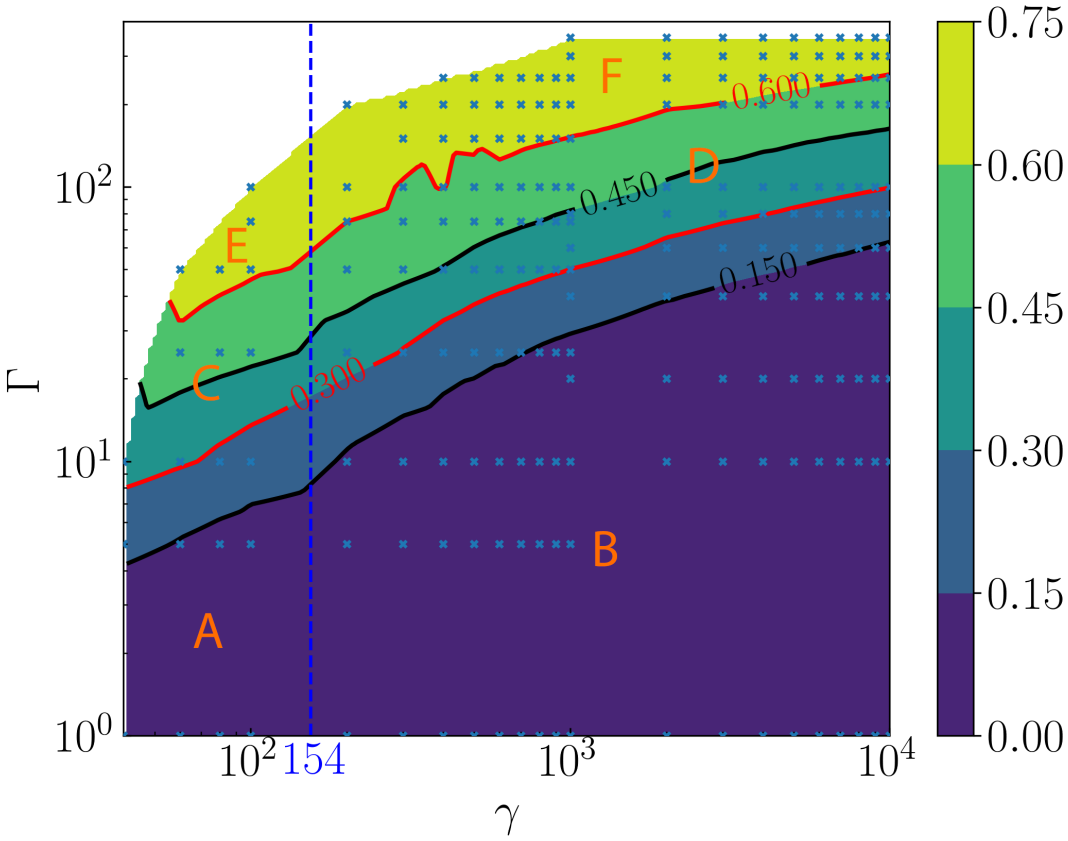

Figure 2.4. A shape diagram for the closed homogeneous magnetoelastic crystalline membranes with the volume constraint. γ is the Föppl-von Kármán (FvK) parameter and Γ is the magnetoelastic parameter. Blue crosses represent data points from simulations. Colors represent the magnetic energy contribution χ_m. Blue vertical dash line indicates the elastic buckling transition point and two red contour lines (30% and 60%) indicate estimations of magnetically induced membrane morphologies transition points. Different regions in the shape diagram correspond to different membrane morphologies: A. spheres; B. icosahedra; C. ellipsoids; D. star shapes with six ridges; E. cylinders; F. star shapes with four ridges.

2.3.2. Curvature distributions of magnetoelastic membranes

Among all these mentioned morphologies of the magnetoelastic membrane, the $\gamma \sim 1000$ cases are particularly interesting because this regime corresponds to a typical FvK parameter of viral shells [**32**]. In this regime, where both nonlinear elasticity and magnetic dipole-dipole interactions can be significant, we find that the magnetoelastic membrane tends to choose configurations that decrease symmetry with increasing external magnetic field strength. This point is illustrated by plotting the mean curvature and energy distribution of the membrane in spherical coordinates [Fig. 2.5].

In the weak field strength limit, the membrane forms an icosahedron [Fig. 2.5a] with five-fold rotational symmetry around the z-axis as shown in Fig. 2.5b and 2.5c. In this limit, the elastic energy dominates and the magnetic energy is negligible [Fig. 2.5d]. With a moderate external magnetic field strength, the membrane morphology has six ridges [Fig. 2.5e]. However, the 12 isolated disclinations prefer to pair up and form ridges connecting each pair of disclinations [**81**]. These disclinations pairs are arranged alternatively to maximize the mutual distance in order to reduce interactions between disclinations [**69**] and ridges [**82**], as shown in Fig. 2.5f and 2.5g. Because of this alternative arrangement, the membrane with six ridges has only three-fold rotational symmetry around the z-axis, which is also reflected by the magnetic energy distribution [Fig. 2.5h]. If the field strength is further increased, the membrane starts to form morphologies with four ridges [Fig. 2.5i]. In this regime, two pairs of disclinations break and there is a single disclination near each of the four concave regions as show in Fig. 2.5j and 2.5k. Therefore, the symmetry of the membrane reduces to two-fold rotational symmetry [Fig. 2.5j, k and l] around the z-axis. In the extremely high field strengths regime, the magnetic

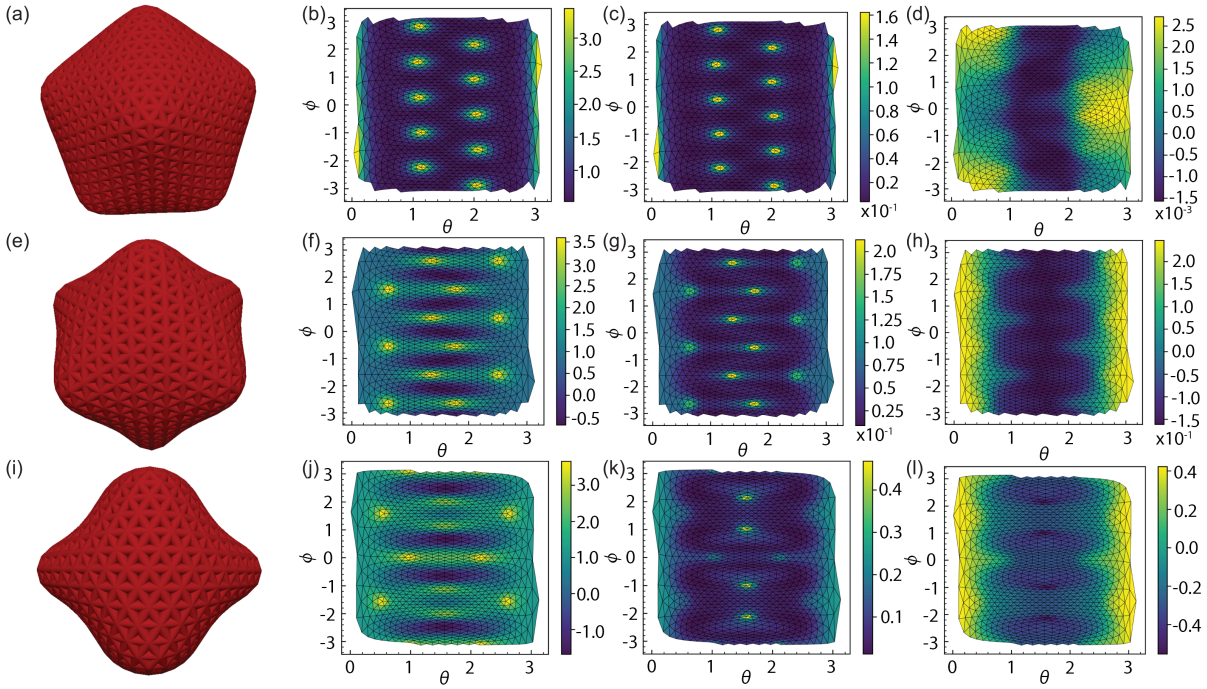

Figure 2.5. membrane morphologies(first column), mean curvature distribution(second column), elastic energy distribution(third column) and magnetic energy distribution(fourth column) showing symmetry of magnetoelastic membranes. Membrane morphologies in the first column are shown from z-direction. All other plots are shown in spherical coordinates. Horizontal axis is polar angle $\theta \in [0, \pi]$ and vertical axis is azimuthal angle $\phi \in (-\pi, \pi]$. Mean curvatures are chose to be signed values where positive values indicate convex regions and negative values indicate concave regions. Elastic energy is sum of stretching energy (bond interaction) and bending energy (dihedral interaction). Magnetic energy is sum of magnetic dipole-dipole interactions. Energy from Lennard-Jones interactions is negligible in all three cases. Parameters pairs (γ, Γ) of membranes in each row are: (1000,1), (1000,100), (1000,200) from top to bottom.

energy completely dominates and the membrane collapses and takes one-fold rotational symmetry (the collapsed state is not shown in Fig. 2.5).

A natural question is to ask why the four-fold rotational symmetry is missing among all these above mentioned morphologies. This is due to two important facts: the ridges connecting each pair of disclinations are energetically expensive to break up [**83**] and

there are effective repulsive interactions between disclinations [**69**] and ridges [**82**]. The existence of four-fold symmetric structures requires that 12 disclinations are divided into 4 groups of 3 disclinations, which needs strong enough external magnetic field strength to break up the ridge structures. Even these 4 groups of 3 disclinations are formed, four-fold symmetric structures are still not energetically favorable since the total energy of the system can be further reduced by choosing an alternative arrangement to increase mutual distances and reduce repulsive interactions between disclinations and ridges. This alternative arrangement brings the system directly into two-fold symmetric structures, which makes four-fold symmetric structures are never observed as a lowest energy configuration in our simulations.

2.3.3. Magnetoelastic membranes without volume constraint

We also explore cases without the volume constraint, which correspond to the situation that materials inside the membrane can freely penetrate the membrane. Possible morphologies of the membranes without the volume constraint are shown in Fig. 2.6.

When compared to the results with the volume constraint [Fig. 2.3], the volume constraint shifts the transition points between different morphologies, which is expected and controlled by the parameters V_{ref} and Λ. The morphologies without the volume constraint generally do not differ significantly from cases with the volume constraint, except in cases with a high magnetic field strength.

For example, as shown in Fig. 2.6e, the membrane morphology becomes "pancake" shape when the membrane is relatively soft ($\gamma < \gamma^*$) in the high field strength limit. The

"pancake" shape brings magnetic dipoles even closer than cylindrical shape [Fig. 2.3e] since there is no additional volume constraint to prevent the membrane from shrinking.

When the membrane is relatively stiff ($\gamma > \gamma^*$) in the high field strength limit, many crumpled states or collapsed states are observed as shown in Fig. 2.7. These morphologies are difficult to describe and generally differ a lot from each other. The magnetoelastic membranes in those cases are highly nonlinear and both magnetic and elastic energy are important. Small fluctuations of the membrane disclinations can change the membrane morphology significantly in those cases and lead to different crumpled states or collapsed states. Without the volume constraint, the membranes resist magnetic dipole-dipole interactions by elasticity (although L-J interactions also help stabilizing the membrane when the membrane is collapsed). After reaching a certain magnetic field strength, the membranes cannot hold a definite shape anymore and are free to crumple or collapse since there is no volume constraint to restrict these crumpling or collapsing processes. This creates a family of complicated morphologies, which are strongly deformed. Selected representative crumpled and collapsed morphologies shown in Fig. 2.7 are repeated with finer mesh size (up to mesh (12,12) which has 4322 vertices) to ensure that these morphologies do not result from insufficient discretization. It is interesting to notice that these morphologies in Fig. 2.7 ($\gamma > \gamma^*$ in high magnetic field strength limit), still roughly maintain two-fold symmetry for some states [Fig. 2.7a, c, and d].

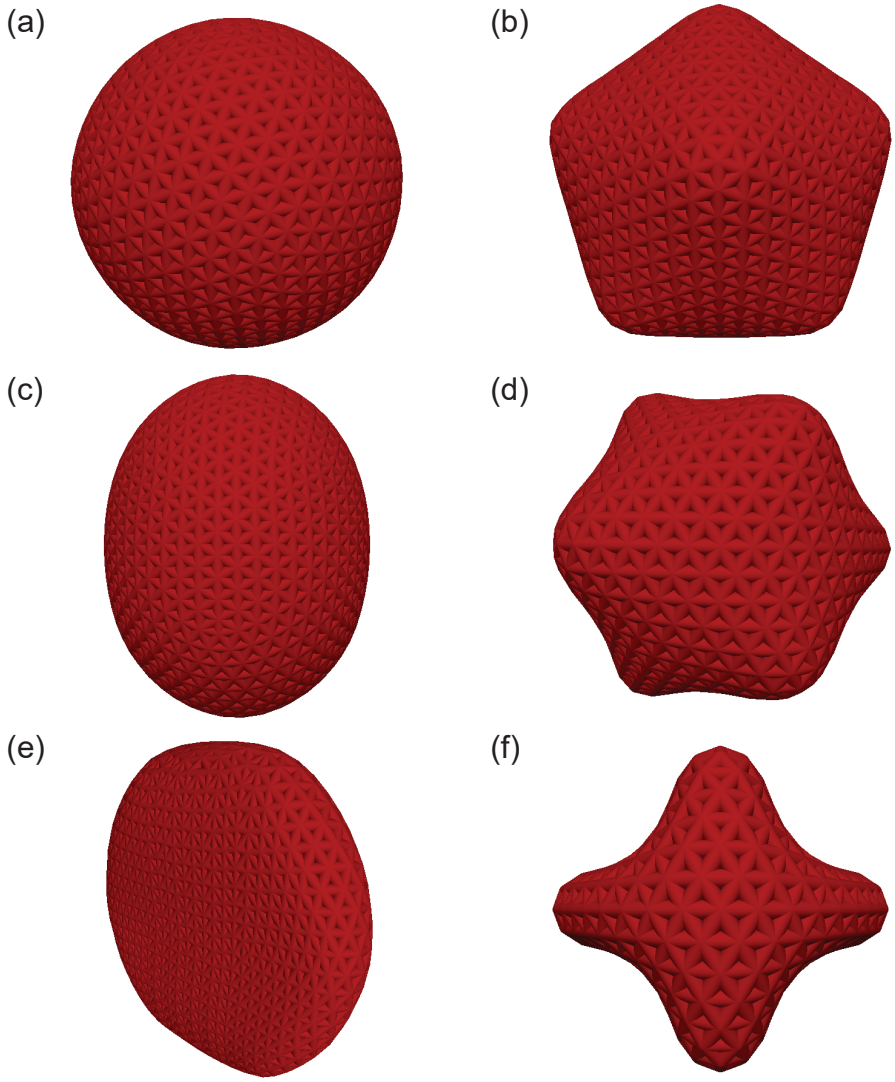

Figure 2.6. A collection of representative minimum energy morphologies of the closed magnetoelastic membrane without the volume constraint. Different parameters pairs (γ, Γ), Föppl-von Kármán (FvK) parameter γ and magnetoelastic parameter Γ, are explored. γ increases from left to right and Γ increases from top to bottom. (a) spherical shape (100,0); (b) icosahedral shape (1000,0); (c) ellipsoidal shape (100,20); (d) star shape with six ridges (1000,80); (e) pancake shape (100,40); (f) star shape with four ridges (1000,150). Note that (a) and (c) are shown from y-direction, (e) is shown in angled view and second column is shown from z-direction to give better illustration of morphologies.

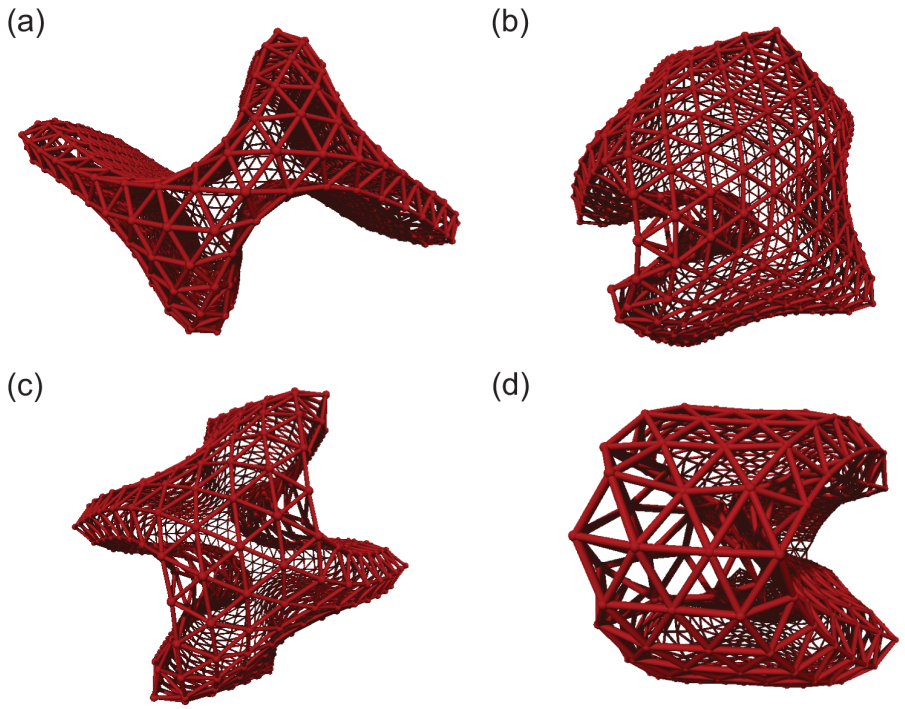

Figure 2.7. Examples of crumpled states and collapsed states. These morphologies are observed in the cases without the volume constraint in the high magnetic field strength limit. Their corresponding parameters pairs (γ, Γ) are: (a) (2000,600); (b) (4000,200); (c) (6000,500); (d) (8000, 400). All of them are shown from z-direction and are represented by triangulation meshes to show overlapping regions.

2.4. Discussion and future works

In summary, crystalline magnetoelastic membranes exhibit concave morphologies beyond the conventional polyhedral shapes found in elastic membranes. Magnetic dipole-dipole interactions give an additional control parameter which is the magnetoelastic parameter Γ. Combining with the Föppl-von Kármán (FvK) parameter γ in the elastic membranes, these two dimensionless parameters provide guidelines for analyzing properties of crystalline magnetoelastic membranes [Eqn. 2.20]. Importantly, since γ is hard to change once a membrane is assembled, the magnetoelastic parameter, which can be

easily manipulated by an external magnetic field, provides a way to tune the membrane morphology between convex shapes and concave shapes with specific symmetry.

Exciting applications, including reversible membrane shape control, design of microcontainers, and targeted drug delivery, are expected for the closed crystalline magnetoelastic membranes. For example, since the volume to surface ratio of magnetoelastic membranes can be highly reduced by imposing an external magnetic field, the concentration inside can be much higher than that in the outside environment. This morphological change induced by the external magnetic field can facilitate release of cargoes. Therefore, the magnetoelastic membrane can be used as a container to carry and protect volatile or toxic molecules and release them in a targeted region labelled by the external magnetic fields.

For future works, it's been a long term pursuit of scientists and engineers to design controllable artificial robots for tasks in microscopic world [**84**–**86**]. Living organisms have been constantly providing inspirations for such challenges [**87**, **88**]. During the long evolution history of those living organisms, *diverse morphologies* and *propulsion mechanism* have been developed to adapt to their unique demands of functionalities and flow environments in the viscous world. An important common feature of all those developed morphologies of living organisms is that there is a membrane structure which separate its interior content from the outer environment. This boundary protects the living organism from taking unwanted elements in the environment and provides an isolated chamber for essential chemical reactions and metabolic processes. Therefore, the closed magnetoelastic membranes are promising candidate materials for the design of microscopic artificial robots. Experimentally, such magnetoelastic membranes are envisioned to be synthesized

by crosslinking super-paramagnetic nano-particles via polymers [**58**, **62**, **89**]. As inspired by biology, possible future efforts can be categorized into two primary directions: membrane morphologies and locomotion mechanisms.

membrane morphologies. As demonstrated in this chapter, even a simple static magnetic field is able to induce diverse morphological changes of magnetoelastic membranes in a controllable manner. A natural extension will be study the dynamic behaviors of magnetoelastic membranes under the influence of a precessing magnetic field. Because the effective magnetic modulus M [Sec. 2.2] changes from positive to negative with an increasing precessing angle [**57**, **64**, **65**], it provides another control parameter for tuning the magnetoelastic parameter Γ in additional to the magnetic field strength and even more diverse morphological changes are expected.

Another direction along the membrane morphologies worth exploring is to introducing heterogeneous elasticity [**45**, **90**–**92**] as it's common to find membranes consisting of multiple components [**28**, **93**] in biology. A simplest construction is a Janus-type two-component magnetoelastic membrane [Fig. 2.8]. Then, each type of materials has its own set of FvK and magnetoelastic parameters (i.e. γ_A, Γ_A and γ_B, Γ_B), which provides a much larger parameter space to design desired membrane morphologies.

locomotion mechanisms. Besides the study of membrane morphologies, a proper design of controllable locomotion is desired for turning an immobile membrane-structure into a "micro-robot". The motility strategies based on flagella [**94**, **95**], cilia [**96**, **97**] and euglenoid movement [**98**] are all successfully locomotion mechanisms observed in living organisms. Due to the constraints of low Reynolds number (Re) environments

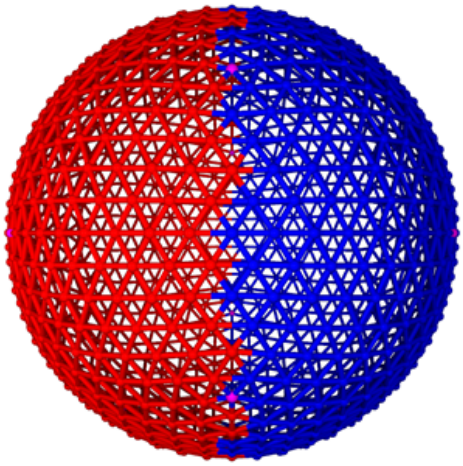

Figure 2.8. A mesh presentation of the Janus-type two-component magnetoelastic membrane. Above figure shows the example of $(6, 6)$ structure and it has 1082 vertices, 3240 edges and 2160 faces. Red and blue colored regions indicates each type of elastic materials. Magenta vertices correspond to the locations of 5-fold disclinations and there are 12 disclinations in total which are located on vertices of an inscribed icosahedron.

[**99**, **100**], all locomotion mechanisms must generate non-reciprocal movements to have net-displacements in viscous fluids. By introducing heterogeneous elasticity as shown in Fig. 2.8 combining with reversible buckling transition induced by external magnetic fields, it's promising to generate non-reciprocal deformations similar to the one demonstrated in [**101**]. In terms of theoretical and numerical study, it's also interesting to integrate the magnetoelastic membrane model developed here with appropriate hydrodynamic models, such as LBM, DPD, MPCD and SD, etc., to systematically investigate the performance of possible locomotion mechanisms [**102**–**106**] at the microscopic scale.

CHAPTER 3

Quincke Oscillators*

3.1. Introduction

The Quincke rotation [**108**] refers to the spontaneous rotation of dielectric particles immersed in a weakly conducting liquid under the application of a direct current (DC) electric field [**109**]. Recently, this phenomenon is attracting increasing interests because of its great potential in the design of the synthetic active system [**110**–**115**]. The boundary-assisted [**114**] or the geometry-assisted [**116**] locomotion, which mimic its biological counterparts, has been theoretically designed and experimentally realized. The mechanism of Quincke rotation was successfully explained with the Taylor-Melcher leaky dielectric model [**117**–**119**], which was developed for studying electrohydrodynamics in 1970s. In the most general form, there are three sets of equations used for describing electrohydrodynamical problems:

(1) the Navier-Stokes (N-S) equations which describe the motion of fluid;

(2) the Maxwell's equations which describe the electromagnetic phenomena;

(3) the Nernst-Planck (N-P) equation which describes the transport phenomena;

Those three sets of equations coupled with each other and make the problem complicated. However, additional simplifications can be made for the case of the Quincke rotation. As

*This chapter is primarily based on the published work [**107**] of Zhengyan Zhang, Hang Yuan, Yong Dou, Monica Olvera de la Cruz† and Kyle J. M. Bishop†, **Quincke Oscillations of Colloids at Planar Electrodes**, *Phys. Rev. Lett.*, Vol. 126, p. 258001, 2021, with modified notations and extended details to comply with the structure of this work.

the particles are generally in the micron scale, the low Reynolds number (Re) allows us to use the Stokes equation instead; In the absence of magnetic fields, the Poisson's equation is sufficient to describe electrostatic phenomena; The weakly conducting liquid (or the leaky dielectric) allows us to ignore the electric double layer (EDL) structure, which is usually important in the case of strong electrolyte. Therefore, all particle-liquid interfaces in the Quincke system can be regarded as sharp boundaries. And net charges only exist at the interfaces such that the electroneutrality holds everywhere in the bulk solution. It also means that the electromechanical coupling [**120**] occurs only at the boundaries between particles and its surrounding liquid, where charges, transported to the interfaces by conduction, accumulate at the interface. Those accumulated free charges modify the local electric field and create the electric stress, which must be balanced by the viscous stress developed by flows of liquid.

With above considerations, the equations used for explaining the Quincke rotation related phenomena can be simplified as:

(1) the Stokes equations which describe the motion of viscous flows;

(2) the Poisson's equations which describe the electrostatics;

(3) the surface charge conservation equation which describe the electric conduction;

Usually, the resistance matrix formulation [**121**] is used instead of solving Stokes equations explicitly. The Poisson's equation and the surface charge conservation equation have been solved with the multipole expansion [**122**, **123**]. With negligible particle inertia, it successfully described the important features of Quincke rotation such as the critical threshold of electric field via linear stability analysis and get the correct scaling of the angular velocity with respect to the electric field strength [Sec. 3.5]. When the particle

inertia is significant, those equations can be mapped into the Lorentz equations [**124**] and the chaotic dynamics is predicted [**125**] in the strong field limit, which is also observed in the experiment [**115**, **126**]. However, the question about the behavior of inertialess particles in the strong field limit does not have a clear answer yet. Interestingly, our experiments [**107**] with inertialess particles (Re$\sim 10^{-3}$) surprisingly discovered a robust periodic oscillation in the strong field limit [Sec. 3.2]. Our primary motivation of this work is to explain this unexpected oscillatory motion.

This chapter is centered around for explaining two observed motion modes of a single Quincke particle, rolling motion and oscillating motion. Sec. 3.2 describes the experimental setup and observed phenomena; Then, the existing theory for explaining the Quincke rotation are explained in details, which includes the general Taylor-Melcher (T-M) leaky dielectric model [Sec. 3.3], the theoretical description of a single Quincke particle [Sec. 3.4] and the multipole model of Quincke rotation [Sec. 3.5]; Based on those theoretical development, the mechanism of rolling motion is explained [Sec. 3.6]. After that, this chapter interludes with emphasizing the important roles of the planar electrode [Sec. 3.7], whose effects are investigated via both numeric [Sec. 3.8] and theoretical [Sec. 3.9] approaches. After realizing the existence of a boundary layer near the electrode surface, the mechanism of oscillatory motions is elucidated [Sec. 3.10] and the whole chapter concludes with a brief discussion and raises possible future works [Sec. 3.11].

3.2. Experimental setup and observations

In the experiment, polystyrene spheres are dispersed at low volume fraction in hexadecane solutions of sodium bis(2-ethylhexyl) sulfosuccinate (AOT) surfactant [Fig. 3.1] to get isolated particle behaviors. The suspension is confined between two parallel electrodes, where the particles sediment under gravity to the lower electrode [Fig. 3.2(a)]. All relevant experiment parameters are documented in table 3.1. On the application of

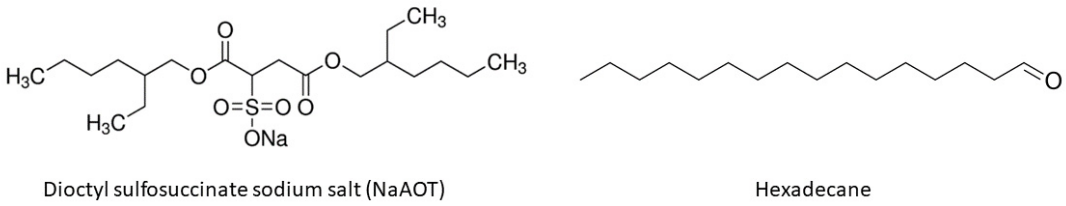

Figure 3.1. Chemical diagrams of NaAOT and hexadecane. Comparing with water, this nonpolar solution has smaller electric conductivity and higher dielectric breakdown voltage.

an external electric field, the particles move on the electrode surface and exhibit three distinct types of particle motion, stationary, rolling and oscillating [Fig. 3.2(b)], depending on the strength of the applied electric field.

For external fields strength weaker than a critical value, particles remain motionless [Fig. 3.2(b), left]. After exceeding this critical value, particles roll along the electrode surface in random directions perpendicular to the applied field with a constant speed [Fig. 3.2(b), middle]. Further increasing the field strength, a second transition, where particles cease to roll and instead oscillate back and forth [Fig. 3.2(c), right], is observed. We characterize those three different particle motions with time averaged particle speed.

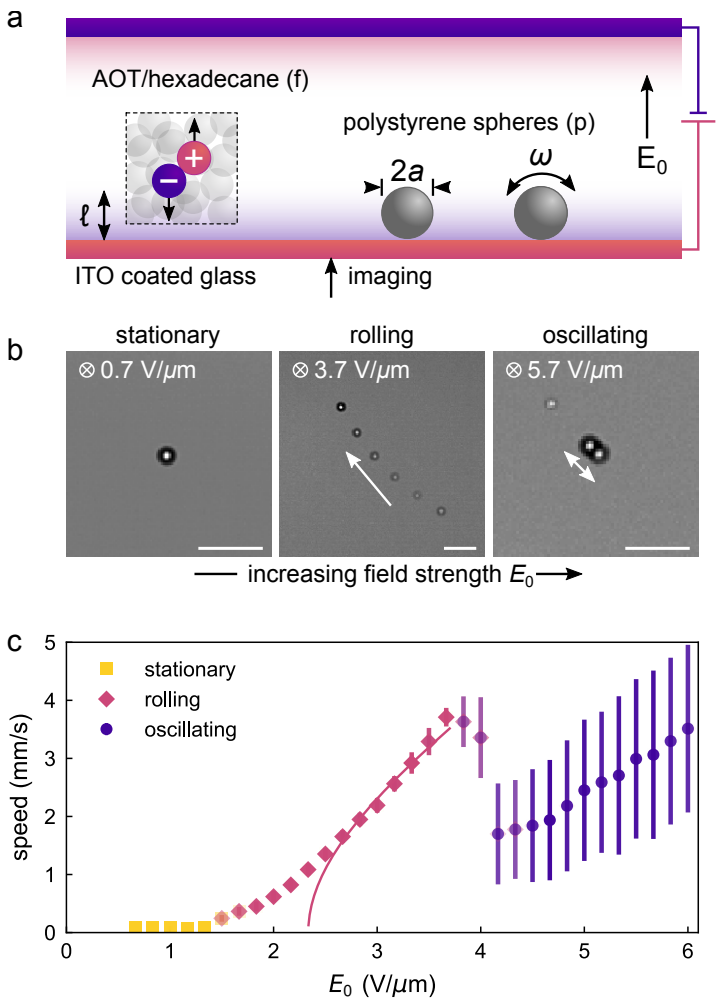

Figure 3.2. (a) Schematic illustration of the experimental setup. (b) Time-lapse microscopy images showing the three observed particle behaviors: stationary, rolling, and oscillating. Here, the particle radius is $a = 5$ μm, the AOT concentration is [AOT] = 150 mM, and the electrode separation is $H = 150$ μm. Scale bars are 40 μm. (c) Time-averaged particle speed vs. external field strength E_e. For each 20 ms trajectory, we compute the mean and standard deviation of the particle speed. Markers denote the median of these mean speeds for ca. 1000 trajectories; error bars denote the median of the corresponding standard deviations. The plotted data are colored based on probability assignments of the Bayesian classifier. The solid curve is a fit of the form $U = (\kappa a/\tau_{mw})[(E_e/E_o)^2 - 1]^{1/2}$ with $\kappa = 0.40$ and $E_o = 2.3$ V/μm; the Maxwell-Wagner relaxation time is $\tau_{mw} = 0.70$ ms from independent conductivity measurements. Note that the fitted value of the field strength E_o differs from that predicted by equation (3.64) for an unbounded sphere, $E_c = 0.91$ V/μm.

During the transition from rolling motion to oscillating motion, temporal variations of particle speed increase from zero to a finite value [Fig. 3.2(c), error bars].

Parameters	Symbols	Values
radius of polystyrene microspheres	a	0.5 - 25.0 μm
height of chamber	H	150 - 300 μm
applied electric potential	V	$0.1 - 1$ kV
particle density(polystyrene)	ρ_p	1.05 g/cm^3
liquid density(0.15M AOT/hexadecane)	ρ_l	0.77 g/cm^3
relative permittivity of the particle	ϵ_p	3
relative permittivity of the liquid	ϵ_l	2
electric conductivity of the particle	σ_p	0 S/cm
electric conductivity of the liquid(0.15M AOT [**127**])	σ_l	0.195×10^{-9} S/cm
dynamic viscosity of the solution	η	3 mPa $\cdot$ s

Table 3.1. Table of experimental parameters of Quincke oscillation system

3.3. Taylor-Melcher leaky dielectric model

This section will revisit the foundation of the Taylor-Melcher leaky dielectric model [**117**] proposed by G. I. Taylor and J. R. Melcher in the 1960s. The leaky dielectric model is extensively used in the electrohydrodynamics, which deals with fluid motion induced by electric fields. The governing equations describing electrohydrodynamics arise from the equations for describing the conservation of mass and momentum [**128**], coupled with the Maxwell's equations [**129**]. The scaling analysis will be used to derive the fundamental equations of the leaky dielectric model from the Nernst-Planck equation, the Navier-Stokes equation and the Maxwell's equation. It will focus on highlighting all assumptions of the leaky dielectric model and show how to arrive at the simplified equations used for explaining the Quincke rotation with the experimental conditions.

3.3.1. Maxwell's equation

According to the Maxwell's equation, the electric and magnetic phenomena are decoupled from each other in the time-independent conditions (or static conditions). In the absence of the magnetic field, the magnetic contributions can be completely ignored. The characteristic time scale of electric phenomena is $\tau_e = \epsilon_r \epsilon_0 / \sigma$, where ϵ_r is the relative electric permittivity of the medium, ϵ_0 is the absolute electric permittivity of vacuum and σ is the electric conductivity of the medium. The characteristic time scale of magnetic phenomena is $\tau_m = \mu_r \mu_0 \sigma L_c^2$, where μ_r is the relative magnetic permeability of the medium, μ_0 is the absolute magnetic permeability of vacuum and L_c is the characteristic length scale. Because $\tau_e \gg \tau_m$ holds for any usual conductivity of liquids considered in this work, the electrostatic approximation holds and the Poisson's equation is sufficient to describe the electric phenomena involved in this work:

$$\boldsymbol{\nabla} \cdot (\epsilon_r \epsilon_0 \boldsymbol{\nabla} \varphi) = -\rho_f \tag{3.1}$$

where φ is the electric potential, ρ_f is the free charge density and the electric field $\mathbf{E} = -\boldsymbol{\nabla}\varphi$. The corresponding boundary conditions at the particle-liquid interface is:

$$\hat{\mathbf{n}}_{12} \cdot [\mathbf{D}_2 - \mathbf{D}_1]_{r=a} = q_s \tag{3.2}$$

where $\mathbf{D}$ is the electric displacement field and $\mathbf{D}_{1(2)} = \mathbf{D}_{p(l)} = \epsilon_{p(l)} \epsilon_0 \mathbf{E}_{p(l)}$ is the electric displacement field of particle (liquid); $\hat{\mathbf{n}}_{12}$ is the outer normal of the interface, pointing from the particle to the liquid; q_s is the free surface charge density. Since the magnetic

contributions are ignored, the Maxwell stress tensor [**129**] only contains electric components:

$$\boldsymbol{\sigma}_e = \epsilon \mathbf{E} \otimes \mathbf{E} - \frac{1}{2}\epsilon(\mathbf{E} \cdot \mathbf{E})\boldsymbol{I} \tag{3.3}$$

where $\epsilon = \epsilon_r \epsilon_0$ is the absolute permittivity of the medium, $\otimes$ denotes the dyadic product and $\boldsymbol{I}$ is the identity tensor. Then, the electric force at the particle-liquid interface $\mathbf{f}_e$ is:

$$\mathbf{f}_e = \hat{\mathbf{n}}_{12} \cdot \left[\boldsymbol{\sigma}_e^2 - \boldsymbol{\sigma}_e^1\right]_{r=a} \tag{3.4}$$

where $\boldsymbol{\sigma}_e^1$ and $\boldsymbol{\sigma}_e^2$ are the respective Maxwell stress tensor of particle $\boldsymbol{\sigma}_e^p$ and liquid $\boldsymbol{\sigma}_e^l$.

3.3.2. Navier-Stokes equation

By the conservation of momentum, the general form of the Navier-Stokes equation [**128**] is:

$$\rho \frac{\mathrm{D}\mathbf{u}}{\mathrm{D}t} = \boldsymbol{\nabla} \cdot \boldsymbol{\sigma} + \rho \mathbf{f} \tag{3.5}$$

where $\mathbf{u}$ is the flow velocity of fluid, ρ is the density of fluid, $\boldsymbol{\sigma}$ is the Cauchy stress tensor, $\mathbf{f}$ is the body force such as gravity and $\frac{\mathrm{D}}{\mathrm{D}t}$ is the material derivative, which is defined as:

$$\frac{\mathrm{D}}{\mathrm{D}t} = \frac{\partial}{\partial t} + \mathbf{u} \cdot \boldsymbol{\nabla} \tag{3.6}$$

In the electrohydrodynamics, the Cauchy stress tensor should include both hydrodynamic and electric contributions, i.e.

$$\boldsymbol{\sigma} = \boldsymbol{\sigma}_h + \boldsymbol{\sigma}_e$$

where $\boldsymbol{\sigma}_e$ is the Maxwell stress tensor as shown in equation 3.3 and $\boldsymbol{\sigma}_h$ is the hydrodynamic stress tensor. Since we only consider simple incompressible Newtonian fluid in this work, the corresponding constitutive relation of the fluid is:

$$\boldsymbol{\sigma}_h = -p\boldsymbol{I} + \mu\left(\boldsymbol{\nabla}\mathbf{u} + \boldsymbol{\nabla}\mathbf{u}^T\right) \tag{3.7}$$

where p is the pressure and μ is the dynamic viscosity of fluid.

Substituting both Eqn. 3.3 and Eqn. 3.7 back into Eqn. 3.5, it gives that

$$\rho\left[\frac{\partial \mathbf{u}}{\partial t} + (\mathbf{u}\cdot\boldsymbol{\nabla})\,\mathbf{u}\right] = -\boldsymbol{\nabla}p - \frac{1}{2}\mathbf{E}\cdot\mathbf{E}\boldsymbol{\nabla}\epsilon + \mu\nabla^2\mathbf{u} + \rho_f\mathbf{E} \tag{3.8}$$

In the right hand side, the first term is the force from the pressure gradient, the second term is the contribution from the dielectric permittivity gradient, the third term is resulted from viscous stress and the fourth term is the possible electric body force caused by the net charges under electric fields. The corresponding boundary conditions at the particle-liquid interface depend on the system and the most commonly used boundary condition is the no-slip boundary condition at the interface:

$$\left[\mathbf{u} - \mathbf{U}_p\right]_{r=a} = 0 \tag{3.9}$$

where $\mathbf{u}$ is the flow velocity of liquid at the interface and $\mathbf{U}_p$ is the velocity at the particle surface.

Besides, the mass conservation gives the continuity equation:

$$\frac{\partial \rho}{\partial t} + \boldsymbol{\nabla}\cdot(\rho\mathbf{u}) = 0 \tag{3.10}$$

and the incompressible condition simplifies the above equation as:

$$\boldsymbol{\nabla} \cdot \mathbf{u} = 0 \tag{3.11}$$

3.3.3. Nernst-Planck equation

To complete the description, we still need the distribution of free charges. In the liquid, the free charges are carried by the ions and the free charge density ρ_f is related to the concentration of each ion species:

$$\rho_f = \sum_i e z_i n_i \tag{3.12}$$

where e is the charge of a proton, z_i is the valence of i-th species and n_i is the number density of i-th species(in the unit of $1/\mathrm{m}^3$). By the conservation of charges, the Nernst-Planck equation is:

$$\frac{\partial n_i}{\partial t} + \boldsymbol{\nabla} \cdot \mathbf{J}_i = r_i \tag{3.13}$$

where r_i is source/sink of i-th species due to related chemical reactions and $\mathbf{J}_i$ is the total flux of i-th species, which includes the diffusion flux $\mathbf{J}_i^d = -D_i \boldsymbol{\nabla} n_i$, the electric migration flux $\mathbf{J}_i^e = \mu_i e z_i n_i \mathbf{E}$ and the convection flux $\mathbf{J}_i^c = n_i \mathbf{u}$, i.e.

$$\mathbf{J}_i = \mathbf{J}_i^d + \mathbf{J}_i^e + \mathbf{J}_i^c = -D_i \boldsymbol{\nabla} n_i + \mu_i e z_i n_i \mathbf{E} + n_i \mathbf{u} \tag{3.14}$$

where D_i is the diffusion constant of i-th species, μ_i is the mobility of i-th species, $\mathbf{E}$ is the electric field and $\mathbf{u}$ is the flow velocity. Here, the Ohmic conductivity is assumed as $\mathbf{J}_i^e = \sigma_i \mathbf{E} = \mu_i e z_i n_i \mathbf{E}$ and σ_i is the electric conductivity of i-th species. The mobility μ_i

of i-th species is related to its diffusion constant D_i via the Einstein relation:

$$\mu_i = \frac{D_i}{k_B T} \tag{3.15}$$

where k_B is the Boltzmann constant and T is the temperature. The inverse of mobility is the friction coefficient ξ, which can be estimated from the Stokes drag, i.e. $\xi_i = \mu_i^{-1} = 6\pi\mu a_i^h$, where μ is the dynamic viscosity of liquid and $a^h{}_i$ is the hydrodynamic radius of i-th species. Plugging Eqn. 3.14 back into Eqn. 3.13, it gives that

$$\frac{\partial n_i}{\partial t} + \boldsymbol{\nabla} \cdot [-\mu_i k_B T \boldsymbol{\nabla} n_i + \mu_i e z_i n_i \mathbf{E} + n_i \mathbf{u}] = r_i \tag{3.16}$$

This is the general of form of Nernst-Planck equation used in electrohydrodynamics. Besides, we are particularly interested in the charge conservation at the particle-liquid interface. Then, we can constrain the above equation at the interface and integrate it across a patch of the interface to get the surface charge conservation equation. Assuming the interface is rigid (deformable interfaces will have additional contribution from the moving boundary) and there is no surface reactions, it gives that

$$\frac{\partial n_i^s}{\partial t} + \boldsymbol{\nabla}_s \cdot [-\mu_i^s k_B T \boldsymbol{\nabla}_s n_i^s + \mu_i^s e z_i n_i^s \mathbf{E} + n_i^s \mathbf{u}] + \hat{\mathbf{n}}_{12} \cdot \left[\mathbf{J}_i^2 - \mathbf{J}_i^1\right] = 0 \tag{3.17}$$

where n_i^s is the surface number density of i-th species, μ_i^s is the surface mobility of i-th species, $\boldsymbol{\nabla}_s \cdot$ is the surface divergence operator and $\boldsymbol{\nabla}_s$ is surface gradient operator; $\hat{\mathbf{n}}_{12}$ is the outer normal of the interface and $\mathbf{J}_i^1(\mathbf{J}_i^2)$ denotes the total flux of i-th species [Eqn. 3.14] in the medium 1(2). Basically, the divergence term describes the change of species concentration from the surface flux (lateral transport processes) and the normal jump

term describes the change of species concentration from the bulk flux (normal transport processes).

3.3.4. Leaky dielectric systems

To summarize, the general formulation of electrohydrodynamics problem consists of the following coupled equations [**117**, **118**]:

$$
\begin{cases}
\boldsymbol{\nabla} \cdot (\epsilon_r \epsilon_0 \mathbf{E}) = \sum_i e z_i n_i \\
\rho \left[\dfrac{\partial \mathbf{u}}{\partial t} + (\mathbf{u} \cdot \boldsymbol{\nabla}) \mathbf{u} \right] = -\boldsymbol{\nabla} p - \dfrac{1}{2} \mathbf{E} \cdot \mathbf{E} \boldsymbol{\nabla} \epsilon + \mu \nabla^2 \mathbf{u} + \rho_f \mathbf{E} \\
\boldsymbol{\nabla} \cdot \mathbf{u} = 0 \\
\dfrac{\partial n_i}{\partial t} = -\boldsymbol{\nabla} \cdot [-\mu_i k_B T \boldsymbol{\nabla} n_i + \mu_i e z_i n_i \mathbf{E} + n_i \mathbf{u}] + r_i, i = 1 \cdots N
\end{cases}
\tag{3.18}
$$

If there are chemical reactions involved in the system($r_i \neq 0$), additional equations describing the relevant chemical reactions also need to be included to close the system of equations.

So far, we have not make any assumptions specific to the leaky dielectric system. For a perfect dielectric medium, there is no free ions and we do not need to concern about the transport processes. It behaves like a perfect insulator and the polarization charges dominate the electrostatic interactions. For a perfect conducting medium, like the strong electrolyte, the solute molecules completely or almost completely break apart into ions in the solution. A large number of free ions make the strong electrolyte a good conductor and generally the transport processes are more important in those systems. Comparing

with those two extreme cases, the leaky dielectric system lies closer to a perfect dielectric system but it's weakly conducting. That's how it gets the name of leaky dielectric. It generally consists of weak electrolyte in a nonpolar solution.

Here, we focus on the 1:1 binary electrolyte and there are one neutral species, one positively charged species and one negatively charged species ($N = 3$). More specifically, we use dioctyl sulfosuccinate sodium salt (NaAOT) dissolve in the nonpolar solvent hexadecane [Sec. 3.2, Fig. 3.1]. The association-disassociation reaction of NaAOT in hexadecane is:

$$\underset{(n_1,z_1=0)}{\mathrm{NaAOT}} \underset{\mathrm{k_-}}{\overset{\mathrm{k_+}}{\rightleftharpoons}} \underset{(n_2,z_2=+1)}{\mathrm{Na^+}} + \underset{(n_3,z_3=-1)}{\mathrm{AOT^-}} \tag{3.19}$$

where k_+ and k_- are the forward and backward reaction rate constants, respectively. Reaction rate constants depend on the chemicals and the solvent used in the system. The corresponding reaction rate equations are:

$$-r_1 = r_2 = r_3 = +k_+ n_1 - k_- n_2 n_3 \tag{3.20}$$

where r_i, n_i, and z_i denote the chemical production rate, the concentration and the valence of each species ($i = 1, 2, 3$). It's worth comparing with the case of strong electrolyte. In the strong electrolyte, solute molecules are completely or almost completely ionized in the solvent and the chemical reaction is almost unidirectional. Generally, the strong electrolyte reaches its equilibrium very quickly. And all chemical reaction rates are zero at the equilibrium.

For the weak electrolyte, the equilibrium constant $K = \frac{[\mathrm{Na}^+][\mathrm{AOT}^-]}{[\mathrm{NaAOT}]} = n_2 n_3/n_1 = k_+/k_-$ is useful for characterizing the degree of disassociation. However, for the case of NaAOT dissolve in hexadecane, it's more complicated as the concentration used in the experiment is much higher than its critical micelle concentration (CMC) (10^{-6}M [**130**]). Therefore, charge carriers include both the ionized monomers and charged reverse-micelles [**127**]. Assume the bulk concentration of NaAOT is n_0. Then, it's convenient to use $\sqrt{n_0 K}$ as the characteristic concentration of all charged species, provided $\sqrt{n_0 K} \ll n_0$. We are most interested in the distribution of charged species. Therefore, we can add Eqn. 3.16 for $i = 2$ and $i = 3$ cases together:

$$\frac{\partial \rho_f}{\partial t} = -\boldsymbol{\nabla} \cdot \left[-k_B T \left(\mu_2 e z_2 \boldsymbol{\nabla} n_2 + \mu_3 e z_3 \boldsymbol{\nabla} n_3 \right) + \left(\mu_2 e^2 z_2^2 n_2 + \mu_3 e^2 z_3^2 n_3 \right) \mathbf{E} + \rho_f \mathbf{u} \right] \tag{3.21}$$

where $z_2 = -z_3 = z$ has been applied to eliminate the reaction terms. In order to see the relative importance of each flux components, we recast the above equation into the dimensionless form:

$$\frac{\tau_D}{\tau_c} \frac{\partial \rho_f}{\partial t} = \nabla^2 \left(\mu_2 \boldsymbol{\nabla} n_2 - \mu_3 \boldsymbol{\nabla} n_3 \right) - \Lambda \boldsymbol{\nabla} \cdot \left[(\mu_2 n_2 + \mu_3 n_3) \mathbf{E} \right] - \mathrm{Pe} \boldsymbol{\nabla} \cdot (\rho_f \mathbf{u}) \tag{3.22}$$

where all quantities are scaled with characteristic scales defined in the table 3.2, $\tau_D = \frac{L_c^2}{k_B T \mu_c} \sim 0.3$ s, $\Lambda = \frac{e z E_c L_c}{k_B T} \sim 400$ and $\mathrm{Pe} = \frac{U_c L_c}{k_B T \mu_c} \sim 60$. The Quincke rotation has very fast dynamics ($\tau_c \sim 1$ms), which gives that $\tau_D/\tau_c \sim 300$. Therefore, all dimensionless quantities are much greater than $\mathcal{O}(1)$, which means that the diffusion process is negligible in our system, i.e.

$$\frac{\tau_D}{\tau_c} \frac{\partial \rho_f}{\partial t} = -\Lambda \boldsymbol{\nabla} \cdot \left[(\mu_2 n_2 + \mu_3 n_3) \mathbf{E} \right] - \mathrm{Pe} \boldsymbol{\nabla} \cdot (\rho_f \mathbf{u}) \tag{3.23}$$

To further simplify the problem, we need to utilize the electroneutrality condition of the system. According to the Debye–Hückel theory, the Debye length λ_D provides a characteristic length scale of the diffusion layer in the strong electrolyte. However, since we are working with the weak electrolyte (NaAOT/hexadecane), we cannot estimate the Debye length with the concentration of NaAOT directly. Experiment measurement has been conducted to estimate the Debye length in NaAOT/hexadecane solution [**130**]. For 0.15 M NaAOT, the Debye length is about 100 nm, which is about 1% of a particle diameter. Therefore, the diffusion layer is very thin comparing with the particle size and the system is mostly electroneutral away from interfaces. With the electroneutrality condition in the bulk region, the equation 3.23 reduces as the classic Ohm's law in the steady state:

$$\boldsymbol{\nabla} \cdot [(\mu_2 n_2 + \mu_3 n_3)\mathbf{E}] = 0 \tag{3.24}$$

Note that the total electric current $\mathbf{J}_e = \sigma_l \mathbf{E} = (\mu_2 e z_2 n_2 + \mu_3 e z_3 n_3)\mathbf{E}$. Besides, the electroneutrality also allows to simplify the Poisson's equation [Eqn. 3.1] for electrostatics as the Laplace's equation:

$$\boldsymbol{\nabla} \cdot (\epsilon_r \epsilon_0 \mathbf{E}) = 0 \tag{3.25}$$

And the equation 3.8 for hydrodyanmics as:

$$\rho \left[\frac{\partial \mathbf{u}}{\partial t} + (\mathbf{u} \cdot \boldsymbol{\nabla})\, \mathbf{u} \right] = -\boldsymbol{\nabla} p + \mu \nabla^2 \mathbf{u} \tag{3.26}$$

where we assumed the change of dielectric permittivity happens only at the interfaces. To sum up, the simplified governing equations for the leaky dielectric systems are:

$$\begin{cases} \boldsymbol{\nabla} \cdot (\epsilon_r \epsilon_0 \mathbf{E}) = 0 \\ \rho \left[\dfrac{\partial \mathbf{u}}{\partial t} + (\mathbf{u} \cdot \boldsymbol{\nabla}) \, \mathbf{u} \right] = -\boldsymbol{\nabla} p + \mu \nabla^2 \mathbf{u} \\ \boldsymbol{\nabla} \cdot \mathbf{u} = 0 \\ \boldsymbol{\nabla} \cdot \mathbf{J}^e = 0 \end{cases} \tag{3.27}$$

The considerations specific to the leaky dielectric systems greatly simplify the original governing equations 3.18, which make these three sets of equations completely decouple from each other everywhere except at the particle-fluid interfaces.

To complete the simplifications, we also need to deal with the couplings at the interfaces. Following the similar scale analysis used for simplifying the N-P equation in the bulk, the general interfacial charge conservation equation [Eqn. 3.17] can be simplified by noticing that [see Table 3.2]:

(1) the diffusion process is negligible comparing with other transport processes;

(2) the convection flux term dominates in the lateral transport processes;

(3) the electric migration flux dominates in the normal transport processes;

It gives that

$$\frac{\partial q_s}{\partial t} + \boldsymbol{\nabla}_s \cdot [q_s \mathbf{u}] + \hat{\mathbf{n}}_{12} \cdot \left[\mathbf{J}_e^2 - \mathbf{J}_e^1 \right] = 0 \tag{3.28}$$

Therefore, the corresponding boundary conditions for the leaky dielectric systems are:

$$\begin{cases} \hat{\mathbf{n}}_{12} \cdot [\mathbf{D}_2 - \mathbf{D}_1]_{r=a} = q_s \\ [\mathbf{u} - \mathbf{U}_p]_{r=a} = 0 \\ \dfrac{\partial q_s}{\partial t} + \boldsymbol{\nabla}_s \cdot [q_s \mathbf{u}] + \hat{\mathbf{n}}_{12} \cdot \left[\mathbf{J}_e^2 - \mathbf{J}_e^1\right] = 0, r = a \end{cases} \tag{3.29}$$

Finally, Eqn. 3.27 and Eqn. 3.29 together form the foundation of theoretical frameworks describing the leaky dielectric systems. The coupling between electrostatics and hydrodynamics is only introduced via the boundary conditions. The great simplifications are achieved by: 1) ignoring the electric double layer structure, which enables treating all boundaries as sharp interfaces and also the electroneutrality condition in the bulk; 2) identifying the dominant transport process and ignoring negligible ones.

Quantities	Symbols	Characteristic values
time	τ_c	1 ms
length	L_c	5 μm
velocity	U_c	1 mm/s
electric field strength	$\sim E_c$	2 V/μ m
mobility	$\mu_c = (6\pi\eta L_c)^{-1}$	2×10^{10}s/kg
diffusion constant	$k_B T \mu_c$	10^{-10}m^2/s
time scale of diffusion	$\tau_D = L_c^2/k_B T \mu_c$	0.3 s
concentration of NaAOT	n_0	0.1 M
Debye length	λ_D	100 nm
Reynolds number	$\mathrm{Re} = \rho_l U_c L_c/\mu$	10^{-3}
Péclet number	$\mathrm{Pe} = \frac{U_c L_c}{k_B T \mu_c}$	100

Table 3.2. Table of characteristic values of relevant quantities and dimensionless parameters of Quincke oscillation system

3.4. Theoretical model of a single Quincke roller

The theoretical description introduced in section 3.3 is general for any leaky dielectric materials and more specific results can be obtained by applying them to the systems of interests. The simplest scenario is to consider a single isolated Quincke particle immersed in a weakly conducting liquid as shown in figure 3.3. Without loss of generality, consider a dielectric particle of radius a with relative dielectric permittivity ϵ_p and conductivity σ_p immersed in a weakly conducting liquid with relative dielectric permittivity ϵ_l and conductivity σ_l. An uniform external electric field $\mathbf{E}_0 = E_0\hat{\mathbf{z}}$ is applied along the z-axis and the dynamic viscosity of the fluid is μ. The particle may exhibit a possible mechanical rotation of angular velocity $\mathbf{\Omega}$. Please refer to table 3.1 for a more concrete sense of these parameters in experimental conditions.

3.4.1. Governing equations of a single Quincke particle

First, we need to apply the general governing equations [Eqn. 3.27] for the case of a single Quincke particle. For the convenience, the external electric fields are split out and the total electric potential φ can be written as:

$$\varphi(\mathbf{r}) = \begin{cases} \varphi_b(\mathbf{r}) + \varphi_d^+(\mathbf{r}) & |\mathbf{r}| > a \\ \varphi_b(\mathbf{r}) + \varphi_d^-(\mathbf{r}) & |\mathbf{r}| < a \end{cases} \tag{3.30}$$

where $\mathbf{r}$ is the position vector and $\varphi_b(\mathbf{r}) = \varphi_b(\mathbf{0}) - \mathbf{r}\cdot\mathbf{E}_0$ is the background electric potential contributed by the external electric fields, which is assumed to be uniform and does not have any gradient components for the moment; φ_d^+ and φ_d^- are respective disturbance

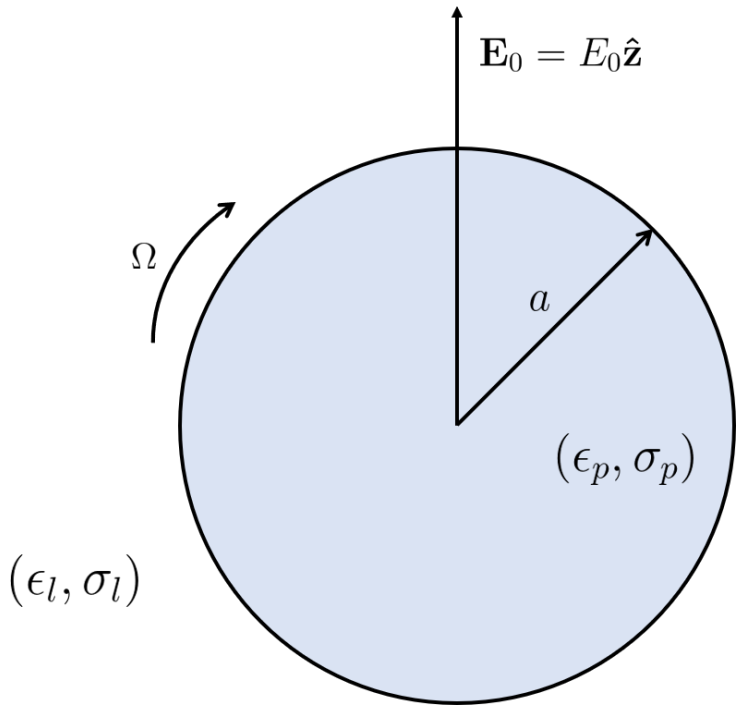

Figure 3.3. Schematic of a single isolated Quincke particle. A dielectric particle of radius a with relative dielectric permittivity ϵ_p and conductivity σ_p immersed in a weakly conducting liquid with relative dielectric permittivity ϵ_l and conductivity σ_l. An uniform external electric field $\mathbf{E}_0 = E_0\hat{\mathbf{z}}$ is applied along the z-axis and the dynamic viscosity of the fluid is μ. The particle may exhibit a possible mechanical rotation of angular velocity $\mathbf{\Omega}$.

potentials inside and outside the particle.

Following the assumptions of the leaky-dielectric model, both disturbance potentials should satisfy the Laplace's equation [Eqn. 3.25], i.e.

$$\nabla^2\varphi_d^+(\mathbf{r}) = \nabla^2\varphi_d^-(\mathbf{r}) = 0 \tag{3.31}$$

Besides, the hydrodynamic equations [Eqn. 3.26] needs to be solved in order to determine the kinetic motion of the particle. Since the typical size of the Quincke roller particle is in the micrometer scale, the low Reynolds number ($\mathrm{Re} = \frac{\rho u L}{\mu} \sim 10^{-3}$) enables the

description of the hydrodynamic behaviors with the Stokes' equation:

$$\begin{cases} \mu\nabla^2\mathbf{u} = \boldsymbol{\nabla} p + \mathbf{f} \\ \boldsymbol{\nabla}\cdot\mathbf{u} = 0 \end{cases} \tag{3.32}$$

In principle, the Stokes' equation needs to be solved to get the viscous stress exerted upon the Quincke particle. Together with electric forces and torques, the kinetic motions of Quincke particle can be calculated through force and torque balances. However, the linearity of the Stokes' equation allows expressing the relationship between kinetic motions and mechanical forces in a mobility matrix form [**121**]:

$$\begin{pmatrix} \mathbf{U} \\ \boldsymbol{\Omega} \end{pmatrix} = \begin{pmatrix} \boldsymbol{M}_{UF} & \boldsymbol{M}_{UT} \\ \boldsymbol{M}_{\Omega F} & \boldsymbol{M}_{\Omega T} \end{pmatrix} \begin{pmatrix} \mathbf{F} \\ \mathbf{T} \end{pmatrix} \tag{3.33}$$

where $\mathbf{U}$ and $\boldsymbol{\Omega}$ are the translational and angular velocity of the particle, respectively; $\mathbf{F}$ and $\mathbf{T}$ are the total forces and torques exerted on the particle; $\boldsymbol{M}_{UF}$, $\boldsymbol{M}_{UT}$, $\boldsymbol{M}_{\Omega F}$ and $\boldsymbol{M}_{\Omega T}$ are corresponding mobility tensors. If those mobility tensors can be determined for the systems of interests, the hydrodynamic equations do not need to be solved explicitly. For an unbound medium [**131**] here, mobility tensors take particularly simple forms and $\boldsymbol{M}_{UF} = (6\pi\eta a)^{-1}\boldsymbol{I}$,$\boldsymbol{M}_{\Omega T} = (8\pi\eta a^3)^{-1}\boldsymbol{I}$ and $\boldsymbol{M}_{UT} = \boldsymbol{M}_{\Omega F} = 0$, where μ is the dynamic viscosity of the liquid and $\boldsymbol{I}$ is the identity tensor.

Finally, the electric currents $\mathbf{J}_e$ in the bulk are just simple constant Ohmic currents [Eqn. 3.24]. Therefore, the only governing equations need to be solved explicitly is the electrostatic equation [Eqn. 3.31].

3.4.2. Boundary conditions of a single Quincke particle

Next, the general boundary conditions [Eqn. 3.29] also need to be satisfied at the fluid-particle interface. First, the electric potentials should be continuous at the interface [**129**]:

$$\varphi_d^+(\mathbf{r}) = \varphi_d^-(\mathbf{r}) \text{ if } |\mathbf{r}| = a \tag{3.34}$$

Second, the free surface charge should be equal to the normal jump of electric displacement fields by the Gauss's law [**129**]:

$$\hat{\mathbf{n}}_{12} \cdot \left[-\epsilon_2 \boldsymbol{\nabla} \varphi_d^-(\mathbf{r}) + \epsilon_1 \boldsymbol{\nabla} \varphi_d^+(\mathbf{r})\right] = q_s \text{ if } \ |\mathbf{r}| = a \tag{3.35}$$

Third, the surface free charges on the interface should be conserved as a result of Ohmic currents from the bulk and charge convection by the flow motion [**132**], i.e.

$$\frac{\partial q_s}{\partial t} + \boldsymbol{\nabla}_s \cdot [q_s \mathbf{u}_s] + \hat{\mathbf{n}}_{12} \cdot \left[\mathbf{J}_e^2 - \mathbf{J}_e^1\right] = 0 \text{ if } \ |\mathbf{r}| = a \tag{3.36}$$

where ${\mathbf{J}_e}^i = \sigma_i \mathbf{E} = -\sigma_i \boldsymbol{\nabla} \varphi(\mathbf{r}), i = 1, 2$ are the respective electric current in the fluid ($i = 1$) and the particle ($i = 2$); $\mathbf{u}_s$ is the surface convection velocity, which is assumed to be the same as the particle surface velocity $\mathbf{u}_s = \boldsymbol{\Omega} \times a\hat{\mathbf{n}}$, where $\boldsymbol{\Omega}$ is the angular velocity of the particle.

Lastly, the disturbance electric potential should decay to zero at the infinity in an unconfined space, i.e.

$$\varphi_d^+(\mathbf{r}) \to 0 \text{ as } \ |\mathbf{r}| \to \infty \tag{3.37}$$

If the system is confined by additional boundaries, the electric potential may not vanish at the boundaries far away. For example, when the particle is near an electrode surface, the above boundary condition should be replaced by a constant potential boundary condition at the electrode surface,

$$\varphi_d^+(\mathbf{r}) \to \varphi_0, \quad \mathbf{r} \in \text{electrode} \tag{3.38}$$

where φ_0 is the constant potential imposed at the electrode surface and this boundary condition will be discussed more in Sec. 3.7.1.

3.5. Multipole expansion in unconfined space

In an unbounded medium, we need to solve Eqn. 3.31 together with boundary conditions Eqn. 3.34, 3.35, 3.36 and 3.37. By restricting the point of interests to be far away from the Quincke particle (i.e. $|\mathbf{r}| \gg a$), the detailed distribution of the surface charge density q_s can be replaced by its moments (dipole moments, quadruple moments, etc.), which reduces the complexities of solving partial differential equations (PDE) into a set of ordinary differential equations (ODE). This approximation can be done systematically via the multipole expansion and most essential properties of the Quincke rotation can be derived via this approach [**116**, **123**, **133**].

3.5.1. Spherical harmonic solutions

To include more general situations, let's assume that the external electric fields in the absence of Quincke particle can be written as:

$$\mathbf{E}_b(\mathbf{r}) = \mathbf{E}_0 + \mathbf{r} \cdot \boldsymbol{\nabla}\mathbf{E}_b|_{\mathbf{r}=\mathbf{0}} + \cdots \tag{3.39}$$

which considers possible gradients of the external electric fields around the particle. Thus, the total electric field inside and outside the particle can be written as:

$$\mathbf{E}^+(\mathbf{r}) = \mathbf{E}_b + \mathbf{E}_d^+, |\mathbf{r}| > a \tag{3.40}$$

$$\mathbf{E}^-(\mathbf{r}) = \mathbf{E}_b + \mathbf{E}_d^-, |\mathbf{r}| < a \tag{3.41}$$

In the unconfined space, the disturbance potentials $\varphi_d^+(\mathbf{r})$ and $\varphi_d^-(\mathbf{r})$ can be written in terms of spherical harmonics [**134**]:

$$\varphi_d^+(\mathbf{r}) = \frac{\mathbf{r} \cdot \mathbf{P}}{r^3} + \frac{1}{2}\frac{\mathbf{rr} : \boldsymbol{Q}}{r^5} + \cdots, |\mathbf{r}| > a \tag{3.42}$$

$$\varphi_d^-(\mathbf{r}) = \frac{\mathbf{r} \cdot \mathbf{P}}{a^3} + \frac{1}{2}\frac{\mathbf{rr} : \boldsymbol{Q}}{a^5} + \cdots, |\mathbf{r}| < a \tag{3.43}$$

where $\mathbf{P}$ and $\boldsymbol{Q}$ are electric dipole and quadrupole moments respectively. Note that the contribution of charge monopole is not included as the Quincke particle is assumed to be charge neutral (because the Debye length λ_D is small comparing with the particle radius

a). Then, the corresponding disturbance electric fields are:

$$\mathbf{E}_d^+(\mathbf{r}) = -\boldsymbol{\nabla}\varphi_d^+(\mathbf{r}) = \left(-\frac{\mathbf{P}}{r^3} + 3\frac{\mathbf{r}\cdot\mathbf{P}}{r^5}\mathbf{r}\right) + \left(-\frac{\boldsymbol{Q}\cdot\mathbf{r}}{r^5} + \frac{5}{2}\frac{\mathbf{rr}:\boldsymbol{Q}}{r^7}\mathbf{r}\right) + \cdots, |\mathbf{r}| > a \tag{3.44}$$

$$\mathbf{E}_d^-(\mathbf{r}) = -\boldsymbol{\nabla}\varphi_d^-(\mathbf{r}) = -\frac{\mathbf{P}}{a^3} - \frac{\boldsymbol{Q}\cdot\mathbf{r}}{a^5} + \cdots, |\mathbf{r}| < a \tag{3.45}$$

The above spherical harmonic expansion automatically satisfies the boundary conditions 3.34 and 3.37.

3.5.2. Surface charge conservation

The free surface charge q_s can be expressed in terms of electric moments by substituting 3.42 and 3.43 into 3.35, which gives that:

$$\begin{aligned} q_s = \hat{\mathbf{n}}_{12}\cdot\left[\epsilon_2\mathbf{E}_2 - \epsilon_1\mathbf{E}_1\right] &= -\left(\epsilon_2 - \epsilon_1\right)\left[\mathbf{E}_0 + a\hat{\mathbf{r}}\cdot\boldsymbol{\nabla}\mathbf{E}_b(\mathbf{0})\right]\cdot\hat{\mathbf{r}} \\ &+ \left(\epsilon_2 + 2\epsilon_1\right)\frac{\mathbf{P}\cdot\hat{\mathbf{r}}}{a^3} + \left(\epsilon_2 + \frac{3}{2}\epsilon_1\right)\frac{\hat{\mathbf{r}}\hat{\mathbf{r}}:\boldsymbol{Q}}{a^4} + \cdots \end{aligned} \tag{3.46}$$

where $\hat{\mathbf{r}} = \mathbf{r}/|\mathbf{r}|$ and $\hat{\mathbf{n}}_{12} = -\hat{\mathbf{r}}$. And the corresponding Euclidean gradient of surface charge is:

$$\begin{aligned} \boldsymbol{\nabla}q_s = &-\left(\epsilon_2 - \epsilon_1\right)\frac{\mathbf{E}_0}{a} - \left(\epsilon_2 - \epsilon_1\right)\left(\boldsymbol{\nabla}\mathbf{E}_b + \boldsymbol{\nabla}\mathbf{E}_b^T\right)\cdot\hat{\mathbf{r}} \\ &+ \left(\epsilon_2 + 2\epsilon_1\right)\frac{\mathbf{P}}{a^4} + \left(\epsilon_2 + \frac{3}{2}\epsilon_1\right)\frac{\left(\boldsymbol{Q} + \boldsymbol{Q}^T\right)\cdot\hat{\mathbf{r}}}{a^5} + \cdots \end{aligned} \tag{3.47}$$

For the case of spherical particles, the surface divergence [**79**] of surface charge currents can be calculated as:

(3.48)

$$\begin{aligned}
&\boldsymbol{\nabla}_s \cdot [q_s \mathbf{u}_s] = \boldsymbol{\nabla} q_s \cdot \mathbf{u}_s \\
&= \left\{ -(\epsilon_2 - \epsilon_1) \left[\frac{\mathbf{E}_0}{a} + \left(\boldsymbol{\nabla}\mathbf{E}_b + \boldsymbol{\nabla}\mathbf{E}_b^T \right) \cdot \hat{\mathbf{r}} \right] + (\epsilon_2 + 2\epsilon_1) \frac{\mathbf{P}}{a^4} + (2\epsilon_2 + 3\epsilon_1) \frac{\boldsymbol{Q} \cdot \hat{\mathbf{r}}}{a^5} \right\} \cdot (\boldsymbol{\Omega} \times a\hat{\mathbf{r}}) \\
&= \hat{\mathbf{r}} \cdot \left\{ \left\{ -(\epsilon_2 - \epsilon_1) \left[\mathbf{E}_0 + \left(\boldsymbol{\nabla}\mathbf{E}_b + \boldsymbol{\nabla}\mathbf{E}_b^T \right) \cdot a\hat{\mathbf{r}} \right] + (\epsilon_2 + 2\epsilon_1) \frac{\mathbf{P}}{a^3} + (2\epsilon_2 + 3\epsilon_1) \frac{\boldsymbol{Q} \cdot \hat{\mathbf{r}}}{a^4} \right\} \times \boldsymbol{\Omega} \right\}
\end{aligned}$$

Lastly, note the electric currents in both medium are assumed to be Ohmic, i.e.

$$\mathbf{J}_e^1 = \sigma_1 \mathbf{E} = \sigma_1 \left(\mathbf{E}_b + \mathbf{E}_d^+ \right), \mathbf{J}_e^2 = \sigma_2 \mathbf{E} = \sigma_2 \left(\mathbf{E}_b + \mathbf{E}_d^- \right) \tag{3.49}$$

Then, the surface charge accumulation due to the bulk electric currents is:

$$\begin{aligned}
\hat{\mathbf{n}}_{12} \cdot \left[\mathbf{J}_e^2 - \mathbf{J}_e^1 \right] = &-(\sigma_2 - \sigma_1) \left[\mathbf{E}_0 + \boldsymbol{\nabla}\mathbf{E}_b \cdot a\hat{\mathbf{r}} \right] \cdot \hat{\mathbf{r}} \\
&+ (\sigma_2 + 2\sigma_1) \frac{\mathbf{P} \cdot \hat{\mathbf{r}}}{a^3} + \left(\sigma_2 + \frac{3}{2}\sigma_1 \right) \frac{\hat{\mathbf{r}}\hat{\mathbf{r}} : \boldsymbol{Q}}{a^4} + \cdots
\end{aligned} \tag{3.50}$$

3.5.3. Time evolution equations of electric moments

Substituting 3.46, 3.48 and 3.50 into 3.36, it gives the time evolution equation for each electric moments by collecting terms of each spherical harmonics:

$$\frac{\mathrm{d}\mathbf{P}}{\mathrm{d}t} = \boldsymbol{\Omega} \times \left[\mathbf{P} - \epsilon_{21}^P a^3 \mathbf{E}_0 \right] - \frac{1}{\tau_{\mathrm{mw}}^P} \left[\mathbf{P} - \sigma_{21}^P a^3 \mathbf{E}_0 \right] \tag{3.51}$$

$$\frac{\mathrm{d}\boldsymbol{Q}}{\mathrm{d}t} = \boldsymbol{\Omega} \times \left[\left(\boldsymbol{Q} - \epsilon_{21}^Q a^5 \boldsymbol{\nabla}\mathbf{E}_b \cdot \hat{\mathbf{r}} \right) + \left(\boldsymbol{Q}^T - \epsilon_{21}^Q a^5 \boldsymbol{\nabla}\mathbf{E}_b^T \cdot \hat{\mathbf{r}} \right) \right] - \frac{1}{\tau_{\mathrm{mw}}^Q} \left(\boldsymbol{Q} - \sigma_{21}^Q a^5 \boldsymbol{\nabla}\mathbf{E}_b \right) \tag{3.52}$$

where τ_{mw}^{P} and τ_{mw}^{Q} are the Maxwell-Wagner (M-W) relaxation time of dipole and quadrupole moments respectively, which are given as:

$$\tau_{mw}^{P} = \frac{\epsilon_2 + 2\epsilon_1}{\sigma_2 + 2\sigma_1}, \quad \tau_{mw}^{Q} = \frac{2\epsilon_2 + 3\epsilon_1}{2\sigma_2 + 3\sigma_1} \tag{3.53}$$

And two dimensionless parameters ϵ_{21} and σ_{21} , which characterize the mismatch of electric permittivity and conductivity between two mediums, are defined as:

$$\epsilon_{21}^{P} = \frac{\epsilon_2 - \epsilon_1}{\epsilon_2 + 2\epsilon_1}, \quad \sigma_{21}^{P} = \frac{\sigma_2 - \sigma_1}{\sigma_2 + 2\sigma_1} \tag{3.54}$$

$$\epsilon_{21}^{Q} = \frac{\epsilon_2 - \epsilon_1}{\epsilon_2 + \frac{3}{2}\epsilon_1}, \sigma_{21}^{Q} = \frac{\sigma_2 - \sigma_1}{\sigma_2 + \frac{3}{2}\sigma_1} \tag{3.55}$$

Please note that the derived results have slightly different forms comparing with the results in [**123**].

3.5.4. Mechanical balances

Since there exists possible free surface charges q_s at the particle-liquid interface, the particle may experience net electric forces $\mathbf{F}_e = \oint \mathbf{f}_e \mathrm{d}S$ and electric torques $\mathbf{T}_e = \oint \mathbf{r} \times \mathbf{f}_e \mathrm{d}S$, where the integral is taken over the particle surface, $\mathbf{f}_e = \hat{\mathbf{n}} \cdot \left[\boldsymbol{\sigma}_l^e - \boldsymbol{\sigma}_p^e\right]_{r=a}$ is the interfacial electric force and $\boldsymbol{\sigma}^e = \epsilon \mathbf{E} \otimes \mathbf{E} - \frac{1}{2}\epsilon(\mathbf{E} \cdot \mathbf{E})\boldsymbol{I}$ is the electric stress tensor .

Similarly, electric forces and torques can be expressed in terms of electric moments by the multipole expansion [**120**, **135**], i.e.

$$\mathbf{F}_e = (\mathbf{P} \cdot \boldsymbol{\nabla})\, \mathbf{E}_0 + \cdots \tag{3.56}$$

and

$$\mathbf{T}_e = \mathbf{P} \times \mathbf{E}_0 + (\boldsymbol{Q} \cdot \boldsymbol{\nabla}) \times \mathbf{E}_0 + \cdots \tag{3.57}$$

With the electric forces and torques, the kinetic motion of the Quincke particle is readily calculated by simply multiplying them with the mobility tensors [Eqn. 3.33]. For example, the rotational motion of the Quincke particle in the bulk solution can be obtained by balancing electric torques and viscous torques:

$$\boldsymbol{\Omega} = \boldsymbol{M}_{\Omega T}\mathbf{T}_e = \left(8\pi\eta a^3\right)^{-1}\mathbf{T}_e \tag{3.58}$$

3.5.5. Steady-state solutions

Now we are ready to derive several important properties of Quincke rotation based on previous results. For simplicity, the external electric field is assumed to be uniform. Thus, the electric torque is dominantly contributed by the electric dipole moment, i.e. $\mathbf{T}_e = \mathbf{P}_{\text{eff}} \times \mathbf{E}_0$. Note that the effective dipole moment should be used [**120**], which is $\mathbf{P}_{\text{eff}} = \epsilon_1\mathbf{P}$ here and ϵ_1 is the dielectric permittivity of the fluid. And the electric dipole moment in the steady state [Eqn. 3.51, $\frac{\mathrm{d}\mathbf{P}}{\mathrm{d}t} = 0$] is given by:

$$\boldsymbol{\Omega} \times \mathbf{P} - \frac{1}{\tau_{mw}^P}\mathbf{P} = \epsilon_{21}^P a^3 \boldsymbol{\Omega} \times \mathbf{E}_0 - \frac{1}{\tau_{mw}^P}\sigma_{21}^P a^3 \mathbf{E}_0 \tag{3.59}$$

Taking inner product and cross product of the above equation with $\boldsymbol{\Omega}$ yields:

$$(\boldsymbol{\Omega} \cdot \mathbf{P})\boldsymbol{\Omega} - (\boldsymbol{\Omega} \cdot \boldsymbol{\Omega})\mathbf{P} - \frac{1}{\tau_{mw}^P}\boldsymbol{\Omega} \times \mathbf{P} = \epsilon_{21}^P a^3 (\boldsymbol{\Omega} \cdot \mathbf{E}_0)\boldsymbol{\Omega} - \epsilon_{21}^P a^3 (\boldsymbol{\Omega} \cdot \boldsymbol{\Omega})\mathbf{E}_0 - \frac{1}{\tau_{mw}^P}\sigma_{21}^P a^3 \boldsymbol{\Omega} \times \mathbf{E}_0$$

and

$$-\frac{1}{\tau_{mw}^{P}}\mathbf{\Omega}\cdot\mathbf{P}=-\frac{1}{\tau_{mw}^{P}}\sigma_{21}^{P}a^{3}\mathbf{\Omega}\cdot\mathbf{E}_{0}$$

It gives the steady state electric dipole moment[†] as:

(3.60)

$$\mathbf{P}=\frac{(\sigma_{21}^{P}-\epsilon_{21}^{P})}{1+\left(\Omega\tau_{mw}^{P}\right)^{2}}a^{3}\left[\left(\mathbf{\Omega}\tau_{mw}^{P}\right)\times\mathbf{E}_{0}+\left(\mathbf{\Omega}\tau_{mw}^{P}\cdot\mathbf{E}_{0}\right)\left(\mathbf{\Omega}\tau_{mw}^{P}\right)\right]+\frac{\epsilon_{21}^{P}\left(\Omega\tau_{mw}^{P}\right)^{2}+\sigma_{21}^{P}}{1+\left(\Omega\tau_{mw}^{P}\right)^{2}}a^{3}\mathbf{E}_{0}$$

Plugging it back into the torque balance [Eqn. 3.58] gives that:

$$8\pi\eta a^{3}\mathbf{\Omega}=4\pi\epsilon_{0}\epsilon_{1}\frac{(\sigma_{21}^{P}-\epsilon_{21}^{P})}{1+\left(\Omega\tau_{mw}^{P}\right)^{2}}a^{3}\left[\left(\mathbf{\Omega}\tau_{mw}^{P}\right)\times\mathbf{E}_{0}+\left(\mathbf{\Omega}\tau_{mw}^{P}\cdot\mathbf{E}_{0}\right)\left(\mathbf{\Omega}\tau_{mw}^{P}\right)\right]\times\mathbf{E}_{0} \tag{3.61}$$

Next, taking the inner product of the above equation with the external electric field $\mathbf{E}_0$ immediately yields that:

$$\mathbf{\Omega}\cdot\mathbf{E}_{0}=0 \tag{3.62}$$

This is the first important result derived from the steady state solution, which states that the direction of the angular velocity of the Quincke particle $\mathbf{\Omega}$ can be any be any random direction perpendicular to the applied external electric field $\mathbf{E}_0$. As for the magnitude of the angular velocity, it can be obtained by taking inner product with the angular velocity $\mathbf{\Omega}$:

$$\Omega^{2}\left[1+\left(\Omega\tau_{mw}^{P}\right)^{2}+\frac{\epsilon_{0}\epsilon_{1}(\sigma_{21}^{P}-\epsilon_{21}^{P})\tau_{mw}^{P}}{2\eta}E_{0}^{2}\right]=0 \tag{3.63}$$

[†]Eqn. 3.51 can be solved via the Laplace transformation to derive the complete time evolution of the electric dipole moment $\mathbf{P}(t)$.

The first solution of the above equation is the stationary solution ($\mathbf{\Omega} = 0$), which corresponds to the absence of particle motion [3.2(b), left]. And the second solution corresponds to the steady rotation of the particle [3.2(b), middle]:

$$\Omega = \pm \frac{1}{\tau_{MW}^P} \sqrt{\left(\frac{E_0}{E_c}\right)^2 - 1} \tag{3.64}$$

The above expression indicates another important feature of Quincke rotation, i.e. the steady rotation only occurs when the external field strength E_0 exceeds a critical field strength E_c, which is given by

$$E_c = \sqrt{\frac{2\eta}{\epsilon_0 \epsilon_1 \tau_{mw}^P (\epsilon_{21}^P - \sigma_{21}^P)}} \tag{3.65}$$

where the Maxwell-Wagner relaxation time $\tau_{mw}^P = \frac{\epsilon_2 + 2\epsilon_1}{\sigma_2 + 2\sigma_1}$ [Eqn. 3.53], the dielectric permittivity mismatch $\epsilon_{21}^P = \frac{\epsilon_2 - \epsilon_1}{\epsilon_2 + 2\epsilon_1}$ and the electric conductivity mismatch $\sigma_{21}^P = \frac{\sigma_2 - \sigma_1}{\sigma_2 + 2\sigma_1}$ [Eqn. 3.54]. The above definition of the critical electric field strength also indicates that the Quincke rotation only occurs when $\epsilon_{21}^P > \sigma_{21}^P$, i.e.

$$\frac{\epsilon_2}{\sigma_2} > \frac{\epsilon_1}{\sigma_1} \tag{3.66}$$

Since the ratio ϵ/σ has the unit of time, it's equivalent to say that the Quincke rotation only happens in the system where the characteristic time scale in the particle (ϵ_2/σ_2) is larger than the one in the liquid (ϵ_1/σ_1).

3.6. From stationary to rolling

Up to this point, we are ready to explain the first transition from stationary state to rolling motion [Fig. 3.2 (b)], which is mathematically described in the previous section [Sec. 3.5]. Here, it's helpful to connect each mathematical descriptions with corresponding experimental phenomena to get more physical understanding of the Quincke rotation.

3.6.1. Mechanism of the Quincke rotation

Under the application of an external electric field, the charge carriers in the liquid are driven by the field and accumulated at the impermeable particle-liquid interface, which dominantly forms a dipolar surface charge distribution.

When the external field strength is below the critical electric field strength, the Quincke particle is motionless ($\mathbf{\Omega}= 0$). According to equation 3.51, the steady state electric dipole moment should be $\mathbf{P}_{eq} = \sigma_{21}^{P} a^3 \mathbf{E}_0$. As the Quincke particle is effectively an insulator and the liquid is a weakly conducting fluid [table 3.1], the dimensionless number σ_{21}^{P} is negative. This indicates that the Quincke particle develops an electric dipole moment anti-parallel to the external electric field in the steady state [Fig. 3.5, left].

With increasing electric field strength, the magnitude of the anti-parallel electric dipole moment grows and the Quincke particle becomes more unstable. Once the external field exceeds the critical field strength E_c, any small perturbations of the Quincke particle will cause a spontaneous rotation of the particle [Eqn. 3.64]. In the steady state, the flux of charge carriers from the bulk solution driven by the electric fields [Eqn. 3.36, third term] is balanced by the surface convection flux of charge carriers [Eqn. 3.36, second term] caused by the particle rotation. The steady state electric dipole moment forms a

finite angle with the external electric field [Fig. 3.5, right; Eqn. 3.60], which generates a constant electric torque $\mathbf{T}_e$ exerting on the particle and results in a constant rotation of the particle.

3.6.2. Boundary effects of the bottom electrode surface

So far, the above description does not include any effects from electrode surfaces, which is commonly used in the experiment [Fig. 3.2 (a)]. As the chamber height is generally much larger than the particle size [table 3.1], the boundary effect is primarily contributed by the bottom electrode surface and the existence of the bottom electrode surface modifies the description of Quincke rotation derived in bulk from two primary aspects.

First, the bottom electrode surface acts as a non-slippery boundary which modifies the mobility tensors [Eqn. 3.33]. With the existence of the bottom floor, the most direct consequence is the off-diagonal mobility tensors become nonzero, i.e. $\boldsymbol{M}_{UT} = \boldsymbol{M}_{\Omega F} \neq 0$. As each particles experience an electric torque $\mathbf{T}_e$, a non-zero $\boldsymbol{M}_{UT}$ enables the coupling between torque and translational motion, which is responsible for the translational motion observed in the Quincke roller experiments [Fig. 3.2(b), middle]. Besides, the bottom electrode surface also modifies the value of diagonal mobility tensors $\boldsymbol{M}_{UF}$ and $\boldsymbol{M}_{\Omega T}$. Depending on the separation distance between the particle and the bottom floor, the values of all those mobility tensors can be calculated via the method of reflection [**136**](see also Sec. 5.3.4.1) or the lubrication theory [**121**, **137**, **138**].

Second, the bottom electrode surface is a conductor, which is an equi-potential surface. The surface charges on the particle surface q_s induces excess charges on the electrode surface, whose effect can be included by introducing an image dipole $\mathbf{P}^*$ [also see Sec. 5.3.4.2]. By the image charge method [**129**], the image dipole $\mathbf{P}^*$ has reflected in-plane dipole moments and unchanged out-of-plane dipole moments, i.e. $\mathbf{P}^* = (-P_x, -P_y, P_z)$ with the real dipole $\mathbf{P} = (P_x, P_y, P_z)$. To include the effect of image charges, the external electric field $\mathbf{E}_0$ in Eqn. 3.51 should include the electric field $\delta\mathbf{E}^*$ generated by the image dipole. Besides, the calculation of electric force and electric torque exerted upon the particle also needs to consider the interactions with the image dipole, i.e. $\delta\mathbf{F}^{e*} \approx (\mathbf{P}\cdot\boldsymbol{\nabla})\,\delta\mathbf{E}^*$ and $\delta\mathbf{T}^{e*} \approx \mathbf{P}\times\delta\mathbf{E}^*$.

Those boundary corrections are only described qualitatively here and do not affect the physical mechanism of Quincke rotation described in this section qualitatively. More quantitative calculations will be discussed in the following section [Sec. 3.7.1].

3.7. The role of the planar electrode

With the first transition from stationary state [Fig. 3.2(b), left] to rolling motion [Fig. 3.2(b), middle] explained successfully by the leaky dielectric model [Sec. 3.4, 3.5 and 3.6], the second transition from rolling motion to oscillating motion [Fig. 3.2(b), right] is difficult to understand within the same framework. As shown in equation 3.64, the angular velocity of Quincke particle should increase monotonically with the external field strength according to the leaky dielectric model, which means that the Quincke particle should just

roll faster with increasing electric fields strength and there is no clue of oscillatory motions.

To isolate what is the possible cause of this unexpected oscillating motion, the controlled experiments are conducted between the Quincke particle near the electrode surface and the Quincke particle in the bulk fluid [Fig. 3.4]. A standing acoustic field is used to levitate particles at the mid-plane between two planar electrodes [**139**] and observe their motion upon application of the electric field. In the absence of the acoustic field, the application of a strong electric field drives the particles to oscillate at the electrode surface. Such oscillations are not observed when the same field is applied to particles levitating at the mid-plane of the chamber. Instead, particles in the bulk fluid exhibit steady rotation consistent with predictions of the leaky dielectric model [Sec. 3.6].

These experiment results show that the oscillating motion is only observed near the planar electrode surface, which indicates that the planar electrode should play an important role in explaining the oscillatory behaviors.

The Quincke particle is expected to be fairly close to the bottom electrode surface and only separated by a thin layer of fluid (nanometer thickness [**115**]). This is because there is a strong attraction force towards the bottom electrode surface due to the interactions between surface charges on the Quincke particle and induced excess charges on the electrode surface. This strong attraction force is balanced by a diverging lubrication force (inversely proportional to the gap distance [**137**, **138**]) in the opposite direction. The balance of those two forces determines the equilibrium height of the Quincke particle.

The theory presented before [Sec. 3.5] is based on the multipole expansion, which in principle is no longer valid when the particle is in proximity of a boundary. To understand

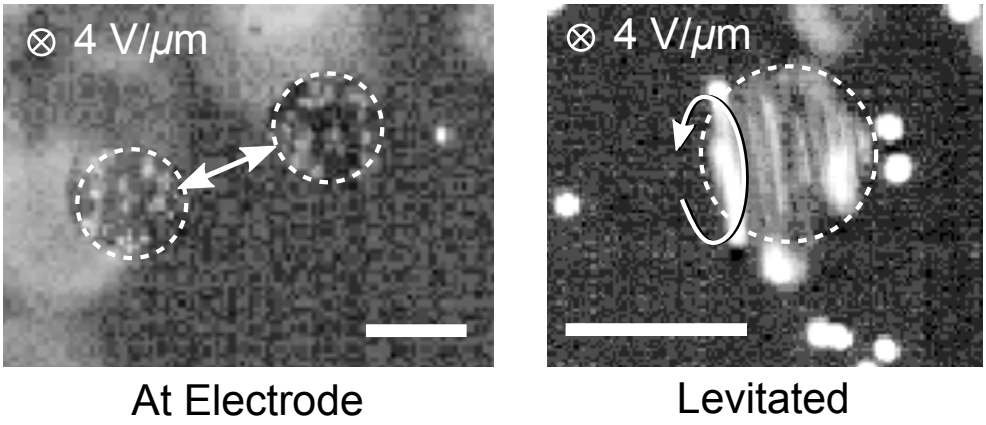

Figure 3.4. Time-lapse microscopy images showing the dynamics of a single particle oscillating at the electrode surface (left) and rotating in the bulk fluid (right). Dashed circles highlight the particle position. The external field strength in both experiments is $E_e = 4$ V/μm. Scale bars are 40 μm. Here, we use 40 μm polyethylene Janus spheres with a white hemisphere coated on black core (HCMS-BLK-WHT-Polymer from Cospheric Inc.). Also visible in the images are 1 μm fluorescent particles (white), which aid in visualizing the motion of the larger particle. Particle levitation is achieved using a piezoelectric transducer adhered to the outside of the top electrode. The transducer is driven by a sinusoidal voltage signal with an amplitude of 10 V and a frequency of 3.6 MHz. The precise frequency is tuned to create a standing acoustic field with wavelength equal to twice the electrode separation $L = 200$ μm. Under these conditions, particles levitate at the mid-plane equidistant from the two parallel electrodes.

the possible effect from the electrode surface, one intuitive attempt is to include the effects from the conducting electrode surface properly to see whether the oscillating motion can be found.

3.7.1. Multipole expansion near a planar electrode

Previous results derived in the bulk fluid [Eqn. 3.51] only consider the contribution from the electric dipole moments as the top and bottom of the system are symmetric. The

existence of the bottom electrode breaks this symmetry and nonvanishing higher order moments of charge distribution are expected. A straightforward approach to include the effect of the electrode surface is to include higher order moments in the leaky dielectric model and also its image counterparts to maintain the constant potential boundary condition at the electrode surface.

More specifically, assume a particle positioned at $(0, 0, h)$ rotates around x-axis, i.e. $\mathbf{\Omega} = \omega\hat{\mathbf{x}}$. The planar electrode is located at $z = 0$ and the external electric fields is applied along the z-axis. Then, the electric dipole $\mathbf{P}$ and quadrupole moments $\boldsymbol{Q}$ can be expressed as the following form:

$$\mathbf{P} = (0, p_y, p_z)\,, \quad \boldsymbol{Q} = \begin{pmatrix} -Q_{yy} - Q_{zz} & 0 & 0 \\ 0 & Q_{yy} & Q_{yz} \\ 0 & Q_{yz} & Q_{zz} \end{pmatrix} \tag{3.67}$$

The corresponding image moments are located at $(0, 0, -h)$ and have the following form:

$$\mathbf{P}^* = (0, -p_y, p_z)\,, \quad \boldsymbol{Q}^* = \begin{pmatrix} Q_{yy} + Q_{zz} & 0 & 0 \\ 0 & -Q_{yy} & Q_{yz} \\ 0 & Q_{yz} & -Q_{zz} \end{pmatrix} \tag{3.68}$$

In addition to the electric potential contributed by the real charges [Eqn. 3.42 and 3.43], the disturbance potential contributed by image charges are:

$$\Delta\varphi^*(\mathbf{r}) = \frac{\mathbf{r} \cdot \mathbf{P}^*}{r^3} + \frac{1}{2}\frac{\mathbf{rr} : \boldsymbol{Q}^*}{r^5} + \cdots\,, \quad z > 0 \tag{3.69}$$

With this setup, similar procedure described in section 3.5 can be executed to get the time evolution equations of high order moments with image charge corrections. In principle, arbitrary orders of charge moments can be include to get accurate results near the planar electrode. However, in practice, the calculation quickly becomes tedious and error-prone with increasing order of moments. The calculation up to quadrupole moments was carried out and the results do not reproduce the oscillatory motion observed in the experiment. For the sake of brevity, those calculations are not recorded here as it can be easily derived by following the derivations in section 3.5.

3.7.2. Analytical results near a planar electrode

The multipole expansion approach has inherent limitations when dealing with near-contact problems. This is because the multipole expansion essentially treats the particle as a point particle with electric moments upon it. This prohibits the multipole expansion solutions from incorporating some important length scales such as the particle radius a and the gap distance δ when the particle is in close contact with the boundary [**140**, **141**]. This point is evidenced by the results derived in the bulk fluid [Eqn. 3.64 and 3.65], where both predicted angular velocity $\mathbf{\Omega}$ and critical field strength E_c depend on neither the size of particle nor the gap distance. This is clearly contradicted to the experiment observations [**107**, **115**] and simulation results [**142**].

Therefore, another more brutal-force way to study the role of bottom electrode is to solve the leaky dielectric model near a planar electrode analytically. This is of course difficult and messy and I did not succeed. Here, I just document some major efforts for reference.

Consider a single Quincke particle is in proximity of a bottom planar electrode surface. The governing equation describing the problem is still the same as previous leaky dielectric model [Sec. 3.4] with additional boundary conditions enforced by the electrode surface. The hydrodynamic part is identical to the lubrication problems, which has been extensively studied and its analytical solutions are readily available in literature [**121**,**137**,**138**,**143**–**145**]. Thus, the rest of this problem becomes solving the Laplace equation with the boundary conditions unique to the Quincke rotation system.

Due to the planar boundary and spherical geometry of the Quincke particle, it turns out the so-called bispherical coordinate system makes the specification of boundary conditions much easier (as both planar and spherical surfaces are the coordinate surfaces of the bispherical coordinate system) at the cost of a more complicated infinite series expression of the general solution of the Laplace equation [see Appx. A.2].

For a purely dielectric particle near a planar boundary, such problem has already been solved in [**146**], where boundary conditions yield a set of infinite recurrence relations. Please refer to [**146**] for more details. Fortunately, the solution of the resulting recurrence relations can be constructed analytically using a Green's function technique for finite difference equations [**147**], which has a form of continued fractions.

Following the same spirit, all boundary conditions of a single Quincke particle near an planar electrode can also be expressed in the bispherical coordinate system. However, the boundary conditions yields a higher order recurrence relations this time, i.e. the recurrence relation depends on the second-nearest-neighbor terms ($A_{n-2}, A_{n-1}, A_n, A_{n+1}, A_{n+2}$ instead of just A_{n-1}, A_n, A_{n+1}). It's not easy to obtain the analytical solution of such

infinite finite difference equations [**147**]. All those inconclusive analytical results can be derived by following [**146**] and will not be reported here for brevity.

3.8. The numerical model of a single Quincke roller

As theoretical attempts based on the multipole expansion 3.7.1 and analytical analysis 3.7.2 encountered difficulties, the numeric approach provides an alternative pathway for understanding the role of planar electrode. With the theoretical description of a single Quincke particle detailed in Sec. 3.4, the Laplace equation 3.31 together with boundary conditions Eqn. 3.34, 3.35,3.36,3.37 and 3.38 can be solved self-consistently to study the behaviors of a single Quincke particle near a planar electrode surface.

The Laplace equation [Eqn. 3.31] and boundary conditions such as the continuity of electric potential [Eqn. 3.34], the normal jump of electric displacement fields [Eqn. 3.35] and constant electric potential [Eqn. 3.37 and 3.38] are standard components of electrostatic solvers of any commonly available Finite Element Method (FEM) simulation packages, such as COMSOL, ABAQUS, FEniCSx, etc. The only exception is the surface charge conservation equation [Eqn. 3.36], which is unique for the Quincke rotation problem and has to be implemented manually. The surface charge conservation equation is a PDE defined on the particle surface and any FEM packages provide the boundary PDE solver can be used for solving the Quincke problems. Below, we will only focus deriving the explicit form of Eqn. 3.36 for the spherical particle case, which in principle can be generalized to any smooth parametrizable surfaces.

3.8.1. Surface charge conservation

As the surface charge conservation equation is defined on a curved surface, it's important to express the quantities defined on the surface to its embedded 3D Euclidean space ($\mathbb{R}^3$).

3.8.1.1. surface fluxes. For a spherical surface, the surface flux $\mathbf{J}_s$ can be written as:

$$\mathbf{J}_s = q_s \mathbf{u}_s = q_s \boldsymbol{\Omega} \times a\hat{\mathbf{n}} \tag{3.70}$$

where $\boldsymbol{\Omega}$ is the angular velocity, $\hat{\mathbf{n}}$ is the unit outer normal vector of the particle surface, q_s is the free surface charges and a is the radius of the particle. As the Quincke rotation occurs in the plane perpendicular to the external electric field, i.e. $\boldsymbol{\Omega} \cdot \mathbf{E}_0 = 0$ [Eqn. 3.62]. By assuming the external field is along the z-axis, the general angular velocity can be expressed as:

$$\boldsymbol{\Omega} = \omega_x \hat{\mathbf{x}} + \omega_y \hat{\mathbf{y}} \tag{3.71}$$

where ω_x and ω_y are the respective x and y component of angular velocity. In the spherical coordinate system [Appx. A.1], $\hat{\mathbf{n}} = \hat{\mathbf{r}} = \sin\theta\cos\phi\hat{\mathbf{x}} + \sin\theta\sin\phi\hat{\mathbf{y}} + \cos\theta\hat{\mathbf{z}}$ and the surface flux $\mathbf{J}_s$ can be rewritten in the spherical coordinates as:

$$\mathbf{J}_s = q_s a(\omega_y \cos\phi - \omega_x \sin\phi)\hat{\boldsymbol{\theta}} - q_s a \cos\theta(\omega_y \sin\phi + \omega_x \cos\phi)\hat{\boldsymbol{\phi}} = T^i \mathbf{t}_i \tag{3.72}$$

where tangent vectors $\mathbf{t}_i$ are defined as:

$$\mathbf{t}_r = \sqrt{g_{rr}}\hat{\mathbf{r}} = \hat{\mathbf{r}}, \quad \mathbf{t}_\theta = \sqrt{g_{\theta\theta}}\hat{\boldsymbol{\theta}} = r\hat{\boldsymbol{\theta}} = a\hat{\boldsymbol{\theta}}, \quad \mathbf{t}_\phi = \sqrt{g_{\phi\phi}}\hat{\boldsymbol{\phi}} = r\sin\theta\hat{\boldsymbol{\phi}} = a\sin\theta\hat{\boldsymbol{\phi}} \tag{3.73}$$

And corresponding contravariant components T^i are:

$$T^r = 0, \quad T^\theta = q_s(\omega_y \cos\phi - \omega_x \sin\phi), \quad T^\phi = -q_s \cot\theta(\omega_y \sin\phi + \omega_x \cos\phi) \tag{3.74}$$

As the surface charge flux is a vector in the tangent space of the particle surface, i.e. $\mathbf{J}_s = T^i \mathbf{t}_i$, the surface divergence operator is just the covariant divergence [**132**, **148**]:

$$\begin{aligned} \boldsymbol{\nabla}_s \cdot \mathbf{J}_s &= T^i_{;i} = T^i_{,i} + \Gamma^i_{ji} T^j = T^r_{,r} + T^\theta_{,\theta} + T^\phi_{,\phi} + \frac{2}{r} T^r + \cot\theta T^\theta \\ &= \frac{\partial q_s}{\partial \theta}(\omega_y \cos\phi - \omega_x \sin\phi) - \frac{\partial q_s}{\partial \phi} \cot\theta(\omega_y \sin\phi + \omega_x \cos\phi) \end{aligned} \tag{3.75}$$

where the subscript $_,$ and $_;$ denote the Euclidean derivative and the covariant derivative, respectively. And Γ^k_{ij} is the Christoffel symbol [Appx. A.1]. As expected, the surface charge flux is non-zero only when there is a gradient of surface charge distribution.

3.8.1.2. bulk fluxes. Another contribution to the surface charge conservation is from the discontinuity of the bulk charge flux, which can easily written in the spherical coordinates as:

$$\hat{\mathbf{n}}_{12} \cdot \left[\mathbf{J}_e^2 - \mathbf{J}_e^1\right] = \hat{\mathbf{r}} \cdot [\sigma_2 \mathbf{E}_2 - \sigma_1 \mathbf{E}_1] \tag{3.76}$$

where ${\mathbf{J}_e}^i = \sigma_i \mathbf{E} = -\sigma_i \boldsymbol{\nabla}\varphi(\mathbf{r}), i = 1, 2$, are the respective electric current in the fluid ($i = 1$) and the particle ($i = 2$).

3.8.1.3. surface charge conservation. Combining the surface flux term and the bulk flux term together, the surface charge conservation equation [Eqn. 3.36] can be expressed in the spherical coordinate system as:

$$\frac{\partial q_s}{\partial t} + \sigma_2 \hat{\mathbf{r}} \cdot \mathbf{E}_2 - \sigma_1 \hat{\mathbf{r}} \cdot \mathbf{E}_1 + \frac{\partial q_s}{\partial \theta}(\omega_y \cos\phi - \omega_x \sin\phi) - \frac{\partial q_s}{\partial \phi} \cot\theta(\omega_y \sin\phi + \omega_x \cos\phi) = 0 \tag{3.77}$$

In most FEM simulation packages, it's more convenient to implement in the Cartesian coordinates and the above equation can be transformed back into Cartesian coordinates:

$$\frac{\partial q_s}{\partial t} + \hat{\mathbf{n}} \cdot [\sigma_2 \mathbf{E}_2 - \sigma_1 \mathbf{E}_1] + \frac{\partial q_s}{\partial x}\omega_y z - \frac{\partial q_s}{\partial y}\omega_x z + \frac{\partial q_s}{\partial z}(\omega_x y - \omega_y x) = 0 \tag{3.78}$$

If we relax the constraint that the angular velocity should be perpendicular to the field direction, i.e. $\boldsymbol{\Omega} \cdot \mathbf{E}_0 = 0$, the surface charge conservation equation can be written in a more familiar form:

$$\frac{\partial q_s}{\partial t} + \hat{\mathbf{n}} \cdot [\sigma_2 \mathbf{E}_2 - \sigma_1 \mathbf{E}_1] + \mathbf{u}_s \cdot \boldsymbol{\nabla} q_s = 0 \tag{3.79}$$

where $\mathbf{u}_s = \boldsymbol{\Omega} \times \mathbf{r}|_{r=a}$ and $\boldsymbol{\nabla}$ is the usual Euclidean gradient operator.

The whole derivation may seem introducing unnecessary complication as Eqn. 3.79 should be a pretty obviously result, which basically projects the gradient of surface charges into the tangent plane of the particle surface. However, this is obvious for the symmetric spherical surface and this method can be modified to derive the explicit form of the surface charge conservation equation for arbitrary parametrizable surfaces.

3.8.2. Self-consistent model of a single Quincke particle

With the explicit expression of the surface charge conservation equation [Eqn. 3.79], it can be implemented as a user-defined PDE via the boundary PDE module of COMSOL while other electrostatic-related equations can be solved by the electrostatic module of COMSOL. The hydrodynamic interactions are treated implicitly via the resistance matrix formulation and the angular velocity of the particle is obtained via the torque balance

as detailed in Sec. 3.5.4. Both modules are solved simultaneously which yield the FEM solutions as shown in Fig. 3.5. Fig. 3.5 (left) shows the surface charge distribution of a stationary Quincke particle, which has an overall anti-parallel electric dipole moment while Fig. 3.5 (right) demonstrates the surface charge distribution of a rotating Quincke particle. It confirms the existence of tilted electric dipole moment, which generates the electric torque with the external electric field for propelling the Quincke particle.

However, although the self-consistent model agrees exceptionally well with the explanation of Quincke rotation [Sec. 3.6], the numeric simulations still do not recover the oscillatory motion observed in the experiment. The numeric simulations indeed unveil some effects of the planar electrode surface, such as inducing higher order electric moments, stabilizing the critical field of rolling motion [Fig. 3.10], etc., but none of them are sufficient for explaining the robust oscillation at the high field limit. Those findings lead us to think that there may have some effects due to the electrode surface are outside the framework of the leaky-dielectric model.

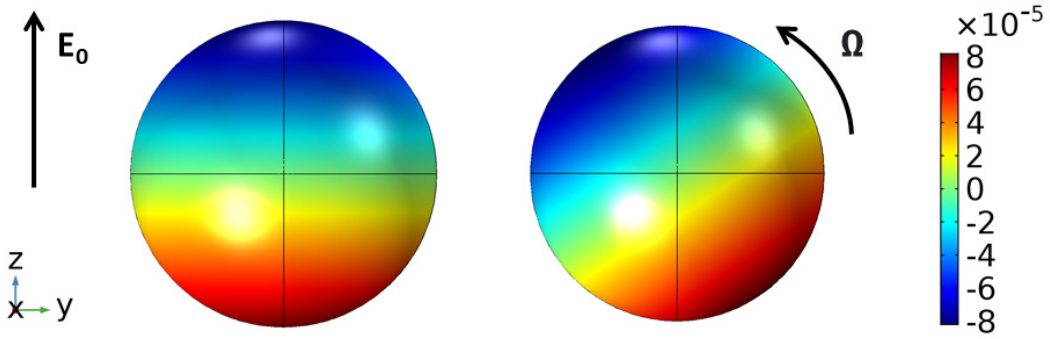

Figure 3.5. Surface charge distribution of stationary (left) and steady rotating (right) Quincke particle. An uniform electric field E_0 is applied along the z-axis and the particle is rotating around the x-axis with angular velocity $\mathbf{\Omega}$. The color depicts the surface charge density. The bottom electrode surface is not depicted in the figure.

3.9. The boundary layer near electrode surface

As informed by the simulation results in Sec. 3.8, we will do a detailed theoretical analysis of the confined electrolyte used in Quincke particle experiments in this section to figure out the possible effects caused by the electrode surface.

3.9.1. Conductivity of AOT/hexadecane solution

The anionic surfactant, sodium bis(2-ethylhexyl) sulfosuccinate (AOT), forms inverse micelles in hexadecane above a critical micelle concentration (CMC) of $\sim 10^{-6}$ M [**130**, **149**]. Small-angle neutron scattering (SANS) data [**150**] suggest that each inverse micelle contains $N\approx$ 20 AOT molecules with a polarizable core of radius $a_c \approx 1$ nm and a hydrodynamic radius of $a^h\approx 1.7$ nm . At equilibrium, the charge fluctuation theory [**151**] predicts the number density of charged micelles to be

$$n_z = n_0 \exp\left(\frac{-z^2\lambda_B}{2a_c}\right) \tag{3.80}$$

where $n_0 \approx \frac{[\mathrm{AOT}]}{N}$ is the concentration of uncharged micelles, z is the valence of charged micelles, and λ_B is the Bjerrum length,

$$\lambda_B = \frac{e^2}{4\pi\epsilon k_B T} \approx 28.5\mathrm{nm} \tag{3.81}$$

where e is the elementary charge, $\epsilon = 2\epsilon_0$ is the permittivity of hexadecane, k_B is the Boltzmann constant, and T= 298 K is the temperature. The fact that $\lambda_B/2a_c \approx 14 \gg 1$ implies that nearly all of the charged micelles have unit valence, $z = \pm 1$. Then, the

conductivity of the whole solution in the equilibrium can be approximated as:

$$\sigma = \sum_z \frac{z^2 e^2 D}{k_B T} n_z \approx \frac{2e^2 D}{k_B T} n_0 \exp\left(-\lambda_B / 2a_c\right) \tag{3.82}$$

Using the Stokes-Einstein (S-E) relation, it can be expressed as:

$$\sigma = \frac{2e^2}{6\pi\eta a_h} n_0 \exp\left(-\lambda_B / 2a_c\right) \tag{3.83}$$

where the mobility of charged micelle is estimated as $\mu = \frac{D}{k_B T} \approx (6\pi\eta a_h)^{-1}$ and $\eta = 3$ mPa·s is the dynamic viscosity of hexadecane [see table 3.1].

3.9.2. Analysis of chemical reactions

Since the experimental concentration of AOT solution ($\sim$ 0.15 M) is well above the CMC ($\sim 10^{-6}$ M), the charge carriers are dominated by the charged micelles and the conductivity increases linearly with the AOT concentration in agreement with previous experiments [**130**]. Therefore, the association-disassociation reaction of interests in the AOT/hexadecane solution is:

$$\underset{(n_1, z_1=0)}{2\,\mathrm{M}} \underset{\mathrm{k_-}}{\overset{\mathrm{k_+}}{\rightleftharpoons}} \underset{(n_2, z_2=+1)}{\mathrm{M^+}} + \underset{(n_3, z_3=-1)}{\mathrm{M^-}} \tag{3.84}$$

where [M] is the concentration of neutral micelles, [M^+] is the concentration of positively charged micelles and [M^-] is the concentration of negatively charged micelles. k_+ is the forward rate constant and k_- is the backward rate constant.

The forward rate constant can be obtained via the chemical equilibrium:

$$\frac{[\mathrm{M}^+][\mathrm{M}^-]}{[\mathrm{M}]^2} = \frac{k_+}{k_-} = \exp\left(-\lambda_B/a_c\right) \tag{3.85}$$

i.e.

$$k_+ = k_- \exp\left(-\lambda_B/a_c\right)$$

Therefore, the reaction rates of each species are:

$$-r_1 = r_2 = r_3 = k_+ n_1^2 - k_- n_2 n_3 = k_- \left[n_1^2 \exp\left(-\lambda_B/a_c\right) - n_2 n_3\right]$$

where r_i is the source/sink of i-th species. Because the concentration of charged species (n_2 and n_3) are very dilute, we can approximate the concentration of the neutral species (n_1) by its equilibrium concentration, i.e. $n_1 \approx n_0$. Then,

$$-r_1 = r_2 = r_3 = k_- \left[n_0^2 \exp\left(-\lambda_B/a_c\right) - n_+ n_-\right] = k_- \left(n_{eq}^2 - n_+ n_-\right) \tag{3.86}$$

where $n_{eq} = n_0^2 \exp\left(-\lambda_B/2a_c\right)$ is the equilibrium concentration of neutral species, $n_+ = n_2$ and $n_- = n_3$ are the concentration of positively and negatively charged species, respectively.

If the recombination of charged species is assumed to be diffusion-limited, the rate constant can be estimated [**118**, **152**] as:

$$k_- = 8\pi D \lambda_B = \frac{2e^2\mu}{\epsilon} \approx 2.9 \times 10^{-17}\ \mathrm{m}^3/\mathrm{s} \tag{3.87}$$

where $D = k_B T \mu$ is the micelle diffusivity. The micelles approach their equilibrium ionization with a characteristic time scale $(2k_- n_{eq})^{-1}$, which is equal to one half of the charge

relaxation time ϵ/σ_0. For a 0.1 M AOT solution, the equilibrium ion concentration is $n_{eq} \approx 7 \times 10^{-8}$ M and the ion relaxation time is $(2k_- n_{eq})^{-1} \geq 0.4$ ms with equality for diffusion-limited recombination [**107**].

Finally, we can solve the Nernst-Planck equation for charged micelles to get the transport behaviors of charge carriers:

$$\frac{\partial n_\pm}{\partial t} + \boldsymbol{\nabla} \cdot \mathbf{J}_\pm = k_r \left(n_{eq}^2 - n_+ n_- \right) \tag{3.88}$$

where the corresponding fluxes of each charged species (ignoring the convective flux) are

$$\mathbf{J}_\pm = -D_\pm \boldsymbol{\nabla} n_\pm \pm \frac{eD_\pm}{k_B T} n_\pm \mathbf{E}$$

and the equilibrium concentration of neutral species is

$$n_{eq} = \frac{[\mathrm{AOT}]}{N} \exp\left(-\lambda_B / 2a_c\right)$$

3.9.3. Analysis of the equilibrium charge distributions

With the understanding of the origin of electric conductivity and relevant chemical reactions in AOT/hexadecane solution, the assumption of zero space charge in the leaky dielectric system [Sec. 3.3] should be relaxed. Including possible nonvanishing space charges, the relevant governing equations become the Poisson-Nernst-Planck (PNP) equations:

$$\begin{cases} \boldsymbol{\nabla} \cdot (\epsilon_r \epsilon_0 \mathbf{E}) = e(n_+ - n_-) \\ \dfrac{\partial n_\pm}{\partial t} + \boldsymbol{\nabla} \cdot \left[-D_\pm \boldsymbol{\nabla} n_\pm \pm \dfrac{eD_\pm}{k_B T} n_\pm \mathbf{E} \right] = k_- \left(n_{eq}^2 - n_+ n_- \right) \end{cases} \tag{3.89}$$

As the system under consideration is confined by two planar electrodes, the problem can be effectively reduced as a 1D problem. Without loss of generality, assume the planar electrodes are placed along the z-axis, then

$$\begin{cases} -\epsilon\dfrac{\partial^2\varphi}{\partial z^2} = e(n_+ - n_-) \\ \dfrac{\partial n_\pm}{\partial t} - D\dfrac{\partial^2 n_\pm}{\partial z^2} \mp \dfrac{eD}{k_BT}\dfrac{\partial}{\partial z}\left(n_\pm\dfrac{\partial\varphi}{\partial z}\right) = k_-(n_{eq}^2 - n_+n_-) \end{cases}$$

Note that the Quincke rotation/oscillation only happens in high electric field strength regime (see table 3.1), i.e. $\varphi \gg \frac{k_BT}{e} \sim 25$ meV. Thus, the diffusion flux is negligible comparing with the electric migration flux and the above equations in the steady state simplify as:

$$\begin{cases} -\epsilon\dfrac{\partial^2\varphi}{\partial z^2} = e(n_+ - n_-) \\ -\dfrac{eD}{k_BT}\dfrac{\partial}{\partial z}\left(n_+\dfrac{\partial\varphi}{\partial z}\right) = k_-(n_0^2 - n_+n_-) \\ \dfrac{eD}{k_BT}\dfrac{\partial}{\partial z}\left(n_-\dfrac{\partial\varphi}{\partial z}\right) = k_-(n_0^2 - n_+n_-) \end{cases} \tag{3.90}$$

Introducing the sum of ion concentrations, $n_s = n_+ + n_-$, and the difference of ion concentrations, $n_d = n_+ - n_-$, the governing equations can be rewritten as

$$\begin{cases} \dfrac{\partial E}{\partial z} = \dfrac{e}{\epsilon}n_d \\ \dfrac{\partial}{\partial z}(n_sE) = 0 \\ e\mu\dfrac{\partial}{\partial z}(n_dE) = 2k_-\left[n_0^2 - \dfrac{1}{4}\left(n_s^2 - n_d^2\right)\right] \end{cases} \tag{3.91}$$

where $\mathbf{E} = -\frac{\partial\varphi}{\partial z}$ is the total electric field and $\mu = \frac{D}{k_BT}$ is the mobility of charged micelles. Integrating the second equation above basically requires that the electric current $\mathbf{J}_e$ should

be constant through out the electrolyte, i.e. $j_e = e^2\mu n_s E$. Since there are nonzero space charges comparing with original equations for the leaky dielectric systems [Eqn. 3.27], we would like to understand how the limited reaction rates in the weak electrolyte will affect equilibrium charge distribution.

3.9.3.1. Semi-infinite weak-electrolyte confined by one boundary. The first simple system is to consider the weak-electrolyte confined by a single boundary. This corresponds to the electrolyte in contact with a single planar electrode surface and extend to infinite in the other direction. Physically, it requires all quantities reduce to its bulk values at infinite:

$$n_d(\infty) = 0, n_s(\infty) = 2n_{eq}, E(\infty) = E_0 \tag{3.92}$$

where n_{eq} is the equilibrium concentration in the bulk and E_0 is the external electric field strength. By the conservation of electric currents, this gives that

$$j_e = e^2\mu n_s E = 2e^2\mu n_{eq} E_0 \tag{3.93}$$

Expressing both n_s and n_d in terms of the electric field E by substituting the Poisson's equation [Eqn. 3.91] and the above equation [Eqn. 3.93], we obtain the following nonlinear equation of the electric field:

$$\frac{\mathrm{d}^2E^2}{\mathrm{d}z^2} = \frac{4k_- n_{eq}^2}{\mu\epsilon}\left[1 - \frac{E_0^2}{E^2} + \frac{1}{E^2}\left(\frac{\epsilon}{4en_{eq}}\frac{\mathrm{d}^2E^2}{\mathrm{d}z^2}\right)^2\right] \tag{3.94}$$

Besides, in the strong field strength limit, all positive charge carriers should be depleted from the electrode surface ($z = 0$) assuming the applied electric field is along the positive

z direction ($E_0 > 0$), i.e.

$$n_+(0) = \frac{1}{2}\left[n_s(0) + n_d(0)\right] = 0 \tag{3.95}$$

which can be expressed in terms of electric fields as

$$\left[2n_{eq}\frac{E_0}{E(z)} + \frac{\epsilon}{e}\frac{\mathrm{d}E}{\mathrm{d}z}\right]_{z=0} = 0 \quad \text{i.e.} \quad \left.\frac{\mathrm{d}^2E^2}{\mathrm{d}z^2}\right|_{z=0} = -\frac{4en_{eq}E_0}{\epsilon} \tag{3.96}$$

The equation 3.91 is a second order ODE with an infinite interval, which can be solved numerically. However, it's more instructive to get further insights via the perturbation analysis before presenting its numeric results. Denote the first order perturbation as $u = E^2 - E_0^2$, it gives that

$$\frac{\mathrm{d}^2u}{\mathrm{d}z^2} = \frac{4k_-n_{eq}^2}{\mu\epsilon E_0^2}u + \mathcal{O}(u^2) \tag{3.97}$$

This equation permits solutions of exponential forms, which indicates that the perturbation due to the existence of electrode surface decays over a length scale defined as:

$$\lambda = \frac{E_0}{2n_{eq}}\sqrt{\frac{\mu\epsilon}{k_-}} = \frac{1}{2}\beta\ell \tag{3.98}$$

For clarity, this new length scale λ is split into another length scale $\ell = e\mu E_0/k_-n_{eq}$ and a dimensionless parameter $\beta = (k_-\epsilon/e^2\mu)^{1/2}$, which characterizes the relative rates of charge formation ($2k_-n_{eq}$) and charge relaxation ($2e^2\mu n_{eq}/\epsilon$). Assuming the diffusion-limited approximation (3.87) for the recombination rate constant k_-, these two rates are approximately equal, $\beta = \sqrt{2}$, as are the two length scales, $\ell/\lambda = \sqrt{2}$. For a 0.1 M

AOT/hexadecane solution subject to an external field of $E_0 = 5$ V/μm, this length is estimated to be $\lambda \approx 5$ μm. For comparison, the Debye length is $\lambda_D = (\epsilon k_B T/2e^2 n_{eq})^{1/2} \approx$ 0.2 μm.

The emergence of this new length scale λ brings us new insights about the system, which is also clearly confirmed by the numeric solutions [Fig. 3.6]. Note that the length scale is proportional to the external field strength E_0 and inversely proportional square root of the backward reaction rate $\sqrt{k_-}$. For a strong electrolyte or weak electric field strength, the length scale λ is small comparing with the Debye length λ_D. And the Debye length ($\lambda_D \sim$ 200 nm) is much smaller than the particle size ($a \sim$ 5 μm). Thus, the original assumptions of the leaky dielectric model [Sec. 3.3] are valid. However, as the experimental conditions push into the regime of strong electric fields, the length scale λ becomes much more significant, even comparable with the particle size (~ 5 μm). It means the electroneutrality condition is no longer valid near the electrode surface.

3.9.3.2. Finite weak-electrolyte confined by two boundaries. After realizing the existence of boundary layer near the electrode surface, a more experimentally relevant example is the case with two boundaries. Instead of confining by a single electrode, let's consider a weak-electrolyte confined by two electrode surfaces. Note that now the electric currents $\mathbf{J}_e$ is no longer determined by the values at infinity [Eqn. 3.93] and need to be determined later from the following potential difference condition:

$$\int_0^H E(z)\mathrm{d}z = E_0 H \tag{3.99}$$

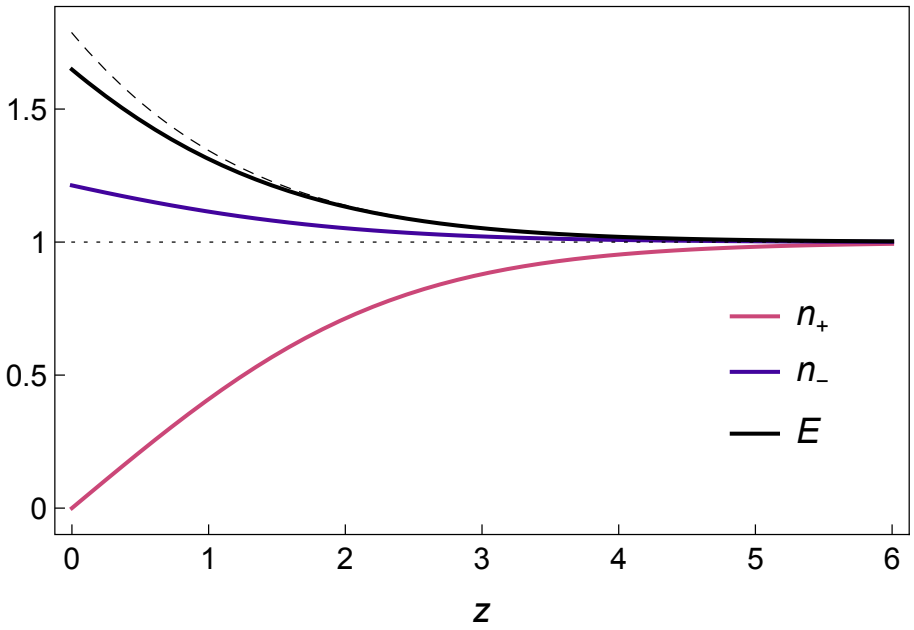

Figure 3.6. Number density of positive and negative charge carriers, n_+ and n_-, and the electric field E as a function of distance z from a planar electrode. Here, number densities are scaled by its equilibrium value n_{eq}, the field by the external field E_0, and position by the characteristic length λ [Eqn. 3.98]. The recombination parameter is $\beta^2 = 2$ corresponding to diffusion-limited recombination. The dashed curve shows the asymptotic prediction of the first order perturbation solution.

where H is the separation distance between two electrodes. Then, the governing equation of the electric fields in its dimensionless form becomes

$$\frac{\mathrm{d}^2 E}{\mathrm{d}z^2} = 1 - \frac{j_e^2}{4E^2} + \frac{\beta^2}{4E^2}\left(\frac{\mathrm{d}E^2}{\mathrm{d}z}\right)^2 \tag{3.100}$$

where the electric field is scaled by E_0, electric current is scaled by $e^2 \mu n_{eq} E_0$ and distance is scaled by the characteristic length λ. Corresponding boundary conditions at each electrode are:

$$\left.\frac{\mathrm{d}^2 E^2}{\mathrm{d}z^2}\right|_{z=0} = -\frac{j_e}{\beta} \quad \text{and} \quad \left.\frac{\mathrm{d}^2 E^2}{\mathrm{d}z^2}\right|_{z=H} = \frac{j_e}{\beta} \tag{3.101}$$

Figure 3.7 (left) shows the electric field and the charge carrier profiles for $H = 1$ and $\beta^2 = 2$. Due to the confined volume in which ions are generated, the associated current is only $j_e = 0.655$ as compared to $j_e = 2$ in the limit of large separations ($H \to \infty$). Figure 3.7 (right) shows the computed current density j_e as a function of the boundary separation H. For $H \ll 2$, the current is limited by the rate at which ions are generated within the electrolyte: $j_e \approx \beta L/2$. In dimensional units, the apparent conductivity of the electrolyte depends linearly the boundary separation as

$$\sigma = \frac{j_e}{E_0} \approx \frac{e k_- n_{eq}^2 H}{E_0} \quad \text{for} \quad H \ll 2\lambda \tag{3.102}$$

The diminishing conductivity for the strongly confined electrolyte has important implications for the Quincke particle under strong electric fields. As the Quincke particle is strongly attracted to the bottom electrode surface and only separated from the electrode by a thin lubrication layer, the gap region between the particle and electrode has limited generation of charge carriers and leads to a smaller conductivity comparing with the bulk conductivity.

3.10. From rolling to oscillating

After identifying the boundary layer near the electrode for the weak-electrolyte under strong electric fields, experiment conditions are systematically tested to map out the necessary conditions for the oscillating motion [Fig. 3.8].

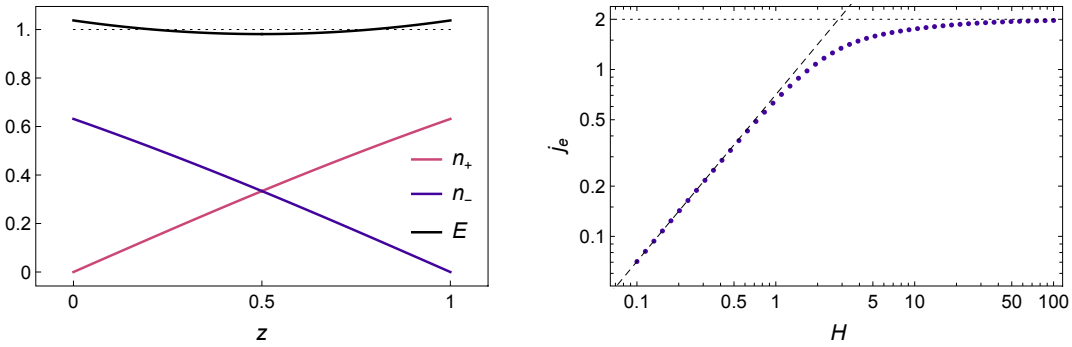

Figure 3.7. (left) Number density of positive and negative charge carriers, n_+ and n_-, and the electric field E as a function of position z between two electrodes separated by $H = 1$. Number densities are scaled by the equilibrium density n_{eq}, the field by the external field E_0, and position by the characteristic length λ. The recombination parameter is $\beta^2 = 2$ corresponding to diffusion-limited recombination. (right) Electric current density j_e (scaled by $e^2\mu n_{eq}E_0$) as a function of the boundary separation H. For small separations ($H \ll 2$), the current is $j_e \approx \beta H/2$; for large separations ($H \gg 2$), it approaches $j_e = 2$.

3.10.1. Phase diagram of observed Quincke particle dynamics

Oscillatory dynamics are reliably observed for strong fields, $E_0/E_c > 3$, when the ratio between the particle radius and the boundary layer thickness is of order unity, $a/\ell \sim 1$ [Fig. 3.8]. With all experiment conditions explored, the resulting boundary layer thickness ℓ varies from 1 to 20 μm depending on the AOT concentration and the external field strength E_0. Notably, large particles ($a/\ell \gg 1$) that extend beyond the boundary region do not oscillate but rather roll at even the highest fields investigated [Fig. 3.8, the line at top]. Small particles ($a/\ell \ll 1$) do not move at all and their otherwise Brownian motion is arrested upon application of the field [Fig. 3.8, the line at bottom].

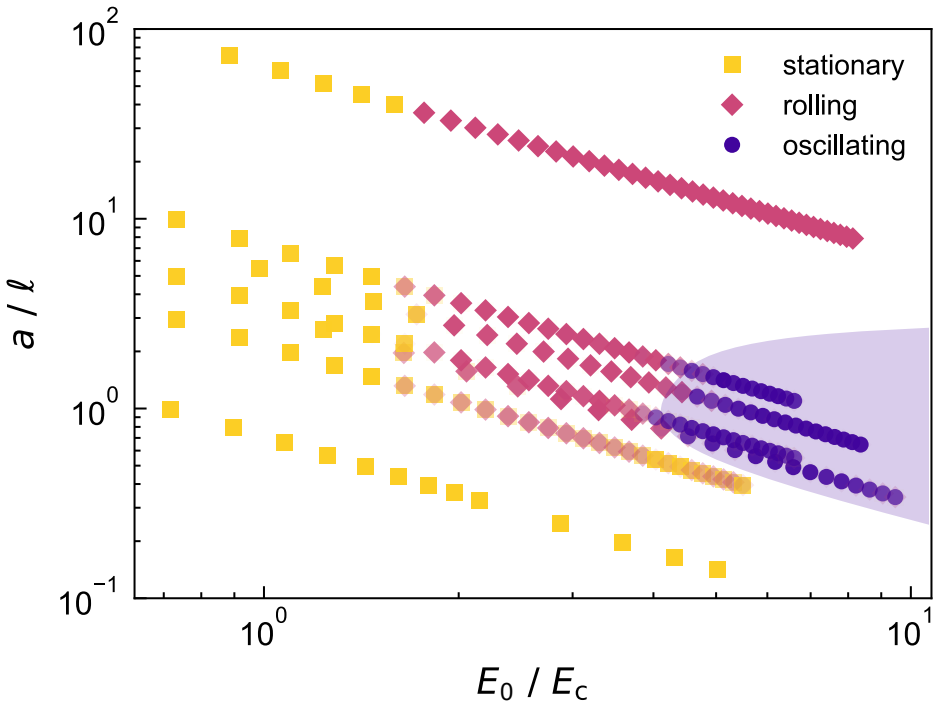

Figure 3.8. Phase diagram showing the observed dynamics as a function of two dimensionless parameters: a/ℓ, the ratio of the particle radius and the boundary layer thickness [Eqn. 3.98]; E_0/E_c, the ratio of the external field strength and the critical field [Eqn. 3.65]. Plotted data correspond to experiments on five different particle sizes $a = 0.5, 1.5, 2.5, 5, 25$ μm (for [AOT] = 150 mM) and three different AOT concentrations [AOT] $= 50, 100, 150$ mM (for $a = 5$ μm).

3.10.2. Characteristics of the oscillatory motions

The oscillation period ω^{-1} is comparable to the dipolar Maxwell-Wagner relaxation time τ^P_{mw} [Fig. 3.9 (a)] and the oscillation frequency ω increases with increasing field strength [Fig. 3.9 (b)]. The peak-to-peak amplitude of the oscillating particle position is approximately $2A \approx \pi a$ [Fig. 3.9 (c)]. This observed quantity is linearly related to the angle $2A/\kappa a$ by which the particle rotates during each half of the oscillation cycle. If one assumes frictional rolling with $\kappa = 1$, the observed amplitude would imply a rotation of

ca. 180°. By contrast, the assumption of hydrodynamic rolling with a thin lubricating film [**121**] requires that $\kappa \leq 1/4$ and implies a rotation of at least two revolutions per half cycle. Below, we present a model for particle oscillations that favors the former interpretation based on frictional rolling.

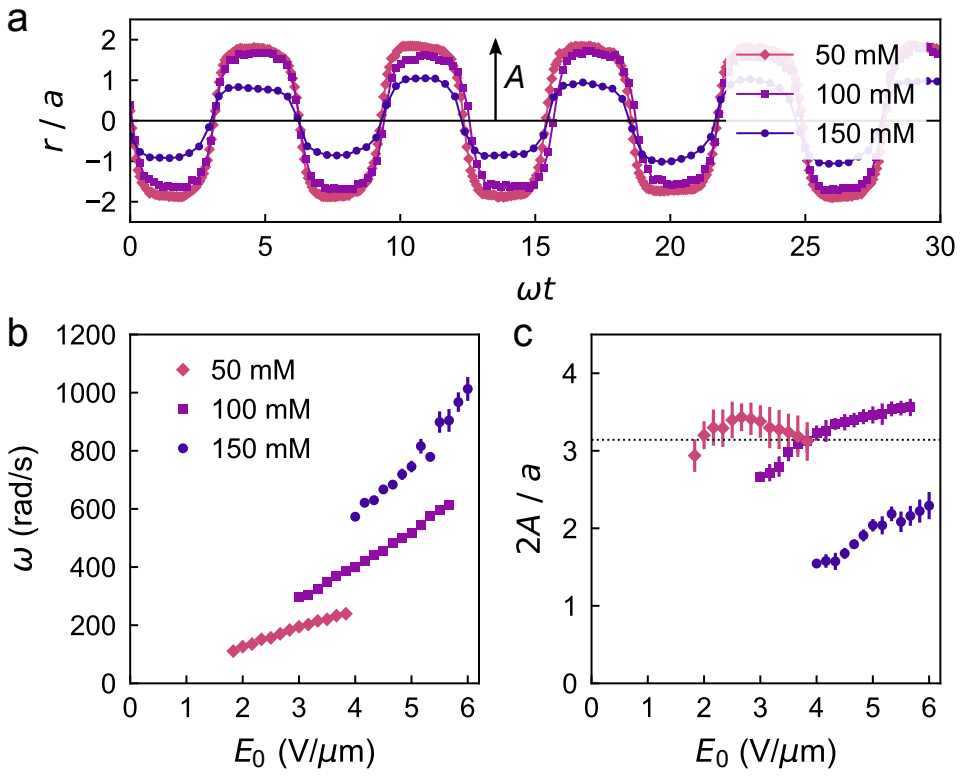

Figure 3.9. (a) Particle position r vs. time t for PS spheres (radius $a = 5\ \mu$m) in different AOT/hexadecane solutions. The applied field is $E_0/E_c = 5.4$, which corresponds to $E_0 = 2.2$, 3.7, and 4.8 V/μm for [AOT] =50, 100, and 150 mM, respectively. (b) Oscillation frequency ω vs. external field strength E_0 for different AOT concentrations. Markers denote the mean frequencies within populations of particle trajectories of equal duration; error bars denote standard deviations of these populations. (c) Peak-to-peak oscillation amplitude $2A$ vs. external field strength E_0 for the three AOT concentrations in (b). Markers denote the mean frequencies; error bars denote standard deviations.

3.10.3. Mechanism of the Quincke oscillations

To understand why particles of intermediate size oscillate near the electrode [Fig. 3.8], we first consider the transport of charged AOT micelles around a stationary sphere near a plane boundary [Fig. 3.10 (a) and (b)]. The electric field and the charge carrier densities are modeled using the Poisson-Nernst-Planck (PNP) equations [Eqn. 3.89] modified to describe the generation and recombination of charged micelles within the electrolyte [**118**, **142**]. At steady state, the solution is characterized by three length scales: the particle radius a, the Debye length $\lambda_D = (\epsilon_f k_B T/2e^2 n_o)^{1/2}$, and the boundary layer thickness ℓ associated with carrier recombination [Eqn. 3.98]. We focus our analysis on the limit of strong fields relevant to our experiments, for which $E_0 \gg k_B T/e\ell$ or, equivalently, $\ell \gg \lambda_D$.

Under these conditions, the behavior of large spheres ($a \gg \ell$) is well described by the leaky dielectric model. Charge accumulates at the particle surface as to redirect the electric field and the associated electric current around the particle [Fig. 3.10 (a)]. The Quincke instability is caused by the relaxation of this dipolar charge distribution via particle rotation [Sec. 3.6].

For small spheres ($a \ll \ell$), however, the accumulation of charge at the particle surface is mitigated by the diffusive-leaking of charge carriers around the sides [Fig. 3.10 (b)]. The comparatively little charge that accumulates does not significantly alter the electric field. Without a sufficiently large dipole moment directed anti-parallel to the external field, there is no Quincke rotation for these small particles [cf. Fig. 3.8]. Moreover, such

particles are characterized by a net charge that contributes additional electrostatic forces directed to the nearby electrode. The attraction of small particles to the electrode surface helps to explain the field-induced arrest of their Brownian motion.

For particles of intermediate size ($a \sim \ell$), the observed oscillations are explained by asymmetries in the rates of charging between the top and bottom of the particle. Within the confined region separating the particle and the electrode, ionic currents are limited by the finite rate of ion formation in the fluid. The effective conductivity within such a region of thickness δ can be approximated as $ek_{-}n_o^2\delta/E_0$, which is smaller than the bulk conductivity, $\sigma_f \approx 2e^2\mu n_o$, by a factor of $\ell/\delta \gg 1$. By modifying the leaky dielectric model to describe variations in the effective conductivity as a function of distance from the electrode surface, numerical simulations are able to reproduce the particle oscillations observed in experiment [Fig. 3.10 (c), pink diamonds & blue circles].

3.10.4. Simulation results of a single Quincke oscillator

In the model, we consider a dielectric sphere of radius a immersed in a conductive fluid at a distance δ from a plane electrode. Application of an external field E_0 drives the accumulation of charge at the particle-fluid interface; the effects of free charge within the electrolyte are neglected. The fluid conductivity is assumed to vary with distance z from the electrode as $\sigma_f z/(2a+\delta)$, approaching the bulk value σ_f at the top of the particle. The angular velocity of the particle (parallel to the plane) is linearly related to the electric torque as $\Omega = L/R$, where $R = 8\pi\eta a^3 f(\delta/a)$ is the relevant resistance coefficient. With these assumptions, the particle dynamics agree qualitatively with the

experimental observations [cf. Fig. 3.2 (c) & 3.10 (c)]. At sufficiently high field strengths—here, greater than 3.7 times the critical field E_c for an unbounded sphere—the particle oscillates back and forth with an peak-to-peak amplitude of ca. 200° [Fig. 3.10 (d)]. The oscillation frequency ω increases in proportion to the external field strength E_0 [Fig. 3.10 (e)].

3.11. Discussion and future works

Physically, particle oscillations combine the basic elements of the traditional Quincke mechanism—namely, charge accumulation and mechanical relaxation—with an added memory effect caused by anisotropic charging within the electric boundary layer, which is fundamentally different from the hydrodynamic memory effect [**153**–**158**] found in the transient Stokes flows. Additional experiments on particles of different shapes suggest that these Quincke oscillations can be achieved for any dielectric particle of suitable size [see [**107**] SI]. This mechanism may therefore provide a useful experimental model for active matter [**159**] comprised of many self-oscillating units, where particle interactions—neglected herein—mediate their collective dynamics. More generally, Quincke oscillations illustrate the potential importance of field-induced boundary layers within nonpolar fluids. Even away from electrode surfaces, such boundary layers are expected to influence the dynamics of micron-scale Quincke swimmers moving within bulk fluids [**116**, **160**–**162**].

It's rare to observe an oscillatory motion via a static field input and such Quincke oscillators might provide some inspirations for the design of colloidal oscillators with other types of active colloidal particles. With a oscillatory mobility unit, it's interesting to explore the collective behaviors of a population of colloidal oscillators [also see Sec.

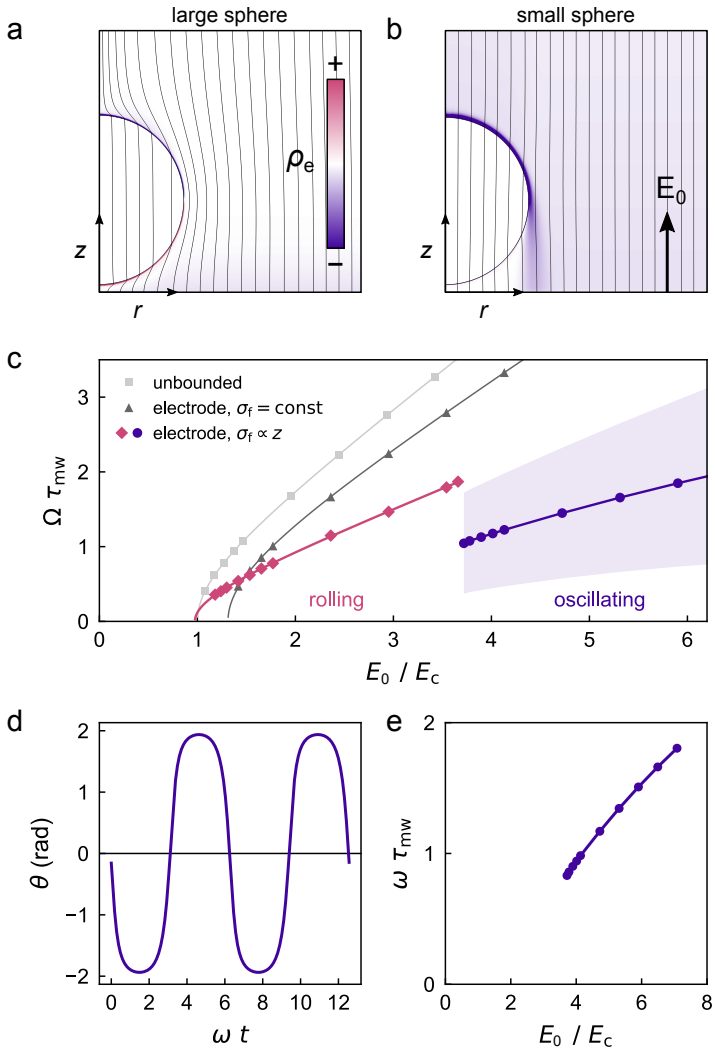

Figure 3.10. (a,b) Simulated electric field around a stationary sphere in a model electrolyte above a plane electrode; color map shows the charge density. The radii of the large (a) and small (b) spheres are $a/\ell = 3.5$ and $a/\ell = 0.14$, respectively. Other parameters include the Debye length $\lambda_D/\ell = 0.028$, the surface separation $\delta/a = 0.1$, the particle permittivity $\epsilon_p/\epsilon_f = 1.2$, and the recombination rate constant $k_-\epsilon_f/e^2\mu = 2$. (c) Time-averaged angular speed Ω scaled by τ_{mw}^{-1} vs. external field strength E_0 scaled by E_c for three variations of the leaky dielectric model: an unbounded sphere, a sphere at a plane electrode with constant fluid conductivity, and a sphere at an electrode with a conductivity gradient. The particle permittivity is $\epsilon_p/\epsilon_f = 1.5$; the surface separation is $\delta/a = 0.1$; the conductivity gradient is $\sigma_f/(2a+\delta)$; the resistance coefficient is $R/8\pi\eta a^3 = 1.45$. The shaded region denotes one standard deviation about the average speed. (d) Angular position θ vs. oscillation phase ωt for $E_0 = 5.3E_c$. (e) Oscillation frequency ω scaled by τ_{mw}^{-1} vs. external field strength E_0 scaled by E_c.

5.5], which might result in very different collective patterns commonly observed for a population of colloidal rollers.

CHAPTER 4

Hydrogel Robots*

4.1. Introduction

The design of miniature robots is an enormous challenge of science and engineering [**164**–**171**]. Building a microrobot, which integrates functionalities to sense its surrounding environment [**172**–**175**], communicate information [**176**–**178**] and actuate itself [**179**–**182**] to any targeted locations [**55**,**183**–**185**] with sustained power supply [**186**–**188**] in a controllable manner [**189**–**191**], is a long-term objective. Because microrobots are subject to the principles of microscopic physics, the mechanism to realize each functionalities differ from those counterparts of conventional large scale robots. Tremendous efforts have been made to successfully realize individual or a combination of those functionalities and shown great potential applications [**59**, **63**, **85**, **186**, **190**, **192**].

Throughout those investigations [**193**–**196**], soft materials have shown great advantages as building blocks of microrobots. Unlike conventional robots connect rigid parts via joints, soft materials allow to build microrobots as a whole, which reduce the complexity of manufacture and assembly. Besides, the unique mechanical properties of soft materials

*This chapter is primarily based on the published work [**163**] of Chuang Li*, Garrett C. Lau*, Hang Yuan*, Aaveg Aggarwal, Victor Lopez Dominguez, Shuangping Liu, Hiroaki Sai, Liam C. Palmer, Nicholas A. Sather, Tyler J. Pearson, Danna E. Freedman, Pedram Khalili Amiri, Monica Olvera de la Cruz† and Samuel I. Stupp†, **Fast and programmable locomotion of hydrogel-metal hybrids under light and magnetic fields**, *Science Robotics*, Vol. 5, No. 49, p.eabb9822, 2020, with modified notations and extended details to comply with the structure of this work.

permit morphological changes with large deformations, which enables flexible manipulations and versatile functions. The soft materials also show excellent bio-compatibility, which make them ideal for medical applications.

More importantly, nowadays it's possible to synthesize soft materials hybridized with various dimensional nanocomponts [**197**], enabling additional responsiveness to various external stimuli. This imparts living characteristics into passive materials and turn it into a microrobots. Like biological microrobots such as bacteria, the responsiveness to external stimuli offer venues to sense its local environment, harness power to actuate itself and carry controlled locomotion. Synthetic microrobots, which respond to heat [**198**, **199**], light [**200**], electric field [**179**, **201**, **202**], magnetic field [**203**, **204**], etc, has been reported and demonstrated similar functionalities of living organism. However, most of previous works focus on only one external stimulus. Inspiring by biological systems, a real microrobots should be able to respond to multiple external stimuli in a coordinated way. It motivates us to study possible design of a soft robot which has multiple responsiveness. Among those possible choices of external stimuli, we are particularly interested in light and magnetic fields because of its non-invasiveness in biological systems. Also, there are existing infrastructures commercially available to generate high temporal and spatial resolution of both light and magnetic fields. Therefore, we will focus on building a microrobots from soft materials which respond to both light and magnetic fields.

In recent years, it has been shown that magnetic fields can remotely direct motions of soft materials containing ferromagnetic components of various dimensions, such as filaments [**59**, **205**], slabs [**55**], 2D sheets [**191**, **204**] and 3D structures [**53**]. In these

examples, specific patterns of magnetization and object geometry were generated by various fabrication techniques, such as lithography, 3D printing and so on. However, once these samples have been prepared, the responsive magnetization profile cannot be reconfigured in the absence of a magnetic field. Moreover, the magnetic components were either embedded in a solid hydrophobic elastomer or supported on a rigid silicon nitride membrane. Hydrogels, which consist of mostly water, offer the possibility to function in water and also have the capacity to exchange fluids with aqueous environments. And hydrogels generally have small elastic moduli, which makes them a lot easier to deform comparing with elastomers. Besides magnetic response, light as a stimulus is useful since it can be delivered remotely and potentially in localized fashion. Recent examples of light responsive materials include polymer films containing cis-trans azobenzene switches [**206**] and hydrogels based on spiropyran chemistry [**207**, **208**] or molecular motors [**209**, **210**].

We report here on the development of hydrogel–metal hybrid materials that are actuated by magnetic fields after exposure to light and also remain reconfigurable by light to alter their magnetic response. This chapter starts with the design of a dual-responsive hydrogel-metal hybrid capable of responding to both light and magnetic fields and experimental characterizations of the materials [Sec. 4.2]. In order to understand the fundamental mechanisms of both light and magnetic responses, a continuum model of the hydrogel-metal hybrid is systematically developed in Sec. 4.3 and corresponding numeric implementation details are discussed in Sec. 4.4. With the understanding of dual-responsiveness to light and magnetic fields [Sec. 4.5], the hydrogel-metal hybrid can perform distinct tasks with remote control over geometry, stiffness, and magnetization using a combination of light and magnetic fields. More specifically, the samples are

prepared by incorporating aligned ferromagnetic nanowires into a photoactive hydrogel matrix that is capable of changing shape in response to light. Macroscopic deformations of the hydrogel upon light irradiation generate complex three-dimensional magnetization profiles that lead to programmable actuation. These hydrogels can perform functions such as walking [Sec. 4.6.1], steering [Sec. 4.6.2], climbing, and delivering cargo [Sec. 4.8] under the control of an external magnetic field and light. Furthermore, small changes in the chemical structure of these systems change the kinetics of light response and thus provide access to a broader range of actuating behaviors [Sec 4.7]. Sec. 4.9 summarizes the whole chapter and concludes with discussions and possible further development of the hydrogel robots.

4.2. Design of the dual-responsive hydrogel-metal hybrid

4.2.1. Synthesis and characterizations

To synthesize the hydrogel–metal samples, nickel (Ni) nanowires were added to a solution containing monomers, crosslinking agents, initiators and a polymerizable photo-switching spiropyran monomer in order to create a light-responsive crosslinked network [Fig. 4.1A, see [**163**] Fig. S2 and methods for synthetic details]. Under dark and acidic conditions, the photoswitch contains a hydrophilic protonated merocyanine (MCH^+) moiety that isomerizes to a hydrophobic spiropyran (SP) form upon exposure to visible light. This isomerization with light exposure results in contraction of the hydrogel due to dehydration, followed by expansion under dark conditions. The ferromagnetic nanowires were aligned under a static magnetic field and then fixed in this configuration by free-radical photopolymerization of the light-responsive hydrogel [Fig. 4.1A and B, also see [**163**] Figs.

S3-4]. Small-angle X-ray scattering (SAXS) confirmed the alignment of the nanowires, as shown by the radial integration of a 2D scattering intensity plot [Fig. 4.1C]. We measured a remnant magnetization of 260 emu/cm^3 parallel to the alignment of the nanowires and the coercive magnetic field required to reverse the magnetization of the sample was found to be 25 mT [Fig. 4.1D]. This is a 1.9-fold enhancement in the coercivity over bulk nickel (13 mT) [**211**], highlighting the utility of the shape anisotropy derived from the nanowire architecture ($\sim$8 μm long on average and 200 nm in diameter). In comparison, magnetization loops measured perpendicular to the alignment direction were noisy and exhibited a much lower magnetization, demonstrating the magnetic anisotropy of the composite material. Samples containing randomly oriented Ni nanowires did not show any macroscopic magnetic anisotropy [see [**163**] Fig. S5]. Also, when spherical Ni nanoparticles formed chained clusters during photopolymerization under a magnetic field, we did not detect any anisotropy since each individual particle can rotate to align its magnetization with the field [see [**163**] Fig. S6]. The magnetic anisotropy of the Ni nanowires was also confirmed by superconducting quantum interference device (SQUID) magnetometry with a rotating stage [see [**163**] Fig. S7]. This indicates that the shape of Ni nanowires is a critical structural feature responsible for the anisotropic magnetic properties of the Ni-hydrogel composites.

4.2.2. Response to light

The as-prepared hydrogel materials were soaked in acidic water for 40 min to obtain an equilibrated swollen state prior to photo-actuation experiments in a large water bath ($\sim$ 100 mL) that contained 5 mM HCl. Upon light exposure, this swollen state underwent

a shrinkage to about 84% of its original volume. Since the actuation occurs in acidic water, the SP1 hydrogel is capable of sequential actuation cycles that did not require additional HCl preconditioning. We found that the flat hydrogel object bends towards the light source upon irradiation from one side and recovers its original flat geometry in the dark. This bending–flattening process is highly reversible, and the hydrogel could maintain its photo-activity with the same maximum bending angle over at least ten cycles by switching the light on and off [see [**163**] Fig. S9].

4.2.3. Response to magnetic fields

Fig. 4.1E (left) shows the calculated water concentration gradient within a hydrogel slab [Sec. 4.3.3] and also the resultant deformation after the light exposure. The deformed light-induced bent geometry leads to a nonuniform 3D magnetization profile of the magnetic nanowires (indicated by the magenta arrows) with respect to the applied magnetic field. This change enables the arch-shaped hydrogel to respond to a spatially uniform external magnetic field $\mathbf{B}_{\text{ext}}$, but remains completely unresponsive in its flat state. Thus, the span of the arch-shaped hydrogel can be increased or decreased by simply applying a static magnetic field parallel or anti-parallel to the nanowires' alignment direction [Fig. 4.1E, right].

4.3. Continuum model of the hydrogel-metal hybrid

In order to understand the fundamental mechanism of the dual-responsiveness of the designed hydrogel-metal hybrid to both light and magnetic fields [Sec. 4.2 and Fig. 4.7 A-C], a continuum model is developed systematically based on elasticity theory [Sec. 4.3.2],

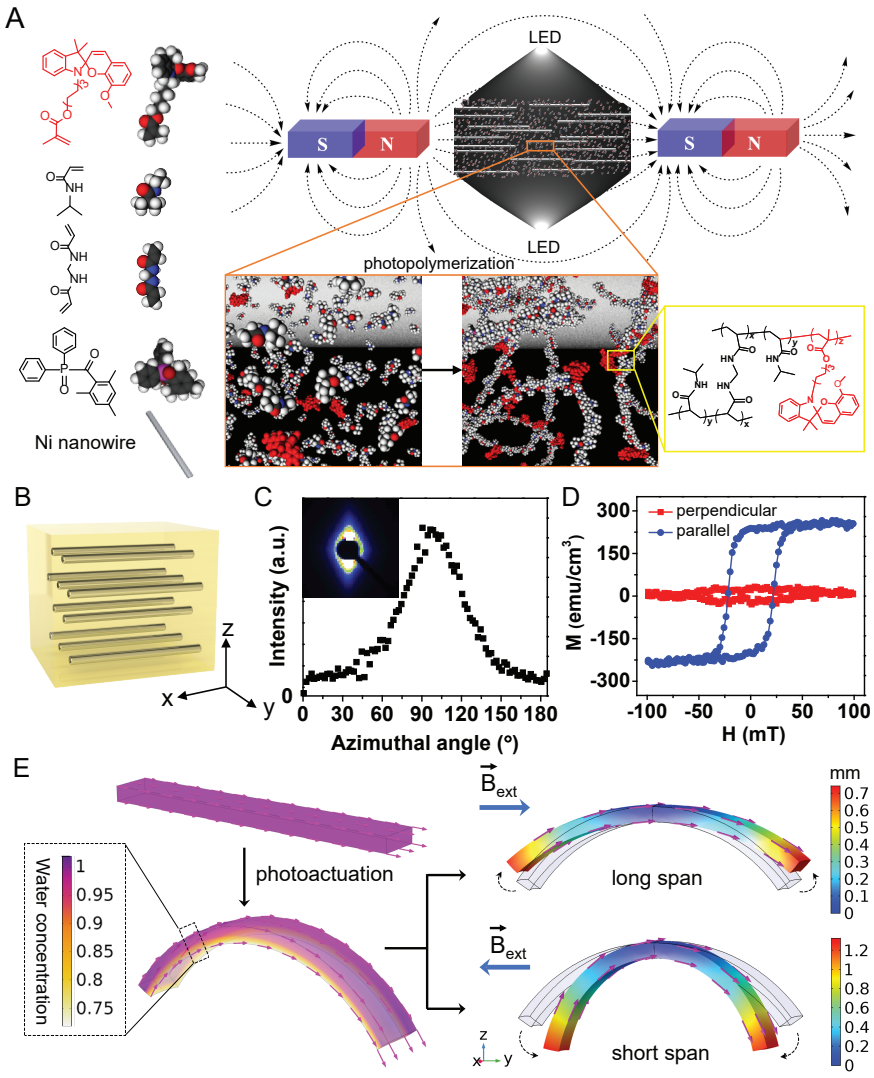

Figure 4.1. **Hydrogels designed for coupled response to light and magnetic fields.** (**A**) Schematic showing Ni nanowires aligned and fixed within a hydrogel network containing photoactive spiropyran moieties using a uniform magnetic field during free radical photopolymerization. (**B**) Schematic representation of aligned Ni nanowires (grey) immobilized in a hydrogel network (yellow). (**C**) Radial integration of 2D SAXS pattern (inset) revealing the macroscopic alignment of Ni nanowires within the hydrogel. (**D**) Magnetization loops parallel and perpendicular to the alignment axis of the nanowires. (**E**) Finite element calculation of the water concentration gradient and deformation in a slab of hydrogel exposed to light (left); finite element calculation of deformation as a result of magnetic field exposure in a hydrogel slab previously bent by light (right). Magenta arrows denote the magnetization of Ni nanowires; blue arrows indicate the direction of the external magnetic fields; dashed arrows represent the movement of both ends after applying magnetic fields; rainbow surface colors represent the deformations relative to its initial configurations (shaded regions).

polymer physics [Sec. 4.3.3] and magnetism [Sec. 4.3.4] to quantitatively describe the behaviors of the hydrogel-metal hybrid [Sec. 4.3.5].

4.3.1. Preliminaries of continuum mechanics

Here, some basic but essential concepts and terminologies related to continuum mechanics will be briefly introduced as the preparation for the development of the continuum model of the hydrogel-metal hybrid. Readers who are familiar with those concepts can skip to Sec. 4.3.2 directly.

4.3.1.1. coordinate systems. In order to describe the motion and deformation of a continuum body in a 3-dimensional space, two types of coordinate systems are commonly employed [**212**]:

(1) Material coordinates

In this coordinate system, each material particles are explicitly tracked. All material particles are labelled by upper case variables (X, Y, Z) in this work, which are uniquely identified by its position in the given initial configuration. Material coordinates are also called as *Lagrangian coordinates* or *reference coordinates*.

(2) Spatial coordinates

This is the physical space which contains the continuum body. In this work, lower case variables (x, y, z) are used to describe positions in this space. In this coordinate system, material particles constitute the continuum body are not labelled but a fixed observation position in the space is labelled by (x, y, z). Spatial coordinates are also called as *Eulerian coordinates*.

By the definition, spatial coordinates and material coordinates coincide with each other in the initial configuration, where displacements of each particles are zero. When the continuum body deforms due to external or internal forces, each material particles keeps its material coordinates but its spatial coordinates change with time and the following relation holds:

$$\mathbf{x} = \mathbf{x}(\mathbf{X}, t) = \mathbf{X} + \mathbf{u}(\mathbf{X}, t) \tag{4.1}$$

where $\mathbf{x}$ and $\mathbf{X}$ are the coordinates in the deformed and reference configuration, respectively; $\mathbf{u}$ is the displacement vector field, which connects the reference (undeformed) configuration with present (deformed) configuration.

4.3.1.2. strains. With the coordinates system defined, we are ready to quantitatively describe deformations of a continuum body. The first important quantity is the *deformation gradient tensor* $\boldsymbol{F}$, which is defined as following:

$$\boldsymbol{F} = \frac{\partial \mathbf{x}}{\partial \mathbf{X}} = \boldsymbol{\nabla} \mathbf{u} + \boldsymbol{I} \tag{4.2}$$

where $\boldsymbol{I}$ is the identity tensor and $\boldsymbol{\nabla}$ is the gradient operator.

The deformation gradient tensor $\boldsymbol{F}$ is generally an asymmetric tensor, which maps reference configuration to present configuration. For example, it describes how an infinitesimal line element is mapped from the reference configuration to the present configuration:

$$\mathrm{d}\mathbf{x} = \frac{\partial \mathbf{x}}{\partial \mathbf{X}} \mathrm{d}\mathbf{X} = \boldsymbol{F} \mathrm{d}\mathbf{X} \tag{4.3}$$

Here, $\boldsymbol{F}$ contains complete information about the local stretching and rotation of the line element. By *right* Polar Decomposition (PD) [**213**], the deformation gradient tensor $\boldsymbol{F}$ can be decomposed as:

$$\boldsymbol{F} = \boldsymbol{R}\boldsymbol{U} \tag{4.4}$$

where $\boldsymbol{R}$ is an unitary tensor ($\det(\boldsymbol{R}) = 1, \boldsymbol{R}^{-1} = \boldsymbol{R}^T$) and $\boldsymbol{U}$ is the *right* stretch tensor, which is positive-definite and symmetric. *Right* (*Left*) refers to the position of stretch tensor $\boldsymbol{U}$ is on the *right* (*left*) side of unitary tensor $\boldsymbol{R}$ and only *right* case decomposition will be shown here for illustration purpose.

Physically, $\boldsymbol{R}$ describes the rotation of system and all information about the deformation of the material is contained in the symmetric tensor $\boldsymbol{U}$. Then, the change of length of an infinitesimal line element is: $\mathrm{d}\mathbf{X} \cdot (\boldsymbol{F}^T\boldsymbol{F}\mathrm{d}\mathbf{X}) - \mathrm{d}\mathbf{X} \cdot \mathrm{d}\mathbf{X} = \mathrm{d}\mathbf{X}(\boldsymbol{F}^T\boldsymbol{F} - \boldsymbol{I})\mathrm{d}\mathbf{X}$, which gives the natural definitions of some deformation measures shown below.
The *right* Cauchy-Green (C-G) deformation tensor $\boldsymbol{C}$ is defined as:

$$\boldsymbol{C} = \boldsymbol{F}^T\boldsymbol{F} = \boldsymbol{U}^2 \tag{4.5}$$

and the Green-Lagrange (G-L) strain tensor $\boldsymbol{\epsilon}$ is defined as:

$$\boldsymbol{\epsilon} = \frac{1}{2}(\boldsymbol{C} - \boldsymbol{I}) = \frac{1}{2}(\boldsymbol{F}^T\boldsymbol{F} - \boldsymbol{I}) \tag{4.6}$$

Plugging in the definition of the deformation gradient tensor [Eqn. 4.2], it gives that

$$\epsilon_{ij} = \frac{1}{2}(u_{i,j} + u_{j,i} + u_{k,i}u_{k,j}) \tag{4.7}$$

The Einstein notation has been used, where repeated index means a summation over that index and the index after comma indicates the derivative with respect to that index, i.e. $u_{i,j} = \nabla_j u_i$.

Both $\boldsymbol{C}$ and $\boldsymbol{\epsilon}$ do not contain any information about rotation as $\boldsymbol{F}^T\boldsymbol{F} = \boldsymbol{U}^T\boldsymbol{R}^T\boldsymbol{R}\boldsymbol{U} = \boldsymbol{U}^2$. And the commonly used Engineering strain [**212**] is an approximation of the Green-Lagrange strain tensor $\boldsymbol{\epsilon}$ for small strains, i.e. $\epsilon_{ij} \approx \frac{1}{2}(u_{i,j} + u_{j,i})$.

4.3.1.3. stresses. Strains describe the state of a continuum body and we also need corresponding quantities to describe external and internal forces acting on such a continuum body, which are termed as stress tensors. The most well-known stress tensor is the Cauchy stress tensor [**214**] $\boldsymbol{\sigma}$, which is defined as:

$$\boldsymbol{\sigma} = \lim_{\Delta S \to 0} \frac{\Delta \mathbf{F}}{\Delta \mathbf{S}} \tag{4.8}$$

where both the force $\Delta\mathbf{F}$ and the area $\Delta\mathbf{S}$ are expressed in the spatial coordinates. However, it may or may not be convenient to measure forces and areas in the spatial coordinates. Thus, there are *first* Piola-Kirchhoff (P-K) stress tensor and *second* Piola-Kirchhoff (P-K) stress tensor:

(1) *first* P-K stress tensor $\boldsymbol{P}$

The force $\Delta\mathbf{F}$ is measured in the spatial coordinates but the area $\Delta\mathbf{S}$ is measured in the material coordinates. It's usually an asymmetric tensor connecting the spatial and material coordinates like the deformation gradient tensor $\boldsymbol{F}$.

(2) *second* P-K stress tensor $\boldsymbol{S}$

Both the force $\Delta\mathbf{F}$ and area $\Delta\mathbf{S}$ are measured in the material coordinates. Thus,

it's a symmetric tensor which resembles the Cauchy stress tensor $\boldsymbol{\sigma}$ but defined in the material coordinates instead.

All three stress tensors are related with each other via the deformation gradient tensor $\boldsymbol{F}$:

$$\boldsymbol{P} = \boldsymbol{F}\boldsymbol{S}, \quad \boldsymbol{\sigma} = J^{-1}\boldsymbol{P}\boldsymbol{F}^T = J^{-1}\boldsymbol{F}\boldsymbol{S}\boldsymbol{F}^T \tag{4.9}$$

where J is the determinant of the deformation gradient tensor, i.e. $J = \det \boldsymbol{F}$. All three stress tensors equivalently describe stresses applied on the continuum body in the view of different coordinates. It's important to note that the Cauchy stress tensor $\boldsymbol{\sigma}$ and *second* P-K stress tensor $\boldsymbol{S}$ are generally symmetric. This is a consequence of the conservation of local angular momentum. Whenever the considered object has asymmetric active or external stresses, all these stress tensors are not guaranteed to be symmetric.

4.3.1.4. equations of motion. With description of both strains and stresses of a continuum body, we are ready to connect them via the conservation of linear momentum (second Newton's law). The equations of motion (EOM) can be expressed in the material frame:

$$\rho_0 \frac{\partial^2 \mathbf{u}}{\partial t^2} = \mathbf{F}_V + \boldsymbol{\nabla}_{\mathbf{X}} \cdot \boldsymbol{P} \tag{4.10}$$

where ρ_0 is the density of material in the initial configuration, the volume force $\mathbf{F}_V$ has components in the present configuration but given with respect to the undeformed volume, $\boldsymbol{P}$ is the *first* P-K stress tensor and the divergence operator $\boldsymbol{\nabla}\cdot$ is computed with respect to material coordinates.

Similarly, the EOM can also be expressed in the more familiar spatial coordinates:

$$\rho \frac{\partial^2 \mathbf{u}}{\partial t^2} = \mathbf{f}_V + \boldsymbol{\nabla}_{\mathbf{x}} \cdot \boldsymbol{\sigma} \tag{4.11}$$

where ρ is the density of material in the deformed configuration, the volume force $\mathbf{f}_V$ has components in the present configuration given with respect to the deformed volume, $\boldsymbol{\sigma}$ is the Cauchy stress tensor and the divergence operator $\boldsymbol{\nabla}\cdot$ is computed with respect to spatial coordinates.

The EOM shown in 4.10 and 4.11 are termed as the strong form, which are elegant in theory but are not friendly for numeric computation since it requires a certain level of differentiability of involved quantities. Another equivalent description of EOM is based on the *principle of virtual works* [**215**], which states that the sum of the internal virtual work and the external work are equal. The internal virtual work is the work done by the current stress state on a variation in strains. The external virtual work is the work done by all external forces with the variation in displacement fields corresponding to the variation in strains. Mathematically, the virtual work $\delta\mathcal{W}$ can be written in the material coordinates as:

$$\delta\mathcal{W} = \int_V (-\delta\boldsymbol{\epsilon} : \boldsymbol{S} + \delta\mathbf{u} \cdot \mathbf{F}_V - \rho_0 \delta\mathbf{u} \cdot \mathbf{u}_{tt}) \, \mathrm{d}v + \int_{\partial V} (\delta\mathbf{u} \cdot \mathbf{F}_S) \, \mathrm{d}s \tag{4.12}$$

where δ means the functional variation, : indicates double contraction between two tensors, i.e. $\epsilon_{ij} S_{ij}$, ∂V denotes the boundary of volume V and $\mathbf{F}_S$ is the traction force at the boundary given with respect to undeformed area. All integrals are taken with respect to the undeformed configuration. Such integral description is termd as the weak form, which is equivalent to the strong form shown in Eqn. 4.10 and commonly employed in numeric

implementations [**216**].

4.3.1.5. material models. Only equations of motion (EOM) do not sufficiently define the continuum mechanics problems. To form a closure of the system of equations, a *constitutive relation* is necessary. Basically, a *constitutive relation* describes the responses of materials with deformations, i.e. $\boldsymbol{\sigma} = \boldsymbol{\sigma}(\boldsymbol{\epsilon})$. Because such responses are material-specific, different materials require different constitutive relations to describe their behaviors, which are so-called material models. This is the most empirical also the most diverse part in the entire elasticity theory. There are many material models proposed for different types of materials. For illustration purpose, the simplest one is for linear elastic solids:

$$\sigma_{ij} = E_{ijkl}\epsilon_{kl} \tag{4.13}$$

where $\boldsymbol{E}$ is a general fourth order elasticity tensor. For a homogeneous isotropic linear elastic solids, the elasticity tensor can be reduced as two independent scalar elastic moduli such as

$$\sigma_{ij} = K\delta_{ij}\delta_{kl} + G(\delta_{ik}\delta_{jl} + \delta_{il}\delta_{jk} - \frac{2}{3}\delta_{ij}\delta_{kl}) \tag{4.14}$$

where K is the bulk modulus and G is the shear modulus.

If the material does not exhibit significant dissipation of elastic energy and history-dependent behaviors, sometimes it's more convenient to express the responses of materials by a scalar elastic strain energy density $\mathcal{W}_{el}$. This type of material models are called

hyperelastic models, where stresses of the material are calculated as:

$$\boldsymbol{\sigma} = 2\frac{\partial \mathcal{W}_{el}(\boldsymbol{\epsilon})}{\partial \boldsymbol{\epsilon}} \tag{4.15}$$

For the case of linear elastic solids shown above, its equivalent constitutive relation expressed by an elastic strain energy density is:

$$\mathcal{W}_{el}(\boldsymbol{\epsilon}) = \frac{1}{2} E_{ijkl}\epsilon_{ij}\epsilon_{kl} \tag{4.16}$$

4.3.2. Elastic model — the standard reinforced model

With relevant basic concepts of continuum mechanics introduced in previous section [Sec. 4.3.1], the goal of this section is to develop a suitable *constitutive relation* which describes the elastic responses of the hydrogel-metal hybrid designed in Sec. 4.2. As a starting point, there are several experimental observations would be helpful for selecting appropriate material models:

(1) The deformations of hydrogel-metal hybrid is comparable to its thickness. This suggests that elastic theory of infinitesimal small strains is not applicable. Instead, elastic theory of finite strains should be used.

(2) Because of the existence of aligned Ni nanowires [Fig. 4.1 A-C], elastic properties of the hydrogel-metal hybrid are not isotropic. It suggests that at least one more elastic parameter is needed to characterize the additional anisotropic response.

(3) The hydrogel-metal hybrid develops intrinsic curvatures with the application of light [Fig. 4.1 E]. It suggests that the reference state of this elastic material is coupled with the photo-sensitive chemical processes. However, experiments [**163**]

show that changes of curvatures are relatively slow, which allow us to ignore the time-dependence of reference state and treat the elastic and light responses separately.

With all above considerations, the hyperelastic model [Sec. 4.3.1.5] is a good choice for modeling the elastic responses of the hydrogel-metal hybrid. For hyperelastic models, elastic responses are defined by its elastic strain energy density $\mathcal{W}_{el}$. Usually, the Cauchy-Green deformation tensor $\boldsymbol{C}$ is used to describe the current state of elastic materials (Other strain measures are also applicable). So, the elastic strain energy density can be expressed as a scalar function of the C-G deformation tensor, i.e. $\mathcal{W}_{el} = \mathcal{W}_{el}(\boldsymbol{C})$.

4.3.2.1. isotropic materials. To illustrate the idea clearer, it's helpful to consider a hyperelastic model for isotropic materials [**217**] first. Due to the isotropy of the material, the elastic strain energy density $\mathcal{W}_{el}$ should remain invariant under arbitrary rotations of the material, i.e.

$$\mathcal{W}_{el}(\boldsymbol{C}) = \mathcal{W}_{el}(\boldsymbol{Q}\boldsymbol{C}\boldsymbol{Q}^T), \quad \boldsymbol{Q} \in \mathrm{SO}(3) \tag{4.17}$$

where $\boldsymbol{Q}$ denotes a rotation matrix and SO(3) is the group of all rotations about the origin of three-dimensional Euclidean space $\mathbb{R}^3$. Such symmetry condition requires that the energy density function $\mathcal{W}_{el}$ must be a function of *rotational invariants* of $\boldsymbol{C}$. Three most commonly used independent rotational invariants of C-G tensor are:

$$I_1 = \mathrm{Tr}\boldsymbol{C}, \quad I_2 = \frac{1}{2}\left[(\mathrm{Tr}\boldsymbol{C})^2 - \mathrm{Tr}(\boldsymbol{C}^2)\right], \quad I_3 = \det \boldsymbol{C} \tag{4.18}$$

Sometimes, it's convenient to splits the deformation gradient tensor $\boldsymbol{F}$ into the volumetric and isochoric components, i.e. $\boldsymbol{F} = \boldsymbol{F}_{vol}\boldsymbol{F}_{iso}$, where $\det \boldsymbol{F}_{vol} = \det \boldsymbol{F} = J$ and $\det \boldsymbol{F}_{iso} = 1$. Then, the isochoric deformation gradient tensor is $\boldsymbol{F}_{iso} = J^{-1/3}\boldsymbol{F}$ and the isochoric C-G strain tensor is $\boldsymbol{C}_{iso} = J^{-2/3}\boldsymbol{C}$, which give the corresponding isochoric rotational invariants as:

$$\bar{I}_1 = \mathrm{Tr}(\mathbf{C}_{iso}) = J^{-2/3}I_1, \quad \bar{I}_2 = J^{-4/3}I_2, \quad \bar{I}_3 = 1 \tag{4.19}$$

Therefore, the elastic strain energy density for isotropic materials should be a function of above three invariants:

$$\mathcal{W}_{el} = \mathcal{W}_{el}(\bar{I}_1, \bar{I}_2, \bar{I}_3) \tag{4.20}$$

Above symmetry argument is not enough for determining the exact functional form of the strain energy density. The next step is to get the functional form in terms of these invariants [Eqn. 4.18], no matter by mathematical considerations (Mooney-Rivlin model) or by experimental measurements (Yeoh and Ogden model). The simplest model for hydrogels derived from its microscopic structure is the Neo-Hookean (N-H) model [**218**, **219**]:

$$\mathcal{W}_{el} = \frac{1}{2}G(\bar{I}_1 - 3) + \frac{1}{2}K(J-1)^2 \tag{4.21}$$

where G is the shear modulus and K is the bulk modulus. The shear modulus G can be connected with properties of hydrogels by $G = Nk_BT$, where N is the number of polymer chains per unit volume, k_B is the Boltzmann constant and T is the temperature. Please

be aware that the above model is only valid for nearly-incompressible materials and the effect of entropy need to be included for compressible hydrogels [**220**].

4.3.2.2. transversely isotropic materials. Next, let's consider isotropic materials with embedded aligned micro-fibers [Fig. 4.1]. Obviously, such materials have less symmetry comparing with fully isotropic materials. The alignment direction of micro-fibers define a local direction, which is denoted as $\mathbf{a}$. Then, the state of system is fully described by C-G deformation tensor $\boldsymbol{C}$ and fibers alignment direction vector $\mathbf{a}$ and the elastic strain energy density should be a function of both, i.e. $\mathcal{W}_{el} = \mathcal{W}_{el}(\boldsymbol{C}, \mathbf{a})$.

Although the existence of fibers breaks the isotropy of materials, materials are still isotropic perpendicular to the fibers' direction or transversely isotropic for short. The elastic strain energy $\mathcal{W}_{el}$ should be invariant for arbitrary rotations around fibers' direction:

$$\mathcal{W}_{el}(\boldsymbol{C}, \mathbf{a}) = \mathcal{W}_{el}(\boldsymbol{Q}\boldsymbol{C}\boldsymbol{Q}^T, \boldsymbol{Q}\mathbf{a}), \quad \boldsymbol{Q} \in \mathrm{SO}(2) \otimes \mathbf{a} \tag{4.22}$$

where $\boldsymbol{Q}$ denotes a rotation matrix and SO(2) is the group of all rotations about the origin of two-dimensional Euclidean space $\mathbb{R}^2$. $\mathrm{SO}(2) \otimes \mathbf{a}$ denotes all rotations around the axis defined by $\mathbf{a}$. Mathematically, besides the three rotational invariants defined for fully isotropic case [Eqn. 4.18], there are two more independent rotational invariants can be constructed [**221**] and their command choices are:

$$I_4 = \mathbf{a} \cdot (\boldsymbol{C}\mathbf{a}), \quad I_5 = \mathbf{a} \cdot (\boldsymbol{C}^2\mathbf{a}) \tag{4.23}$$

And corresponding isochoric invariants can be similarly defined [Eqn. 4.19]:

$$\bar{I}_4 = J^{-2/3} I_4, \quad \bar{I}_5 = J^{-4/3} I_5 \tag{4.24}$$

Thus, the general form of elastic strain energy density for a transversely isotropic material can be written as:

$$\mathcal{W}_{el} = \mathcal{W}_{el}(\bar{I}_1, \bar{I}_2, \bar{I}_3, \bar{I}_4, \bar{I}_5) \tag{4.25}$$

It's pretty complicated to include all possible invariants and determine the exact functional form of $\mathcal{W}_{el}$. Fortunately, previous works [**221**] show that not all of these invariants are equally important to capture essential behaviors of fiber-reinforced materials. The simplest one is the so-called *standard reinforcement model* [**221**]:

$$\mathcal{W}_{el} = \frac{1}{2} G(\bar{I}_1 - 3) + \frac{1}{2} \gamma G(\bar{I}_4 - 1)^2 + \frac{K}{2}(J-1)^2 \tag{4.26}$$

where γ is a parameter which reflects stiffness caused by aligned fibers. This model is almost the same as the N-H model [Eqn. 4.21] except one additional term (second term) which describes the anisotropic elastic responses of such transversely isotropic materials.

4.3.3. Light-responsive hydrogel model

In addition to the pure elastic responses [Sec. 4.3.2], the underlying elastic medium of the designed hydrogel-metal hybrid [Sec. 4.2] is a light-responsive hydrogel [Fig. 4.1 A]. In order to describe its light-induced deformation, appropriate light-response model is needed.

4.3.3.1. Photochemistry. Upon light radiation, the spiropyran chromophores grafted on the polymer chains of the hydrogels undergo a chemical reaction from hydrophilic protonated merocyanine (MCH^+) form to hydrophobic spiropyran (SP) form:

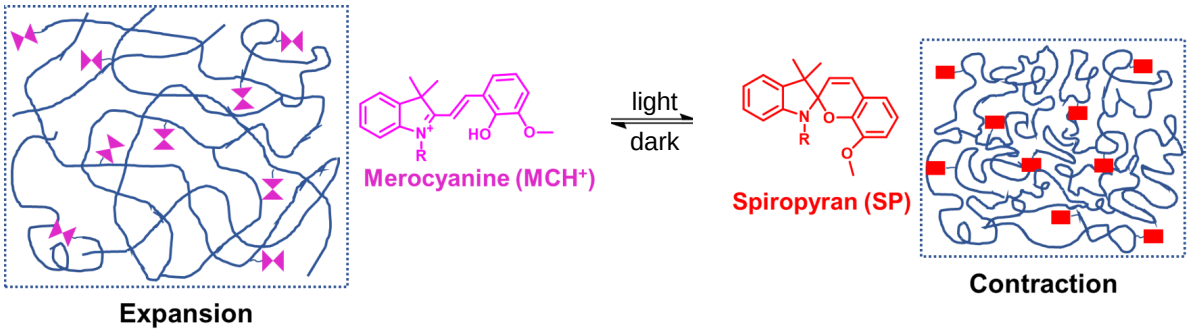

Figure 4.2. Photochemical reaction of spiropyran chromophores, whose hydrophilic protonated merocyanine (MCH^+) form converts to hydrophobic spiropyran (SP) form upon the light radiation. And such photochemical reaction can be reversed in the dark condition.

The reaction rate equation of above photochemical reaction can be expressed:

$$\frac{\partial r_{sp}}{\partial t} = k_+(I) r_{mch^+} - k_- r_{sp} \tag{4.27}$$

where r_{sp} and r_{mch^+} are the fractions of chromophores in SP and MCH^+, respectively. k_+ and k_- are the forward and backward reaction rate constant. More specifically, k_- refers to the ring-opening process, which is usually a constant value at a given substituent, temperature and pH [**222**]; While k_+ refers to the ring-closing process, which is dependent on the incident light intensity I. For an unidirectional and monochromatic light source of angular frequency ω, the light intensity dependence of k_+ can be written as [**223**]:

$$k_+ = \frac{\psi_{\omega,mch^+}}{\hbar\omega} \epsilon_{\omega,mch^+} I \tag{4.28}$$

where ψ_{ω,mch^+} and ϵ_{ω,mch^+} are the quantum yield (number of reactions per photon) and molar absorptivity of the MCH^+ chromophore, respectively. $\hbar$ is the reduced Planck constant. For the steady state ($\frac{\partial r_{sp}}{\partial t} = 0$), the equilibrium concentration of SP chromophores is

$$r_{sp} = \frac{k_+(I)}{k_+(I) + k_-} \tag{4.29}$$

4.3.3.2. light propagation. As light propagates across a medium, the light can be absorbed, scattered and diffracted , etc., which generally results in a reduction of light intensity. Here, the Beer–Lambert (B-L) law is employed to describe the attenuation of light and the light intensity distribution for a monochromatic light traveling along z-direction is given by:

$$\frac{\mathrm{d}I(z)}{\mathrm{d}z} + k_\omega I = 0 \tag{4.30}$$

where k_ω denotes the overall light absorption coefficient. The decay of the light intensity in a photo-responsive hydrogel results from two major contributions [**223**]: the absorption of light by the photochemical reaction and the absorption of light by the hydrogel' polymer matrix. Then, the overall light absorption coefficient can therefore be expressed as:

$$k_\omega = \frac{k_{gel}}{J} + k_{\omega,sp} \tag{4.31}$$

where k_{gel} denotes the absorption of light by the dry polymer matrix, which is rescaled by J ($= \det\boldsymbol{F}$) due to the volumetric changes; $k_{\omega,sp}$ is the absorption of light due to the

SP photochemical reaction, which depends on the concentration of MCH^+ chromophores:

$$k_{\omega,sp} = \epsilon_{\omega,mch^+} r_{mch^+} \left(\frac{f\phi}{V_m N_A} \right) \tag{4.32}$$

where ϕ is the volume fraction and f is the fraction of monomers containing a chromophore; V_m is the volume of a chromophore; N_A is the Avogadro constant.

4.3.3.3. light-responsive hydrogel. Comparing with a usual elastic materials described in Sec. 4.3.2, a hydrogel has additional contributions in two primary aspects:

(1) A hydrogel is basically a network of polymer chains, which interaction with environmental solvent molecules;

(2) The chromophore molecules grafted on the hydrogel provide its light responsiveness, which also modifies the hydrophobicity of polymer chains ($MCH^+ \leftrightarrow SP$) with surrounding solvent molecules.

The Flory–Huggins (F-H) model [**219**, **224**–**226**] provides a description of interaction energy of a hydrogel with its surrounding solvents molecules as:

$$U_{mix} = \frac{k_B T}{V_m} \left[(1-\phi)\ln(1-\phi) + \chi\phi(1-\phi) \right] \tag{4.33}$$

where χ describes the interaction between hydrogel monomers and solvent molecules, V_m is the volume of the hydrogel monomer, ϕ is the volume fraction, k_B is the Boltzmann constant and T is the temperature.

As for the energy contribution due to the chromophores, a simple model similar to the F-H model is proposed, which express the additional contribution due to the hydrogel's

interaction with light as:

$$U_{photo} = \frac{zf}{V_m} r_{sp}(u_{sw} - u_{mw})\phi(1-\phi) \tag{4.34}$$

where u_{sp} and u_{mw} denotes the interaction energy of SP and MCH^+ with solvent molecules, respectively; z is a parameter (coordinate number, which is 6 in 3D) of the F-H model.

Finally, both interaction energies U_{mix} and U_{photo} can be rescaled by its volume fraction ϕ which yields the corresponding energy densities as $\mathcal{W}_{mixing} = U_{mix}/\phi$ and $\mathcal{W}_{photo} = U_{photo}/\phi$. Combining with the passive elastic energy density $\mathcal{W}_{el}$ [Eqn. 4.26], it provides a theoretical description of the light-responsive hydrogel within the framework of hyperelastic model [Sec. 4.3.1.5] as:

$$\mathcal{W}_{gel} = \mathcal{W}_{el} + \mathcal{W}_{mix} + \mathcal{W}_{photo} \tag{4.35}$$

4.3.4. Magnetic model — the ideal hard magnet

Besides its elastic responses [Sec. 4.3.2] and light responses [Sec. 4.3.3], another *constitutive relation* is needed to describe its magnetic responses because of the dual responsiveness of the hydrogel-metal hybrid [Fig. 4.1]. The Ni nanowires embedded in the hydrogel interacts with magnetic fields imposed by an external magnet. As the time-varying effects are negligible and no free-currents exist in the experimental setup, the Maxwell's equations for the magnetostatics [**129**] is sufficient to describe the relevant magnetic phenomena:

$$\begin{cases} \boldsymbol{\nabla} \times \mathbf{H} = 0 \\ \boldsymbol{\nabla} \cdot \mathbf{B} = 0 \end{cases} \tag{4.36}$$

where $\mathbf{H}$ is the magnetic field strength and $\mathbf{B}$ is the magnetic flux density. As the magnetic field strength $\mathbf{H}$ is curl-free, a magnetic scalar potential φ_m can be introduced:

$$\mathbf{H} = -\boldsymbol{\nabla}\varphi_m + \mathbf{H}_b \tag{4.37}$$

where the background magnetic field $\mathbf{H}_b$ is explicitly split out for convenience. The above equation automatically satisfies the curl-free condition and the problem reduced to solve for a scalar potential function analogous to the electrostatics problems.

Similar to elastic problems [Sec. 4.3.1.5], a material model $\mathbf{B} = \mathbf{B}(\mathbf{H})$ is needed to complete the system of equations for magnetostatics. The magnetic hysteresis curve of Ni nanowires is measured in experiments [Fig. 4.3], which gives the relationship between $\mathbf{B}$ and $\mathbf{H}$. Since the imposed external magnetic field strength is relatively weak (≤ 16 mT), the magnetic responses of Ni nanowires stay in the linear response regime (red dash line in Fig. 4.3) and can be treat as *ideal hard magnets* for simplicity, i.e.

$$\mathbf{B} = \mu_r\mu_0\left(\mathbf{H} + \mathbf{M}_0\right) \tag{4.38}$$

where μ_r is the relative magnetic permeability of Ni nanowires, μ_0 is the absolute magnetic permeability of vacuum and $\mathbf{M}_0$ is the residual magnetization. Please be aware that $\mu_r\mu_0$ should choose the magnetic permeability of Ni nanowires ($\sim 3.58 \times 10^{-5}$ H/m [**163**]) only if the whole composite consists of pure Ni nanowires. However, in the design of our hydrogel-metal hybrid, the weight percent of Ni nanowires is only about 0.5% and most content is essentially water, which is non-magnetizable. Therefore, the magnetic permeability of the hydrogel-metal hybrid should be close to vacuum, i.e. $\mu_r \sim 1$.

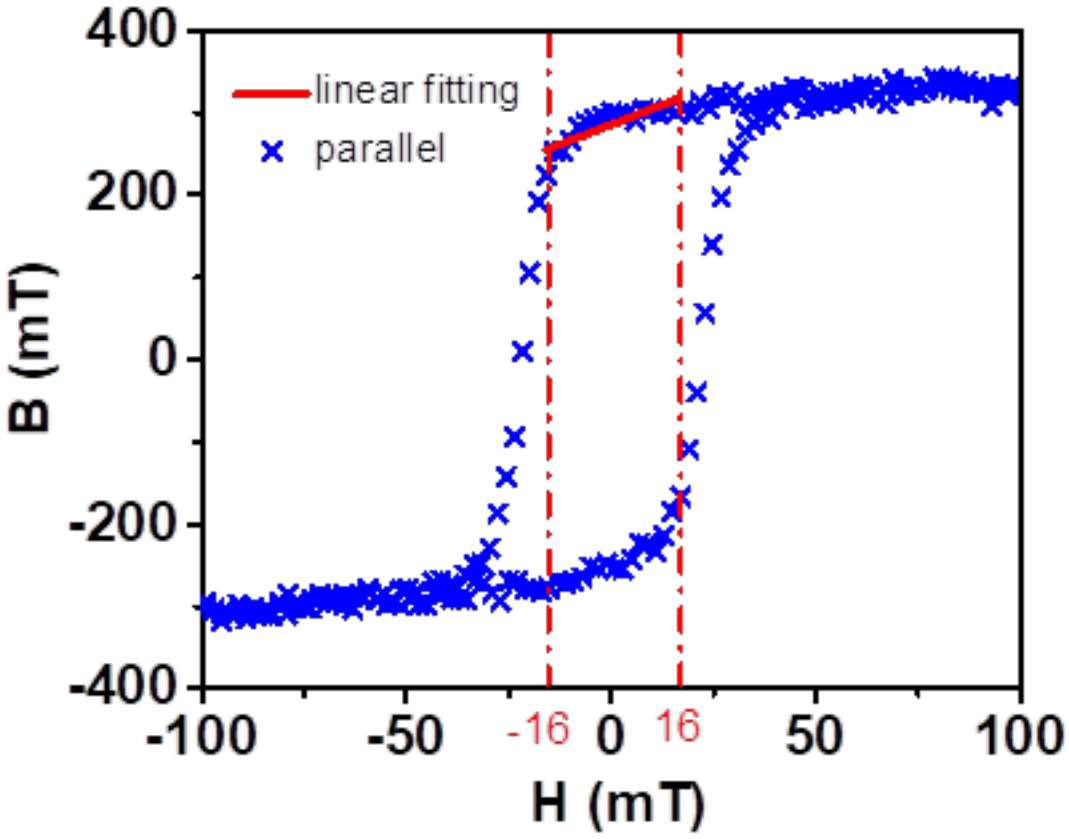

Figure 4.3. Hysteresis curve parallel to the alignment of Ni nanowires (blue cross). A linear fitting is shown by red line within the operational range (between two vertical red lines) of the magnetic field strength.

4.3.5. Magnetoelastic model

So far, both elastic and magnetic responses of the hydrogel-metal hybrid [Sec. 4.3.2 and 4.3.4] have been treat separately. However, apparently, there exists coupling between elastic and magnetic responses. The magnetization of Ni nanowires interacts with magnetic fields **B**, which creates magnetic torques on the nanowires. Because the nanowires are fixed within the hydrogel, these magnetic torques cause elastic stresses on the hydrogel matrix

and result in macroscopic deformations. To include the coupling between magnetism and elasticity, it's tempting to simply add the magnetic fields dependence into the elastic energy, i.e. $\mathcal{W}_{el} = \mathcal{W}_{el}(\boldsymbol{C}, \mathbf{a}, \mathbf{B})$ and construct invariants [**227**] following previous symmetry arguments [Sec. 4.3.2]. However, it's important to notice that the hydrogel-metal hybrid under an external magnetic field is not even transversely isotropic as the magnetic external field defines another preferred direction, which further reduces the symmetry of the whole system. It clearly that the hydrogel-metal hybrid has different energies when the external magnetic field is imposed in different directions. In other words, unlike the pure elastic strain free energy $\mathcal{W}_{el}$ [Eqn. 4.26], the total magnetoelastic energy of the system is orientation dependent, which implies that the C-G deformation tensor $\boldsymbol{C}$ is not sufficient for fully characterizing the current state of the system because $\boldsymbol{C}$ does not contain any information about rotation [Sec. 4.3.1.2]. In order to preserve orientational information of the system, a more fundamental strain measure quantity ($\boldsymbol{C} = \boldsymbol{F}^T\boldsymbol{F}$), the deformation gradient tensor $\boldsymbol{F}$, should be used instead. It suggests that the additional magnetic energy density function $\mathcal{W}_m$ should be a function of the deformation gradient tensor $\boldsymbol{F}$ and magnetic flux density $\mathbf{B}$ (or magnetic field strength $\mathbf{H}$), i.e. $\mathcal{W}_m = \mathcal{W}_m(\boldsymbol{F}, \mathbf{B})$.

We assume that Ni nanowires move with the hydrogel matrix without slipping. Then, the magnetization in the deformed configuration is $\boldsymbol{F}\mathbf{M}/J$, where $\mathbf{M}$ denotes the magnetization in the reference configuration. Ignoring the higher order energy contributions from $\mathbf{M}$ and $\mathbf{B}$, the magnetic energy density in the deformed configuration can be written as $-(\boldsymbol{F}\mathbf{M}/J)\cdot\mathbf{B}$. Therefore, the magnetic energy density $\mathcal{W}_m$ in the reference configuration

can be expressed as:

$$\mathcal{W}_m = -J(\boldsymbol{F}\mathbf{M}/J)\cdot\mathbf{B} = -\boldsymbol{F}\mathbf{M}\cdot\mathbf{B} \tag{4.39}$$

Adding the elastic energy density [Eqn. 4.26] and the magnetic energy density [Eqn. 4.39] together, the total magnetoelastic energy density $\mathcal{W}_{me}$ can be written as:

$$\mathcal{W}_{me} = \frac{1}{2}G(\bar{I}_1 - 3) + \frac{1}{2}\gamma G(\bar{I}_4 - 1)^2 + \frac{K}{2}(J-1)^2 - \boldsymbol{F}\mathbf{M}\cdot\mathbf{B} \tag{4.40}$$

This magnetoelastic energy density function defines the *constitutive relation* of the fiber-reinforced magnetoelastic materials, which can be shown explicitly by calculating corresponding stresses.

4.3.5.1. elastic stresses. For calculating elastic stresses, it's convenient to split elastic energy density function $\mathcal{W}_{el}$ into volumetric and isochoric parts for nearly-impressible materials:

$$\mathcal{W}_{el} = \mathcal{W}_{el}^{iso} + \mathcal{W}_{el}^{vol} \tag{4.41}$$

where the isochoric and volumetric elastic strain energy density are defined as

$$\mathcal{W}_{iso} = \frac{1}{2}G(\bar{I}_1 - 3) + \frac{1}{2}\gamma G(\bar{I}_4 - 1)^2, \quad \mathcal{W}_{vol} = \frac{1}{2}K(J-1)^2 \tag{4.42}$$

Then, the *second* P-K elastic stress tensor is calculated by taking derivatives with respect to the C-G strain tensor:

$$\boldsymbol{S}_{el} = 2\frac{\partial \mathcal{W}_{el}}{\partial \boldsymbol{C}} = 2\frac{\partial \mathcal{W}_{el}^{iso}}{\partial \bar{I}_1}\frac{\partial \bar{I}_1}{\partial \boldsymbol{C}} + 2\frac{\partial \mathcal{W}_{el}^{iso}}{\partial \bar{I}_4}\frac{\partial \bar{I}_4}{\partial \boldsymbol{C}} + 2\frac{\partial \mathcal{W}_{vol}}{\partial J}\frac{\partial J}{\partial \boldsymbol{C}} \tag{4.43}$$

The derivatives of energy density functions with respect to the isochoric invariants are straightforward to compute:

$$\frac{\partial \mathcal{W}_{el}^{iso}}{\partial \bar{I}_1} = \frac{1}{2}G, \quad \frac{\partial \mathcal{W}_{el}^{iso}}{\partial \bar{I}_4} = \gamma G(\bar{I}_4 - 1), \quad \frac{\partial \mathcal{W}_{el}^{vol}}{\partial J} = K(J-1) \tag{4.44}$$

By the chain rules, the derivatives of the isochoric invariants [Eqn. 4.19] with respect to the C-G strain tensor are:

$$\begin{aligned} \frac{\partial \bar{I}_1}{\partial \boldsymbol{C}} &= \frac{\partial (J^{-2/3} I_1)}{\partial \boldsymbol{C}} = -\frac{2}{3} J^{-5/3}\frac{\partial J}{\partial \boldsymbol{C}} I_1 + J^{-2/3}\frac{\partial I_1}{\partial \boldsymbol{C}} \\ \frac{\partial \bar{I}_4}{\partial \mathbf{C}} &= \frac{\partial (J^{-2/3} I_4)}{\partial \boldsymbol{C}} = -\frac{2}{3} J^{-5/3}\frac{\partial J}{\partial \boldsymbol{C}} I_4 + J^{-2/3}\frac{\partial I_4}{\partial \boldsymbol{C}} \\ \frac{\partial J}{\partial \boldsymbol{C}} &= \frac{\partial I_3}{\partial \boldsymbol{C}} = \frac{\partial \det \boldsymbol{C}}{\partial \boldsymbol{C}} \end{aligned} \tag{4.45}$$

It still needs derivatives of invariants [Eqn. 4.18] with respect to the C-G strain tensor:

$$\frac{\partial I_1}{\partial \boldsymbol{C}} = \frac{\partial C_{KK}}{\partial C_{IJ}} = \boldsymbol{I}, \quad \frac{\partial I_4}{\partial \boldsymbol{C}} = \frac{\partial C_{KL} a_K a_L}{\partial C_{IJ}} = \mathbf{a} \otimes \mathbf{a} \tag{4.46}$$

The derivative of J with respect to $\boldsymbol{C}$ is more difficult to calculate as the determinant operator is a nonlinear function. By using the linearization of the determinant of a tensor [**228**], it gives that:

$$\frac{\partial I_3}{\partial \boldsymbol{C}} = \frac{\partial \det \boldsymbol{C}}{\partial \boldsymbol{C}} = \frac{1}{2} J \boldsymbol{C}^{-1} \tag{4.47}$$

Finally, combining all intermediate results together and plugging back into Eqn. 4.43 yields the *second* P-K elastic stress tensor as

$$\begin{aligned}\boldsymbol{S}_{el} &= GJ^{-2/3}\left(-\frac{\boldsymbol{C}:\boldsymbol{I}}{3}\boldsymbol{C}^{-1}+\boldsymbol{I}\right)+K(J-1)J\boldsymbol{C}^{-1}\\ &\quad+2\gamma GJ^{-2/3}\left(\boldsymbol{C}:\mathbf{a}\otimes\mathbf{a}-1\right)\left(-\frac{\boldsymbol{C}:\mathbf{a}\otimes\mathbf{a}}{3}\boldsymbol{C}^{-1}+\mathbf{a}\otimes\mathbf{a}\right)\end{aligned} \tag{4.48}$$

where : and $\otimes$ denote double contraction and dyadic product, respectively.

It's more useful to convert the *second* P-K stress tensor as the Cauchy stress tensor [Eqn. 4.9], i.e.

$$\begin{aligned}\boldsymbol{\sigma}_{el} &= J^{-1}\boldsymbol{F}\boldsymbol{S}_{el}\boldsymbol{F}^{T}\\ &= GJ^{-5/3}\left[-\frac{\boldsymbol{C}:\boldsymbol{I}}{3}\boldsymbol{I}+\boldsymbol{F}\boldsymbol{F}^{T}\right]+K(J-1)\boldsymbol{I}\\ &\quad+2\gamma GJ^{-5/3}\left(\boldsymbol{C}:\mathbf{a}\otimes\mathbf{a}-1\right)\left[-\frac{\boldsymbol{C}:\mathbf{a}\otimes\mathbf{a}}{3}\boldsymbol{I}+\boldsymbol{F}\left(\mathbf{a}\otimes\mathbf{a}\right)\boldsymbol{F}^{T}\right]\end{aligned} \tag{4.49}$$

which gives the elastic stresses of fiber-reinforced materials in the spatial coordinates.

4.3.5.2. magnetic stresses. Due to the magnetoelastic coupling, the magnetic energy $\mathcal{W}_m$ also creates stresses. Based on the work-conjugation [**228**], the conjugate variable [**229**] of the deformation gradient tensor $\boldsymbol{F}$ is the *first* P-K stress tensor, i.e.

$$\boldsymbol{P}_m = \frac{\partial \mathcal{W}_m}{\partial \boldsymbol{F}} \tag{4.50}$$

Note the relation between the *first* P-K stress tensor and the Cauchy stress tensor [Eqn. 4.9], it gives the magnetic stress tensor as

$$\begin{aligned}\boldsymbol{\sigma}_m &= \frac{1}{J}\frac{\partial \mathcal{W}_m}{\partial \boldsymbol{F}}\boldsymbol{F}^T = -J^{-1}\frac{\partial\left(\boldsymbol{F}\mathbf{M}\cdot\mathbf{B}\right)}{\partial \boldsymbol{F}}\boldsymbol{F}^T \\ &= -J^{-1}\frac{\partial(F_{kL}M_LB_k)}{\partial F_{iN}}F_{Nj} = -J^{-1}\delta_{ik}\delta_{NL}M_LB_kF_{Nj} = -J^{-1}F_{Nj}M_NB_i \\ &= -J^{-1}\mathbf{B}\otimes\boldsymbol{F}\mathbf{M}\end{aligned} \tag{4.51}$$

Unlike the Cauchy elastic stress tensor $\boldsymbol{\sigma}_{el}$ [Eqn. 4.49], the Cauchy magnetic stress tensor $\boldsymbol{\sigma}_m$ is usually asymmetric, which leads to local magnetic torques $\boldsymbol{\tau}_m = J^{-1}(\boldsymbol{F}\mathbf{M})\times\mathbf{B}$. This point will be discussed in more details in Sec. 4.4.3.3.

4.3.5.3. constitutive relation of magnetoelastic materials. Finally, adding the elastic stresses [Eqn. 4.49] and the magnetic stresses [Eqn. 4.51] together, the constitutive relation of the fiber-reinforced magnetoelastic materials defined by the magnetoelastic energy density $\mathcal{W}_{me}$ [Eqn. 4.40] can be expressed as:

$$\boldsymbol{\sigma}_{me} = \boldsymbol{\sigma}_{me}(\boldsymbol{F}) = \boldsymbol{\sigma}_{el}(\boldsymbol{C}) + \boldsymbol{\sigma}_m(\boldsymbol{F}) \tag{4.52}$$

This concludes the development of the material model of the hydrogel-metal hybrid and details of numeric implementations will be discussed in the next section.

4.4. Finite element simulations

4.4.1. Overview of numeric implementations

The continuum model of the hydrogel-metal hybrid was solved in two steps using the commercial finite-element software COMSOL. The first step calculates the deformation

of the hydrogel under the influence of light and the second step uses the deformed geometry as the reference configuration to calculate the dynamic behavior of the robot under an external magnetic field. For the first step, we used the solid mechanics module of COMSOL and modeled the hydrogel as a hyperelastic material to calculate its response to light. Since the photo component of the free energy density of the material depends on the concentration of chromophores in the SP form [Eqn. 4.34], the general form partial differential equations (PDE) module of COMSOL was also used to calculate the light intensity [Eqn. 4.30] and hence the concentration of SP chromophores [Eqn. 4.29] in the bulk of the material. For the second part of the simulation, the magnetic field [Eqn. 4.37 and 4.38] was solved via the AC/DC module of COMSOL. The model developed for the fiber-reinforced magnetoelastic materials [Eqn. 4.40] was implemented as a user-defined hyperelastic model in the Structural Mechanics module of COMSOL. The contribution from asymmetric magnetic Cauchy stress tensor $\boldsymbol{\sigma}_m$ [Eqn. 4.51 and 4.62] was implemented via the weak contribution functionality of COMSOL. The contacts between the hydrogel robot and the floor are assumed to be non-slippery and the contact events are detected via the Events module of COMSOL, which triggers time-dependent non-slippery boundary conditions. Besides, both volumetric gravitational and frictional forces were also added into the continuum model to take into account the effect of gravity and the viscosity of the liquid environment, respectively.

4.4.2. Magnetism related simulation details

Solving the governing equations of magnetostatics [Eqn. 4.36] together with the magnetic constitutive relation [Eqn. 4.38] gives the distribution of overall magnetic fields $\mathbf{B}$.

It's rather cumbersome to impose a rotating external magnetic field via time-dependent boundary conditions and the AC/DC module of COMSOL supports solving magnetostatic problems by splitting out the background magnetic field as shown in Eqn. 4.37. Thus, a rotating external magnetic field in the y-z plane $\mathbf{H}_b$ can be imposed by simply setting $\mathbf{H}_b = H_0(0, \cos(2\pi ft), \sin(2\pi ft))$, where H_0 is the field strength and f is the field frequency.

In this work, the magnetization profile is usually modulated by a preceding light-actuation process [Fig. 4.7 (A) and (B)], which results in a non-uniform position-dependent distribution of magnetization, i.e. $\mathbf{M}_0 = \mathbf{M}_0(\mathbf{X})$. Therefore, the magnetization profile is obtained from the final state of the light-actuation simulation [Sec. 4.3.3], which starts from a flat uniform magnetization profile, and serves as an input to the magnetic material model [Eqn. 4.38].

Another side note is the magnetic scalar potential φ_m permits arbitrary shifts by a constant value [Eqn. 4.37]. Therefore, to ensure the convergence of magnetic simulations, it's important to impose additional constraints to provide a reference point for the magnetic scalar potential.

4.4.3. Elasticity related simulation details

In principle, solving the governing equations of elasticity [Eqn. 4.11] together with the material model [Eqn. 4.52] yields the elastic deformations of the materials $\mathbf{u}$. However, difficulties arise as the hyperelastic model implemented in COMSOL only supports taking derivatives of energy density with respect to the symmetric C-G strain tensor $\boldsymbol{C}$ but the magnetoelastic energy density $\mathcal{W}_{me}$ depends on the asymmetric deformation gradient

tensor $\boldsymbol{F}$. The Cauchy stress tensor in the Structural Mechanics module of COMSOL is internally assummed to be symmetric. As a workaround, the elastic energy density $\mathcal{W}_{el}$ [Eqn. 4.26], which only depends on the C-G strain tensor, can still be implemented via the built-in hyperelastic model provided by COMSOL but the magnetic energy density $\mathcal{W}_m$ [Eqn. 4.39] is included separately via the weak form contribution.

4.4.3.1. weak form in terms of the deformation gradient tensor. It's important to notice that the usual weak form of EOM [Eqn. 4.12] assumes stress tensors to be symmetric during the derivation [**215**], which is invalid for the magnetic stress tensors [Eqn. 4.51]. Besides, the weak form in terms of the G-L strain tensor $\boldsymbol{\epsilon}$ cannot capture the rotational motion of the system. This point can be illustrated by considering a rigid body rotation of whole system, in which case strain tensor of system is unchanged and gives that $\delta\boldsymbol{\epsilon} = 0$. Therefore, to properly compute the stresses due to the magnetic energy, the weak form expression must be able to capture rotational variations of displacement vector fields. This motivates re-expressing the strong form of EOM in terms of the *first* P-K stress tensor $\boldsymbol{P}$:

$$\rho_0 u_{i,tt} = F_{Vi} + P_{iJ,J} \tag{4.53}$$

and the corresponding weak form can be derived as:

(4.54)
$$\begin{aligned}\int_V (F_{Vi} + P_{iJ,J} - \rho_0 u_{i,tt})\delta u_i \mathrm{d}v &= \int_V (F_{Vi} - \rho_0 u_{i,tt})u_i \mathrm{d}v + \int_V P_{iJ,J}\delta u_i \mathrm{d}v \\ &= \int_V (F_{Vi} - \rho_0 u_{i,tt})u_i \mathrm{d}v + \int_V \left[(P_{iJ}\delta u_i)_{,J} - P_{iJ}\delta u_{i,j}\right] \mathrm{d}v \\ &= \int_V (-P_{iJ}\delta u_{i,j} + F_{Vi}\delta u_i - \rho_0 u_{i,tt}\delta u_i)\mathrm{d}v + \int_{\partial V} P_{iJ}\delta u_i N_j \mathrm{d}s \\ &= \int_V (-P_{iJ}\delta u_{i,j} + F_{Vi}\delta u_i - \rho_0 u_{i,tt}\delta u_i)\mathrm{d}v + \int_{\partial V} F_{Si}\delta u_i \mathrm{d}s\end{aligned}$$

Symmetry properties of the stress tensors are not needed to derive the above result. Therefore, such formulation is compatible with asymmetric stress tensors and it can be written in vectorial notation as:

$$\delta\mathcal{W} = \int_V \left(-\delta\boldsymbol{F} : \boldsymbol{P} + \delta\mathbf{u}\cdot\mathbf{F}_V - \rho_0\delta\mathbf{u}\cdot\mathbf{u}_{tt}\right)\mathrm{d}v + \int_{\partial V}\left(\delta\mathbf{u}\cdot\mathbf{F}_S\right)\mathrm{d}s \tag{4.55}$$

Since deformation gradient tensor contains information about rotation, the weak form shown in Eqn. 4.55 can capture energy variations caused by rotational motions.

4.4.3.2. torque balance. The strong form [Eqn. 4.53] and weak form [Eqn. 4.55] expression of EOM compatible with asymmetric stress tensors have been derived in previous section. However, besides the conservation of linear momentum, the conservation of angular momentum also need to be satisfied. For the case without external torques, local torque balance is automatically fulfilled as long as the stress tensor is symmetric [**212**], i.e. $\sigma_{ij} = \sigma_{ji}$. For our case, the system has magnetization in the deformed configuration as $J^{-1}\boldsymbol{F}\mathbf{M}$, which exert an additional magnetic torque:

$$\boldsymbol{\tau}_m = J^{-1}(\boldsymbol{F}\mathbf{M}) \times \mathbf{B} \tag{4.56}$$

The existence of local magnetic torque is reflected by the fact that the magnetic stress tensor $\boldsymbol{\sigma}_m$ [Eqn. 4.51] is no longer symmetric, i.e. $\sigma^m_{ij} \neq \sigma^m_{ji}$. However, the overall torque balance of the system still holds as the consequence of the conservation of linear angular momentum, i.e.

$$\int_{\partial V} \mathbf{r} \times \mathbf{T}_{tot} \mathrm{d}s + \int_V \mathbf{r} \times \mathbf{f}_V \mathrm{d}v + \int_V \mathbf{r} \times \left(-\rho \frac{\partial^2 \mathbf{u}}{\partial t^2} \right) = \int_V \boldsymbol{\tau}_m \mathrm{d}v \tag{4.57}$$

where $\mathbf{T}_{tot}$ denotes the total traction force (from both elastic and magnetic stresses) at the boundary ∂V and $\mathbf{r}$ is the position vector is defined relative to any arbitrary reference point chose for the torque calculations. The above torque balance can be directly verified as:

$$\begin{aligned}
&\int_{\partial V} \epsilon_{ijk} r_j T^{tot}_k \mathrm{d}s + \int_V \epsilon_{ijk} r_j f_{Vk} \mathrm{d}v + \int_V \epsilon_{ijk} r_j (-\rho u_{k,tt}) \\
&= \int_{\partial V} \epsilon_{ijk} r_j (\sigma^{el}_{kl} + \sigma^m_{kl}) n_l \mathrm{d}s + \int_V \epsilon_{ijk} r_j (f_{Vk} - \rho u_{k,tt}) \mathrm{d}v \\
&= \int_V \left[\epsilon_{ijk} r_j (\sigma^{el}_{kl} + \sigma^m_{kl}) \right]_{,l} \mathrm{d}v + \int_V \epsilon_{ijk} r_j (f_{Vk} - \rho u_{k,tt}) \mathrm{d}v \\
&= \int_V \epsilon_{ijk} r_{j,l} (\sigma^{el}_{kl} + \sigma^m_{kl}) \mathrm{d}v + \int_V \epsilon_{ijk} r_j (\sigma^{el}_{kl,l} + \sigma^m_{kl,l}) \mathrm{d}v + \int_V \epsilon_{ijk} r_j (f_{Vk} - \rho u_{k,tt}) \mathrm{d}v \\
&= \int_V \epsilon_{ijk} r_{j,l} \sigma^m_{kl} \mathrm{d}v + \int_V \epsilon_{ijk} r_{j,l} \sigma^{el}_{kl} \mathrm{d}v + \int_V \epsilon_{ijk} r_j [f_{Vk} - \rho u_{k,tt} + (\sigma^{el}_{kl} + \sigma^m_{kl})_{,l}] \mathrm{d}v \\
&= \int_V \epsilon_{ijk} \delta_{jl} \sigma^m_{kl} \mathrm{d}v + \int_V \epsilon_{ijk} \delta_{jl} \sigma^{el}_{kl} \mathrm{d}v = \int_V \epsilon_{ijk} \sigma^m_{kj} \mathrm{d}v + \int_V \epsilon_{ijk} \sigma^{el}_{kj} \mathrm{d}v \\
&= \int_V \epsilon_{ijk} \sigma^m_{kj} \mathrm{d}v = \int_V \epsilon_{ijk} (-J^{-1} B_k F_{jK} M_K) \mathrm{d}v = \int_V \epsilon_{ijk} \left(J^{-1} F_{jK} M_K \right) B_k \mathrm{d}v
\end{aligned} \tag{4.58}$$

where the EOM and the symmetric property of elastic stress tensor ($\sigma^{el}_{ij} = \sigma^{el}_{ji}$) have been applied. As the conservation of angular momentum is automatically fulfilled [Eqn. 4.57],

only the EOM shown in Eqn. 4.55 need to be solved.

4.4.3.3. explicit expressions of magnetic stresses. As shown by the weak form EOM [Eqn. 4.55], the energy variations due to the magnetic stresses can be computed as:

$$\delta \mathcal{W}_m = \int_V -\delta \boldsymbol{F} : \boldsymbol{P}_m \mathrm{d}v \tag{4.59}$$

The Cauchy magnetic stress tensor is given by Eqn. 4.51 and also note the transformation relation [Eqn. 4.9], then the *first* P-K magnetic stress tensor is:

$$\boldsymbol{P}_m = J\boldsymbol{\sigma}_m \mathbf{F}^{-T} \tag{4.60}$$

or explicitly written in its component wise form:

$$\boldsymbol{P}_m = \begin{pmatrix} P_{xX} & P_{xY} & P_{xZ} \\ P_{yX} & P_{yY} & P_{yZ} \\ P_{zX} & P_{zY} & P_{zZ} \end{pmatrix} \tag{4.61}$$

where

(4.62)

$$P_{xX} = \mathrm{F_{xY}}\,\mathrm{F_{yZ}}\,\sigma^m_{\mathrm{xz}} - \mathrm{F_{xZ}}\,\mathrm{F_{yY}}\,\sigma^m_{\mathrm{xz}} - \mathrm{F_{xY}}\,\mathrm{F_{zZ}}\,\sigma^m_{\mathrm{xy}} + \mathrm{F_{xZ}}\,\mathrm{F_{zY}}\,\sigma^m_{\mathrm{xy}} + \mathrm{F_{yY}}\,\mathrm{F_{zZ}}\,\sigma^m_{\mathrm{xx}} - \mathrm{F_{yZ}}\,\mathrm{F_{zY}}\,\sigma^m_{\mathrm{xx}}$$

$$P_{xY} = \mathrm{F_{xZ}}\,\mathrm{F_{yX}}\,\sigma^m_{\mathrm{xz}} - \mathrm{F_{xX}}\,\mathrm{F_{yZ}}\,\sigma^m_{\mathrm{xz}} + \mathrm{F_{xX}}\,\mathrm{F_{zZ}}\,\sigma^m_{\mathrm{xy}} - \mathrm{F_{xZ}}\,\mathrm{F_{zX}}\,\sigma^m_{\mathrm{xy}} - \mathrm{F_{yX}}\,\mathrm{F_{zZ}}\,\sigma^m_{\mathrm{xx}} + \mathrm{F_{yZ}}\,\mathrm{F_{zX}}\,\sigma^m_{\mathrm{xx}}$$

$$P_{xZ} = \mathrm{F_{xX}}\,\mathrm{F_{yY}}\,\sigma^m_{\mathrm{xz}} - \mathrm{F_{xY}}\,\mathrm{F_{yX}}\,\sigma^m_{\mathrm{xz}} - \mathrm{F_{xX}}\,\mathrm{F_{zY}}\,\sigma^m_{\mathrm{xy}} + \mathrm{F_{xY}}\,\mathrm{F_{zX}}\,\sigma^m_{\mathrm{xy}} + \mathrm{F_{yX}}\,\mathrm{F_{zY}}\,\sigma^m_{\mathrm{xx}} - \mathrm{F_{yY}}\,\mathrm{F_{zX}}\,\sigma^m_{\mathrm{xx}}$$

$$P_{Yx} = \mathrm{F_{xY}}\,\mathrm{F_{yZ}}\,\sigma^m_{\mathrm{yz}} - \mathrm{F_{xZ}}\,\mathrm{F_{yY}}\,\sigma^m_{\mathrm{yz}} - \mathrm{F_{xY}}\,\mathrm{F_{zZ}}\,\sigma^m_{\mathrm{yy}} + \mathrm{F_{xZ}}\,\mathrm{F_{zY}}\,\sigma^m_{\mathrm{yy}} + \mathrm{F_{yY}}\,\mathrm{F_{zZ}}\,\sigma^m_{\mathrm{yx}} - \mathrm{F_{yZ}}\,\mathrm{F_{zY}}\,\sigma^m_{\mathrm{yx}}$$

$$P_{yY} = \mathrm{F_{xZ}}\,\mathrm{F_{yX}}\,\sigma^m_{\mathrm{yz}} - \mathrm{F_{xX}}\,\mathrm{F_{yZ}}\,\sigma^m_{\mathrm{yz}} + \mathrm{F_{xX}}\,\mathrm{F_{zZ}}\,\sigma^m_{\mathrm{yy}} - \mathrm{F_{xZ}}\,\mathrm{F_{zX}}\,\sigma^m_{\mathrm{yy}} - \mathrm{F_{yX}}\,\mathrm{F_{zZ}}\,\sigma^m_{\mathrm{yx}} + \mathrm{F_{yZ}}\,\mathrm{F_{zX}}\,\sigma^m_{\mathrm{yx}}$$

$$P_{yZ} = \mathrm{F_{xX}}\,\mathrm{F_{yY}}\,\sigma^m_{\mathrm{yz}} - \mathrm{F_{xY}}\,\mathrm{F_{yX}}\,\sigma^m_{\mathrm{yz}} - \mathrm{F_{xX}}\,\mathrm{F_{zY}}\,\sigma^m_{\mathrm{yy}} + \mathrm{F_{xY}}\,\mathrm{F_{zX}}\,\sigma^m_{\mathrm{yy}} + \mathrm{F_{yX}}\,\mathrm{F_{zY}}\,\sigma^m_{\mathrm{yx}} - \mathrm{F_{yY}}\,\mathrm{F_{zX}}\,\sigma^m_{\mathrm{yx}}$$

$$P_{zX} = \mathrm{F_{xY}}\,\mathrm{F_{yZ}}\,\sigma^m_{\mathrm{zz}} - \mathrm{F_{xZ}}\,\mathrm{F_{yY}}\,\sigma^m_{\mathrm{zz}} - \mathrm{F_{xY}}\,\mathrm{F_{zZ}}\,\sigma^m_{\mathrm{zy}} + \mathrm{F_{xZ}}\,\mathrm{F_{zY}}\,\sigma^m_{\mathrm{zy}} + \mathrm{F_{yY}}\,\mathrm{F_{zZ}}\,\sigma^m_{\mathrm{zx}} - \mathrm{F_{yZ}}\,\mathrm{F_{zY}}\,\sigma^m_{\mathrm{zx}}$$

$$P_{zY} = \mathrm{F_{xZ}}\,\mathrm{F_{yX}}\,\sigma^m_{\mathrm{zz}} - \mathrm{F_{xX}}\,\mathrm{F_{yZ}}\,\sigma^m_{\mathrm{zz}} + \mathrm{F_{xX}}\,\mathrm{F_{zZ}}\,\sigma^m_{\mathrm{zy}} - \mathrm{F_{xZ}}\,\mathrm{F_{zX}}\,\sigma^m_{\mathrm{zy}} - \mathrm{F_{yX}}\,\mathrm{F_{zZ}}\,\sigma^m_{\mathrm{zx}} + \mathrm{F_{yZ}}\,\mathrm{F_{zX}}\,\sigma^m_{\mathrm{zx}}$$

$$P_{zZ} = \mathrm{F_{xX}}\,\mathrm{F_{yY}}\,\sigma^m_{\mathrm{zz}} - \mathrm{F_{xY}}\,\mathrm{F_{yX}}\,\sigma^m_{\mathrm{zz}} - \mathrm{F_{xX}}\,\mathrm{F_{zY}}\,\sigma^m_{\mathrm{zy}} + \mathrm{F_{xY}}\,\mathrm{F_{zX}}\,\sigma^m_{\mathrm{zy}} + \mathrm{F_{yX}}\,\mathrm{F_{zY}}\,\sigma^m_{\mathrm{zx}} - \mathrm{F_{yY}}\,\mathrm{F_{zX}}\,\sigma^m_{\mathrm{zx}}$$

These explicit expressions are recorded only because COMSOL does not support matrix operations for the version I was working with (version 5.3) and it's recommended to generate those expressions via any popular Symbolic Algebra System (SAS) (such as MATLAB or Mathematica) to avoid mistakes.

4.4.3.4. weak contributions. Finally, the weak-form EOM for the magnetoelastic materials can be written explicitly as:

$$\delta\mathcal{W} = \int_V \left(-\delta\boldsymbol{F} : \boldsymbol{P}_m - \delta\boldsymbol{\epsilon} : \boldsymbol{S}_{el} + \delta\mathbf{u}\cdot\mathbf{F}_V - \rho_0\delta\mathbf{u}\cdot\mathbf{u}_{tt}\right)\mathrm{d}v + \int_{\partial V}\left(\delta\mathbf{u}\cdot\mathbf{F}_S\right)\mathrm{d}s \tag{4.63}$$

The elastic stresses are implemented as a user-defined hyperelastic model with energy density function given by Eqn. 4.26 and the magnetic stresses are implemented as additional external stresses whose expressions are explicitly computed via Eqn. 4.62. Common FEM software (such as COMSOL and FEniCSx) all support input of the weak-form equations. But different software use different terminologies. In COMSOL, the built-in *test()* function servers as the role of functional variation operator δ in Eqn. 4.63 and the deformation gradient tensor $\boldsymbol{F}$ is readily available as internal variables in the Structural Mechanics module. Therefore, after the computation of *first* P-K magnetic stress tensor $\boldsymbol{P}_m$, the contribution due to magnetic stresses can be straightforwardly implemented as

$$\delta \mathcal{W}_m = -\int_V \sum_{i=x,y,z} \sum_{J=X,Y,Z} test\left(F_{iJ}\right) P^m_{iJ} \mathrm{d}v \tag{4.64}$$

via the *weak contribution* functionality of COMSOL.

4.4.3.5. Contact boundary conditions. For a complete dynamic simulation of the whole robotic behaviors (such as walking/steering motions), the mechanical contacts between the hydrogel robot and the support glass floor are necessary modeling ingredients and need extra cautions. The complete analysis of the contacts, in principle, requires the simulation model to include corresponding mechanical frictions and contact pressures at the contact locations. This needs a separate friction model, which is still largely empirical and generally difficult to integrate into the FEM simulation. In order to capture the essential physics without introducing too much technical complexities, we assume all contacts are non-slippery during walking. Specifically, it means that once a leg of the hydrogel robot lands on the floor, the landed leg is not allowed to have translational displacement. However, rotational movement around the center of the landed leg is allowed to give its

steering capability. Besides, we assume all contacts are perfectly inelastic collisions, which means that the kinetic energy of the hydrogel robot gets dissipated immediately when a leg lands on the ground.

With above assumptions, we track the positions of each legs of the hydrogel robot during the time-dependent simulation and trigger a contact event once any leg hits the floor. For each contact event, the boundary condition of the landed leg is switched as a fixed boundary condition. At the same time, the boundary condition of the other leg is switched as a free boundary condition. The kinetic energy of the hydrogel robot is also dissipated completely during each contact events. This contact event-driven boundary condition allows us to recover the dynamic behaviors of the hydrogel robots observed in the experiment and quantitatively study possible robotic functions of the hydrogel robots.

4.4.4. Benchmark with analytic solutions

In order to confirm the numerical model is implemented correctly, it's important to benchmark FEM solution with available analytic solutions. Here, the analytic solutions of magnetoelastic materials of a simple cube geometry under uniaxial stretch or compression are derived to serve as a test example.

For simplicity, the external magnetic field $\mathbf{H}_b$, the direction of embedded fibers $\mathbf{a}$ and the residual magnetization $\mathbf{M}_0$ are all assumed to be uniformly distributed along z-direction. All elastic deformations should be along each axes in such setup and three principal stretches are denoted as λ_x, λ_y and λ_z. Due to the symmetry of the problem setup, it requires that $\lambda_x = \lambda_y$. Besides, the materials are assumed to be nearly-impressible such that $J = \lambda_x\lambda_y\lambda_z = 1$, then the deformation gradient tensor has the following simple

diagonal form:

$$\boldsymbol{F} = \begin{pmatrix} \lambda_z^{-1/2} & 0 & 0 \\ 0 & \lambda_z^{-1/2} & 0 \\ 0 & 0 & \lambda_z \end{pmatrix} \tag{4.65}$$

and also note that

$$\boldsymbol{C} = \boldsymbol{F}^T\boldsymbol{F} = \begin{pmatrix} \lambda_z^{-1} & 0 & 0 \\ 0 & \lambda_z^{-1} & 0 \\ 0 & 0 & \lambda_z^2 \end{pmatrix}, \quad \mathbf{a} = \begin{pmatrix} 0 \\ 0 \\ 1 \end{pmatrix}, \quad \mathbf{M} = M_0 \begin{pmatrix} 0 \\ 0 \\ 1 \end{pmatrix}, \quad \mathbf{B} = B_{ext} \begin{pmatrix} 0 \\ 0 \\ 1 \end{pmatrix} \tag{4.66}$$

where M_0 is the magnitude of the residual magnetization and B_{ext} denotes the external magnetic flux density.

Plugging above expressions into the stress tensors [Eqn. 4.49, 4.51 and 4.52], it gives the magnetoelastic stress tensor as:

(4.67)

$$\boldsymbol{\sigma}_{me} = G\left[-\frac{\lambda_z^2 + 2\lambda_z^{-1}}{3}\boldsymbol{I} + \boldsymbol{F}\boldsymbol{F}^T\right] + 2\gamma G\left(\lambda_z^2 - 1\right)\left[-\frac{\lambda_z^2}{3}\boldsymbol{I} + \boldsymbol{F}\left(\mathbf{a}\otimes\mathbf{a}\right)\boldsymbol{F}^T\right] - p\boldsymbol{I} - \mathbf{B}\otimes\boldsymbol{F}\mathbf{M}$$

where the volumetric pressure p is defined as:

$$p = -K(J-1) \tag{4.68}$$

In the component form, it gives that

$$\sigma_{xx}^{me} = \sigma_{yy}^{me} = \frac{1}{3}G(\lambda_z^{-1} - \lambda_z^2) - \frac{2}{3}\gamma G\lambda_z^2(\lambda_z^2 - 1) - p \tag{4.69a}$$

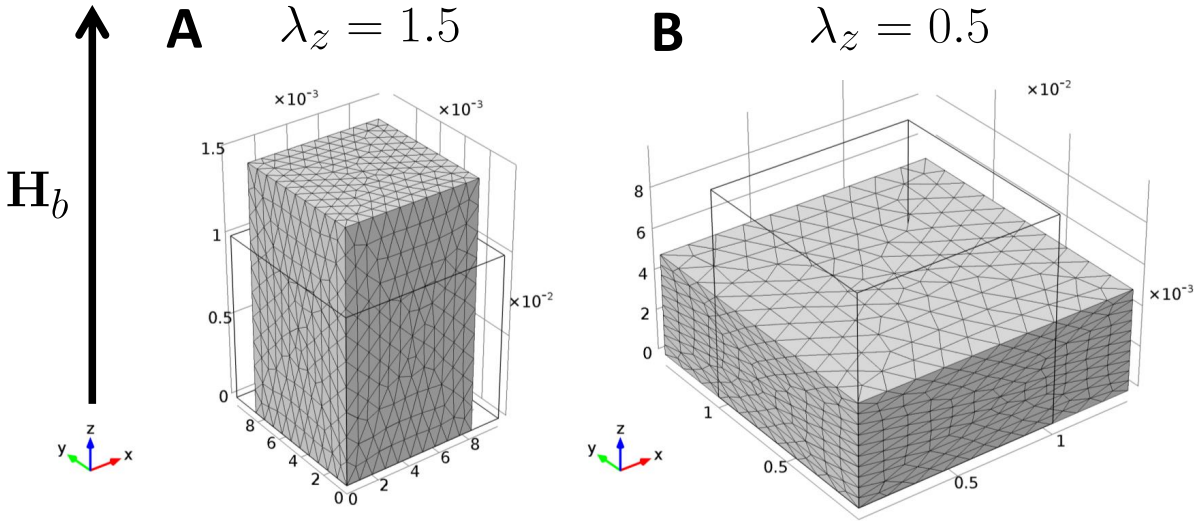

Figure 4.4. Uniaxial stretch (**A**, $\lambda_z = 1.5$) and compression (**B**, $\lambda_z = 0.5$) of a magnetoelastic cube under external magnetic fields. The residual magnetization (not shown), direction of embedded fibers (not shown) and the external magnetic field are uniformly distributed along the z-axis. The cubic outlines indicate the initial shape and only an octant is shown for simplicity.

$$\sigma_{zz}^{me} = \frac{2}{3}G(\lambda_z^2 - \lambda_z^{-1}) + \frac{4}{3}\gamma G\lambda_z^2(\lambda_z^2 - 1) - p - B_{ext}M_0\lambda_z \tag{4.69b}$$

The traction-free boundary condition requires that

$$\sigma_{xx}^{me} = \sigma_{yy}^{me} = \sigma_{zz}^{me} = 0 \tag{4.70}$$

Therefore, the deformation of a magnetoelastic cube under external magnetic fields is given as:

$$(\lambda_z - \lambda_z^{-2}) + 2\gamma\lambda_z(\lambda_z^2 - 1) = \frac{B_{ext}M_0}{G} \tag{4.71}$$

For a given set of material parameters (G, γ, $\mathbf{M}_0$) and experiment conditions ($\mathbf{B}_{ext}$), above nonlinear dimensionless equation can be solved to obtain the induced stretch or compression (λ_z). As indicated by the above equation, λ_z only depends on two dimensionless parameters γ and $\frac{B_{ext}M_0}{G}$, which is plotted solid lines in Fig. 4.5. Corresponding FEM simulation is set up with $K \gg G$ to ensure the incompressibility of the materials. Simulation results are marked as cross symbols in Fig. 4.5, and they match consistently with analytic solutions, which validate numeric implementations of the continuum model of fiber-reinforced magnetoelastic materials.

4.4.5. Calibration of parameters

After validating numeric implementations of the material model, all material parameters (G, K, γ, $\mathbf{M}$) [see Eqn. 4.40] need to be calibrated from actual experiment measurements. For magnetic properties, the magnetization is obtain via SQUID measurement [**163**]. As for elastic properties, Dynamic Mechanical Analysis (DMA) is conducted to characterize the elastic responses of the materials via a uniaxial compression. Then, the calibration process is done by the reverse modeling and implemented via the Optimization module in COMSOL. More specifically, the calibration process is formulated as an optimization problem to find elastic parameters matching experimental results best, where the objective function and the optimization solver are chosen as least square function and Sparse Nonlinear OPTimizer (SNOPT), respectively.

For the calibration purpose, identical circular samples with the diameter of 8 mm and thickness of 0.536 mm are cut by mold for uniaxial compression test. The nominal stresses of samples without Ni nanowires (control sample), samples with Ni nanowires

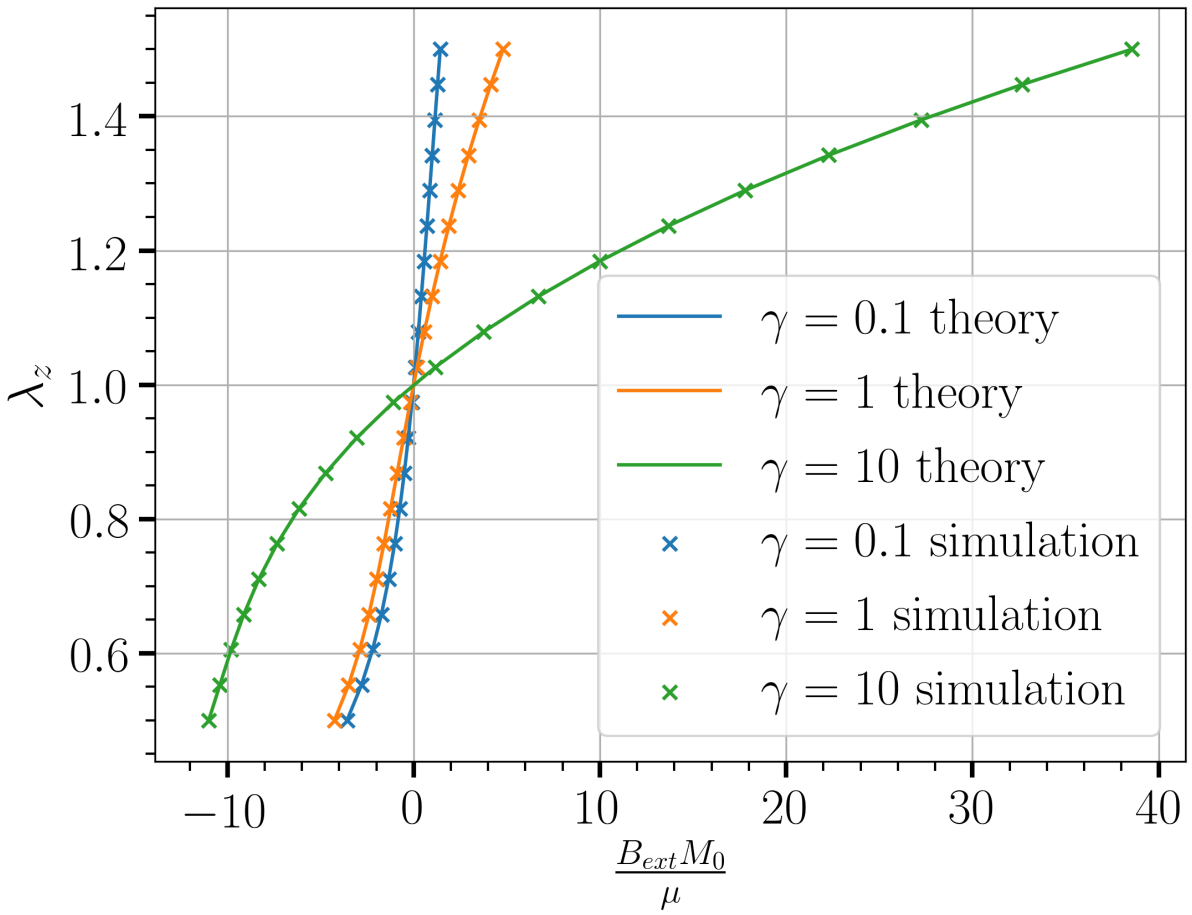

Figure 4.5. Comparison between the numeric solutions (cross symbols) and the corresponding analytic solutions (solid lines) of the fiber-reinforced magnetoelastic materials with a simple cubic geometry.

aligned perpendicular to bottom surface (perpendicular sample) and samples with Ni nanowires aligned parallel to bottom surface (parallel sample) are measured with respect to the strain, which are shown as cross symbols in Fig. 4.6.

For the control sample, corresponding continuum model reduces as the N-H model since it does not contain anisotropic contribution from the Ni nanowires. The best fitting

extracts corresponding elastic parameters of the hydrogel as: G= 3.6 kPa, K= 17.5 kPa [see blue solid line in Fig. 4.6].

The same set of elastic parameters are used to fit experimental data of both the perpendicular and parallel samples simultaneously. The continuum model of perpendicular sample only differs at Ni nanowires' orientation with the parallel sample. Since the concentration of the Ni nanowires is low ($\sim$ 0.5 % weight percentage), the bulk modulus of fiber-reinforced materials is assumed to be roughly the same as the bulk modulus of the control sample. The best fitting extracts corresponding elastic parameters of the fiber-reinforced hydrogel as: G= 5.2 kPa, γ= 0.9, K= 17.5 kPa [see green and yellow solid lines in Fig. 4.6].

4.5. Mechanism of dual-responsiveness to light and magnetic fields

4.5.1. Mechanism of photoelastic response

The fundamental mechanism of deformation under the action of light in the materials investigated is rooted in the creation of a spatial gradient in the population of hydrophilic and hydrophobic moieties within the hydrogel (protonated merocyanine (MCH^+) versus spiropyran (SP) segments). This should result in a decrease of water concentration within the material as the density of SP units increases, leading in turn to mechanical deformation, either bending up or down depending on the irradiation direction. A phenomenological model [**230**] has been developed to describe such photoinduced hydrophobicity in gels with an additional contribution to the free energy proportional to $r_{sp}\,(1-\phi)$, where ϕ is the monomer volume fraction and r_{sp} is the fraction of chromophores in the SP configuration. Here we derived the additional contribution to be $\alpha\phi\,(1-\phi)$, where α is given

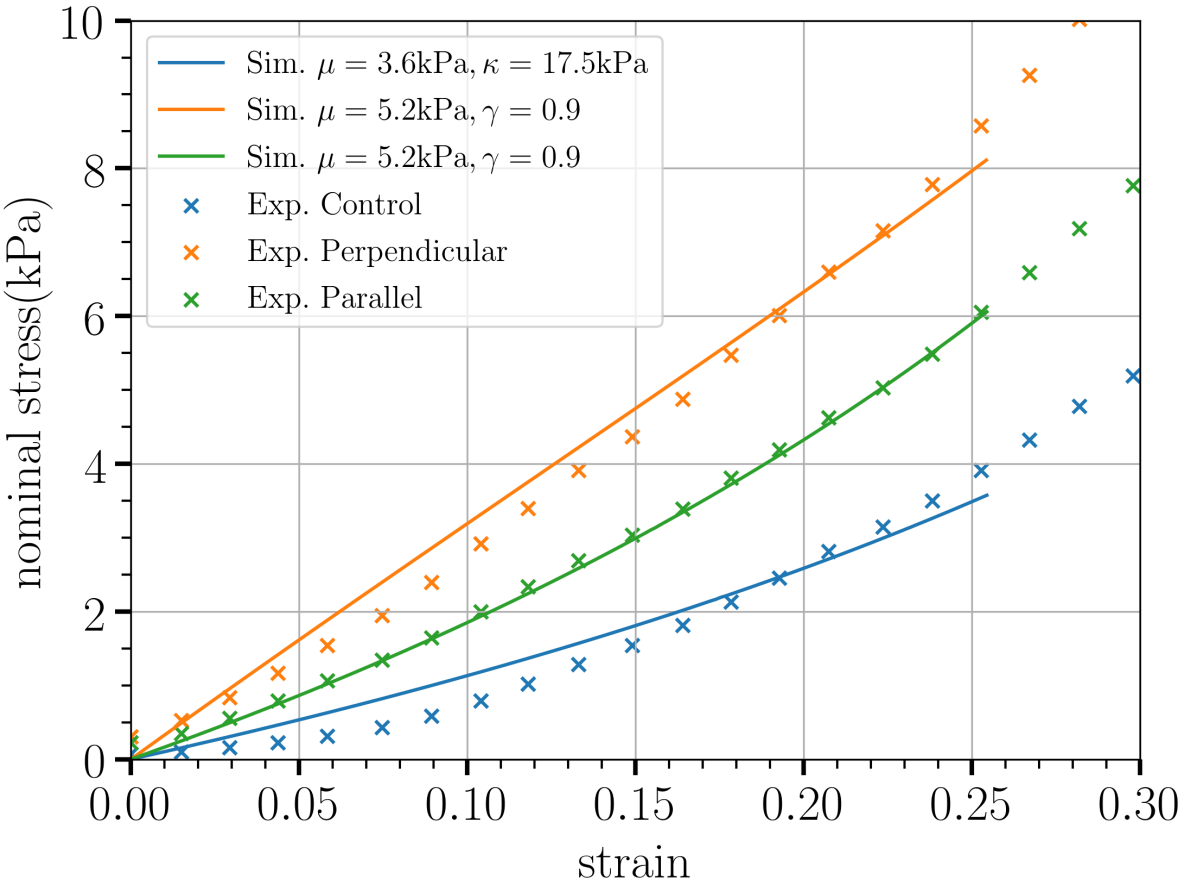

Figure 4.6. Calibration of the elastic parameters from the DMA measurement after light irradiation. The experiment results are shown as cross symbols and the corresponding simulation results are shown as solid lines.

by,

$$\alpha = \frac{zf}{k_B T}(u_{sw} - u_{mw}) r_{sp} \tag{4.72}$$

where u_{sw} and u_{mw} are the interaction energies of the SP and MCH^+ moieties with water, respectively, z is the coordination number of the lattice, and f is the fraction of monomers containing a chromophore. Moreover, r_{sp} is described by the kinetics of the

chemical reaction, $MCH^+ \leftrightarrow SP$ and can be calculated by computing the light intensity as a function of spatial coordinates in the hydrogel objects [see Sec 4.3.3].

4.5.2. Mechanism of magnetoelastic response

To quantitatively characterize deformations of the hydrogel, we developed a continuum model of fiber-reinforced magnetoelastic materials. An external magnetic field induces local torques since Ni nanowires prefer to align with the field. We solve Maxwell's equations in the limit of a static magnetic field (the magnetostatics) [Eqn.4.36] to obtain the distribution of the magnetic flux density $\mathbf{B}$, which couples with the magnetization of Ni nanowires and creates magnetic torques on the nanowires [Eqn. 4.56]. Given that the nanowires are immobilized by the hydrogel ([**163**] Fig. S3), these magnetic torques transmit stresses that collectively result in macroscopic deformation of the material. Since the interaction between the field and magnetized material is orientation dependent, strain tensors are not enough to fully describe the state of the system. Instead, we used here the deformation gradient tensor $\boldsymbol{F}$, which takes into account the rotational deformation to develop a free energy density function of fiber-reinforced magnetoelastic materials, $\mathcal{W}_{me}$, given by,

$$\mathcal{W}_{me} = \frac{1}{2}G(\bar{I}_1 - 3) + \frac{1}{2}\gamma G(\bar{I}_4 - 1)^2 + \frac{K}{2}(J-1)^2 - \boldsymbol{F}\mathbf{M}\cdot\mathbf{B}$$

where G and K are the shear and bulk modulus, respectively; γ is a stiffness parameter resulting from mechanical reinforcement by the aligned nanowires [**221**]; $J = \det \boldsymbol{F}$ characterizes volumetric changes with respect to the initial state; $\bar{I}_1$ [Eqn. 4.19] describes shape changes and $\bar{I}_4$ [Eqn. 4.24] describes the deformation along the direction of nanowires;

$\mathbf{B}$ is the magnetic flux density; and $\mathbf{M}$ is the magnetization field in the reference configuration [see Sec. 4.3.5 for details]. The magnetic energy term $\mathcal{W}_m = -(\boldsymbol{F}\mathbf{M}) \cdot \mathbf{B}$ [Eqn. 4.39] corresponds to the magnetic stress tensor $\boldsymbol{\sigma}_m = -J^{-1}\mathbf{B} \otimes \boldsymbol{F}\mathbf{M}$ [Eqn. 4.51]. This model demonstrates a clear coupling between light and magnetic actuation via elastic deformation. With light exposure, the light propagates through the hydrogel and creates differential shrinking, which induces macroscopic deformations $\boldsymbol{F}$ of the hydrogel and enables the light actuation. Since the Ni nanowires are trapped within the hydrogel, the elastic deformation will change the spatial orientation of Ni nanowires $\boldsymbol{F}\mathbf{M}$. This change in Ni nanowire orientation ultimately modifies magnetic actuation ($\boldsymbol{\sigma}_m$). In this model, the Ni nanowires move with the hydrogel without slipping and the higher order energy contributions in $\mathbf{B}$ to the free energy density $\mathcal{W}_{me}$ are ignored [**53**, **205**]. The strength of external magnetic field stays in the linear response region of Ni nanowires [Fig. 4.3] and all elastic parameters are calibrated from experimental measurements [Fig. 4.6]. This continuum model was solved using finite element methods [Sec. 4.4] and benchmarked with analytic solutions [Fig. 4.5]. It provides a quantitative analysis for the dynamic behavior of the hydrogels in magnetic fields.

4.6. Programmed walking and steering motions

4.6.1. Walking motions

To develop robotic functions, we prepared cross-shaped hydrogel films containing aligned Ni nanowires [Fig. 4.7A]. The film thickness was fixed around 0.5 mm to obtain an optimal photoisomerization speed and deformation stability based on our previous results [**231**]. After light irradiation, the flat sample bends up as an object with two walking legs (w1,

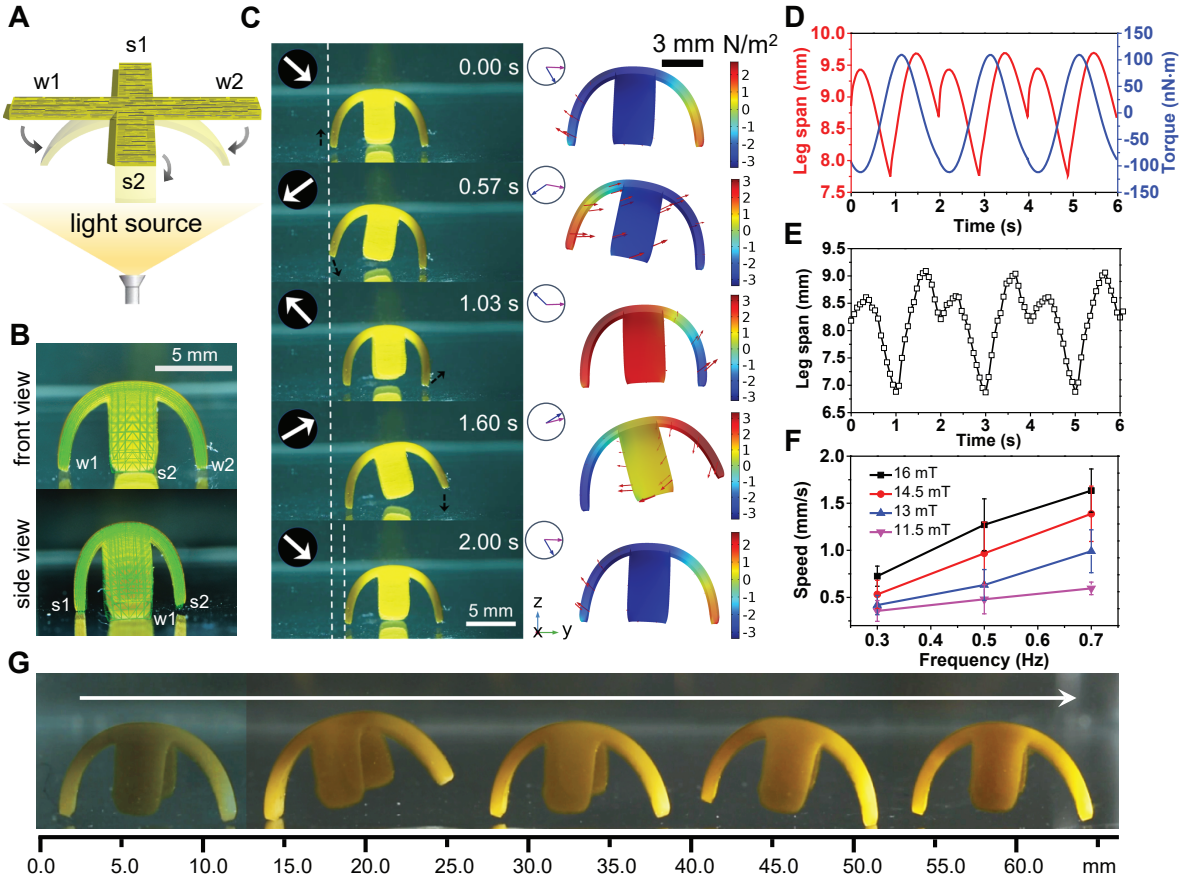

Figure 4.7. **Light triggered walking under rotating magnetic fields.** (**A**) Schematic of a cross-shaped hydrogel film containing aligned Ni nanowires irradiated from below. (**B**) Photographs of the bent hydrogels (front and side views) superimposed with green wireframe representations of the calculated photo-actuation using a finite element method. (**C**) (Left) Photographs of the hydrogel walking from left to right for one cycle (white arrows indicate direction of the magnetic fields). (Right) Calculated snapshots from a finite element simulation of the walking motion (color scale used on the object's surface represents the x-component of the magnetic torque density). Red arrows indicate the instantaneous velocity field, blue arrows indicate the direction of the external magnetic field, and magenta arrows indicate the direction of the average magnetization. (**D**) Plot of the x-component of the magnetic torque (blue) and leg span (red) obtained from the simulation. (**E**) Plot of the experimental leg span of samples as a function of time over multiple walking cycles. (**F**) Plot of the walking speed of samples as a function of rotating frequency at various magnetic field strengths (error bars represent standard deviations of data collected from three separate samples). (**G**) Time-lapsed photographs of hydrogel walking (collected every four cycles, ~8.3 s) over macroscopic distances under a rotating magnetic field (14.5 mT, 0.7 Hz).

w2) and two stabilizing arms (s1, s2) [Fig. 4.7B]. The alignment of the wires within the object creates an anisotropic mechanical response and therefore the span between w1 and w2 (see front view) is larger than that between s1 and s2 (see side view). We calculated photo-actuation of these samples using the model described before and generated the green wireframes shown in Fig. 4.7B. The wireframes overlap exactly with the actual bending geometry of the hydrogels, observed both from front and side views, suggesting there is clear agreement between the calculated and actual light-induced deformation observed in the photographs. It is therefore possible to exploit this mechanical anisotropy caused by the aligned Ni nanowires to modulate photo-actuation in hydrogel samples with simple geometries such as squares [see [**163**] Figs. S13-S15]. We found that when the hybrid hydrogel-metal hybrids are illuminated and bent by the light, a nonuniform 3D magnetization profile is established that enables walking under the influence of an external rotating magnetic field [Fig. 4.7C]. As a control, samples containing unaligned Ni nanowires or aligned chains of Ni nanoparticles exhibited minimal movement under the same magnetic field and were not capable of walking [[**163**] Fig. S16]. The average magnetization (purple arrow) and the external magnetic field (blue arrow) lie within the y-z plane and the magnetic torque density is given by $\boldsymbol{\tau}_m = \boldsymbol{F}\mathbf{M}/J \times \mathbf{B}$. Therefore, only the x-component of the magnetic torque is a nonzero quantity. The rotating magnetic field in the y-z plane generates an oscillatory x-component of the magnetic torque that causes the objects to rotate alternately clockwise and counterclockwise around the x-axis (perpendicular to the walking direction) [Fig. 4.7D]. Because of the combination of magnetic torque and gravity, the object lands on its front and back legs in alternating fashion [Fig. 4.7C]. Our model assumes friction between the legs and the floor is large

enough to avoid slippage during walking [Sec. 4.4.3.5]. Magnetoelastic coupling results in a periodic change in the hydrogel's leg span (distance between w1 and w2) [Fig. 4.7D and E], which enables the net displacement of the hydrogel along the y-axis. Furthermore, longer side arms were found to be important in stabilizing the hydrogel's movement and optimizing its lift during walking due to a larger magnetic torque [[**163**] Fig. S17]. Also, the walking speed was found to be faster with higher frequencies (0.3–0.7 Hz) or stronger magnetic fields (11.5–16.0 mT) [Fig. 4.7F]. With a fixed frequency (0.7 Hz) and field strength (14.5 mT), it was possible to achieve walking over macroscopic distances (∼53 mm) [Fig. 4.7G] and reduction of the hydrogels to millimeter size scales did not change the mechanism of motion [**163**].

4.6.2. Steering motions

The hybrid hydrogels can also achieve steering motion in arbitrary directions while walking along x-y plane by controlling the applied magnetic field to produce an additional torque in the z direction (i.e. normal to the walking plane). Using simulations we predicted that the objects could turn 90° in 30° increments [Fig. 4.8A] by programming the applied field in the x, y, and z directions to achieve the required torque [Fig. 4.8B and C]. The predicted motion using simulations was in fact observed experimentally as shown in Fig. 4.8A. The two modes of motion (walking and steering) allow our hydrogel sample to reach any arbitrary destination on a two-dimensional level or inclined surface. Fig. 4.8D shows a designed arbitrary path with multiple turns and Fig. 4.8E its corresponding experimental realization. We therefore conclude that the experimental samples of these

materials can have robotic functions, which in this case involve following continuous paths over macroscopic distances.

4.7. Effect of photoswitch chemistry on walking trajectories

To develop more complex robotic functions, we synthesized hydrogels with different molecular photoswitches to tune the kinetics of photo-actuation. Hydrogels made of SP1 can maintain their bending curvature under variable light intensities (96–190 mW/cm^2) through the duration of our experiments [Fig. 4.9A], confirmed by the change of leg span [Fig. 4.9C, black]. We also synthesized a photoswitch (SP2) that could be covalently incorporated in the polymeric network, which lacks the methoxy group and displays faster photoisomerization to the closed ring form [[**163**] Figs. S18-19]. The hydrogel component of the hybrid samples containing SP2 bend and then flatten in response to relatively low light intensities (23.5–33.0 mW/cm^2) [Fig. 4.9B and C, red], since prolonged irradiation destroys the initial light-induced hydrophobicity gradient associated with bending of the material. Since the bending angle is highly tunable by changing irradiation conditions [[**163**] Fig. S20] and the walking behaviors depend directly on the bending geometry, a permanent walker made of SP1 walks with a constant speed while one made of SP2 gradually loses its walking ability with continuous irradiation [Fig. 4.9D, [**163**] Fig S21], and is therefore a transient walker. Note the walking speed of SP2 samples has a large standard deviation probably due to the rapidly increasing stiffness upon light irradiation [[**163**] Fig. S14] as well as some uncontrolled slippage and rotation of the walker. The walking speed can be controlled by programmed sequences of light intensity. As shown in Fig. 4.9E and F, samples containing SP1 hydrogel were found to bend and walk faster as

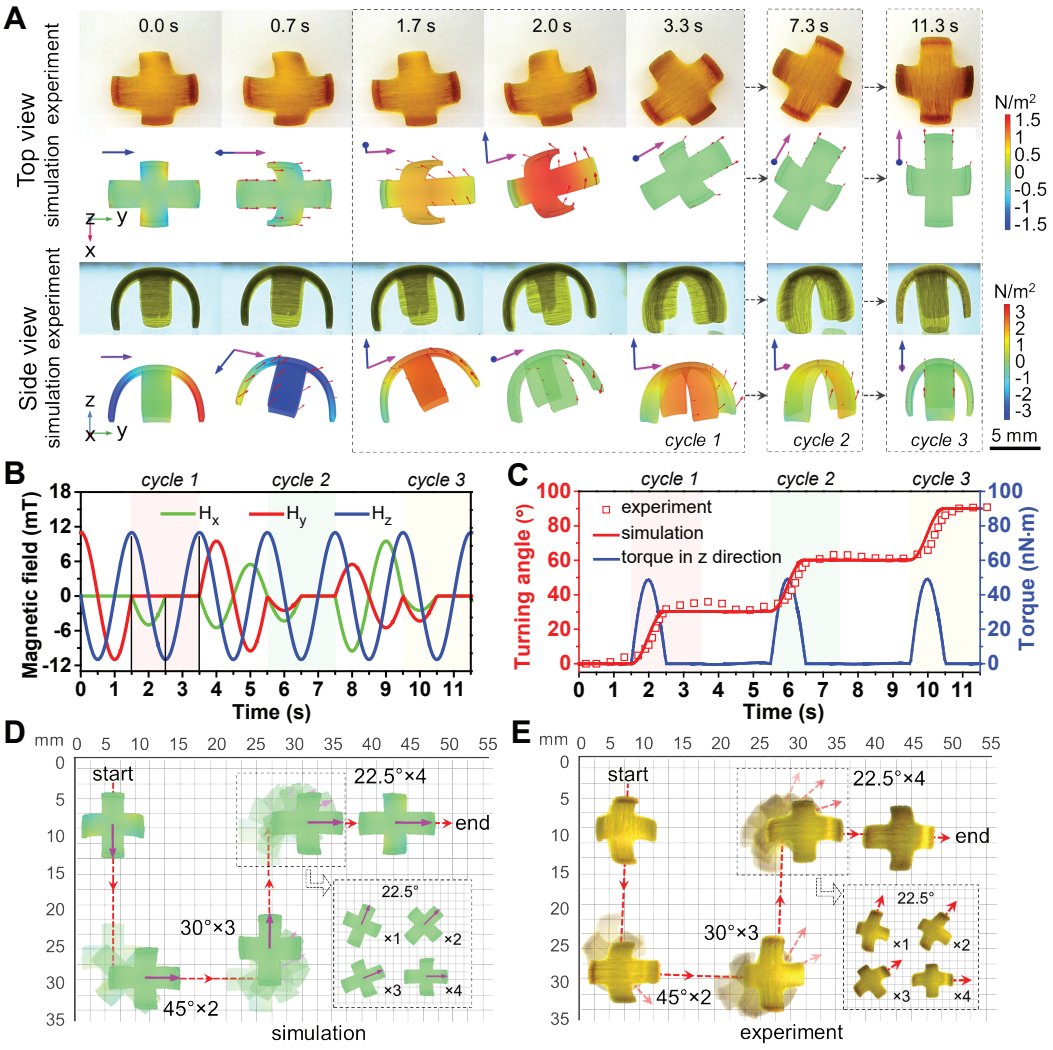

Figure 4.8. **Steering motion and path followed by samples under rotating magnetic fields.** (**A**) Snapshots of three periods of steering motion from both experiment and simulation shown in the top view (top) and side view (bottom). Red arrows depict the instantaneous velocity field, blue arrows depict the direction of external rotating magnetic fields, purple arrows depict the direction of the average magnetization and surface colors represent the z- and x-components of the magnetic torque density in the top and side views, respectively. (**B**) The x, y and z components of the external rotating magnetic fields as functions of time. (**C**) Turning angle of the hydrogel robot from the experiment (red square) and the simulation (red line) and the z component of the total magnetic torque (blue line). Arbitrary path of the hydrogel from simulations (**D**) and experiment (**E**). The surface colors represent the z-component of the magnetic torque density; dashed red line indicates the motion trajectory; magenta arrows indicate the direction of the average magnetization. Insets show a 90° turn in four 22.5° increments. "x1, x2, x3, x4" indicate the number of turning increments made while steering along a 90° turn.

the light intensity increases. The walking speed of SP1 hydrogels after 10 min of sequential irradiation at low and then higher intensity [see Fig. 4.9F] was faster (1.2 mm/s) than the speed after 10 min of exposure to a constant light intensity (0.7 mm/s) [Fig. 4.9D]. We suggest that light irradiation history leads to variations in bending curvature and mechanical properties. For example, Fig. 4.9E and F show plateaus in leg span and walking speed during the first 10 min. A full understanding of this phenomenon is beyond the scope of this paper, but we can suggest that equilibration rate of structures during irradiation will be sensitively dependent to light exposure history. Also the SP1 hydrogel was able to selectively bend and its walking accelerated along a section of its path where the light source was localized, offering another possibility for adaptive response to the surrounding environment. This permanent walker gradually stops walking when light is turned off [[**163**] Fig. S22], since the bending hydrogel returns to its initial flat geometry and the hydrophobicity gradient disappears. In contrast to the SP1 samples, prolonged light irradiation of SP2 leads to rapid penetration of light and the disappearance of the hydrophobicity gradient through the thickness of samples. Therefore, increasing the light intensity did not cause samples containing SP2 to walk faster, but rather accelerated flattening of bent samples [[**163**] Fig. S23].

4.8. Demonstration of robotic functions

We also found that we can create objects with different walking modes by controlling the alignment direction of the nanowires during preparation of the Ni-hydrogel composites [[**163**] Figs. S24]. Objects with nanowires aligned diagonally relative to their legs

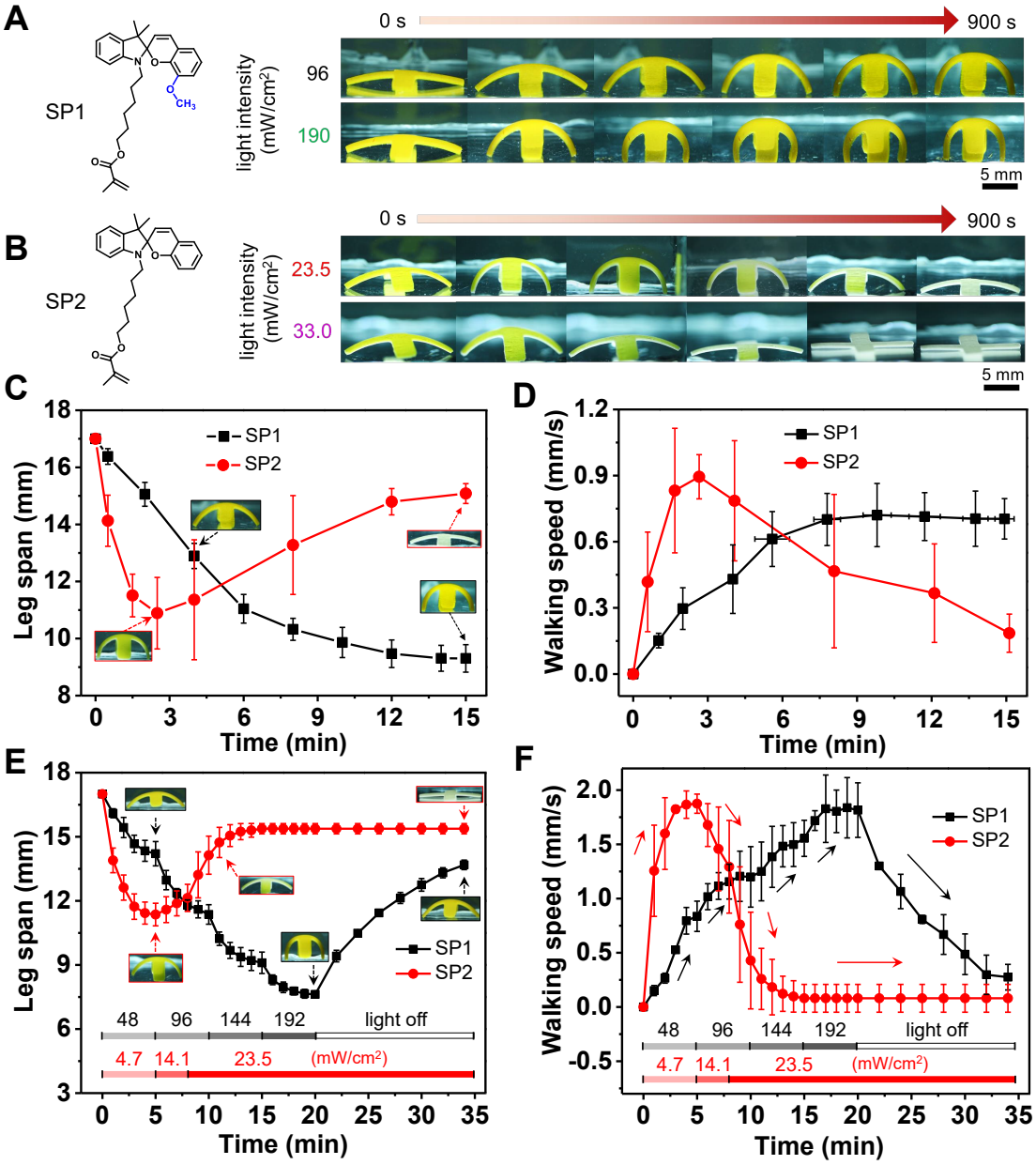

Figure 4.9. **Chemical design and bimodal control of the hydrogel robots.** (**A**, **B**) Molecular structures of SP1 and SP2 and snapshots of the corresponding hydrogel robots under constant light irradiation over 900 s. (**C**) Leg span and (**D**) walking speed under irradiation with 96 mW/cm^2 for SP1 and 23.5 mW/cm^2 for SP2 (error bars represent standard deviations of data collected from three separate samples). (**E**, **F**) Variable light intensity applied over 2100 s to program leg span and walking speed, respectively (black bar, four different light intensities (48, 96, 144, 192 mW/cm^2) were sequentially applied on SP1 samples every 5 min followed by a dark time for 15 min; red bar, three different light intensities (4.7, 14.1, 23,5 mW/cm^2) were sequentially applied on SP2 samples for 5 min, 3 min and 27 min, respectively).

exhibited a walking motion by lifting two legs simultaneously under the rotating magnetic field [Fig. 4.10A]. Objects with nanowires aligned perpendicular to the films walk similarly to those with nanowires in the plane of the film but do not rotate their bodies when the magnetic field is reoriented from the y-z to the x-z plane due to lack of magnetic anisotropy [Fig. 4.10B].

In addition to walking across a flat plane, the hydrogel objects can also climb inclined surfaces [Fig. 4.11A] and therefore displayed a different walking speed during the ascending and descending process [Fig. 4.11B]. The hydrogel–metal hybrid samples can transport and release cargos using light and magnetic field exposure. Irradiating samples with high intensity light (4800 mW/cm^2) from below caused the hydrogel to curl into a spheroidal object, wrapping around an alginate hydrogel bead (cargo) that had been placed underneath it [Fig. 4.11C, top]. We point out that substantial photothermal or photobleaching effects were not observed when using this short exposure to high intensity irradiation [[**163**] Fig. S25]. The rolling motion of the ball-like object under a rotating magnetic field can be guided to different directions without dropping the alginate bead, allowing delivery of the cargo to any arbitrary destination [Fig. 4.11C, middle]. By shining light continuously on the convex side of the object, we can eliminate the photoisomerization gradient to flatten the object first, followed by continuous irradiation from the bottom to create an opposing gradient, thus causing the object to bend up and release its cargo [Fig. 4.11C, bottom]. In addition to using the rolling motion, our robot was also able to transport cargo using the walking motion. Since the MCH^+ is positively charged, the hydrogel robots can transport negatively charged cargo (alginate bead) adhered to

the top of the object through electrostatic attractions, and deliver the cargo to any destination by walking and subsequent release by fast spinning [Fig. 4.11D]. These results offer proof-of-concept on the use of programmed light and magnetic fields to externally and remotely stimulate materials to transport and release cargo.

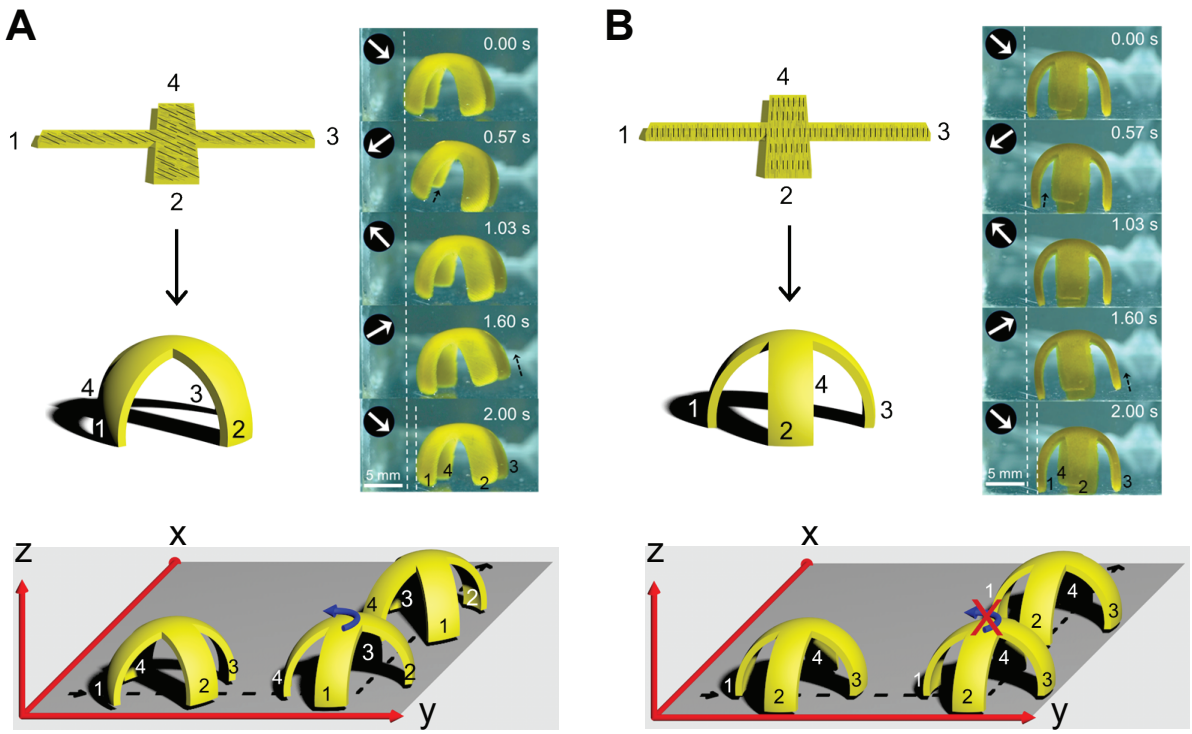

Figure 4.10. **Walking modes of the hydrogel robots in response to nanowire orientation.** Top left, schematic representation of a cross-shaped hydrogel object irradiated from below with the Ni nanowires aligned diagonally (**A**) or perpendicularly (**B**). Top right, photographs of the diagonal (**A**) and perpendicular (**B**) hydrogel object after irradiation walking from left to right for one cycle by lifting two legs simultaneously (1, 4) or (2, 3) (**A**), or by lifting leg 1 or 3 alternately (**B**). White arrows indicate direction of the magnetic fields. Black arrows indicate the lifting of legs. Bottom, the diagonal hydrogel object rotates its body 90° counterclockwise as it turns (**A**), while the perpendicular hydrogel object does not rotate its body (**B**) when the rotation direction of magnetic fields changes from the y-z plane to the x-z plane.

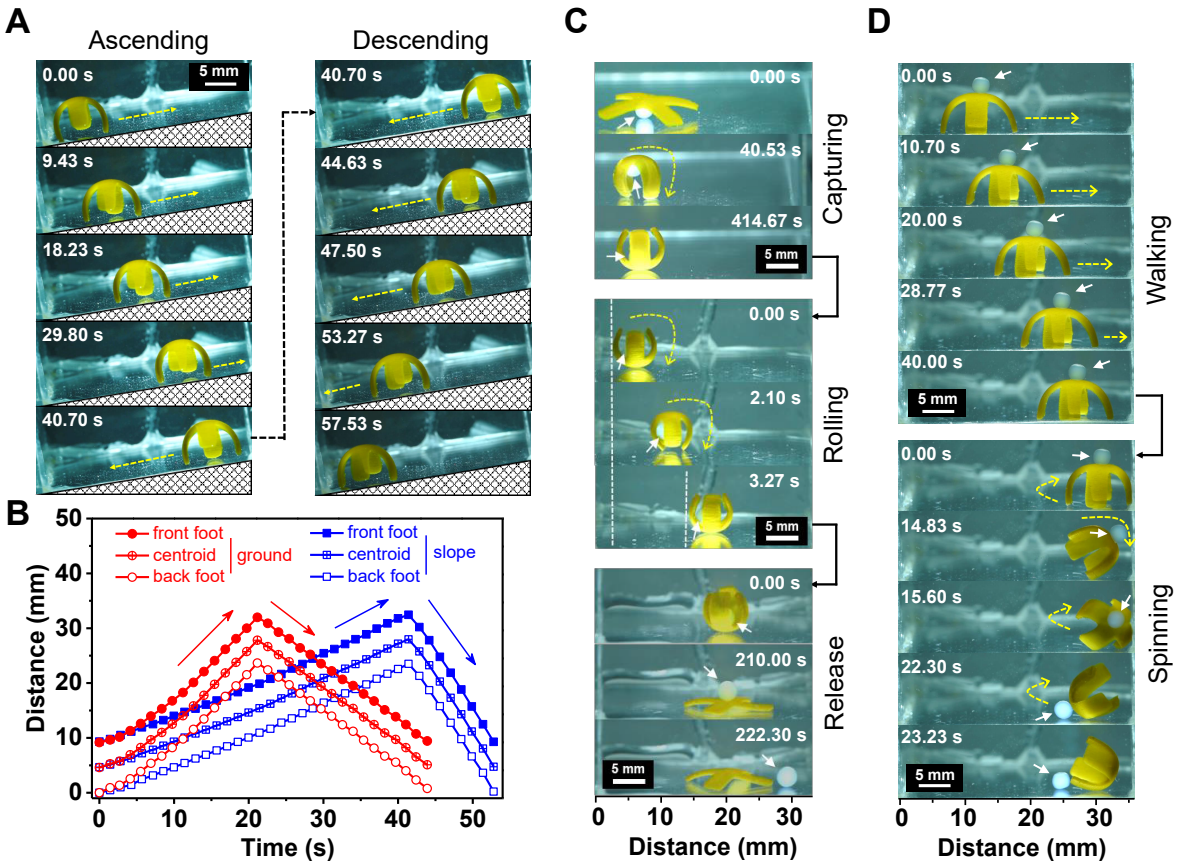

Figure 4.11. **Hydrogel robots for performing work under rotating magnetic fields.** (**A**) Photographs of ascending (left) and descending (right) processes of the hydrogel object containing the SP1 moiety on a glass surface with an inclined angle of 9° under a magnetic field rotating in y-z plane. (**B**) Plot of centroid, front and back feet of the hydrogel object vs time when it walks on an inclined surface (blue) and a flat surface (red) under the same rotating magnetic field. (**C**) Alginate bead captured underneath a flat walker upon irradiation with strong white light from below, transported by rolling under magnetic fields and released by irradiation to invert the sample curvature. (**D**) Alginate bead adhered to the top of the hydrogel object, transported by walking under magnetic fields and subsequently released by fast spinning.

4.9. Discussion and future works

In this work we have investigated the design of highly hydrated soft matter with the capability to respond to both light and magnetic fields in order to emulate locomotion and other functions observed in living organisms. This coupling is achieved by embedding rigid and macroscopically aligned ferromagnetic nanowires in a soft photoactive hydrogel. Compared with conventional polymers or liquid crystal elastomers (LCEs) that have been widely investigated, hydrogels offer great potential in bio-related applications due to their high-water content and mechanical similarity to soft tissues. At the same time, the high aspect ratio of the Ni nanowires used to create the experimental materials allows the possibility of aligning the magnetic scaffold of the hydrogels. Thus, these hybrid materials have potential as systems that can be designed to have anisotropic properties. In this context, the common spherical and irregularly shaped magnetic particles (such as NdFeB) used in previous work lack well-defined shapes and magnetic anisotropy. In those earlier systems, a high content of the magnetic component ($\sim$10 wt%) or a large magnetic field is required to activate a considerable response. In contrast, a very low content of aligned Ni nanowires (0.5 wt%) is sufficient in the hybrid hydrogels to generate a large magnetic response for robotic functions using a relatively weak magnetic field strength ($\leq$16 mT). This advantage is supported by the product of the weight percentage of magnetic material and the applied field strength in our system, which is about three times lower than those used with previous systems. Also whereas the responses of our system to light and magnetic fields are driven by different mechanisms, they are interestingly coupled strongly via elastic deformation. The magnetic response depends on the geometry induced by photo-actuation (light direction, intensity, and irradiation time), while the magnetic

response only appears to affect photo-actuation by changing the object's orientation with respect to incident light [[**163**] Fig. S26]. As demonstrated above, chemical changes in the photo-switching molecules can also alter the programmable shape changes upon light exposure and in this way change the magnetically driven robotic functions. The photo-switching approach via molecular isomerization offers the advantage of activation using relatively low light intensity [**208**, **232**, **233**]. This is in contrast to the commonly used photothermal agents which require high intensity light [**197**, **200**, **234**].

In miniaturized form, the materials developed in this work could be potentially used to transport and release cargoes in aqueous media through narrow passages with complex routes. In the experiments reported here, a rotating external field precessing at a 90° angle to the walking direction was selected because it maximizes the magnetic torque that drives actuation when the fibers are aligned along the bending direction of the hydrogel. However, the actuation mechanisms investigated here could be used in the future to explore other modes of locomotion and functions by designing objects with other shapes and fields precessing at other angles with respect to the magnetization of the nanowires. The coupling principle developed here between shape-morphing and responsive actuation provides a general framework to create more complex bio-inspired motions and functions.

Given the hydrogel nature of our materials, they can potentially collect from aqueous solutions molecular components and deliver them at another point by expelling water. Future directions could also include developing much smaller objects for drug delivery in tissues or to specific cells. In this respect, our understanding of the synergy between light and magnetic actuation will be important in design geometries suited for swimming and locomotion in low Reynolds number environments [**235**]. The walking mechanism

reported here can occur on any flat or inclined surface without relying on ratchets, which is comparable with previous photothermal [**236**], thermal [**237**] or electrically [**238**, **239**] driven walkers. The walking speed reached in our system (∼2 mm/s) is fast from the perspective of previously observed light-induced locomotion but is comparable to other examples of magnetic actuation. However, we point out that in our system exposure of the objects to photons and the magnetic field are physically inseparable factors in the observed actuation. As we approach the walking speed in biologically relevant systems (∼1 body length per second), the walking speed of our systems (∼0.3 body length per second) is comparable or lower than that of light actuated robots [**240**, **241**], which is limited by the viscous drag from the liquid environment and surface friction. With increasing walking speed, the viscous drag creates higher resistance forces and slippage occurs during walking because of insufficient friction with the surface. Given the possibility to match the mechanical properties and water content of molecularly designed hydrogels to those of cells and tissues, these systems may allow us to recreate in synthetic robots the locomotion modes and other actuation behaviors observed in living organisms. We conclude that by theoretically integrating magnetoelasticity, polymer physics, and photochemical kinetics, we learned how to control locomotion and shape changes in soft materials responding to both light and magnetic fields.

Part 2

Collective Behaviors

CHAPTER 5

Collective Behaviors of Quincke Particles*

5.1. Introduction

It is fascinating to observe in nature that simple entities with little or no intelligence, such as birds [**243**], fishes, bacteria [**244**–**247**], cells [**248**], filaments [**249**–**251**], etc., coordinate each other within a limited range and self-organize themselves into highly complex but also highly ordered spatial or temporal structures at a much larger scale. Those collective behaviors of active entities are clearly out-of-equilibrium, which have been attracting scientists to uncover the underlying principles in those complex systems [**252**, **253**]. As the original observations in nature are generally highly complicated, scientists prefer synthetic systems consisting of a few clearly identified components and the resulting phenomena are easy to observe and highly reproducible for systematical investigations. Therefore, active colloidal particles [**254**–**258**] are ideal candidates to serve as a synthetic counterpart for studying collective behaviors of those widely existing active entities. In recent years, active colloidal particles driven by chemicals [**253**, **259**–**261**], electric fields [**262**, **263**], magnetic fields [**264**–**266**] and light [**267**–**269**], etc., have been synthesized and found exhibiting a diverse range of interesting collective behaviors [**159**, **270**–**273**].

*This chapter is primarily based on the published work [**242**] of Bo Zhang, Hang Yuan, Andrey Sokolov, Monica Olvera de la Cruz and Alexey Snezhko†, **Polar state reversal in active fluids**, *Nature Physics*, Vol. 18, No. 2, p. 154-159, 2022, with modified notations and extended details to comply with the structure of this work.

Meanwhile, those experimental findings also promote the development of theoretical and numeric modeling of those active systems. Interestingly, some models, such as the Vicsek model [**274**], the active Brownian particle, etc., focus on the "external" spatial behaviors of active systems without considering the "internal" dynamics of its self-propulsion mechanism. On the other hand, some models, such as the Kuramoto model [**275**, **276**], etc., focus more on the "internal" temporal behaviors of active systems but ignoring its "external" spatial motility behaviors. In principle, the dynamics of internal degrees of freedom (DOF) responsible for self-propulsion can affect the motility of externally observed spatial motions, and vice versa. As a simple example, a model for a population of active entities including two external DOFs (position $\mathbf{r}$ and orientation $\boldsymbol{\theta}$) and one internal DOF (phase $\boldsymbol{\phi}$) can be written phenomenologically as [**277**]:

$$\frac{\mathrm{d}\mathbf{r}_i}{\mathrm{d}t} = \mathbf{U}_0(\boldsymbol{\theta}_i, \boldsymbol{\phi}_i, t) + \left\langle I_{ij}(\mathbf{r}_j - \mathbf{r}_i, \boldsymbol{\theta}_j - \boldsymbol{\theta}_i, \boldsymbol{\phi}_j - \boldsymbol{\phi}_i \right\rangle_j + \boldsymbol{\xi}^r(t) \tag{5.1a}$$

$$\frac{\mathrm{d}\boldsymbol{\theta}_i}{\mathrm{d}t} = \left\langle \Theta_{ij}(\mathbf{r}_j - \mathbf{r}_i, \boldsymbol{\theta}_j - \boldsymbol{\theta}_i, \boldsymbol{\phi}_j - \boldsymbol{\phi}_i) \right\rangle_j + \boldsymbol{\xi}^\theta(t) \tag{5.1b}$$

$$\frac{\mathrm{d}\boldsymbol{\phi}_i}{\mathrm{d}t} = \left\langle \Phi_{ij}(\mathbf{r}_j - \mathbf{r}_i, \boldsymbol{\theta}_j - \boldsymbol{\theta}_i, \boldsymbol{\phi}_j - \boldsymbol{\phi}_i) \right\rangle_j + \boldsymbol{\xi}^\phi(t) \tag{5.1c}$$

where $\mathbf{r}_i$, $\boldsymbol{\theta}_i$ and $\boldsymbol{\phi}_i$ are the position, orientation and phase of i-th particle ($i = 1 \cdots N$); $\boldsymbol{\xi}_i^r$, $\boldsymbol{\xi}_i^\theta$ and $\boldsymbol{\xi}_i^\phi$ are the corresponding random noises acting on each DOFs of i-th particle; I_{ij}, Θ_{ij} and Φ_{ij} denote the pairwise interactions resulted position, orientation and phase changes of i-th particle due to j-th particle; $\mathbf{U}_0$ is the self-propulsion velocity of i-th particle, which may or may not depend on its orientation and phase. And $\langle \cdot \rangle$ indicates

the average for surrounding particles, which can be short-ranged or long-ranged depending on the nature of interactions.

The actual functional forms of $\mathbf{U}_0$, I_{ij}, Θ_{ij}, and Φ_{ij} in Eqn. 5.1 are usually system-dependent, which varies for different propulsion mechanisms and pairwise interactions. More commonly, simple functional forms are proposed to capture the most essential features of experimental observations. For example, the Vicsek model uses simple average between neighboring particles to describe the "alignment interactions" as active particles in many systems tend to align their directions with neighboring particles. And the Kuramoto mode also chooses a simple constant coupling relative to the mean phases to describe the synchronization phenomena. However, all those models still describes the active systems in a phenomenological level and certain physical details are smeared out in such models. It will be interesting to understand how those phenomenological interactions emerge from microscopic interactions in the system.

In this chapter, a model for studying collective behaviors of active colloidal particles, which possess both external and internal degrees of freedom, will be constructed from relevant physical microscopic interactions. More specially, this chapter will particularly focus on hydrodynamically-interacting colloidal particles. It is a long lasting interests to simulate a collection of hydrodynamically interacting particles, which dates back to 1970s [**278**–**281**]. However, the long range nature of hydrodynamic interactions makes direct simulations [**282**, **283**] very expensive ($\mathcal{O}(N^3)$) and severely limits the simulation system size. In order to include inter-particle hydrodynamic interactions in simulations

with acceptable simulation costs, many numeric formulations have been proposed. Examples include explicitly solvent approaches, such as the grid-based algorithms Lattice Boltzmann Method (LBM) [**284**–**289**] and the coarse-grained methods like Dissipative Particle Dynamics (DPD) [**290**–**293**] and Multi-particle Collision Dynamics (MPCD) [**294**–**299**]; implicit solvent approaches, such as Brownian Dynamics (BD) [**300**, **301**] or Stokesian Dynamics (SD) [**302**–**305**]. There are also formulations based on directly solving the Stokes' equation [**306**, **307**], boundary element methods [**216**, **308**], or fluctuating hydrodynamics [**309**, **310**], etc. This list can keep going and each of the above mentioned methods have its own advantages and limitations. In this work, we will follow the approach of Stokesian Dynamics [**302**], which treats the solvent implicitly describes by the Stokes' equation, which enables deriving the explicit functional forms of hydrodynamic interactions [Sec. 5.2].

Following that, the Quincke particle is selected to serve as a concrete example of active colloidal particles with both external (rolling motion) and internal (electric dipole moments) DOFs to illustrate the ideas. Based on the understanding of a single Quincke particle [Chap. 3], the propulsion mechanism of Quincke particles is combined with the Stokesian Dynamics, which yields a particle-based simulation model for a population of Quincke particles [Sec. 5.3] constructed from its relevant microscopic interactions [**110**]. Then, an interesting polar state reversal phenomenon in suspension of Quincke rollers confined by a circular well [**242**] is discussed and also demonstrate how such type of simulation models with both external and internal dynamics help elucidating the important roles of relevant microscopic interactions [Sec. 5.4]. Finally, the whole chapter concludes with a short discussion and possible future development [Sec. 5.5].

5.2. Stokesian Dynamics

In this section, the basics of Stokesian Dynamics (SD) will be systematically introduced in details. Through out this chapter, only simple incompressible Newtonian fluids will be considered, which assumes the constitutive relation of fluid as:

$$\boldsymbol{\sigma}^h = -p\boldsymbol{I} + \mu\left(\boldsymbol{\nabla}\mathbf{u} + \boldsymbol{\nabla}\mathbf{u}^T\right) \tag{5.2}$$

where p and μ are the pressure and the dynamic viscosity of fluid, respectively; $\mathbf{u}$ is the velocity filed of fluid and $\boldsymbol{\sigma}^h$ is the hydrodynamic stress tensor. By the conservation of mass and linear momentum, the general motions of fluid are described by the Navier-Stokes (N-S) equations [Eqn-3.5] [**128**]:

$$\begin{cases} \rho\dfrac{\mathrm{D}\mathbf{u}}{\mathrm{D}t} = \boldsymbol{\nabla}\cdot\boldsymbol{\sigma}^h + \rho\mathbf{f} \\ \boldsymbol{\nabla}\cdot\mathbf{u} = 0 \end{cases} \tag{5.3}$$

where $\frac{\mathrm{D}}{\mathrm{D}t}$ is the material derivative [Eqn. 3.6], ρ is the density of fluid and $\mathbf{f}$ is any possible external volumetric forces. Denoting the relevant characteristic length, time and velocity scales as L_c, τ_c and U_c respectively, then the above N-S equations can be rendered into a dimensionless form as [**121**]:

$$\mathrm{Re\ St}\ \frac{\partial\mathbf{u}}{\partial t} + \mathrm{Re}\ \mathbf{u}\cdot\boldsymbol{\nabla}\mathbf{u} = -\boldsymbol{\nabla}p + \nabla^2\mathbf{u} \tag{5.4}$$

Two dimensionless numbers, Reynolds number (Re) and Strouhal number (St), naturally emerge, which are given as:

$$\mathrm{Re} = \frac{\rho U_c L_c}{\mu} \tag{5.5a}$$

$$\mathrm{St} = \frac{L_c}{U_c \tau_c} \tag{5.5b}$$

For the system of interest, a collection of micrometer size colloids ($a\sim$ 1 μm) immersed in a viscous fluid with a typical speed of micrometers per second, the corresponding Re of the system is very small ($\sim 10^{-3} - 10^{-1}$). Besides, the interested phenomena here usually happen in the diffusion time scale ($\tau_D = 6\pi\mu a^3/k_B T \sim 1$ s) or longer, which results in a small St and the effect due to transient Stokes' flows is negligible. Therefore, the N-S equations reduce as the Stokes' equations [Eqn. 5.4, $\mathrm{Re}, \mathrm{St} \to 0$]:

$$\begin{cases} \mu \nabla^2 \mathbf{u} = \boldsymbol{\nabla} p + \mathbf{f} \\ \boldsymbol{\nabla} \cdot \mathbf{u} = 0 \end{cases} \tag{5.6}$$

where $\mathbf{u}$ is the velocity field of fluid, p is the pressure, μ is the dynamic viscosity of fluid and $\mathbf{f}$ is the external body force.

5.2.1. Integral representation

As shown in Eqn. 5.6, the Stokes' equations are linear equations and the Green's function of Stokes' equation [**145**, **311**] in the unconfined space is known as the Oseen tensor:

$$\boldsymbol{J}(\mathbf{r}) = \frac{\boldsymbol{I}}{r} + \frac{\mathbf{rr}}{r^3} \tag{5.7}$$

where $r = |\mathbf{r}|$ and $\mathbf{r}$ is the position vector. For the convenience, following expressions in this section adopt the Einstein notation unless explicitly written in the vectorial form. Then, the flow field generated by a point force $\mathbf{F}$ at origin is given as:

$$u_i^{PF} = \frac{1}{8\pi\mu} J_{ij}(\mathbf{r}) F_j \tag{5.8}$$

Thus, by the linearity of the Stokes' equations, the total flow field induced by a collection of finite size rigid particles can be written as:

$$u_i(\mathbf{x}) = u_i^{\infty}(\mathbf{x}) + \frac{1}{8\pi\mu} \sum_{\alpha=1}^{N} \int_{S^\alpha} J_{ij}(\mathbf{x}-\mathbf{y}) f_j(\mathbf{y}) \mathrm{d}S(\mathbf{y}) \tag{5.9}$$

where u_i^{∞} $(i = x, y, z)$ is the background linear velocity field, S^α is the surface of α-th particle $(\alpha = 1, \cdots, N)$, $\mathbf{y}$ is the location at the particle surface, $f_j(\mathbf{y})$ is the force density (or traction force) distributed over the particle surface and

$$f_j(\mathbf{y}) = \sigma_{jk}(\mathbf{y}) n_k(\mathbf{y}) \tag{5.10}$$

where σ_{jk} is the stress tensor and n_k is the outer normal vector of particle surface. The equation 5.9 is known as the integral representation of the solution of Stokes' equation [**131**]. Although this solution is exact, it requires detailed knowledge of force density distribution $\mathbf{f}$ (or stress tensor $\boldsymbol{\sigma}$), which it's generally not known from an experimental point of view. Besides, this formulation relies on the Green's function of the Stokes' equation, which makes it difficult to extend to confinement of complex geometry.

5.2.2. Multipole expansion

Analogous to electrostatics [**129**], the multipole expansion method can be applied to get the leading order contributions of flow fields in Eqn. 5.9 at large distance. Unlike the case of electrostatics which deals with scalar quantities (electric potential φ and electric charges q), here vectorial quantities (flow velocity $\mathbf{u}$ and force density $\mathbf{f}$) and anisotropic Green's function [Eqn. 5.7] add additional mathematical complexities but also result in richer physical interactions. Considering the flow field far away from the particle, i.e. $|\mathbf{x}-\mathbf{y}| \gg |\mathbf{x}^\alpha - \mathbf{y}|$, the Tarloy expansion of the Oseen tensor is:

$$J_{ij}(\mathbf{x}-\mathbf{y}) = J_{ij}(\mathbf{x}-\mathbf{x}^\alpha) + (x_k^\alpha - y_k)\nabla_k J_{ij}(\mathbf{x}-\mathbf{x}^\alpha) + \cdots \tag{5.11}$$

If we truncate the above expansion at the linear order and plug it back into the integral representation [Eqn. 5.9], it gives that

$$u_i(\mathbf{x}) \approx u_i^\infty(\mathbf{x}) + \frac{1}{8\pi\mu}\sum_{\alpha=1}^{N}\int_{S^\alpha}\left[J_{ij}(\mathbf{x}-\mathbf{x}^\alpha) + (x_k^\alpha - y_k)\nabla_k J_{ij}(\mathbf{x}-\mathbf{x}^\alpha)\right] f_j(\mathbf{y})\mathrm{d}S(\mathbf{y}) \tag{5.12}$$

Next, the integrals in above expression will be executed to derive the corresponding expression in terms of force moments.

5.2.2.1. force. The integral of the first term is straightforward to evaluate,

$$\int_{S^\alpha} J_{ij}(\mathbf{x}-\mathbf{x}^\alpha) f_j(\mathbf{y})\mathrm{d}S(\mathbf{y}) = J_{ij}(\mathbf{x}-\mathbf{x}^\alpha)F_j^\alpha \tag{5.13}$$

where F_j^α is the zero-th order moment of force density or the total forces acting on α-th particle. And the propagator of the force (or stokeslet) is simply the Oseen tensor J_{ij}.

The integral of the second term can be rewritten as a more familiar form:

(5.14)
$$\int_{S^\alpha}(x_k^\alpha - y_k)\nabla_k J_{ij}(\mathbf{x}-\mathbf{x}^\alpha)f_j(\mathbf{y})\mathrm{d}S(\mathbf{y}) = -\nabla_k J_{ij}(\mathbf{x}-\mathbf{x}^\alpha)\int_{S^\alpha}(y_k - x_k^\alpha)f_j(\mathbf{y})\mathrm{d}S(\mathbf{y})$$
$$= -\nabla_k J_{ij}\int_{S^\alpha} X_k f_j \mathrm{d}S = -\nabla_k J_{ij}\int_{S^\alpha} M_{jk}\mathrm{d}S$$

where $X_k = y_k - x_k^\alpha$ is the relative distance between particle surface and particle center. And the first moment of surface traction force M_{jk} is defined as:

(5.15)
$$M_{jk} = f_j X_k$$

To connect the first moment of force density $\boldsymbol{M}$ with more familiar mechanical quantities, note that any rank-2 tensor can be decomposed as the sum of scalar, symmetric tensor and anti-symmetric tensor [**312**]:

(5.16)
$$M_{jk} = f_j X_k = \frac{1}{3}f_l X_l \delta_{jk} + \frac{1}{2}(f_j X_k - f_k X_j) + \left[\frac{1}{2}(f_j X_k + f_k X_j) - \frac{1}{3}f_l X_l \delta_{jk}\right]$$

where δ_{ij} is the Kronecker delta, which is 1 if the indexes are equal, and 0 otherwise. The scalar component (trace of the first order moments) does not contribute to the flow field in unconfined space as

(5.17)
$$-\nabla_k J_{ij}\int_{S^\alpha}\frac{1}{3}f_l X_l \delta_{jk}\mathrm{d}S = -\nabla_k J_{ik}\int_{S^\alpha}\frac{1}{3}f_l X_l \mathrm{d}S = 0$$

where the fact that the Oseen tensor is divergence-free ($\nabla_k J_{ik} = 0$) [Appx. B.1] has been applied.

5.2.2.2. torque. The anti-symmetric components of the first order moments $\boldsymbol{M}$ correspond to contributions from the torque,

(5.18)
$$\begin{aligned}
-\nabla_k J_{ij} \int_{S^\alpha} \frac{1}{2}(f_j X_k - f_k X_j)\mathrm{d}S &= \int_{S^\alpha} \left(\frac{1}{2}\nabla_k J_{ij} f_k X_j - \frac{1}{2}\nabla_k J_{ij} f_j X_k \right) \mathrm{d}S \\
&= \int_{S^\alpha} \left(\frac{1}{2}\nabla_k J_{ij} f_n X_m \delta_{nk}\delta_{mj} - \frac{1}{2}\nabla_k J_{ij} f_n X_m \delta_{mk}\delta_{nj} \right) \mathrm{d}S \\
&= \int_{S^\alpha} \frac{1}{2}\nabla_k J_{ij} f_n X_m \left(\delta_{nk}\delta_{mj} - \delta_{nj}\delta_{mk} \right) \mathrm{d}S \\
&= \int_{S^\alpha} \frac{1}{2}\nabla_k J_{ij} f_n X_m \varepsilon_{lnm}\varepsilon_{lkj} = \int_{S^\alpha} \frac{1}{2}\varepsilon_{lkj}\nabla_k J_{ij}\varepsilon_{lnm} f_n X_m \mathrm{d}S \\
&= \left(-\frac{1}{2}\varepsilon_{jkl}\nabla_k J_{il} \right) \int_{S^\alpha} \left(\varepsilon_{jmn} X_m f_n \right) \mathrm{d}S \\
&= R_{ij} \int_{S^\alpha} \tau_j \mathrm{d}S = R_{ij} T_j^\alpha
\end{aligned}$$

where ε_{ijk} is the 3D Levi-Civita symbol, which is 1 if (i, j, k) is an even permutation of $(1, 2, 3)$, -1 if it is an odd permutation, and 0 if any index is repeated. And τ_j is the torque density:

(5.19)
$$\tau_j = \varepsilon_{jmn} X_m f_n$$

and the total torque on α-th particle is:

(5.20)
$$T_j^\alpha = \int_{S^\alpha} \tau_j \mathrm{d}S$$

and R_{ij} is the propagator of torque (or rotlet):

(5.21)
$$R_{ij} = \frac{1}{2}\varepsilon_{ikl}\nabla_k J_{jl}$$

5.2.2.3. stresslet. The symmetric components of the first order moments $\boldsymbol{M}$ correspond to contributions from the stresslet,

(5.22)
$$
\begin{aligned}
&-\nabla_k J_{ij}\int_{S^\alpha}\left[\frac{1}{2}\left(f_j X_k + f_k X_j\right) - \frac{1}{3} f_l X_l \delta_{jk}\right]\mathrm{d}S = -\nabla_k J_{ij}\int_{S^\alpha}\frac{1}{2}\left(f_j X_k + f_k X_j\right)\mathrm{d}S \\
&= -\left[\left(\frac{1}{2}\nabla_k J_{ij} + \frac{1}{2}\nabla_j J_{ik}\right) + \left(\frac{1}{2}\nabla_k J_{ij} - \frac{1}{2}\nabla_j J_{ik}\right)\right]\int_{S^\alpha}\frac{1}{2}\left(f_j X_k + f_k X_j\right)\mathrm{d}S \\
&= -\left(\frac{1}{2}\nabla_k J_{ij} + \frac{1}{2}\nabla_j J_{ik}\right)\int_{S^\alpha}\frac{1}{2}\left(f_j X_k + f_k X_j\right)\mathrm{d}S = -K_{ijk}\int_{S^\alpha} s_{jk}\mathrm{d}S = -K_{ijk}S^\alpha_{jk}
\end{aligned}
$$

where the scalar components have been dropped [Eqn. 5.17] and also note that the double contraction between symmetric and anti-symmetric tensor is zero. The stresslet density s_{jk} is defined as:

$$
s_{jk} = \frac{1}{2}\left(f_j X_k + f_k X_j\right) \tag{5.23}
$$

and the total stresslet on α-th particle is:

$$
S^\alpha_{jk} = \int_{S^\alpha} s_{jk}\mathrm{d}S \tag{5.24}
$$

and the propagator of stresslet is a third-rank tensor:

$$
K_{ijk} = \frac{1}{2}\nabla_k J_{ij} + \frac{1}{2}\nabla_j J_{ik} \tag{5.25}
$$

Please be aware that we can drop the trace part of S_{jk} relies on the choice of the Green's function. It's valid for the Oseen tensor[Eqn. 5.7] but not always for other

choices. More generally, the stresslet should incorporate the scalar part, i.e.

$$s_{ij} = \left[\frac{1}{2}\left(f_i X_j + f_j X_i\right) - \frac{1}{3} f_k X_k \delta_{ij}\right] \tag{5.26}$$

5.2.2.4. flow fields. Finally, the multipole expansion of the integral representation[Eqn.5.9] is obtained by adding flows induced by each force moments together:

$$u_i(\mathbf{x}) \approx u_i^{\infty}(\mathbf{x}) + \frac{1}{8\pi\mu}\sum_{\alpha=1}^{N}\left[J_{ij}(\mathbf{x}-\mathbf{x}^{\alpha})F_j^{\alpha} + R_{ij}(\mathbf{x}-\mathbf{x}^{\alpha})T_j^{\alpha} - K_{ijk}(\mathbf{x}-\mathbf{x}^{\alpha})S_{jk}^{\alpha}\right] \tag{5.27}$$

As shown in the above equation, the flow field depends *linearly* on all force density moments, such as force, torque and stresslet, etc. This is the most important feature of the Stokesian Dynamics (SD), which builds upon the linearity of the Stokes' equation. In principle, the multipole expansion procedure can extend to arbitrary orders. For our interests of system, it suffices to retain only up to the linear order since we care most about the force and torque parts.

The Eqn. 5.27 has a truncation error term of $\mathcal{O}(a/\left|\mathbf{x}-\mathbf{x}^{\alpha}\right|^3)$, where a is the radius of particles. For the case of hard spherical particles, it turns out that the multipole expansion terminates quickly and the error term can be further reduced by introducing curvature terms related to the finite size of particles, which are exact for isolated particles [**121**,**283**]:

$$\begin{aligned} u_i(\mathbf{x}) \approx u_i^{\infty}(\mathbf{x}) + \frac{1}{8\pi\mu}\sum_{\alpha=1}^{N}\Bigg[&\left(1+\frac{1}{6}a^2\nabla^2\right)J_{ij}(\mathbf{x}-\mathbf{x}^{\alpha})F_j^{\alpha} + R_{ij}(\mathbf{x}-\mathbf{x}^{\alpha})T_j^{\alpha} \\ &- \left(1+\frac{1}{10}a^2\nabla^2\right)K_{ijk}(\mathbf{x}-\mathbf{x}^{\alpha})S_{jk}^{\alpha}\Bigg] \end{aligned} \tag{5.28}$$

It shows that the far-field flow induced by a finite size spherical particle can be represented exactly as a force monopole and degenerate force quadrupole; a torque monopole; a stresslet monopole and degenerate stresslet octupole.

For simplicity, only mono-dispersed suspension ($a^\alpha = a, \quad \alpha = 1 \cdots N$) will be discussed in this work. And the theoretical framework introduced here can be easily extended to poly-dispersed suspension [**313**].

5.2.3. Faxén laws

If the mechanical quantities acting on each particles ($\mathbf{F}^\alpha, \mathbf{T}^\alpha, \boldsymbol{S}^\alpha$) are known, the equation 5.28 enables the calculation of flow fields $\mathbf{u}$ providing the observation point $\mathbf{x}$ is sufficiently far away from every particles. However, we are more interested in calculating the kinetic motions of each particles ($\mathbf{U}^\alpha, \boldsymbol{\Omega}^\alpha, \boldsymbol{E}^\alpha$), where $\mathbf{U}^\alpha$ is the translational velocity, $\boldsymbol{\Omega}^\alpha$ is the angular velocity and $\boldsymbol{E}^\alpha$ is the straining velocity of α-th particle. Therefore, those kinetic variables need to be calculated from the flow velocity $\mathbf{u}$.

5.2.3.1. Direct interaction. The simplest situation is the force moments ($\mathbf{F}^\beta, \mathbf{T}^\beta, \boldsymbol{S}^\beta$) acting directly on the particle of interest with motions ($\mathbf{U}^\alpha, \boldsymbol{\Omega}^\alpha, \boldsymbol{E}^\alpha$), i.e. $\alpha = \beta$. In such scenarios, each particle motion modes (translation, rotation and straining) can be solved analytically by balancing the viscous force moments with external force moments [**121**, **131**], which relates the particle motions with external force moments as:

$$\mathbf{F}^\alpha = 6\pi\mu a(\mathbf{U}^\alpha - \mathbf{U}^\infty) \tag{5.29a}$$

$$\mathbf{T}^\alpha = 8\pi\mu a^3(\boldsymbol{\Omega}^\alpha - \boldsymbol{\Omega}^\infty) \tag{5.29b}$$

$$\boldsymbol{S}^\alpha = \frac{20}{3}\pi\mu a^3(\boldsymbol{E}^\alpha - \boldsymbol{E}^\infty) \tag{5.29c}$$

where an externally imposed linear background flow is included,

$$\mathbf{u}^{\infty}(\mathbf{x}) = \mathbf{U}^{\infty} + \boldsymbol{\Omega}^{\infty} \times \mathbf{x} + \boldsymbol{E}^{\infty} \cdot \mathbf{x} \tag{5.30}$$

Therefore, the motion of an isolated particle can be obtained directly from the above expressions.

5.2.3.2. Indirect interaction. A more common situation is the ambient flow generated by force moments $(\mathbf{F}^{\beta}, \mathbf{T}^{\beta}, \boldsymbol{S}^{\beta})$ acting on β-th particle affect the motion of α-th particle $(\mathbf{U}^{\alpha}, \boldsymbol{\Omega}^{\alpha}, \boldsymbol{E}^{\alpha})$, i.e. $\alpha \neq \beta$. The ambient flow field induced by all other particles excluding the α-th particle can be written as:

(5.31)

$$\begin{aligned} u_i'(\mathbf{x}) \approx u_i^{\infty}(\mathbf{x}) + \frac{1}{8\pi\mu} \sum_{\beta=1,\beta\neq\alpha}^{N} \Bigg[& \left(1 + \frac{1}{6}a^2\nabla^2\right) J_{ij}(\mathbf{x}-\mathbf{x}^{\beta}) F_j^{\beta} + R_{ij}(\mathbf{x}-\mathbf{x}^{\beta}) T_j^{\beta} \\ & - \left(1 + \frac{1}{10}a^2\nabla^2\right) K_{ijk}(\mathbf{x}-\mathbf{x}^{\beta}) S_{jk}^{\beta} \Bigg] \\ = u_i^{\infty}(\mathbf{x}) + \frac{1}{8\pi\mu} \sum_{\beta=1,\beta\neq\alpha}^{N} & \left\{ \mathcal{F}\left[J_{ij}(\mathbf{x}-\mathbf{x}^{\beta})\right] F_j^{\beta} + \mathcal{T}\left[J_{ij}(\mathbf{x}-\mathbf{x}^{\beta})\right] T_j^{\beta} - \mathcal{S}\left[J_{ij}(\mathbf{x}-\mathbf{x}^{\beta})\right] S_{jk}^{\beta} \right\} \end{aligned}$$

where $\mathcal{F}\left[J_{ij}(\mathbf{x}-\mathbf{y})\right]$, $\mathcal{T}\left[J_{ij}(\mathbf{x}-\mathbf{y})\right]$ and $\mathcal{S}\left[J_{ij}(\mathbf{x}-\mathbf{y})\right]$ denote linear functions which describe the far-field response to external forces, torques, stresslets respectively, and are functions of the Oseen tensor [Eqn. 5.7] and its derivatives [Appx. B.1]:

$$\mathcal{F}\left[J_{ij}(\mathbf{x}-\mathbf{y})\right] = \left(1 + \frac{a^2}{6}\nabla^2\right) J_{ij}(\mathbf{x}-\mathbf{y}), \quad |\mathbf{x}-\mathbf{y}| > 2a \tag{5.32a}$$

$$\mathcal{T}\left[J_{ij}(\mathbf{x}-\mathbf{y})\right] = R_{ij}(\mathbf{x}-\mathbf{y}) = \frac{1}{2}\varepsilon_{ikl}\nabla_k J_{jl}(\mathbf{x}-\mathbf{y}), \quad |\mathbf{x}-\mathbf{y}| > 2a \tag{5.32b}$$

(5.32c)

$$\mathcal{S}\left[J_{ij}(\mathbf{x}-\mathbf{y})\right]=\left(1+\frac{a^2}{10}\nabla^2\right)K_{ijk}(\mathbf{x}-\mathbf{y})=\left(1+\frac{a^2}{10}\nabla^2\right)\frac{1}{2}\left(\nabla_k J_{ij}+\nabla_j J_{ik}\right),\quad |\mathbf{x}-\mathbf{y}|>2a$$

5.2.3.3. the Faxén laws in differential form. If we follow the calculation procedure for a single isolated particle [Eqn. 5.29], we should compute the corresponding stress generated by the ambient flow $\mathbf{u}'$ and balance it with the viscous stress to determine the particle motions. Fortunately, the so-called Faxén laws provide elegant shortcuts to the results. By leveraging the Lorentz Reciprocal Theorem (LRT) [Sec. 5.2.4.1], resulting kinetic motions of α-th particle due to the ambient flow $\mathbf{u}'$ induced by other particles ($\beta \neq \alpha$) can be written as [**121**]:

$$\begin{cases} U_i^\alpha - U_i^\infty(\mathbf{x}^\alpha)=\mathcal{F}\left[u_i'(\mathbf{x});\mathbf{x}^\alpha\right]=\left(1+\dfrac{a^2}{6}\nabla^2\right)u_i'(\mathbf{x}^\alpha) \\ \Omega_i^\alpha - \Omega_i^\infty(\mathbf{x}^\alpha)=\mathcal{T}[u_i'(\mathbf{x});\mathbf{x}^\alpha]=\dfrac{1}{2}\varepsilon_{ijk}\nabla_j u_k'(\mathbf{x}^\alpha) \\ E_{ij}^\alpha - E_{ij}^\infty(\mathbf{x}^\alpha)=\mathcal{S}[u_i'(\mathbf{x});\mathbf{x}^\alpha]=\left(1+\dfrac{a^2}{10}\nabla^2\right)\dfrac{1}{2}\left[\nabla_j u_i'(\mathbf{x}^\alpha)+\nabla_i u_j'(\mathbf{x}^\alpha)\right] \end{cases} \tag{5.33}$$

where $\mathcal{F}\left[u_i'(\mathbf{x});\mathbf{x}^\alpha\right]$, $\mathcal{T}\left[u_i'(\mathbf{x});\mathbf{x}^\alpha\right]$ and $\mathcal{S}\left[u_i'(\mathbf{x});\mathbf{x}^\alpha\right]$ are the same linear functions used in Eqn. 5.31 but applied to the ambient flow $\mathbf{u}'(\mathbf{x})$ and evaluated at the position of α-th particle $\mathbf{x}^\alpha$ instead. As $\mathcal{F}\left[\,\cdot\,\right]$, $\mathcal{T}\left[\,\cdot\,\right]$ and $\mathcal{S}\left[\,\cdot\,\right]$ are linear differential operators, the above relations[Eqn. 5.33] is referred as the Faxén laws in differential form.

5.2.4. Far-field mobility tensors

Next, the kinetic motions of particles are readily available by substituting the ambient flow[Eqn. 5.31] into the Faxén laws[Eqn. 5.33]. As all operators involved are linear due

to the linearity of Stokes' equation, the relation connecting kinetic motions $(\mathbf{U}^\alpha, \boldsymbol{\Omega}^\alpha, \boldsymbol{E}^\alpha)$ and force moments $(\mathbf{F}^\alpha, \mathbf{T}^\alpha, \boldsymbol{S}^\alpha)$ can be written in a matrix form:

$$\begin{pmatrix} \mathbf{U}^\alpha - \mathbf{U}^\infty \\ \boldsymbol{\Omega}^\alpha - \boldsymbol{\Omega}^\infty \\ \boldsymbol{E}^\alpha - \boldsymbol{E}^\infty \end{pmatrix} = \mathcal{M}_\infty \begin{pmatrix} \mathbf{F}^\alpha \\ \mathbf{T}^\alpha \\ \boldsymbol{S}^\alpha \end{pmatrix} \tag{5.34}$$

where $\mathcal{M}_\infty$ is the far-field grand mobility tensor as it's essentially based on the far-field multipole expansion. In the above expression, only quantities of α-th particle are explicitly written insides the parentheses for compactness, which actually denotes quantities of every particles all stacked together into a single vector. To be clear, the grand mobility tensor can be decomposed into a block-wise form:

$$\mathcal{M}_\infty = \begin{pmatrix} \boldsymbol{M}^\infty_{UF} & \boldsymbol{M}^\infty_{UT} & \boldsymbol{M}^\infty_{US} \\ \boldsymbol{M}^\infty_{\Omega F} & \boldsymbol{M}^\infty_{\Omega T} & \boldsymbol{M}^\infty_{\Omega S} \\ \boldsymbol{M}^\infty_{EF} & \boldsymbol{M}^\infty_{ET} & \boldsymbol{E}^\infty_{ES} \end{pmatrix} \tag{5.35}$$

where $\boldsymbol{M}^\infty_{XY}$ denotes the far-field mobility tensor connecting the kinetic motion X ($X = U, \Omega$ or E) resulted from the force moment Y ($Y = F, T$ or S) between N particles. For

the mobility tensors between two different particles ($\alpha \neq \beta$),

$$\boldsymbol{M}_{UF}^{\alpha\beta} = \left(M_{UF}{}^{\alpha\beta}{}_{ij}\right) = \frac{1}{8\pi\mu}\left(1+\frac{a^2}{6}\nabla^2\right)\left(1+\frac{a^2}{6}\nabla^2\right) J_{ij}(\mathbf{x}^\alpha - \mathbf{x}^\beta) \tag{5.36a}$$

$$\boldsymbol{M}_{UT}^{\alpha\beta} = \left(M_{UT}{}^{\alpha\beta}{}_{ij}\right) = \frac{1}{8\pi\mu}\left(1+\frac{a^2}{6}\nabla^2\right) R_{ij}(\mathbf{x}^\alpha - \mathbf{x}^\beta) \tag{5.36b}$$

$$\boldsymbol{M}_{US}^{\alpha\beta} = \left(M_{US}{}^{\alpha\beta}{}_{ijk}\right) = -\frac{1}{8\pi\mu}\left(1+\frac{a^2}{6}\nabla^2\right)\left(1+\frac{a^2}{10}\nabla^2\right) K_{ijk}(\mathbf{x}^\alpha - \mathbf{x}^\beta) \tag{5.36c}$$

$$\boldsymbol{M}_{\Omega T}^{\alpha\beta} = \left(M_{\Omega T}{}^{\alpha\beta}{}_{ij}\right) = \frac{1}{8\pi\mu}\frac{1}{2}\varepsilon_{ikl}\nabla_k R_{lj}(\mathbf{x}^\alpha - \mathbf{x}^\beta) \tag{5.36d}$$

$$\boldsymbol{M}_{\Omega S}^{\alpha\beta} = \left(M_{\Omega S}{}^{\alpha\beta}{}_{ijk}\right) = -\frac{1}{8\pi\mu}\frac{1}{2}\varepsilon_{ilm}\nabla_l\left(1+\frac{a^2}{10}\nabla^2\right) K_{mjk}(\mathbf{x}^\alpha - \mathbf{x}^\beta) \tag{5.36e}$$

$$\boldsymbol{M}_{ES}^{\alpha\beta} = \left(M_{ES}{}^{\alpha\beta}{}_{ijkl}\right) = -\frac{1}{8\pi\mu}\left(1+\frac{a^2}{10}\nabla^2\right)\left(1+\frac{a^2}{10}\nabla^2\right) \tag{5.36f}$$

$$\frac{1}{2}\left[\nabla_j K_{ikl}(\mathbf{x}^\alpha - \mathbf{x}^\beta) + \nabla_i K_{jkl}(\mathbf{x}^\alpha - \mathbf{x}^\beta)\right]$$

and for the mobility tensors of each particles themselves ($\alpha = \beta$),

$$\boldsymbol{M}_{UF}^{\alpha\alpha} = \left(M_{UF}{}^{\alpha\alpha}{}_{ij}\right) = \frac{1}{6\pi\mu a}\delta_{ij} \tag{5.37a}$$

$$\boldsymbol{M}_{UT}^{\alpha\alpha} = \left(M_{UT}{}^{\alpha\alpha}{}_{ij}\right) = 0 \tag{5.37b}$$

$$\boldsymbol{M}_{US}^{\alpha\alpha} = \left(M_{US}{}^{\alpha\alpha}{}_{ij}\right) = 0 \tag{5.37c}$$

$$\boldsymbol{M}_{\Omega T}^{\alpha\alpha} = \left(M_{\Omega T}{}^{\alpha\alpha}{}_{ij}\right) = \frac{1}{8\pi\mu a^3}\delta_{ij} \tag{5.37d}$$

$$\boldsymbol{M}_{\Omega S}^{\alpha\alpha} = \left(M_{\Omega S}{}^{\alpha\alpha}{}_{ij}\right) = 0 \tag{5.37e}$$

$$\boldsymbol{M}_{ES}^{\alpha\alpha} = \left(M_{ES}{}^{\alpha\alpha}{}_{ijkl}\right) = \frac{3}{20\pi\mu a^3}\delta_{ijkl} \tag{5.37f}$$

where superscripts α and β denote the mobility tensor is between α-th and β-th particle, subscripts i, j, k, l indicate the Cartesian components of each tensors and δ_{ijkl} is the fourth-rank deviatoric traceless unit tensor:

$$\delta_{ijkl} = \frac{1}{2}\left(\delta_{ik}\delta_{jl} + \delta_{il}\delta_{jk} - \frac{2}{3}\delta_{ij}\delta_{kl}\right) \tag{5.38}$$

Note that the Oseen tensor is biharmonic, i.e. $\nabla^4 J_{ij}(\mathbf{r}) = 0$ [Appx. B.1.1], which enables further simplification of mobility tensors. The explicit expressions of all far-field mobility tensors can be found at Appx. B.4.2.

Only the upper half of the grand mobility tensor [Eqn. 5.35] need to be computed because of the symmetry relations between mobility tensors. Actually, the so-called Lorentz Reciprocal Theorem (LRT) imposes constraints on symmetries of mobility tensors.

5.2.4.1. Lorentz reciprocal theorem. Suppose that $(\mathbf{u}^{(1)}, \boldsymbol{\sigma}^{(1)})$ and $(\mathbf{u}^{(2)}, \boldsymbol{\sigma}^{(2)})$ are two different solutions of the Stokes' equation with the same geometry but subjected to different boundary conditions. The Lorentz Reciprocal Theorem states that:

$$\oint_S \mathbf{u}^{(1)} \cdot (\boldsymbol{\sigma}^{(2)} \cdot \hat{\mathbf{n}}) \mathrm{d}S - \int_V \mathbf{u}^{(1)} \cdot (\boldsymbol{\nabla} \cdot \boldsymbol{\sigma}^{(2)}) \mathrm{d}V = \oint_S \mathbf{u}^{(2)} \cdot (\boldsymbol{\sigma}^{(1)} \cdot \hat{\mathbf{n}}) \mathrm{d}S - \int_V \mathbf{u}^{(2)} \cdot (\boldsymbol{\nabla} \cdot \boldsymbol{\sigma}^{(1)}) \mathrm{d}V \tag{5.39}$$

In the absence of the external forces ($\boldsymbol{\nabla} \cdot \boldsymbol{\sigma} = 0$), it reduces as:

$$\oint_S \mathbf{u}^{(1)} \cdot (\boldsymbol{\sigma}^{(2)} \cdot \hat{\mathbf{n}}) \mathrm{d}S = \oint_S \mathbf{u}^{(2)} \cdot (\boldsymbol{\sigma}^{(1)} \cdot \hat{\mathbf{n}}) \mathrm{d}S \tag{5.40}$$

The proof of Lorentz Reciprocal Theorem can be found in many microhydrodynamic books [**121**, **131**, **145**]. Here, the proof will be repeated to emphasize its assumptions

during the derivations. By applying the divergence theorem, it's equivalent to prove that

$$\nabla_i \left(u_j^{(1)} \sigma_{ij}^{(2)} \right) - u_i^{(1)} \nabla_j \sigma_{ij}^{(2)} = \nabla_i \left(u_j^{(2)} \sigma_{ij}^{(1)} \right) - u_i^{(2)} \nabla_j \sigma_{ij}^{(1)} \tag{5.41}$$

Note that

$$\sigma_{ij}^{(2)} \nabla_j u_i^{(1)} = \nabla_j \left(\sigma_{ij}^{(2)} u_i^{(1)} \right) - u_i^{(1)} \nabla_j \sigma_{ij}^{(2)} = \nabla_i \left(u_j^{(1)} \sigma_{ij}^{(2)} \right) - u_i^{(1)} \nabla_j \sigma_{ij}^{(2)} \tag{5.42a}$$

$$\sigma_{ij}^{(1)} \nabla_j u_i^{(2)} = \nabla_j \left(\sigma_{ij}^{(1)} u_i^{(2)} \right) - u_i^{(2)} \nabla_j \sigma_{ij}^{(1)} = \nabla_i \left(u_j^{(2)} \sigma_{ij}^{(1)} \right) - u_i^{(2)} \nabla_j \sigma_{ij}^{(1)} \tag{5.42b}$$

where stress tensors are symmetric ($\sigma_{ij}^{(1)} = \sigma_{ji}^{(1)}$ and $\sigma_{ij}^{(2)} = \sigma_{ji}^{(2)}$) as long as there is no external angular momentum in the system [see Sec. 4.57]. For a general linear constitutive relation of Newtonian liquid, the relation between stress tensor and strain tensor can be written as

$$\sigma_{ij}^{(1)} = \mu_{ijkl} \nabla_l u_k^{(1)}, \quad \sigma_{ij}^{(2)} = \mu_{ijkl} \nabla_l u_k^{(2)} \tag{5.43}$$

Thus,

$$\sigma_{ij}^{(2)} \nabla_j u_i^{(1)} = \mu_{ijkl} \nabla_l u_k^{(2)} \nabla_j u_i^{(1)}, \quad \sigma_{ij}^{(1)} \nabla_j u_i^{(2)} = \mu_{ijkl} \nabla_l u_k^{(1)} \nabla_j u_i^{(2)} \tag{5.44}$$

For the LRT to hold everywhere ($\sigma_{ij}^{(2)} \nabla_j u_i^{(1)} = \sigma_{ij}^{(1)} \nabla_j u_i^{(2)}$), it requires that

$$\mu_{ijkl} = \mu_{klij} \tag{5.45}$$

The viscosity tensor must be invariant under the exchange of index pairs ($ij \leftrightarrow kl$), which corresponds to the time reversal symmetry [see Sec. 6.3.1 and 6.3.6.1 for more discussions].

5.2.4.2. symmetry relations. There are many symmetry relations of mobility tensors constrained by symmetry properties of system. These symmetry relations will come in handy to speed up numeric implementations by skipping redundant computations. For a complete set of symmetry relations, please refer to Appx. B.4.4.

Every symmetry property of system should be reflected in the derived mathematical expressions of mobility tensors [Eqn. 5.36]. There are symmetry relations of component indices (i, j, k, l) [Appx. B.4.4.1] and particle indices (α, β) [Appx. B.4.4.2], which reflects the space symmetry and the parity symmetry of system, respectively. These symmetry relations should be easy to identify and are provided without proof. Besides, there are also symmetry relations constrained by the Lorentz Reciprocal Theorem [Appx. B.4.4.3], which reflects the time reversal symmetry of system. These symmetry relations are provided with its brief proofs. Finally, there are also three symmetry relations can be derived by the definition of the Faxén laws [Appx. B.4.4.4]. These three relations are actually redundant and can be derived from previous three sets of symmetry relations. It serves as a consistency check and also a convenient reference.

Now it should be clear that the grand mobility tensor $\mathcal{M}_\infty$ [Eqn. 5.35] is "symmetric" and only the upper (or lower) half of the matrix needs to be computed as

$$M_{\Omega F}{}^{\alpha\beta}{}_{ij} = M_{UT}{}^{\alpha\beta}{}_{ij}, \quad M_{EF}{}^{\alpha\beta}{}_{ijk} = -M_{US}{}^{\alpha\beta}{}_{kij}, \quad M_{ET}{}^{\alpha\beta}{}_{ijk} = M_{\Omega S}{}^{\alpha\beta}{}_{kij} \tag{5.46}$$

5.2.4.3. positive definiteness. Physically, any valid construction of the grand mobility tensor must ensure the energy dissipation is always positive, i.e.

$$\mathcal{P} = \mathbf{F}^T\mathbf{U} = \mathbf{F}^T\mathcal{M}\mathbf{F} > 0, \quad \forall \mathbf{F} \neq \mathbf{0} \tag{5.47}$$

Mathematically, the above expression is a quadratic form and it is equivalent to say that the grand mobility tensor $\mathcal{M}$ is *positive definite*.

5.2.5. Near-field resistance tensors - lubrication theory

So far, the far-field mobility tensors $\mathcal{M}_\infty$ enable the computation of particle motions as long as the average distance between particles are sufficiently larger than the particle radius ($\left|\mathbf{x}^\alpha - \mathbf{x}^\beta\right| \gg 2a$). This corresponds to the scenario of dilute suspension. However, for the case of dense suspension, particles are commonly close to each other or nearly in contact ($\left|\mathbf{x}^\alpha - \mathbf{x}^\beta\right| \sim 2a$). The original multipole expansion based calculation[Eqn. 5.11] converges slowly in such conditions and requires an in-practically large number of higher order moments to obtain sufficient accuracy. In order to overcome these difficulties in the short range, methods based on analytic solutions and asymptotic analysis are developed [**313**–**316**] to calculate the short range hydrodynamic interactions (or lubrication interactions) between two particles accurately and efficiently.

If only two-body interactions are considered for the near-field hydrodynamic interactions, the near-field hydrodynamic interactions are pairwise additive and can be similarly

expressed in a matrix form:

$$\begin{pmatrix} \mathbf{F}^{\alpha} \\ \mathbf{T}^{\alpha} \\ \boldsymbol{S}^{\alpha} \end{pmatrix} = \mathcal{R}_{\delta} \begin{pmatrix} \mathbf{U}^{\alpha} - \mathbf{U}^{\infty} \\ \boldsymbol{\Omega}^{\alpha} - \boldsymbol{\Omega}^{\infty} \\ \boldsymbol{E} - \boldsymbol{E}^{\infty} \end{pmatrix} \tag{5.48}$$

where is $\mathcal{R}_{\delta}$ the near-field grand resistance tensor, which takes into account of the lubrication interactions for two closely spaced spherical particles and is constructed by summing the resistance tensors between all particle pairs within a cutoff distance d^c:

$$\mathcal{R}_{\delta} = \sum_{(\alpha,\beta):\left|\mathbf{x}^{\alpha}-\mathbf{x}^{\beta}\right|<d^c} \left(\mathcal{R}_{\delta}^{\alpha\beta}\right) \tag{5.49}$$

where $\mathcal{R}_{\delta}^{\alpha\beta}$ is the resistance tensor between α-th particle and β-th particle. And, the full resistance tensor $\mathcal{R}_{\delta}$ can be written in a block-wise form:

$$\mathcal{R}_{\delta} = \begin{pmatrix} \boldsymbol{R}_{FU}^{\delta} & \boldsymbol{R}_{F\Omega}^{\delta} & \boldsymbol{R}_{FE}^{\delta} \\ \boldsymbol{R}_{TU}^{\delta} & \boldsymbol{R}_{T\Omega}^{\delta} & \boldsymbol{R}_{TE}^{\delta} \\ \boldsymbol{R}_{SU}^{\delta} & \boldsymbol{R}_{S\Omega}^{\delta} & \boldsymbol{R}_{SE}^{\delta} \end{pmatrix} \tag{5.50}$$

where $\boldsymbol{R}_{YX}$ denotes the near-field resistance tensor connecting the force moment Y ($Y = F, T$ or S) due to the kinetic motion X ($X = U, \Omega$ or E) between N particles. Each of

these resistance tensors between α-th particle and β-th particle are:

$$\boldsymbol{R}_{FU}^{\alpha\beta} = \left({R_{FU}}^{\alpha\beta}{}_{ij} \right) = \mathsf{X}_{FU}^{\gamma} L_{ij}^{1} + \mathsf{Y}_{FU}^{\gamma} L_{ij}^{2} \tag{5.51a}$$

$$\boldsymbol{R}_{TU}^{\alpha\beta} = \left({R_{TU}}^{\alpha\beta}{}_{ij} \right) = \mathsf{Y}_{TU}^{\gamma} L_{ij}^{3} \tag{5.51b}$$

$$\boldsymbol{R}_{SU}^{\alpha\beta} = \left({R_{SU}}^{\alpha\beta}{}_{ijk} \right) = \mathsf{X}_{SU}^{\gamma} L_{ijk}^{4} + \mathsf{Y}_{SU}^{\gamma} L_{ijk}^{5} \tag{5.51c}$$

$$\boldsymbol{R}_{T\Omega}^{\alpha\beta} = \left({R_{T\Omega}}^{\alpha\beta}{}_{ij} \right) = \mathsf{X}_{T\Omega}^{\gamma} L_{ij}^{1} + \mathsf{Y}_{T\Omega}^{\gamma} L_{ij}^{2} \tag{5.51d}$$

$$\boldsymbol{R}_{S\Omega}^{\alpha\beta} = \left({R_{S\Omega}}^{\alpha\beta}{}_{ijk} \right) = \mathsf{Y}_{S\Omega}^{\gamma} L_{ijk}^{6} \tag{5.51e}$$

$$\boldsymbol{R}_{SE}^{\alpha\beta} = \left({R_{SE}}^{\alpha\beta}{}_{ijkl} \right) = \mathsf{X}_{SE}^{\gamma} L_{ijkl}^{7} + \mathsf{Y}_{SE}^{\gamma} L_{ijkl}^{8} + \mathsf{Z}_{SE}^{\gamma} L_{ijkl}^{9} \tag{5.51f}$$

where $\mathsf{X}_{YX}^{\gamma}\left(\left|\mathbf{r}^{\alpha} - \mathbf{r}^{\beta}\right|\right)$,$\mathsf{Y}_{YX}^{\gamma}\left(\left|\mathbf{r}^{\alpha} - \mathbf{r}^{\beta}\right|\right)$ and $\mathsf{Z}_{YX}^{\gamma}\left(\left|\mathbf{r}^{\alpha} - \mathbf{r}^{\beta}\right|\right)$ ($Y = F, T$ or S and $X = U, \Omega$ or E) are scalar resistance functions of the resistance tensor $\boldsymbol{R}_{YX}^{\alpha\beta}$, which only depend on the relative distance between α-th particle and β-th particle (also the particle size ratio if particles are not equal sized). The superscript γ is a parameter used for distinguishing self and mutual cases, which is defined as:

$$\gamma = \begin{cases} 1 & \alpha = \beta \\ 2 & \alpha \neq \beta \end{cases} \tag{5.52}$$

and $\boldsymbol{L}^{i}, i = 1, 2, \cdots, 9$ are unit displacement tensors representing each independent relative motion modes between two particles (for example, $\boldsymbol{L}^{1}$, $\boldsymbol{L}^{2}$ and $\boldsymbol{L}^{3}$ correspond to squeezing,

shearing and vortical motion respectively):

$$L^1_{ij} = \hat{r}_i\hat{r}_j \tag{5.53a}$$

$$L^2_{ij} = \delta_{ij} - \hat{r}_i\hat{r}_j \tag{5.53b}$$

$$L^3_{ij} = \varepsilon_{ijk}\hat{r}_k \tag{5.53c}$$

$$L^4_{ijk} = \left(\hat{r}_i\hat{r}_j - \frac{1}{3}\delta_{ij}\right)\hat{r}_k \tag{5.53d}$$

$$L^5_{ijk} = \hat{r}_i\delta_{jk} + \hat{r}_j\delta_{ik} - 2\hat{r}_i\hat{r}_j\hat{r}_k \tag{5.53e}$$

$$L^6_{ijk} = \varepsilon_{ikl}\hat{r}_l\hat{r}_j + \varepsilon_{jkl}\hat{r}_l\hat{r}_i \tag{5.53f}$$

$$L^7_{ijkl} = \frac{3}{2}\left(\hat{r}_i\hat{r}_j - \frac{1}{3}\delta_{ij}\right)\left(\hat{r}_k\hat{r}_l - \frac{1}{3}\delta_{kl}\right) \tag{5.53g}$$

$$L^8_{ijkl} = \frac{1}{2}\left(\hat{r}_i\delta_{jl}\hat{r}_k + \hat{r}_j\delta_{il}\hat{r}_k + \hat{r}_i\delta_{jk}\hat{r}_l + \hat{r}_j\delta_{ik}\hat{r}_l - 4\hat{r}_i\hat{r}_j\hat{r}_k\hat{r}_l\right) \tag{5.53h}$$

$$\begin{aligned} L^9_{ijkl} = \frac{1}{2}\big(&\delta_{ik}\delta_{jl} + \delta_{jk}\delta_{il} - \delta_{ij}\delta_{kl} + \hat{r}_i\hat{r}_j\delta_{kl} + \delta_{ij}\hat{r}_k\hat{r}_l \\ &-\hat{r}_i\delta_{jl}\hat{r}_k - \hat{r}_j\delta_{il}\hat{r}_k - \hat{r}_i\delta_{jk}\hat{r}_l - \hat{r}_j\delta_{ik}\hat{r}_l + \hat{r}_i\hat{r}_j\hat{r}_k\hat{r}_l\big) \end{aligned} \tag{5.53i}$$

where $\hat{r}_i$ is the i-th component of the unit direction vector $\hat{\mathbf{r}} = (\mathbf{r}^\alpha - \mathbf{r}^\beta)/\left|\mathbf{r}^\alpha - \mathbf{r}^\beta\right|$.

Therefore, the key of the lubrication interactions is to determine those scalar resistance functions $\mathsf{X}^\gamma_{YX}\left(\left|\mathbf{r}^\alpha - \mathbf{r}^\beta\right|\right)$,$\mathsf{Y}^\gamma_{YX}\left(\left|\mathbf{r}^\alpha - \mathbf{r}^\beta\right|\right)$ and $\mathsf{Z}^\gamma_{YX}\left(\left|\mathbf{r}^\alpha - \mathbf{r}^\beta\right|\right)$. If we can find explicit expressions of those scalar resistance functions, the near-field resistance tensors can be similarly computed just like the far-field mobility tensors. Unfortunately, it turns out that it's rather difficult to find explicit expressions of those scalar resistance functions work well for a wide range of particle separation. For example, asymptotic expressions of each scalar resistance functions [**121**,**317**] are derived when the gap distance between two

particles δ is very small. By using the Lamb's solution of Stokes' equation and the Method of Reflections [**316**], numeric values of each scalar resistance functions can be numerically evaluated. The multipole expansion can also be utilized to evaluate those scalar resistance functions providing sufficient higher order terms [**314**, **318**]. Each of those methods have their own applicable range of separation distance. A convenient practice is to numerically evaluate those scalar resistance functions using different methods at various separation distance and get the full range of numeric values by interpretation [**313**, **319**]. As shown in figure 5.1, values of scalar resistance functions (for simplicity, only X^{γ}_{FU}, Y^{γ}_{FU}, Y^{γ}_{TU}, $\mathsf{X}^{\gamma}_{T\Omega}$ and $\mathsf{Y}^{\gamma}_{T\Omega}$ are shown) can be obtain via interpretation at any particular particle separation distance, which in turn can be used for constructing the near-field resistance tensors [Eqn. 5.50].

5.2.6. Near-field mobility tensors - RPY approximation

From a physic point of view, when the gap distance δ between two particles is in nanometer scale, additional effects other than pure hydrodynamic interactions may become more important, such as the frictional contacts [**320**–**323**]. The lubrication interactions derived for an ideally smooth spherical particle may not be able to describe short range behaviors in systems such as a dense suspension.

From a simulation point of view, as two particles are closely separated or even in contact, the diverging nature of lubrication interactions ($1/\delta$ for squeezing motion and $\log(\delta)$ for shearing motion) [Fig. 5.1] generally create an ill-conditioned near-field resistance matrix, which deteriorate the convergence of iterative solvers. Direct solvers can be used to invert the ill-conditioned matrix but it's generally costly unless specifically optimized

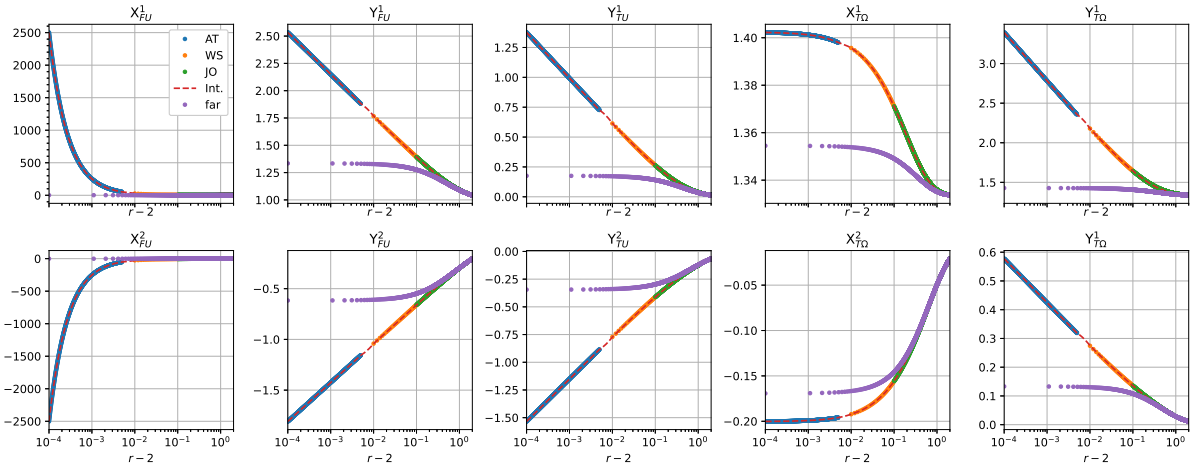

Figure 5.1. Plots of scalar resistance functions of resistance tensors $\boldsymbol{R}_{FU}$, $\boldsymbol{R}_{TU}$ and $\boldsymbol{R}_{T\Omega}$ evaluated by different methods with respect to scaled separation distance $\delta = r - 2 = \left|\mathbf{r}^{\alpha} - \mathbf{r}^{\beta}\right| / a - 2$. The x-axis is shown in logarithmic scale. The first and second row of subplots correspond to the case $\gamma = 1$ and $\gamma = 2$ respectively. The blue dots are the asymptotic values given by [**317**]; the orange dots are the numeric values derived by the Lamb's solution and the Method of Reflections [**316**]; the green dots are the numeric values derived by the multipole expansion [**314**, **318**]. The red dash line indicates a linear interpretation of all three method over the whole tabulated range [**313**, **319**]. The purple dots correspond to the far-field values by directly inverting the far-field mobility tensors[Eqn. 5.35], which matches with near-field values smoothly at large distance.

with special properties of the ill-conditioned matrix [see Sec. 5.3.6]. It's intuitive to prevent two particles from overlapping by introducing a strong repulsion between particles. However, a strong short-range repulsion severely limits the maximum time step of the simulation [**324**], especially for the dense suspension, which limits the access to the long time behaviors like diffusion, sedimentation, etc.

Therefore, although the near-field hydrodynamic interactions can be in principle computed accurately from lubrication theory [Sec. 5.2.5], it's practically more convenient to simply regularize the interactions between overlapping particles, especially when the

near-field interactions are not important in the system. Such regularized interactions can be systematically derived based on the Rotne-Prager-Yamakawa (RPY) approximation [**278**, **300**, **325**] shown below.

5.2.6.1. ambient flow - integral form. As shown in equation 5.31, the ambient flow induced by other particles at large distance($\left|\mathbf{x}-\mathbf{x}^{\beta}\right| \gg 2a$) excluding the α-th itself can be written as:

$$u_i'(\mathbf{x}) - u_i^{\infty}(\mathbf{x}) \approx$$

$$\frac{1}{8\pi\mu}\sum_{\beta=1,\beta\neq\alpha}^{N}\left\{\mathcal{F}\left[J_{ij}(\mathbf{x}-\mathbf{x}^{\beta})\right]F_j^{\beta} + \mathcal{T}\left[J_{ij}(\mathbf{x}-\mathbf{x}^{\beta})\right]T_j^{\beta} - \mathcal{S}\left[J_{ij}(\mathbf{x}-\mathbf{x}^{\beta})\right]S_{jk}^{\beta}\right\}, \left|\mathbf{x}-\mathbf{x}^{\beta}\right| \gg 2a$$

where the functional forms of $\mathcal{F}\left[J_{ij}(\mathbf{x}-\mathbf{y})\right]$, $\mathcal{T}\left[J_{ij}(\mathbf{x}-\mathbf{y})\right]$ and $\mathcal{S}\left[J_{ij}(\mathbf{x}-\mathbf{y})\right]$ are given in equation 5.32, which are expressed in differential forms and only valid at large distance. However, keep in mind that the multipole expansion actually treat each particle as a point particle with each order of moments acting on it. To consider the interactions between two closely separated particles of finite size, the most naive approximation is to simply assume each force moments uniformly distributed on the particle surface, i.e.

(5.54)
$$u_i'(\mathbf{x}) - u_i^{\infty}(\mathbf{x}) \approx \frac{1}{8\pi\mu}\sum_{\beta=1,\beta\neq\alpha}^{N}\oint_{S^{\beta}} J_{ij}(\mathbf{x}-\mathbf{y})\left[\frac{F_j^{\beta}}{4\pi a^2} + \frac{3}{8\pi a^3}\epsilon_{jkl}T_k^{\beta}n_l\mathrm{d}S + \frac{3}{4\pi a^3}S_{jk}^{\beta}n_k\right]\mathrm{d}S$$

We can prove that the far-field expansion of the above integral expression of ambient flow matches with the differential form shown in equation 5.31 [see Appx. B.3.1]. Therefore, the integral forms of $\mathcal{F}\left[J_{ij}(\mathbf{x}-\mathbf{y})\right]$, $\mathcal{T}\left[J_{ij}(\mathbf{x}-\mathbf{y})\right]$ and $\mathcal{S}\left[J_{ij}(\mathbf{x}-\mathbf{y})\right]$ can be defined

as:

$$\mathcal{F}\left[J_{ij}(\mathbf{x}-\mathbf{y});S\right]=\frac{1}{4\pi a^2}\oint_S \widetilde{J}_{ij}(\mathbf{x}-\mathbf{y})\mathrm{d}S(\mathbf{y}) \tag{5.55a}$$

$$\mathcal{T}\left[J_{ij}(\mathbf{x}-\mathbf{y});S\right]=\frac{3}{8\pi a^3}\oint_S \widetilde{R}_{ij}(\mathbf{x}-\mathbf{y})\mathrm{d}S(\mathbf{y}) \tag{5.55b}$$

$$\mathcal{S}\left[J_{ij}(\mathbf{x}-\mathbf{y});S\right]=\frac{3}{4\pi a^3}\oint_S \widetilde{K}_{ijk}(\mathbf{x}-\mathbf{y})\mathrm{d}S(\mathbf{y}) \tag{5.55c}$$

where the integral is evaluated at the surface S and propagators of each force moments are redefined as:

$$\widetilde{J}_{ij}(\mathbf{x}-\mathbf{y})=J_{ij}(\mathbf{x}-\mathbf{y}) \tag{5.56a}$$

$$\widetilde{R}_{ij}(\mathbf{x}-\mathbf{y})=J_{ik}(\mathbf{x}-\mathbf{y})\varepsilon_{kjl}n_l \tag{5.56b}$$

$$\widetilde{K}_{ijk}(\mathbf{x}-\mathbf{y})=\frac{1}{2}\left[J_{ij}(\mathbf{x}-\mathbf{y})n_k+J_{ik}(\mathbf{x}-\mathbf{y})n_j\right] \tag{5.56c}$$

Although the assumption of uniform distribution of force moments might be too strong for general geometry of particles, it works nicely for spherical particles as there is no reason for force moments to deviate from uniform distribution due to the spherical symmetry. Therefore, we obtain the expression of ambient flow in integral form, which works even for closely touching particles:

(5.57)

$$u_i'(\mathbf{x})-u_i^{\infty}(\mathbf{x})\approx\frac{1}{8\pi\mu}\sum_{\beta=1,\beta\neq\alpha}^{N}\left\{\mathcal{F}\left[J_{ij}(\mathbf{x}-\mathbf{x}^{\beta})\right]F_j^{\beta}+\mathcal{T}\left[J_{ij}(\mathbf{x}-\mathbf{x}^{\beta})\right]T_j^{\beta}+\mathcal{S}\left[J_{ij}(\mathbf{x}-\mathbf{x}^{\beta})\right]S_{jk}^{\beta}\right\}$$

Particularly, it can be shown that [see Appx. B.2.1]:

$$M_{ij}^{F}(\mathbf{x}) = \frac{1}{8\pi\mu}\mathcal{F}\left[J_{ij}(\mathbf{x}-\mathbf{y}); S^{\beta}\right] = \begin{cases} \left(1+\frac{a^2}{6}\nabla^2\right)\frac{J_{ij}(\mathbf{x}-\mathbf{x}^{\beta})}{8\pi\mu} & \left|\mathbf{x}-\mathbf{x}^{\beta}\right| > a \\ \frac{1}{6\pi\mu a}\delta_{ij} & \left|\mathbf{x}-\mathbf{x}^{\beta}\right| \leq a \end{cases} \tag{5.58a}$$

$$M_{ij}^{T}(\mathbf{x}) = \frac{1}{8\pi\mu}\mathcal{T}\left[J_{ij}(\mathbf{x}-\mathbf{y}); S^{\beta}\right] = \begin{cases} \frac{R_{ij}(\mathbf{x}-\mathbf{x}^{\beta})}{8\pi\mu} & \left|\mathbf{x}-\mathbf{x}^{\beta}\right| > a \\ \frac{1}{8\pi\mu a^3}\varepsilon_{ijk}\left(x_k - x_k^{\beta}\right) & \left|\mathbf{x}-\mathbf{x}^{\beta}\right| \leq a \end{cases} \tag{5.58b}$$

$$M_{ijk}^{S}(\mathbf{x}) = \frac{1}{8\pi\mu}\mathcal{S}\left[J_{ij}(\mathbf{x}-\mathbf{y}); S^{\beta}\right] = \begin{cases} -\left(1+\frac{a^2}{10}\nabla^2\right)\frac{K_{ijk}(\mathbf{x}-\mathbf{x}^{\beta})}{8\pi\mu} & \left|\mathbf{x}-\mathbf{x}^{\beta}\right| > a \\ \frac{1}{\frac{20}{3}\pi\mu a^3}\left(x_l - x_l^{\beta}\right)\delta_{lijk} & \left|\mathbf{x}-\mathbf{x}^{\beta}\right| \leq a \end{cases} \tag{5.58c}$$

5.2.6.2. the Faxén Laws in integral form. Similarly to previous derivations of the Faxén Laws in differential form [Sec. 5.2.3], the same argument still holds with all linear functions $\mathcal{F}[\,\cdot\,]$, $\mathcal{T}[\,\cdot\,]$ and $\mathcal{S}[\,\cdot\,]$ replaced with its integral forms [Eqn. 5.55], i.e.

$$\begin{cases} U_i^{\alpha} - U_i^{\infty}(\mathbf{x}^{\alpha}) = \mathcal{F}\left[u_i'(\mathbf{x}); S^{\alpha}\right] = \dfrac{1}{4\pi a^2}\oint_{S^{\alpha}} u_i'(\mathbf{x})\mathrm{d}S^{\alpha}(\mathbf{x}) \\ \Omega_i^{\alpha} - \Omega_i^{\infty}(\mathbf{x}^{\alpha}) = \mathcal{T}\left[u_i'(\mathbf{x}); S^{\alpha}\right] = \dfrac{3}{8\pi a^3}\oint_{S^{\alpha}} \varepsilon_{ijk}n_j u_k'(\mathbf{x})\mathrm{d}S^{\alpha}(\mathbf{x}) \\ E_{ij}^{\alpha} - E_{ij}^{\infty}(\mathbf{x}^{\alpha}) = \mathcal{S}[u_i'(\mathbf{x}); S^{\alpha}] = \dfrac{3}{4\pi a^3}\oint_{S^{\alpha}} \dfrac{1}{2}\left[u_i'(\mathbf{x})n_j + u_j'(\mathbf{x})n_i\right]\mathrm{d}S^{\alpha}(\mathbf{x}) \end{cases} \tag{5.59}$$

where $\mathcal{F}\left[u_i'(\mathbf{x}); S^{\alpha}\right]$, $\mathcal{T}\left[u_i'(\mathbf{x}); S^{\alpha}\right]$ and $\mathcal{S}\left[u_i'(\mathbf{x}); S^{\alpha}\right]$ are the same linear functions used in Eqn. 5.57 but applied to the ambient flow $\mathbf{u}'(\mathbf{x})$ and evaluated at the surface of α-th

particle S^α instead. As $\mathcal{F}[\,\cdot\,]$, $\mathcal{T}[\,\cdot\,]$ and $\mathcal{S}[\,\cdot\,]$ are linear integral operators, the above relations [Eqn. 5.59] is referred as the Faxén laws in integral form.

5.2.6.3. near-field mobility tensors. Then, plugging the expression of ambient flow [Eqn. 5.57] into the Faxén laws in integral form [Eqn. 5.59], the mobility tensors [Eqn. 5.36] can be similarly defined in its integral form ($\alpha \neq \beta$):

$$\boldsymbol{M}_{UF}^{\alpha\beta} = \left(M_{UF}{}^{\alpha\beta}{}_{ij}\right) = \frac{1}{8\pi\mu}\frac{1}{(4\pi a^2)^2}\oint_{S^\alpha}\oint_{S^\beta}\widetilde{J}_{ij}(\mathbf{x}-\mathbf{y})\mathrm{d}S^\alpha\mathrm{d}S^\beta \tag{5.60a}$$

$$\boldsymbol{M}_{UT}^{\alpha\beta} = \left(M_{UT}{}^{\alpha\beta}{}_{ij}\right) = \frac{1}{8\pi\mu}\frac{1}{4\pi a^2}\frac{3}{8\pi a^3}\oint_{S^\alpha}\oint_{S^\beta}\widetilde{R}_{ij}(\mathbf{x}-\mathbf{y})\mathrm{d}S^\alpha\mathrm{d}S^\beta \tag{5.60b}$$

$$\boldsymbol{M}_{US}^{\alpha\beta} = \left(M_{US}{}^{\alpha\beta}{}_{ijk}\right) = \frac{1}{8\pi\mu}\frac{1}{4\pi a^2}\frac{3}{4\pi a^3}\oint_{S^\alpha}\oint_{S^\beta}\widetilde{K}_{ijk}(\mathbf{x}-\mathbf{y})\mathrm{d}S^\alpha\mathrm{d}S^\beta \tag{5.60c}$$

$$\boldsymbol{M}_{\Omega T}^{\alpha\beta} = \left(M_{\Omega T}{}^{\alpha\beta}{}_{ij}\right) = \frac{1}{8\pi\mu}\left(\frac{3}{8\pi a^3}\right)^2\oint_{S^\alpha}\oint_{S^\beta}\varepsilon_{ikl}n_k\widetilde{R}_{lj}(\mathbf{x}-\mathbf{y})\mathrm{d}S^\alpha\mathrm{d}S^\beta \tag{5.60d}$$

$$\boldsymbol{M}_{\Omega S}^{\alpha\beta} = \left(M_{\Omega S}{}^{\alpha\beta}{}_{ijk}\right) = \frac{1}{8\pi\mu}\frac{3}{8\pi a^3}\frac{3}{4\pi a^3}\oint_{S^\alpha}\oint_{S^\beta}\varepsilon_{ilm}n_l\widetilde{K}_{mjk}(\mathbf{x}-\mathbf{y})\mathrm{d}S^\alpha\mathrm{d}S^\beta \tag{5.60e}$$

$$\boldsymbol{M}_{ES}^{\alpha\beta} = \left(M_{ES}{}^{\alpha\beta}{}_{ijkl}\right) = \frac{1}{8\pi\mu}\left(\frac{3}{4\pi a^3}\right)^2 \oint_{S^\alpha}\oint_{S^\beta}\frac{1}{2}\left[\widetilde{K}_{ikl}(\mathbf{x}-\mathbf{y})n_j + \widetilde{K}_{jkl}(\mathbf{x}-\mathbf{y})n_i\right]\mathrm{d}S^\alpha\mathrm{d}S^\beta \tag{5.60f}$$

For large separation distance ($\left|\mathbf{x}^\alpha - \mathbf{x}^\beta\right| \gg 2a$), the above integral expressions of mobility tensors can be expanded, which reduce into the differential form of mobility tensors [Eqn. 5.36]. Here, we are particularly interested in cases where two particles overlap ($\left|\mathbf{x}^\alpha - \mathbf{x}^\beta\right| \leq 2a$). The evaluations of those surface integrals are rather involved and the details of calculation can be found at Appx. B.3.1. The explicit expressions of near-field

mobility tensors can be found at Appx. B.4.3.

5.2.6.4. limiting behaviors. According to the explicit expressions of near-field mobility tensors [Appx. B.4.3], we can show that all regularized expression reduce as the self-mobilities [Appx. B.4.1] when the separation distance goes to zero:

$$\lim_{r\to 0} M_{UF}{}^{\alpha\beta}{}_{ij} = \frac{1}{6\pi\mu a}\delta_{ij} \tag{5.61a}$$

$$\lim_{r\to 0} M_{UT}{}^{\alpha\beta}{}_{ij} = 0 \tag{5.61b}$$

$$\lim_{r\to 0} M_{US}{}^{\alpha\beta}{}_{ijk} = 0 \tag{5.61c}$$

$$\lim_{r\to 0} M_{\Omega T}{}^{\alpha\beta}{}_{ij} = \frac{1}{8\pi\mu a^3}\delta_{ij} \tag{5.61d}$$

$$\lim_{r\to 0} M_{\Omega S}{}^{\alpha\beta}{}_{ijk} = 0 \tag{5.61e}$$

$$\lim_{r\to 0} M_{ES}{}^{\alpha\beta}{}_{ijkl} = \frac{3}{20\pi\mu a^3}\delta_{ijkl} \tag{5.61f}$$

Also the near-field mobility tensors [Appx. B.4.3] and the far-field mobility tensors [Appx. B.4.2] transit continuously at the particle interface:

$$\lim_{r\to 2a^-} M_{UF}{}^{\alpha\beta}{}_{ij} = \lim_{r\to 2a^+} M_{UF}{}^{\alpha\beta}{}_{ij} \tag{5.62a}$$

$$\lim_{r\to 2a^-} M_{UT}{}^{\alpha\beta}{}_{ij} = \lim_{r\to 2a^+} M_{UT}{}^{\alpha\beta}{}_{ij} \tag{5.62b}$$

$$\lim_{r\to 2a^-} M_{US}{}^{\alpha\beta}{}_{ijk} = \lim_{r\to 2a^+} M_{US}{}^{\alpha\beta}{}_{ijk} \tag{5.62c}$$

$$\lim_{r\to 2a^-} M_{\Omega T}{}^{\alpha\beta}{}_{ij} = \lim_{r\to 2a^+} M_{\Omega T}{}^{\alpha\beta}{}_{ij} \tag{5.62d}$$

$$\lim_{r\to 2a^-} M_{\Omega S}{}^{\alpha\beta}{}_{ijk} = \lim_{r\to 2a^+} M_{\Omega S}{}^{\alpha\beta}{}_{ijk} \tag{5.62e}$$

$$\lim_{r\to 2a^-} M_{ES}{}^{\alpha\beta}{}_{ijkl} = \lim_{r\to 2a^+} M_{ES}{}^{\alpha\beta}{}_{ijkl} \tag{5.62f}$$

Both far-field mobility tensors [Eqn. 5.35] and lubrication resistance tensors [Eqn. 5.51] become singular when two particles overlap. The Rotne-Prager-Yamakawa (RPY) approximation [**301**, **326**] provides an intuitive way to remove those singularities for overlapping particles. It regularizes mobility tensors in a way that continuously transit from pair mobilities to self mobilities when two particles approach each other. From a theoretical perspective, the RPY still truncates at finite force moments and is less accurate comparing with the lubrication theory. From a numeric perspective, the RPY approximation is easier to implement and more robust for temporary particles overlapping in the simulation.

5.2.7. Full-range mobility tensors

With both near-field [Sec. 5.2.5 or Sec. 5.2.6] and far-field [Sec. 5.2.4] hydrodynamic interactions treated separately, the Stokesian Dynamics (SD) basically proposed to combine both descriptions together to get the hydrodynamic interactions over a full range of particle separations [Fig. 5.2]. Mathematically, the hydrodynamic interactions in SD can be written as:

$$\mathcal{M} = \mathcal{M}_\infty + (\mathcal{R}_\delta - \mathcal{R}_\delta^\infty)^{-1} \tag{5.63}$$

where $\mathcal{M}$ is the full grand mobility tensor which contains both near-field and far-field hydrodynamic interactions; $\mathcal{M}_\infty$ is the far-field grand mobility tensor [Eqn. 5.35, Appx. B.4.2], which is a dense matrix as it's constructed for every pairs of particles [Eqn. 5.36 and 5.37]; and $\mathcal{R}_\delta$ is the near-field grand resistance tensor [Eqn. 5.50], which is a sparse matrix as it only has nonzero elements for particle pairs within a cutoff distance d^c [Eqn. 5.49]. The far-field grand resistance tensor $\mathcal{R}_\delta^\infty$ is the inverse of the far-field grand mobility tensor $\mathcal{M}_\infty$, which is substracted from the near-field grand resistance tensor $\mathcal{R}_\delta$ to avoid double counting of far-field hydrodynamic interactions.

Depending on the problems of interest, the full grand mobility tensor $\mathcal{M}$ can be used for solving mobility problems, i.e. the force moments acting on each particles $(\mathbf{F}^\alpha, \mathbf{T}^\alpha, \boldsymbol{S}^\alpha)$ are known and kinetic motions of each particles $(\mathbf{U}^\alpha, \boldsymbol{\Omega}^\alpha, \boldsymbol{E}^\alpha)$ are unknown:

$$\begin{pmatrix} \mathbf{U}^\alpha - \mathbf{U}^\infty \\ \boldsymbol{\Omega}^\alpha - \boldsymbol{\Omega}^\infty \\ \boldsymbol{E}^\alpha - \boldsymbol{E}^\infty \end{pmatrix} = \mathcal{M} \begin{pmatrix} \mathbf{F}^\alpha \\ \mathbf{T}^\alpha \\ \boldsymbol{S}^\alpha \end{pmatrix} \tag{5.64}$$

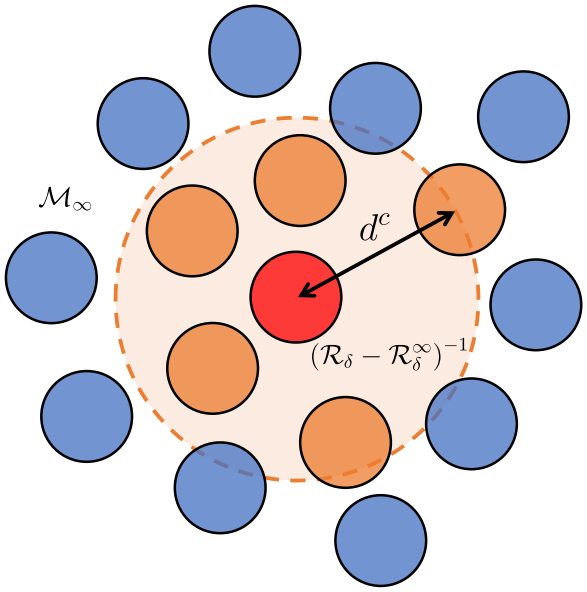

Figure 5.2. A schematic showing the hydrodynamic interactions in Stokesian Dynamics (SD). For an arbitrarily picked center particle (red), it interacts with all neighboring particles (orange) within a cutoff distance d^c via the near-field grand resistance tensor $\mathcal{R}_\delta$. The corresponding far-field grand resistance tensor $\mathcal{R}_\delta^\infty$ is subtracted to avoid double counting of far-field hydrodynamic interactions. All of rest particles outside the cutoff distance (blue) interact with the center particle by the far-field grand mobility tensor $\mathcal{M}_\infty$. Overall, both near-field and far-field hydrodynamic interactions can be combined together and described by a single effective grand mobility tensor $\mathcal{M}$ [Eqn. 5.63].

or resistance problems, i.e. the kinetic motions of each particles $(\mathbf{U}^\alpha, \boldsymbol{\Omega}^\alpha, \boldsymbol{E}^\alpha)$ are known and the force moments acting on each particles $(\mathbf{F}^\alpha, \mathbf{T}^\alpha, \boldsymbol{S}^\alpha)$ are unknown instead:

$$\begin{pmatrix} \mathbf{F}^\alpha \\ \mathbf{T}^\alpha \\ \mathbf{S}^\alpha \end{pmatrix} = \mathcal{M}^{-1} \begin{pmatrix} \mathbf{U}^\alpha - \mathbf{U}^\infty \\ \boldsymbol{\Omega}^\alpha - \boldsymbol{\Omega}^\infty \\ \boldsymbol{E}^\alpha - \boldsymbol{E}^\infty \end{pmatrix} \tag{5.65}$$

Please be aware that these are just theoretical formulations and do not consider the performance of numeric implementations here [see Sec. 5.3.6 for discussion of efficient numeric implementations]. For example, it's more common to use iterative solvers to avoid direct inversion of the grand mobility tensor $\mathcal{M}$ in the resistance formulation.

5.3. Dynamic simulation of a population of Quincke rollers

With the understanding of a single Quincke roller dynamics discussed in Sec. 3.5 and appropriate description of hydrodynamic interactions (HI) between colloidal particles developed in Sec. 5.2, we are ready to extend the description of a single Quincke roller [Chap. 3] to a population of Quincke rollers based on their microscopic interactions.

5.3.1. Dynamics of Quincke rollers

As discussed in Sec. 3.6, a tilted electric dipole moment due to the balance between surface and bulk fluxes of charge carriers is responsible for the steady rolling motion of Quincke particles. Although the surface charge distribution of Quincke rollers is not purely dipolar, especially when rollers are near the electrode surface [Sec. 3.8.2 and Fig. 3.5], the dominant effect should still be contributed by its dipolar components of surface charge distribution of each Quincke rollers. To leading order of approximation [**122**,**123**], each particle effectively carries an electric dipole moment resulting from the dominant dipolar interfacial charge at each particle-fluid interface and evolves according to the surface charge conservation equation [Eqn. 3.51]:

$$\frac{\mathrm{d}\mathbf{P}^{\alpha}}{\mathrm{d}t} = \mathbf{\Omega}^{\alpha} \times (\mathbf{P}^{\alpha} - \chi^{\infty}\mathbf{E}^{\alpha}) - \frac{1}{\tau_{mw}^{P}} \left(\mathbf{P}^{\alpha} - \chi^{0}\mathbf{E}^{\alpha}\right) \tag{5.66}$$

where $\mathbf{P}^\alpha$ and $\mathbf{\Omega}^\alpha$ are the electric dipole moment and the angular velocity of the α-th particle, $\mathbf{E}^\alpha = \mathbf{E}_0 + \delta\mathbf{E}^\alpha$ is the electric field at α-th particle's location, $\mathbf{E}_0$ is the external electric field and $\delta\mathbf{E}^\alpha$ includes contributions from both the surrounding particles and their image dipoles; $\chi^\infty = 4\pi\epsilon_0 a^3 \frac{\epsilon_p - \epsilon_l}{\epsilon_p + 2\epsilon_l}$ and $\chi^0 = 4\pi\epsilon_0 a^3 \frac{\sigma_p - \sigma_l}{\sigma_p + 2\sigma_l}$ are the respective high-frequency and low-frequency polarizability; $\tau^P_{mw} \frac{\epsilon_p + 2\epsilon_l}{\sigma_p + 2\sigma_l}$ is the Maxwell-Wagner relaxation time of dipole moments [**120**]. Please be noted that Eqn. 5.66 does not depend on the fluid flow velocity, which essentially ignores possible electro-osmotic flow effects on the dynamics of surface charge transport.

5.3.2. Electrostatic interactions

Due to the dipolar surface charge distribution, each Quincke particle interacts with the external electric fields:

$$\mathbf{T}^\alpha_{\text{ext}} = \mathbf{P}^\alpha \times \mathbf{E}_0 \tag{5.67}$$

and also with its surrounding rollers via the screened dipole-dipole interaction:

$$U^{\alpha\beta}_{\text{d}}(\mathbf{r}) = \varepsilon_{\text{d}} \exp\left(-\kappa_{\text{d}} r\right) \left[\frac{1}{r^3}\left(\mathbf{P}^\alpha \cdot \mathbf{P}^\beta\right) - \frac{3}{r^5}\left(\mathbf{P}^\alpha \cdot \mathbf{r}\right)\left(\mathbf{P}^\beta \cdot \mathbf{r}\right)\right] \tag{5.68}$$

and Coulombic interaction:

$$U^{\alpha\beta}_{\text{q}}(r) = \varepsilon_q \frac{\exp\left(-\kappa_{\text{q}} r\right)}{r} \tag{5.69}$$

where $\mathbf{r}= \mathbf{r}^\alpha - \mathbf{r}^\beta$, $r = |\mathbf{r}|$ and $\mathbf{r}^\alpha$ is the position of α-th particle; ε_q and κ_q^{-1} are the interaction strength and the screening length of the Coulombic interaction, which is included to account for steric interactions and possible net charges on each particles. Since the concentration of AOT is 150 mM, the κ_q^{-1} is estimated [**149**] as $0.2a$ (500 nm), which makes the Coulombic interaction highly short-ranged and ϵ_q is adjusted to ensure particles do not overlap during simulations. The interaction strength and the screening length of the dipole-dipole interaction are ε_d and κ_d^{-1}, respectively; $\epsilon_d = 1.0$ and $\kappa_d^{-1} \approx 5a \gg \kappa_q^{-1}$ to ensure that each particle can interact with its neighbors about one particle diameter away.

Note that the inter-particle forces and torques due to the *un-screened* dipole-dipole interactions (Eqn. 5.68 without the exponential screening factor) can be computed by taking derivatives with respect to particle positions:

$$\mathbf{F}_{dd}^{\alpha\beta} = \frac{3}{r^5}\left(\mathbf{P}^\alpha \cdot \mathbf{P}^\beta\right)\mathbf{r} - \frac{15}{r^7}\left(\mathbf{P}^\alpha \cdot \mathbf{r}\right)\left(\mathbf{P}^\beta \cdot \mathbf{r}\right)\mathbf{r} + \frac{3}{r^5}\left[\left(\mathbf{P}^\beta \cdot \mathbf{r}\right)\mathbf{P}^\alpha + \left(\mathbf{P}^\alpha \cdot \mathbf{r}\right)\mathbf{P}^\beta\right] \tag{5.70a}$$

$$\mathbf{F}_{dd}^{\beta\alpha} = -\mathbf{F}_{dd}^{\alpha\beta} \tag{5.70b}$$

$$\mathbf{T}_{dd}^{\alpha\beta} = -\frac{1}{r^3}\left(\mathbf{P}^\alpha \times \mathbf{P}^\beta\right) + \frac{3}{r^5}\left(\mathbf{P}^\beta \cdot \mathbf{r}\right)\left(\mathbf{P}^\alpha \times \mathbf{r}\right) \tag{5.71a}$$

$$\mathbf{T}_{dd}^{\beta\alpha} = -\frac{1}{r^3}\left(\mathbf{P}^\beta \times \mathbf{P}^\alpha\right) + \frac{3}{r^5}\left(\mathbf{P}^\alpha \cdot \mathbf{r}\right)\left(\mathbf{P}^\beta \times \mathbf{r}\right) \tag{5.71b}$$

As for the *screened* dipole-dipole interaction described in Eqn. 5.68, a simple chain rule will yield similar force and torques expressions for the screened dipole-dipole interactions.

5.3.3. Hydrodynamic interactions

The total force $\mathbf{F}^\alpha$ and the total torque $\mathbf{T}^\alpha$ acting on α-th particles can be obtained by summing over all electrostatic interactions (EI). Then, the corresponding motion of each particles are calculated via the mobility matrix formulation [Eqn. 5.64] based on the configuration of N particles [**121**]:

$$\begin{pmatrix} \mathbf{U}^\alpha - \mathbf{U}^\infty \\ \boldsymbol{\Omega}^\alpha - \boldsymbol{\Omega}^\infty \\ -\boldsymbol{E}^\infty \end{pmatrix} = \mathcal{M} \begin{pmatrix} \mathbf{F}^\alpha \\ \mathbf{T}^\alpha \\ \boldsymbol{S}^\alpha \end{pmatrix} \tag{5.72}$$

where each particles have been assumed to be rigid ($\boldsymbol{E}^\alpha = 0$). Furthermore, for simplicity, we ignore the contribution from stresslet as we do not intend to study rheological properties of the suspension and also will not consider very dense suspension in this work. Thus, the mobility matrix formulation simplifies as:

$$\begin{pmatrix} \mathbf{U}^\alpha - \mathbf{U}^\infty \\ \boldsymbol{\Omega}^\alpha - \boldsymbol{\Omega}^\infty \end{pmatrix} = \mathcal{M} \begin{pmatrix} \mathbf{F}^\alpha \\ \mathbf{T}^\alpha \end{pmatrix} \tag{5.73}$$

where $\mathbf{U}^\alpha$ and $\boldsymbol{\Omega}^\alpha$ are the translational and angular velocity of $\alpha-$th particle ($\alpha = 1 \cdots N$), respectively; $\mathbf{F}^\alpha$ and $\mathbf{T}^\alpha$ are the force and torque of α-th particle ($\alpha = 1 \cdots N$), respectively; $\mathcal{M}(\mathbf{r}^1, \cdots, \mathbf{r}^N)$ is the grand mobility tensor, which maps the applied forces and torques into the respective translational and angular velocities of each particles.

The explicit expressions of the mobility tensor in an unbound medium have been derived via the multipole expansion method for well-separated pair of particles [Sec. 5.2.4] [**121**, **302**] or using the Rotne-Prager-Yamakawa (RPY) approximation for overlapping

particles [Sec. 5.2.6] [**300**,**301**]. Furthermore, additional wall corrections of these mobility tensors have also been derived for the case near an infinite no-slip boundary based on the method of reflection [**136**,**327**,**328**]. In this work, the hydrodynamic interactions between Quincke rollers are modelled with the Rotne-Prager-Blake tensor with wall corrections [**329**–**331**].

5.3.4. Wall corrections

The existence of bottom electrode surface is an necessary component for creating the rolling motion of Quincke particles [Sec. 3.6], which inevitably introduces additional complexities due to boundary conditions of the system:

1) the no-slip boundary condition for hydrodynamic interactions (HI);
2) the equi-potential boundary condition for electrostatic interactions (EI).

Because of the simple planar geometry of the bottom conducting electrode, both boundary effects can be systematically included by adding wall corrections to both hydrodynamic interactions and electrostatic interactions derived without any confinement.

5.3.4.1. hydrodynamic interactions. Firstly, the bottom electrode surface acts as a non-slippery boundary which modifies the bulk mobility tensors. The most direct consequence of these wall corrections is a non-zero torque-translation coupling, which enables the self-propulsion of Quincke rollers. Depending on the separation distance between the particle and the bottom electrode, the wall corrections of the mobility tensors can be calculated via the method of reflection [**136**] or the lubrication theory [**121**, **137**]. In this work, we follow the former approach to include the wall corrections.

In the presence of a no-slip wall, the overall flow fields can be split as two parts:

$$\mathbf{u}(\mathbf{x}) - \mathbf{u}^{\infty}(\mathbf{x}) = \mathbf{u}^{f}(\mathbf{x}) + \mathbf{u}^{w}(\mathbf{x}) \tag{5.74}$$

where $\mathbf{u}$ and $\mathbf{u}^{\infty}$ are the total and background flow fields respectively, $\mathbf{u}^{f}$ is the flow fields induced by particles in an unconfined space [Eqn. 5.9] and $\mathbf{u}^{w}$ is the additional flow fields due to the presence of a no-slip wall in order to maintain the boundary condition:

$$\mathbf{u}^{f}(\mathbf{x}) + \mathbf{u}^{w}(\mathbf{x}) = 0, \quad \forall \mathbf{x} \in \text{wall} \tag{5.75}$$

Analogous to the image charge construction to fulfill vanishing potential in electrostatics at a conducting surface [**129**], such constraint of vanishing flow fields at no-slip wall can be satisfied by introducing image stokeslets. Without loss of generality, let's assume that there is an infinite planar wall at $z = 0$, the location of particle is $\mathbf{y}$ and the point of interests is $\mathbf{x}$, then the free-space Green's function is given by the Oseen tensor [Eqn. 5.7]:

$$\boldsymbol{J}(\mathbf{x} - \mathbf{y}) = \frac{\boldsymbol{I}}{r} + \frac{\mathbf{rr}}{r^3}$$

and the additional Green's function due to the no-slip wall is [**136**, **327**]:

$$J^{w}_{ij}(\mathbf{x}, \mathbf{y}) = -J_{ij}(\mathbf{x} - \mathbf{y}') + h^2 P_{jk} \nabla^2 J_{ik}(\mathbf{x} - \mathbf{y}') - 2h P_{jk} \nabla_{R_k}(J_{il}\delta_{l3}) \tag{5.76}$$

where $h = y_3$ is the height above the no-slip wall, $\mathbf{y}' = \mathbf{y} - 2h\mathbf{n}$ is the location of image, $\mathbf{R} = \mathbf{x} - \mathbf{y}'$ and the projection operator $\mathbf{P} = \boldsymbol{I} - 2\mathbf{nn}$. Thus, the Green's function with

the wall correction can be constructed as:

$$J_{ij}^{ns}(\mathbf{x},\mathbf{y}) = J_{ij}(\mathbf{x}-\mathbf{y}) + J_{ij}^{w}(\mathbf{x},\mathbf{y}) \tag{5.77}$$

such that $J_{ij}^{ns}(\mathbf{x},\mathbf{y}) = 0, \forall \mathbf{x} \in$ wall. With this modified Green's function which fulfills the no-slip boundary condition, previous derivations for far-field mobility tensors [Sec. 5.2.4] still hold and additional wall correction terms of free-space mobility tensors [Eqn. 5.36] can be obtained by replacing the Oseen tensor $\boldsymbol{J}(\mathbf{x}-\mathbf{y})$ with the no-slip Green's function $\boldsymbol{J}^{ns}(\mathbf{x},\mathbf{y})$. The explicit expressions of those wall correction terms can be found at [**136**].

5.3.4.2. electrostatic interactions. Secondly, the bottom electrode is a conductor, whose surface can be treated as an equi-potential surface. The surface charges carried by Quincke particles induce excess charges on the electrode surface. If we only consider this effect to the dipolar level (the leading order effect), such induced charges on the electrode can be effectively replaced by an image dipole $\mathbf{P}^*$. By the image charge method [**129**], an electric dipole moment $\mathbf{P}$ positioned at (x, y, z) induces an image dipole $\mathbf{P}^*$ positioned at $(x, y, -z)$ which has reflected in-plane dipole moments and unchanged out-of-plane dipole moments, i.e., $\mathbf{P}^* = (-P_x, -P_y, P_z)$. Here, we again assume that the electrode surface is at $z = 0$. To include the effect of image charges, the electric field in Eqn. 5.66 should include contributions from the image dipoles. Besides, the calculation of electric forces and torques exerted upon the particle [Eqn. 5.70 and 5.71] also should include the interactions with image dipoles.

5.3.5. Equations of motion

For a collection of particles immersed in a viscous, incompressible fluid, their behaviors generally can be described by two equivalent theoretical approaches: the Fokker-Planck (F-P) description and the Langevin description. As we are interested in the dynamic behaviors of each particles, the particle-based Langevin description is preferred. Particularly, for low Reynolds number (Re) systems, the Langevin equation reduces as the Brownian equation by considering the time interval beyond the momentum relaxation time scale [**279**–**283**, **332**], which gives the equations of motion (EOM) as:

$$\frac{\mathrm{d}\mathbf{r}}{\mathrm{d}t} = \mathcal{M}\mathbf{F} + \sqrt{2k_BT}\mathcal{M}^{1/2}\mathcal{W} + k_BT\boldsymbol{\nabla}\cdot\mathcal{M} \tag{5.78}$$

where $\mathbf{r}$ and $\mathbf{F}$ should be treat as general configurational and mechanical variables, respectively. $\mathbf{F}$ can be any order of force density moments such as forces, torques and stresslets, etc. And $\mathbf{r}$ denotes the corresponding order of configurational variables such as positions, orientations and deformations, etc. Here, only $\mathbf{r}$ and $\mathbf{F}$ are explicitly written out for the brevity of notations. The first term is the deterministic displacements due to external force moments and $\mathcal{M}$ is the grand mobility tensor; The second term is the stochastic Brownian displacements, where k_B is the Boltzmann constant, T is the temperature and $\mathcal{W}$ is a vector of independent and identically distributed (i.i.d.) standard Gaussian noise, which is linearly transformed by the "square root" of the grand mobility tensor $\mathcal{M}^{1/2}$ to fulfill the Fluctuation-Dissipation Theorem (FDT) [**280**, **282**]:

$$\mathrm{Cov}\left[\Delta\mathbf{r}(t)\right] = 2\mathcal{M}k_BT \tag{5.79}$$

It requires that the covariance of hydrodynamically-correlated stochastic displacements should be equal to the grand mobility tensor with a factor of $2k_BT$. And the third term is the so-called thermal drift term [**331**, **333**], which involves the divergence of the grand mobility tensor. For commonly used mobility tensors such as the Oseen tensors [Eqn. 5.36] or the RPY tensors [Eqn. 5.60], they all possess the divergence-free property so the thermal drift term vanishes for those choices of mobility tensors. However, for systems under confinements such as the case near a planar wall [Sec. 5.3.4.1], the fundamental Green's function has additional corrections [Eqn. 5.76], which may not preserve the divergence-free property of the original Oseen tensor [Eqn. 5.7] and inclusion of the thermal drift term is necessary in such scenarios.

5.3.6. Numeric implementations

In principle, with the grand mobility tensor constructed [Eqn. 5.63] and particle interactions evaluated [Eqn. 5.67 5.68, 5.69], the EOM shown in Eqn. 5.78 is ready to be numerically solved. However, if we look carefully at each terms in the EOM, it's not a trivial task to solve such an equation efficiently and accurately:

(1) deterministic part $\mathcal{M}\mathbf{F}$

This is a deterministic contribution, which involves the multiplication between the grand mobility tensor and the external forces vector. A simple implementation of direct matrix-vector multiplication inevitably introduces both time and space complexity of $\mathcal{O}(N^2)$.

(2) stochastic part $\sqrt{2k_BT}\mathcal{M}^{1/2}\mathcal{W}$

This is a stochastic contribution as it requires generating correlated Gaussian noises. There are efficient algorithms for generating i.i.d. Gaussian random variables [**334**] but it's not easy to generate correlated Gaussian random variables. A straightforward approach is to get the square root of targeted covariance via the Cholesky decomposition [**335**], which involves $\mathcal{O}(N^3)$ time complexity for a direct implementation.

(3) thermal drift $k_BT\boldsymbol{\nabla}\cdot\mathcal{M}$

This term involves the divergence of the mobility tensor, which is also an expensive operation. As even a simple finite difference approach, it requires additional evaluations of the grand mobility tensor to get derivatives of the mobility tensor, which introduces time complexity $\mathcal{O}(N^2)$.

As discussed above, each terms in the EOM requires at least quadratic time complexity for a direct numeric implementation, which prevents practical simulations of experimental scale systems with usual computation powers nowadays. Recent works [**303**–**305**] have successfully reduced the time complexity of the Stokesian Dynamics (SD) simulation as $\mathcal{O}(N)$ by utilizing an Ewald-like formulation, which splits the hydrodynamic interaction and correlated thermal fluctuations into long-ranged and short-ranged parts. This progress makes the large scale simulation of colloidal suspension practical. However, to avoid introducing complicated numerical techniques and obscuring the essential physics, I will follow a more "brutal-force" approach [**328**,**330**,**331**], which is essentially still $\mathcal{O}(N^2)$ algorithm but works in practice by heavily utilizing the parallel computing capability of

modern graphics processing unit (GPU).

5.3.6.1. deterministic part. The computation of deterministic part is a matrix-vector multiplication, which can be easily paralleled as the full grand mobility tensor can be decomposed into a block-wise form:

$$\mathcal{M} = \begin{pmatrix} \boldsymbol{M}_{UF} & \boldsymbol{M}_{UT} & \boldsymbol{M}_{US} \\ \boldsymbol{M}_{\Omega F} & \boldsymbol{M}_{\Omega T} & \boldsymbol{M}_{\Omega S} \\ \boldsymbol{M}_{EF} & \boldsymbol{M}_{ET} & \boldsymbol{E}_{ES} \end{pmatrix} \tag{5.80}$$

For each sub-block of the grand mobility tensor, the interactions between each pair of particles are completely independent and all those computations can be launched simultaneously. However, all those mobility tensors should not be constructed explicitly in the memory to avoid the limitation of memory size and, more importantly, avoid the additional time cost for accessing data from the memory. Instead, a matrix-free implementation is more efficient, which constructs the mobility tensors on-demand for each pair of particles and no explicit arrays needed for storing the mobility tensors. To make this point clear, a simple pseudo code excerpt which computes the $\boldsymbol{M}_{UF}$ block is shown below to demonstrate the typical code structure:

```
@parallel # launch each particle pairs (i,j) in parallel
for i,j in zip(range(N),range(N)):
    # get relative distance from global position arrays of i and j particles
    rij = r[i] - r[j]
    # get forces acting on j particle from global force arrays
```

```
    force = force[j]
    # compute M_{UF} between i and j particles on-the-fly
    M_UF = mobility_UF(i,j,rij) # here, M_UF is only a 3x3 matrix
    # (optional) wall corrections
    M_UF+= mobility_UF_wall(i,j,rij)
    # compute velocities of i particle due to j particle
    velocity = M_UF * force
    # accumulate into the global velocity array of i particle
    U[i] += velocity

@kernel # kernel function executed on each parallel thread
def mobility_UF(self, i, j, rvec):
    if (i==j):
        # construct 3x3 self-mobility tensor M_UF of i particle
        M_UF = self_mobility()
    else:
        # construct 3x3 pair-mobility tensor M_UF between i and j particles
        M_UF = pair_mobility(rvec)
    return M_UF
```

All other sub-blocks of the grand mobility tensor can be computed in parallel in a similar way. There are many available open-source libraries for implementing parallelization, such as OpenCL, CUDA, PyCUDA, Numba and Taichi, etc. All libraries metioned are able to achieve the demand of parallelization here and the choice depends on the targeted

computing architectures and also the familiarity with those packages. Please refer to the documentations of those libraries for more details.

Besides, the full grand mobility tensor consist of both near-field and far-field parts [Eqn. 5.63, which has different numeric characteristics. The far-field mobility tensors $\mathcal{M}_\infty$ are constructed for every pair of particles [Eqn. 5.36], which result in a dense matrix ($\sim \mathcal{O}(N^2)$ nonvanishing matrix elements); On the contrary, the near-filed resistance tensors $\mathcal{R}_\delta$ are only constructed for neighboring particles within a given cutoff distance d^c, which result in a sparse matrix ($\sim \mathcal{O}(6N)$ nonvanishing matrix elements). Therefore, numeric solvers specifically optimized for dense or sparse matrix, for example, Basic Linear Algebra Subprograms (BLAS) [**336**] and Linear Algebra Package (LAPACK) [**337**], can be leveraged to further speed up the computation. A common practice is to tabulate numeric values of near-field scalar resistance functions [Fig. 5.1] and construct the near-field resistance tensors $\mathcal{R}_\delta$ explicitly [**305**, **319**]. Because of the sparse nature of the near-field resistance tensors, those tensors scale linearly with the number of particles and allow very efficient matrix construction and matrix operations such as Cholesky decomposition [**338**]. And, the full grand mobility tensor [Eqn. 5.63] can be rearranged as:

$$\mathcal{M} = \left[\boldsymbol{I} + \mathcal{M}_\infty \left(\mathcal{R}_\delta - \mathcal{R}_\delta^\infty\right)\right]^{-1} \mathcal{M}_\infty$$

and the corresponding deterministic velocities are:

$$\mathbf{U} = \left[\boldsymbol{I} + \mathcal{M}_\infty \left(\mathcal{R}_\delta - \mathcal{R}_\delta^\infty\right)\right]^{-1} \mathcal{M}_\infty \mathbf{F}$$

which is equivalent to solve the following linear equations:

$$[\boldsymbol{I} + \mathcal{M}_\infty (\mathcal{R}_\delta - \mathcal{R}_\delta^\infty)] \mathbf{U} = \mathcal{M}_\infty \mathbf{F} \tag{5.81}$$

As discussed before, the multiplication with the dense far-field mobility tensor $\mathcal{M}_\infty$ is parallelizable. And the spare matrix $\mathcal{R}_\delta - \mathcal{R}_\delta^\infty$ can be tabulated and efficiently constructed on the fly. To avoid direct matrix inversion, Eqn. 5.81 should be solved by iterative linear solvers such as Generalized Minimal Residual Method (GMRES) [**339**]. Depending on the system configurations, appropriate preconditioning matrices [**340**] can also be included for better convergence rate.

5.3.6.2. stochastic part. As the full grand mobility tensor $\mathcal{M}$ is still a dense matrix, a direct Cholesky decomposition ($\sim \mathcal{O}(N^3)$) of the mobility tensor ($\mathcal{M}^{1/2}$) to generate correlated fluctuations is very expensive and will severely limit the overall performance of the simulation. Instead, iterative methods such as a Fixman method [**341**] or a Lanczos-like method are proposed [**342**, **343**] to avoid a direct Cholesky decomposition. Such iterative methods still involve application of the grand mobility tensor so it's still a $\mathcal{O}(N^2)$ algorithm. However, given the fact that the application of the grand mobility tensor is parallelizable and computation usually converge in a modest number of iterations [**319**, **330**, **331**], such iterative methods generally provide a better performance comparing with direct methods and are able to achieve performance in the same order of the deterministic part.

5.3.6.3. thermal drift. In principle, the thermal drift term is deterministic and requires multiple evaluations of derivatives of the grand mobility tensor to get its divergence. However, since there already exists stochastic term due to Brownian noise, the divergence of the grand mobility tensor does not necessarily need to be accurate at each moment but can be relaxed to converge to its true value in a statistically sense. That's the so-called Random Finite Difference (RFD) approach:

$$\boldsymbol{\nabla} \cdot \mathcal{M} \approx \frac{1}{\epsilon} \left\langle \left[\mathcal{M}(\mathbf{r} + \frac{\epsilon}{2}\mathcal{W}^D) - \mathcal{M}(\mathbf{r} - \frac{\epsilon}{2}\mathcal{W}^D) \right] \mathcal{W}^D \right\rangle \tag{5.82}$$

where ϵ is a small parameter which depends on the desired accuracy, $\mathcal{W}^D$ is a standard Gaussian random vector representing random displacements of each particles and $\langle \cdot \rangle$ denotes the statistical average. This is basically a random version of the FDM, which can be proved to converge to the divergence of the grand mobility tensor on average [**331**] but only requires two simple evaluations of the grand mobility tensor at each time step.

5.3.6.4. time integrators. With efficient and accurate computation of all three terms on the right hand side of the EOM [Eqn. 5.78], an appropriate time integrator is also needed to evolve the whole system in time at desired accuracy. Because Eqn. 5.78 is essentially a system of ordinary differential equations, all numeric solvers developed for ODE [**344**] in principle can be applied here although its stochastic nature makes the proof of accuracy more difficult. The design of efficient and accurate numeric schemes is not the focus of this work and there have been lots of discussion of temporal integrator schemes [**328**, **331**, **345**]. Please refer to those works for more details. Unless explicitly specified, a simple second-order Adams-Bashforth (A-B) method [**346**] is used to solve

the EOM throughout this work:

$$\mathbf{r}(t+\Delta t) = \mathbf{r}(t) + \Delta t \left[\frac{3}{2}\mathbf{v}(t) - \frac{1}{2}\mathbf{v}(t-\Delta t)\right] \tag{5.83}$$

where $\mathbf{r}(t)$ is the general configurational variables at time t, $\mathbf{v}(t)$ is the corresponding general velocities (the sum of all three terms on the right hand side of Eqn. 5.78) at time t and Δt is the time step.

5.3.6.5. numeric implementations specific to Quincke particles. So far, all numeric implementations discussed are centered around the EOM [Eqn. 5.78], which works for a general Brownian Dynamics (BD) simulation. In the next, numeric implementations specific to the Quincke system will be elaborated. As mentioned before [Sec. 5.3.2], electrostatic interactions also need to be taken into account for a population of Quincke particles, which relies on a separate equation to describe the dynamics of its internal states (electric dipole moments here [Sec. 5.3.1]). The strength and orientation of electric dipole moments carried by each Quincke particles determine the dipole-dipole interactions and how active forces enter the BD simulation, which ultimately leads to the self-propulsion of Quincke particles. Therefore, a good description of the dynamics of internal states of active particles is important for an accurate simulation of its collective behaviors. Here, by extending the multipole model of a single Quincke particle [Eqn. 3.51] to many particles case, a simple model [Eqn. 5.66] is proposed for describing the time evolution of electric dipole moments of each Quincke particles. Since Eqn. 5.66 is an ODE and also to be consistent with the solver accuracy chose for solving the hydrodynamics [Eqn. 5.83], a second order Runge-Kutta (R-K) method is used for solving the dynamics of electric

dipole moments:

$$\frac{\mathrm{d}\mathbf{P}^{\alpha}(t)}{\mathrm{d}t} = \boldsymbol{\Omega}^{\alpha} \times \left[\mathbf{P}^{\alpha}(t) - \chi^{\infty}\mathbf{E}^{\alpha}\right] - \frac{1}{\tau_{MW}^{P}}\left[\mathbf{P}^{\alpha}(t) - \chi^{0}\mathbf{E}^{\alpha}\right] = f\left[\mathbf{P}^{\alpha}(t), \boldsymbol{\Omega}^{\alpha}(t), \mathbf{E}^{\alpha}(t)\right] \tag{5.84}$$

where the time-dependence of dipole moments is written out explicitly and the corresponding discretized form is:

$$\begin{aligned} \mathbf{P}^{\alpha}(t+\Delta t^{*}) &= \mathbf{P}^{\alpha}(t) + \frac{1}{2}\Delta t^{*}\left(k_1 + k_2\right) \\ k_1 &= f\left[\mathbf{P}^{\alpha}(t), \boldsymbol{\Omega}^{\alpha}(t), \mathbf{E}^{\alpha}(t)\right] \\ k_2 &= f\left[\mathbf{P}^{\alpha}(t) + \Delta t^{*}k_1, \boldsymbol{\Omega}^{\alpha}(t+\Delta t^{*}), \mathbf{E}^{\alpha}(t+\Delta t^{*})\right] \end{aligned} \tag{5.85}$$

The time step used for evolving the electric dipole moment Δt^{*} is usually set as $0.1\Delta t$ to better resolve the dynamics of electric dipole moments. To avoid executing expensive computations multiple times during a single hydrodynamic time step Δt [Eqn. 5.83], the angular velocities and the electric fields are assumed to be constant during the evolution of dipole moment, i.e. $k_2 \approx f\left[\mathbf{P}^{\alpha}(t) + \Delta t^{*}k_1, \boldsymbol{\Omega}^{\alpha}(t), \mathbf{E}^{\alpha}(t)\right]$.

With the electric dipole moments on each Quincke particles, the relevant electrostatic interactions between Quincke particles [Sec. 5.3.2] are ready to be computed. There are many techniques available for efficient implementation of pairwise interaction calculations. For example, by utilizing the neighbor-list or any fast solvers like Ewald summation [**347**], PPPM [**78**], etc, the time cost for computing electrostatic interactions will not be the limiting factor of the overall performance. Detailed implementation of those computation will not be discussed in this work and please refer to common molecular dynamic simulation

packages such as LAMMPS or HOOMD for examples.

After obtaining the external forces acting on each Quincke particles, the hydrodynamic interactions can be computed via the procedures detailed for a general BD simulation [Eqn. 5.78]. However, several features of Quincke particles system setup allow further simplifications.

(1) Firstly, the effect of stresslet is ignored considering the fact that the system is not very dense and the interested phenomena are not related to rheological properties of the whole system [Eqn. 5.73];

(2) Secondly, the packing fraction under consideration is usually about 10% and the lubrication effect is negligible; Thus, the deterministic velocities are simply given by the far-field mobility tensors , i.e.

$$\begin{pmatrix} \mathbf{U}^{\alpha} - \mathbf{U}^{\infty} \\ \boldsymbol{\Omega}^{\alpha} - \boldsymbol{\Omega}^{\infty} \end{pmatrix} = \mathcal{M}^{\infty} \begin{pmatrix} \mathbf{F}^{\alpha} \\ \mathbf{T}^{\alpha} \end{pmatrix}$$

(3) Thirdly, for a typical Quincke roller system, the active velocity (~ 1 mm/s) driven by external electric fields is much large than the diffusive velocity (~ 0.1 μm/s) caused by the thermal energy. The Brownian noise is only important when the roller just starts moving and is negligible once the roller picks up speed. For simplicity, the uncorrelated Brownian noise is used instead:

$$\boldsymbol{\xi} \approx \sqrt{2k_B\chi T}\mathcal{M}_{bulk}^{1/2}\mathcal{W}$$

where $\mathcal{M}_{bulk}$ is the diagonal grand mobility tensor in an unbound medium and $\chi \approx 0.1$ is a factor which accounts for the diffusion hindrance near the boundary [**348**].

All those considerations greatly simplify the simulation complexity and enable simulations close to experiments in both length and time scales. Relevant simulation parameters are list in Table. 5.1 for reference. As a rough reference, a typical simulation performance of 4096 particles on a Nvidia Tesla v100 GPU is about 50 time steps per second including the overhead of I/O operations (still have lots of room of optimizations).

Parameters	Symbols	Values
unit of length	L_c	1 μm
unit of time	τ_c	1 s
unit of mass	M_c	1 mg
number of particles	N	4096
radius of particles	a	2.5 μ m
diameter of circular well	D	1000 μm
applied electric field	E_0	~ 2 V/μm
relative permittivity of the particle	ϵ_p	3
relative permittivity of the liquid	ϵ_l	2
electric conductivity of the particle	σ_p	0 S/cm
electric conductivity of the liquid	σ_l	2×10^{-8} S/cm
dynamic viscosity of the solution	η	3 mPa $\cdot$ s
gap distance	δ	0.1 a
time step	Δt	0.1 - 0.001 ms
dipole steps per time step	Δt^*	0.1 Δt

Table 5.1. Table of simulation parameters for the system of a population of Quincke rollers

5.4. Polar state reversal in suspension of Quincke rollers

Ensembles of interacting self-propelled particles, or active matter, exhibit a plethora of remarkable collective phenomena which have been widely observed and studied in both

biological and artificial systems [**110**, **112**, **349**–**355**]. Many synthetic active systems are realized by ensembles of externally energized particles [**264**,**267**,**329**,**356**–**359**]. The onset of globally correlated vortical states in active ensembles is associated with a spontaneous symmetry breaking between two equally probably chiral states (characterized by clockwise or counterclockwise rotations). Once the global state is formed, it is often robust and stable [**360**, **361**]. Subsequent control of such polar states, however, remains elusive and largely unexplored. Here we use a model system of colloidal rollers powered by the Quincke electro-rotation mechanism [**362**, **363**] to demonstrate a control over the polar states in active liquids.

5.4.1. Experimental observations

The experimental system consists of polystyrene spheres dispersed in a weakly conductive liquid that are sandwiched between two ITO-coated glass slides and energized by a static (DC) electric field [Fig. 5.3a]. The particles continuously roll with a typical speed of v_0 ∼0.7 mm s^{-1}, while energized by a uniform DC electric field $E = 2.7$ V μm^{-1}. The rollers experience hydrodynamic and electrostatic interactions that promote alignment of their translational velocities [**110**]. As reported in [**360**], the rollers move randomly and resemble the dynamics of an isotropic gas at low particle number densities. When the density increases above a certain threshold, the rollers self-organize into a single stable vortex [Fig. 5.3] when confined in a well [**360**]. Trajectories of Quincke rollers in the vortex are nearly circular, and the average tangential velocity $\mathbf{v}_t$ increases with the distance from the center [Fig. 5.3a,b].

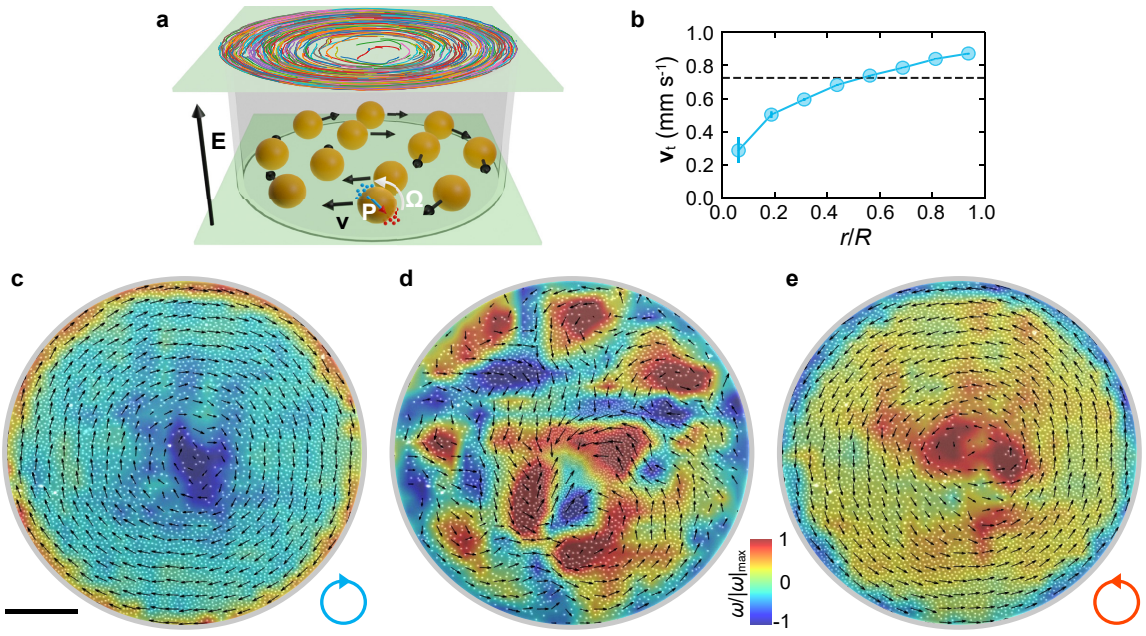

Figure 5.3. **a**, A sketch of the experimental setup. Red and blue specks illustrate induced positive and negative charges around a particle. Particles develop a tilted dipole **P** and rotate with an angular velocity **Ω** resulting in a translational velocity **v** along the surface. Particle trajectories in a typical self-organized vortex of rollers are illustrated as an insert on the top cell surface. The local particle density in the vortex is not uniform with a noticeable depletion in the center of the well. **b**, Averaged tangential velocities v_t of particles in the roller vortex as a function of the distance from the center. R is the radius of the well. The dash line shows the averaged velocity v_0 of an isolated roller measured in a dilute sample under the same experimental conditions. The error bars are standard deviations of the mean. **c-e**, Snapshots of superimposed velocity (arrows) and vorticity (background color) fields of the rollers during a vortex reversal under a temporal modulation of the activity. **c**, A stable initial roller vortex with a clockwise rotation. **d**, Intermittent flocking after re-activation of the system. Rollers initially move mostly towards the center of the cell. **e**, A stable vortex with a counter-clockwise rotation evolved from the state shown in **d**. The blue and red circles with an arrow illustrate the chirality of the states. The scale bar is 0.2 mm. The field strength $E = 2.7$ V μm^{-1}, the particle area fraction $\phi = 0.12$.

The roller vortex is robust and remains stable as long as the system is energized. Typical velocity and vorticity fields in a stable vortex are shown in Fig. 5.3c. Two possible chiral states of the vortex, clockwise (CW) or counter-clockwise (CCW), are equally probable, and the system spontaneously selects one in the course of the vortex self-assembly from initially random distribution of particles. When the electric field is switched off, particles come to rest within a time scale given by the Maxwell-Wagner relaxation time τ_{MW} and viscous time scale τ_ν that are both of the order of 1 ms for our system. The effect of Brownian motion on 4.8 μm particles used in the experiments is negligible, and the system behaves as a granular counterpart- once stopped particles preserve their positions. The particle arrangements appear to be random and the direction of the original vortex cannot be easily identified. A cessation of the activity beyond $\tau_{\mathrm{MW}} = (\epsilon_{\mathrm{p}} + 2\epsilon_{\mathrm{f}})/(\sigma_{\mathrm{p}} + 2\sigma_{\mathrm{f}})$ [Eqn. 3.53], where $\epsilon_{\mathrm{p,f}}$ and $\sigma_{\mathrm{p,f}}$ are respective particle and fluid permittivities and conductivities, preserves the particle positions but erases their previous velocities, polarizations and resets aligning forces. Once the system is re-energized by the same DC electric field, particles initially move mostly toward the center of the well where the density is the lowest [see Fig. 5.3d]. Eventually the rollers redistribute over the well and form a single vortex with the direction of rotation opposite to the state preceding the cessation of the activity [Fig. 5.3e].

The probability of the vortex reversal, P, achieves 1 in a wide range of explored experimental parameters [see Fig. 5.4a-c]. The activity cessation time τ_{off} in a range from 10 ms up to 5 minutes has been probed and resulted in no significant effect on the reversal probability upon the re-energizing the system. This observation allows us to exclude the effects caused by remnant hydrodynamic flows or polarization. When τ_{off} is comparable

to τ_{MW} and τ_{ν}, the vortex reversal is not triggered. Persistence of the rotation at small τ_{off} is supported by the incomplete depolarization of the particles and the inertia of a macroscopic hydrodynamic flow.

The robustness of the chiral state reversal long after the termination of the activity suggests the development of certain particle positional arrangements in the ensemble.

The reversal probability depends on the system diameter, D, and particle area fraction ϕ [see Fig. 5.4b, c]. For small diameters the persistence length of roller trajectories is reduced by the high curvature of the walls and the vortex formation probability decreases. The chiral state reversal is robust in a wide range of the particle number densities ($0.04 < \phi < 0.12$). For dilute area fractions ($\phi < 0.03$), the inter-particle interactions are weak and motion of the rollers is uncorrelated. At higher area fractions ($\phi > 0.19$), while the vortex formation probability is high, the reversal probability decreases. This is because the repulsion between the particles at high particle number density reduce the degree of density variations in the system, leading to a more symmetric arrangement of particles.

5.4.2. Vortex reversal

While the observed chiral state reversal is a remarkably robust phenomenon, the formation of a new polar state upon re-activation proceeds through a seemingly chaotic process. In a stable vortex illustrated in Fig. 5.5a, all particles initially move CCW with an average tangential velocity of $\mathbf{v}_{\mathrm{t}} = 0.82$ mm s^{-1} and nearly zero normal velocity. When the DC electric field is switched off, all particles cease to roll without significant alteration of their relative positions set during the vortex rotation [Fig. 5.5b]. After the field is restored, the particles restart motion in seemingly random directions [Fig. 5.5c]. Flocks

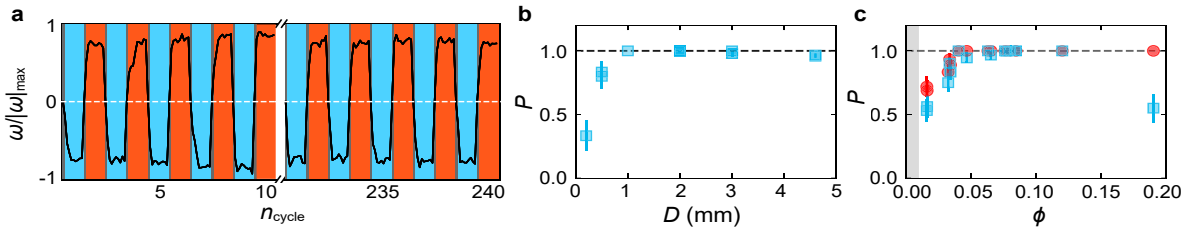

Figure 5.4. **a**, Cycling of the vortex chiral state by a temporal termination and subsequent restoration of the electric field. The black curve shows normalized magnitude of the vorticity in the vortex center. Blue spans indicate CW vortices, and red spans correspond to CCW vortices. The vortex reversal is observed for every one of 240 cycles. The particle area fraction $\phi = 0.08$. **b**, The reversal probability P as a function of the well diameter D. The particle area fraction $\phi = 0.07 \pm 0.01$. $P = N_r/N_t$, where N_r is the number of times the vortex reversal is observed during N_t activity cycles. **c**, The reversal probability P (blue squares) as a function of the particles area fraction ϕ for $D = 2$ mm. Red circles illustrate the probability of the vortex formation in the same system. A shaded area indicates the area fractions $\phi < 0.01$ where no stable vortex is observed. Dash lines depict $P = 1$. Error bars are standard deviations of the mean.

of rollers with spatially correlated velocities form [Fig. 5.5d,e]. The center of the well becomes the densest part of the system in a fraction of a second, and within the next few seconds, particles redistribute into a new stable vortex with a depletion zone in the center [Fig. 5.5f]. The process is characterized by the behavior of the average tangential and normal components of the rollers velocities shown in Fig. 5.5g. At the very first moments upon reactivation, the tangential motion of particles is mostly chaotic, manifested by the emergence of small flocks of rollers moving in both CW and CCW directions. In contrast, the normal component of the average roller velocities sharply increases at re-activation and eventually subside to zero. While initial fractions of particles moving CCW and CW are approximately the same, the CW fraction steadily grows with time and eventually

plateaus with the average tangential velocity reaching $\mathbf{v}_\mathrm{t} = -0.82$ mm s^{-1} (equal in magnitude but opposite in the direction to the initial vortex).

5.4.3. Emergence of local asymmetry

The chirality of the collective motion can be similarly reversed in an annulus [Fig. 5.6a]. However, in contrast to the cylindrical confinement, particle traveling bands with a visible local density gradient along the direction of motion are observed in these experiments. The traveling density bands carry the information about the chirality of the polar state. It is possible to identify the direction of the band motion preceding the activity termination from a snapshot of the track when particles are at rest. In a stable CCW-rotating band shown in Fig. 5.6a, the local particle density ϕ_loc increases slowly with an azimuth angle toward the front of the band, and then abruptly drops at the frontier. When the system is re-energized, the inter-particle repulsive interactions push rollers away from the high-density regions resulting in a reversal of the band motion.

As the width of the track grows, the tangential density gradient (i.e., the band structure) dissolves and completely vanishes in the case of a well [Fig. 5.6b]. Nevertheless, the reversal of the vortex chiral state upon temporal modulation of activity is preserved. It suggests that a structural asymmetry reflected in the local particle positions is now hidden by being redistributed over the whole ensemble. To unveil intrinsic asymmetries in the positional arrangements of rollers in a vortex, we introduce two local order parameters A_n and A_t.

$$A_\mathrm{n,t} = \langle \mathbf{F}_i \cdot \mathbf{u}^i_\mathrm{n,t} \rangle_i. \tag{5.86}$$

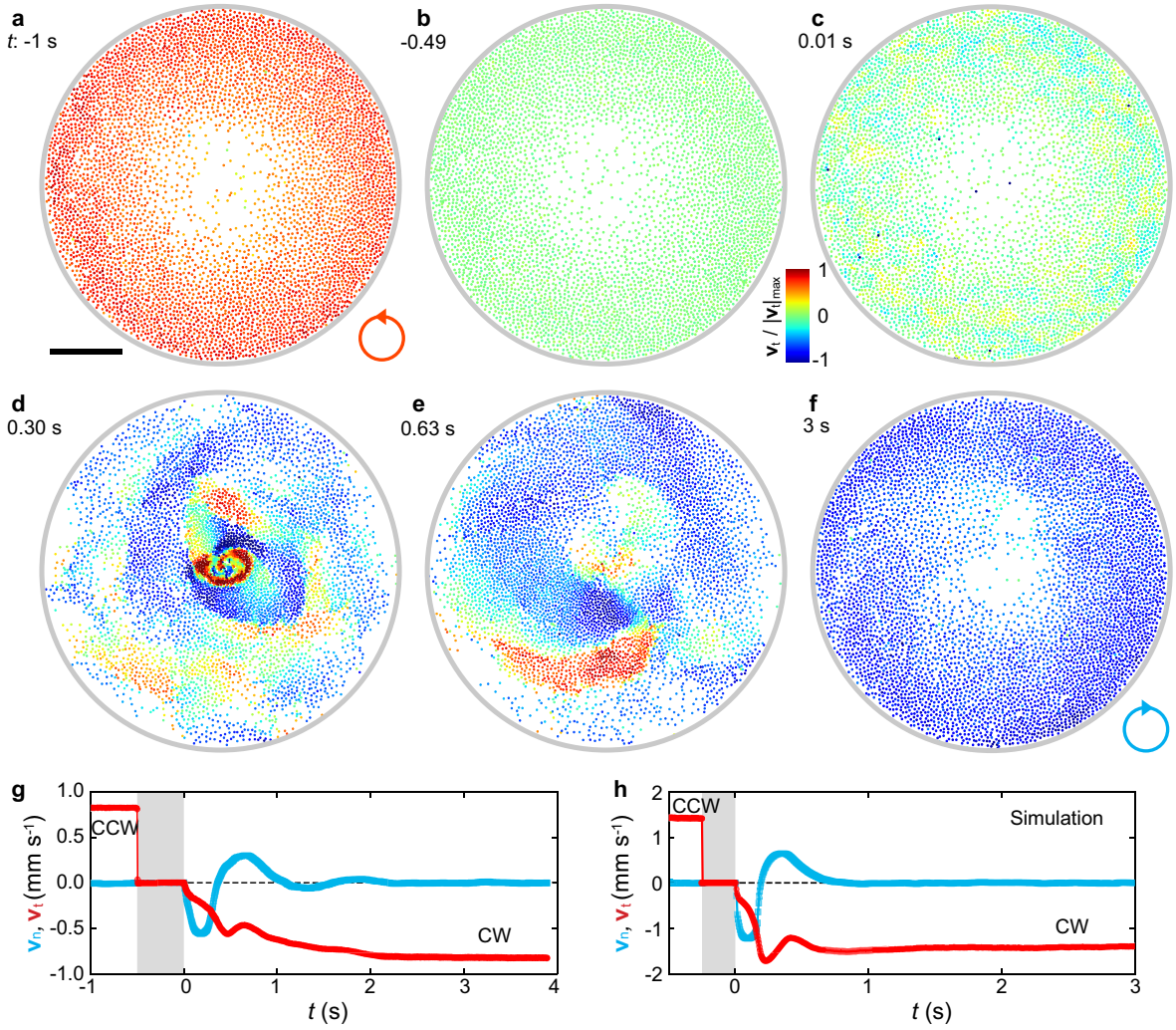

Figure 5.5. **a-f**, Snapshots of a roller vortex undergoing the chiral state reversal. The electric field is reapplied at $t = 0$ s after a short cessation of activity, τ_{off}= 0.5 s. Rollers are shown as circles colored according to the magnitude of the tangential velocity $\mathbf{v}_{\text{t}}$. **a**, Particles in a stable CCW vortex. **b**, Particles are at rest when the electric field is off. **c**, Rollers ensemble moments after the system is re-energized. **d**, Most of the particles move towards the center of the well. CW (blue) and CCW (red) roller flocks are formed. **e**, Particles redistribute over the well. The CW rotating flocks start to dominate over those with CCW rotation. **f**, A stable CW vortex is formed. The scale bar is 0.2 mm. **g**, Time evolution of the average normal (blue) and tangential (red) velocities during the chiral state reversal. **h**, Same process as in **g** is calculated in simulations [see Sec. 5.3]. Gray areas indicate the state with the electric filed off.

Here, $\mathbf{F}_i$ is a model repulsive unit force acting on the particle i from the the nearest neighbors, and $\mathbf{u}^i_{\mathrm{n,t}}$ are normal and tangential unit vectors respectively at the position of the particle i. $\langle ... \rangle_i$ indicates averaging over all particles. We can simplify the averaging over the neighbors by taking into account only a single nearest particle in Eq. 5.86.

Equipped with two order parameters we analyze the reversal process in a circular track and a well. The non-zero value of A_{t} in the track during a stable collective motion indicates the density gradient along the tangential direction, see Fig. 5.6c. Meanwhile, A_{n} is zero within the noise level during the band motion, indicating the absence of normal particle density gradients in a track. Both A_{n} and A_{t} remain nearly constant while the system is in a stable dynamic state. The positive (or negative) value of A_{t} indicates a CW (or CCW) vortex or band. In a well, the value of A_{t} also exhibits stable non-zero values comparable in magnitude to those observed in narrow tracks, even though the density bands are absent [Fig. 5.6d]. The local values of the ${A_{\mathrm{t}}}^i = \mathbf{F}_i \cdot \mathbf{u}^i_{\mathrm{t}}$ are uniformly distributed over the whole system [see [**242**] Fig. S6] with no apparent clustering of the ${A_{\mathrm{t}}}^i$ values that can be directly linked to the subsequent intermittent flocks.

5.4.4. Reversal mechanism

To elucidate the physics underlying the robust chiral state reversal in the ensemble of active rollers, we develop a particle-based simulation model of the Quincke rollers suspension [Sec. 5.3]. Following the work of [**110**, **360**], we similarly identify the essential microscopic interactions. Instead of using the mean-field Fokker-Plank description for the large-scale behaviors [**110**], we develop here the many-particle simulation by coupling the

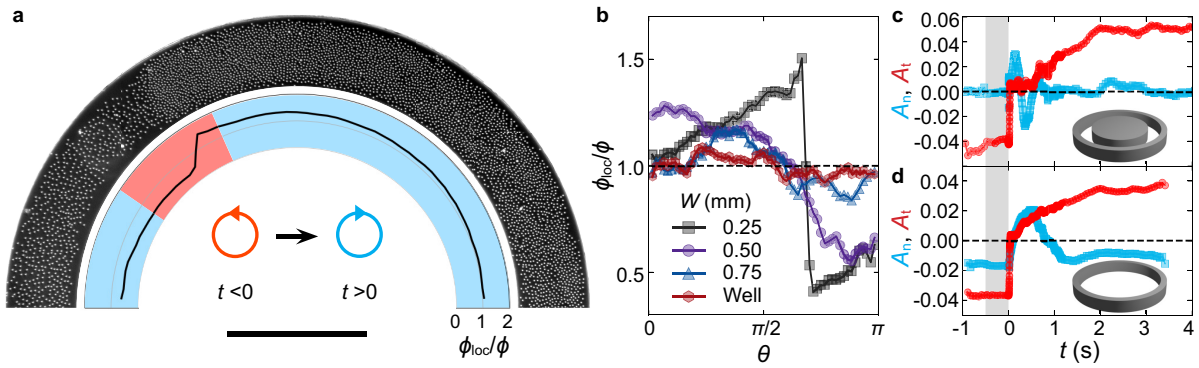

Figure 5.6. **a**, Microscopic image illustrates the spatial distribution of rollers in a circular track (only half of the track is shown) with a width $W = 0.25$ mm. Particles move CCW and form a stable traveling band along the track. The black curve in the inner ring illustrate the average azimuthal particle density. The background color of the inner ring indicates the direction of initial rollers velocities at the moment when the DC electric field is re-applied. The scale bar is 0.5 mm. **b**, Azimuthal density distribution of rollers in circular tracks with outer diameter $D = 2$ mm and the width $W = 0.25$ mm (black), 0.50 mm (purple), 0.75 mm (blue) and in the well (red) as a function of azimuthal angle. Average particles area fraction $\phi = 0.12$. A half of the track (or well) is shown. **c-d**, Evolutions of local order parameters A_{n} (blue) and A_{t} (red) in a track of the width $W = 0.25$ mm (**c**) and a well with $D = 2$ mm (**d**) during a vortex reversal. The initial direction of the vortex is CCW. The area fraction $\phi = 0.12$. Oscillations of A_{n} at the initial stage of the band formation in a track correspond to the reflections of density bands from the walls. A non-zero value of A_{n} reflects the existence of a particle density gradient along the normal direction in the well. Shaded areas indicate field-off time.

Quincke rotation mechanism [**110**, **122**, **123**, **362**, **363**] [Sec. 3.6] with Stokesian Dynamics [**121**, **136**, **283**, **300**–**302**, **327**, **330**] [Sec. 5.2]. The simulations correctly capture all essential phenomenology observed in the roller ensemble upon temporal modulation of the activity [Fig. 5.3h].

In ensembles of Quincke rollers both electrostatic interactions (EI) and hydrodynamic interactions (HI) contribute to the velocity alignment processes resulting in a coherent large-scale motion [**110**]. To identify the microscopic mechanisms driving the emergence

of intrinsic positional order asymmetries, we investigate the behavior of the system when either EI or HI are "turned off" in the simulations. Without EI, a stable vortex still forms and has a structure similar to a regular vortex with both types of interactions present [see Fig. 5.7a,b]. The absence of the EI does not affect significantly the overall particle distribution in the vortex as indicated by a radial particle density distribution [Fig. 5.7d] and pair correlation function, $g(r)$ [Fig. 5.7e]. The vortex also preserves the non-zero local order parameter A_{t} indicating the presence of the local positional order asymmetries [Fig. 5.7f]. However, the chiral state of each vortex was randomly selected upon each re-activation. The results imply that, in general, the development of the local particle arrangement asymmetries alone is not enough to support correlations of the subsequent chiral states of the system upon re-activations.

In contrast, the absence of the long-range HI results in particle accumulation near the boundary of the well [Fig. 5.7c-d]. The vortex forms, however, with most of the particles densely packed near the boundary as indicated by multiple peaks of $g(r)$ [see Fig. 5.7e]. Importantly, the order parameter A_{t} is at the noise level, see Fig. 5.7f, indicative that the local asymmetries along the tangential direction disappear. The plots of the order parameter A_{t} as the system undergoes activity-inactivity cycles demonstrate that in both cases of truncated interactions no robust vortex reversal is observed, and the probability of the reversal is close to 0.5 suggestive that each time the system randomly selects the chiral state. It implies very specific roles of those two interactions. The HI are responsible for the development of asymmetries in the local positional order within the vortex that effectively encode the chiral state. EI on the other hand facilitate a mechanism by which

the particle distributions become relevant in the process of vortex formation. In particular, the locally asymmetric particles distributions in conjunction with EI dictate the subsequent chiral states of the ensemble. When both ingredients (EI and HI) are present the system exhibits remarkable reversibility of its chiral state upon temporal control of the activity by the external field. Upon restarting the field, multiple small flocks arise in random positions and chiral states due to the local fluctuations of the order parameter (Fig. S2), and the system evolves towards the final polar state with the reversed chirality through the coalescence and annihilation of the counter-rotating flocks in a similar fashion as the initial vortex. In a closely related system of ferromagnetic rollers carrying permanent magnetic dipoles rotating together with the particles in a uniaxial alternating magnetic field [**264**,**361**], while both systems share similar hydrodynamic interactions the electrostatic repulsive interactions are replaced with time-averaged magnetic dipole-dipole interactions of permanent rotating dipoles, and the reported phenomenon is absent - all subsequent chiral states upon arbitrary reactivations are random.

5.5. Discussion and future works

In this chapter, we demonstrate that active liquids formed by Quincke particles are capable of preserving their dynamic state information in seemingly random arrangements of the particles. We show that a global vortex formed in an ensemble of Quincke rollers leads to a globally correlated state with local inter-particle positional arrangement asymmetries. Remarkably, a relatively weak level of the local arrangement asymmetry is enough to prescribe the direction of the global vortex motion with high fidelity.

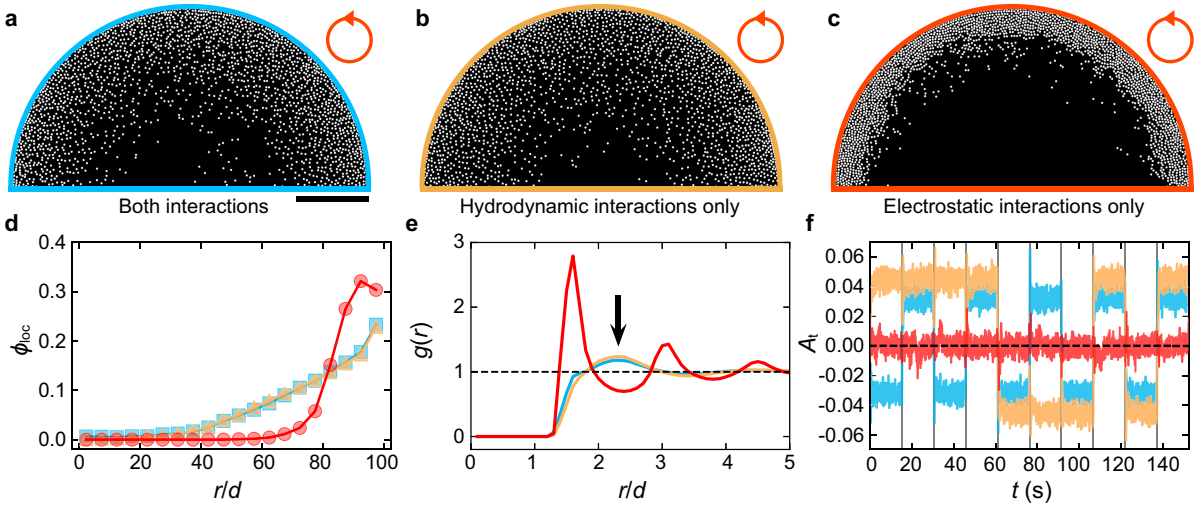

Figure 5.7. **a-c**, Simulation snapshots of stable spontaneous vortices formed under three different scenarios. **a**, Both electrostatic and hydrodynamic interactions between rollers are included in the model. **b**, only hydrodynamic interactions drive rollers dynamics. **c**, only electrostatic interactions contribute to the collective dynamics. Only half of the wells are shown. The scale bar is 0.2 mm. The particle area fraction $\phi = 0.10$ and the field strength is $E = 2.0$ V μm^{-1}. **d**, Radial variations of local particle density, ϕ_{loc}, in a stable vortex formed with both electrostatic and hydrodynamic interactions (blue), only hydrodynamic (orange), and only electrostatic (red) interactions. r is the distance of particles from the center of the well. **e**, Positional pair correlation functions g(r) of particles in stable vortices shown in **a-c**. The same color coding is used as in **d**. The black arrow in **e** points to the identical location of a first peak for scenarios **a** and **b**. **f**, Local order parameter A_{t} calculated for 10 activity cessation cycles. The ensemble does not develop asymmetries in the positional order when only electrostatic interactions govern collective dynamics of the rollers (red curve). Local positional order asymmetries in the ensemble develop only for scenarios including hydrodynamic interactions (blue, orange). Nevertheless, robust reversal is observed only when both hydrodynamic and electrostatic interactions are present(blue).

With the simulation model constructed from microscopic interactions, we isolate the role of hydrodynamics as a driving force in the development of the local particle positional asymmetries and reveal the crucial role of electrostatic repulsive interactions as

a key mechanism making the spatial distribution of particles relevant in the formation of the subsequent chiral states of the ensemble upon reactivation. The dynamics of the global chiral state reversal involve seemingly chaotic evolution of multiple flocks. Nevertheless, the reversal process is robust, and a temporal control of the activity can be exploited to systematically command the subsequent polar states of the active liquid. We further demonstrate that the local particle arrangement asymmetries alone do not result in polar state reversal, and, in general, isotropic short-range repulsions between active units and velocity alignment interactions are necessary for the rise of correlations between subsequent chiral states upon activity modulations.

Perhaps more generally, our results suggest that regardless of the dimension of the problem seemingly disordered dynamic patterns tend to develop local structural asymmetries in response to competing repulsive and aligning interactions between active particles, and within diffusion timescale, these asymmetries could be exploited to systematically control self-organized dynamic states with the aid of temporal modulation of activity.

As a physical example of the general framework [Eqn. 5.1] for describing active particles with both external and internal DOFs, this chapter demonstrates that how to construct the functional forms of the usually phenomenological interaction functions from relevant microscopic interactions. By embedding the rolling motion mechanism of Quincke particles [Sec. 3.6] into the Stokesian Dynamics, we developed a particle-based model which includes dynamics of both external and internal degrees of freedom. More generally, the self-propulsion mechanism and the interaction models, in principle, can be replaced with any other active-driving mechanisms and relevant interactions of the interested systems. For example, the dynamic equations describing the internal DOF of

rolling Quincke particles [Eqn. 5.3.1] can to extended to include the dynamics in the oscillation regime [Sec. 3.10], which enables studying collective behaviors of a population of oscillating Quincke particles.

CHAPTER 6

Collective Behaviors of Magnetic Spinners*

6.1. Introduction

Active colloidal particles typically perform mechanical motions in response to external stimuli from environment [**364**–**368**]. The constant injection of external energy signals the non-equilibrium nature of those active particles, where diverse steady-state collective behaviors sharply contrast to those commonly seen in the equilibrium systems have been reported [**369**–**373**]. So far, most of the works about active colloidal particles have been focusing on the active colloidal particles themselves and very limited attention has been put on the medium which mediates the interactions between active colloidal particles. Since almost all collective behaviors of active colloidal particles are studied in an aqueous environment, this inevitable introduces hydrodynamic interactions (HI) between particles [**159**, **271**], which may or may not be important for the observed collective behaviors depending on the system of interests. However, it should be realized that the HI in such active colloidal particle systems is a common cornerstone for understanding its resulting collective behaviors. Due to the constant input of external energy in active systems, the mechanical motions of active units also constantly disturb the surrounding aqueous environment, which induce active flows absent in usual passive fluids. In recent years, active fluids composed of self-propelling particles [**374**,**375**] with broken time reversal symmetry

*This chapter originates from the unpublished collaborative efforts with Dr. Michael Wang and Prof. Paul M. Chaikin at New York University, who conducted all experiment measurements in this chapter.

(TRS) have been attracting increasing interests due to possible new hydrodynamic effects. From a theoretical perspective, the broken TRS permits the emergence of the so-called odd viscosity [**376**] and it's interesting to extend conventional hydrodynamic models to explore possible physical effects of odd viscosity [**377**–**380**]; Experimentally, it's also worth designing an active system [**381**,**382**], which isolate hydrodynamic interactions from other interfering interactions entirely with controllable activity for a systematical investigation of the effects due to induced active flows.

Among all possible candidates of active colloidal particles, the colloid particle embedded with a tiny ferromagnetic component driven by external magnetic fields seem an ideal model system [**319**, **329**, **383**] for studying active flows. With carefully designed microscopic interactions, the magnetostatic and electrostatic interactions are essentially negligible comparing with the thermal energy [**329**], which leaves the hydrodynamic interactions as the solely dominant interaction in the system. The magnetic responsiveness of particles allows continuous tuning of the system activity level via an external magnetic field, which enables exploring how the hydrodynamic interactions depend on the system activity level.

In this chapter, a controllable effective gravity is purposefully introduced into a suspension of magnetic colloidal particles driven by a rotating external magnetic field. The "active" hydrodynamic interactions compete with such an effective gravity, which results in a sedimentation of active colloidal particles depending on its activity level [Sec. 6.2]. The traditional Stokesian Dynamics (SD) [Sec. 5.2] turns out to be inadequate for describing the observed collective motions due to active flows. By realizing the experimental

system has a broken TRS, the odd viscosity is incorporated into the existing SD framework [Sec. 6.3]. With the extended SD with odd viscosity, a simulation model for a population of magnetic spinners is developed to understand the experimental phenomena [Sec. 6.4]. In the end, this chapter concludes with a brief summary and discussion about open questions [Sec. 6.5].

6.2. Sedimentation of magnetic spinners

6.2.1. Experiment setup

The experiment is conducted with polymer colloids with radius about 1 μm with an embedded haematite cube [**384**], which gives each colloids a small permanent magnetic moment $\mathbf{m}$, allowing the manipulations of particles via an external magnetic field. The inter-particle magnetic interactions are small comparing with thermal energy ($< 0.1\ k_BT$) [**329**]. A suspension of such magnetic colloidal particles is prepared inside a chamber, which is slightly tilted by an angle θ allowing the sedimentation [**385**] of particles under gravity [Fig. 6.1]. The proposed experimental setup is very similar to the previous work [**386**] except the field directions and the inclination angle [see Table 6.1]. Here, the external magnetic field is rotating in the plane [Fig. 6.1 B], which drives mechanical rotations of magnetic colloidal particles with angular velocity $\boldsymbol{\omega}$ perpendicular to the chamber floor. Besides, the inclination angle is deliberately chosen to be very small (about 2°) [Fig. 6.1 C], which makes the effective weight of particles comparable to the thermal energy ($k_BT/mg\sin\theta \sim 2.7$). The active rotation of magnetic colloidal particles in our experiment does not directly generate translational motions like Quincke particles [**110**] or magnetic rollers [**256**,**329**]. This mitigates the interference of boundary effects due to the

surrounding chamber walls. Thus, the driven magnetic colloidal particles interacts with each other with a rather clean active rotational flows. If there are any significant effects due to the active flows induced by mechanical rotations of magnetic colloidal particles, the small effective particle weight acts as a sensitive probe for detecting such effects. By measuring the steady particle distribution along the settling direction, it allows the quantitative study of hydrodynamic interactions in such active fluids.

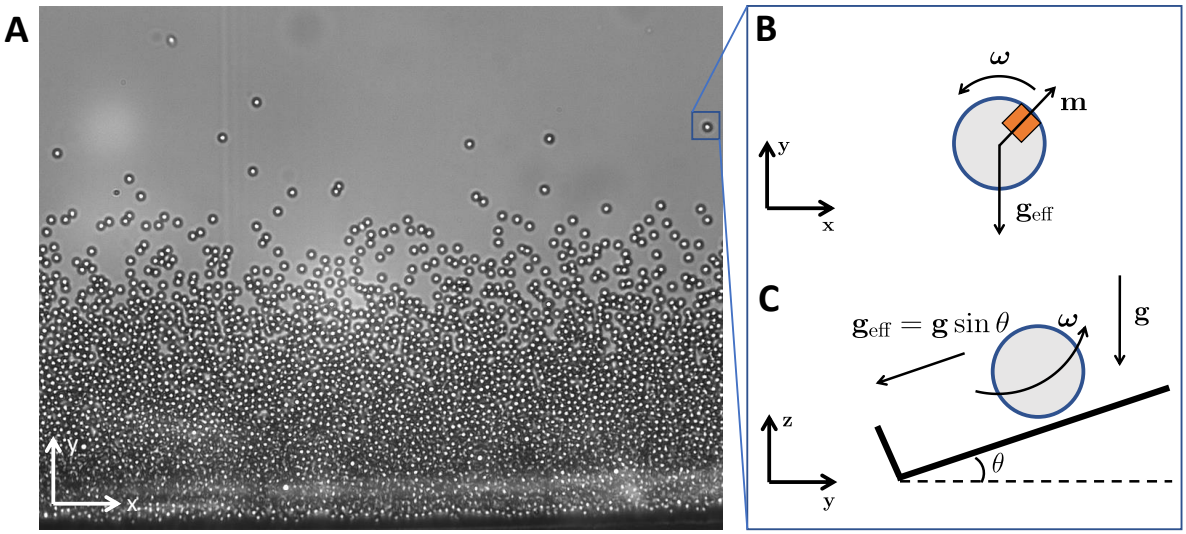

Figure 6.1. Sedimentation experiments of magnetic colloidal particles. **A**, the top view experimental optical microscope image of the magnetic spinners suspension (courtesy of Dr. Michael Wang, NYU). **B** and **C** are schematics of zoom-in views of a single magnetic spinner from the top and side views, respectively. **B**, the top view schematic of a settling colloidal particle (light gray) with embedded ferromagnetic components (orange), which is driven by a rotating external magnetic field, rotates with angular velocity $\boldsymbol{\omega}$. **C**, the side view schematic of the same magnetic colloidal particle, which settles above an inclined floor of angle θ with an effective gravity $g\sin\theta$, where g is the acceleration of gravity.

Parameters	Symbols	Values
radius of particles	a	$1\ \mu m$
gravity	g	$9.8\ \mathrm{m/s^2}$
estimated particle weight	mg	$\sim 4.41 \times 10^{-14}$ N
inclination angle	θ	2°
effective particle weight	$mg \sin\theta$	$\sim 1.54 \times 10^{-15}$ N
field frequency	f	$0 - 5$ Hz
dynamic viscosity of the solution	η	$\sim 0.89 - 1.8$ mPa $\cdot$ s
estimated magnetic torques	$T_m = 8\pi\eta a^3\omega$	$\sim 1.5791 \times 10^{-19}$ N $\cdot$ m
gravitational height	$k_BT/mg\cos\theta$	$\sim 1.094\ \mu m$
characteristic diffusive time	$\tau_D = 6\pi\eta a^3/k_BT$	~ 4.59 s
temperature	T	300 K

Table 6.1. Table of experiment parameters for the sedimentation of magnetic spinners

6.2.2. Experiment observations

The rotation speed of magnetic spinners is directly controlled by the frequency of external magnetic fields [**329**], which enables a continuous tuning of system activity level. The sedimentation experiments of magnetic spinners are conducted under the influence of a rotating magnetic field with frequency 0 - 5 Hz and the corresponding area fraction distribution of magnetic spinners is shown in Fig. 6.2 A. Interestingly, the experimental measurements show a significant deviation from the equilibrium distribution of passive magnetic spinners with a higher field frequency. By comparing the experimental images of the equilibrium suspension [Fig. 6.2 B] and driven suspension [Fig. 6.2 C], it shows clearly that the driven suspension is much more spread upwards against the effective gravity, which signifies possible extra repulsive interactions between particles.

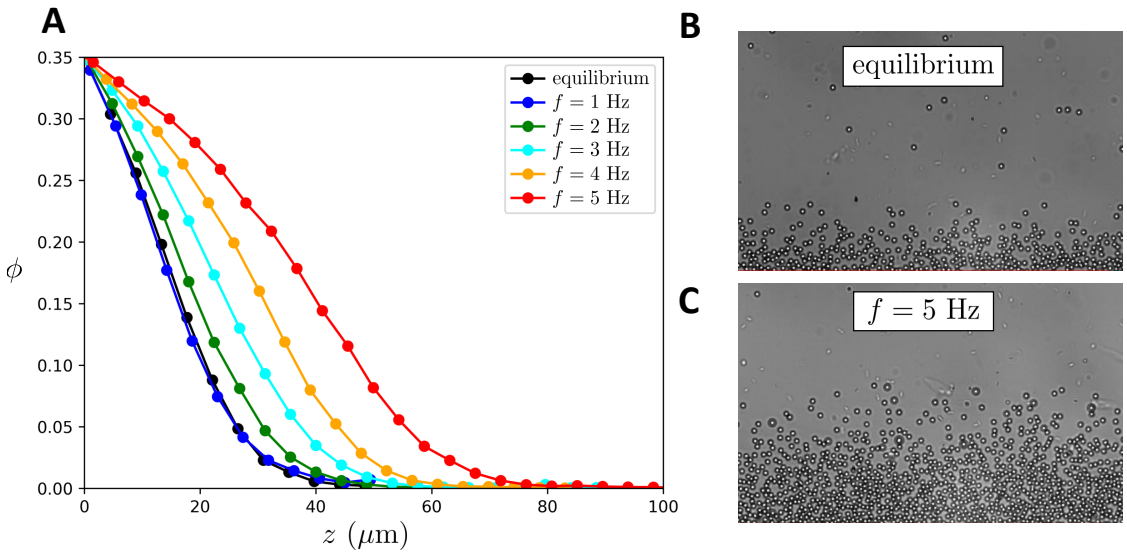

Figure 6.2. Density profiles of settled magnetic colloidal particles with various external magnetic field frequency (courtesy of Dr. Michael Wang, NYU). **A**, the area fraction of magnetic spinners driven by a rotating magnetic field of frequency 0 - 5 Hz as a function of height. **B** and **C** are respective representative experimental optical microscope images of passive magnetic spinners and magnetic spinners driven by a rotating magnetic field of frequency 5 Hz.

Such experimental results are particularly interesting from a physics point of view. For an equilibrium system, hydrodynamic interactions do not affect its thermodynamic equilibrium states as any equation of states of equilibrium systems [**387**, **388**] do not depend on HI. For a non-equilibrium system, there is no general theoretical framework yet. However, the experimental system here is clearly out-of-equilibrium, whose results indicate that the HI of those active colloidal particles clearly modify the steady state of the system. The active flows create certain effective repulsion between particles, which actually support the weight of particles and creates a large spread of density distribution

[Fig. 6.2 B and C]. It is of great interests to understand how those active flows induced by driven magnetic spinners change the steady states of system, as it might provide some insights for uncovering the principles of non-equilibrium systems.

As discussed before, such magnetic spinners primarily interact with HI, which makes the Stokesian Dynamics [Sec. 5.2] an ideal numeric method for simulating a suspension of magnetic spinners. As a starting point, all magnetic spinners are assumed to be rotating with the same frequency as the external magnetic field. Then, each magnetic spinner is approximately driven by a magnetic torque $\mathbf{T}_m = 8\pi\mu a^3\boldsymbol{\omega}$. Besides, each spinners also feels the same effective gravity $\mathbf{F}_g = m\mathbf{g}\sin\theta$, where m is the mass of colloidal particle. These are essentially all external forces and torques of the system, combining with appropriate hard-core interactions to avoid overlapping, the usual SD simulations are performed. Unfortunately, these simulations are not able to reproduce the significant upward spread of magnetic spinners and stay pretty close to equilibrium particle distribution even for the highest field frequency investigated. By realizing that all magnetic spinners are rotating in a prescribed direction determined by the external magnetic field, the system actually has a broken time reversal symmetry (TRS), which motivates the development of an extended Stokesian Dynamics with odd viscosity presented in the next section.

6.3. Stokesian Dynamics with odd viscosity

In this section, I will develop an extended Stokesian Dynamics (SD) formalism [Sec. 5.2], which takes into account of the effects from odd viscosity.

6.3.1. Odd viscosity

First, the concept of odd viscosity will be briefly introduced [**376**, **389**–**392**]. Similarly to the case of linear elastic solids [Sec.4.3.1.5], the general linear constitutive relation of a fluid can be written as:

$$\sigma_{ij} = -p\delta_{ij} + \mu_{ijkl}\nabla_l u_k \tag{6.1}$$

where p is the hydrostatic pressure and $\boldsymbol{\mu}$ is a general fourth order viscosity tensor. For a conventional homogeneous and isotropic passive fluid, the system has both rotational symmetry and time-reversal symmetry. Based on the Curie's Symmetry Principle (CSP) [**393**], the spatial symmetry property simplifies the general viscosity tensor as [**394**]:

$$\mu^e_{ijkl} = \mu_b\delta_{ij}\delta_{kl} + \mu_s(\delta_{ik}\delta_{jl} + \delta_{jk}\delta_{il}) \tag{6.2}$$

where μ_b and μ_s are the bulk and shear viscosity, respectively. Such viscosity tensor μ^e_{ijkl} only depends on two independent material properties, which have analogous roles of bulk and shear modulus in linear elastic solids [Eqn. 4.14].

Furthermore, symmetry properties of the system enforce three important symmetry relations, which the viscosity tensor μ^e_{ijkl} must fulfill. Firstly, the rotational invariance of system requires that $\mu^e_{ijkl} = \mu^e_{ijlk}$; Secondly, the conservation of local angular momentum (passive fluid) requires that the stress tensor to be symmetric [see Sec. 4.4.3.2], i.e. $\sigma_{ij} = \sigma_{ji}$, which enforces that $\mu^e_{ijkl} = \mu^e_{jikl}$; Thirdly, according to the Onsager reciprocal relations (ORR) [**395**, **396**], the time-reversal symmetry requires that $\mu^e_{ijkl} = \mu^e_{klij}$. It's easy to verify that the above viscosity μ^e_{ijkl} [Eqn. 6.2] fulfill all three symmetry relations.

The superscript e indicates that it's even under the time-reversal transformation and the corresponding viscosity is therefore termed as *even viscosity*.

As an extension of the above symmetry considerations, Avron et al. [**376**] considers the system with an external magnetic field **B**. The time-reversal symmetry states that the particles consisting the system should retrace its former paths when their velocities are reversed. However, for example, when there is an magnetic field, the external magnetic field also needs to be reversed (-**B**) due to the fact that the Lorentz force [**129**] couples the velocity and the magnetic fields ($\mathbf{F} = q\mathbf{u} \times \mathbf{B}$). Therefore, ORR needs to be modified for the case with a broken time reversal symmetry [**394**], which yields that

$$\mu^o_{ijkl} = -\mu^o_{klij} \tag{6.3}$$

where the superscript o indicates that the viscosity is odd under the time-reversal transformation and μ^o_{ijkl} is thus termed as *odd viscosity*.

For the spatial symmetry, previous considerations still hold, which require that $\mu^o_{ijkl} = \mu^o_{ijlk}$ and $\mu^o_{ijkl} = \mu^o_{jikl}$. By considering the rotational degrees of freedom of microscopic particles and starting from a microscopic Hamiltonian, Lubensky et al. [**390**] derive the general form of odd viscosity in a 3D system as:

$$\mu^o_{ijkl} = \ell_n(\varepsilon_{jln}\delta_{ik} + \varepsilon_{iln}\delta_{jk} + \varepsilon_{ikn}\delta_{jl} + \varepsilon_{jkn}\delta_{il}) \tag{6.4}$$

where ε_{ijk} is the 3D Levi-Civita symbol and δ_{ij} is the Kronecker delta. And $\boldsymbol{\ell}$ is the angular momentum density of constituting particles. It can be directly verified that all three symmetric relations are fulfilled. For a quasi-2D system where $\boldsymbol{\ell} = \mu_o\hat{\mathbf{z}}$, the above

general expression in 3D can be simplified as:

$$\mu^o_{ijkl} = \mu_o(\epsilon_{jl}\delta_{ik} + \epsilon_{il}\delta_{jk} + \epsilon_{ik}\delta_{jl} + \epsilon_{jk}\delta_{il}) \tag{6.5}$$

where ε_{ij} is the 2D Levi-Civita symbol, i.e. $\varepsilon_{ij} = \varepsilon_{ijz}$. In this case, only a single scalar odd viscosity μ_o is needed to determine the odd viscosity tensor.

Finally, for a system containing both even and odd interactions under the time-reversal transformation, the general linear constitutive relation can be written as:

$$\sigma_{ij} = -p\delta_{ij} + \left(\mu^e_{ijkl} + \mu^o_{ijkl}\right)\nabla_l u_k \tag{6.6}$$

where even and odd viscosity are given by Eqn. 6.2 and 6.4, respectively.

6.3.2. Odd Stokes' equations

With the constitutive relation of the fluid with both even and odd viscosity [Eqn. 6.6], the Stokes' equations are ready to be derived via the balance of linear momentum. For simplicity, we only consider quasi-2D systems here and the overall stress tensor is given as:

$$\begin{aligned}\sigma_{ij} = -p\delta_{ij} + (\mu^e_{ijkl} + \mu^o_{ijkl})\nabla_l u_k = -p\delta_{ij} + \mu_b\nabla_k u_k\delta_{ij} + \mu_s\left(\nabla_j u_i + \nabla_i u_j\right) \\ + \mu_o\left(\varepsilon_{jl}\nabla_l u_i + \varepsilon_{il}\nabla_l u_j + \nabla_i\varepsilon_{jl}u_l + \nabla_j\varepsilon_{il}u_l\right)\end{aligned} \tag{6.7}$$

Taking the divergence of the stress tensor gives that

$$-\nabla_i\left[p - (\mu_b + \mu_s)\nabla_j u_j + \mu_o\epsilon_{jl}\nabla_j u_l\right] + \mu_s\nabla^2 u_i + \mu_o\epsilon_{il}\nabla_l\nabla_j u_j + \mu_o\epsilon_{il}\nabla^2 u_l = 0 \tag{6.8}$$

For an incompressible fluid, $\nabla_j u_j = 0$, and it gives that the Stokes' equations with odd viscosity as

$$-\nabla_i \left(p + \mu_o \epsilon_{jl} \nabla_j u_l\right) + \mu_s \nabla^2 u_i + \mu_o \epsilon_{il} \nabla^2 u_l = 0 \tag{6.9}$$

The above equations can be expressed in an equivalent matrix form as:

$$\begin{pmatrix} \mu_s & \mu_o & 0 \\ -\mu_o & \mu_s & 0 \\ 0 & 0 & \mu_s \end{pmatrix} \nabla^2 \mathbf{u} = \boldsymbol{\nabla} \tilde{p} + \mathbf{f} \tag{6.10}$$

where the modified pressure $\tilde{p} = p + \mu_o \epsilon_{jl} \nabla_j u_l$ and possible external volumetric forces $\mathbf{f}$ are also added into the equation. Note that the above equation reduces as the conventional Stokes' equation [Eqn. 5.6] when $\mu_o = 0$ as expected and the odd viscosity μ_o emerges only at off-diagonal elements which introduces coupling between x and y components.

6.3.3. Odd Oseen tensor

As shown in Eqn. 6.10, the Stokes' equations with odd viscosity are still linear equations. Similarly to the Oseen tensor [Eqn. 5.7] derived for the usual Stokes' equations with only even viscosity, we would like to derive the corresponding *Green's function* of the generalized Stokes' equations with odd viscosity, which starts by consider a point force

$-\mathbf{F}$ applied at position $\mathbf{r}$ [**134**]:

$$\begin{pmatrix} \mu_s & \mu_o & 0 \\ -\mu_o & \mu_s & 0 \\ 0 & 0 & \mu_s \end{pmatrix} \nabla^2 \mathbf{u} = \boldsymbol{\nabla} p - \mathbf{F}\delta(\mathbf{r}) \tag{6.11}$$

Please note that the modified pressure $\tilde{p}$ [Eqn. 6.10] is denoted as p for brevity. The linearity of the Stokes' equation requires that both the pressure p and flow field $\mathbf{u}$ should be proportional to the apply point force $\mathbf{F}$. Since $p(\mathbf{r})$ is a scalar field and $\mathbf{u}(\mathbf{r})$ is a vector field, they can be expressed as:

$$p(\mathbf{r}) = P_j(\mathbf{r}) F_j \tag{6.12a}$$

$$\mathbf{u}(\mathbf{r}) = G_{ij}(\mathbf{r}) F_j \tag{6.12b}$$

where $P_i(\mathbf{r})$ and $G_{ij}(\mathbf{r})$ are the Green's function of the pressure field and flow field, respectively.

6.3.3.1. Green's function in k-space. As the problem is easier to solve in the k-space, the Fourier transformation is applied to both the pressure and flow field:

$$\mathbf{u}(\mathbf{r}) = \mathcal{F}^{-1}\left[\widehat{\mathbf{u}}(\mathbf{k})\right] = \frac{1}{(2\pi)^3} \int_{\mathbb{R}^3} \mathrm{d}\mathbf{k} \widehat{\mathbf{u}}(\mathbf{k}) e^{i\mathbf{k}\cdot\mathbf{r}} \tag{6.13a}$$

$$p(\mathbf{r}) = \mathcal{F}^{-1}\left[\widehat{p}(\mathbf{k})\right] = \frac{1}{(2\pi)^3} \int_{\mathbb{R}^3} \mathrm{d}\mathbf{k} \widehat{p}(\mathbf{k}) e^{i\mathbf{k}\cdot\mathbf{r}} \tag{6.13b}$$

where $\mathcal{F}^{-1}$ is the inverse Fourier transformation, $\mathbf{k}$ is the wave vector and $\widehat{\mathbf{u}}(\mathbf{k})$ and $\widehat{p}(\mathbf{k})$ are the corresponding pressure and flow field in the k-space. Plugging above expressions back into the Stokes' equations [Eqn. 6.11] yields that

$$-\mu_{ij}k^2\widehat{u}_j(\mathbf{k}) = ik_i\widehat{p}(\mathbf{k}) - F_i \tag{6.14}$$

where the second order viscosity matrix μ_{ij} is defined as:

$$\mu_{ij} = \begin{pmatrix} \mu_s & \mu_o & 0 \\ -\mu_o & \mu_s & 0 \\ 0 & 0 & \mu_s \end{pmatrix} \tag{6.15}$$

Also note that the k-space expressions of Eqn. 6.12 are:

$$\widehat{p}(\mathbf{k}) = \widehat{P}_j(\mathbf{k})F_j, \quad \widehat{\mathbf{u}}(\mathbf{k}) = \widehat{G}_{ij}(\mathbf{k})F_j$$

which enables the elimination of external forces F_i:

$$-k^2\mu_{ij}\widehat{G}_{jk}(\mathbf{k})F_k = ik_i\widehat{P}_j(\mathbf{k})F_j - \delta_{ij}F_j$$

i.e.

$$-k^2\mu_{ik}\widehat{G}_{kj}(\mathbf{k}) = ik_i\widehat{P}_j(\mathbf{k}) - \delta_{ij} \tag{6.16}$$

The incompressibility condition ($\boldsymbol{\nabla}\cdot\mathbf{u} = 0$) in the k-space reads as

$$\widehat{G}_{ij}(\mathbf{k})k_i = 0 \tag{6.17}$$

Taking the inner product of Eqn. 6.16 with k_i yields that

$$-k^2\mu_{ik}k_i\widehat{G}_{kj}(\mathbf{k}) = -k^2\mu_0\varepsilon_{ik}k_i\widehat{G}_{kj}(\mathbf{k}) = ik^2\widehat{P}_j(\mathbf{k}) - k_j$$

It gives the Green's function of the pressure field in the k-space as:

$$\widehat{P}_j(\mathbf{k}) = -\frac{ik_j}{k^2} + i\mu_0\varepsilon_{ik}k_i\widehat{G}_{kj}(\mathbf{k}) \tag{6.18}$$

where $\mu_{ij} = \mu_s\delta_{ik} + \mu_o\varepsilon_{ik}$ by definition [Eqn. 6.15] and the second term is the additional pressure contribution due to the odd viscosity. Plugging the above expression back into Eqn. 6.16 gives that:

$$\begin{pmatrix} \mu_s + \mu_o\frac{k_xk_y}{k^2} & \mu_o\left(1-\frac{k_x^2}{k^2}\right) & 0 \\ \mu_o(-1+\frac{k_y^2}{k^2}) & \mu_s - \mu_o\frac{k_yk_x}{k^2} & 0 \\ \mu_o\frac{k_yk_z}{k^2} & -\mu_o\frac{k_xk_z}{k^2} & \mu_s \end{pmatrix}\widehat{G}_{kj}(\mathbf{k}) = -\frac{k_ik_j}{k^4} + \frac{\delta_{ij}}{k^2} \tag{6.19}$$

The right-hand side is exactly the k-space expression of the Oseen tensor [**311**] and the matrix on the left-hand side can be directly inverted, which gives the k-space expression of the Green's function of the flow field as:

$$\widehat{G}_{ij}(\mathbf{k}) = \frac{1}{\mu_s}\frac{1}{\Sigma^2(\mathbf{k})}\begin{pmatrix} \frac{k_y^2+k_z^2}{k^4} & -\frac{k_xk_y}{k^4} - \chi\frac{k_z^2}{k^4} & -\frac{k_xk_z}{k^4} + \chi\frac{k_yk_z}{k^4} \\ -\frac{k_xk_y}{k^4} + \chi\frac{k_z^2}{k^4} & \frac{k_x^2+k_z^2}{k^4} & -\frac{k_yk_z}{k^4} - \chi\frac{k_xk_z}{k^4} \\ -\frac{k_xk_z}{k^4} - \chi\frac{k_yk_z}{k^4} & -\frac{k_yk_z}{k^4} + \chi\frac{k_xk_z}{k^4} & \frac{k_x^2+k_y^2}{k^4} \end{pmatrix} \tag{6.20}$$

where two auxiliary variables are introduced as:

$$\Sigma^2(\mathbf{k}) = 1 + \chi^2\frac{k_z^2}{k^2}, \quad \chi = \frac{\mu_o}{\mu_s} \tag{6.21}$$

Particularly, the dimensionless number χ is the ratio between odd viscosity μ_o and even viscosity μ_s, which characterizes the effects due to the odd viscosity. Moreover, as any second order tensor can be decomposed into symmetric and anti-symmetric parts, the above k-space Green's function can be split as:

$$\widehat{G}_{ij}(\mathbf{k}) = \widehat{G}_{(ij)}(\mathbf{k}) + \widehat{G}_{[ij]}(\mathbf{k}) \tag{6.22a}$$

$$\widehat{G}_{(ij)}(\mathbf{k}) = \frac{1}{\mu_s}\frac{1}{\Sigma^2(\mathbf{k})}\left(-\frac{k_i k_j}{k^4} + \frac{\delta_{ij}}{k^2}\right) \tag{6.22b}$$

$$\widehat{G}_{[ij]}(\mathbf{k}) = -\frac{1}{\mu_s}\frac{\chi}{\Sigma^2(\mathbf{k})}\varepsilon_{ijk}k_k\frac{k_z}{k^4} \tag{6.22c}$$

where indices in parentheses and brackets indicate symmetrizing and anti-symmetrizing the orginal tensor, respectively.

6.3.3.2. Green's function in real-space. With the k-space Green's function for both the pressure field and flow field [Eqn. 6.18 and 6.20], the corresponding real-space expressions can be obtained via the inverse Fourier transformation, i.e.

$$G_{ij}(\mathbf{r}) = \mathcal{F}^{-1}\left[\widehat{G}_{ij}(\mathbf{k})\right], \quad P_i(\mathbf{r}) = \mathcal{F}^{-1}\left[\widehat{P}_i(\mathbf{k})\right] \tag{6.23}$$

However, the additional k-dependence introduced by $\Sigma^2(\mathbf{k})$ for non-vanishing odd viscosity makes the exact analytical calculation difficult. For simplicity, we focused on the fluid with *weak activity* (this approximation is also supported by actual experimental measurements [**397**]). Then, the viscosity ratio χ serves as a natural parameter to characterize the activity level of the system. For the weak activity limit, i.e. $\chi \to 0$, the

inverse of $\Sigma^2(\mathbf{k})$ can be expanded as:

$$\frac{1}{\Sigma^2(\mathbf{k})} = \frac{1}{1+\chi^2\frac{k_z^2}{k^2}} = \sum_{n=0}^{\infty}(-1)^n\left(\frac{k_z^2}{k^2}\chi^2\right)^n = 1 - \frac{k_z^2}{k^2}\chi^2 + \mathcal{O}(\chi^4) \tag{6.24}$$

Then, the expansions of the symmetric and anti-symmetric parts of the k-space Green's function [Eqn. 6.22] can be written as:

$$\widehat{G}_{(ij)}(\mathbf{k}) = \frac{1}{\mu_s}\sum_{n=0}^{\infty}(-1)^n\left(\frac{k_z^2}{k^2}\chi^2\right)^n\left(-\frac{k_ik_j}{k^4}+\frac{\delta_{ij}}{k^2}\right) = \left[\widehat{G}^{(0)}_{(ij)} + \widehat{G}^{(2)}_{(ij)}\right] + \mathcal{O}(\chi^4) \tag{6.25a}$$

$$\widehat{G}_{[ij]}(\mathbf{k}) = -\frac{\chi}{\mu_s}\sum_{n=0}^{\infty}(-1)^n\left(\frac{k_z^2}{k^2}\chi^2\right)^n\left(\varepsilon_{ijk}k_k\frac{k_z}{k^4}\right) = \left[\widehat{G}^{(1)}_{[ij]} + \widehat{G}^{(3)}_{[ij]}\right] + \mathcal{O}(\chi^5) \tag{6.25b}$$

where n-th order expansion of the symmetric and anti-symmetric parts are defined as:

$$\widehat{G}^{(2n)}_{(ij)}(\mathbf{k}) = \frac{(-1)^n}{\mu_s}\left(\frac{k_z^2}{k^2}\chi^2\right)^n\left(-\frac{k_ik_j}{k^4}+\frac{\delta_{ij}}{k^2}\right), \quad n\in\mathbb{N} \tag{6.26a}$$

$$\widehat{G}^{(2n+1)}_{[ij]}(\mathbf{k}) = -\chi\frac{(-1)^n}{\mu_s}\left(\frac{k_z^2}{k^2}\chi^2\right)^n\left(\varepsilon_{ijk}\frac{k_kk_z}{k^4}\right), \quad n\in\mathbb{N} \tag{6.26b}$$

where $\mathbb{N}$ is the set of natural numbers. The inverse Fourier transformation of the lowest order expressions is easy to compute:

$$G^{(0)}_{(ij)}(\mathbf{r}) = \mathcal{F}^{-1}\left[\widehat{G}^{(0)}_{(ij)}(\mathbf{k})\right] = \frac{1}{\mu_s}\mathcal{F}^{-1}\left[-\frac{k_ik_j}{k^4}+\frac{\delta_{ij}}{k^2}\right] = \frac{1}{8\pi\mu_s}\left(\frac{\delta_{ij}}{r}+\frac{r_ir_j}{r^3}\right) \tag{6.27a}$$

$$G^{(1)}_{[ij]}(\mathbf{r}) = \mathcal{F}^{-1}\left[\widehat{G}^{(1)}_{[ij]}(\mathbf{k})\right] = -\frac{1}{\mu_s}\mathcal{F}^{-1}\left[\varepsilon_{ijk}\frac{k_kk_z}{k^4}\right] = -\frac{\chi}{8\pi\mu_s}\varepsilon_{ijk}\left(\frac{\delta_{k3}}{r}-\frac{r_kr_3}{r^3}\right) \tag{6.27b}$$

Note the expression of Oseen tensor [Eqn. 5.7], the above expressions can be rewritten as:

$$G^{(0)}_{(ij)}(\mathbf{r}) = \frac{1}{8\pi\mu_s} J_{ij}(\mathbf{r}) \tag{6.28a}$$

$$G^{(1)}_{[ij]}(\mathbf{r}) = -\frac{\chi}{8\pi\mu_s}\varepsilon_{ijk}\delta_{l3}\left(\frac{\delta_{kl}}{r} - \frac{r_k r_l}{r^3}\right) = -\frac{\chi}{8\pi\mu_s}\varepsilon_{ijk}\delta_{l3}J^s_{kl}(\mathbf{r}) = -\frac{\chi}{8\pi\mu_s}J^o_{ij}(\mathbf{r}) \tag{6.28b}$$

where J_{ij} is the usual Oseen tensor and a similar *odd* Oseen tensor is defined as:

$$J^o_{ij}(\mathbf{r}) = \varepsilon_{ijk}\delta_{l3}J^s_{kl}(\mathbf{r}) = \varepsilon_{ijk}\delta_{l3}\left(\frac{\delta_{kl}}{r} - \frac{r_k r_l}{r^3}\right) \tag{6.29}$$

For convenience, an auxiliary symmetric tensor $J^s_{ij}(\mathbf{r})$ is also defined, which only differs with the symmetric Oseen tensor $\boldsymbol{J}$ by a minus sign of the anisotropic term:

$$J^s_{ij}(\mathbf{r}) = \frac{\delta_{ij}}{r} - \frac{r_i r_j}{r^3} \tag{6.30}$$

As for the higher order terms, it can be constructed from the lower order solutions by noting the following properties:

$$\frac{\partial^2}{\partial z^2} f(\mathbf{r}) = \frac{1}{(2\pi)^3}\int \mathrm{d}\mathbf{k}(-k_z^2)\widehat{f}(\mathbf{k})e^{i\mathbf{k}\cdot\mathbf{r}} \tag{6.31}$$

$$\nabla^2 f(\mathbf{r}) = \frac{1}{(2\pi)^3}\int \mathrm{d}\mathbf{k}(-k^2)\widehat{f}(\mathbf{k})e^{i\mathbf{k}\cdot\mathbf{r}} \tag{6.32}$$

Therefore, the next order solutions can be constructed as:

$$G^{(2)}_{(ij)}(\mathbf{r}) = -\chi^2 \mathcal{F}^{-1}\left[\frac{k_z^2}{k^2}\widehat{G}^{(0)}_{(ij)}(\mathbf{k})\right] = -\chi^2 \frac{\partial^2}{\partial z^2}\nabla^{-2}\left[\mathcal{F}^{-1}\left[\widehat{G}^{(0)}_{(ij)}(\mathbf{k})\right]\right] \tag{6.33a}$$

$$G^{(3)}_{[ij]}(\mathbf{r}) = -\chi^2 \mathcal{F}^{-1}\left[\frac{k_z^2}{k^2}\widehat{G}^{(1)}_{[ij]}(\mathbf{k})\right] = -\chi^2 \frac{\partial^2}{\partial z^2}\nabla^{-2}\left[\mathcal{F}^{-1}\left[\widehat{G}^{(1)}_{[ij])}(\mathbf{k})\right]\right] \tag{6.33b}$$

where ∇^{-2} is the inverse Laplace operator defined as:

$$\nabla^{-2} = \int_{\mathbb{R}^3} \mathrm{d}\mathbf{r}' G(\mathbf{r}-\mathbf{r}'), \quad G(\mathbf{r}) = -\frac{1}{4\pi r} \tag{6.34}$$

and $G(\mathbf{r})$ is the Green's function of the 3D Laplace's equation. Also please be aware that the inverse Laplace operator ∇^{-2} is spherically symmetric but the double derivative in z-direction $\frac{\partial^2}{\partial z^2}$ is not. Thus, it's important to choose a proper order between two operators to maintain the desired symmetry for intermediate steps.

In the next, both symmetric and anti-symmetric parts $\left(G^{(2)}_{(ij)}(\mathbf{r}) \text{ and } G^{(3)}_{[ij]}(\mathbf{r})\right)$ will be calculated as an illustration and higher order terms can be computed in a similar manner.

- the symmetric part $G^{(2)}_{(ij)}(\mathbf{r})$

  For the symmetric part, the inverse Laplace operator can be computed as:

$$\begin{aligned}
\nabla^{-2}\left[\mathcal{F}^{-1}\left[G^{(0)}_{(ij)}\right]\right] &= \frac{1}{8\pi\mu_s}\nabla^{-2}\left[\frac{\delta_{ij}}{r} + \frac{r_i r_j}{r^3}\right] \\
&= \frac{1}{8\pi\mu_s}\int_{\mathbb{R}^3} \mathrm{d}\mathbf{r}' G(\mathbf{r}-\mathbf{r}')\left(\frac{\delta_{ij}}{r'} + \frac{r'_i r'_j}{r'^3}\right) \\
&= \frac{1}{8\pi\mu_s}\int_{\mathbb{R}^3} \mathrm{d}\mathbf{r}' G(\mathbf{r}-\mathbf{r}') J_{ij}(\mathbf{r}')
\end{aligned} \tag{6.35}$$

The inverse Laplace operator of the Oseen tensor can be evaluated in the spherical coordinates, which gives that:

$$\nabla^{-2}\left[J_{ij}(\mathbf{r})\right] = \frac{3}{4} r\delta_{ij} - \frac{1}{4}\frac{r_i r_j}{r} \tag{6.36}$$

Then, the double derivative in z-direction is straightforward to calculate, which gives the real-space expression of the symmetric part as

$$\begin{aligned} G^{(2)}_{(ij)}(\mathbf{r}) &= -\frac{\chi^2}{8\pi\mu_s}\frac{\partial^2}{\partial z^2}\left(\frac{3}{4} r\delta_{ij} - \frac{1}{4}\frac{r_i r_j}{r}\right) \\ &= -\frac{\chi^2}{8\pi\mu_s}\left[\frac{3}{4}\left(1-\frac{r_3^2}{r^2}\right)\frac{1}{r}\delta_{ij} + \frac{1}{4}\left(1-3\frac{z^2}{r^2}\right)\frac{r_i r_j}{r^3}\right. \\ &\left. +\frac{1}{2}\frac{r_3}{r^3}\left(\delta_{i3} r_j + r_i\delta_{j3}\right) - \frac{1}{2}\frac{1}{r}\delta_{i3}\delta_{j3}\right] \end{aligned} \tag{6.37}$$

- the anti-symmetric part $G^{(3)}_{[ij]}(\mathbf{r})$

  For the anti-symmetric part, the inverse Laplace operator can be calculated as:

$$\begin{aligned} \nabla^{-2}\left[\mathcal{F}^{-1}\left[G^{(1)}_{[ij]}\right]\right] &= -\frac{\chi}{8\pi\mu_s}\varepsilon_{ijk}\delta_{l3}\nabla^{-2}\left[\frac{\delta_{kl}}{r} - \frac{r_k r_l}{r^3}\right] \\ &= -\frac{\chi}{8\pi\mu_s}\varepsilon_{ijk}\delta_{l3}\nabla^{-2}\int_{\mathbb{R}^3} \mathrm{d}\mathbf{r}' G(\mathbf{r}-\mathbf{r}')\left(\frac{\delta_{ij}}{r'} - \frac{r'_i r'_j}{r'^3}\right) \\ &= -\frac{\chi}{8\pi\mu_s}\varepsilon_{ijk}\delta_{l3}\nabla^{-2}\int_{\mathbb{R}^3} \mathrm{d}\mathbf{r}' G(\mathbf{r}-\mathbf{r}') J^s_{ij}(\mathbf{r}') \end{aligned} \tag{6.38}$$

The inverse Laplace operator of $J^s_{ij}(\mathbf{r})$ can be similarly evaluated in the spherical coordinates, which gives that:

$$\nabla^{-2}\left[J^s_{ij}(\mathbf{r})\right] = \frac{1}{4} r\delta_{ij} + \frac{1}{4}\frac{r_i r_j}{r} \tag{6.39}$$

Then, plugging it back and evaluate the double derivative in z-direction yields the real-space expression of the anti-symmetric part as:

$$
\begin{aligned}
G^{(3)}_{[ij]}(\mathbf{r}) &= \frac{\chi^3}{8\pi\mu_s}\varepsilon_{ijk}\delta_{l3}\frac{\partial^2}{\partial z^2}\left(\frac{1}{4}r\delta_{kl}+\frac{1}{4}\frac{r_k r_l}{r}\right) \\
&= \frac{\chi^3}{8\pi\mu_s}\varepsilon_{ijk}\delta_{l3}\left[\frac{1}{4}\left(1-\frac{r_3^2}{r^2}\right)\frac{1}{r}\delta_{kl}-\frac{1}{4}\left(1-3\frac{z^2}{r^2}\right)\frac{r_k r_l}{r^3}\right. \\
&\left.-\frac{1}{2}\frac{r_3}{r^3}\left(\delta_{k3}r_l+r_k\delta_{l3}\right)+\frac{1}{2}\frac{1}{r}\delta_{k3}\delta_{l3}\right] \\
&= \frac{\chi^3}{8\pi\mu_s}\left[\frac{3}{4}\left(1-\frac{r_3^2}{r^2}\right)\frac{1}{r}\varepsilon_{ij3}-\frac{3}{4}\left(1-\frac{r_3^2}{r^2}\right)\frac{r_3}{r^3}\varepsilon_{ijk}r_k\right]
\end{aligned}
\tag{6.40}
$$

Finally, the Green's function in the real-space can be expressed as:

$$G_{ij}(\mathbf{r}) = G_{(ij)}(\mathbf{r}) + G_{[ij]}(\mathbf{r}) \tag{6.41a}$$

$$G_{(ij)}(\mathbf{r}) = G^{(0)}_{(ij)}(\mathbf{r}) + G^{(2)}_{(ij)}(\mathbf{r}) + \mathcal{O}(\chi^4) \tag{6.41b}$$

$$G_{[ij]}(\mathbf{r}) = G^{(1)}_{[ij]}(\mathbf{r}) + G^{(3)}_{[ij]}(\mathbf{r}) + \mathcal{O}(\chi^5) \tag{6.41c}$$

where the explicit expressions of the symmetric Green's functions are given by Eqn. 6.28a and 6.37; the explicit expressions of the anti-symmetric Green's functions are given by Eqn. 6.28b and 6.40.

6.3.4. Integral representation

With the Green's function [Eqn. 6.41] of the odd Stokes' equations [Eqn. 6.10] derived in previous section, the flow field induced by a point force $\mathbf{F}$ at origin is:

$$u_i^{PF}(\mathbf{r}) = G_{ij}(\mathbf{r})F_j = \left[G_{(ij)}(\mathbf{r}) + G_{[ij]}(\mathbf{r})\right] F_j \tag{6.42}$$

As a starting point, only the first order effect due to odd viscosity will be explored here for simplicity but the formalism developed below in principle can be extended to arbitrary orders. If we only retain the first order term of viscosity ratio χ [Eqn. 6.28a and 6.28b], the exact Green's function reduces as

$$\begin{aligned} G_{ij}(\mathbf{r}) &= G^{(0)}_{(ij)}(\mathbf{r}) + G^{(1)}_{[ij]}(\mathbf{r}) + \mathcal{O}(\chi^2) \\ &\approx \frac{1}{8\pi\mu}\left[J_{ij}(\mathbf{r}) - \chi J^o_{ij}(\mathbf{r})\right] \end{aligned} \tag{6.43}$$

where $J_{ij}(\mathbf{r})$ and $J^o_{ij}(\mathbf{r})$ are the even [Eqn. 5.7] and odd Oseen tensor [Eqn. 6.29], respectively. And from now on, the shear viscosity μ_s will be denoted as μ for short. Then, by the linearity of the odd Stokes' equation, the total flow field induced by a collection of finite size rigid particles can be written as [see Sec. 5.2.1]:

$$u_i(\mathbf{x}) = u_i^{\infty}(\mathbf{x}) + \frac{1}{8\pi\mu}\sum_{\alpha=1}^{N}\int_{S^\alpha}\left[J_{ij}(\mathbf{r}) - \chi J^o_{ij}(\mathbf{r})\right] f_j(\mathbf{y})\mathrm{d}S(\mathbf{y}) \tag{6.44}$$

where u_i^∞ $(i = x, y, z)$ is the background linear velocity field, S^α is the surface of α-th particle ($\alpha = 1, \cdots, N$), $\mathbf{y}$ is the location at the particle surface, $f_j(\mathbf{y})$ is the force density (or traction force) distributed over the particle surface.

6.3.5. Multipole expansion

Comparing with the integral representation of only even viscosity [Eqn. 5.9], the above integral representation with odd viscosity has one additional term due to the first order effect of the odd viscosity $-\chi J^o_{ij}(\mathbf{r})$. However, the exactly same multipole expansion procedure can still be carried out as detailed in Sec. 5.2.2. The whole procedure does not depend on the explicit form of the Green's function, therefore, the multipole expansion of the integral representation with odd viscosity [Eqn. 6.44] can be written as:

$$\begin{aligned} u_i(\mathbf{x}) \approx u_i^{\infty}(\mathbf{x}) &+ \frac{1}{8\pi\mu}\sum_{\alpha=1}^{N}\left[J_{ij}(\mathbf{x}-\mathbf{x}^\alpha)F_j^\alpha + R_{ij}(\mathbf{x}-\mathbf{x}^\alpha)T_j^\alpha - K_{ijk}(\mathbf{x}-\mathbf{x}^\alpha)S_{jk}^\alpha\right] \\ &- \frac{\chi}{8\pi\mu}\sum_{\alpha=1}^{N}\left[J^o_{ij}(\mathbf{x}-\mathbf{x}^\alpha)F_j^\alpha + R^o_{ij}(\mathbf{x}-\mathbf{x}^\alpha)T_j^\alpha - K^o_{ijk}(\mathbf{x}-\mathbf{x}^\alpha)S_{jk}^\alpha\right] \end{aligned} \tag{6.45}$$

where J_{ij}, R_{ij} and K_{ijk} are the usual even viscosity propagators of force, torque and stresslet, respectively [Eqn. 5.7, 5.21 and 5.24]. The additional flows contributed by the odd viscosity are explicitly split out and the corresponding propagators can be obtained by simply replacing the even Oseen tensor J_{ij} with the odd Oseen tensor J^o_{ij}:

$$J^o_{ij}(\mathbf{r}) = \frac{\varepsilon_{ij3}}{r} - \frac{\varepsilon_{ijk}r_k r_3}{r^3} \tag{6.46a}$$

$$R^o_{ij}(\mathbf{r}) = \frac{1}{2}\varepsilon_{ikl}\nabla_k J^o_{jl} \tag{6.46b}$$

$$K^o_{ijk}(\mathbf{r}) = \frac{1}{2}\left[\nabla_k J^o_{ij}(\mathbf{r}) + \nabla_j J^o_{ik}(\mathbf{r})\right] \tag{6.46c}$$

The above multipole expansion is truncated at the first order and such expansion can proceed to higher order terms [see Sec. 5.2.2]. For rigid spherical particles, such expansion terminate quickly and the exact solution can be obtained for isolated particles [see

Eqn. 5.28]. However, for the next order of multipole expansion involved the gradients of propagators, the results indeed depend on the properties of the propagators (for example, R_{ij} is anti-symmetric while R^o_{ij} is symmetric). Therefore, those higher order terms need to be constructed from singularity solutions of steady flow of each motion modes [**121**]. In the following, the proper correction terms for propagators due to the odd viscosity are given directly and their proof will be postponed to Sec. 6.3.8:

(6.47)

$$
\begin{aligned}
u_i(\mathbf{x}) \approx u_i^{\infty}(\mathbf{x}) + \frac{1}{8\pi\mu}\sum_{\alpha=1}^{N}\Bigg[&\left(1+\frac{1}{6}a^2\nabla^2\right)J_{ij}(\mathbf{x}-\mathbf{x}^\alpha)F_j^\alpha + R_{ij}(\mathbf{x}-\mathbf{x}^\alpha)T_j^\alpha \\
&-\left(1+\frac{1}{10}a^2\nabla^2\right)K_{ijk}(\mathbf{x}-\mathbf{x}^\alpha)S_{jk}^\alpha\Bigg] \\
-\frac{\chi}{8\pi\mu}\sum_{\alpha=1}^{N}\Bigg[&\left(1+\frac{1}{6}a^2\nabla^2\right)J^o_{ij}(\mathbf{x}-\mathbf{x}^\alpha)F_j^\alpha - \left(1+\frac{1}{10}a^2\nabla^2\right)R^o_{ij}(\mathbf{x}-\mathbf{x}^\alpha)T_j^\alpha \\
&-\left(1+\frac{1}{10}a^2\nabla^2\right)K^o_{ijk}(\mathbf{x}-\mathbf{x}^\alpha)S_{jk}^\alpha\Bigg]
\end{aligned}
$$

6.3.6. Generalized Faxén laws

As shown in Sec. 5.2.3, the Faxén laws provide a bridge for connecting the kinetic motions $(\mathbf{U}^\alpha, \mathbf{\Omega}^\alpha, \boldsymbol{E}^\alpha)$ with corresponding mechanical quantities $(\mathbf{F}^\beta, \mathbf{T}^\beta, \boldsymbol{S}^\beta)$ of each particles. However, the validity of the Faxén laws with even viscosity relies on the Lorentz Reciprocal Theorem (LRT) and symmetry properties of the Oseen tensor [**121**]. In the following, a generalized LRT including odd viscosity will be derived firstly. Then, the Faxén laws with odd viscosity will be proved based on the generalized LRT.

6.3.6.1. generalized Lorentz reciprocal theorem. Suppose that $(\mathbf{u}^{(1)}, \boldsymbol{\sigma}^{(1)})$ and $(\mathbf{u}^{(2)}, \boldsymbol{\sigma}^{(2)})$ are two different solutions of the *odd* Stokes' equations with the same geometry but subjected to different boundary conditions. Due to the linearity of the viscosity tensor [Eqn. 6.6], the overall stress tensor can be separated into stresses contributed by even and odd viscosity, i.e. $\boldsymbol{\sigma} = \boldsymbol{\sigma}_e + \boldsymbol{\sigma}_o$. Then, the generalized Lorentz Reciprocal Theorem states that:

$$\begin{aligned} &\oint_S \mathbf{u}^{(1)} \cdot \left[\left(\boldsymbol{\sigma}_e^{(2)} + \boldsymbol{\sigma}_o^{(2)} \right) \cdot \hat{\mathbf{n}} \right] \mathrm{d}S - \int_V \mathbf{u}^{(1)} \cdot \left[\boldsymbol{\nabla} \cdot \left(\boldsymbol{\sigma}_e^{(2)} + \boldsymbol{\sigma}_o^{(2)} \right) \right] \mathrm{d}V \\ &= \oint_S \mathbf{u}^{(2)} \cdot \left[\left(\boldsymbol{\sigma}_e^{(2)} - \boldsymbol{\sigma}_o^{(2)} \right) \cdot \hat{\mathbf{n}} \right] \mathrm{d}S - \int_V \mathbf{u}^{(2)} \cdot \left[\boldsymbol{\nabla} \cdot \left(\boldsymbol{\sigma}_e^{(2)} - \boldsymbol{\sigma}_o^{(2)} \right) \right] \mathrm{d}V \end{aligned} \tag{6.48}$$

In the absence of the external forces ($\boldsymbol{\nabla} \cdot \boldsymbol{\sigma} = 0$), it reduces as:

$$\oint_S \mathbf{u}^{(1)} \cdot \left[\left(\boldsymbol{\sigma}_e^{(2)} + \boldsymbol{\sigma}_o^{(2)} \right) \cdot \hat{\mathbf{n}} \right] \mathrm{d}S = \oint_S \mathbf{u}^{(2)} \cdot \left[\left(\boldsymbol{\sigma}_e^{(2)} - \boldsymbol{\sigma}_o^{(2)} \right) \cdot \hat{\mathbf{n}} \right] \mathrm{d}S \tag{6.49}$$

The proof of the above generalized version of LRT is very similar to the one detailed in Sec. 5.2.4.1. The only difference of the proof is to note that the constitutive relation now becomes:

$$\sigma_{ij}^{(1)} = \left(\mu_{ijkl}^e + \mu_{ijkl}^o \right) \nabla_l u_k^{(1)}, \quad \sigma_{ij}^{(2)} = \left(\mu_{ijkl}^e + \mu_{ijkl}^o \right) \nabla_l u_k^{(2)} \tag{6.50}$$

and relevant symmetry properties of even and odd viscosity tensors are:

$$\mu_{ijkl}^e = \mu_{klij}^e, \quad \mu_{ijkl}^o = -\mu_{klij}^o \tag{6.51}$$

Then, one can easily prove the generalized Lorentz Reciprocal Theorem by following the steps given in Sec. 5.2.4.1. As discussed in Sec. 6.3.1, those symmetry properties of

viscosity tensors ($ij \leftrightarrow kl$) are actually connected to the time-reversal symmetry. The additional minus sign of the odd viscosity under the time-reversal transformation is reflected in the odd stress terms in the generalized LRT.

6.3.6.2. generalized Faxén laws. With the generalized LRT, a generalized Faxén laws can be derived. For example [**121**], considering a particle translates in the fluid with velocity $\mathbf{U}_1$, which has a corresponding flow field $\mathbf{u}_1$, and another particle is stationary but there is a point $\mathbf{F}$ applied at location $\mathbf{y}$ outside the particle. Then, the generalized LRT gives that:

$$\mathbf{U}_1 \cdot \mathbf{F}_2 - \mathbf{u}_1(\mathbf{y}) \cdot \mathbf{F} = 0 \tag{6.52}$$

where $\mathbf{F}_2$ is the force acting on the stationary particle due to the corresponding flow field $\mathbf{u}_2(\mathbf{x})$ induced by the point force $\mathbf{F}$. Because of the linearity of the *odd* Stokes' equations, the ambient flow for the translating particle can be expressed as:

$$\mathbf{u}_1(\mathbf{x}) = \left\{ \mathcal{F}_e \left[\frac{J_{ij}(\mathbf{x} - \boldsymbol{\xi})}{8\pi\mu} \right] + \mathcal{F}_o \left[\frac{-\chi J^o_{ij}(\mathbf{x} - \boldsymbol{\xi})}{8\pi\mu} \right] \right\} \cdot \mathbf{U}_1 \tag{6.53}$$

where $\mathcal{F}_e$ and $\mathcal{F}_o$ represent a linear function for the even and odd viscosity, respectively. $\mathcal{F}_e$ and $\mathcal{F}_o$ may or may not have the same functional form. And $\boldsymbol{\xi}$ denotes the region where source force densities are distributed. Plugging it back enables the elimination of $\mathbf{U}_1$, which yields that

$$F^2_i = \left\{ \mathcal{F}_e \left[\frac{J_{ji}(\mathbf{x} - \boldsymbol{\xi})}{8\pi\mu} \right] + \mathcal{F}_o \left[\frac{-\chi J^o_{ji}(\mathbf{x} - \boldsymbol{\xi})}{8\pi\mu} \right] \right\} F_j \tag{6.54}$$

Note the symmetry properties of both even and odd Oseen tensors:

$$J_{ji}(\mathbf{x}-\boldsymbol{\xi}) = J_{ij}(\mathbf{x}-\boldsymbol{\xi}), \quad J^o_{ji}(\mathbf{x}-\boldsymbol{\xi}) = -J^o_{ij}(\mathbf{x}-\boldsymbol{\xi}) \tag{6.55a}$$

$$J_{ij}(\mathbf{x}-\boldsymbol{\xi}) = J_{ij}(\boldsymbol{\xi}-\mathbf{x}), \quad J^o_{ij}(\mathbf{x}-\boldsymbol{\xi}) = J^o_{ij}(\boldsymbol{\xi}-\mathbf{x}) \tag{6.55b}$$

Therefore, the linear function $\mathcal{F}$ evaluated at the translating particle in the $\mathbf{u}_1$ problem is the same linear function $\mathcal{F}$ evaluated at the stationary particle in the $\mathbf{u}_2$ problem, i.e.

$$F_i^2 = \mathcal{F}_e\left[\frac{J_{ij}(\boldsymbol{\xi}-\mathbf{y})}{8\pi\mu}F_j\right] + \mathcal{F}_o\left[\chi\frac{J^o_{ij}(\boldsymbol{\xi}-\mathbf{y})}{8\pi\mu}F_j\right] \tag{6.56}$$

As informed by the multipole expansion results 6.47] (or from the Green's function directly), the flows contributed by even and odd viscosity induced by a point force $\mathbf{F}$ are:

$$\mathbf{u}^e(\boldsymbol{\xi}) = \frac{1}{8\pi\mu}\lim_{a\to 0}\left(1+\frac{a^2}{6}\nabla^2\right)J_{ij}(\boldsymbol{\xi}-\mathbf{y})F_j = \frac{J_{ij}(\boldsymbol{\xi}-\mathbf{y})}{8\pi\mu}F_j \tag{6.57a}$$

$$\mathbf{u}^o(\boldsymbol{\xi}) = -\frac{\chi}{8\pi\mu}\lim_{a\to 0}\left(1+\frac{a^2}{6}\nabla^2\right)J^o_{ij}(\boldsymbol{\xi}-\mathbf{y})F_j = -\chi\frac{J^o_{ij}(\boldsymbol{\xi}-\mathbf{y})}{8\pi\mu}F_j \tag{6.57b}$$

where $\mathbf{u}^e(\boldsymbol{\xi})$ and $\mathbf{u}^o(\boldsymbol{\xi})$ denote the flow contributed by the even and odd viscosity, respectively. Thus, the terms inside the brackets are identified as just the induced ambient flow, which gives that

$$\mathbf{F}_2 = \mathcal{F}_e\left[\mathbf{u}^e(\boldsymbol{\xi})\right] - \mathcal{F}_o\left[\mathbf{u}^o(\boldsymbol{\xi})\right] \tag{6.58}$$

Finally, it shows that there is just an additional minus sign for the flow contributed the odd viscosity in the generalized Faxén laws. Follow the above construction, one can prove similar relations for torques and stresslets, i.e.

$$\mathbf{T} = \mathcal{T}_e\left[\mathbf{u}^e(\boldsymbol{\xi})\right] - \mathcal{T}_o\left[\mathbf{u}^o(\boldsymbol{\xi})\right] \tag{6.59a}$$

$$\boldsymbol{S} = \mathcal{S}_e\left[\mathbf{u}^e(\boldsymbol{\xi})\right] - \mathcal{S}_o\left[\mathbf{u}^o(\boldsymbol{\xi})\right] \tag{6.59b}$$

In the next, only additional new contributions due to the odd viscosity will be covered as the Faxén laws for the even viscosity have been discussed in Sec. 5.2.3. Similar to Eqn. 5.31, for a collection of spherical particles, the linear superposition enables writing the ambient *odd* flow field $\mathbf{u}^{o\prime}$ induced by all other particles excluding the α-th particle itself as:

(6.60)
$$u_i^{o\prime}(\mathbf{x}) \approx -\frac{\chi}{8\pi\mu}\sum_{\beta=1,\beta\neq\alpha}^{N}\left\{\mathcal{F}\left[J_{ij}^o(\mathbf{x}-\mathbf{x}^\beta)\right]F_j^\beta + \mathcal{T}\left[J_{ij}^o(\mathbf{x}-\mathbf{x}^\beta)\right]T_j^\beta + \mathcal{S}\left[J_{ij}^o(\mathbf{x}-\mathbf{x}^\beta)\right]S_{jk}^\beta\right\}$$

where $\mathcal{F}\left[J_{ij}^o(\mathbf{x}-\mathbf{y})\right]$, $\mathcal{T}\left[J_{ij}^o(\mathbf{x}-\mathbf{y})\right]$ and $\mathcal{S}\left[J_{ij}^o(\mathbf{x}-\mathbf{y})\right]$ denote linear functions which describe the odd viscosity related response to external forces, torques, stresslets respectively. Based on the results derived in Eqn. 6.58, 6.59a and 6.59b, the kinetic motions of α-th particle due to the ambient *odd* flow $\mathbf{u}^{o\prime}$ induced by other particles ($\beta \neq \alpha$) can be written

as:

$$\begin{cases} U_i^\alpha - U_i^\infty(\mathbf{x}^\alpha) = -\mathcal{F}\left[u_i^{o\prime}(\mathbf{x}); \mathbf{x}^\alpha\right] \\ \Omega_i^\alpha - \Omega_i^\infty(\mathbf{x}^\alpha) = -\mathcal{T}[u_i^{o\prime}(\mathbf{x}); \mathbf{x}^\alpha] \\ E_{ij}^\alpha - E_{ij}^\infty(\mathbf{x}^\alpha) = -\mathcal{S}[u_i^{o\prime}(\mathbf{x}); \mathbf{x}^\alpha] \end{cases} \tag{6.61}$$

The above relations are the Faxén laws for the odd viscosity, which differ with the Faxén laws for the even viscosity [Eqn. 5.33] by a minus sign.

6.3.7. Near-field mobility tensors

So far, the explicit functional forms of linear response functions $\mathcal{F}\left[J_{ij}^o(\mathbf{x}-\mathbf{y})\right]$, $\mathcal{T}\left[J_{ij}^o(\mathbf{x}-\mathbf{y})\right]$ and $\mathcal{S}\left[J_{ij}^o(\mathbf{x}-\mathbf{y})\right]$ have not been determined. Their expressions may be obtained by directly comparing with the ambient flow formula given by the multipole expansion [Eqn. 6.47] just like the way did for even viscosity [Sec. 5.2.3]. However, the validity of Eqn. 6.47 has not been justified yet. Here, I am going to develop the theory in a slightly different order. First, the Rotne-Prager-Yamakawa (RPY) approximation will be used to derive the near-field results in this section. After that, the Eqn. 6.47 will be proved as the far-field expansion of the near-field results [Sec. 6.3.8].

6.3.7.1. integral forms of response functions. Based on the idea of RPY approximation [see Sec. 5.2.6], each force moments are assumed to be uniformly distributed over the particle surface [Eqn. 5.54] and the integral form of ambient *odd* flow can therefore

be expressed as:

(6.62)

$$u_i^{o\prime}(\mathbf{x}) - u_i^{\infty}(\mathbf{x}) \approx -\frac{\chi}{8\pi\mu} \sum_{\beta=1,\beta\neq\alpha}^{N} \oint_{S^\beta} J_{ij}^o(\mathbf{x}-\mathbf{y}) \left[\frac{F_j^\beta}{4\pi a^2} + \frac{3}{8\pi a^3}\epsilon_{jkl} T_k^\beta n_l \mathrm{d}S + \frac{3}{4\pi a^3} S_{jk}^\beta n_k \right] \mathrm{d}S$$

Such integral form expression only replies on the Green's function of the odd Stokes' equations which are derived in Sec. 6.3.3. Then, the integral forms of response functions $\mathcal{F}\left[J_{ij}^o(\mathbf{x}-\mathbf{y})\right]$, $\mathcal{T}\left[J_{ij}^o(\mathbf{x}-\mathbf{y})\right]$ and $\mathcal{S}\left[J_{ij}^o(\mathbf{x}-\mathbf{y})\right]$ can be defined as:

(6.63a) $$\mathcal{F}\left[J_{ij}^o(\mathbf{x}-\mathbf{y}); S\right] = \frac{1}{4\pi a^2} \oint_S \widetilde{J}_{ij}^o(\mathbf{x}-\mathbf{y}) \mathrm{d}S(\mathbf{y})$$

(6.63b) $$\mathcal{T}\left[J_{ij}^o(\mathbf{x}-\mathbf{y}); S\right] = \frac{3}{8\pi a^3} \oint_S \widetilde{R}_{ij}^o(\mathbf{x}-\mathbf{y}) \mathrm{d}S(\mathbf{y})$$

(6.63c) $$\mathcal{S}\left[J_{ij}^o(\mathbf{x}-\mathbf{y}); S\right] = \frac{3}{4\pi a^3} \oint_S \widetilde{K}_{ijk}^o(\mathbf{x}-\mathbf{y}) \mathrm{d}S(\mathbf{y})$$

where the integral is evaluated at the particle surface S and propagators of each force moments are:

(6.64a) $$\widetilde{J}_{ij}^o(\mathbf{x}-\mathbf{y}) = J_{ij}^o(\mathbf{x}-\mathbf{y})$$

(6.64b) $$\widetilde{R}_{ij}^o(\mathbf{x}-\mathbf{y}) = J_{ik}^o(\mathbf{x}-\mathbf{y})\varepsilon_{kjl} n_l$$

(6.64c) $$\widetilde{K}_{ijk}^o(\mathbf{x}-\mathbf{y}) = \frac{1}{2}\left[J_{ij}^o(\mathbf{x}-\mathbf{y}) n_k + J_{ik}^o(\mathbf{x}-\mathbf{y}) n_j\right]$$

These are almost identical to the even viscosity case [Eqn. 5.55] with the even Oseen tensor replaced with the odd Oseen tensor. Besides, the single spherical surface integrals

of response functions can be evaluated analytically, which yield that [see Appx. B.2.2]:

$$M^o_{Fij}(\mathbf{x}) = \frac{1}{8\pi\mu}\mathcal{F}\left[J^o_{ij}(\mathbf{x}-\mathbf{y}); S^\beta\right] = \begin{cases} \left(1+\frac{a^2}{6}\nabla^2\right)\frac{J^o_{ij}(\mathbf{x}-\mathbf{x}^\beta)}{8\pi\mu} & \left|\mathbf{x}-\mathbf{x}^\beta\right| > a \\ \frac{1}{12\pi\mu a}\varepsilon_{ij3} & \left|\mathbf{x}-\mathbf{x}^\beta\right| \le a \end{cases} \tag{6.65a}$$

(6.65b)

$$M^o_{Tij}(\mathbf{x}) = \frac{1}{8\pi\mu}\mathcal{T}\left[J^o_{ij}(\mathbf{x}-\mathbf{y}); S^\beta\right] = \begin{cases} -\left(1+\frac{1}{10}\nabla^2\right)\frac{R^o_{ij}(\mathbf{x}-\mathbf{x}^\beta)}{8\pi\mu} & \left|\mathbf{x}-\mathbf{x}^\beta\right| > a \\ \frac{1}{8\pi\mu a^3}\left[-\frac{3}{5}\left(x_l - x_l^\beta\right)\delta_{lij3}\right. & \\ \left. -\frac{1}{2}\delta_{ij}\left(z-z^\beta\right)+\frac{1}{2}\delta_{i3}(x_j-x_j^\beta)\right] & \left|\mathbf{x}-\mathbf{x}^\beta\right| \le a \end{cases}$$

(6.65c)

$$M^o_{Sijk}(\mathbf{x}) = \frac{1}{8\pi\mu}\mathcal{S}\left[J^o_{ij}(\mathbf{x}-\mathbf{y}); S^\beta\right] = \begin{cases} -\left(1+\frac{a^2}{10}\nabla^2\right)\frac{K^o_{ijk}(\mathbf{x}-\mathbf{x}^\beta)}{8\pi\mu} & \left|\mathbf{x}-\mathbf{x}^\beta\right| > a \\ \frac{1}{40\pi\mu a^3}\left\{\left[\varepsilon_{ij3}\left(x_k-x_k^\beta\right)+\varepsilon_{ik3}\left(x_j-x_j^\beta\right)\right]\right. & \\ \left. +\left(\varepsilon_{ijm}\delta_{k3}+\varepsilon_{ikm}\delta_{j3}\right)\left(x_m-x_m^\beta\right)\right\} & \left|\mathbf{x}-\mathbf{x}^\beta\right| \le a \end{cases}$$

6.3.7.2. the Faxén laws in integral form. With the integral forms of response functions [Eqn. 6.63], the integral form of Faxén laws with odd viscosity can be written explicitly as:

$$\begin{cases} U_i^\alpha - U_i^\infty(\mathbf{x}^\alpha) = -\mathcal{F}\left[u_i'(\mathbf{x}); S^\alpha\right] = -\dfrac{1}{4\pi a^2}\oint_{S^\alpha} u_i'(\mathbf{x})\mathrm{d}S^\alpha(\mathbf{x}) \\ \Omega_i^\alpha - \Omega_i^\infty(\mathbf{x}^\alpha) = -\mathcal{T}\left[u_i'(\mathbf{x}); S^\alpha\right] = -\dfrac{3}{8\pi a^3}\oint_{S^\alpha} \varepsilon_{ijk}n_j u_k'(\mathbf{x})\mathrm{d}S^\alpha(\mathbf{x}) \\ E_{ij}^\alpha - E_{ij}^\infty(\mathbf{x}^\alpha) = -\mathcal{S}[u_i'(\mathbf{x}); S^\alpha] = -\dfrac{3}{4\pi a^3}\oint_{S^\alpha}\dfrac{1}{2}\left[u_i'(\mathbf{x})n_j + u_j'(\mathbf{x})n_i\right]\mathrm{d}S^\alpha(\mathbf{x}) \end{cases} \tag{6.66}$$

where $\mathcal{F}\left[u_i'(\mathbf{x}); S^\alpha\right]$, $\mathcal{T}\left[u_i'(\mathbf{x}); S^\alpha\right]$ and $\mathcal{S}\left[u_i'(\mathbf{x}); S^\alpha\right]$ are the same linear functions defined by Eqn. 6.63 but applied to the ambient *odd* flow $\mathbf{u}^{o\prime}(\mathbf{x})$ given by Eqn. 6.62 and evaluated at the surface of α-th particle S^α instead.

6.3.7.3. near-field mobility tensors. Then, the integral form pair mobility tensors ($\alpha \neq \beta$) can be obtained by plugging the expression of ambient flow [Eqn. 6.62] into the Faxén laws in integral form [Eqn. 6.66], which yields that:

$$\boldsymbol{M}_{UF}^{\alpha\beta} = \left(M^o{}_{UF}{}^{\alpha\beta}{}_{ij}\right) = \frac{\chi}{8\pi\mu}\frac{1}{\left(4\pi a^2\right)^2}\oint_{S^\alpha}\oint_{S^\beta}\widetilde{J}_{ij}^o(\mathbf{x}-\mathbf{y})\mathrm{d}S^\alpha\mathrm{d}S^\beta \tag{6.67a}$$

$$\boldsymbol{M}_{UT}^{\alpha\beta} = \left(M^o{}_{UT}{}^{\alpha\beta}{}_{ij}\right) = \frac{\chi}{8\pi\mu}\frac{1}{4\pi a^2}\frac{3}{8\pi a^3}\oint_{S^\alpha}\oint_{S^\beta}\widetilde{R}_{ij}^o(\mathbf{x}-\mathbf{y})\mathrm{d}S^\alpha\mathrm{d}S^\beta \tag{6.67b}$$

$$\boldsymbol{M}_{US}^{\alpha\beta} = \left(M^o{}_{US}{}^{\alpha\beta}{}_{ijk}\right) = \frac{\chi}{8\pi\mu}\frac{1}{4\pi a^2}\frac{3}{4\pi a^3}\oint_{S^\alpha}\oint_{S^\beta}\widetilde{K}_{ijk}^o(\mathbf{x}-\mathbf{y})\mathrm{d}S^\alpha\mathrm{d}S^\beta \tag{6.67c}$$

$$\boldsymbol{M}_{\Omega T}^{\alpha\beta} = \left(M^o{}_{\Omega T}{}^{\alpha\beta}{}_{ij}\right) = \frac{\chi}{8\pi\mu}\left(\frac{3}{8\pi a^3}\right)^2\oint_{S^\alpha}\oint_{S^\beta}\varepsilon_{ikl}n_k\widetilde{R}_{lj}^o(\mathbf{x}-\mathbf{y})\mathrm{d}S^\alpha\mathrm{d}S^\beta \tag{6.67d}$$

$$\boldsymbol{M}_{\Omega S}^{\alpha\beta} = \left(M^o{}_{\Omega S}{}^{\alpha\beta}{}_{ijk}\right) = \frac{\chi}{8\pi\mu}\frac{3}{8\pi a^3}\frac{3}{4\pi a^3}\oint_{S^\alpha}\oint_{S^\beta}\varepsilon_{ilm}n_l\widetilde{K}_{mjk}^o(\mathbf{x}-\mathbf{y})\mathrm{d}S^\alpha\mathrm{d}S^\beta \tag{6.67e}$$

$$\begin{aligned}\boldsymbol{M}_{ES}^{\alpha\beta} = \left(M^o{}_{ES}{}^{\alpha\beta}{}_{ijkl}\right) &= \frac{\chi}{8\pi\mu}\left(\frac{3}{4\pi a^3}\right)^2 \\ &\oint_{S^\alpha}\oint_{S^\beta}\frac{1}{2}\left[\widetilde{K}_{ikl}^o(\mathbf{x}-\mathbf{y})n_j + \widetilde{K}_{jkl}^o(\mathbf{x}-\mathbf{y})n_i\right]\mathrm{d}S^\alpha\mathrm{d}S^\beta\end{aligned} \tag{6.67f}$$

Again, the evaluations of such double surface integrals are rather tedious and details of calculation can be found at Appx. B.3.2 and the explicit expressions of near-field *odd* mobility tensors are also documented at Appx. B.5.3.

6.3.7.4. self-mobility tensors. Traditionally, the self-mobility tensors are derived from the analytical solutions of each motion modes for an isolated particle [see Sec. 5.2.3.1]. However, starting from only Green's functions, the RPY approach provides an way to derive the self-mobility tensors without solving each boundary-value problems as the near-field mobility tensors [Appx. B.5.3] should reduce to the self-mobility tensors when the separation distance goes to zero [see Sec. 5.2.6.4]. Below, the self-mobility tensors are calculated by taking the limits of the near-field mobility tensors [Appx. B.5.1]:

$$M^o_{UF}{}^{\alpha\alpha}_{ij} = \lim_{r\to 0} M^o_{UF}{}^{\alpha\beta}_{ij} = \frac{\chi}{12\pi\mu a}\varepsilon_{ij3} \tag{6.68a}$$

$$M^o_{UT}{}^{\alpha\alpha}_{ij} = \lim_{r\to 0} M^o_{UT}{}^{\alpha\beta}_{ij} = 0 \tag{6.68b}$$

$$M^o_{US}{}^{\alpha\alpha}_{ijk} = \lim_{r\to 0} M^o_{US}{}^{\alpha\beta}_{ijk} = 0 \tag{6.68c}$$

$$M^o_{\Omega T}{}^{\alpha\alpha}_{ij} = \lim_{r\to 0} M^o_{\Omega T}{}^{\alpha\beta}_{ij} = \frac{\chi}{16\pi\mu a^3}\varepsilon_{ij3} \tag{6.68d}$$

$$M^o_{\Omega S}{}^{\alpha\alpha}_{ijk} = \lim_{r\to 0} M^o_{\Omega S}{}^{\alpha\beta}_{ijk} = \frac{3\chi}{40\pi\mu a^3}\delta_{3ijk} \tag{6.68e}$$

$$M^o_{ES}{}^{\alpha\alpha}_{ijkl} = \lim_{r\to 0} M^o_{ES}{}^{\alpha\beta}_{ijkl} = \frac{\chi}{80\pi\mu a^3}\left[(\varepsilon_{ik3}\delta_{lj} + \varepsilon_{il3}\delta_{kj}) + (\varepsilon_{jk3}\delta_{li} + \varepsilon_{jl3}\delta_{ki})\right] \tag{6.68f}$$

6.3.8. Far-field mobility tensors

6.3.8.1. differential forms of response functions. With the integral form of ambient flow [Eqn. 6.62] and the far-field results of the single surface integrals of propagators [Eqn. 6.65, $\left|\mathbf{x} - \mathbf{x}^\beta\right| > a$], we can immediately show that the far-field expression of the near-field

ambient flow [Eqn. 6.62] is:

(6.69)

$$u_i^{o\prime}(\mathbf{x}) - u_i^{\infty}(\mathbf{x}) \approx -\frac{\chi}{8\pi\mu}\sum_{\beta=1,\beta\neq\alpha}^{N}\left[\left(1+\frac{1}{6}a^2\nabla^2\right)J_{ij}^{o}(\mathbf{x}-\mathbf{x}^{\beta})F_j^{\beta} - \left(1+\frac{1}{10}a^2\nabla^2\right)R_{ij}^{o}(\mathbf{x}-\mathbf{x}^{\beta})T_j^{\beta}\right.$$
$$\left. - \left(1+\frac{1}{10}a^2\nabla^2\right)K_{ijk}^{o}(\mathbf{x}-\mathbf{x}^{\beta})S_{jk}^{\beta}\right], \quad \left|\mathbf{x}-\mathbf{x}^{\beta}\right| > a$$
$$= -\frac{\chi}{8\pi\mu}\sum_{\beta=1,\beta\neq\alpha}^{N}\left\{\mathcal{F}\left[J_{ij}^{o}(\mathbf{x}-\mathbf{x}^{\beta})\right]F_j^{\beta} - \mathcal{T}\left[J_{ij}^{o}(\mathbf{x}-\mathbf{x}^{\beta})\right]T_j^{\beta} - \mathcal{S}\left[J_{ij}^{o}(\mathbf{x}-\mathbf{x}^{\beta})\right]S_{jk}^{\beta}\right\}$$

where the approximation sign is due to the many-body effects and the above results are exact for an infinitely dilute system. This justifies the validity of higher order corrections in Eqn. 6.47 and the differential form of linear response functions $\mathcal{F}\left[J_{ij}^{o}(\mathbf{x}-\mathbf{y})\right]$, $\mathcal{T}\left[J_{ij}^{o}(\mathbf{x}-\mathbf{y})\right]$ and $\mathcal{S}\left[J_{ij}^{o}(\mathbf{x}-\mathbf{y})\right]$ can be defined as:

(6.70a) $$\mathcal{F}\left[J_{ij}^{o}(\mathbf{x}-\mathbf{y})\right] = \left(1+\frac{a^2}{6}\nabla^2\right)J_{ij}^{o}(\mathbf{x}-\mathbf{y}), \quad |\mathbf{x}-\mathbf{y}| > 2a$$

(6.70b) $$\mathcal{T}\left[J_{ij}^{o}(\mathbf{x}-\mathbf{y})\right] = \left(1+\frac{a^2}{10}\nabla^2\right)R_{ij}^{o}(\mathbf{x}-\mathbf{y}), \quad |\mathbf{x}-\mathbf{y}| > 2a$$

(6.70c) $$\mathcal{S}\left[J_{ij}^{o}(\mathbf{x}-\mathbf{y})\right] = \left(1+\frac{a^2}{10}\nabla^2\right)K_{ijk}^{o}(\mathbf{x}-\mathbf{y}), \quad |\mathbf{x}-\mathbf{y}| > 2a$$

6.3.8.2. the Faxén laws in differential form. With the differential forms of response functions [Eqn. 6.70], the differential form of Faxén laws with odd viscosity can be written

explicitly as:

$$
\text{(6.71)}\quad \begin{cases} U_i^\alpha - U_i^\infty(\mathbf{x}^\alpha) = -\mathcal{F}_o\left[u_i^{o\prime}(\mathbf{x}); \mathbf{x}^\alpha\right] = -\left(1 + \dfrac{a^2}{6}\nabla^2\right) u_i'(\mathbf{x}^\alpha) \\ \Omega_i^\alpha - \Omega_i^\infty(\mathbf{x}^\alpha) = -\mathcal{T}_o[u_i^{o\prime}(\mathbf{x}); \mathbf{x}^\alpha] = -\left(1 + \dfrac{a^2}{10}\nabla^2\right) \dfrac{1}{2}\varepsilon_{ijk}\nabla_j u_k'(\mathbf{x}^\alpha) \\ E_{ij}^\alpha - E_{ij}^\infty(\mathbf{x}^\alpha) = -\mathcal{S}_o[u_i^{o\prime}(\mathbf{x}); \mathbf{x}^\alpha] = -\left(1 + \dfrac{a^2}{10}\nabla^2\right) \dfrac{1}{2}\left[\nabla_j u_i'(\mathbf{x}^\alpha) + \nabla_i u_j'(\mathbf{x}^\alpha)\right] \end{cases}
$$

where $\mathcal{F}\left[u_i'(\mathbf{x}); S^\alpha\right]$, $\mathcal{T}\left[u_i'(\mathbf{x}); S^\alpha\right]$ and $\mathcal{S}\left[u_i'(\mathbf{x}); S^\alpha\right]$ are the same linear functions defined by Eqn. 6.70 but applied to the ambient *odd* flow $\mathbf{u}^{o\prime}(\mathbf{x})$ given by Eqn. 6.69 and evaluated at the surface of α-th particle S^α instead.

6.3.8.3. far-field mobility tensors. With the differential form Faxén laws [Eqn. 6.71] and the expression of ambient flow [Eqn. 6.69], the far-field pair mobility tensors ($\alpha \neq \beta$) can be derived as:

$$
\text{(6.72a)}\quad \boldsymbol{M}_{UF}^{\alpha\beta} = \left(M^o{}_{UF}{}^{\alpha\beta}_{ij}\right) = \frac{\chi}{8\pi\mu}\left(1 + \frac{a^2}{6}\nabla^2\right)\left(1 + \frac{a^2}{6}\nabla^2\right) J_{ij}^o(\mathbf{x}^\alpha - \mathbf{x}^\beta)
$$

$$
\text{(6.72b)}\quad \boldsymbol{M}_{UT}^{\alpha\beta} = \left(M^o{}_{UT}{}^{\alpha\beta}_{ij}\right) = \frac{-\chi}{8\pi\mu}\left(1 + \frac{a^2}{6}\nabla^2\right)\left(1 + \frac{a^2}{10}\nabla^2\right) R_{ij}^o(\mathbf{x}^\alpha - \mathbf{x}^\beta)
$$

$$
\text{(6.72c)}\quad \boldsymbol{M}_{US}^{\alpha\beta} = \left(M^o{}_{US}{}^{\alpha\beta}_{ijk}\right) = \frac{-\chi}{8\pi\mu}\left(1 + \frac{a^2}{6}\nabla^2\right)\left(1 + \frac{a^2}{10}\nabla^2\right) K_{ijk}^o(\mathbf{x}^\alpha - \mathbf{x}^\beta)
$$

$$
\text{(6.72d)}\quad \boldsymbol{M}_{\Omega T}^{\alpha\beta} = \left(M^o{}_{\Omega T}{}^{\alpha\beta}_{ij}\right) = \frac{-\chi}{8\pi\mu}\left(1 + \frac{a^2}{10}\nabla^2\right)\left(1 + \frac{a^2}{10}\nabla^2\right) \frac{1}{2}\varepsilon_{ikl}\nabla_k R_{lj}^o(\mathbf{x}^\alpha - \mathbf{x}^\beta)
$$

$$
\text{(6.72e)}\quad \boldsymbol{M}_{\Omega S}^{\alpha\beta} = \left(M^o{}_{\Omega S}{}^{\alpha\beta}_{ijk}\right) = \frac{-\chi}{8\pi\mu}\left(1 + \frac{a^2}{10}\nabla^2\right)\left(1 + \frac{a^2}{10}\nabla^2\right) \frac{1}{2}\varepsilon_{ilm}\nabla_l K_{mjk}^o(\mathbf{x}^\alpha - \mathbf{x}^\beta)
$$

$$
\text{(6.72f)}\quad \boldsymbol{M}_{ES}^{\alpha\beta} = \left(M^o{}_{ES}{}^{\alpha\beta}_{ijkl}\right) = \frac{-\chi}{8\pi\mu}\left(1 + \frac{a^2}{10}\nabla^2\right)\left(1 + \frac{a^2}{10}\nabla^2\right)
$$

$$
\frac{1}{2}\left[\nabla_j K_{ikl}^o(\mathbf{x}^\alpha - \mathbf{x}^\beta) + \nabla_i K_{jkl}^o(\mathbf{x}^\alpha - \mathbf{x}^\beta)\right]
$$

Note that the odd Oseen tensor is also biharmonic, i.e. $\nabla^4 J^o_{ij}(\mathbf{r}) = 0$ [Appx. B.1.2], which enables further simplification of mobility tensors. The explicit expressions of all far-field odd mobility tensors can be found at Appx. B.5.2.

6.3.8.4. continuity between near-field and far-field mobility tensors. By construction, the near-field mobility tensors [Appx. B.5.3] should match with the far-field mobility tensors [Appx. B.5.2] continuously at the particle surface [Sec. 5.2.6.4]. Such continuity requirement can be checked explicitly as:

$$\lim_{r\to 2a^-} {M^o_{UF}}^{\alpha\beta}{}_{ij} = \lim_{r\to 2a^+} {M^o_{UF}}^{\alpha\beta}{}_{ij} \tag{6.73a}$$

$$\lim_{r\to 2a^-} {M^o_{UT}}^{\alpha\beta}{}_{ij} = \lim_{r\to 2a^+} {M^o_{UT}}^{\alpha\beta}{}_{ij} \tag{6.73b}$$

$$\lim_{r\to 2a^-} {M^o_{US}}^{\alpha\beta}{}_{ijk} = \lim_{r\to 2a^+} {M^o_{US}}^{\alpha\beta}{}_{ijk} \tag{6.73c}$$

$$\lim_{r\to 2a^-} {M^o_{\Omega T}}^{\alpha\beta}{}_{ij} = \lim_{r\to 2a^+} {M^o_{\Omega T}}^{\alpha\beta}{}_{ij} \tag{6.73d}$$

$$\lim_{r\to 2a^-} {M^o_{\Omega S}}^{\alpha\beta}{}_{ijk} = \lim_{r\to 2a^+} {M^o_{\Omega S}}^{\alpha\beta}{}_{ijk} \tag{6.73e}$$

$$\lim_{r\to 2a^-} {M^o_{ES}}^{\alpha\beta}{}_{ijkl} = \lim_{r\to 2a^+} {M^o_{ES}}^{\alpha\beta}{}_{ijkl} \tag{6.73f}$$

6.3.8.5. Symmetry of mobility tensors. Similar to the case of even viscosity [Sec. 5.2.4.2], there are also many symmetry relations of mobility tensors of odd viscosity constrained by symmetry properties of system. For a complete list of symmetry relations, please refer to Appx. B.5.4.

Due to the existence of odd viscosity, some symmetry properties of system are changed, which yields different sets of symmetry relations comparing with those of even viscosity.

There are symmetry relations of component indices (i, j, k, l) [Appx. B.5.4.1] and particle indices (α, β) [Appx. B.5.4.2], which reflects the space symmetry and the parity symmetry of system, respectively. Besides, there are also symmetry relations constrained by the generalized Lorentz Reciprocal Theorem [Appx. B.5.4.3], which reflects the time reversal symmetry of system. Because all these relations can be proved similarly as shown for even viscosity case [Appx. B.4.4], all these symmetry relations are provided without proof.

With all those symmetry relations of mobility tensors, it can be shown that the grand mobility tensor of odd viscosity $\mathcal{M}^o_\infty$ [Eqn. 6.72] is "symmetric" and only the upper (or lower) half of the matrix needs to be computed as [Appx. B.5.4.4]:

$$M^o{}_{\Omega F}{}^{\alpha\beta}{}_{ij} = M^o{}_{UT}{}^{\alpha\beta}{}_{ij}, \quad M^o{}_{EF}{}^{\alpha\beta}{}_{ijk} = -M^o{}_{US}{}^{\alpha\beta}{}_{kij}, \quad M^o{}_{ET}{}^{\alpha\beta}{}_{ijk} = -M^o{}_{\Omega S}{}^{\alpha\beta}{}_{kij} \tag{6.74}$$

6.3.9. Full-range mobility tensors

Finally, with both near-field [Sec. 6.3.7] and far-field [Sec. 6.3.8] *odd* mobility tensors constructed, the Stokesian Dynamics (SD) formalism can be modified to incorporate the leading order effects due to odd viscosity. Mathematically, the hydrodynamic interactions in SD with both even and odd viscosity can be written as:

$$\mathcal{M} = \mathcal{M}^e_\infty + \mathcal{M}^o_\infty \tag{6.75}$$

where $\mathcal{M}$ is the full grand mobility tensor which contains hydrodynamic interactions from both even and odd viscosity; $\mathcal{M}^e_\infty$ is the grand mobility tensor due to even viscosity, which including both near-field [Eqn. 5.60 and Appx. B.4.3] and far-field [Eqn. 5.36 and Appx. B.4.2] even mobility tensors; $\mathcal{M}^o_\infty$ is the grand mobility tensor due to odd viscosity, which

including both near-field [Eqn. 6.67 and Appx. B.5.3] and far-field [Eqn. 6.72 and Appx. B.5.2] odd mobility tensors.

To be more clear, as the lubrication theory with odd viscosity has not been developed, the above formalism is not exactly the same as the existing SD framework [Eqn. 5.63] and in principle only works for well-separated particles i.e. dilute suspension. However, empirically, this is not a strict limitation as long as the system of interests is not very dense. In terms of numeric aspects, the grand mobility tensor $\mathcal{M}$ becomes a purely dense matrix due to the lack of near-field lubrication theory with odd viscosity. Therefore, all problem formalism and numeric techniques related to dense matrix discussed before [Sec. 5.2.7 and Sec. 5.3.6] still can directly apply to the new extended grand mobility tensor.

6.4. Simulation of a population of magnetic spinners

So far, this part of work is not fully complete yet and I will only sketch the plan of using the developed odd Stokesian Dynamics [Sec. 6.3] to simulate a collection of magnetic spinners in the near future. By the time of final revision, more simulation results are expected.

6.4.1. Outlook of simulations

6.4.1.1. Equations of motion. Similar to the pure SD simulation discussed in Sec. 6.2, a magnetic torque, $\mathbf{T}_m = 8\pi\mu a^3\boldsymbol{\omega}$ and an effective gravitational force $\mathbf{F}_g = m\mathbf{g}\sin\theta$ are applied to each magnetic colloidal particle. Then, the deterministic translational and

angular velocity of each particle can be computed by the mobility formulation, i.e.

$$\begin{pmatrix} \mathbf{U}^{\alpha} - \mathbf{U}^{\infty} \\ \boldsymbol{\Omega}^{\alpha} - \boldsymbol{\Omega}^{\infty} \end{pmatrix} = \mathcal{M} \begin{pmatrix} \mathbf{F}^{\alpha} \\ \mathbf{T}^{\alpha} \end{pmatrix} \tag{6.76}$$

where the grand mobility tensor $\mathcal{M}$ now should include contributions from both even and odd viscosity, i.e. $\mathcal{M} = \mathcal{M}^{o}_{\infty} + \mathcal{M}^{o}_{\infty}$. The ratio between thermal energy and effective gravity, $k_B T/mg\sin\theta$, gives an estimation of the spread height of steady state density profile of sedimentation, which makes the thermal fluctuation an intrinsic component for sedimentation process, the equations of motion governing the dynamics of magnetic spinners should be Brownian equations [Sec. 5.3.5 and Eqn. 5.78]:

$$\frac{\mathrm{d}\mathbf{r}}{\mathrm{d}t} = \mathcal{M}\mathbf{F} + \sqrt{2k_B T}\mathcal{M}^{1/2}\mathcal{W} + k_B T\boldsymbol{\nabla}\cdot\mathcal{M}$$

6.4.1.2. chamber walls. Unlike the case for simulating a collection of Quincke rollers [Sec. 5.3.6] constrained to a 2D plane, the simulation of a collection of magnetic spinners is in fully 3D space confined by chamber walls. As sketched in Fig. 6.1, there are two important walls: one is the titled chamber floor acting against the major component of gravity ($mg\cos\theta$) and another one is the bottom wall located along y-axis which stops particles from further sedimentation. A wall-particle interaction is included to reproduce the experimental conditions in a 3D setting.

6.4.1.3. simulations. In order to validate the development of odd Stokesian Dynamics, the plan is to simulate the sedimentation of a collection of magnetic spinners to see whether any significant effects can be observed comparing with conventional even viscosity only simulations. Due to the recent theoretical works [**390**], the odd viscosity is proportional to

the activity level of the system, which is reflected by the external magnetic field frequency $\boldsymbol{\omega}$. Note that the magnetic torque $\mathbf{T}_m \propto \boldsymbol{\omega}$ is also proportional to the frequency, which makes such attempt promising to uncover possible effects with quadratic dependence on system activity level. This is clearly beyond the traditional framework of Stokesian Dynamics, where only linear dependence is expected.

6.5. Discussion and future works

There are still lots of open questions need to be addressed in these non-equilibrium active fluid systems. For the continual development of the Stokesian Dynamics with odd viscosity, the corresponding wall corrections [**136**, **327**] and lubrication theory [**137**, **138**, **143**] are still missing and worth investigating. From a more general perspective, it's also very interesting to check whether the Fluctuation-Dissipation Theorem [**398**–**404**] still holds in such active systems.

In terms of numeric technique development, it's helpful to automate the numeric implementation process for the Stokesian Dynamics community. Since the SD relies on the analytic expressions of mobility tensors, which are ultimately derived from the Green's function of the system, the whole theoretical derivations of SD formalism can be automated by a Symbolic Algebra System, such as SymPy. Then, the corresponding analytic expressions of mobility tensors can be generated automatically by simply changing the fundamental Green's function, such as replacing the Oseen tensor with the odd Oseen tensor [Sec. 6.3]. More importantly, such symbolic expressions can be used for the generation of kernels on targeted device (such as the CUDA code for GPU devices), where automatic code optimization can be applied to have highly-efficient device-specific implementations.

Therefore, physicists can focus on the development of theory and leave the difficulties of numeric implementation to computer. This idea of automation is not new and has already been implemented in other fields such as LBM (lbmpy [**405**]), which is becoming increasingly popular to archive superior performance by the design of a domain-specific compiler.

CHAPTER 7

Concluding Remarks

"More is different."

—*Anderson, P. W.*

This work provides a holistic overview of research problems encountered while *engineering responses of soft materials* at hierarchical length and time scales from both individual [Part 1] and collective [Part 2] perspectives. I hope it helps us to appreciate the famous quote — "More is different [**406**]." — from *Anderson* in 1972. The hybrid between the "hard" and "soft" materials is creating a portfolio of diverse materials has never been explored and this work only presents a glimpse of those emerging materials. As shown in this work, understanding of soft material systems at different scales requires theoretical and computational tools developed for the corresponding scales. For example, the microscopic simulation technique, Molecular Dynamics, is employed for studying morphologies of nanometer scale magnetoelastic shells [Chap. 2]; the mesoscopic simulation technique, Stokesian Dynamics, is used for understanding hydrodynamic interactions between micrometer scale colloidal particles [Chap. 5 and 6]; And the macroscopic simulation technique, Finite Element Method, is utilized to solve the continuum model of the millimeter scale hydrogel-metal hybrid for quantitative study their dynamic robotic behaviors [Chap. 4]. This work demonstrates clearly that a set of multi-scales theoretical and computational tools is important for understanding the underlying mechanisms governing the complex emerging behaviors in soft material systems. The fundamental first-principle

approach is valuable for illuminating important elements at the atomic level. However, when it comes to calculating the behaviors of a Avogadro number (N_A) of atoms in a time scale like a second, the "curse of dimensionality" always emerge [**407**], which is a common issue in other domains such as optimization, sampling, machine learning and data mining, etc. In order to deal with the dimensionality problem, all the multi-scales tools employed in this work are "simplified" models with different level of coarse-graining and I hope this work provides confirmative evidence that those coarse-grained models are useful for understanding the responses of soft materials in a length and time scale more relevant to our daily life. With the continual fusion between "hard" and "soft" materials, the synthesis of new materials will keep inspiring the merging of separate branches of theoretical descriptions of material responses and this work only provides several initial attempts. More and more natural/synthetic soft materials with controlled responses are expected to be engineered in the future as the understanding of those soft materials deepening. Considering the exceptional flexibility and bio-compatibility of soft materials, such advances will lay a solid foundation for future living-system related technology development.

References

[1] R. Hooke. *Lectures de Potentia Restitutiva, Or of Spring Explaining the Power of Springing Bodies*. Cutlerian lecture. John Martyn, 1678.

[2] G. G. Stokes. On the Effect of the Internal Friction of Fluids on the Motion of Pendulums. *Transactions of the Cambridge Philosophical Society*, 9:8, January 1851.

[3] Adolf Fick. Ueber diffusion. *Annalen der Physik*, 170(1):59–86, 1855.

[4] Georg Ohm. *Die galvanische Kette, mathematisch bearbeitet*. 1827.

[5] Joseph Fourier. *Théorie analytique de la chaleur*. 1822.

[6] Marvin L. Cohen. Essay: Fifty years of condensed matter physics. *Phys. Rev. Lett.*, 101:250001, Dec 2008.

[7] W. Kohn. An essay on condensed matter physics in the twentieth century. *Rev. Mod. Phys.*, 71:S59–s77, Mar 1999.

[8] Linjie Zhou, Zhenwu Wang, Changsong Wu, Yang Cong, Rui Zhang, and Jun Fu. Highly sensitive pressure and strain sensors based on stretchable and recoverable ion-conductive physically cross-linked double-network hydrogels. *ACS Appl. Mater. Interfaces*, 12(46):51969–51977, November 2020.

[9] Jens W. Neubauer, Nicolas Hauck, Max J. Männel, Maximilian Seuss, Andreas Fery, and Julian Thiele. Mechanoresponsive hydrogel particles as a platform for three-dimensional force sensing. *ACS Appl. Mater. Interfaces*, 11(29):26307–26313, July 2019.

[10] Andreas Richter, Georgi Paschew, Stephan Klatt, Jens Lienig, Karl-Friedrich Arndt, and Hans-Jürgen P. Adler. Review on hydrogel-based ph sensors and microsensors. *Sensors*, 8(1):561–581, 2008.

[11] Hui Liu, Xi Xiang, Jianbo Huang, Bihui Zhu, Liyun Wang, Yuanjiao Tang, Fangxue Du, Ling Li, Feng Yan, Lang Ma, and Li Qiu. Ultrasound augmenting injectable

chemotaxis hydrogel for articular cartilage repair in osteoarthritis. *Chinese Chemical Letters*, 32(5):1759–1764, 2021.

[12] Nicholas Kellaris, Vidyacharan Gopaluni Venkata, Garrett M. Smith, Shane K. Mitchell, and Christoph Keplinger. Peano-hasel actuators: Muscle-mimetic, electrohydraulic transducers that linearly contract on activation. *Science Robotics*, 3(14), Jan 24 2018.

[13] Yufeng Chen, Huichan Zhao, Jie Mao, Pakpong Chirarattananon, E. Farrell Helbling, Nak-seung Patrick Hyun, David R. Clarke, and Robert J. Wood. Controlled flight of a microrobot powered by soft artificial muscles. *Nature*, 575(7782):324–329, 2019.

[14] Mengmeng Sun, Chenyao Tian, Liyang Mao, Xianghe Meng, Xingjian Shen, Bo Hao, Xin Wang, Hui Xie, and Li Zhang. Reconfigurable magnetic slime robot: Deformation, adaptability, and multifunction. *Advanced Functional Materials*, page 2112508, 2022.

[15] Nitin S. Satarkar and J. Zach Hilt. Magnetic hydrogel nanocomposites for remote controlled pulsatile drug release. *Journal of Controlled Release*, 130(3):246–251, 2008.

[16] Zhenjun Qiu, Haitao Yu, Jinbo Li, Yu Wang, and Yan Zhang. Spiropyran-linked dipeptide forms supramolecular hydrogel with dual responses to light and to ligand–receptor interaction. *Chem. Commun.*, pages 3342–3344, 2009.

[17] S. R. Sershen, S. L. Westcott, N. J. Halas, and J. L. West. Temperature-sensitive polymer–nanoshell composites for photothermally modulated drug delivery. *Journal of Biomedical Materials Research*, 51(3):293–298, 2000.

[18] Ke Hu, Jianfei Sun, Zhaobin Guo, Peng Wang, Qiang Chen, Ming Ma, and Ning Gu. A novel magnetic hydrogel with aligned magnetic colloidal assemblies showing controllable enhancement of magnetothermal effect in the presence of alternating magnetic field. *Advanced Materials*, 27(15):2507–2514, 2015.

[19] Susana Carregal-Romero, Pablo Guardia, Xiang Yu, Raimo Hartmann, Teresa Pellegrino, and Wolfgang J. Parak. Magnetically triggered release of molecular cargo from iron oxide nanoparticle loaded microcapsules. *Nanoscale*, 7:570–576, 2015.

[20] Joyce C. Breger, ChangKyu Yoon, Rui Xiao, Hye Rin Kwag, Martha O. Wang, John P. Fisher, Thao D. Nguyen, and David H. Gracias. Self-folding thermomagnetically responsive soft microgrippers. *ACS Appl. Mater. Interfaces*, 7(5):3398–3405, February 2015.

[21] Seog-Jin Jeon, Adam W. Hauser, and Ryan C. Hayward. Shape-morphing materials from stimuli-responsive hydrogel hybrids. *Accounts Of Chemical Research*, 50(2):161–169, Feb 2017.

[22] Michael C. Koetting, Jonathan T. Peters, Stephanie D. Steichen, and Nicholas A. Peppas. Stimulus-responsive hydrogels: Theory, modern advances, and applications. *Materials Science and Engineering: R: Reports*, 93:1–49, 2015.

[23] Yong Qiu and Kinam Park. Environment-sensitive hydrogels for drug delivery. *Advanced Drug Delivery Reviews*, 53(3):321–339, 2001. Triggering in Drug Delivery Systems.

[24] S.J. Ebbens. Active colloids: Progress and challenges towards realising autonomous applications. *Current Opinion in Colloid & Interface Science*, 21:14–23, 2016.

[25] Canhui Yang and Zhigang Suo. Hydrogel ionotronics. *Nature Reviews Materials*, 3(6):125–142, 2018.

[26] Hang Yuan and Monica Olvera de la Cruz. Crystalline membrane morphology beyond polyhedra. *Phys. Rev. E*, 100:012610, Jul 2019.

[27] H. W. Kroto, J. R. Heath, S. C. O'Brien, R. F. Curl, and R. E. Smalley. C60: Buckminsterfullerene. *Nature*, 318(6042):162–163, November 1985.

[28] Chenguang Fan, Shouqiang Cheng, Yu Liu, Cristina M. Escobar, Christopher S. Crowley, Robert E. Jefferson, Todd O. Yeates, and Thomas A. Bobik. Short n-terminal sequences package proteins into bacterial microcompartments. *Proc Natl Acad Sci USA*, 107(16):7509, April 2010.

[29] C. I. Zoldesi, I. L. Ivanovska, C. Quilliet, G. J. L. Wuite, and A. Imhof. Elastic properties of hollow colloidal particles. *Phys. Rev. E*, 78:051401, Nov 2008.

[30] Carmen I. Zoldesi, Cornelis A. van Walree, and Arnout Imhof. Deformable hollow hybrid silica/siloxane colloids by emulsion templating. *Langmuir*, 22(9):4343–4352, April 2006.

[31] Jissy Jose, Marlous Kamp, Alfons van Blaaderen, and Arnout Imhof. Unloading and reloading colloidal microcapsules with apolar solutions by controlled and reversible buckling. *Langmuir*, 30(9):2385–2393, March 2014.

[32] Jack Lidmar, Leonid Mirny, and David R. Nelson. Virus shapes and buckling transitions in spherical shells. *Phys. Rev. E*, 68:051910, Nov 2003.

[33] Siyu Li, Polly Roy, Alex Travesset, and Roya Zandi. Why large icosahedral viruses need scaffolding proteins. *Proc Natl Acad Sci USA*, 115(43):10971, October 2018.

[34] Edward J. Banigan, Andrew D. Stephens, and John F. Marko. Mechanics and buckling of biopolymeric shells and cell nuclei. *Biophysical Journal*, 113(8):1654–1663, October 2017.

[35] Maxim O. Lavrentovich, Eric M. Horsley, Asja Radja, Alison M. Sweeney, and Randall D. Kamien. First-order patterning transitions on a sphere as a route to cell morphology. *Proc Natl Acad Sci USA*, 113(19):5189, May 2016.

[36] Eric Raspaud, Bruno Pitard, Dominique Durand, Olivier Aguerre-Chariol, Juan Pelta, Gerardo Byk, Daniel Scherman, and Françoise Livolant. Polymorphism of dna/multi-cationic lipid complexes driven by temperature and salts. *J. Phys. Chem. B*, 105(22):5291–5297, June 2001.

[37] Graziano Vernizzi and Monica Olvera de la Cruz. Faceting ionic shells into icosahedra via electrostatics. *Proc Natl Acad Sci USA*, 104(47):18382, November 2007.

[38] Y. Chushak and A. Travesset. Solid domains in lipid vesicles and scars. *Europhysics Letters (EPL)*, 72(5):767–773, December 2005.

[39] François Quemeneur, Catherine Quilliet, Magalie Faivre, Annie Viallat, and Brigitte Pépin-Donat. Gel phase vesicles buckle into specific shapes. *Prl*, 108(10):108303, March 2012.

[40] Sebastian Knoche and Jan Kierfeld. Buckling of spherical capsules. *Pre*, 84(4):046608, October 2011.

[41] Sujit S. Datta, Shin-Hyun Kim, Jayson Paulose, Alireza Abbaspourrad, David R. Nelson, and David A. Weitz. Delayed buckling and guided folding of inhomogeneous capsules. *Phys. Rev. Lett.*, 109:134302, Sep 2012.

[42] G. A. Vliegenthart and G. Gompper. Compression, crumpling and collapse of spherical shells and capsules. *New Journal of Physics*, 13(4):045020, April 2011.

[43] Roya Zandi, David Reguera, Robijn F. Bruinsma, William M. Gelbart, and Joseph Rudnick. Origin of icosahedral symmetry in viruses. *Proc Natl Acad Sci U S A*, 101(44):15556, November 2004.

[44] H. S. Seung and David R. Nelson. Defects in flexible membranes with crystalline order. *Phys. Rev. A*, 38:1005–1018, Jul 1988.

[45] Graziano Vernizzi, Rastko Sknepnek, and Monica Olvera de la Cruz. Platonic and archimedean geometries in multicomponent elastic membranes. *Proceedings of the National Academy of Sciences*, 108(11):4292–4296, 2011.

[46] Ee Hou Yong, David R. Nelson, and L. Mahadevan. Elastic platonic shells. *Phys. Rev. Lett.*, 111:177801, Oct 2013.

[47] Jon Dobson. Magnetic nanoparticles for drug delivery. *Drug Development Research*, 67(1):55–60, 2006.

[48] Simona Mura, Julien Nicolas, and Patrick Couvreur. Stimuli-responsive nanocarriers for drug delivery. *Nature Materials*, 12:991, October 2013.

[49] Theresa M. Allen and Pieter R. Cullis. Liposomal drug delivery systems: From concept to clinical applications. *Advanced Drug Delivery Reviews*, 65(1):36–48, January 2013.

[50] Hang Xing, Kevin Hwang, and Yi Lu. Recent developments of liposomes as nanocarriers for theranostic applications. *Theranostics*, 6(9):1336, 2016.

[51] Vikas Nandwana, Abhalaxmi Singh, Marisa M. You, Gefei Zhang, John Higham, Tiffany S. Zheng, Yue Li, Pottumarthi V. Prasad, and Vinayak P. Dravid. Magnetic lipid nanocapsules (mlncs): self-assembled lipid-based nanoconstruct for non-invasive theranostic applications. *J. Mater. Chem. B*, 6:1026–1034, 2018.

[52] Veronika Magdanz, Maria Guix, Franziska Hebenstreit, and Oliver G. Schmidt. Dynamic polymeric microtubes for the remote-controlled capture, guidance, and release of sperm cells. *Advanced Materials*, 28(21):4084–4089, 2016.

[53] Yoonho Kim, Hyunwoo Yuk, Ruike Zhao, Shawn A. Chester, and Xuanhe Zhao. Printing ferromagnetic domains for untethered fast-transforming soft materials. *Nature*, 558(7709):274–279, June 2018.

[54] Guo Zhan Lum, Zhou Ye, Xiaoguang Dong, Hamid Marvi, Onder Erin, Wenqi Hu, and Metin Sitti. Shape-programmable magnetic soft matter. *Proceedings of the National Academy of Sciences*, 113(41):E6007–e6015, 2016.

[55] Wenqi Hu, Guo Zhan Lum, Massimo Mastrangeli, and Metin Sitti. Small-scale soft-bodied robot with multimodal locomotion. *Nature*, 554:81, January 2018.

[56] H.-W. Huang, F. E. Uslu, P. Katsamba, E. Lauga, M. S. Sakar, and B. J. Nelson. Adaptive locomotion of artificial microswimmers. *Science Advances*, 5(1):eaau1532, 2019.

[57] Chase Austyn Brisbois, Mykola Tasinkevych, Pablo Vázquez-Montejo, and Monica Olvera de la Cruz. Actuation of magnetoelastic membranes in precessing magnetic fields. *Proc Natl Acad Sci USA*, 116(7):2500, February 2019.

[58] C. Goubault, P. Jop, M. Fermigier, J. Baudry, E. Bertrand, and J. Bibette. Flexible magnetic filaments as micromechanical sensors. *Phys. Rev. Lett.*, 91:260802, Dec 2003.

[59] Rémi Dreyfus, Jean Baudry, Marcus L. Roper, Marc Fermigier, Howard A. Stone, and Jérôme Bibette. Microscopic artificial swimmers. *Nature*, 437:862, October 2005.

[60] Hui Wang, Yifei Yu, Yubin Sun, and Qianwang Chen. Magnetic nanochains: a review. *Nano*, 06(01):1–17, October 2011.

[61] Jiachen Wei, Fan Song, and Jure Dobnikar. Assembly of superparamagnetic filaments in external field. *Langmuir*, 32(36):9321–9328, September 2016.

[62] Tao Yang, Brennan Sprinkle, Yang Guo, Jun Qian, Daoben Hua, Aleksandar Donev, David W. M. Marr, and Ning Wu. Reconfigurable microbots folded from simple colloidal chains. *Proceedings of the National Academy of Sciences*, 117(31):18186–18193, 2020.

[63] Mariana Medina-Sánchez, Lukas Schwarz, Anne K. Meyer, Franziska Hebenstreit, and Oliver G. Schmidt. Cellular cargo delivery: Toward assisted fertilization by sperm-carrying micromotors. *Nano Lett.*, 16(1):555–561, January 2016.

[64] Joshua M. Dempster, Pablo Vázquez-Montejo, and Monica Olvera de la Cruz. Contractile actuation and dynamical gel assembly of paramagnetic filaments in fast precessing fields. *Phys. Rev. E*, 95:052606, May 2017.

[65] Pablo Vázquez-Montejo, Joshua M. Dempster, and Mónica Olvera de la Cruz. Paramagnetic filaments in a fast precessing field: Planar versus helical conformations. *Phys. Rev. Materials*, 1:064402, Nov 2017.

[66] Valera P. Shcherbakov and Michael Winklhofer. Bending of magnetic filaments under a magnetic field. *Phys. Rev. E*, 70:061803, Dec 2004.

[67] R. Car and M. Parrinello. Unified approach for molecular dynamics and density-functional theory. *Phys. Rev. Lett.*, 55:2471–2474, Nov 1985.

[68] R. D. Kamien. The geometry of soft materials: a primer. *Reviews of Modern Physics*, 74:953–971, September 2002.

[69] Mark J. Bowick, David R. Nelson, and Alex Travesset. Interacting topological defects on frozen topographies. *Phys. Rev. B*, 62:8738–8751, Oct 2000.

[70] D. L. D. Caspar and A. Klug. Physical principles in the construction of regular viruses. *Cold Spring Harbor Symposia on Quantitative Biology*, 27:1–24, 1962.

[71] G. Gompper and D. M. Kroll. Random surface discretizations and the renormalization of the bending rigidity. *J. Phys. I France*, 6(10):1305–1320, October 1996.

[72] D. R. Nelson, T. Piran, and S. Weinberg. *Statistical Mechanics of Membranes and Surfaces*. World Scientific Pub., 2004.

[73] A. Libai and J.G. Simmonds. *The Nonlinear Theory of Elastic Shells*. Cambridge University Press, 1998.

[74] Pablo Vázquez-Montejo and Mónica Olvera de la Cruz. Flexible paramagnetic membranes in fast precessing fields. *Phys. Rev. E*, 98:032603, Sep 2018.

[75] Jean-Paul Ryckaert, Giovanni Ciccotti, and Herman J.C Berendsen. Numerical integration of the cartesian equations of motion of a system with constraints: molecular dynamics of n-alkanes. *Journal of Computational Physics*, 23(3):327–341, 1977.

[76] T. A. Witten. Stress focusing in elastic sheets. *Rev. Mod. Phys.*, 79:643–675, Apr 2007.

[77] Steve Plimpton. Fast parallel algorithms for short-range molecular dynamics. *Journal of Computational Physics*, 117(1):1–19, March 1995.

[78] Juan J. Cerdà, V. Ballenegger, O. Lenz, and C. Holm. P3m algorithm for dipolar interactions. *The Journal of chemical physics*, 129:234104, Dec 2008.

[79] M.P. do Carmo. *Differential Geometry of Curves and Surfaces*. Prentice-Hall, 1976.

[80] Mark Meyer, Mathieu Desbrun, Peter Schröder, and Alan H. Barr. Discrete differential-geometry operators for triangulated 2-manifolds. In Hans-Christian Hege and Konrad Polthier, editors, *Visualization and Mathematics III*, pages 35–57, Berlin, Heidelberg, 2003. Springer Berlin Heidelberg.

[81] Alex Lobkovsky, Sharon Gentges, Hao Li, David Morse, and T. A. Witten. Scaling properties of stretching ridges in a crumpled elastic sheet. *Science*, 270(5241):1482, December 1995.

[82] Alexander E. Lobkovsky and T. A. Witten. Properties of ridges in elastic membranes. *Phys. Rev. E*, 55:1577–1589, Feb 1997.

[83] B. A. DiDonna and T. A. Witten. Anomalous strength of membranes with elastic ridges. *Phys. Rev. Lett.*, 87:206105, Oct 2001.

[84] Metin Sitti. Voyage of the microrobots. *Nature*, 458:1121, April 2009.

[85] Jeffrey L. Moran and Jonathan D. Posner. Phoretic self-propulsion. *Annual Review of Fluid Mechanics*, 49(1):511–540, 2017.

[86] Jinxing Li, Isaac Rozen, and Joseph Wang. Rocket science at the nanoscale. *ACS Nano*, 10(6):5619–5634, June 2016.

[87] Jeffrey S. Guasto, Roberto Rusconi, and Roman Stocker. Fluid mechanics of planktonic microorganisms. *Annual Review of Fluid Mechanics*, 44(1):373–400, 2012.

[88] Antonio DeSimone, Antonio DeSimone, Benoît Perthame, Alfio Quarteroni, and Lev Truskinovsky. Cell motility and locomotion by shape control. In Davide Ambrosi and Pasquale Ciarletta, editors, *The Mathematics of Mechanobiology: Cetraro, Italy 2018*, pages 1–41. Springer International Publishing, Cham, 2020.

[89] Tao Yang, David W.M. Marr, and Ning Wu. Superparamagnetic colloidal chains prepared via michael-addition. *Colloids and Surfaces A: Physicochemical and Engineering Aspects*, 540:23–28, 2018.

[90] Rastko Sknepnek, Graziano Vernizzi, and Monica Olvera de la Cruz. Buckling of multicomponent elastic shells with line tension. *Soft Matter*, 8:636–644, 2012.

[91] Siyu Li, Daniel A. Matoz-Fernandez, and Monica Olvera de la Cruz. Effect of mechanical properties on multicomponent shell patterning. *ACS Nano*, 15(9):14804–14812, September 2021.

[92] Siyu Li, Daniel A. Matoz-Fernandez, Aaveg Aggarwal, and Monica Olvera de la Cruz. Chemically controlled pattern formation in self-oscillating elastic shells. *Proceedings of the National Academy of Sciences*, 118(10):e2025717118, 2021.

[93] Yaohua Li, Nolan W. Kennedy, Siyu Li, Carolyn E. Mills, Danielle Tullman-Ercek, and Monica Olvera de la Cruz. Computational and experimental approaches to controlling bacterial microcompartment assembly. *ACS Cent. Sci.*, 7(4):658–670, April 2021.

[94] Sonia L. Bardy, Sandy Y. M. Ng, and Ken F. Jarrell. Prokaryotic motility structures. *Microbiology*, 149(2):295–304, 2003.

[95] Sonja-Verena Albers and Ken F. Jarrell. The archaellum: how archaea swim. *Frontiers in Microbiology*, 6:23, 2015.

[96] L T Haimo and J L Rosenbaum. Cilia, flagella, and microtubules. *Journal of Cell Biology*, 91(3):125s–130s, 02 1981.

[97] William Gilpin, Matthew Storm Bull, and Manu Prakash. The multiscale physics of cilia and flagella. *Nature Reviews Physics*, 2(2):74–88, 2020.

[98] Marino Arroyo, Luca Heltai, Daniel Millán, and Antonio DeSimone. Reverse engineering the euglenoid movement. *Proc Natl Acad Sci USA*, 109(44):17874, October 2012.

[99] E. M. Purcell. Life at low reynolds number. *American Journal of Physics*, 45(1):3–11, August 1976.

[100] Alfred Shapere and Frank Wilczek. Self-propulsion at low reynolds number. *Phys. Rev. Lett.*, 58:2051–2054, May 1987.

[101] Adel Djellouli, Philippe Marmottant, Henda Djeridi, Catherine Quilliet, and Gwennou Coupier. Buckling instability causes inertial thrust for spherical swimmers at all scales. *Phys. Rev. Lett.*, 119:224501, Nov 2017.

[102] Wenxiao Pan, Bruce Caswell, and George Em Karniadakis. A low-dimensional model for the red blood cell. *Soft Matter*, 6(18):4366–4376, 2010.

[103] Kristina Pickl. *Fully Resolved Simulation of Self-propelled Microorganisms on Supercomputers*. PhD thesis, Friedrich-Alexander-Universität Erlangen-Nürnberg (FAU), 2016.

[104] Jinglei Hu, Mingcheng Yang, Gerhard Gompper, and Roland G. Winkler. Modelling the mechanics and hydrodynamics of swimming e. coli. *Soft Matter*, 11:7867–7876, 2015.

[105] Davod Alizadehrad, Timothy Krüger, Markus Engstler, and Holger Stark. Simulating the complex cell design of trypanosoma brucei and its motility. *PLOS Computational Biology*, 11(1):e1003967, January 2015.

[106] S. Toppaladoddi and N. J. Balmforth. Slender axisymmetric stokesian swimmers. *Journal of Fluid Mechanics*, 746:273–299, 2014.

[107] Zhengyan Zhang, Hang Yuan, Yong Dou, Monica Olvera de la Cruz, and Kyle J. M. Bishop. Quincke oscillations of colloids at planar electrodes. *Phys. Rev. Lett.*, 126:258001, Jun 2021.

[108] G. Quincke. Ueber rotationen im constanten electrischen felde. *Ann. Phys.*, 295(11):417–486, January 1896.

[109] W. Weiler. Zur darstellung elektrischer kraftlinien. *Z phys. chem. Unterricht*, Iv:194–195, April 1893.

[110] Antoine Bricard, Jean-Baptiste Caussin, Nicolas Desreumaux, Olivier Dauchot, and Denis Bartolo. Emergence of macroscopic directed motion in populations of motile colloids. *Nature*, 503:95, November 2013.

[111] Bo Zhang, Benjamin Hilton, Christopher Short, Anton Souslov, and Alexey Snezhko. Oscillatory chiral flows in confined active fluids with obstacles. *Phys. Rev. Research*, 2:043225, Nov 2020.

[112] Bo Zhang, Andrey Sokolov, and Alexey Snezhko. Reconfigurable emergent patterns in active chiral fluids. *Nature Communications*, 11(1):4401, 2020.

[113] Bo Zhang, Alexey Snezhko, and Andrey Sokolov. Guiding self-assembly of active colloids by temporal modulation of activity. *Phys. Rev. Lett.*, 128:018004, Jan 2022.

[114] Hamid Karani, Gerardo E. Pradillo, and Petia M. Vlahovska. Tuning the random walk of active colloids: From individual run-and-tumble to dynamic clustering. *Phys. Rev. Lett.*, 123:208002, Nov 2019.

[115] Gerardo E. Pradillo, Hamid Karani, and Petia M. Vlahovska. Quincke rotor dynamics in confinement: rolling and hovering. *Soft Matter*, 15:6564–6570, 2019.

[116] Debasish Das and Eric Lauga. Active particles powered by quincke rotation in a bulk fluid. *Phys. Rev. Lett.*, 122:194503, May 2019.

[117] J. R. Melcher and G. I. Taylor. Electrohydrodynamics: A review of the role of interfacial shear stresses. *Annu. Rev. Fluid Mech.*, 1(1):111–146, January 1969.

[118] D. A. Saville. Electrohydrodynamics: The taylor-melcher leaky dielectric model. *Annu. Rev. Fluid Mech.*, 29(1):27–64, January 1997.

[119] T. B. Jones. Quincke rotation of spheres. *IEEE Transactions on Industry Applications*, Ia-20(4):845–849, 1984.

[120] Thomas B. Jones. *Electromechanics of Particles*. Cambridge University Press, 2005.

[121] Seppo J. Karrila Sangtae Kim. *Microhydrodynamics - Principles and Selected Applications*. Dover Publications, Inc., 2005.

[122] N. Pannacci, L. Lobry, and E. Lemaire. How insulating particles increase the conductivity of a suspension. *Phys. Rev. Lett.*, 99:094503, Aug 2007.

[123] Debasish Das and David Saintillan. Electrohydrodynamic interaction of spherical particles under quincke rotation. *Phys. Rev. E*, 87:043014, Apr 2013.

[124] Edward N. Lorenz. Deterministic nonperiodic flow. *J. Atmos. Sci.*, 20(2):130–141, March 1963.

[125] E. Lemaire and L. Lobry. Chaotic behavior in electro-rotation. *Physica A: Statistical Mechanics and its Applications*, 314(1):663–671, 2002.

[126] François Peters, Laurent Lobry, and Elisabeth Lemaire. Experimental observation of lorenz chaos in the quincke rotor dynamics. *Chaos*, 15(1):013102, September 2005.

[127] Jochen Schmidt, Rodolphe Prignitz, Dirk Peschka, Andreas Münch, Barbara Wagner, Eberhard Bänsch, and Wolfgang Peukert. Conductivity in nonpolar media: Experimental and numerical studies on sodium aot-hexadecane, lecithin-hexadecane and aluminum(iii)-3,5-diisopropyl salicylate-hexadecane systems. *Journal of Colloid and Interface Science*, 386(1):240–251, 2012.

[128] L. D. Landau and E. M. Lifshitz. *Fluid Mechanics, Second Edition: Volume 6 (Course of Theoretical Physics)*. Course of theoretical physics / by L. D. Landau and E. M. Lifshitz, Vol. 6. Butterworth-Heinemann, 2 edition, 1987.

[129] John David Jackson. *Classical electrodynamics*. Wiley, 1925.

[130] Sunil K. Sainis, Jason W. Merrill, and Eric R. Dufresne. Electrostatic interactions of colloidal particles at vanishing ionic strength. *Langmuir*, 24(23):13334–13337, December 2008.

[131] Élisabeth Guazzelli and Jeffrey F. Morris. *A Physical Introduction to Suspension Dynamics*. Cambridge University Press, Cambridge, 2011.

[132] Henk F. Arnoldus. Conservation of charge at an interface. *Optics Communications*, 265(1):52–59, 2006.

[133] Quentin Brosseau, Gregory Hickey, and Petia M. Vlahovska. Electrohydrodynamic quincke rotation of a prolate ellipsoid. *Phys. Rev. Fluids*, 2:014101, Jan 2017.

[134] Philip M. Morse and Herman Feshbach. *Methods of theoretical physics*. New York, McGraw-Hill, 1953.

[135] L. D. Landau and E. M. Lífshíts. *Electrodynamics of Continuous Media*. Pergamon, 1984.

[136] James W. Swan and John F. Brady. Simulation of hydrodynamically interacting particles near a no-slip boundary. *Physics of Fluids*, 19(11):113306, 2007.

[137] A. J. Goldman, R. G. Cox, and H. Brenner. Slow viscous motion of a sphere parallel to a plane wall–i motion through a quiescent fluid. *Chemical Engineering Science*, 22(4):637–651, April 1967.

[138] A. J. Goldman, R. G. Cox, and H. Brenner. Slow viscous motion of a sphere parallel to a plane wall–ii couette flow. *Chemical Engineering Science*, 22(4):653–660, April 1967.

[139] Syeda Sabrina, Mykola Tasinkevych, Suzanne Ahmed, Allan M. Brooks, Monica Olvera de la Cruz, Thomas E. Mallouk, and Kyle J. M. Bishop. Shape-directed microspinners powered by ultrasound. *ACS Nano*, 12(3):2939–2947, March 2018.

[140] Jian Qin, Juan J. de Pablo, and Karl F. Freed. Image method for induced surface charge from many-body system of dielectric spheres. *J. Chem. Phys.*, 145(12):124903, September 2016.

[141] Jian Qin. Charge polarization near dielectric interfaces and the multiple-scattering formalism. *Soft Matter*, 15:2125–2134, 2019.

[142] F. Peters, L. Lobry, A. Khayari, and E. Lemaire. Size effect in quincke rotation: A numerical study. *The Journal of Chemical Physics*, 130(19):194905, 2009.

[143] M. E. O'Neill and K. Stewartson. On the slow motion of a sphere parallel to a nearby plane wall. *Journal of Fluid Mechanics*, 27(4):705–724, 1967.

[144] L. I. U. QIANLONG and A. N. D. R. E. A. PROSPERETTI. Wall effects on a rotating sphere. *Journal of Fluid Mechanics*, 657:1–21, 2010.

[145] Michael D. Graham. *Microhydrodynamics, Brownian Motion, and Complex Fluids*. Cambridge University Press, Cambridge, 2018.

[146] L. O. V. E. John D. Dielectric sphere-sphere and sphere-plane problems in electrostatics. *The Quarterly Journal of Mechanics and Applied Mathematics*, 28(4):449–471, 1975.

[147] L. M. Milne Thomson. *The Calculus Of Finite Differences*. Macmillan And Company., Limited, 1933.

[148] Frank Schmidt. The laplace-beltrami-operator on riemannian manifolds the laplace-beltrami-operator on riemannian manifolds. 2014.

[149] Sunil K. Sainis, Vincent Germain, Cecile O. Mejean, and Eric R. Dufresne. Electrostatic interactions of colloidal particles in nonpolar solvents: Role of surface chemistry and charge control agents. *Langmuir*, 24(4):1160–1164, February 2008.

[150] Michael Kotlarchyk, John S. Huang, and Sow Hsin Chen. Structure of aot reversed micelles determined by small-angle neutron scattering. *J. Phys. Chem.*, 89(20):4382–4386, September 1985.

[151] Dennis C. Prieve, Benjamin A. Yezer, Aditya S. Khair, Paul J. Sides, and James W. Schneider. Formation of charge carriers in liquids. *Advances in Colloid and Interface Science*, 244:21–35, 2017.

[152] P. Debye. Reaction rates in ionic solutions. *Transactions of The Electrochemical Society*, 82(1):265, 1942.

[153] Alfred Barnard Basset and John William Strutt. Iii. on the motion of a sphere in a viscous liquid. *Philosophical Transactions of the Royal Society of London. (A.)*, 179:43–63, January 1888.

[154] F. FEUILLEBOIS and A. LASEK. On the rotational historic term in non-stationary stokes flow. *The Quarterly Journal of Mechanics and Applied Mathematics*, 31(4):435–443, 1978.

[155] E. Gavze. The accelerated motion of rigid bodies in non-steady stokes flow. *International Journal of Multiphase Flow*, 16(1):153–166, 1990.

[156] B. J. Alder and T. E. Wainwright. Decay of the velocity autocorrelation function. *Phys. Rev. A*, 1:18–21, Jan 1970.

[157] Robert Zwanzig and Mordechai Bixon. Hydrodynamic theory of the velocity correlation function. *Phys. Rev. A*, 2:2005–2012, Nov 1970.

[158] Sean L. Seyler and Steve Pressé. Long-time persistence of hydrodynamic memory boosts microparticle transport. *Phys. Rev. Research*, 1:032003, Oct 2019.

[159] M. C. Marchetti, J. F. Joanny, S. Ramaswamy, T. B. Liverpool, J. Prost, Madan Rao, and R. Aditi Simha. Hydrodynamics of soft active matter. *Rev. Mod. Phys.*, 85:1143–1189, Jul 2013.

[160] Lailai Zhu and Howard A. Stone. Propulsion driven by self-oscillation via an electrohydrodynamic instability. *Phys. Rev. Fluids*, 4:061701, Jun 2019.

[161] Endao Han, Lailai Zhu, Joshua W. Shaevitz, and Howard A. Stone. Low-reynolds-number, biflagellated quincke swimmers with multiple forms of motion. *Proceedings of the National Academy of Sciences*, 118(29), 2021.

[162] Wen-Zhen Fang, Francesco Viola, Simone Camarri, Chun Yang, and Lailai Zhu. A low-reynolds-number actuator driven by instability: rotating or oscillating. *Nonlinear Dynamics*, 106(3):2005–2019, 2021.

[163] Chuang Li, Garrett C. Lau, Hang Yuan, Aaveg Aggarwal, Victor Lopez Dominguez, Shuangping Liu, Hiroaki Sai, Liam C. Palmer, Nicholas A. Sather, Tyler J. Pearson, Danna E. Freedman, Pedram Khalili Amiri, Monica Olvera de la Cruz, and Samuel I. Stupp. Fast and programmable locomotion of hydrogel-metal hybrids under light and magnetic fields. *Science Robotics*, 5(49):eabb9822, December 2020.

[164] Stefano Palagi and Peer Fischer. Bioinspired microrobots. *Nature Reviews Materials*, 3(6):113–124, 2018.

[165] Hongbo Wang, Massimo Totaro, and Lucia Beccai. Toward perceptive soft robots: Progress and challenges. *Advanced Science*, 5(9):1800541, 2018.

[166] Bradley J. Nelson, Ioannis K. Kaliakatsos, and Jake J. Abbott. Microrobots for minimally invasive medicine. *Annu. Rev. Biomed. Eng.*, 12(1):55–85, June 2010.

[167] Chengzhi Hu, Salvador Pané, and Bradley J. Nelson. Soft micro- and nanorobotics. *Annual Review of Control, Robotics, and Autonomous Systems*, 1(1):53–75, 2018.

[168] M. A. McEvoy and N. Correll. Materials that couple sensing, actuation, computation, and communication. *Science*, 347(6228), 2015.

[169] Hakan Ceylan, Joshua Giltinan, Kristen Kozielski, and Metin Sitti. Mobile microrobots for bioengineering applications. *Lab Chip*, 17:1705–1724, 2017.

[170] Xiaoguang Dong, Guo Zhan Lum, Wenqi Hu, Rongjing Zhang, Ziyu Ren, Patrick R. Onck, and Metin Sitti. Bioinspired cilia arrays with programmable nonreciprocal motion and metachronal coordination. *Science Advances*, 6(45), 2020.

[171] Mahdi Ilami, Hosain Bagheri, Reza Ahmed, E. Olga Skowronek, and Hamid Marvi. Materials, actuators, and sensors for soft bioinspired robots. *Advanced Materials*, 33(19):2003139, 2021.

[172] Wei Gao, Sam Emaminejad, Hnin Yin Yin Nyein, Samyuktha Challa, Kevin Chen, Austin Peck, Hossain M. Fahad, Hiroki Ota, Hiroshi Shiraki, Daisuke Kiriya, Der-Hsien Lien, George A. Brooks, Ronald W. Davis, and Ali Javey. Fully integrated wearable sensor arrays for multiplexed in situ perspiration analysis. *Nature*, 529(7587):509–514, 2016.

[173] C. Larson, B. Peele, S. Li, S. Robinson, M. Totaro, L. Beccai, B. Mazzolai, and R. Shepherd. Highly stretchable electroluminescent skin for optical signaling and tactile sensing. *Science*, 351(6277):1071–1074, 2016.

[174] Jayoung Kim, Alan S. Campbell, Berta Esteban-Fernández de Ávila, and Joseph Wang. Wearable biosensors for healthcare monitoring. *Nature Biotechnology*, 37(4):389–406, 2019.

[175] Zhenwu Wang, Yang Cong, and Jun Fu. Stretchable and tough conductive hydrogels for flexible pressure and strain sensors. *J. Mater. Chem. B*, 8:3437–3459, 2020.

[176] Simiao Niu, Naoji Matsuhisa, Levent Beker, Jinxing Li, Sihong Wang, Jiechen Wang, Yuanwen Jiang, Xuzhou Yan, Youngjun Yun, William Burnett, Ada S. Y. Poon, Jeffery B.-H. Tok, Xiaodong Chen, and Zhenan Bao. A wireless body area sensor network based on stretchable passive tags. *Nature Electronics*, 2(8):361–368, 2019.

[177] Jiajie Liang, Lu Li, Xiaofan Niu, Zhibin Yu, and Qibing Pei. Elastomeric polymer light-emitting devices and displays. *Nature Photonics*, 7(10):817–824, 2013.

[178] Jeonghyun Kim, Anthony Banks, Huanyu Cheng, Zhaoqian Xie, Sheng Xu, Kyung-In Jang, Jung Woo Lee, Zhuangjian Liu, Philipp Gutruf, Xian Huang, Pinghung Wei, Fei Liu, Kan Li, Mitul Dalal, Roozbeh Ghaffari, Xue Feng, Yonggang Huang, Sanjay Gupta, Ungyu Paik, and John A. Rogers. Epidermal electronics with advanced capabilities in near-field communication. *Small*, 11(8):906–912, 2015.

[179] E. Acome, S. K. Mitchell, T. G. Morrissey, M. B. Emmett, C. Benjamin, M. King, M. Radakovitz, and C. Keplinger. Hydraulically amplified self-healing electrostatic actuators with muscle-like performance. *Science*, 359(6371):61, January 2018.

[180] Yichao Tang, Yinding Chi, Jiefeng Sun, Tzu-Hao Huang, Omid H. Maghsoudi, Andrew Spence, Jianguo Zhao, Hao Su, and Jie Yin. Leveraging elastic instabilities for amplified performance: Spine-inspired high-speed and high-force soft robots. *Science Advances*, 6(19):eaaz6912, 2020.

[181] Wei Tang, Yangqiao Lin, Chao Zhang, Yuwen Liang, Jinrong Wang, Wei Wang, Chen Ji, Maoying Zhou, Huayong Yang, and Jun Zou. Self-contained soft electrofluidic actuators. *Science Advances*, 7(34):eabf8080, 2021.

[182] David Quashie, Prateek Benhal, Zhi Chen, Zihan Wang, Xueliang Mu, Xiaoxia Song, Teng Jiang, Yukun Zhong, U Kei Cheang, and Jamel Ali. Magnetic bio-hybrid micro actuators. *Nanoscale*, 14:4364–4379, 2022.

[183] Hamed Shahsavan, Amirreza Aghakhani, Hao Zeng, Yubing Guo, Zoey S. Davidson, Arri Priimagi, and Metin Sitti. Bioinspired underwater locomotion of light-driven liquid crystal gels. *Proceedings of the National Academy of Sciences*, 117(10):5125–5133, 2020.

[184] Haojian Lu, Mei Zhang, Yuanyuan Yang, Qiang Huang, Toshio Fukuda, Zuankai Wang, and Yajing Shen. A bioinspired multilegged soft millirobot that functions in both dry and wet conditions. *Nature Communications*, 9(1):3944, 2018.

[185] Xuemin Du, Huanqing Cui, Tiantian Xu, Chenyang Huang, Yunlong Wang, Qilong Zhao, Yangsheng Xu, and Xinyu Wu. Reconfiguration, camouflage, and color-shifting for bioinspired adaptive hydrogel-based millirobots. *Advanced Functional Materials*, 30(10):1909202, 2020.

[186] Sam Kriegman, Douglas Blackiston, Michael Levin, and Josh Bongard. A scalable pipeline for designing reconfigurable organisms. *Proceedings of the National Academy of Sciences*, 117(4):1853–1859, 2020.

[187] Seungyong Han, Jeonghyun Kim, Sang Min Won, Yinji Ma, Daeshik Kang, Zhaoqian Xie, Kyu-Tae Lee, Ha Uk Chung, Anthony Banks, Seunghwan Min, Seung Yun Heo, Charles R. Davies, Jung Woo Lee, Chi-Hwan Lee, Bong Hoon Kim, Kan Li, Yadong Zhou, Chen Wei, Xue Feng, Yonggang Huang, and John A. Rogers. Battery-free, wireless sensors for full-body pressure and temperature mapping. *Science Translational Medicine*, 10(435):eaan4950, 2018.

[188] Michael Wehner, Ryan L. Truby, Daniel J. Fitzgerald, Bobak Mosadegh, George M. Whitesides, Jennifer A. Lewis, and Robert J. Wood. An integrated design and fabrication strategy for entirely soft, autonomous robots. *Nature*, 536(7617):451–455, 2016.

[189] Ambarish Ghosh and Peer Fischer. Controlled propulsion of artificial magnetic nanostructured propellers. *Nano Lett.*, 9(6):2243–2245, June 2009.

[190] Hui Xie, Mengmeng Sun, Xinjian Fan, Zhihua Lin, Weinan Chen, Lei Wang, Lixin Dong, and Qiang He. Reconfigurable magnetic microrobot swarm: Multimode transformation, locomotion, and manipulation. *Sci. Robotics*, 4(28):eaav8006, March 2019.

[191] Tianqi Xu, Jiachen Zhang, Mohammad Salehizadeh, Onaizah Onaizah, and Eric Diller. Millimeter-scale flexible robots with programmable three-dimensional magnetization and motions. *Sci. Robotics*, 4(29):eaav4494, April 2019.

[192] Li Zhang, Jake J. Abbott, Lixin Dong, Bradley E. Kratochvil, Dominik Bell, and Bradley J. Nelson. Artificial bacterial flagella: Fabrication and magnetic control. *Appl. Phys. Lett.*, 94(6):064107, June 2009.

[193] Robert F. Shepherd, Filip Ilievski, Wonjae Choi, Stephen A. Morin, Adam A. Stokes, Aaron D. Mazzeo, Xin Chen, Michael Wang, and George M. Whitesides. Multigait soft robot. *Proc Natl Acad Sci USA*, 108(51):20400, December 2011.

[194] T. Tolley Michael, F. Shepherd Robert, Mosadegh Bobak, C. Galloway Kevin, Wehner Michael, Karpelson Michael, J. Wood Robert, and M. Whitesides George. A resilient, untethered soft robot. *Soft Robotics*, 1(3):213–223, 2014.

[195] Nicholas W. Bartlett, Michael T. Tolley, Johannes T. B. Overvelde, James C. Weaver, Bobak Mosadegh, Katia Bertoldi, George M. Whitesides, and Robert J. Wood. A 3d-printed, functionally graded soft robot powered by combustion. *Science*, 349(6244):161, July 2015.

[196] Michael Wehner, Ryan L. Truby, Daniel J. Fitzgerald, Bobak Mosadegh, George M. Whitesides, Jennifer A. Lewis, and Robert J. Wood. An integrated design and fabrication strategy for entirely soft, autonomous robots. *Nature*, 536:451, August 2016.

[197] Im Kyung Han, Taehun Chung, Jihoon Han, and Youn Soo Kim. Nanocomposite hydrogel actuators hybridized with various dimensional nanomaterials for stimuli responsiveness enhancement. *Nano Convergence*, 6(1):18, 2019.

[198] Zhichen Zhu, Erkan Senses, Pinar Akcora, and Svetlana A. Sukhishvili. Programmable light-controlled shape changes in layered polymer nanocomposites. *ACS Nano*, 6(4):3152–3162, April 2012.

[199] Satoshi Watanabe, Hiroshi Era, and Masashi Kunitake. Two-wavelength infrared responsive hydrogel actuators containing rare-earth photothermal conversion particles. *Scientific Reports*, 8(1):13528, 2018.

[200] Eddie Wang, Malav S. Desai, and Seung-Wuk Lee. Light-controlled graphene-elastin composite hydrogel actuators. *Nano Lett.*, 13(6):2826–2830, June 2013.

[201] Aslan Miriyev, Kenneth Stack, and Hod Lipson. Soft material for soft actuators. *Nature Communications*, 8(1):596, September 2017.

[202] Daehoon Han, Cindy Farino, Chen Yang, Tracy Scott, Daniel Browe, Wonjoon Choi, Joseph W. Freeman, and Howon Lee. Soft robotic manipulation and locomotion with a 3d printed electroactive hydrogel. *ACS Appl. Mater. Interfaces*, 10(21):17512–17518, May 2018.

[203] Tuncer Caykara, Döne Yörük, and Serkan Demirci. Preparation and characterization of poly(n-tert-butylacrylamide-co-acrylamide) ferrogel. *J. Appl. Polym. Sci.*, 112(2):800–804, April 2009.

[204] Jizhai Cui, Tian-Yun Huang, Zhaochu Luo, Paolo Testa, Hongri Gu, Xiang-Zhong Chen, Bradley J. Nelson, and Laura J. Heyderman. Nanomagnetic encoding of shape-morphing micromachines. *Nature*, 575(7781):164–168, November 2019.

[205] Yoonho Kim, German A. Parada, Shengduo Liu, and Xuanhe Zhao. Ferromagnetic soft continuum robots. *Sci. Robotics*, 4(33):eaax7329, August 2019.

[206] Anne Helene Gelebart, Dirk Jan Mulder, Michael Varga, Andrew Konya, Ghislaine Vantomme, E. W. Meijer, Robin L. B. Selinger, and Dirk J. Broer. Making waves in a photoactive polymer film. *Nature*, 546(7660):632–636, 2017.

[207] Wayne Francis, Aishling Dunne, Colm Delaney, Larisa Florea, and Dermot Diamond. Spiropyran based hydrogels actuators–walking in the light. *Sensors and Actuators B: Chemical*, 250:608–616, 2017.

[208] Rafal Klajn. Spiropyran-based dynamic materials. *Chem. Soc. Rev.*, 43:148–184, 2014.

[209] Jiawen Chen, Franco King-Chi Leung, Marc C. A. Stuart, Takashi Kajitani, Takanori Fukushima, Erik van der Giessen, and Ben L. Feringa. Artificial muscle-like

function from hierarchical supramolecular assembly of photoresponsive molecular motors. *Nature Chemistry*, 10(2):132–138, 2018.

[210] Franco King-Chi Leung, Takashi Kajitani, Marc C. A. Stuart, Takanori Fukushima, and Ben L. Feringa. Dual-controlled macroscopic motions in a supramolecular hierarchical assembly of motor amphiphiles. *Angewandte Chemie International Edition*, 58(32):10985–10989, 2019.

[211] Bo Gao, Liang Qiao, Jianbo Wang, Qingfang Liu, Fashen Li, Jie Feng, and Desheng Xue. Microwave absorption properties of the ni nanowires composite. *Journal of Physics D: Applied Physics*, 41(23):235005, 2008.

[212] W Michael Lai W Michael Lai David Rubin Erhard Krempl. *Introduction to Continuum Mechanics*. Butterworth-Heinemann, 2009.

[213] B.C. Hall. *Lie Groups, Lie Algebras, and Representations: An Elementary Introduction*. Graduate Texts in Mathematics. Springer New York, 2010.

[214] L. D. Landau and E. M. Lifshitz. *Theory of Elasticity*. Elsevier, 1986.

[215] Ted Belytschko, W. K. Liu, and B. Moran. *Nonlinear finite elements for continua and structures*. Wiley, 2000.

[216] C. Pozrikidis. *A Practical Guide to Boundary Element Methods with the Software Library BEMLIB*. CRC Press, 2002.

[217] Ray W. Ogden Luis Dorfmann. *Nonlinear Theory of Electroelastic and Magnetoelastic Interactions*. Springer, 2014.

[218] Allan F. Bower. *Applied Mechanics of Solids*. CRC Press, 2009.

[219] Masao Doi. *Soft matter physics*. Oxford University Press, 2013.

[220] Mario M. Attard. Finite strain–isotropic hyperelasticity. *International Journal of Solids and Structures*, 40(17):4353–4378, August 2003.

[221] G. Y. Qiu and T. J. Pence. Remarks on the behavior of simple directionally reinforced incompressible nonlinearly elastic solids. *Journal of Elasticity*, 49(1):1–30, October 1997.

[222] Taku Satoh, Kimio Sumaru, Toshiyuki Takagi, Katsuki Takai, and Toshiyuki Kanamori. Isomerization of spirobenzopyrans bearing electron-donating and

electron-withdrawing groups in acidic aqueous solutions. *Phys. Chem. Chem. Phys.*, 13:7322–7329, 2011.

[223] Mohammad Dehghany, Haohui Zhang, Reza Naghdabadi, and Yuhang Hu. A thermodynamically-consistent large deformation theory coupling photochemical reaction and electrochemistry for light-responsive gels. *Journal of the Mechanics and Physics of Solids*, 116:239–266, July 2018.

[224] P. G. de Gennes. *Scaling Concepts in Polymer Physics*. Cornell University Press, 1979.

[225] M. Doi and S. F. Edwards. *The Theory of Polymer Dynamics*. Clarendon Press, 1988.

[226] Masao Doi. Gel dynamics. *J. Phys. Soc. Jpn.*, 78(5):052001, August 2009.

[227] Roger Bustamante. Transversely isotropic nonlinear magneto-active elastomers. *Acta Mechanica*, 210(3):183–214, March 2010.

[228] J. Bonet and R. D. Wood. *Nonlinear Continuum Mechanics for Finite Element Analysis*. Cambridge University Press, 2008.

[229] Herbert Goldstein. *Classical Mechanics*. Addison-Wesley, 1980.

[230] Olga Kuksenok and Anna C. Balazs. Modeling the photoinduced reconfiguration and directed motion of polymer gels. *Advanced Functional Materials*, 23(36):4601–4610, 2013.

[231] Chuang Li, Aysenur Iscen, Hiroaki Sai, Kohei Sato, Nicholas A. Sather, Stacey M. Chin, Zaida Álvarez, Liam C. Palmer, George C. Schatz, and Samuel I. Stupp. Supramolecular-covalent hybrid polymers for light-activated mechanical actuation. *Nature Materials*, 19(8):900–909, 2020.

[232] Maria-Melanie Russew and Stefan Hecht. Photoswitches: From molecules to materials. *Adv. Mater.*, 22(31):3348–3360, August 2010.

[233] Federico Lancia, Alexander Ryabchun, and Nathalie Katsonis. Life-like motion driven by artificial molecular machines. *Nature Reviews Chemistry*, 3(9):536–551, 2019.

[234] Hamed Shahsavan, Amirreza Aghakhani, Hao Zeng, Yubing Guo, Zoey S. Davidson, Arri Priimagi, and Metin Sitti. Bioinspired underwater locomotion of light-driven liquid crystal gels. *Proc Natl Acad Sci USA*, 117(10):5125, March 2020.

[235] Bahareh Behkam and Metin Sitti. Design methodology for biomimetic propulsion of miniature swimming robots. *J. Dyn. Sys., Meas., Control*, 128(1):36–43, September 2005.

[236] Ivan Rehor, Charlie Maslen, Pepijn G. Moerman, Bas G. P. van Ravensteijn, Renee van Alst, Jan Groenewold, Huseyin Burak Eral, and Willem K. Kegel. Photoresponsive hydrogel microcrawlers exploit friction hysteresis to crawl by reciprocal actuation. *Soft Robotics*, 8(1):10–18, April 2020.

[237] O. J. Sul, M. R. Falvo, R. M. Taylor, S. Washburn, and R. Superfine. Thermally actuated untethered impact-driven locomotive microdevices. *Appl. Phys. Lett.*, 89(20):203512, November 2006.

[238] Daniel Morales, Etienne Palleau, Michael D. Dickey, and Orlin D. Velev. Electroactuated hydrogel walkers with dual responsive legs. *Soft Matter*, 10:1337–1348, 2014.

[239] B.R. Donald, C.G. Levey, C.D. McGray, I. Paprotny, and D. Rus. An untethered, electrostatic, globally controllable mems micro-robot. *Journal of Microelectromechanical Systems*, 15(1):1–15, 2006.

[240] Ahmed Mourran, Hang Zhang, Rostislav Vinokur, and Martin Möller. Soft microrobots employing nonequilibrium actuation via plasmonic heating. *Advanced Materials*, 29(2):1604825, 2017.

[241] Hao Zeng, Piotr Wasylczyk, Camilla Parmeggiani, Daniele Martella, Matteo Burresi, and Diederik Sybolt Wiersma. Light-fueled microscopic walkers. *Advanced Materials*, 27(26):3883–3887, 2015.

[242] Bo Zhang, Hang Yuan, Andrey Sokolov, Monica Olvera de la Cruz, and Alexey Snezhko. Polar state reversal in active fluids. *Nature Physics*, 18(2):154–159, 2022.

[243] Andrea Cavagna and Irene Giardina. Bird flocks as condensed matter. *Annual Review of Condensed Matter Physics*, 5(1):183–207, 2014.

[244] Enkeleida Lushi, Hugo Wioland, and Raymond E. Goldstein. Fluid flows created by swimming bacteria drive self-organization in confined suspensions. *Proceedings of the National Academy of Sciences*, 111(27):9733–9738, 2014.

[245] Daiki Nishiguchi, Igor S. Aranson, Alexey Snezhko, and Andrey Sokolov. Engineering bacterial vortex lattice via direct laser lithography. *Nature Communications*, 9(1):4486, 2018.

[246] He Li, Xia qing Shi, Mingji Huang, Xiao Chen, Minfeng Xiao, Chenli Liu, Hugues Chaté, and H. P. Zhang. Data-driven quantitative modeling of bacterial active nematics. *Proceedings of the National Academy of Sciences*, 116(3):777–785, 2019.

[247] Mingji Huang, Wensi Hu, Siyuan Yang, Quan-Xing Liu, and H. P. Zhang. Circular swimming motility and disordered hyperuniform state in an algae system. *Proceedings of the National Academy of Sciences*, 118(18), 2021.

[248] Tzer Han Tan, Jinghui Liu, Pearson W. Miller, Melis Tekant, Jörn Dunkel, and Nikta Fakhri. Topological turbulence in the membrane of a living cell. *Nature Physics*, 16(6):657–662, 2020.

[249] Tim Sanchez, Daniel T. N. Chen, Stephen J. DeCamp, Michael Heymann, and Zvonimir Dogic. Spontaneous motion in hierarchically assembled active matter. *Nature*, 491:431, November 2012.

[250] Felix C. Keber, Etienne Loiseau, Tim Sanchez, Stephen J. DeCamp, Luca Giomi, Mark J. Bowick, M. Cristina Marchetti, Zvonimir Dogic, and Andreas R. Bausch. Topology and dynamics of active nematic vesicles. *Science*, 345(6201):1135–1139, 2014.

[251] Sebastian Fürthauer, Bezia Lemma, Peter J. Foster, Stephanie C. Ems-McClung, Che-Hang Yu, Claire E. Walczak, Zvonimir Dogic, Daniel J. Needleman, and Michael J. Shelley. Self-straining of actively crosslinked microtubule networks. *Nature Physics*, 15(12):1295–1300, 2019.

[252] Delphine Geyer, Alexandre Morin, and Denis Bartolo. Sounds and hydrodynamics of polar active fluids. *Nature Materials*, 17(9):789–793, 2018.

[253] Ivo Buttinoni, Julian Bialké, Felix Kümmel, Hartmut Löwen, Clemens Bechinger, and Thomas Speck. Dynamical clustering and phase separation in suspensions of self-propelled colloidal particles. *Phys. Rev. Lett.*, 110:238301, Jun 2013.

[254] Tamás Vicsek and Anna Zafeiris. Collective motion. *Physics Reports*, 517(3):71–140, August 2012.

[255] Igor S Aranson. Active colloids. *Physics-Uspekhi*, 56(1):79–92, 2013.

[256] Michelle Driscoll and Blaise Delmotte. Leveraging collective effects in externally driven colloidal suspensions: experiments and simulations. *Current Opinion in Colloid & Interface Science*, 40:42–57, 2019.

[257] Clemens Bechinger, Roberto Di Leonardo, Hartmut Löwen, Charles Reichhardt, Giorgio Volpe, and Giovanni Volpe. Active particles in complex and crowded environments. *Rev. Mod. Phys.*, 88:045006, Nov 2016.

[258] Andreas M. Menzel. Tuned, driven, and active soft matter. *Physics Reports*, 554:1–45, 2015. Tuned, driven, and active soft matter.

[259] Shuang Zhou, Andrey Sokolov, Oleg D. Lavrentovich, and Igor S. Aranson. Living liquid crystals. *Proceedings of the National Academy of Sciences*, 111(4):1265–1270, 2014.

[260] Jie Zhang, Bartosz A. Grzybowski, and Steve Granick. Janus particle synthesis, assembly, and application. *Langmuir*, 33(28):6964–6977, July 2017.

[261] Katherine Villa and Martin Pumera. Fuel-free light-driven micro/nanomachines: artificial active matter mimicking nature. *Chem. Soc. Rev.*, 48:4966–4978, 2019.

[262] Delphine Geyer, David Martin, Julien Tailleur, and Denis Bartolo. Freezing a flock: Motility-induced phase separation in polar active liquids. *Phys. Rev. X*, 9:031043, Sep 2019.

[263] Jing Yan, Ming Han, Jie Zhang, Cong Xu, Erik Luijten, and Steve Granick. Reconfiguring active particles by electrostatic imbalance. *Nature Materials*, 15(10):1095–1099, 2016.

[264] Gasper Kokot and Alexey Snezhko. Manipulation of emergent vortices in swarms of magnetic rollers. *Nature communications*, 9(1):2344, 2018.

[265] Koohee Han, C. Wyatt Shields IV, and Orlin D. Velev. Engineering of self-propelling microbots and microdevices powered by magnetic and electric fields. *Advanced Functional Materials*, 28(25):1705953, 2018.

[266] Fernando Martinez-Pedrero, Eloy Navarro-Argemí, Antonio Ortiz-Ambriz, Ignacio Pagonabarraga, and Pietro Tierno. Emergent hydrodynamic bound states between magnetically powered micropropellers. *Science Advances*, 4(1):eaap9379, 2018.

[267] Palacci Jeremie, Sacanna Stefano, Steinberg Asher Preska, J. Pine David, and M. Chaikin Paul. Living crystals of light-activated colloidal surfers. *Science*, 339(6122):936–940, February 2013.

[268] Dhruv P. Singh, Udit Choudhury, Peer Fischer, and Andrew G. Mark. Non-equilibrium assembly of light-activated colloidal mixtures. *Advanced Materials*, 29(32):1701328, 2017.

[269] Leilei Xu, Fangzhi Mou, Haotian Gong, Ming Luo, and Jianguo Guan. Light-driven micro/nanomotors: from fundamentals to applications. *Chem. Soc. Rev.*, 46:6905–6926, 2017.

[270] Alexey Snezhko. Complex collective dynamics of active torque-driven colloids at interfaces. *Current Opinion in Colloid & Interface Science*, 21:65–75, 2016.

[271] Andreas Zöttl and Holger Stark. Hydrodynamics determines collective motion and phase behavior of active colloids in quasi-two-dimensional confinement. *Physical review letters*, 112(11):118101, 2014.

[272] Kun-Ta Wu, Jean Bernard Hishamunda, Daniel T. N. Chen, Stephen J. DeCamp, Ya-Wen Chang, Alberto Fernández-Nieves, Seth Fraden, and Zvonimir Dogic. Transition from turbulent to coherent flows in confined three-dimensional active fluids. *Science*, 355(6331), 2017.

[273] Antoine Aubret, Mena Youssef, Stefano Sacanna, and Jérémie Palacci. Targeted assembly and synchronization of self-spinning microgears. *Nature Physics*, 14(11):1114–1118, 2018.

[274] Tamás Vicsek, András Czirók, Eshel Ben-Jacob, Inon Cohen, and Ofer Shochet. Novel type of phase transition in a system of self-driven particles. *Phys. Rev. Lett.*, 75:1226–1229, Aug 1995.

[275] Arthur T. Winfree. Biological rhythms and the behavior of populations of coupled oscillators. *Journal of Theoretical Biology*, 16(1):15–42, 1967.

[276] Steven H. Strogatz. From kuramoto to crawford: exploring the onset of synchronization in populations of coupled oscillators. *Physica D: Nonlinear Phenomena*, 143(1):1–20, 2000.

[277] Kevin P. O'Keeffe, Hyunsuk Hong, and Steven H. Strogatz. Oscillators that sync and swarm. *Nature Communications*, 8(1):1504, 2017.

[278] Hiromi Yamakawa. Transport properties of polymer chains in dilute solution: Hydrodynamic interaction. *J. Chem. Phys.*, 53(1):436–443, December 1970.

[279] J. M. Deutch and Irwin Oppenheim. Molecular theory of brownian motion for several particles. *J. Chem. Phys.*, 54(8):3547–3555, December 1971.

[280] T. J. Murphy and J. L. Aguirre. Brownian motion of n interacting particles. i. extension of the einstein diffusion relation to the n-particle case. *J. Chem. Phys.*, 57(5):2098–2104, December 1972.

[281] Gerald Wilemski. On the derivation of smoluchowski equations with corrections in the classical theory of brownian motion. *Journal of Statistical Physics*, 14(2):153–169, February 1976.

[282] Donald L. Ermak and J. A. McCammon. Brownian dynamics with hydrodynamic interactions. *J. Chem. Phys.*, 69(4):1352–1360, December 1978.

[283] L. Durlofsky, J. F. Brady, and G. Bossis. Dynamic simulation of hydrodynamically interacting particles. *Journal of Fluid Mechanics*, 180:21–49, 1987.

[284] Anthony J. C. Ladd, Michael E. Colvin, and Daan Frenkel. Application of lattice-gas cellular automata to the brownian motion of solids in suspension. *Phys. Rev. Lett.*, 60:975–978, Mar 1988.

[285] T. Krüger, H. Kusumaatmaja, A. Kuzmin, O. Shardt, G. Silva, and E. M. Viggen. *The Lattice Boltzmann Method: Principles and Practice*. Springer International Publishing, 2016.

[286] R. Benzi, S. Succi, and M. Vergassola. The lattice boltzmann equation: theory and applications. *Physics Reports*, 222(3):145–197, 1992.

[287] F.E. Mackay, S.T.T. Ollila, and C. Denniston. Hydrodynamic forces implemented into lammps through a lattice-boltzmann fluid. *Computer Physics Communications*, 184(8):2021–2031, 2013.

[288] I. Cimrák, M. Gusenbauer, and I. Jan**c**igová. An espresso implementation of elastic objects immersed in a fluid. *Computer Physics Communications*, 185(3):900–907, 2014.

[289] Martin Bauer, Sebastian Eibl, Christian Godenschwager, Nils Kohl, Michael Kuron, Christoph Rettinger, Florian Schornbaum, Christoph Schwarzmeier, Dominik Thönnes, Harald Köstler, and Ulrich Rüde. walberla: A block-structured high-performance framework for multiphysics simulations. *Computers & Mathematics with Applications*, 81:478–501, 2021. Development and Application of Open-source Software for Problems with Numerical PDEs.

[290] Pep Español. Hydrodynamics from dissipative particle dynamics. *Phys. Rev. E*, 52:1734–1742, Aug 1995.

[291] Robert D. Groot and Patrick B. Warren. Dissipative particle dynamics: Bridging the gap between atomistic and mesoscopic simulation. *The Journal of Chemical Physics*, 107(11):4423–4435, October 1997.

[292] N. Mai-Duy, D. Pan, N. Phan-Thien, and B. C. Khoo. Dissipative particle dynamics modeling of low reynolds number incompressible flows. *Journal of Rheology*, 57(2):585–604, October 2013.

[293] E. MOEENDARBARY, N. G. T. Y., and M. ZANGENEH. Dissipative particle dynamics: Introduction, methodology and complex fluid applications – a review. *Int. J. Appl. Mechanics*, 01(04):737–763, September 2018.

[294] Anatoly Malevanets and Raymond Kapral. Mesoscopic model for solvent dynamics. *J. Chem. Phys.*, 110(17):8605–8613, April 1999.

[295] Michael P. Howard, Arash Nikoubashman, and Jeremy C. Palmer. Modeling hydrodynamic interactions in soft materials with multiparticle collision dynamics. *Current Opinion in Chemical Engineering*, 23:34–43, 2019.

[296] Simón Poblete, Adam Wysocki, Gerhard Gompper, and Roland G. Winkler. Hydrodynamics of discrete-particle models of spherical colloids: A multiparticle collision dynamics simulation study. *Phys. Rev. E*, 90:033314, Sep 2014.

[297] E. Tüzel, M. Strauss, T. Ihle, and D. M. Kroll. Transport coefficients for stochastic rotation dynamics in three dimensions. *Phys. Rev. E*, 68:036701, Sep 2003.

[298] N. Kikuchi, C. M. Pooley, J. F. Ryder, and J. M. Yeomans. Transport coefficients of a mesoscopic fluid dynamics model. *J. Chem. Phys.*, 119(12):6388–6395, September 2003.

[299] Michael P. Howard, Athanassios Z. Panagiotopoulos, and Arash Nikoubashman. Efficient mesoscale hydrodynamics: Multiparticle collision dynamics with massively parallel gpu acceleration. *Computer Physics Communications*, 230:10–20, 2018.

[300] Jens Rotne and Stephen Prager. Variational treatment of hydrodynamic interaction in polymers. *J. Chem. Phys.*, 50(11):4831–4837, December 1969.

[301] Eligiusz Wajnryb, Krzysztof A. Mizerski, Pawel J. Zuk, and Piotr Szymczak. Generalization of the rotne-prager-yamakawa mobility and shear disturbance tensors. *Journal of Fluid Mechanics*, 731(R3):R3, 2013.

[302] J F Brady and G. Bossis. Stokesian dynamics. *Annual Review of Fluid Mechanics*, 20(1):111–157, 1988.

[303] James W. Swan and Gang Wang. Rapid calculation of hydrodynamic and transport properties in concentrated solutions of colloidal particles and macromolecules. *Physics of Fluids*, 28(1):011902, 2016.

[304] Andrew M. Fiore, Florencio Balboa Usabiaga, Aleksandar Donev, and James W. Swan. Rapid sampling of stochastic displacements in brownian dynamics simulations. *J. Chem. Phys.*, 146(12):124116, December 2017.

[305] Andrew M. Fiore and James W. Swan. Fast stokesian dynamics. *Journal of Fluid Mechanics*, 878:544–597, 2019.

[306] Xujun Zhao, Jiyuan Li, Xikai Jiang, Dmitry Karpeev, Olle Heinonen, Barry Smith, Juan P. Hernandez-Ortiz, and Juan J. de Pablo. Parallel o(n) stokes' solver towards scalable brownian dynamics of hydrodynamically interacting objects in general geometries. *The Journal of Chemical Physics*, 146(24):244114, September 2018.

[307] Abhinendra Singh, Jiyuan Li, Xikai Jiang, Juan P. Hernández-Ortiz, Heinrich M. Jaeger, and Juan J. de Pablo. Shape induced segregation and anomalous particle transport under spherical confinement. *Physics of Fluids*, 32(5):053307, May 2020.

[308] C. Pozrikidis. *Boundary Integral and Singularity Methods for Linearized Viscous Flow*. Cambridge Texts in Applied Mathematics. Cambridge University Press, 1992.

[309] Steven Delong, Florencio Balboa Usabiaga, Rafael Delgado-Buscalioni, Boyce E. Griffith, and Aleksandar Donev. Brownian dynamics without green's functions. *J. Chem. Phys.*, 140(13):134110, April 2014.

[310] Eric E. Keaveny. Fluctuating force-coupling method for simulations of colloidal suspensions. *Journal of Computational Physics*, 269:61–79, July 2014.

[311] Maciej Lisicki. Four approaches to hydrodynamic green's functions–the oseen tensors. *arXiv preprint arXiv:1312.6231*, 2013.

[312] J. J. Sakurai and J. Napolitano. *Modern Quantum Mechanics*. Cambridge University Press, 2017.

[313] Adam Kenneth Townsend. *The mechanics of suspensions*. PhD thesis, University College London, 2017.

[314] D. J. Jeffrey and Y. Onishi. Calculation of the resistance and mobility functions for two unequal rigid spheres in low-reynolds-number flow. *Journal of Fluid Mechanics*, 139:261–290, 1984.

[315] D. J. Jeffrey. The calculation of the low reynolds number resistance functions for two unequal spheres. *Physics of Fluids A: Fluid Dynamics*, 4(1):16–29, January 1992.

[316] Helen J. Wilson. Stokes flow past three spheres. *Journal of Computational Physics*, 245:302–316, July 2013.

[317] Adam K. Townsend. Generating, from scratch, the near-field asymptotic forms of scalar resistance functions for two unequal rigid spheres in low-reynolds-number flow, 2019.

[318] J. Happel and H. Brenner. *Low Reynolds number hydrodynamics: with special applications to particulate media*. Springer Netherlands, 1981.

[319] Brennan Sprinkle, Ernest B. van der Wee, Yixiang Luo, Michelle M. Driscoll, and Aleksandar Donev. Driven dynamics in dense suspensions of microrollers. *Soft Matter*, 16:7982–8001, 2020.

[320] Ryohei Seto, Romain Mari, Jeffrey F. Morris, and Morton M. Denn. Discontinuous shear thickening of frictional hard-sphere suspensions. *Phys. Rev. Lett.*, 111:218301, November 2013.

[321] Romain Mari, Ryohei Seto, Jeffrey F. Morris, and Morton M. Denn. Shear thickening, frictionless and frictional rheologies in non-brownian suspensions. *Journal of Rheology*, 58(6):1693–1724, September 2014.

[322] Romain Mari, Ryohei Seto, Jeffrey F. Morris, and Morton M. Denn. Discontinuous shear thickening in brownian suspensions by dynamic simulation. *Proceedings of the National Academy of Sciences*, 112(50):15326–15330, 2015.

[323] Stefan Luding. Cohesive, frictional powders: contact models for tension. *Granular Matter*, 10(4):235, 2008.

[324] D. I. Dratler and W. R. Schowalter. Dynamic simulation of suspensions of non-brownian hard spheres. *Journal of Fluid Mechanics*, 325:53–77, 1996.

[325] Hiromi Yamakawa. *Modern Theory of Polymer Solutions*. Harper & Row, 1971.

[326] P. J. Zuk, E. Wajnryb, K. A. Mizerski, and P. Szymczak. Rotne-prager-yamakawa approximation for different-sized particles in application to macromolecular bead models. *Journal of Fluid Mechanics*, 741(R5):R5, 2014.

[327] J. R. Blake. A note on the image system for a stokeslet in a no-slip boundary. *Mathematical Proceedings of the Cambridge Philosophical Society*, 70(2):303–310, sep 1971.

[328] Steven Delong, Florencio Balboa Usabiaga, and Aleksandar Donev. Brownian dynamics of confined rigid bodies. *J. Chem. Phys.*, 143(14):144107, October 2015.

[329] Michelle Driscoll, Blaise Delmotte, Mena Youssef, Stefano Sacanna, Aleksandar Donev, and Paul Chaikin. Unstable fronts and motile structures formed by microrollers. *Nature Physics*, 13(4):375–379, 2017.

[330] Florencio Balboa Usabiaga, Blaise Delmotte, and Aleksandar Donev. Brownian dynamics of confined suspensions of active microrollers. *J. Chem. Phys.*, 146(13):134104, April 2017.

[331] Brennan Sprinkle, Florencio Balboa Usabiaga, Neelesh A. Patankar, and Aleksandar Donev. Large scale brownian dynamics of confined suspensions of rigid particles. *J. Chem. Phys.*, 147(24):244103, December 2017.

[332] R. C. Ball and J. R. Melrose. A simulation technique for many spheres in quasi-static motion under frame-invariant pair drag and brownian forces. *Physica A: Statistical Mechanics and its Applications*, 247(1):444–472, 1997.

[333] Markus Hütter and Hans Christian Öttinger. Fluctuation-dissipation theorem, kinetic stochastic integral and efficient simulations. *J. Chem. Soc., Faraday Trans.*, 94:1403–1405, 1998.

[334] David B. Thomas, Wayne Luk, Philip H.W. Leong, and John D. Villasenor. Gaussian random number generators. *ACM Comput. Surv.*, 39(4):11–es, nov 2007.

[335] V. Srinivasan and M. Viswanathan. *Wireless Communication Systems in Matlab: (Color Edition)*. Independently Published, 2019.

[336] L Susan Blackford, Antoine Petitet, Roldan Pozo, Karin Remington, R Clint Whaley, James Demmel, Jack Dongarra, Iain Duff, Sven Hammarling, Greg Henry, et al. An updated set of basic linear algebra subprograms (blas). *ACM Transactions on Mathematical Software*, 28(2):135–151, 2002.

[337] E. Anderson, Z. Bai, C. Bischof, S. Blackford, J. Demmel, J. Dongarra, J. Du Croz, A. Greenbaum, S. Hammarling, A. McKenney, and D. Sorensen. *LAPACK Users' Guide*. Society for Industrial and Applied Mathematics, Philadelphia, PA, third edition, 1999.

[338] Yanqing Chen, Timothy A. Davis, William W. Hager, and Sivasankaran Rajamanickam. Algorithm 887: Cholmod, supernodal sparse cholesky factorization and update/downdate. *ACM Trans. Math. Softw.*, 35(3), oct 2008.

[339] C. C. Paige and M. A. Saunders. Solution of sparse indefinite systems of linear equations. *SIAM Journal on Numerical Analysis*, 12(4):617–629, 1975.

[340] Michele Benzi, Gene H. Golub, and Jörg Liesen. Numerical solution of saddle point problems. *Acta Numerica*, 14:1–137, 2005.

[341] Marshall Fixman. Construction of langevin forces in the simulation of hydrodynamic interaction. *Macromolecules*, 19(4):1204–1207, April 1986.

[342] Tadashi Ando, Edmond Chow, Yousef Saad, and Jeffrey Skolnick. Krylov subspace methods for computing hydrodynamic interactions in brownian dynamics simulations. *J. Chem. Phys.*, 137(6):064106, August 2012.

[343] Edmond Chow and Yousef Saad. Preconditioned krylov subspace methods for sampling multivariate gaussian distributions. *SIAM Journal on Scientific Computing*, 36(2):A588–a608, 2014.

[344] J.D. Lambert. *Numerical Methods for Ordinary Differential Systems: The Initial Value Problem*. John Wiley and Sons, 1991.

[345] Steven Delong, Boyce E. Griffith, Eric Vanden-Eijnden, and Aleksandar Donev. Temporal integrators for fluctuating hydrodynamics. *Phys. Rev. E*, 87:033302, Mar 2013.

[346] J.C. Butcher. *Numerical Methods for Ordinary Differential Equations*. Wiley, 2003.

[347] D. Frenkel and B. Smit. *Understanding Molecular Simulation: From Algorithms to Applications*. Computational science series. Elsevier Science, 2001.

[348] Yutaka Kazoe and Minami Yoda. Measurements of the near-wall hindered diffusion of colloidal particles in the presence of an electric field. *Appl. Phys. Lett.*, 99(12):124104, September 2011.

[349] Fernando Peruani, Jörn Starruß, Vladimir Jakovljevic, Lotte Søgaard-Andersen, Andreas Deutsch, and Markus Bär. Collective motion and nonequilibrium cluster formation in colonies of gliding bacteria. *Physical review letters*, 108(9):098102, 2012.

[350] Volker Schaller, Christoph Weber, Christine Semmrich, Erwin Frey, and Andreas R Bausch. Polar patterns of driven filaments. *Nature*, 467(7311):73–77, 2010.

[351] Yutaka Sumino, Ken H Nagai, Yuji Shitaka, Dan Tanaka, Kenichi Yoshikawa, Hugues Chaté, and Kazuhiro Oiwa. Large-scale vortex lattice emerging from collectively moving microtubules. *Nature*, 483(7390):448–452, 2012.

[352] Andrey Sokolov and Igor S Aranson. Physical properties of collective motion in suspensions of bacteria. *Physical review letters*, 109(24):248109, 2012.

[353] Jing Yan, Ming Han, Jie Zhang, Cong Xu, Erik Luijten, and Steve Granick. Reconfiguring active particles by electrostatic imbalance. *Nature materials*, 15(10):1095–1099, 2016.

[354] Gasper Kokot, Shibananda Das, Roland G Winkler, Gerhard Gompper, Igor S Aranson, and Alexey Snezhko. Active turbulence in a gas of self-assembled spinners. *Proceedings of the National Academy of Sciences*, 114(49):12870–12875, 2017.

[355] Amin Doostmohammadi, Jordi Ignés-Mullol, Julia M Yeomans, and Francesc Sagués. Active nematics. *Nature communications*, 9(1):3246, 2018.

[356] James E Martin and Alexey Snezhko. Driving self-assembly and emergent dynamics in colloidal suspensions by time-dependent magnetic fields. *Reports on Progress in Physics*, 76(12):126601, 2013.

[357] Christoph A Weber, Timo Hanke, J Deseigne, S Léonard, Olivier Dauchot, Erwin Frey, and Hugues Chaté. Long-range ordering of vibrated polar disks. *Physical review letters*, 110(20):208001, 2013.

[358] Helena Massana-Cid, Joan Codina, Ignacio Pagonabarraga, and Pietro Tierno. Active apolar doping determines routes to colloidal clusters and gels. *Proceedings of the National Academy of Sciences*, 115(42):10618–10623, 2018.

[359] Koohee Han, Gasper Kokot, Shibananda Das, Roland G Winkler, Gerhard Gompper, and Alexey Snezhko. Reconfigurable structure and tunable transport in synchronized active spinner materials. *Science advances*, 6(12):eaaz8535, 2020.

[360] Antoine Bricard, Jean-Baptiste Caussin, Debasish Das, Charles Savoie, Vijayakumar Chikkadi, Kyohei Shitara, Oleksandr Chepizhko, Fernando Peruani, David Saintillan, and Denis Bartolo. Emergent vortices in populations of colloidal rollers. *Nature Communications*, 6(1):7470, 2015.

[361] Andreas Kaiser, Alexey Snezhko, and Igor S Aranson. Flocking ferromagnetic colloids. *Science advances*, 3(2):e1601469, 2017.

[362] G Quincke. Ueber rotationen im constanten electrischen felde. *Annalen der Physik*, 295(11):417–486, 1896.

[363] JR Melcher and GI Taylor. Electrohydrodynamics: a review of the role of interfacial shear stresses. *Annual review of fluid mechanics*, 1(1):111–146, 1969.

[364] Teun Vissers, Alfons van Blaaderen, and Arnout Imhof. Band formation in mixtures of oppositely charged colloids driven by an ac electric field. *Phys. Rev. Lett.*, 106:228303, Jun 2011.

[365] Celia Lozano, Borge ten Hagen, Hartmut Löwen, and Clemens Bechinger. Phototaxis of synthetic microswimmers in optical landscapes. *Nature Communications*, 7(1):12828, 2016.

[366] M. Belkin, A. Snezhko, I. S. Aranson, and W.-K. Kwok. Driven magnetic particles on a fluid surface: Pattern assisted surface flows. *Phys. Rev. Lett.*, 99:158301, Oct 2007.

[367] Walter F. Paxton, Kevin C. Kistler, Christine C. Olmeda, Ayusman Sen, Sarah K. St. Angelo, Yanyan Cao, Thomas E. Mallouk, Paul E. Lammert, and Vincent H. Crespi. Catalytic nanomotors: Autonomous movement of striped nanorods. *J. Am. Chem. Soc.*, 126(41):13424–13431, October 2004.

[368] Sumit Gangwal, Olivier J. Cayre, Martin Z. Bazant, and Orlin D. Velev. Induced-charge electrophoresis of metallodielectric particles. *Phys. Rev. Lett.*, 100:058302, Feb 2008.

[369] J. Elgeti, R. G. Winkler, and G. Gompper. Physics of microswimmers-single particle motion and collective behavior: a review. *Reports On Progress In Physics*, 78(5), May 2015.

[370] Andreas Zöttl and Holger Stark. Emergent behavior in active colloids. *J. Phys.: Condens. Matter*, 28(253001), 2016.

[371] M. Reza Shaebani, Adam Wysocki, Roland G. Winkler, Gerhard Gompper, and Heiko Rieger. Computational models for active matter. *Nature Reviews Physics*, 2(4):181–199, 2020.

[372] Kai Qi, Elmar Westphal, Gerhard Gompper, and Roland G. Winkler. Emergence of active turbulence in microswimmer suspensions due to active hydrodynamic stress and volume exclusion. *Communications Physics*, 5(1):49, 2022.

[373] Qun-Li Lei and Ran Ni. Hydrodynamics of random-organizing hyperuniform fluids. *Proceedings of the National Academy of Sciences*, 116(46):22983–22989, 2019.

[374] M. Belovs, M. Brics, and A. Cebers. Rotating-field-driven ensembles of magnetic particles. *Phys. Rev. E*, 99:042605, Apr 2019.

[375] Xiang Yang, Chenyang Ren, Kangjun Cheng, and H. P. Zhang. Robust boundary flow in chiral active fluid. *Phys. Rev. E*, 101:022603, Feb 2020.

[376] JE Avron. Odd viscosity. *Journal of statistical physics*, 92(3):543–557, 1998.

[377] Tali Khain, Colin Scheibner, Michel Fruchart, and Vincenzo Vitelli. Stokes flows in three-dimensional fluids with odd and parity-violating viscosities. *Journal of Fluid Mechanics*, 934:A23, 2022.

[378] Arghya Samanta. Role of odd viscosity in falling viscous fluid. *Journal of Fluid Mechanics*, 938:A9, 2022.

[379] Ming Han, Michel Fruchart, Colin Scheibner, Suriyanarayanan Vaikuntanathan, Juan J. de Pablo, and Vincenzo Vitelli. Fluctuating hydrodynamics of chiral active fluids. *Nature Physics*, 17(11):1260–1269, 2021.

[380] Yuto Hosaka, Shigeyuki Komura, and David Andelman. Hydrodynamic lift of a two-dimensional liquid domain with odd viscosity. *Phys. Rev. E*, 104:064613, Dec 2021.

[381] Somayeh Farhadi, Sergio Machaca, Justin Aird, Bryan O. Torres Maldonado, Stanley Davis, Paulo E. Arratia, and Douglas J. Durian. Dynamics and thermodynamics of air-driven active spinners. *Soft Matter*, 14:5588–5594, 2018.

[382] Marcel Workamp, Gustavo Ramirez, Karen E. Daniels, and Joshua A. Dijksman. Symmetry-reversals in chiral active matter. *Soft Matter*, 14:5572–5580, 2018.

[383] Quanliang Cao, Qi Fan, Qi Chen, Chunting Liu, Xiaotao Han, and Liang Li. Recent advances in manipulation of micro- and nano-objects with magnetic fields at small scales. *Mater. Horiz.*, 7:638–666, 2020.

[384] Stefano Sacanna, Laura Rossi, and David J. Pine. Magnetic click colloidal assembly. *J. Am. Chem. Soc.*, 134(14):6112–6115, April 2012.

[385] P. N. Segrè, F. Liu, P. Umbanhowar, and D. A. Weitz. An effective gravitational temperature for sedimentation. *Nature*, 409(6820):594–597, 2001.

[386] Brennan Sprinkle, Sam Wilken, Shake Karapetyan, Michio Tanaka, Zhe Chen, Joseph R. Cruise, Blaise Delmotte, Michelle M. Driscoll, Paul Chaikin, and Aleksandar Donev. Sedimentation of a colloidal monolayer down an inclined plane. *Phys. Rev. Fluids*, 6:034202, Mar 2021.

[387] Douglas Henderson. A simple equation of state for hard discs. *Molecular Physics*, 30(3):971–972, September 1975.

[388] Norman F. Carnahan and Kenneth E. Starling. Equation of state for nonattracting rigid spheres. *J. Chem. Phys.*, 51(2):635–636, December 2018.

[389] Yuto Hosaka, Shigeyuki Komura, and David Andelman. Nonreciprocal response of a two-dimensional fluid with odd viscosity. *Phys. Rev. E*, 103:042610, Apr 2021.

[390] Tomer Markovich and Tom C. Lubensky. Odd viscosity in active matter: Microscopic origin and 3d effects. *Phys. Rev. Lett.*, 127:048001, Jul 2021.

[391] Tomer Markovich, Elsen Tjhung, and Michael E Cates. Chiral active matter: microscopic 'torque dipoles' have more than one hydrodynamic description. *New Journal of Physics*, 21(11):112001, nov 2019.

[392] Debarghya Banerjee, Anton Souslov, Alexander G. Abanov, and Vincenzo Vitelli. Odd viscosity in chiral active fluids. *Nature Communications*, 8(1):1573, 2017.

[393] Curie, P. Sur la symétrie dans les phénomènes physiques, symétrie d'un champ électrique et d'un champ magnétique. *J. Phys. Theor. Appl.*, 3(1):393–415, 1894.

[394] Sybren Ruurds de Groot and Peter Mazur. *Non-equilibrium Thermodynamics*. Courier Corporation, 1984.

[395] Lars Onsager. Reciprocal relations in irreversible processes. i. *Phys. Rev.*, 37:405–426, Feb 1931.

[396] L.D. Landau and E.M. Lifshitz. *Statistical Physics*, volume 5. Elsevier Science, 2013.

[397] Vishal Soni, Ephraim S. Bililign, Sofia Magkiriadou, Stefano Sacanna, Denis Bartolo, Michael J. Shelley, and William T. M. Irvine. The odd free surface flows of a colloidal chiral fluid. *Nature Physics*, 15(11):1188–1194, 2019.

[398] Henry C. W. Chu and Roseanna N. Zia. Toward a nonequilibrium stokes-einstein relation via active microrheology of hydrodynamically interacting colloidal dispersions. *Journal of Colloid and Interface Science*, 539:388–399, 2019.

[399] Eric W. Burkholder and John F. Brady. Fluctuation-dissipation in active matter. *J. Chem. Phys.*, 150(18):184901, May 2019.

[400] Sara Dal Cengio, Demian Levis, and Ignacio Pagonabarraga. Fluctuation-dissipation relations in the absence of detailed balance: formalism and applications to active matter, 2020.

[401] Jean Colombani, Laure Petit, Christophe Ybert, and Catherine Barentin. Probing the fluctuation-dissipation theorem in a perrin-like experiment. *Phys. Rev. Lett.*, 107:130601, Sep 2011.

[402] Clara del Junco, Laura Tociu, and Suriyanarayanan Vaikuntanathan. Energy dissipation and fluctuations in a driven liquid. *Proceedings of the National Academy of Sciences*, 115(14):3569–3574, 2018.

[403] A. Sarracino and A. Vulpiani. On the fluctuation-dissipation relation in non-equilibrium and non-hamiltonian systems. *Chaos*, 29(8):083132, August 2019.

[404] Lennart Dabelow, Stefano Bo, and Ralf Eichhorn. Irreversibility in active matter systems: Fluctuation theorem and mutual information. *Phys. Rev. X*, 9:021009, Apr 2019.

[405] Martin Bauer, Harald Köstler, and Ulrich Rüde. lbmpy: Automatic code generation for efficient parallel lattice boltzmann methods. *Journal of Computational Science*, 49:101269, 2021.

[406] P. W. Anderson. More is different. *Science*, 177(4047):393–396, 1972.

[407] C.R. Taylor. *Applications Of Dynamic Programming To Agricultural Decision Problems*. CRC Press, 2019.

[408] P. Moon and D. E. Spencer. *Field Theory Handbook*. Springer-Verlag Berlin Heidelberg, 1988.

APPENDIX A

Coordinate Systems

In this appendix, selected properties of both the spherical and bispherical coordinate systems used in this work are compiled for reference [**408**].

A.1. Spherical coordinate system

- Coordinates transformation

$$\begin{cases} x = r\sin\theta\cos\phi \\ y = r\sin\theta\sin\phi \\ z = r\cos\theta \end{cases} \tag{A.1}$$

where $0 \leq r < \infty, \quad 0 \leq \theta \leq \pi, \quad 0 \leq \phi < 2\pi.$

- Coordinate surfaces

$$\begin{cases} x^2 + y^2 + z^2 = r^2 \\ \tan\theta = (x^2 + y^2)^{1/2}/z \\ \tan\phi = \dfrac{y}{x} \end{cases} \tag{A.2}$$

- Base vectors transformation

$$\begin{pmatrix} \hat{\mathbf{x}} \\ \hat{\mathbf{y}} \\ \hat{\mathbf{z}} \end{pmatrix} = \begin{pmatrix} \sin\theta\cos\phi & \cos\theta\cos\phi & -\sin\phi \\ \sin\theta\sin\phi & \cos\theta\sin\phi & \cos\phi \\ \cos\theta & -\sin\theta & 0 \end{pmatrix} \begin{pmatrix} \hat{\mathbf{r}} \\ \hat{\boldsymbol{\theta}} \\ \hat{\boldsymbol{\phi}} \end{pmatrix} \tag{A.3}$$

$$\begin{pmatrix} \hat{\mathbf{r}} \\ \hat{\boldsymbol{\theta}} \\ \hat{\boldsymbol{\phi}} \end{pmatrix} = \begin{pmatrix} \sin\theta\cos\phi & \sin\theta\sin\phi & \cos\theta \\ \cos\theta\cos\phi & \cos\theta\sin\phi & -\sin\theta \\ -\sin\phi & \cos\phi & 0 \end{pmatrix} \begin{pmatrix} \hat{\mathbf{x}} \\ \hat{\mathbf{y}} \\ \hat{\mathbf{z}} \end{pmatrix} \tag{A.4}$$

- Metrics

$$g_{ij} = \delta_{kl} \frac{\partial x^k}{\partial u^i} \frac{\partial x^l}{\partial u^j} \tag{A.5}$$

$$g_{11} = 1, g_{22} = r^2, g_{33} = r^2 \sin^2\theta, g^{1/2} = r^2 \sin\theta \tag{A.6}$$

$$g_{ij} = \begin{pmatrix} 1 & 0 & 0 \\ 0 & r^2 & 0 \\ 0 & 0 & r^2 \sin^2\theta \end{pmatrix} \tag{A.7}$$

- Christoffel symbols

$$\Gamma^{\beta}_{\mu\nu} = \frac{1}{2} g^{\beta\alpha} (g_{\alpha\mu,\nu} + g_{\alpha\nu,\mu} - g_{\mu\nu,\alpha}) \tag{A.8}$$

(A.9) $$\Gamma^r_{\mu\nu} = \begin{pmatrix} 0 & 0 & 0 \\ 0 & -r & 0 \\ 0 & 0 & -r\sin^2\theta \end{pmatrix}$$

(A.10) $$\Gamma^\theta_{\mu\nu} = \begin{pmatrix} 0 & \frac{1}{r} & 0 \\ \frac{1}{r} & 0 & 0 \\ 0 & 0 & -\sin\theta\cos\theta \end{pmatrix}$$

(A.11) $$\Gamma^\phi_{\mu\nu} = \begin{pmatrix} 0 & 0 & \frac{1}{r} \\ 0 & 0 & \cot\theta \\ \frac{1}{r} & \cot\theta & 0 \end{pmatrix}$$

- Covariant derivatives

(A.12) $$A^\mu_{;\nu} = A^\mu_{,\nu} + \Gamma^\mu_{\beta\nu} A^\beta$$

(A.13) $$A_{\mu;\nu} = A_{\mu,\nu} - \Gamma^\beta_{\mu\nu} A_\beta$$

- Covariant divergence

(A.14) $$A^\mu_{;\mu} = A^\mu_{,\mu} + \Gamma^\mu_{\beta\mu} A^\beta = \frac{1}{\sqrt{g}} \left(\sqrt{g} A^\mu\right)_{,\mu}$$

(A.15) $$A^r_{;r} = A^r_{,r} + \Gamma^r_{\beta r} A^\beta = A^r_{,r}$$

$$A^{\theta}_{;\theta} = A^{\theta}_{,\theta} + \Gamma^{\theta}_{\beta\theta} A^{\beta} = A^{\theta}_{,\theta} + \frac{1}{r} A^{r} \tag{A.16}$$

$$A^{\phi}_{;\phi} = A^{\phi}_{,\phi} + \Gamma^{\phi}_{\beta\phi} A^{\beta} = A^{\phi}_{,\phi} + \frac{1}{r} A^{r} + \cot\theta A^{\theta} \tag{A.17}$$

$$A^{\mu}_{;\mu} = A^{r}_{,r} + A^{\theta}_{,\theta} + A^{\phi}_{,\phi} + \frac{2}{r} A^{r} + \cot\theta A^{\theta} \tag{A.18}$$

- Laplace-Beltrami operator

$$\left(\boldsymbol{\nabla} f\right)^{i} = \partial^{i} f = g^{ij} \partial_{j} f = g^{ij} f_{,j} \tag{A.19}$$

$$\nabla^{2} f = \frac{1}{\sqrt{g}} \left(\sqrt{g} g^{\mu\nu} f_{,\nu}\right)_{,\mu} \tag{A.20}$$

A.2. Bispherical coordinate system

- Coordinates transformation

$$\begin{cases} x = \dfrac{c \sin\theta \cos\psi}{\cosh\eta - \cos\theta} \\ y = \dfrac{c \sin\theta \sin\psi}{\cosh\eta - \cos\theta} \\ z = \dfrac{c \sinh\eta}{\cosh\eta - \cos\theta} \end{cases} \tag{A.21}$$

where $-\infty < \eta < \infty, \quad 0 \leq \theta < 2\pi, \quad 0 \leq \psi < 2\pi.$

- Coordinate surfaces

$$\text{(A.22)}\qquad \begin{cases} x^2+y^2+(z-c\coth\eta)^2=\dfrac{c^2}{\sinh^2\eta} \\ x^2+y^2+z^2-2c(x^2+y^2)^{1/2}\cot\theta=c^2 \\ \tan\psi=\dfrac{y}{x} \end{cases}$$

- Base vector transformations

$$\text{(A.23)}\qquad \begin{pmatrix} \hat{\mathbf{e}}_\eta \\ \hat{\mathbf{e}}_\theta \\ \hat{\mathbf{e}}_\psi \end{pmatrix} = \begin{pmatrix} -\frac{\sin\theta\cos\psi\sinh\eta}{\cosh\eta-\cos\theta} & -\frac{\sin\theta\sin\psi\sinh\eta}{\cosh\eta-\cos\theta} & -\frac{\cos\theta\cosh\eta-1}{\cosh\eta-\cos\theta} \\ \frac{(\cos\theta\cosh\eta-1)\cos\psi}{\cosh\eta-\cos\theta} & \frac{(\cos\theta\cosh\eta-1)\sin\psi}{\cosh\eta-\cos\theta} & -\frac{\sin\theta\sinh\eta}{\cosh\eta-\cos\theta} \\ -\sin\psi & \cos\psi & 0 \end{pmatrix} \begin{pmatrix} \hat{\mathbf{x}} \\ \hat{\mathbf{y}} \\ \hat{\mathbf{z}} \end{pmatrix}$$

$$\text{(A.24)}\qquad \begin{pmatrix} \hat{\mathbf{x}} \\ \hat{\mathbf{y}} \\ \hat{\mathbf{z}} \end{pmatrix} = \begin{pmatrix} -\frac{\sin\theta\cos\psi\sinh\eta}{\cosh\eta-\cos\theta} & \frac{(\cos\theta\cosh\eta-1)\cos\psi}{\cosh\eta-\cos\theta} & -\sin\psi \\ -\frac{\sin\theta\sin\psi\sinh\eta}{\cosh\eta-\cos\theta} & \frac{(\cos\theta\cosh\eta-1)\sin\psi}{\cosh\eta-\cos\theta} & \cos\psi \\ -\frac{\cos\theta\cosh\eta-1}{\cosh\eta-\cos\theta} & -\frac{\sin\theta\sinh\eta}{\cosh\eta-\cos\theta} & 0 \end{pmatrix} \begin{pmatrix} \hat{\mathbf{e}}_\eta \\ \hat{\mathbf{e}}_\theta \\ \hat{\mathbf{e}}_\psi \end{pmatrix}$$

- Gradient operator

$$\text{(A.25)}\qquad \boldsymbol{\nabla}\varphi=\frac{1}{c}(\cosh\eta-\cos\theta)\left[\hat{\mathbf{e}}_\eta\frac{\partial\varphi}{\partial\eta}+\hat{\mathbf{e}}_\theta\frac{\partial\varphi}{\partial\theta}+\frac{\hat{\mathbf{e}}_\psi}{\sin\theta}\frac{\partial\varphi}{\partial\psi}\right]$$

- the Laplace's equation

  Separated solution:

$$\text{(A.26)}\qquad \varphi=(\cosh\eta-\cos\theta)^{1/2}H(\eta)\Theta(\theta)\Psi(\psi)$$

Separated equation:

$$\text{(A.27)} \qquad \begin{cases} \dfrac{\mathrm{d}^2 H}{\mathrm{d}\eta^2} - \left(\dfrac{1}{4} + \alpha_2\right) H = 0 \\ \dfrac{\mathrm{d}^2 \Theta}{\mathrm{d}\theta^2} + \cot\theta \dfrac{\mathrm{d}\Theta}{\mathrm{d}\theta} + \left(\alpha_2 - \dfrac{\alpha_3}{\sin^2\theta}\right)\Theta = 0 \\ \dfrac{\mathrm{d}^2 \Psi}{\mathrm{d}\psi^2} + \alpha_3 \Psi = 0 \end{cases}$$

(1) when $\alpha_2 = n(n+1)$ and $\alpha_3 = m^2$

$$\text{(A.28)} \qquad \begin{cases} \dfrac{\mathrm{d}^2 H}{\mathrm{d}\eta^2} - \left(n + \dfrac{1}{2}\right)^2 H = 0 \\ (1-\xi^2)\dfrac{\mathrm{d}^2 \Theta}{\mathrm{d}\xi^2} - 2\xi \dfrac{\mathrm{d}\Theta}{\mathrm{d}\xi} + \left(n(n+1) - \dfrac{m^2}{1-\xi^2}\right)\Theta = 0 \\ \dfrac{\mathrm{d}^2 \Psi}{\mathrm{d}\psi^2} + m^2 \Psi = 0 \end{cases}$$

$$\text{(A.29)} \qquad \begin{cases} H = A e^{(n+\frac{1}{2})\eta} + B e^{-(n+\frac{1}{2})\eta} \\ \Theta = A \mathscr{P}_n^m(\cos\theta) + B \mathscr{Q}_n^m(\cos\theta) \\ \Psi = A \sin(m\psi) + B \cos(m\psi) \end{cases}$$

(2) when $\alpha_2 = n(n+1)$ and $\alpha_3 = 0$

$$\text{(A.30)} \qquad \begin{cases} \dfrac{\mathrm{d}^2 H}{\mathrm{d}\eta^2} - \left(n + \dfrac{1}{2}\right)^2 H = 0 \\ (1-\xi^2)\dfrac{\mathrm{d}^2 \Theta}{\mathrm{d}\xi^2} - 2\xi \dfrac{\mathrm{d}\Theta}{\mathrm{d}\xi} + \left(n(n+1) - \dfrac{m^2}{1-\xi^2}\right)\Theta = 0 \\ \dfrac{\mathrm{d}^2 \Psi}{\mathrm{d}\psi^2} = 0 \end{cases}$$

(A.31)
$$\begin{cases} H = Ae^{(n+\frac{1}{2})\eta} + Be^{-(n+\frac{1}{2})\eta} \\ \Theta = A\mathscr{P}_n(\cos\theta) + B\mathscr{Q}_n(\cos\theta) \\ \Psi = A + B\psi \end{cases}$$

(3) when $\alpha_2 = 0$ and $\alpha_3 = 0$

(A.32)
$$\begin{cases} \dfrac{\mathrm{d}^2 H}{\mathrm{d}\eta^2} - \dfrac{1}{4}H = 0 \\ (1-\xi^2)\dfrac{\mathrm{d}^2\Theta}{\mathrm{d}\xi^2} - 2\xi\dfrac{\mathrm{d}\Theta}{\mathrm{d}\xi} = 0 \\ \dfrac{\mathrm{d}^2\Psi}{\mathrm{d}\psi^2} = 0 \end{cases}$$

(A.33)
$$\begin{cases} H = Ae^{\frac{\eta}{2}} + Be^{-\frac{\eta}{2}} \\ \Theta = A + B\ln\cot(\theta/2) \\ \Psi = A + B\psi \end{cases}$$

- The general solution of Laplace's equation

(A.34)

$$\varphi(\eta,\theta,\psi) = (\cosh\eta - \cos\theta)^{\frac{1}{2}}$$
$$\sum_{n=1}^{\infty}\sum_{m=1}^{\infty}\left[A_n^m e^{(n+\frac{1}{2})\eta} + B_n^m e^{-(n+\frac{1}{2})\eta}\right]\left[C_n^m\mathscr{P}_n^m(\cos\theta) + D_n^m\mathscr{Q}_n^m(\cos\theta)\right]\left[E_n^m\sin(m\psi) + F_n^m\cos(m\psi)\right]$$
$$+\sum_{n=1}^{\infty}\left[A_n^0 e^{(n+\frac{1}{2})\eta} + B_n^0 e^{-(n+\frac{1}{2})\eta}\right]\left[C_n^0\mathscr{P}_n(\cos\theta) + D_n^0\mathscr{Q}_n(\cos\theta)\right]\left[E_n^0 + F_n^0\psi\right]$$
$$+\left[A_0^0 e^{\frac{\eta}{2}} + B_0^0 e^{-\frac{\eta}{2}}\right]\left[C_0^0 + D_0^0\ln\cot\left(\frac{\theta}{2}\right)\right]\left[E_0^0 + F_0^0\psi\right]$$

APPENDIX B

Stokesian Dynamics

This appendix compiles all Stokesian Dynamics (SD) related reference, which includes derivatives of Oseen tensors [Appx. B.1], single surface integrals of Oseen tensors [Appx. B.2], double surface integrals of Oseen tensors [Appx. B.3], explicit expressions of mobility tensors [Appx. B.4 and B.5].

B.1. Derivatives of Oseen tensors

B.1.1. Oseen tensor with even viscosity

In this section, the explicit expressions of stokeslet, rotlet, stresslet derived for even viscosity [Sec. 5.2] and their corresponding higher order derivatives are documented for reference.

B.1.1.1. Propagators.

$$J_{ij}(\mathbf{r}) = \frac{\delta_{ij}}{r} + \frac{r_i r_j}{r^3} \tag{B.1a}$$

$$R_{ij}(\mathbf{r}) = \frac{1}{2}\varepsilon_{ikl}\nabla_k J_{jl} = \epsilon_{ijk}\frac{r_k}{r^3} \tag{B.1b}$$

$$K_{ijk}(\mathbf{r}) = \frac{1}{2}\left[\nabla_k J_{ij}(\mathbf{r}) + \nabla_j J_{ik}(\mathbf{r})\right] = \frac{1}{r^3}\delta_{jk}r_i - \frac{3}{r^5}r_i r_j r_k \tag{B.1c}$$

B.1.1.2. Relevant derivatives.

$$\nabla_i r = \frac{r_i}{r} \tag{B.2a}$$

(B.2b) $$\nabla^2 r = \frac{2}{r}$$

(B.2c) $$\nabla_k J_{ij}(\mathbf{r}) = \frac{1}{r^3}\left(-\delta_{ij}r_k + \delta_{jk}r_i + \delta_{ki}r_j\right) - \frac{3}{r^5}r_i r_j r_k$$

(B.2d) $$\nabla_j J_{ij}(\mathbf{r}) = 0$$

(B.2e) $$\begin{aligned}\nabla_l \nabla_k J_{ij}(\mathbf{r}) = {} & \frac{1}{r^3}\left(-\delta_{ij}\delta_{kl} + \delta_{ik}\delta_{jl} + \delta_{jk}\delta_{il}\right) + \frac{15}{r^7}r_i r_j r_k r_l \\ & - \frac{3}{r^5}\left(-\delta_{ij}r_k r_l + \delta_{ik}r_j r_l + \delta_{jk}r_i r_l + \delta_{il}r_j r_k + \delta_{jl}r_i r_k + \delta_{kl}r_i r_j\right)\end{aligned}$$

(B.2f) $$\nabla_k R_{ij}(\mathbf{r}) = -\frac{1}{2}\varepsilon_{jmn}\nabla_k \nabla_m J_{in}(\mathbf{r})$$

(B.2g) $$\begin{aligned}\nabla_l K_{ijk}(\mathbf{r}) &= \frac{1}{2}\left(\nabla_l \nabla_k J_{ij}(\mathbf{r}) + \nabla_l \nabla_j J_{ik}(\mathbf{r})\right) \\ &= \frac{1}{r^3}\delta_{il}\delta_{jk} + \frac{15}{r^7}r_i r_j r_k r_l \\ &\quad - \frac{3}{r^5}\left(r_i \delta_{jk} r_l + r_i r_j \delta_{kl} + r_i \delta_{jl} r_k + \delta_{il} r_j r_k\right)\end{aligned}$$

(B.2h) $$\begin{aligned}\frac{1}{2}\left(\nabla_l K_{ijk} + \nabla_i K_{ljk}\right) &= \frac{1}{r^3}\delta_{il}\delta_{jk} + \frac{15}{r^7}r_i r_j r_k r_l - \frac{3}{r^5}\left(r_i \delta_{jk} r_l + \delta_{il} r_j r_k\right) \\ &\quad - \frac{3}{r^5}\left[\frac{1}{2}\left(r_i r_j \delta_{kl} + r_l r_j \delta_{ki}\right) + \frac{1}{2}\left(r_i \delta_{jl} r_k + r_l \delta_{ji} r_k\right)\right] \\ &= \frac{1}{2}\left(\nabla_l K_{ikj} + \nabla_i K_{lkj}\right)\end{aligned}$$

(B.2i) $$\frac{1}{2}\left(\nabla_i K_{ijk} + \nabla_i K_{ijk}\right) = \frac{1}{2}\left(\nabla_l K_{ijj} + \nabla_i K_{ljj}\right) = 0$$

(B.2j) $$\nabla^2 J_{ij}(\mathbf{r}) = \frac{2\delta_{ij}}{r^3} - \frac{6r_i r_j}{r^5}$$

(B.2k) $$\nabla_k \nabla^2 J_{ij}(\mathbf{r}) = -\frac{6}{r^5}\left(\delta_{ij}r_k + \delta_{jk}r_i + \delta_{ki}r_j\right) + \frac{30}{r^7} r_i r_j r_k$$

(B.2l) $$\nabla^2 R_{ij}(\mathbf{r}) = -\frac{1}{2}\varepsilon_{jkl}\nabla_k \nabla^2 J_{il}(\mathbf{r}) = 0$$

(B.2m) $$\nabla^2 K_{ijk}(\mathbf{r}) = \nabla_k \nabla^2 J_{ij}(\mathbf{r})$$

(B.2n)
$$\begin{aligned}\nabla_l \nabla^2 K_{ijk}(\mathbf{r}) &= \nabla_l \nabla_k \nabla^2 J_{ij}(\mathbf{r}) \\ &= -\frac{6}{r^5}\left(\delta_{ij}\delta_{kl} + \delta_{jk}\delta_{il} + \delta_{ki}\delta_{jl}\right) - \frac{210}{r^9} r_i r_j r_k r_l \\ &\quad + \frac{30}{r^7}\left(\delta_{ij}r_k r_l + \delta_{jk}r_i r_l + \delta_{ki}r_j r_l + \delta_{il}r_j r_k + \delta_{jl}r_i r_k + \delta_{kl}r_i r_j\right)\end{aligned}$$

(B.2o) $$\frac{1}{2}\left(\nabla_l \nabla^2 K_{ijk} + \nabla_i \nabla^2 K_{ljk}\right) = \nabla_l \nabla^2 K_{ijk}$$

(B.2p) $$\nabla^4 J_{ij}(\mathbf{r}) = 0$$

B.1.2. Oseen tensor with odd viscosity

In this section, the explicit expressions of stokeslet, rotlet, stresslet derived for odd viscosity [Sec. 6.3] and their corresponding higher order derivatives are documented for reference.

B.1.2.1. Propagators.

(B.3a)

$$J^o_{ij}(\mathbf{r}) = \varepsilon_{ijk}\delta_{l3}J^s_{kl}(\mathbf{r}) = \frac{\varepsilon_{ij3}}{r} - \frac{\varepsilon_{ijk}r_k r_3}{r^3}, \quad J^s_{ij}(\mathbf{r}) = \frac{\delta_{ij}}{r} - \frac{r_i r_j}{r^3}$$

(B.3b)

$$R^o_{ij}(\mathbf{r}) = \frac{1}{2}\varepsilon_{ikl}\nabla_k J^o_{jl} = R^s_{ijk}(\mathbf{r})\delta_{k3}, \quad R^s_{ijk}(\mathbf{r}) = \frac{1}{2}\left[\nabla_j J^s_{ik}(\mathbf{r}) - \delta_{ij}\nabla_l J^s_{kl}(\mathbf{r})\right]$$

(B.3c)

$$K^o_{ijk}(\mathbf{r}) = \frac{1}{2}\left[\nabla_k J^o_{ij}(\mathbf{r}) + \nabla_j J^o_{ik}(\mathbf{r})\right] = K^s_{ijkl}(\mathbf{r})\delta_{l3}, \quad K^s_{ijkl}(\mathbf{r}) = \frac{1}{2}\left[\varepsilon_{ijm}\nabla_k J^s_{ml}(\mathbf{r}) + \varepsilon_{ikm}\nabla_j J^s_{ml}(\mathbf{r})\right]$$

B.1.2.2. Relevant derivatives.

(B.4a) $$\nabla_k J^o_{ij}(\mathbf{r}) = \varepsilon_{ijl}\delta_{m3}\nabla_k J^s_{lm}(\mathbf{r}), \quad \nabla_k J^s_{ij}(\mathbf{r}) = -\frac{1}{r^3}\left(\delta_{ij}r_k + \delta_{ki}r_j + \delta_{jk}r_i\right) + \frac{3}{r^5}r_i r_j r_k$$

(B.4b) $$\nabla_j J^o_{ij}(\mathbf{r}) = 0, \quad \nabla_j J^s_{ij}(\mathbf{r}) = -\frac{2r_i}{r^3}$$

(B.4c)
$$\begin{aligned}\nabla_l\nabla_k J^s_{ij}(\mathbf{r}) = &-\frac{1}{r^3}\left(\delta_{ij}\delta_{kl} + \delta_{ik}\delta_{jl} + \delta_{jk}\delta_{il}\right) - \frac{15}{r^7}r_i r_j r_k r_l \\ &+ \frac{3}{r^5}\left(\delta_{ij}r_k r_l + \delta_{ik}r_j r_l + \delta_{jk}r_i r_l + \delta_{il}r_j r_k + \delta_{jl}r_i r_k + \delta_{kl}r_i r_j\right)\end{aligned}$$

(B.4d) $$\nabla^2 J^o_{ij}(\mathbf{r}) = -\frac{2}{r^3}\varepsilon_{ij3} + 6\frac{\varepsilon_{ijk}r_k r_3}{r^5}, \quad \nabla^2 J^s_{ij}(\mathbf{r}) = -\frac{2}{r^3}\delta_{ij} + \frac{6r_i r_j}{r^5}$$

(B.4e) $$\nabla_k\nabla^2 J^s_{ij}(\mathbf{r}) = \frac{6}{r^5}\left(\delta_{ij}r_k + \delta_{jk}r_i + \delta_{ki}r_j\right) - \frac{30}{r^7}r_i r_j r_k$$

(B.4f) $$\nabla_j \nabla^2 J^s_{ij}(\mathbf{r}) = 0$$

(B.4g) $$\nabla_j \nabla_k J^s_{ik}(\mathbf{r}) = -\frac{2\delta_{ij}}{r^3} + \frac{6 r_i r_j}{r^5}$$

(B.4h) $$\begin{aligned}\nabla_l \nabla_k \nabla^2 J^s_{ij}(\mathbf{r}) = {} & \frac{6}{r^5}\left(\delta_{ij}\delta_{kl} + \delta_{il}\delta_{jk} + \delta_{ik}\delta_{jl}\right) + \frac{210}{r^9} r_i r_j r_k r_l \\ & - \frac{30}{r^7}\left(\delta_{ij} r_k r_l + \delta_{kl} r_i r_j + \delta_{jk} r_i r_l + \delta_{jl} r_i r_k + \delta_{ik} r_j r_l + \delta_{il} r_j r_k\right)\end{aligned}$$

(B.4i) $$R^o_{ij}(\mathbf{r}) = R^s_{ijk}(\mathbf{r})\delta_{k3}, \quad R^s_{ijk}(\mathbf{r}) = \frac{1}{2r^3}\left(\delta_{ij} r_k - \delta_{ki} r_j - \delta_{jk} r_i\right) + \frac{3}{2r^5} r_i r_j r_k$$

(B.4j) $$\begin{aligned}\nabla_l R^s_{ijk}(\mathbf{r}) = {} & -\frac{1}{2r^3}\left(-\delta_{ij}\delta_{kl} + \delta_{ik}\delta_{jl} + \delta_{jk}\delta_{il}\right) - \frac{15}{2r^7} r_i r_j r_k r_l \\ & + \frac{3}{2r^5}\left(-\delta_{ij} r_k r_l + \delta_{ik} r_j r_l + \delta_{jk} r_i r_l + \delta_{il} r_j r_k + \delta_{jl} r_i r_k + \delta_{kl} r_i r_j\right)\end{aligned}$$

(B.4k) $$\varepsilon_{ilm}\nabla_l R^s_{mjk}(\mathbf{r}) = -\frac{1}{r^3}\varepsilon_{ijk} + \frac{3}{r^5}\varepsilon_{ijl} r_l r_k$$

(B.4l) $$\nabla^2 R^s_{ijk}(\mathbf{r}) = \frac{1}{2}\nabla_j \nabla^2 J^s_{ik}(\mathbf{r})$$

(B.4m)
$$\begin{aligned}K^s_{ijkl}(\mathbf{r}) &= \frac{1}{2}\left[\varepsilon_{ijm}\nabla_k J^s_{ml}(\mathbf{r}) + \varepsilon_{ikm}\nabla_j J^s_{ml}(\mathbf{r})\right] \\ &= -\frac{1}{2r^3}\left(\varepsilon_{ijl} r_k + \varepsilon_{ikl} r_j\right) - \frac{1}{2r^3}\left(\varepsilon_{ijm}\delta_{kl} + \varepsilon_{ikm}\delta_{lj}\right) r_m + \frac{3}{2r^5}\left(\varepsilon_{ijm} r_k + \varepsilon_{ikm} r_j\right) r_m r_l\end{aligned}$$

$$\begin{aligned}\nabla_m K^s_{ijkl}(\mathbf{r}) &= \frac{1}{2}\left[\varepsilon_{ijn}\nabla_m\nabla_k J^s_{nl}(\mathbf{r}) + \varepsilon_{ikn}\nabla_m\nabla_j J^s_{nl}(\mathbf{r})\right] \\ &= -\frac{1}{2r^3}\left[\left(\varepsilon_{ijl}\delta_{km} + \varepsilon_{ikl}\delta_{jm}\right) + \left(\varepsilon_{ijm}\delta_{lk} + \varepsilon_{ikm}\delta_{lj}\right)\right] \\ &- \frac{15}{2r^7}\left(\varepsilon_{ijn}r_n r_k + \varepsilon_{ikn}r_n r_j\right) r_l r_m \\ &+ \frac{3}{2r^5}\left[\left(\varepsilon_{ijl}r_k r_m + \varepsilon_{ikl}r_j r_m\right) + \left(\varepsilon_{ijm}r_l r_k + \varepsilon_{ikm}r_l r_j\right)\right. \\ &\left.+\varepsilon_{ijn}r_n\left(\delta_{kl}r_m + \delta_{km}r_l + \delta_{ml}r_k\right) + \varepsilon_{ikn}r_n\left(\delta_{jl}r_m + \delta_{jm}r_l + \delta_{ml}r_j\right)\right]\end{aligned} \tag{B.4n}$$

$$\begin{aligned}\varepsilon_{imn}\nabla_m K^s_{njkl}(\mathbf{r}) &= \frac{1}{2}\left(\delta_{ij}\nabla_k + \delta_{ik}\nabla_j\right)\nabla_m J^s_{ml}(\mathbf{r}) - \nabla_k\nabla_j J^s_{il}(\mathbf{r}) \\ &= \frac{1}{r^3}\delta_{il}\delta_{kj} + \frac{15}{r^7}r_i r_j r_k r_l - \frac{3}{r^5}\left(\delta_{il}r_k r_j + \delta_{kl}r_i r_j + \delta_{jl}r_i r_k + \delta_{jk}r_i r_l\right)\end{aligned} \tag{B.4o}$$

$$\begin{aligned}\nabla^2 K^s_{ijkl}(\mathbf{r}) &= \frac{1}{2}\left[\varepsilon_{ijm}\nabla_k\nabla^2 J^s_{ml}(\mathbf{r}) + \varepsilon_{ikm}\nabla_j\nabla^2 J^s_{ml}(\mathbf{r})\right] \\ &= \frac{3}{r^5}\left(\varepsilon_{ijl}r_k + \varepsilon_{ikl}r_j\right) + \frac{3}{r^5}\left(\varepsilon_{ijm}\delta_{kl} + \varepsilon_{ikm}\delta_{jl}\right) r_m - \frac{15}{r^7}\left(\varepsilon_{ijm}r_k + \varepsilon_{ikm}r_j\right) r_m r_l\end{aligned} \tag{B.4p}$$

$$\begin{aligned}\nabla_m\nabla^2 K^s_{ijkl}(\mathbf{r}) &= \frac{1}{2}\left[\varepsilon_{ijn}\nabla_m\nabla_k\nabla^2 J^s_{nl}(\mathbf{r}) + \varepsilon_{ikn}\nabla_m\nabla_j\nabla^2 J^s_{nl}(\mathbf{r})\right] \\ &= -\frac{3}{r^5}\left[\left(\varepsilon_{ijl}\delta_{km} + \varepsilon_{ikl}\delta_{jm}\right) + \left(\varepsilon_{ijm}\delta_{lk} + \varepsilon_{ikm}\delta_{lj}\right)\right] \\ &- \frac{105}{r^9}\left(\varepsilon_{ijn}r_n r_k + \varepsilon_{ikn}r_n r_j\right) r_l r_m \\ &+ \frac{15}{r^7}\left[\left(\varepsilon_{ijl}r_k r_m + \varepsilon_{ikl}r_j r_m\right) + \left(\varepsilon_{ijm}r_l r_k + \varepsilon_{ikm}r_l r_j\right)\right. \\ &\left.+\varepsilon_{ijn}r_n\left(\delta_{kl}r_m + \delta_{km}r_l + \delta_{ml}r_k\right) + \varepsilon_{ikn}r_n\left(\delta_{jl}r_m + \delta_{jm}r_l + \delta_{ml}r_j\right)\right]\end{aligned} \tag{B.4q}$$

$$\varepsilon_{imn}\nabla_m\nabla^2 K^s_{njkl}(\mathbf{r}) = -\nabla_j\nabla_k\nabla^2 J_{il}(\mathbf{r}) \tag{B.4r}$$

(B.4s) $$\nabla^4 J^o_{ij}(\mathbf{r}) = 0$$

B.2. Single surface integrals of Oseen tensors

This section documents single spherical surface integrals of both the even and odd Oseen tensor, which are useful for deriving the near-field mobility tensors [Sec. 5.2.6 and 6.3.7] by the Rotne-Prager-Yamakawa (RPY) approximation. As shown in Fig. B.1, the center of β-th ($\beta = 1 \cdots N$) particle is set as the origin of the Cartesian coordinate system (x, y, z) and also the origin of the spherical coordinate system (r, θ, ϕ). Then, any arbitrary position at the spherical surface can be written as $\mathbf{y} = a\hat{\mathbf{n}}$, where a is the particle radius and $\hat{\mathbf{n}} = (\sin\theta\cos\phi, \sin\theta\sin\phi, \cos\theta)$ is the outer unit surface normal vector. Without loss of generality, the observation point is assumed to be along the z-axis, i.e. $\mathbf{x} = (0, 0, \rho)$. Therefore, the relative position vector $\mathbf{r} = \mathbf{x} - \mathbf{y} = (-a\sin\theta\cos\phi, -a\sin\theta\sin\phi, \rho - a\cos\theta)$ and relative distance $r = |\mathbf{r}| = \sqrt{a^2 + \rho^2 - 2a\rho\cos\theta}$. For simplicity, following results are evaluated for $\mathbf{x}$ along z-axis only but the general results can be easily obtained by permutation as long as each axis is equivalent.

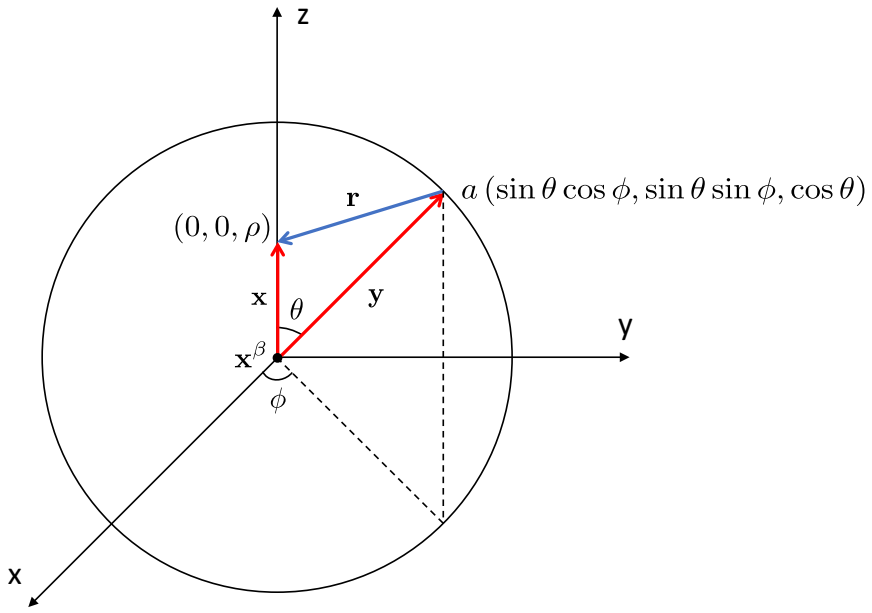

Figure B.1. A schematic drawing defines the coordinate system and notations for single spherical surface integral evaluations.

B.2.1. Single surface integrals of the even Oseen tensor

B.2.1.1. Propagators. Corresponding propagators used in the surface integral evaluations are [Sec. 5.2.6]:

(B.5a) $$\widetilde{J}_{ij}(\mathbf{r}) = \frac{\delta_{ij}}{r} + \frac{r_i r_j}{r^3}$$

(B.5b) $$\widetilde{R}_{ij}(\mathbf{r}) = J_{ik}(\mathbf{r})\varepsilon_{kjl}n_l$$

(B.5c) $$\widetilde{K}_{ijk}(\mathbf{r}) = \frac{1}{2}\left[J_{ij}(\mathbf{r})n_k + J_{ik}(\mathbf{r})n_j\right]$$

B.2.1.2. Single surface integrals. Here, single spherical surface integrals of the stokeslet, rotlet and stresslet are calculated:

(1) surface integral of stokeslet

(B.6a)
$$\hat{M}_{ij}^{F}(\rho\hat{\mathbf{z}}) = \frac{a}{4\pi a^2}\oint_{S^\beta}\widetilde{J}_{ij}(\rho\hat{\mathbf{z}}-\mathbf{y})\mathrm{d}S(\mathbf{y}) = \begin{cases} \left(\frac{1}{\rho}+\frac{1}{3}\frac{1}{\rho^3}\right)\delta_{ij}+\left(\frac{1}{\rho}-\frac{1}{\rho^3}\right)\delta_{i3}\delta_{j3} & \rho > a \\ \frac{4}{3}\delta_{ij} & \rho \le a \end{cases}$$

(B.6b)
$$\hat{M}_{ij}^{F}(\rho\hat{\mathbf{z}}) \overset{\text{sym}}{=} \hat{M}_{ij}^{F}(\mathbf{x}) = \begin{cases} \left(\frac{1}{r}+\frac{1}{3}\frac{1}{r^3}\right)\delta_{ij}+\left(\frac{1}{r}-\frac{1}{r^3}\right)\frac{r_i r_j}{r^2} = \left(1+\frac{1}{6}\nabla^2\right)J_{ij}(\mathbf{x}-\mathbf{x}^\beta) & \left|\mathbf{x}-\mathbf{x}^\beta\right| > a \\ \frac{4}{3}\delta_{ij} & \left|\mathbf{x}-\mathbf{x}^\beta\right| \le a \end{cases}$$

(2) surface integral of rotlet

(B.7a)
$$\hat{M}_{ij}^{T}(\rho\hat{\mathbf{z}}) = \frac{3a^2}{8\pi a^3}\oint_{S}\widetilde{R}_{ij}(\rho\hat{\mathbf{z}}-\mathbf{y})\mathrm{d}S(\mathbf{y}) = \begin{cases} \frac{1}{\rho^2} & \rho > a \\ \rho\varepsilon_{ij3} & \rho \le a \end{cases}$$

(B.7b)
$$\hat{M}_{ij}^{T}(\rho\hat{\mathbf{z}}) \overset{\text{sym}}{=} \hat{M}_{ij}^{T}(\mathbf{x}) = \begin{cases} \varepsilon_{ijk}\frac{r_k}{r^3} = R_{ij}(\mathbf{x}-\mathbf{x}^\beta) & \left|\mathbf{x}-\mathbf{x}^\beta\right| > a \\ \varepsilon_{ijk}r_k & \left|\mathbf{x}-\mathbf{x}^\beta\right| \le a \end{cases}$$

(3) surface integral of stresslet

$$\hat{M}_{ijk}^{S}(\rho\hat{\mathbf{z}}) = \frac{3a^2}{4\pi a^3}\oint_{S}\widetilde{K}_{ijk}(\mathbf{x}-\mathbf{y})\mathrm{d}S(\mathbf{y})$$

(B.8a)
$$= \begin{cases} \frac{6}{5}\frac{1}{\rho^4}\delta_{3ijk}-(\frac{1}{\rho^2}-\frac{1}{\rho^4})\delta_{i3}\delta_{jk}+3\left(\frac{1}{\rho^2}-\frac{1}{\rho^4}\right)\delta_{i3}\delta_{j3}\delta_{k3} & \rho > a \\ \frac{6}{5}\rho\delta_{3ijk} & \rho \le a \end{cases}$$

(B.8b)

$$\hat{M}^S_{ijk}(\rho\hat{\mathbf{z}}) \overset{\text{sym}}{=} \hat{M}^S_{ijk}(\mathbf{x}) = \begin{cases} \frac{6}{5}\frac{1}{r^4}\frac{r_l}{r}\delta_{lijk} - \left(1-\frac{1}{r^2}\right)\frac{1}{r^2}\frac{r_i}{r}\delta_{jk} + 3\left(1-\frac{1}{r^2}\right)\frac{1}{r^2}\frac{r_i r_j r_k}{r^3} & \left|\mathbf{x}-\mathbf{x}^\beta\right| > a \\ \frac{6}{5} r_l \delta_{lijk} & \left|\mathbf{x}-\mathbf{x}^\beta\right| \leq a \end{cases}$$

$$= \begin{cases} -\left(1+\frac{1}{10}\nabla^2\right) K_{ijk}(\mathbf{x}-\mathbf{x}^\beta) & \left|\mathbf{x}-\mathbf{x}^\beta\right| > a \\ \frac{6}{5} r_l \delta_{lijk} & \left|\mathbf{x}-\mathbf{x}^\beta\right| \leq a \end{cases}$$

B.2.2. Single surface integrals of the odd Oseen tensor

B.2.2.1. Propagators. Corresponding propagators used in the surface integral evaluations are [Sec. 6.3.7]:

(B.9a)

$$\widetilde{J}^o_{ij}(\mathbf{r}) = \varepsilon_{ijk}\delta_{l3} J^s_{kl}(\mathbf{r}), \quad J^s_{ij}(\mathbf{r}) = \frac{\delta_{ij}}{r} - \frac{r_i r_j}{r^3}$$

(B.9b)

$$\widetilde{R}^o_{ij}(\mathbf{r}) = J^o_{ik}\varepsilon_{kjl} n_l = \widetilde{R}^s_{ijk}(\mathbf{r})\delta_{k3}, \quad \widetilde{R}^s_{ijk}(\mathbf{r}) = n_i J^s_{jk}(\mathbf{r}) - \delta_{ij} J^s_{lk}(\mathbf{r}) n_l$$

(B.9c)

$$\widetilde{K}^o_{ijk}(\mathbf{r}) = \frac{1}{2}\left[J^o_{ij}(\mathbf{r})n_k + J^o_{ik}(\mathbf{r})n_j\right] = \widetilde{K}^s_{ijkl}(\mathbf{r})\delta_{l3}, \quad \widetilde{K}^s_{ijkl}(\mathbf{r}) = \frac{1}{2}\left[\varepsilon_{ijm} J^s_{ml}(\mathbf{r}) n_k + \varepsilon_{ikm} J^s_{ml}(\mathbf{r}) n_j\right]$$

B.2.2.2. Single surface integrals. Here, single spherical surface integrals of the stokeslet, rotlet and stresslet are calculated:

(1) surface integral of stokeslet

(B.10a)
$$\hat{M}^s_{Fij}(\rho\hat{\mathbf{z}}) = \frac{a}{4\pi a^2}\oint_{S^\beta} \widetilde{J}^s_{ij}(\rho\hat{\mathbf{z}}-\mathbf{y})\mathrm{d}S(\mathbf{y}) = \begin{cases} \left(\frac{1}{\rho}-\frac{1}{3}\frac{1}{\rho^3}\right)\delta_{ij} - \left(\frac{1}{\rho}-\frac{1}{\rho^3}\right)\delta_{i3}\delta_{j3} & \rho > a \\ \frac{2}{3}\delta_{ij} & \rho \le a \end{cases}$$

(B.10b)
$$\hat{M}^s_{Fij}(\rho\hat{\mathbf{z}}) \overset{\text{sym}}{=} \hat{M}^s_{Fij}(\mathbf{x}) = \begin{cases} \left(\frac{1}{r}-\frac{1}{3}\frac{1}{r^3}\right)\delta_{ij} - \left(\frac{1}{r}-\frac{1}{r^3}\right)\frac{r_i r_j}{r^2} & \left|\mathbf{x}-\mathbf{x}^\beta\right| > a \\ \frac{2}{3}\delta_{ij} & \left|\mathbf{x}-\mathbf{x}^\beta\right| \le a \end{cases}$$

(B.10c)
$$\begin{aligned} \hat{M}^o_{Fij}(\mathbf{x}) &= \varepsilon_{ijk}\delta_{l3}\hat{M}^s_{Fkl}(\mathbf{x}) \\ &= \begin{cases} \left(\frac{1}{r}-\frac{1}{3}\frac{1}{r^3}\right)\varepsilon_{ij3} - \left(\frac{1}{r}-\frac{1}{r^3}\right)\varepsilon_{ijk}\frac{r_k r_3}{r^2} & \left|\mathbf{x}-\mathbf{x}^\beta\right| > a \\ \frac{2}{3}\varepsilon_{ij3} & \left|\mathbf{x}-\mathbf{x}^\beta\right| \le a \end{cases} \\ &= \begin{cases} \left(1+\frac{1}{6}\nabla^2\right) J^o_{ij}(\mathbf{x}-\mathbf{x}^\beta) & \left|\mathbf{x}-\mathbf{x}^\beta\right| > a \\ \frac{2}{3}\varepsilon_{ij3} & \left|\mathbf{x}-\mathbf{x}^\beta\right| \le a \end{cases} \end{aligned}$$

(2) surface integral of rotlet

(B.11a)
$$\begin{aligned} \hat{M}^s_{Tijk}(\rho\hat{\mathbf{z}}) &= \frac{3a^2}{8\pi a^3}\oint_{S^\beta} \widetilde{R}^s_{ijk}(\rho\hat{\mathbf{z}}-\mathbf{y})\mathrm{d}S(\mathbf{y}) \\ &= \begin{cases} \frac{3}{10}\left(\frac{3}{\rho^2}-5\right)\frac{\delta_{3ijk}}{\rho^2} - \frac{1}{4}\left(\frac{3}{\rho^2}-1\right)\frac{\delta_{ij}\delta_{k3}}{\rho^2} \\ -\frac{1}{4}\left(\frac{3}{\rho^2}-5\right)\frac{\delta_{ik}\delta_{j3}}{\rho^2} + \frac{3}{2}\left(\frac{1}{\rho^2}-1\right)\frac{\delta_{i3}\delta_{j3}\delta_{k3}}{\rho^2} & \rho > a \\ -\frac{3}{5}\rho\delta_{3ijk} - \frac{1}{2}\rho\delta_{ij}\delta_{k3} + \frac{1}{2}\rho\delta_{ik}\delta_{j3} & \rho \le a \end{cases} \end{aligned}$$

$$\hat{M}^s_{Tijk}(\rho\hat{\mathbf{z}}) \overset{\text{sym}}{=} \hat{M}^s_{Tijk}(\mathbf{x})$$

(B.11b)
$$= \begin{cases} \frac{3}{10}\left(\frac{3}{r^2}-5\right)\frac{r_l\delta_{lijk}}{r^3} - \frac{1}{4}\left(\frac{3}{r^2}-1\right)\frac{\delta_{ij}r_k}{r^3} & \\ -\frac{1}{4}\left(\frac{3}{r^2}-5\right)\frac{\delta_{ik}r_j}{r^3} + \frac{3}{2}\left(\frac{1}{r^2}-1\right)\frac{r_ir_jr_k}{r^5} & \left|\mathbf{x}-\mathbf{x}^\beta\right| > a \\ -\frac{3}{5}r_l\delta_{lijk} - \frac{1}{2}\delta_{ij}r_k + \frac{1}{2}\delta_{ik}r_j & \left|\mathbf{x}-\mathbf{x}^\beta\right| \le a \end{cases}$$

$$\hat{M}^o_{Tij}(\mathbf{x}) = \hat{M}^s_{Tijk}(\mathbf{x})\delta_{k3}$$

(B.11c)
$$= \begin{cases} \frac{3}{10}\left(\frac{3}{r^2}-5\right)\frac{r_l\delta_{lij3}}{r^3} - \frac{1}{4}\left(\frac{3}{r^2}-1\right)\frac{\delta_{ij}r_3}{r^3} & \\ -\frac{1}{4}\left(\frac{3}{r^2}-5\right)\frac{\delta_{i3}r_j}{r^3} + \frac{3}{2}\left(\frac{1}{r^2}-1\right)\frac{r_ir_jr_3}{r^5} & \left|\mathbf{x}-\mathbf{x}^\beta\right| > a \\ -\frac{3}{5}r_l\delta_{lij3} - \frac{1}{2}\delta_{ij}r_3 + \frac{1}{2}\delta_{i3}r_j & \left|\mathbf{x}-\mathbf{x}^\beta\right| \le a \end{cases}$$

$$= \begin{cases} -\left(1+\frac{1}{10}\nabla^2\right)R^o_{ij}(\mathbf{x}-\mathbf{x}^\beta) & \left|\mathbf{x}-\mathbf{x}^\beta\right| > a \\ -\frac{3}{5}r_l\delta_{lij3} - \frac{1}{2}\delta_{ij}r_3 + \frac{1}{2}\delta_{i3}r_j & \left|\mathbf{x}-\mathbf{x}^\beta\right| \le a \end{cases}$$

(3) surface integral of stresslet

$$\hat{M}^s_{Sijkl}(\rho\hat{\mathbf{z}}) = \frac{3a^2}{4\pi a^3}\oint_{S^\beta}\widetilde{K}^s_{ijkl}(\mathbf{x}-\mathbf{y})\mathrm{d}S(\mathbf{y})$$

(B.12a)
$$= \begin{cases} \frac{1}{2\rho^2}\left(1-\frac{3}{5}\frac{1}{\rho^2}\right)\left[\left(\varepsilon_{ijl}\delta_{k3}+\varepsilon_{ikl}\delta_{j3}\right)+\left(\varepsilon_{ij3}\delta_{kl}+\varepsilon_{ik3}\delta_{jl}\right)\right] & \\ +\frac{3}{2\rho^2}\left(\frac{1}{\rho^2}-1\right)\left(\varepsilon_{ij3}\delta_{k3}+\varepsilon_{ik3}\delta_{j3}\right)\delta_{l3} & \rho > a \\ \frac{\rho}{5}\left[\left(\varepsilon_{ijl}\delta_{k3}+\varepsilon_{ikl}\delta_{j3}\right)+\left(\varepsilon_{ij3}\delta_{kl}+\varepsilon_{ik3}\delta_{jl}\right)\right] & \rho \le a \end{cases}$$

(B.12b)

$$\hat{M}^s_{Sijkl}(\rho\hat{\mathbf{z}}) \overset{\text{sym}}{=} \hat{M}^s_{Sijkl}(\mathbf{x})$$

$$= \begin{cases} \frac{1}{2r^3}\left(1-\frac{3}{5}\frac{1}{r^2}\right)\left[\left(\varepsilon_{ijl}r_k+\varepsilon_{ikl}r_j\right)+\left(\varepsilon_{ijm}\delta_{kl}+\varepsilon_{ikm}\delta_{jl}\right)r_m\right] & \\ +\frac{3}{2r^5}\left(\frac{1}{r^2}-1\right)\left(\varepsilon_{ijm}r_k+\varepsilon_{ikm}r_j\right)r_m r_l & \left|\mathbf{x}-\mathbf{x}^\beta\right|>a \\ \frac{1}{5}\left[\left(\varepsilon_{ijl}r_k+\varepsilon_{ikl}r_j\right)+\left(\varepsilon_{ijm}\delta_{kl}+\varepsilon_{ikm}\delta_{jl}\right)r_m\right] & \left|\mathbf{x}-\mathbf{x}^\beta\right|\le a \end{cases}$$

(B.12c)

$$\hat{M}^o_{Sijk}(\mathbf{x}) = \hat{M}^s_{Sijkl}(\mathbf{x})\delta_{l3}$$

$$= \begin{cases} \frac{1}{2r^3}\left(1-\frac{3}{5}\frac{1}{r^2}\right)\left[\left(\varepsilon_{ij3}r_k+\varepsilon_{ik3}r_j\right)+\left(\varepsilon_{ijm}\delta_{k3}+\varepsilon_{ikm}\delta_{j3}\right)r_m\right] & \\ +\frac{3}{2r^5}\left(\frac{1}{r^2}-1\right)\left(\varepsilon_{ijm}r_k+\varepsilon_{ikm}r_j\right)r_3 & \left|\mathbf{x}-\mathbf{x}^\beta\right|>a \\ \frac{1}{5}\left[\left(\varepsilon_{ij3}r_k+\varepsilon_{ik3}r_j\right)+\left(\varepsilon_{ijm}\delta_{k3}+\varepsilon_{ikm}\delta_{j3}\right)r_m\right] & \left|\mathbf{x}-\mathbf{x}^\beta\right|\le a \end{cases}$$

$$= \begin{cases} -\left(1+\frac{1}{10}\nabla^2\right)K^o_{ijk}(\mathbf{x}-\mathbf{x}^\beta) & \left|\mathbf{x}-\mathbf{x}^\beta\right|>a \\ \frac{1}{5}\left[\left(\varepsilon_{ij3}r_k+\varepsilon_{ik3}r_j\right)+\left(\varepsilon_{ijm}\delta_{k3}+\varepsilon_{ikm}\delta_{j3}\right)r_m\right] & \left|\mathbf{x}-\mathbf{x}^\beta\right|\le a \end{cases}$$

B.3. Double surface integrals of Oseen tensors

This section documents double spherical surface integrals of both the even and odd Oseen tensor, which are useful for deriving the near-field mobility tensors [Sec. 5.2.6 and 6.3.7] by the Rotne-Prager-Yamakawa (RPY) approximation. As shown in Fig. B.2, the center of β-th ($\beta = 1 \cdots N$) particle $\mathbf{x}^\beta$ is set as the origin of the Cartesian coordinate system (x, y, z) and also the origin of the spherical coordinate system (r, θ, ϕ). Then, any

arbitrary position at the β-th spherical particle's surface can be written as $\mathbf{y} = a\hat{\mathbf{n}}$, where a is the particle radius and $\hat{\mathbf{n}} = (\sin\theta\cos\phi, \sin\theta\sin\phi, \cos\theta)$ is the outer unit surface normal vector. Without loss of generality, the position of α-th particle is assumed to be along the z-axis, i.e. $\mathbf{x}^\alpha = (0, 0, \rho)$. Therefore, arbitrary position at α-th particle surface relative to the center of β-th particle is $\mathbf{r} = \mathbf{x} - \mathbf{x}^\beta = (a\sin\theta\cos\phi, a\sin\theta\sin\phi, \rho + a\cos\theta)$ and relative distance is $r = |\mathbf{r}| = \sqrt{a^2 + \rho^2 + 2a\rho\cos\theta}$. The critical polar angle used for distinguishing non-overlapping ($\theta < \theta_0$) and overlapping ($\theta > \theta_0$) regions is defined as $\theta_0 = \arccos\left(-\frac{\rho}{2a}\right)$. For simplicity, following results are evaluated for $\mathbf{x}^\alpha$ along z-axis only but the general results can be easily obtained by permutation as long as each axis is equivalent.

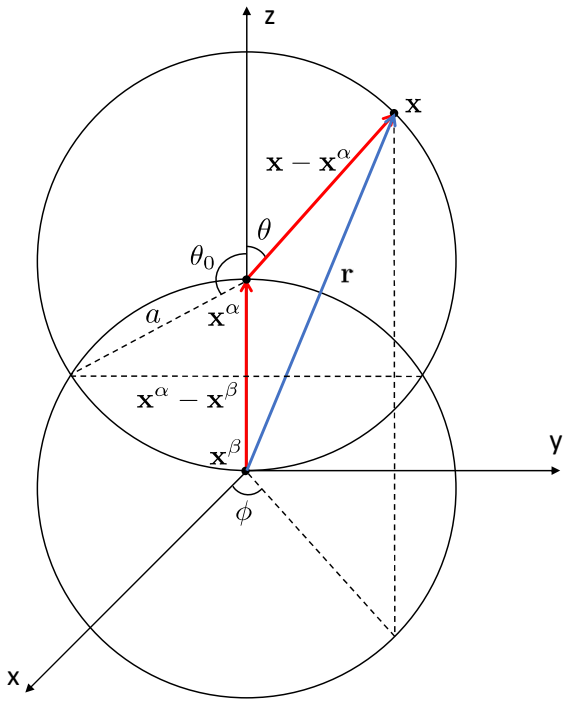

Figure B.2. A schematic drawing defines the coordinate system and notations for double spherical surface integral evaluations.

B.3.1. Double surface integrals of the even Oseen tensor

Note that the first surface integrals of the even Oseen tensor on the β-th particle surface have already been evaluated in Appx. B.2.1, the following calculations will only focus on the second surface integral on the α-th particle surface.

B.3.1.1. $\boldsymbol{M}_{UF}^{\alpha\beta}$.

$$\begin{aligned}\hat{M}_{UF}{}^{\alpha\beta}{}_{ij}(\rho\hat{\mathbf{z}}) &= \frac{a}{(4\pi a^2)^2}\oint_{S^\alpha}\oint_{S^\beta}\widetilde{J}_{ij}(\mathbf{x}-\mathbf{y})\mathrm{d}S^\alpha\mathrm{d}S^\beta = \frac{1}{4\pi a^2}\oint_{S^\alpha}\hat{M}^F_{ij}(\mathbf{x}-\mathbf{x}^\beta)\mathrm{d}S^\alpha \\ &= \left(\frac{4}{3}-\frac{3}{8}\rho\right)\delta_{ij}+\frac{1}{8}\rho\delta_{i3}\delta_{j3}, \quad \rho<2a\end{aligned} \tag{B.13}$$

$$\hat{M}_{UF}{}^{\alpha\beta}{}_{ij}(\rho\hat{\mathbf{z}}) \overset{\text{sym}}{=} \hat{M}_{UF}{}^{\alpha\beta}{}_{ij}(\mathbf{x}) = \left(\frac{4}{3}-\frac{3}{8}r\right)\delta_{ij}+\frac{1}{8}r\frac{r_i r_j}{r^2}, \quad \left|\mathbf{x}^\alpha-\mathbf{x}^\beta\right|\le 2a \tag{B.14}$$

(B.15)

$$\begin{aligned}\hat{M}_{UF}{}^{\alpha\beta}{}_{ij}(\mathbf{x}) &= \frac{1}{4\pi a^2}\oint_{S^\alpha}\hat{M}^F_{ij}(\mathbf{x}-\mathbf{x}^\beta)\mathrm{d}S^\alpha = \frac{a}{4\pi a^2}\oint_{S^\alpha}\left(1+\frac{1}{6}\nabla^2\right)J_{ij}(\mathbf{x}-\mathbf{x}^\beta)\mathrm{d}S^\alpha \\ &= \left(1+\frac{1}{6}\nabla^2\right)\frac{a}{4\pi a^2}\oint_{S^\alpha}\widetilde{J}_{ij}(\mathbf{x}-\mathbf{x}^\beta)\mathrm{d}S^\alpha \\ &= \left(1+\frac{1}{6}\nabla^2\right)\frac{a}{4\pi a^2}\oint_{S^\alpha}\widetilde{J}_{ij}(\mathbf{x}^\beta-\mathbf{x})\mathrm{d}S^\alpha \\ &= \left(1+\frac{1}{6}\nabla^2\right)\left(1+\frac{1}{6}\nabla^2\right)J_{ij}(\mathbf{x}^\alpha-\mathbf{x}^\beta), \quad \left|\mathbf{x}^\alpha-\mathbf{x}^\beta\right|>2a\end{aligned}$$

B.3.1.2. $\boldsymbol{M}_{UT}^{\alpha\beta}$.

(B.16)

$$\hat{M}_{UT}{}^{\alpha\beta}_{ij}(\rho\hat{\mathbf{z}}) = \frac{1}{4\pi a^2}\frac{3a^2}{8\pi a^3}\oint_{S^\alpha}\oint_{S^\beta}\widetilde{R}_{ij}(\mathbf{x}-\mathbf{y})\mathrm{d}S^\alpha\mathrm{d}S^\beta = \frac{1}{4\pi a^2}\oint_{S^\alpha}\hat{M}^T_{ij}(\mathbf{x}-\mathbf{x}^\beta)\mathrm{d}S^\alpha$$
$$= \left(\frac{1}{2}-\frac{3}{16}\rho\right)\rho\varepsilon_{ij3}, \quad \rho < 2a$$

(B.17)
$$\hat{M}_{UT}{}^{\alpha\beta}_{ij}(\rho\hat{\mathbf{z}}) \overset{\text{sym}}{=} \hat{M}_{UT}{}^{\alpha\beta}_{ij}(\mathbf{x}) = \left(\frac{1}{2}-\frac{3}{16}r\right)\varepsilon_{ijk}r_k, \quad \left|\mathbf{x}^\alpha-\mathbf{x}^\beta\right| \le 2a$$

(B.18)
$$\begin{aligned}
\hat{M}_{UT}{}^{\alpha\beta}_{ij}(\mathbf{x}) &= \frac{1}{4\pi a^2}\oint_{S^\alpha}\hat{M}^T_{ij}(\mathbf{x}-\mathbf{x}^\beta)\mathrm{d}S^\alpha = \frac{a^2}{4\pi a^2}\oint_{S^\alpha}R_{ij}(\mathbf{x}-\mathbf{x}^\beta)\mathrm{d}S^\alpha \\
&= \frac{a^2}{4\pi a^2}\oint_{S^\alpha}\frac{1}{2}\varepsilon_{ikl}\nabla_k J_{jl}(\mathbf{x}-\mathbf{x}^\beta)\mathrm{d}S^\alpha \\
&= \frac{1}{2}\varepsilon_{ikl}\nabla_k\frac{a^2}{4\pi a^2}\oint_{S^\alpha}\widetilde{J}_{jl}(\mathbf{x}^\beta-\mathbf{x})\mathrm{d}S^\alpha \\
&= \frac{1}{2}\varepsilon_{ikl}\nabla_k\left(1+\frac{1}{6}\nabla^2\right)J_{jl}(\mathbf{x}^\alpha-\mathbf{x}^\beta) \\
&= \left(1+\frac{1}{6}\nabla^2\right)R_{ij}(\mathbf{x}^\alpha-\mathbf{x}^\beta), \quad \left|\mathbf{x}^\alpha-\mathbf{x}^\beta\right| > 2a
\end{aligned}$$

B.3.1.3. $\boldsymbol{M}_{US}^{\alpha\beta}$.

(B.19)

$$\hat{M}_{US}{}^{\alpha\beta}_{ijk}(\rho\hat{\mathbf{z}}) = \frac{1}{4\pi a^2}\frac{3}{4\pi a^3}\oint_{S^\alpha}\oint_{S^\beta}\widetilde{K}_{ijk}(\mathbf{x}-\mathbf{y})\mathrm{d}S^\alpha\mathrm{d}S^\beta = -\frac{1}{4\pi a^2}\oint_{S^\alpha}\hat{M}^S_{ijk}(\mathbf{x}-\mathbf{x}^\beta)\mathrm{d}S^\alpha$$
$$= \left(\frac{3}{5}-\frac{\rho}{4}\right)\rho\delta_{3ijk} - \frac{\rho^2}{48}\delta_{i3}\delta_{jk} + \frac{\rho^2}{16}\delta_{i3}\delta_{j3}\delta_{k3}, \quad \rho < 2a$$

$$\hat{M}_{US}{}^{\alpha\beta}_{ijk}(\rho\hat{\mathbf{z}}) \overset{\text{sym}}{=} \hat{M}_{US}{}^{\alpha\beta}_{ijk}(\mathbf{x})$$
$$= \left(\frac{3}{5} - \frac{r}{4}\right) r_l \delta_{lijk} - \frac{r}{48} r_i \delta_{jk} + \frac{1}{16} \frac{r_i r_j r_k}{r}, \quad \left|\mathbf{x}^\alpha - \mathbf{x}^\beta\right| \leq 2a \tag{B.20}$$

(B.21)
$$\hat{M}_{US}{}^{\alpha\beta}_{ijk}(\mathbf{x}) = \frac{1}{4\pi a^2} \oint_{S^\alpha} \hat{M}^S_{ijk}(\mathbf{x} - \mathbf{x}^\beta) \mathrm{d}S^\alpha = -\frac{a^2}{4\pi a^2} \oint_{S^\alpha} \left(1 + \frac{1}{10}\nabla^2\right) K_{ijk}(\mathbf{x} - \mathbf{x}^\beta) \mathrm{d}S^\alpha$$
$$= -\left(1 + \frac{1}{10}\nabla^2\right) \frac{a^2}{4\pi a^2} \oint_{S^\alpha} K_{ijk}(\mathbf{x} - \mathbf{x}^\beta) \mathrm{d}S^\alpha$$
$$= \left(1 + \frac{1}{10}\nabla^2\right) \frac{a^2}{4\pi a^2} \oint_{S^\alpha} K_{ijk}(\mathbf{x}^\beta - \mathbf{x}) \mathrm{d}S^\alpha$$
$$= \left(1 + \frac{1}{10}\nabla^2\right) \frac{a^2}{4\pi a^2} \oint_{S^\alpha} \frac{1}{2} \left[\nabla_k J_{ij}(\mathbf{x}^\beta - \mathbf{x}) + \nabla_j J_{ik}(\mathbf{x}^\beta - \mathbf{x})\right] \mathrm{d}S^\alpha$$
$$= \left(1 + \frac{1}{10}\nabla^2\right) \left(1 + \frac{1}{6}\nabla^2\right) \frac{1}{2} \left[\nabla_k J_{ij}(\mathbf{x}^\beta - \mathbf{x}^\alpha) + \nabla_j J_{ik}(\mathbf{x}^\beta - \mathbf{x}^\alpha)\right]$$
$$= -\left(1 + \frac{1}{10}\nabla^2\right) \left(1 + \frac{1}{6}\nabla^2\right) K_{ijk}(\mathbf{x}^\alpha - \mathbf{x}^\beta), \quad \left|\mathbf{x}^\alpha - \mathbf{x}^\beta\right| > 2a$$

B.3.1.4. $\boldsymbol{M}^{\alpha\beta}_{\Omega T}$.

$$\hat{M}_{\Omega T}{}^{\alpha\beta}_{ij}(\rho\hat{\mathbf{z}}) = \left(\frac{3a}{8\pi a^3}\right)^2 \oint_{S^\alpha} \oint_{S^\beta} \varepsilon_{ikl} n_k \widetilde{R}_{lj}(\mathbf{x} - \mathbf{y}) \mathrm{d}S^\alpha \mathrm{d}S^\beta$$
$$= \frac{3}{8\pi a^3} \oint_{S^\alpha} \varepsilon_{ikl} n_k \hat{M}^T_{lj}(\mathbf{x} - \mathbf{x}^\beta) \mathrm{d}S^\alpha \tag{B.22}$$
$$= \left(1 - \frac{27}{32}\rho + \frac{5}{64}\rho^3\right) \delta_{ij} + \left(\frac{9}{32}\rho - \frac{3}{64}\rho^3\right) \delta_{i3}\delta_{j3}, \quad \rho < 2a$$

$$\hat{M}_{\Omega T}{}^{\alpha\beta}_{ij}(\rho\hat{\mathbf{z}}) \overset{\text{sym}}{=} \hat{M}_{\Omega T}{}^{\alpha\beta}_{ij}(\mathbf{x})$$
$$= \left(1 - \frac{27}{32}r + \frac{5}{64}r^3\right) \delta_{ij} + \left(\frac{9}{32}r - \frac{3}{64}r^3\right) \frac{r_i r_j}{r^2}, \quad \left|\mathbf{x}^\alpha - \mathbf{x}^\beta\right| \leq 2a \tag{B.23}$$

$$
\begin{aligned}
\hat{M}_{\Omega T}{}^{\alpha\beta}_{ij}(\mathbf{x}) &= \frac{3}{8\pi a^3}\oint_{S^\alpha}\varepsilon_{ikl}n_k\hat{M}^T_{lj}(\mathbf{x}-\mathbf{x}^\beta)\mathrm{d}S^\alpha = \frac{3a^2}{8\pi a^3}\oint_{S^\alpha}\varepsilon_{ikl}n_kR_{lj}(\mathbf{x}-\mathbf{x}^\beta)\mathrm{d}S^\alpha \\
&= \frac{3a^2}{8\pi a^3}\oint_{S^\alpha}\varepsilon_{ikl}n_k\left[\frac{1}{2}\varepsilon_{lmn}\nabla_m J_{jn}(\mathbf{x}-\mathbf{x}^\beta)\right]\mathrm{d}S^\alpha \\
&= \frac{1}{2}\varepsilon_{ikl}\nabla_m\frac{3a^2}{8\pi a^3}\oint_{S^\alpha}J_{jn}(\mathbf{x}-\mathbf{x}^\beta)\varepsilon_{nlm}n_k\mathrm{d}S^\alpha \\
&= \frac{1}{2}\varepsilon_{ikl}\nabla_k\frac{3a^2}{8\pi a^3}\oint_{S^\alpha}J_{jn}(\mathbf{x}^\beta-\mathbf{x})\varepsilon_{nlm}n_m\mathrm{d}S^\alpha \\
&= \frac{1}{2}\varepsilon_{ikl}\nabla_k\frac{3a^2}{8\pi a^3}\oint_{S^\alpha}\widetilde{R}_{jl}(\mathbf{x}^\beta-\mathbf{x})\mathrm{d}S^\alpha \\
&= \frac{1}{2}\varepsilon_{ikl}\nabla_kR_{jl}(\mathbf{x}^\beta-\mathbf{x}^\alpha) = \frac{1}{2}\varepsilon_{ikl}\nabla_kR_{lj}(\mathbf{x}^\alpha-\mathbf{x}^\beta), \quad \left|\mathbf{x}^\alpha-\mathbf{x}^\beta\right|>2a
\end{aligned}
\tag{B.24}
$$

B.3.1.5. $\boldsymbol{M}^{\alpha\beta}_{\Omega S}$.

$$
\begin{aligned}
\hat{M}_{\Omega S}{}^{\alpha\beta}_{ijk}(\rho\hat{\mathbf{z}}) &= \frac{3}{8\pi a^3}\frac{3a^2}{4\pi a^3}\oint_{S^\alpha}\oint_{S^\beta}\varepsilon_{ilm}n_l\widetilde{K}_{mjk}(\mathbf{x}-\mathbf{y})\mathrm{d}S^\alpha\mathrm{d}S^\beta \\
&= \frac{3}{8\pi a^3}\oint_{S^\alpha}\varepsilon_{ilm}n_l\hat{M}^S_{mjk}(\mathbf{x}-\mathbf{x}^\beta)\mathrm{d}S^\alpha \\
&= \left(\frac{9}{32}\rho-\frac{3}{64}\rho^3\right)\left(\varepsilon_{ij3}\delta_{k3}+\varepsilon_{ik3}\delta_{j3}\right), \quad \rho<2a
\end{aligned}
\tag{B.25}
$$

(B.26)

$$
\hat{M}_{\Omega S}{}^{\alpha\beta}_{ijk}(\rho\hat{\mathbf{z}}) \overset{\text{sym}}{=} \hat{M}_{\Omega S}{}^{\alpha\beta}_{ijk}(\mathbf{x}) = \left(\frac{9}{32}r-\frac{3}{64}r^3\right)\left(\varepsilon_{ijl}r_k+\varepsilon_{ikl}r_j\right)\frac{r_l}{r^2}, \quad \left|\mathbf{x}^\alpha-\mathbf{x}^\beta\right|\le 2a
$$

(B.27)

$$
\begin{aligned}
\hat{M}_{\Omega S}{}^{\alpha\beta}_{ijk}(\mathbf{x}) &= \frac{3}{8\pi a^3}\oint_{S^\alpha}\varepsilon_{ilm}n_l\hat{M}^S_{mjk}(\mathbf{x}-\mathbf{x}^\beta)\mathrm{d}S^\alpha \\
&= -\frac{3a^2}{8\pi a^3}\oint_{S^\alpha}\varepsilon_{ilm}n_l\left(1+\frac{1}{10}\nabla^2\right)K_{mjk}(\mathbf{x}-\mathbf{x}^\beta)\mathrm{d}S^\alpha \\
&= -\left(1+\frac{1}{10}\nabla^2\right)\frac{3a^2}{8\pi a^3}\oint_{S^\alpha}\varepsilon_{ilm}n_l\frac{1}{2}\left[\nabla_k J_{mj}(\mathbf{x}-\mathbf{x}^\beta)+\nabla_j J_{mk}(\mathbf{x}-\mathbf{x}^\beta)\right]\mathrm{d}S^\alpha \\
&= -\left(1+\frac{1}{10}\nabla^2\right)\frac{3a^2}{8\pi a^3}\oint_{S^\alpha}\frac{1}{2}\left[\nabla_k \widetilde{R}_{ji}(\mathbf{x}-\mathbf{x}^\beta)+\nabla_j \widetilde{R}_{ki}(\mathbf{x}-\mathbf{x}^\beta)\right]\mathrm{d}S^\alpha \\
&= -\left(1+\frac{1}{10}\nabla^2\right)\frac{1}{2}\left[\nabla_k R_{ij}(\mathbf{x}^\alpha-\mathbf{x}^\beta)+\nabla_j R_{ik}(\mathbf{x}^\alpha-\mathbf{x}^\beta)\right] \\
&= -\left(1+\frac{1}{10}\nabla^2\right)\frac{1}{2}\varepsilon_{ilm}\nabla_l\frac{1}{2}\left[\nabla_k J_{jm}(\mathbf{x}^\alpha-\mathbf{x}^\beta)+\nabla_j J_{km}(\mathbf{x}^\alpha-\mathbf{x}^\beta)\right] \\
&= -\frac{1}{2}\varepsilon_{ilm}\nabla_l\left(1+\frac{1}{10}\nabla^2\right)K_{mjk}(\mathbf{x}^\alpha-\mathbf{x}^\beta), \quad \left|\mathbf{x}^\alpha-\mathbf{x}^\beta\right|>2a
\end{aligned}
$$

B.3.1.6. $\boldsymbol{M}^{\alpha\beta}_{ES}$.

(B.28)

$$
\begin{aligned}
\hat{M}_{ES}{}^{\alpha\beta}_{ijkl}(\rho\hat{\mathbf{z}}) &= \left(\frac{3a}{4\pi a^3}\right)^2\oint_{S^\alpha}\oint_{S^\beta}\frac{1}{2}\left[\widetilde{K}_{ikl}(\mathbf{x}-\mathbf{y})n_j+\widetilde{K}_{jkl}(\mathbf{x}-\mathbf{y})n_i\right]\mathrm{d}S^\alpha\mathrm{d}S^\beta \\
&= \frac{3}{4\pi a^3}\oint_{S^\alpha}\frac{1}{2}\left[\hat{M}^S_{ikl}(\mathbf{x}-\mathbf{x}^\beta)n_j+\hat{M}^S_{jkl}(\mathbf{x}-\mathbf{x}^\beta)n_i\right]\mathrm{d}S^\alpha \\
&= \left(\frac{6}{5}-\frac{3}{4}\rho+\frac{3}{64}\rho^3\right)\delta_{ijkl}+\left(-\frac{1}{16}\rho+\frac{1}{128}\rho^3\right)\delta_{ij}\delta_{kl} \\
&+ \left(\frac{3}{16}\rho-\frac{3}{128}\rho^3\right)(\delta_{ij}\delta_{k3}\delta_{l3}+\delta_{kl}\delta_{i3}\delta_{j3}) \\
&+ \left(-\frac{3}{32}\rho+\frac{3}{128}\rho^3\right)(\delta_{ik}\delta_{j3}\delta_{l3}+\delta_{il}\delta_{j3}\delta_{k3}+\delta_{jk}\delta_{i3}\delta_{l3}+\delta_{jl}\delta_{i3}\delta_{k3}) \\
&- \left(\frac{3}{16}\rho-\frac{3}{128}\rho^3\right)\delta_{i3}\delta_{j3}\delta_{k3}\delta_{l3}, \quad \rho<2a
\end{aligned}
$$

$$
\begin{aligned}
\hat{M}_{ES}{}^{\alpha\beta}{}_{ijkl}(\rho\hat{\mathbf{z}}) &\overset{\text{sym}}{=} \hat{M}_{ES}{}^{\alpha\beta}{}_{ijkl}(\mathbf{x}) \\
&= \left(\frac{6}{5} - \frac{3}{4}r + \frac{3}{64}r^3\right)\delta_{ijkl} + \left(-\frac{1}{16}r + \frac{1}{128}r^3\right)\delta_{ij}\delta_{kl} \\
&+ \left(\frac{3}{16}r - \frac{3}{128}r^3\right)\left(\delta_{ij}\frac{r_k r_l}{r^2} + \delta_{kl}\frac{r_i r_j}{r^2}\right) \\
&+ \left(-\frac{3}{32}r + \frac{3}{128}r^3\right)\left(\delta_{ik}\frac{r_j r_l}{r^2} + \delta_{il}\frac{r_j r_k}{r^2} + \delta_{jk}\frac{r_i r_l}{r^2} + \delta_{jl}\frac{r_i r_k}{r^2}\right) \\
&- \left(\frac{3}{16}r - \frac{3}{128}r^3\right)\frac{r_i r_j r_k r_l}{r^4}, \quad \left|\mathbf{x}^\alpha - \mathbf{x}^\beta\right| \le 2a
\end{aligned}
\tag{B.29}
$$

(B.30)

$$
\begin{aligned}
&\hat{M}_{ES}{}^{\alpha\beta}{}_{ijkl}(\mathbf{x}) = \frac{3}{4\pi a^3}\oint_{S^\alpha}\frac{1}{2}\left[\hat{M}^S_{ikl}(\mathbf{x}-\mathbf{x}^\beta)n_j + \hat{M}^S_{jkl}(\mathbf{x}-\mathbf{x}^\beta)n_i\right]\mathrm{d}S^\alpha \\
&= -\left(1+\frac{1}{10}\nabla^2\right)\frac{3a^2}{4\pi a^3}\oint_{S^\alpha}\frac{1}{2}\left[K_{ikl}(\mathbf{x}-\mathbf{x}^\beta)n_j + K_{jkl}(\mathbf{x}-\mathbf{x}^\beta)n_i\right]\mathrm{d}S^\alpha \\
&= -\left(1+\frac{1}{10}\nabla^2\right)\frac{3a^2}{4\pi a^3}\oint_{S^\alpha}\frac{1}{2}\left[\frac{1}{2}\left(\nabla_l J_{ik} + \nabla_k J_{il}\right)n_j + \frac{1}{2}\left(\nabla_l J_{jk} + \nabla_k J_{jl}\right)n_i\right]\mathrm{d}S^\alpha \\
&= -\left(1+\frac{1}{10}\nabla^2\right)\frac{3a^2}{4\pi a^3}\oint_{S^\alpha}\frac{1}{2}\left[\nabla_l\frac{1}{2}\left(J_{ik}n_j + J_{jk}n_i\right) + \nabla_k\frac{1}{2}\left(J_{il}n_j + J_{jl}n_i\right)\right]\mathrm{d}S^\alpha \\
&= -\left(1+\frac{1}{10}\nabla^2\right)\frac{3a^2}{4\pi a^3}\oint_{S^\alpha}\frac{1}{2}\left[\nabla_l\widetilde{K}_{kij}(\mathbf{x}^\beta-\mathbf{x}) + \nabla_k\widetilde{K}_{lij}(\mathbf{x}^\beta-\mathbf{x})\right]\mathrm{d}S^\alpha \\
&= \left(1+\frac{1}{10}\nabla^2\right)\left(1+\frac{1}{10}\nabla^2\right)\frac{1}{2}\left[\nabla_l K_{kij}(\mathbf{x}^\beta-\mathbf{x}^\alpha) + \nabla_k K_{lij}(\mathbf{x}^\beta-\mathbf{x}^\alpha)\right] \\
&= -\left(1+\frac{1}{10}\nabla^2\right)\left(1+\frac{1}{10}\nabla^2\right)\frac{1}{2}\left[\nabla_l K_{kij}(\mathbf{x}^\alpha-\mathbf{x}^\beta) + \nabla_k K_{lij}(\mathbf{x}^\alpha-\mathbf{x}^\beta)\right], \quad \left|\mathbf{x}^\alpha-\mathbf{x}^\beta\right| > 2a
\end{aligned}
$$

B.3.2. Double surface integrals of the odd Oseen tensor

Note that the first surface integrals of the odd Oseen tensor on the β-th particle surface have already been evaluated in Appx. B.2.2, the following calculations will only focus on the second surface integral on the α-th particle surface.

B.3.2.1. $\boldsymbol{M}^{\alpha\beta}_{UF}$.

(B.31)

$$\begin{aligned}\hat{M}^{s}{}_{UF}{}^{\alpha\beta}_{ij}(\rho\hat{\mathbf{z}}) &= -\frac{a}{(4\pi a^2)^2}\oint_{S^\alpha}\oint_{S^\beta}\widetilde{J}^{s}_{ij}(\mathbf{x}-\mathbf{y})\mathrm{d}S^\alpha\mathrm{d}S^\beta = -\frac{1}{4\pi a^2}\oint_{S^\alpha}\hat{M}^{s}_{Fij}(\mathbf{x}-\mathbf{x}^\beta)\mathrm{d}S^\alpha \\ &= -\left(\frac{2}{3}-\frac{1}{8}\rho\right)\delta_{ij}+\frac{1}{8}\delta_{i3}\delta_{j3}, \quad \rho<2a\end{aligned}$$

(B.32) $$\hat{M}^{s}{}_{UF}{}^{\alpha\beta}_{ij}(\rho\hat{\mathbf{z}}) \overset{\text{sym}}{=} \hat{M}^{s}{}_{UF}{}^{\alpha\beta}_{ij}(\mathbf{x}) = -\left(\frac{2}{3}-\frac{1}{8}r\right)\delta_{ij}+\frac{1}{8}r\frac{r_i r_j}{r^2}, \quad \left|\mathbf{x}^\alpha-\mathbf{x}^\beta\right|\le 2a$$

(B.33)

$$\hat{M}^{o}{}_{UF}{}^{\alpha\beta}_{ij}(\mathbf{x}) = \varepsilon_{ijk}\delta_{l3}\hat{M}^{s}{}_{UF}{}^{\alpha\beta}_{kl}(\mathbf{x}) = -\left(\frac{2}{3}-\frac{1}{8}r\right)\varepsilon_{ij3}+\frac{1}{8}r\varepsilon_{ijk}\frac{r_k r_3}{r^2}, \quad \left|\mathbf{x}^\alpha-\mathbf{x}^\beta\right|\le 2a$$

(B.34)

$$\begin{aligned}\hat{M}^{o}{}_{UF}{}^{\alpha\beta}_{ij}(\mathbf{x}) &= -\frac{1}{4\pi a^2}\oint_{S^\alpha}\hat{M}^{o}_{Fij}(\mathbf{x}-\mathbf{x}^\beta)\mathrm{d}S^\alpha = -\frac{a}{4\pi a^2}\oint_{S^\alpha}\left(1+\frac{1}{6}\nabla^2\right)J^{o}_{ij}(\mathbf{x}-\mathbf{x}^\beta)\mathrm{d}S^\alpha \\ &= -\left(1+\frac{1}{6}\nabla^2\right)\frac{a}{4\pi a^2}\oint_{S^\alpha}\widetilde{J}^{o}_{ij}(\mathbf{x}-\mathbf{x}^\beta)\mathrm{d}S^\alpha \\ &= -\left(1+\frac{1}{6}\nabla^2\right)\frac{a}{4\pi a^2}\oint_{S^\alpha}\widetilde{J}^{o}_{ij}(\mathbf{x}^\beta-\mathbf{x})\mathrm{d}S^\alpha \\ &= -\left(1+\frac{1}{6}\nabla^2\right)\left(1+\frac{1}{6}\nabla^2\right)J^{o}_{ij}(\mathbf{x}^\alpha-\mathbf{x}^\beta), \quad \left|\mathbf{x}^\alpha-\mathbf{x}^\beta\right|>2a\end{aligned}$$

B.3.2.2. $\boldsymbol{M}^{\alpha\beta}_{UT}$.

(B.35)

$$\begin{aligned}\hat{M}^{s}{}_{UT}{}^{\alpha\beta}_{ijk}(\rho\hat{\mathbf{z}}) &= -\frac{1}{4\pi a^2}\frac{3a^2}{8\pi a^3}\oint_{S^\alpha}\oint_{S^\beta}\widetilde{R}^{s}_{ijk}(\mathbf{x}-\mathbf{y})\mathrm{d}S^\alpha\mathrm{d}S^\beta = -\frac{1}{4\pi a^2}\oint_{S^\alpha}\hat{M}^{s}_{Tijk}(\mathbf{x}-\mathbf{x}^\beta)\mathrm{d}S^\alpha \\ &= \frac{3}{160}\left(16\rho-5\rho^2\right)\delta_{3ijk}+\frac{1}{64}\left(16\rho-7\rho^2\right)\delta_{ij}\delta_{k3}+\frac{1}{64}\left(-16\rho+5\rho^2\right)\delta_{ik}\delta_{j3} \\ &+\frac{1}{32}\rho^2\delta_{i3}\delta_{j3}\delta_{k3}, \quad \rho<2a\end{aligned}$$

$$\hat{M}^{s}_{UT}{}^{\alpha\beta}_{ijk}(\rho\hat{\mathbf{z}}) \overset{\text{sym}}{=} \hat{M}^{s}_{UT}{}^{\alpha\beta}_{ijk}(\mathbf{x})$$

$$= \frac{3}{160}(16-5r)\, r_l \delta_{lijk} + \frac{1}{64}(16-7r)\,\delta_{ij} r_k + \frac{1}{64}(-16+5r)\,\delta_{ik} r_j + \frac{1}{32}\frac{1}{r} r_i r_j r_k, \quad \left|\mathbf{x}^\alpha - \mathbf{x}^\beta\right| < 2a \tag{B.36}$$

$$\hat{M}^{o}_{UT}{}^{\alpha\beta}_{ij}(\mathbf{x}) = \hat{M}^{s}_{UT}{}^{\alpha\beta}_{ijk}(\mathbf{x})\delta_{k3}$$

$$= \frac{3}{160}(16-5r)\, r_l \delta_{lij3} + \frac{1}{64}(16-7r)\,\delta_{ij} r_3 + \frac{1}{64}(-16+5r)\,\delta_{i3} r_j + \frac{1}{32}\frac{1}{r} r_i r_j r_3, \quad \left|\mathbf{x}^\alpha - \mathbf{x}^\beta\right| < 2a \tag{B.37}$$

$$\hat{M}^{o}_{UT}{}^{\alpha\beta}_{ij}(\mathbf{x}) = -\frac{1}{4\pi a^2}\oint_{S^\alpha} \hat{M}^{o}_{Tij}(\mathbf{x}-\mathbf{x}^\beta)\mathrm{d}S^\alpha = \frac{a^2}{4\pi a^2}\oint_{S^\alpha} R^{o}_{ij}(\mathbf{x}-\mathbf{x}^\beta)\mathrm{d}S^\alpha$$

$$= \left(1+\frac{1}{10}\nabla^2\right)\frac{a^2}{4\pi a^2}\oint_{S^\alpha}\frac{1}{2}\varepsilon_{ikl}\nabla_k J^{o}_{jl}(\mathbf{x}-\mathbf{x}^\beta)\mathrm{d}S^\alpha$$

$$= \left(1+\frac{1}{10}\nabla^2\right)\frac{1}{2}\varepsilon_{ikl}\nabla_k \frac{a^2}{4\pi a^2}\oint_{S^\alpha}\widetilde{J}^{o}_{jl}(\mathbf{x}^\beta-\mathbf{x})\mathrm{d}S^\alpha$$

$$= \left(1+\frac{1}{10}\nabla^2\right)\frac{1}{2}\varepsilon_{ikl}\nabla_k \left(1+\frac{1}{6}\nabla^2\right) J^{o}_{jl}(\mathbf{x}^\alpha-\mathbf{x}^\beta)$$

$$= \left(1+\frac{1}{6}\nabla^2\right)\left(1+\frac{1}{10}\nabla^2\right) R^{o}_{ij}(\mathbf{x}^\alpha-\mathbf{x}^\beta), \quad \left|\mathbf{x}^\alpha - \mathbf{x}^\beta\right| > 2a \tag{B.38}$$

B.3.2.3. $\boldsymbol{M}^{\alpha\beta}_{US}$.

$$\hat{M}^{s}_{US}{}^{\alpha\beta}_{ijkl}(\rho\hat{\mathbf{z}}) = -\frac{1}{4\pi a^2}\frac{3}{4\pi a^3}\oint_{S^\alpha}\oint_{S^\beta}\widetilde{K}^{s}_{ijkl}(\mathbf{x}-\mathbf{y})\mathrm{d}S^\alpha\mathrm{d}S^\beta = -\frac{1}{4\pi a^2}\oint_{S^\alpha}\hat{M}^{s}_{Sijkl}(\mathbf{x}-\mathbf{x}^\beta)\mathrm{d}S^\alpha$$

$$= -\frac{1}{160}\left(16\rho-5\rho^2\right)\left[(\varepsilon_{ijl}\delta_{k3}+\varepsilon_{ikl}\delta_{j3})+(\varepsilon_{ij3}\delta_{kl}+\varepsilon_{ik3}\delta_{jl})\right]$$

$$+\frac{1}{32}\rho^2\left(\varepsilon_{ij3}\delta_{k3}+\varepsilon_{ik3}\delta_{j3}\right)\delta_{l3}, \quad \rho < 2a \tag{B.39}$$

$$\hat{M}^{s}{}_{US}{}^{\alpha\beta}{}_{ijkl}(\rho\hat{\mathbf{z}}) \overset{\text{sym}}{=} \hat{M}^{s}{}_{US}{}^{\alpha\beta}{}_{ijkl}(\mathbf{x})$$

$$= -\frac{1}{160}(16-5r)\left[(\varepsilon_{ijl}r_k+\varepsilon_{ikl}r_j)+(\varepsilon_{ijm}\delta_{kl}+\varepsilon_{ikm}\delta_{jl})\,r_m\right] \tag{B.40}$$

$$+\frac{1}{32}\frac{1}{r}(\varepsilon_{ijm}r_k+\varepsilon_{ikm}r_j)\,r_m r_l, \quad \left|\mathbf{x}^\alpha-\mathbf{x}^\beta\right|<2a$$

$$\hat{M}^{o}{}_{US}{}^{\alpha\beta}{}_{ijk}(\mathbf{x}) = \hat{M}^{s}{}_{US}{}^{\alpha\beta}{}_{ijkl}(\mathbf{x})\delta_{l3}$$

$$= -\frac{1}{160}(16-5r)\left[(\varepsilon_{ij3}r_k+\varepsilon_{ik3}r_j)+(\varepsilon_{ijm}\delta_{k3}+\varepsilon_{ikm}\delta_{j3})\,r_m\right] \tag{B.41}$$

$$+\frac{1}{32}\frac{1}{r}(\varepsilon_{ijm}r_k+\varepsilon_{ikm}r_j)\,r_m r_3, \quad \left|\mathbf{x}^\alpha-\mathbf{x}^\beta\right|<2a$$

(B.42)

$$\hat{M}^{o}{}_{US}{}^{\alpha\beta}{}_{ijk}(\mathbf{x}) = -\frac{1}{4\pi a^2}\oint_{S^\alpha}\hat{M}^{o}_{Sijk}(\mathbf{x}-\mathbf{x}^\beta)\mathrm{d}S^\alpha = \frac{a^2}{4\pi a^2}\oint_{S^\alpha}\left(1+\frac{1}{10}\nabla^2\right)K^{o}_{ijk}(\mathbf{x}-\mathbf{x}^\beta)\mathrm{d}S^\alpha$$

$$= -\left(1+\frac{1}{10}\nabla^2\right)\frac{a^2}{4\pi a^2}\oint_{S^\alpha}K^{o}_{ijk}(\mathbf{x}^\beta-\mathbf{x})\mathrm{d}S^\alpha$$

$$= -\left(1+\frac{1}{10}\nabla^2\right)\frac{a^2}{4\pi a^2}\oint_{S^\alpha}\frac{1}{2}\left[\nabla_k J^{o}_{ij}(\mathbf{x}^\beta-\mathbf{x})+\nabla_j J^{o}_{ik}(\mathbf{x}^\beta-\mathbf{x})\right]\mathrm{d}S^\alpha$$

$$= -\left(1+\frac{1}{10}\nabla^2\right)\left(1+\frac{1}{6}\nabla^2\right)\frac{1}{2}\left[\nabla_k J^{o}_{ij}(\mathbf{x}^\beta-\mathbf{x}^\alpha)+\nabla_j J^{o}_{ik}(\mathbf{x}^\beta-\mathbf{x}^\alpha)\right]$$

$$= \left(1+\frac{1}{6}\nabla^2\right)\left(1+\frac{1}{10}\nabla^2\right)K^{o}_{ijk}(\mathbf{x}^\alpha-\mathbf{x}^\beta), \quad \left|\mathbf{x}^\alpha-\mathbf{x}^\beta\right|>2a$$

B.3.2.4. $\boldsymbol{M}^{\alpha\beta}_{\Omega T}$.

$$\hat{M}^{s}{}_{\Omega T}{}^{\alpha\beta}{}_{ijk}(\rho\hat{\mathbf{z}}) = -\left(\frac{3a}{8\pi a^3}\right)^2\oint_{S^\alpha}\oint_{S^\beta}\varepsilon_{ilm}n_l\widetilde{R}^{s}_{mjk}(\mathbf{x}-\mathbf{y})\mathrm{d}S^\alpha\mathrm{d}S^\beta$$

$$= -\frac{3}{8\pi a^3}\oint_{S^\alpha}\varepsilon_{ilm}n_l\hat{M}^{s}_{Tmjk}(\mathbf{x}-\mathbf{x}^\beta)\mathrm{d}S^\alpha \tag{B.43}$$

$$= -\frac{1}{2}\left(1-\frac{9}{16}\rho+\frac{1}{32}\rho^3\right)\varepsilon_{ijk}+\frac{3}{64}(6\rho-\rho^3)\varepsilon_{ij3}\delta_{k3}, \quad \rho<2a$$

(B.44)

$$\hat{M}^{s}{}_{\Omega T}{}^{\alpha\beta}{}_{ijk}(\rho\hat{\mathbf{z}}) \overset{\text{sym}}{=} \hat{M}^{s}{}_{\Omega T}{}^{\alpha\beta}{}_{ijk}(\mathbf{x})$$
$$= -\frac{1}{2}\left(1 - \frac{9}{16}r + \frac{1}{32}r^3\right)\varepsilon_{ijk} + \frac{3}{64}(6r - r^3)\varepsilon_{ijl}\frac{r_l r_k}{r^2}, \quad \left|\mathbf{x}^\alpha - \mathbf{x}^\beta\right| < 2a$$

(B.45)

$$\hat{M}^{o}{}_{\Omega T}{}^{\alpha\beta}{}_{ij}(\mathbf{x}) = \hat{M}^{s}{}_{\Omega T}{}^{\alpha\beta}{}_{ijk}(\mathbf{x})\delta_{k3}$$
$$= -\frac{1}{2}\left(1 - \frac{9}{16}r + \frac{1}{32}r^3\right)\varepsilon_{ij3} + \frac{3}{64}(6r - r^3)\varepsilon_{ijl}\frac{r_l r_3}{r^2}, \quad \left|\mathbf{x}^\alpha - \mathbf{x}^\beta\right| < 2a$$

(B.46)

$$\hat{M}^{o}{}_{\Omega T}{}^{\alpha\beta}{}_{ij}(\mathbf{x}) = -\frac{3}{8\pi a^3}\oint_{S^\alpha}\varepsilon_{ikl}n_k\hat{M}^{o}_{Tlj}(\mathbf{x} - \mathbf{x}^\beta)\mathrm{d}S^\alpha$$
$$= \frac{3a^2}{8\pi a^3}\oint_{S^\alpha}\varepsilon_{ikl}n_k\left(1 + \frac{1}{10}\nabla^2\right)R^{o}_{lj}(\mathbf{x} - \mathbf{x}^\beta)\mathrm{d}S^\alpha$$
$$= \left(1 + \frac{1}{10}\nabla^2\right)\frac{3a^2}{8\pi a^3}\oint_{S^\alpha}\varepsilon_{ikl}n_k\left[\frac{1}{2}\varepsilon_{lmn}\nabla_m J^{o}_{jn}(\mathbf{x} - \mathbf{x}^\beta)\right]\mathrm{d}S^\alpha$$
$$= \left(1 + \frac{1}{10}\nabla^2\right)\frac{1}{2}\varepsilon_{ikl}\nabla_m\frac{3a^2}{8\pi a^3}\oint_{S^\alpha}J^{o}_{jn}(\mathbf{x} - \mathbf{x}^\beta)\varepsilon_{nlm}n_k\mathrm{d}S^\alpha$$
$$= \left(1 + \frac{1}{10}\nabla^2\right)\frac{1}{2}\varepsilon_{ikl}\nabla_k\frac{3a^2}{8\pi a^3}\oint_{S^\alpha}J^{o}_{jn}(\mathbf{x}^\beta - \mathbf{x})\varepsilon_{nlm}n_m\mathrm{d}S^\alpha$$
$$= \left(1 + \frac{1}{10}\nabla^2\right)\frac{1}{2}\varepsilon_{ikl}\nabla_k\frac{3a^2}{8\pi a^3}\oint_{S^\alpha}\widetilde{R}^{o}_{jl}(\mathbf{x}^\beta - \mathbf{x})\mathrm{d}S^\alpha$$
$$= -\left(1 + \frac{1}{10}\nabla^2\right)\left(1 + \frac{1}{10}\nabla^2\right)\frac{1}{2}\varepsilon_{ikl}\nabla_k R^{o}_{jl}(\mathbf{x}^\beta - \mathbf{x}^\alpha)$$
$$= \left(1 + \frac{1}{10}\nabla^2\right)\left(1 + \frac{1}{10}\nabla^2\right)\frac{1}{2}\varepsilon_{ikl}\nabla_k R^{o}_{lj}(\mathbf{x}^\alpha - \mathbf{x}^\beta), \quad \left|\mathbf{x}^\alpha - \mathbf{x}^\beta\right| > 2a$$

B.3.2.5. $M^{\alpha\beta}_{\Omega S}$.

(B.47)

$$\begin{aligned}
\hat{M}^{s}{}_{\Omega S}{}^{\alpha\beta}{}_{ijkl}(\rho\hat{\mathbf{z}}) &= -\frac{3}{8\pi a^3}\frac{3a^2}{4\pi a^3}\oint_{S^\alpha}\oint_{S^\beta}\varepsilon_{ipq}n_p\widetilde{K}^{s}_{qjkl}(\mathbf{x}-\mathbf{y})\mathrm{d}S^\alpha\mathrm{d}S^\beta \\
&= -\frac{3}{8\pi a^3}\oint_{S^\alpha}\varepsilon_{ipq}n_p\hat{M}^{s}_{qjkl}(\mathbf{x}-\mathbf{x}^\beta)\mathrm{d}S^\alpha \\
&= \left(\frac{1}{5}-\frac{3}{32}\rho+\frac{1}{256}\rho^3\right)\delta_{il}\delta_{kj}-\left(\frac{3}{10}-\frac{3}{16}\rho+\frac{3}{256}\rho^3\right)(\delta_{ij}\delta_{kl}+\delta_{ik}\delta_{jl}) \\
&+ \frac{3}{256}\left(8\rho+\rho^3\right)\delta_{i3}\delta_{j3}\delta_{k3}\delta_{l3}+\frac{3}{256}\left(16\rho-3\rho^3\right)(\delta_{ik}\delta_{j3}\delta_{l3}+\delta_{ij}\delta_{k3}\delta_{l3}) \\
&- \frac{3}{256}\left(8\rho-\rho^3\right)(\delta_{il}\delta_{k3}\delta_{j3}+\delta_{kl}\delta_{i3}\delta_{j3}+\delta_{jl}\delta_{i3}\delta_{k3}+\delta_{jk}\delta_{i3}\delta_{l3}), \quad \rho<2a
\end{aligned}$$

(B.48)

$$\begin{aligned}
\hat{M}^{s}{}_{\Omega S}{}^{\alpha\beta}{}_{ijkl}(\rho\hat{\mathbf{z}}) &\overset{\text{sym}}{=} \hat{M}^{s}{}_{\Omega S}{}^{\alpha\beta}{}_{ijkl}(\mathbf{x}) \\
&= \left(\frac{1}{5}-\frac{3}{32}r+\frac{1}{256}r^3\right)\delta_{il}\delta_{kj}-\left(\frac{3}{10}-\frac{3}{16}r+\frac{3}{256}r^3\right)(\delta_{ij}\delta_{kl}+\delta_{ik}\delta_{jl}) \\
&+ \frac{3}{256}\left(8r+r^3\right)\frac{r_ir_jr_kr_l}{r^4}+\frac{3}{256}\left(16r-3r^3\right)\left(\delta_{ik}\frac{r_jr_l}{r^2}+\delta_{ij}\frac{r_kr_l}{r^2}\right) \\
&- \frac{3}{256}\left(8r-r^3\right)\left(\delta_{il}\frac{r_kr_j}{r^2}+\delta_{kl}\frac{r_ir_j}{r^2}+\delta_{jl}\frac{r_ir_k}{r^2}+\delta_{jk}\frac{r_ir_l}{r^2}\right), \quad \left|\mathbf{x}^\alpha-\mathbf{x}^\beta\right|<2a
\end{aligned}$$

(B.49)

$$\begin{aligned}
\hat{M}^{o}{}_{\Omega S}{}^{\alpha\beta}{}_{ijk}(\mathbf{x}) &= \hat{M}^{s}{}_{\Omega S}{}^{\alpha\beta}{}_{ijkl}(\mathbf{x})\delta_{l3} \\
&= \left(\frac{1}{5}-\frac{3}{32}r+\frac{1}{256}r^3\right)\delta_{i3}\delta_{kj}-\left(\frac{3}{10}-\frac{3}{16}r+\frac{3}{256}r^3\right)(\delta_{ij}\delta_{k3}+\delta_{ik}\delta_{j3}) \\
&+ \frac{3}{256}\left(8r+r^3\right)\frac{r_ir_jr_kr_3}{r^4}+\frac{3}{256}\left(16r-3r^3\right)\left(\delta_{ik}\frac{r_jr_3}{r^2}+\delta_{ij}\frac{r_kr_3}{r^2}\right) \\
&- \frac{3}{256}\left(8r-r^3\right)\left(\delta_{i3}\frac{r_kr_j}{r^2}+\delta_{k3}\frac{r_ir_j}{r^2}+\delta_{j3}\frac{r_ir_k}{r^2}+\delta_{jk}\frac{r_ir_3}{r^2}\right), \quad \left|\mathbf{x}^\alpha-\mathbf{x}^\beta\right|<2a
\end{aligned}$$

$$
\begin{aligned}
\hat{M}^{o}{}_{\Omega S}{}^{\alpha\beta}_{ijk}(\mathbf{x}) &= -\frac{3}{8\pi a^3}\oint_{S^\alpha}\varepsilon_{ilm}n_l\hat{M}^{o}_{Smjk}(\mathbf{x}-\mathbf{x}^\beta)\mathrm{d}S^\alpha \\
&= \frac{3a^2}{8\pi a^3}\oint_{S^\alpha}\varepsilon_{ilm}n_l\left(1+\frac{1}{10}\nabla^2\right)K^{o}_{mjk}(\mathbf{x}-\mathbf{x}^\beta)\mathrm{d}S^\alpha \\
&= \left(1+\frac{1}{10}\nabla^2\right)\frac{3a^2}{8\pi a^3}\oint_{S^\alpha}\varepsilon_{ilm}n_l\frac{1}{2}\left[\nabla_k J^{o}_{mj}(\mathbf{x}-\mathbf{x}^\beta)+\nabla_j J^{o}_{mk}(\mathbf{x}-\mathbf{x}^\beta)\right]\mathrm{d}S^\alpha \\
&= \left(1+\frac{1}{10}\nabla^2\right)\frac{3a^2}{8\pi a^3}\oint_{S^\alpha}\frac{1}{2}\left[\nabla_k \widetilde{R}^{o}_{ji}(\mathbf{x}-\mathbf{x}^\beta)+\nabla_j \widetilde{R}^{o}_{ki}(\mathbf{x}-\mathbf{x}^\beta)\right]\mathrm{d}S^\alpha \qquad \text{(B.50)} \\
&= -\left(1+\frac{1}{10}\nabla^2\right)\left(1+\frac{1}{10}\nabla^2\right)\frac{1}{2}\left[\nabla_k R^{o}_{ij}(\mathbf{x}^\alpha-\mathbf{x}^\beta)+\nabla_j R^{o}_{ik}(\mathbf{x}^\alpha-\mathbf{x}^\beta)\right] \\
&= -\left(1+\frac{1}{10}\nabla^2\right)\left(1+\frac{1}{10}\nabla^2\right)\frac{1}{2}\varepsilon_{ilm}\nabla_l\frac{1}{2}\left[\nabla_k J^{o}_{jm}(\mathbf{x}^\alpha-\mathbf{x}^\beta)+\nabla_j J^{o}_{km}(\mathbf{x}^\alpha-\mathbf{x}^\beta)\right] \\
&= \left(1+\frac{1}{10}\nabla^2\right)\left(1+\frac{1}{10}\nabla^2\right)\frac{1}{2}\varepsilon_{ilm}\nabla_l K^{o}_{mjk}(\mathbf{x}^\alpha-\mathbf{x}^\beta), \quad \left|\mathbf{x}^\alpha-\mathbf{x}^\beta\right|>2a
\end{aligned}
$$

B.3.2.6. $M^{\alpha\beta}_{ES}$.

(B.51)

$$
\begin{aligned}
\hat{M}^{s}{}_{ES}{}^{\alpha\beta}_{ijklm}(\rho\hat{\mathbf{z}}) &= -\left(\frac{3a}{4\pi a^3}\right)^2\oint_{S^\alpha}\oint_{S^\beta}\frac{1}{2}\left[\widetilde{K}^{s}_{iklm}(\mathbf{x}-\mathbf{y})n_j+\widetilde{K}^{s}_{jklm}(\mathbf{x}-\mathbf{y})n_i\right]\mathrm{d}S^\alpha\mathrm{d}S^\beta \\
&= -\frac{3}{4\pi a^3}\oint_{S^\alpha}\frac{1}{2}\left[\hat{M}^{s}_{Siklm}(\mathbf{x}-\mathbf{x}^\beta)n_j+\hat{M}^{s}_{Sjklm}(\mathbf{x}-\mathbf{x}^\beta)n_i\right]\mathrm{d}S^\alpha \\
&= \left(-\frac{1}{10}+\frac{3}{64}\rho-\frac{1}{512}\rho^3\right)\left[(\varepsilon_{ikm}\delta_{lj}+\varepsilon_{ilm}\delta_{kj})+(\varepsilon_{jkm}\delta_{li}+\varepsilon_{jlm}\delta_{ki})\right] \\
&\quad -\frac{3}{512}\left(8\rho+\rho^3\right)\left[\left(\varepsilon_{ik3}\delta_{l3}+\varepsilon_{il3}\delta_{k3}\right)\delta_{j3}+\left(\varepsilon_{jk3}\delta_{l3}+\varepsilon_{jl3}\delta_{k3}\right)\delta_{i3}\right]\delta_{m3} \\
&\quad +\frac{3}{512}\left(8\rho-\rho^3\right)\left[\left(\varepsilon_{ikm}\delta_{l3}+\varepsilon_{ilm}\delta_{k3}\right)\delta_{j3}+\left(\varepsilon_{jkm}\delta_{l3}+\varepsilon_{jlm}\delta_{k3}\right)\delta_{i3}\right. \\
&\quad +\varepsilon_{ik3}\left(\delta_{lm}\delta_{j3}+\delta_{lj}\delta_{m3}+\delta_{jm}\delta_{l3}\right)+\varepsilon_{il3}\left(\delta_{km}\delta_{j3}+\delta_{kj}\delta_{m3}+\delta_{jm}\delta_{k3}\right) \\
&\quad \left.+\varepsilon_{jk3}\left(\delta_{lm}\delta_{i3}+\delta_{li}\delta_{m3}+\delta_{im}\delta_{l3}\right)+\varepsilon_{jl3}\left(\delta_{km}\delta_{i3}+\delta_{ki}\delta_{m3}+\delta_{im}\delta_{k3}\right)\right], \quad \rho<2a
\end{aligned}
$$

(B.52)

$$\hat{M}^{s}{}_{ES}{}^{\alpha\beta}{}_{ijklm}(\rho\hat{\mathbf{z}}) \overset{\text{sym}}{=} \hat{M}^{s}{}_{ES}{}^{\alpha\beta}{}_{ijklm}(\mathbf{x})$$

$$= \left(-\frac{1}{10} + \frac{3}{64}r - \frac{1}{512}r^3\right)\left[(\varepsilon_{ikm}\delta_{lj} + \varepsilon_{ilm}\delta_{kj}) + (\varepsilon_{jkm}\delta_{li} + \varepsilon_{jlm}\delta_{ki})\right]$$

$$- \frac{3}{512}\left(8r + r^3\right)\left[\left(\varepsilon_{ikn}\frac{r_l}{r} + \varepsilon_{iln}\frac{r_k}{r}\right)\frac{r_j}{r} + \left(\varepsilon_{jkn}\frac{r_l}{r} + \varepsilon_{jln}\frac{r_k}{r}\right)\frac{r_i}{r}\right]\frac{r_n r_m}{r^2}$$

$$+ \frac{3}{512}\left(8r - r^3\right)\left[\left(\varepsilon_{ikm}\frac{r_l}{r} + \varepsilon_{ilm}\frac{r_k}{r}\right)\frac{r_j}{r} + \left(\varepsilon_{jkm}\frac{r_l}{r} + \varepsilon_{jlm}\frac{r_k}{r}\right)\frac{r_i}{r}\right.$$

$$+ \varepsilon_{ikn}\frac{r_n}{r}\left(\delta_{lm}\frac{r_j}{r} + \delta_{lj}\frac{r_m}{r} + \delta_{jm}\frac{r_l}{r}\right) + \varepsilon_{iln}\frac{r_n}{r}\left(\delta_{km}\frac{r_j}{r} + \delta_{kj}\frac{r_m}{r} + \delta_{jm}\frac{r_k}{r}\right)$$

$$\left. + \varepsilon_{jkn}\frac{r_n}{r}\left(\delta_{lm}\frac{r_i}{r} + \delta_{li}\frac{r_m}{r} + \delta_{im}\frac{r_l}{r}\right) + \varepsilon_{jln}\frac{r_n}{r}\left(\delta_{km}\frac{r_i}{r} + \delta_{ki}\frac{r_m}{r} + \delta_{im}\frac{r_k}{r}\right)\right], \quad \left|\mathbf{x}^{\alpha} - \mathbf{x}^{\beta}\right| > 2a$$

(B.53)

$$\hat{M}^{o}{}_{ES}{}^{\alpha\beta}{}_{ijkl}(\mathbf{x}) = \hat{M}^{s}{}_{ES}{}^{\alpha\beta}{}_{ijklm}(\mathbf{x})\delta_{m3}$$

$$= \left(-\frac{1}{10} + \frac{3}{64}r - \frac{1}{512}r^3\right)\left[(\varepsilon_{ik3}\delta_{lj} + \varepsilon_{il3}\delta_{kj}) + (\varepsilon_{jk3}\delta_{li} + \varepsilon_{jl3}\delta_{ki})\right]$$

$$- \frac{3}{512}\left(8r + r^3\right)\left[\left(\varepsilon_{ikn}\frac{r_l}{r} + \varepsilon_{iln}\frac{r_k}{r}\right)\frac{r_j}{r} + \left(\varepsilon_{jkn}\frac{r_l}{r} + \varepsilon_{jln}\frac{r_k}{r}\right)\frac{r_i}{r}\right]\frac{r_n r_3}{r^2}$$

$$+ \frac{3}{512}\left(8r - r^3\right)\left[\left(\varepsilon_{ik3}\frac{r_l}{r} + \varepsilon_{il3}\frac{r_k}{r}\right)\frac{r_j}{r} + \left(\varepsilon_{jk3}\frac{r_l}{r} + \varepsilon_{jl3}\frac{r_k}{r}\right)\frac{r_i}{r}\right.$$

$$+ \varepsilon_{ikn}\frac{r_n}{r}\left(\delta_{l3}\frac{r_j}{r} + \delta_{lj}\frac{r_3}{r} + \delta_{j3}\frac{r_l}{r}\right) + \varepsilon_{iln}\frac{r_n}{r}\left(\delta_{k3}\frac{r_j}{r} + \delta_{kj}\frac{r_3}{r} + \delta_{j3}\frac{r_k}{r}\right)$$

$$\left. + \varepsilon_{jkn}\frac{r_n}{r}\left(\delta_{l3}\frac{r_i}{r} + \delta_{li}\frac{r_3}{r} + \delta_{i3}\frac{r_l}{r}\right) + \varepsilon_{jln}\frac{r_n}{r}\left(\delta_{k3}\frac{r_i}{r} + \delta_{ki}\frac{r_3}{r} + \delta_{i3}\frac{r_k}{r}\right)\right], \quad \left|\mathbf{x}^{\alpha} - \mathbf{x}^{\beta}\right| > 2a$$

(B.54)

$$\hat{M}^{o}_{ES}{}^{\alpha\beta}_{ijkl}(\mathbf{x}) = -\frac{3}{4\pi a^3}\oint_{S^\alpha}\frac{1}{2}\left[\hat{M}^{o}_{Sikl}(\mathbf{x}-\mathbf{x}^\beta)n_j + \hat{M}^{o}_{Sjkl}(\mathbf{x}-\mathbf{x}^\beta)n_i\right]\mathrm{d}S^\alpha$$

$$= \left(1+\frac{1}{10}\nabla^2\right)\frac{3a^2}{4\pi a^3}\oint_{S^\alpha}\frac{1}{2}\left[K^{o}_{ikl}(\mathbf{x}-\mathbf{x}^\beta)n_j + K^{o}_{jkl}(\mathbf{x}-\mathbf{x}^\beta)n_i\right]\mathrm{d}S^\alpha$$

$$= \left(1+\frac{1}{10}\nabla^2\right)\frac{3a^2}{4\pi a^3}\oint_{S^\alpha}\frac{1}{2}\left[\frac{1}{2}\left(\nabla_l J^{o}_{ik}+\nabla_k J^{o}_{il}\right)n_j + \frac{1}{2}\left(\nabla_l J^{o}_{jk}+\nabla_k J^{o}_{jl}\right)n_i\right]\mathrm{d}S^\alpha$$

$$= \left(1+\frac{1}{10}\nabla^2\right)\frac{3a^2}{4\pi a^3}\oint_{S^\alpha}\frac{1}{2}\left[\nabla_l\frac{1}{2}\left(J^{o}_{ik}n_j + J^{o}_{jk}n_i\right) + \nabla_k\frac{1}{2}\left(J^{o}_{il}n_j + J^{o}_{jl}n_i\right)\right]\mathrm{d}S^\alpha$$

$$= \left(1+\frac{1}{10}\nabla^2\right)\frac{3a^2}{4\pi a^3}\oint_{S^\alpha}\frac{1}{2}\left[\nabla_l\widetilde{K}^{o}_{kij}(\mathbf{x}^\beta-\mathbf{x}) + \nabla_k\widetilde{K}^{o}_{lij}(\mathbf{x}^\beta-\mathbf{x})\right]\mathrm{d}S^\alpha$$

$$= -\left(1+\frac{1}{10}\nabla^2\right)\left(1+\frac{1}{10}\nabla^2\right)\frac{1}{2}\left[\nabla_l K^{o}_{kij}(\mathbf{x}^\beta-\mathbf{x}^\alpha) + \nabla_k K^{o}_{lij}(\mathbf{x}^\beta-\mathbf{x}^\alpha)\right]$$

$$= \left(1+\frac{1}{10}\nabla^2\right)\left(1+\frac{1}{10}\nabla^2\right)\frac{1}{2}\left[\nabla_l K_{kij}(\mathbf{x}^\alpha-\mathbf{x}^\beta) + \nabla_k K_{lij}(\mathbf{x}^\alpha-\mathbf{x}^\beta)\right], \quad \left|\mathbf{x}^\alpha-\mathbf{x}^\beta\right| > 2a$$

B.4. Explicit expressions of the even mobility tensors

In this section, the explicit expressions of even mobility tensors are documented for reference. All N particles are assumed to be equal size of radius a, i.e. $a^\alpha = a^\beta = a$. All distance quantities are normalized by the particle radius, such as $r = \left|\mathbf{x}^\alpha - \mathbf{x}^\beta\right|/a$. All mobility expressions are normalized by $8\pi\mu a^n$, where the exponent n is chose to make the corresponding mobility tensor dimensionless, i.e. $\hat{M}_{XY}{}^{\alpha\beta}_{ij} = 8\pi\mu a^n M_{XY}{}^{\alpha\beta}_{ij}$. The hat symbol $\hat{}$ indicates the quantity is dimensionless; The subscript XY means the mobility tensor describes the coupling between kinetic motions X ($X = U$, Ω or E) and force moments Y ($Y = F$, T or S); The superscript $\alpha\beta$ specifies the mobility tensor describes the interaction between α-th and β-th particles ($\alpha, \beta = 1 \cdots N$); The subscript $ijkl$ indicates the Cartesian components of the mobility tensor ($i, j, k, l = 1, 2, 3$). δ_{ij} is the Kronecker delta and ε_{ijk} is the right-handed Levi-Civita symbol. Only six out of nine

mobility tensors are given and the rest can be obtained by the symmetry relations of mobility tensors [Sec. B.4.4].

B.4.1. Self-mobility tensors

The dimensionless expressions of mobility tensors for a single isolated particle ($\alpha = \beta$) are shown below and its corresponding dimensional forms can be found at Eqn. 5.37 [Sec. 5.2.4].

(B.55a) $$\hat{M}_{UF}{}^{\alpha\alpha}{}_{ij} = \frac{4}{3}\delta_{ij}$$

(B.55b) $$\hat{M}_{UT}{}^{\alpha\alpha}{}_{ij} = 0$$

(B.55c) $$\hat{M}_{US}{}^{\alpha\alpha}{}_{ijk} = 0$$

(B.55d) $$\hat{M}_{\Omega T}{}^{\alpha\alpha}{}_{ij} = \delta_{ij}$$

(B.55e) $$\hat{M}_{\Omega S}{}^{\alpha\alpha}{}_{ijk} = 0$$

(B.55f) $$\hat{M}_{ES}{}^{\alpha\alpha}{}_{ijkl} = \frac{6}{5}\delta_{ijkl}$$

As the stresslet is symmetric and traceless, δ_{ijkl} is chosen as the fourth-rank deviatoric traceless unit tensor:

(B.56) $$\delta_{ijkl} = \frac{1}{2}\left(\delta_{ik}\delta_{jl} + \delta_{il}\delta_{jk}\right) - \frac{1}{3}\delta_{ij}\delta_{kl}$$

B.4.2. Pair-mobility tensors ($r > 2a$)

The definitions of far-field mobility tensors between two different non-overlapping particles ($\alpha \neq \beta$ and $r > 2a$) are given at Eqn. 5.36 [Sec. 5.2.4] and its corresponding dimensionless explicit expressions are shown below:

$$\text{(B.57a)} \qquad \hat{M}_{UF}{}^{\alpha\beta}_{ij} = \frac{1}{r}\left[\left(1+\frac{2}{3r^2}\right)\delta_{ij} + \left(1-\frac{2}{r^2}\right)\frac{r_i r_j}{r^2}\right]$$

$$\text{(B.57b)} \qquad \hat{M}_{UT}{}^{\alpha\beta}_{ij} = \frac{1}{r^3}\varepsilon_{ijk} r_k$$

$$\text{(B.57c)} \qquad \hat{M}_{US}{}^{\alpha\beta}_{ijk} = \left(\frac{3}{r^2}-\frac{8}{r^4}\right)\frac{r_i r_j r_k}{r^3} + \left(-\frac{1}{r^2}+\frac{8}{5r^4}\right)\delta_{jk}\frac{r_i}{r} + \frac{8}{5r^4}\left(\delta_{ij}\frac{r_k}{r}+\delta_{ik}\frac{r_j}{r}\right)$$

$$\text{(B.57d)} \qquad \hat{M}_{\Omega T}{}^{\alpha\beta}_{ij} = -\frac{1}{4}\nabla^2 J_{ij} = -\frac{1}{2r^3}\left(\delta_{ij}-\frac{3r_i r_j}{r^2}\right)$$

$$\text{(B.57e)} \qquad \hat{M}_{\Omega S}{}^{\alpha\beta}_{ijk} = -\frac{1}{2}\varepsilon_{ilm}\nabla_l K_{mjk} = -\frac{3}{2r^3}\left(\varepsilon_{imj}\frac{r_m r_k}{r^2}+\varepsilon_{imk}\frac{r_m r_j}{r^2}\right)$$

$$\begin{aligned}\text{(B.57f)} \qquad \hat{M}_{ES}{}^{\alpha\beta}_{ijkl} &= \left(-\frac{1}{r^3}+\frac{6}{5r^5}\right)\delta_{ij}\delta_{kl} + \frac{6}{5r^5}\left(\delta_{ik}\delta_{lj}+\delta_{il}\delta_{kj}\right)\\ &+ \left(\frac{3}{r^3}-\frac{6}{r^5}\right)\left(\delta_{kl}\frac{r_i r_j}{r^2}+\delta_{ij}\frac{r_k r_l}{r^2}\right)\\ &+ \left(\frac{3}{2r^3}-\frac{6}{r^5}\right)\left(\delta_{lj}\frac{r_i r_k}{r^2}+\delta_{li}\frac{r_k r_j}{r^2}+\delta_{kj}\frac{r_i r_l}{r^2}+\delta_{ik}\frac{r_l r_j}{r^2}\right)\\ &+ \left(-\frac{15}{r^3}+\frac{42}{r^5}\right)\frac{r_i r_j r_k r_l}{r^4}\end{aligned}$$

B.4.3. Pair-mobility tensors ($r \leq 2a$)

The definitions of near-field mobility tensors between two different overlapping particles ($\alpha \neq \beta$ and $r \leq 2a$) are given at Eqn. 5.60 [Sec. 5.2.6] and its corresponding dimensionless explicit expressions are shown below:

$$\text{(B.58a)} \quad \hat{M}_{UF}{}^{\alpha\beta}_{ij} = \frac{4}{3}\left[\left(1-\frac{9r}{32}\right)\delta_{ij} + \frac{3r}{32}\frac{r_i r_j}{r^2}\right]$$

$$\text{(B.58b)} \quad \hat{M}_{UT}{}^{\alpha\beta}_{ij} = \frac{1}{2}\left(r-\frac{3}{8}r^2\right)\varepsilon_{ijk}\frac{r_k}{r}$$

$$\text{(B.58c)} \quad \hat{M}_{US}{}^{\alpha\beta}_{ijk} = \left(\frac{3}{10}r-\frac{1}{8}r^2\right)\left(\delta_{ij}\frac{r_k}{r}+\delta_{ik}\frac{r_j}{r}\right)+\left(-\frac{1}{5}r+\frac{1}{16}r^2\right)\frac{r_i}{r}\delta_{jk}+\frac{r^2}{16}\frac{r_i r_j r_k}{r^3}$$

$$\text{(B.58d)} \quad \hat{M}_{\Omega T}{}^{\alpha\beta}_{ij} = \left(1-\frac{27}{32}r+\frac{5}{64}r^3\right)\delta_{ij}+\left(\frac{9}{32}r-\frac{3}{64}r^3\right)\frac{r_i r_j}{r^2}$$

$$\text{(B.58e)} \quad \hat{M}_{\Omega S}{}^{\alpha\beta}_{ijk} = \left(-\frac{9}{32}r+\frac{3}{64}r^3\right)\left(\varepsilon_{imj}\frac{r_m r_k}{r^2}+\varepsilon_{imk}\frac{r_m r_j}{r^2}\right)$$

$$\begin{aligned}\text{(B.58f)} \quad \hat{M}_{ES}{}^{\alpha\beta}_{ijkl} = {} & \left(-\frac{2}{5}+\frac{3}{16}r-\frac{1}{128}r^3\right)\delta_{ij}\delta_{kl}+\left(\frac{3}{5}-\frac{3}{8}r+\frac{3}{128}r^3\right)(\delta_{ik}\delta_{lj}+\delta_{il}\delta_{kj}) \\ & +\left(\frac{3}{16}r-\frac{3}{128}r^3\right)\left(\delta_{kl}\frac{r_i r_j}{r^2}+\delta_{ij}\frac{r_k r_l}{r^2}\right) \\ & +\left(-\frac{3}{32}r+\frac{3}{128}r^3\right)\left(\delta_{lj}\frac{r_i r_k}{r^2}+\delta_{li}\frac{r_k r_j}{r^2}+\delta_{kj}\frac{r_i r_l}{r^2}+\delta_{ik}\frac{r_l r_j}{r^2}\right) \\ & -\left(\frac{3}{16}r+\frac{3}{128}r^3\right)\frac{r_i r_j r_k r_l}{r^4}\end{aligned}$$

B.4.4. Symmetry relations

A complete list of symmetry relations of mobility tensors [Sec. 5.2.4.2] between component indices (i, j, k, l), pairs indices (α, β) and coupling indices (X, Y) ($X = U$, Ω or E and $Y = F$, T or S) is compiled below.

B.4.4.1. Components indices.

$$\hat{M}_{UF}{}^{\alpha\beta}{}_{ij} = \hat{M}_{UF}{}^{\alpha\beta}{}_{ji} \tag{B.59a}$$

$$\hat{M}_{UT}{}^{\alpha\beta}{}_{ij} = -\hat{M}_{UT}{}^{\alpha\beta}{}_{ji} \tag{B.59b}$$

$$\hat{M}_{US}{}^{\alpha\beta}{}_{ijk} = \hat{M}_{US}{}^{\alpha\beta}{}_{ikj} \tag{B.59c}$$

$$\hat{M}_{\Omega T}{}^{\alpha\beta}{}_{ij} = \hat{M}_{\Omega T}{}^{\alpha\beta}{}_{ji} \tag{B.59d}$$

$$\hat{M}_{\Omega S}{}^{\alpha\beta}{}_{ijk} = \hat{M}_{\Omega S}{}^{\alpha\beta}{}_{ikj} \tag{B.59e}$$

$$\hat{M}_{ES}{}^{\alpha\beta}{}_{ijkl} = \hat{M}_{ES}{}^{\alpha\beta}{}_{ijlk} = \hat{M}_{ES}{}^{\alpha\beta}{}_{jikl} \tag{B.59f}$$

B.4.4.2. Pairs indices.

$$\hat{M}_{UF}{}^{\alpha\beta}{}_{ij} = \hat{M}_{UF}{}^{\beta\alpha}{}_{ij} \tag{B.60a}$$

$$\hat{M}_{UT}{}^{\alpha\beta}{}_{ij} = -\hat{M}_{UT}{}^{\beta\alpha}{}_{ij} \tag{B.60b}$$

$$\hat{M}_{US}{}^{\alpha\beta}{}_{ijk} = -\hat{M}_{US}{}^{\beta\alpha}{}_{ijk} \tag{B.60c}$$

$$\hat{M}_{\Omega T}{}^{\alpha\beta}{}_{ij} = \hat{M}_{\Omega T}{}^{\beta\alpha}{}_{ij} \tag{B.60d}$$

$$\hat{M}_{\Omega S}{}^{\alpha\beta}{}_{ijk} = \hat{M}_{\Omega S}{}^{\beta\alpha}{}_{ijk} \tag{B.60e}$$

$$\hat{M}_{ES}{}^{\alpha\beta}{}_{ijkl} = \hat{M}_{ES}{}^{\beta\alpha}{}_{ijkl} \tag{B.60f}$$

B.4.4.3. Lorentz reciprocal theorem. Based on the Lorentz Reciprocal Theorem [Sec. 5.2.4.1], six symmetry relations can be derived by applying it to different motion modes. As the proof for many particle cases are similar to the single particle case, detailed proof for both cases are only provided for the translation-force mobility tensor

case as an example. For rest of symmetry relations, only proof of single particle case will be presented (particle indices such as α and β will be omitted for brevity).

(B.61a) $$\hat{M}_{UF}{}^{\alpha\beta}_{ij} = \hat{M}_{UF}{}^{\beta\alpha}_{ji}$$

(B.61b) $$\hat{M}_{\Omega T}{}^{\alpha\beta}_{ij} = \hat{M}_{\Omega T}{}^{\beta\alpha}_{ji}$$

(B.61c) $$\hat{M}_{ES}{}^{\alpha\beta}_{ijkl} = \hat{M}_{ES}{}^{\beta\alpha}_{klij}$$

(B.61d) $$\hat{M}_{\Omega F}{}^{\alpha\beta}_{ij} = \hat{M}_{UT}{}^{\beta\alpha}_{ji}$$

(B.61e) $$\hat{M}_{EF}{}^{\alpha\beta}_{ijk} = \hat{M}_{US}{}^{\beta\alpha}_{kij}$$

(B.61f) $$\hat{M}_{ET}{}^{\alpha\beta}_{ijk} = \hat{M}_{\Omega S}{}^{\beta\alpha}_{kij}$$

- translation-force mobility tensor $\boldsymbol{M}_{UF}$.

  For a single particle, let's assume the particle move at velocity $\mathbf{U}^\alpha$ due to a force $\mathbf{F}^\alpha$, and the corresponding surface velocity $\mathbf{u}$ and surface stress $\boldsymbol{\sigma}$ are solutions of the Stokes' equation. Then, consider two set of possible solutions:

$$(\mathbf{U}_1^\alpha, \mathbf{F}_1^\alpha) : (\mathbf{u}_1, \boldsymbol{\sigma}_1 \cdot \hat{\mathbf{n}})|_{\mathbf{x}=S^\alpha} = \left(\mathbf{U}_1^\alpha, \frac{\mathbf{F}_1^\alpha}{4\pi a^2}\right)$$
$$(\mathbf{U}_2^\alpha, \mathbf{F}_2^\alpha) : (\mathbf{u}_2, \boldsymbol{\sigma}_2 \cdot \hat{\mathbf{n}})|_{\mathbf{x}=S^\alpha} = \left(\mathbf{U}_2^\alpha, \frac{\mathbf{F}_2^\alpha}{4\pi a^2}\right)$$

  By the LRT, it gives that $\mathbf{U}_1^\alpha \cdot \mathbf{F}_2^\alpha = \mathbf{U}_2^\alpha \cdot \mathbf{F}_1^\alpha$. And also note the mobility relations, $\mathbf{U}_1^\alpha = \boldsymbol{M}_{UF}^{\alpha\alpha} \cdot \mathbf{F}_1^\alpha, \mathbf{U}_2^\alpha = \boldsymbol{M}_{UF}^{\alpha\alpha} \cdot \mathbf{F}_2^\alpha$. Therefore,

$$M_{UF}{}^{\alpha\alpha}_{ij} F_1{}^{\alpha}_{j} F_2{}^{\alpha}_{i} = M_{UF}{}^{\alpha\alpha}_{ij} F_2{}^{\alpha}_{j} F_1{}^{\alpha}_{i} = M_{UF}{}^{\alpha\alpha}_{ji} F_2{}^{\alpha}_{i} F_1{}^{\alpha}_{j}$$

As the choices of $\mathbf{F}_1^\alpha$ and $\mathbf{F}_2^\alpha$ are arbitrary, it requires that

$$M_{UF}{}^{\alpha\alpha}{}_{ij} = M_{UF}{}^{\alpha\alpha}{}_{ji} \tag{B.62}$$

For a pair of particles, the proof is similar by considering two sets of possible solutions:

$$(\mathbf{U}_1^\alpha, \mathbf{F}_1^\alpha) : (\mathbf{u}_1, \boldsymbol{\sigma}_1 \cdot \hat{\mathbf{n}})|_{\mathbf{x}=S^\alpha} = \left(\mathbf{U}_1^\alpha, \frac{\mathbf{F}_1^\alpha}{4\pi a^2}\right), (\mathbf{U}_1^\beta, \mathbf{F}_1^\beta) : (\mathbf{u}_1, \boldsymbol{\sigma}_1 \cdot \hat{\mathbf{n}})|_{\mathbf{x}=S^\beta} = \left(\mathbf{U}_1^\beta, \frac{\mathbf{F}_1^\beta}{4\pi a^2}\right)$$

$$(\mathbf{U}_2^\alpha, \mathbf{F}_2^\alpha) : (\mathbf{u}_2, \boldsymbol{\sigma}_2 \cdot \hat{\mathbf{n}})|_{\mathbf{x}=S^\alpha} = \left(\mathbf{U}_2^\alpha, \frac{\mathbf{F}_2^\alpha}{4\pi a^2}\right), (\mathbf{U}_2^\beta, \mathbf{F}_2^\beta) : (\mathbf{u}_2, \boldsymbol{\sigma}_2 \cdot \hat{\mathbf{n}})|_{\mathbf{x}=S^\beta} = \left(\mathbf{U}_2^\beta, \frac{\mathbf{F}_2^\beta}{4\pi a^2}\right)$$

And again the LRT yields that $\mathbf{U}_1^\alpha \cdot \mathbf{F}_2^\alpha + \mathbf{U}_1^\beta \cdot \mathbf{F}_2^\beta = \mathbf{U}_2^\alpha \cdot \mathbf{F}_1^\alpha + \mathbf{U}_2^\beta \cdot \mathbf{F}_1^\beta$. Also note the mobility relations: $\mathbf{U}_1^\alpha = \boldsymbol{M}_{UF}^{\alpha\alpha} \cdot \mathbf{F}_1^\alpha + \boldsymbol{M}_{UF}^{\alpha\beta} \cdot \mathbf{F}_1^\beta, \mathbf{U}_2^\alpha = \boldsymbol{M}_{UF}^{\alpha\alpha} \cdot \mathbf{F}_2^\alpha + \boldsymbol{M}_{UF}^{\alpha\beta} \cdot \mathbf{F}_2^\beta$. Therefore,

$$M_{UF}{}^{\alpha\beta}{}_{ij} F_1{}^{\beta}{}_i F_2{}^{\alpha}{}_j + M_{UF}{}^{\beta\alpha}{}_{ij} F_1{}^{\alpha}{}_i F_2{}^{\beta}{}_j = M_{UF}{}^{\alpha\beta}{}_{ij} F_2{}^{\beta}{}_i F_1{}^{\alpha}{}_j + M_{UF}{}^{\beta\alpha}{}_{ij} F_2{}^{\alpha}{}_i F_1{}^{\beta}{}_j$$

For the above identity to hold, it requires that

$$M_{UF}{}^{\alpha\beta}{}_{ij} = M_{UF}{}^{\beta\alpha}{}_{ji} \tag{B.63}$$

- translation-torque mobility tensor $\boldsymbol{M}_{UT}$ and rotation-force mobility tensor $\boldsymbol{M}_{\Omega F}$. Consider a solution $(\mathbf{u}_1, \boldsymbol{\sigma}_1)$ corresponds to a particle translates at velocity $\mathbf{U}_1$ due a torque $\mathbf{T}_1$; And another solution $(\mathbf{u}_2, \boldsymbol{\sigma}_2)$ corresponds to a particle rotates

at angular velocity $\mathbf{\Omega}_2$ due a force $\mathbf{F}_2$, i.e.

$$(\mathbf{U}_1, \mathbf{T}_1) : (\mathbf{u}_1, \boldsymbol{\sigma}_1 \cdot \hat{\mathbf{n}})|_{\mathbf{x}=S} = \left(U_i^1, \frac{3}{8\pi a^3} \varepsilon_{ijk} T_j^1 n_k \right)$$
$$(\mathbf{\Omega}_2, \mathbf{F}_2) : (\mathbf{u}_2, \boldsymbol{\sigma}_2 \cdot \hat{\mathbf{n}})|_{\mathbf{x}=S} = \left(\varepsilon_{ijk} \Omega_j^2 x_k, \frac{F_i^2}{4\pi a^2} \right)$$

By the LRT, $U_i^1 F_i^2 = \Omega_i^2 T_i^1$. Also note the mobility relations, $U_i^1 = {M_{UT}}^{\alpha\alpha}{}_{ij} T_j^1, \Omega_i^2 = {M_{\Omega F}}^{\alpha\alpha}{}_{ij} F_j^2$. Therefore,

$${M_{UT}}^{\alpha\alpha}{}_{ij} T_j^1 F_i^2 = {M_{\Omega F}}^{\alpha\alpha}{}_{ij} F_j^2 T_i^1 = {M_{\Omega F}}^{\alpha\alpha}{}_{ji} F_i^2 T_j^1$$

It gives that

$$ {M_{UT}}^{\alpha\alpha}{}_{ij} = {M_{\Omega F}}^{\alpha\alpha}{}_{ji} \tag{B.64}$$

This can be generalized to many particles case:

$$ {M_{UT}}^{\alpha\beta}{}_{ij} = {M_{\Omega F}}^{\beta\alpha}{}_{ji} \tag{B.65}$$

- translation-stresslet mobility tensor $\boldsymbol{M}_{US}$ and strain-force mobility tensor $\boldsymbol{M}_{EF}$.

$$(\mathbf{U}_1, \boldsymbol{S}_1), (\mathbf{u}_1, \boldsymbol{\sigma}_1 \cdot \hat{\mathbf{n}})|_{\mathbf{x}=S} = \left(U_i^1, \frac{3}{4\pi a^3} S_{ij}^1 n_j \right)$$
$$(\boldsymbol{E}_2, \mathbf{F}_2), (\mathbf{u}_2, \boldsymbol{\sigma}_2 \cdot \hat{\mathbf{n}})|_{\mathbf{x}=S} = \left(E_{ij}^2 x_j, \frac{F_i^2}{4\pi a^2} \right)$$

By the LRT, $U_i^1 F_i^2 = E_{ij}^2 S_{ij}^1$. Also note the mobility relations, $U_i^1 = {M_{US}}^{\alpha\alpha}{}_{ijk} S_{jk}^1, E_{ij}^2 = {M_{EF}}^{\alpha\alpha}{}_{ijk} F_k^2$. Therefore,

$${M_{US}}^{\alpha\alpha}{}_{ijk} S_{jk}^1 F_i^2 = {M_{EF}}^{\alpha\alpha}{}_{ijk} F_k^2 S_{ij}^1 = {M_{EF}}^{\alpha\alpha}{}_{jki} F_i^2 S_{jk}^1$$

It gives that

$$M_{US}{}^{\alpha\alpha}{}_{ijk} = M_{EF}{}^{\alpha\alpha}{}_{jki} \tag{B.66}$$

This can be generalized to many particles case:

$$M_{US}{}^{\alpha\beta}{}_{ijk} = M_{EF}{}^{\beta\alpha}{}_{jki} \tag{B.67}$$

- rotation-torque mobility tensor $\boldsymbol{M}_{\Omega T}$.

$$(\boldsymbol{\Omega}_1, \mathbf{T}_1), (\mathbf{u}_1, \boldsymbol{\sigma}_1 \cdot \hat{\mathbf{n}})|_{\mathbf{x}=S} = \left(\varepsilon_{ijk}\Omega_j^1 x_k, \frac{3}{8\pi a^3}\varepsilon_{ijk}T_j^1 n_k\right)$$
$$(\boldsymbol{\Omega}_2, \mathbf{T}_2), (\mathbf{u}_2, \boldsymbol{\sigma}_2 \cdot \hat{\mathbf{n}})|_{\mathbf{x}=S} = \left(\varepsilon_{ijk}\Omega_j^2 x_k, \frac{3}{8\pi a^3}\varepsilon_{ijk}T_j^2 n_k\right)$$

By the LRT, $\Omega_i^1 T_i^2 = \Omega_i^2 T_i^1$. Also note the mobility relations, $\Omega_i^1 = M_{\Omega T}{}^{\alpha\alpha}{}_{ij} T_j^1$, $\Omega_i^2 = M_{\Omega F}{}^{\alpha\alpha}{}_{ij} T_j^2$. Therefore,

$$M_{\Omega T}{}^{\alpha\alpha}{}_{ij} T_j^1 T_i^2 = M_{\Omega T}{}^{\alpha\alpha}{}_{ij} T_j^2 T_i^1 = M_{\Omega T}{}^{\alpha\alpha}{}_{ji} T_i^2 T_j^1$$

It gives that

$$M_{\Omega T}{}^{\alpha\alpha}{}_{ij} = M_{\Omega T}{}^{\alpha\alpha}{}_{ji} \tag{B.68}$$

This can be generalized to many particles case:

$$M_{\Omega T}{}^{\alpha\beta}{}_{ij} = M_{\Omega T}{}^{\beta\alpha}{}_{ji} \tag{B.69}$$

- rotation-stresslet mobility tensor $\boldsymbol{M}_{\Omega S}$ and strain-torque mobility tensor $\boldsymbol{M}_{ET}$.

$$(\boldsymbol{\Omega}_1, \boldsymbol{S}_1), (\mathbf{u}_1, \boldsymbol{\sigma}_1 \cdot \hat{\mathbf{n}})|_{\mathbf{x}=S} = \left(\varepsilon_{ijk} \Omega_j^1 x_k, \frac{3}{4\pi a^3} S_{ij}^1 n_j \right)$$
$$(\boldsymbol{E}_2, \mathbf{T}_2), (\mathbf{u}_2, \boldsymbol{\sigma}_2 \cdot \hat{\mathbf{n}})|_{\mathbf{x}=S} = \left(E_{ij}^2 x_j, \frac{3}{8\pi a^3} \varepsilon_{ijk} T_j^2 n_k \right)$$

By the LRT, $\Omega_i^1 T_i^2 = E_{ij}^2 S_{ij}^1$. Also note the mobility relations, $\Omega_i^1 = {M_{\Omega S}}^{\alpha\alpha}{}_{ijk} S_{jk}^1, E_{ij}^2 = {M_{ET}}^{\alpha\alpha}{}_{ijk} T_k^2$. Therefore,

$${M_{\Omega S}}^{\alpha\alpha}{}_{ijk} S_{jk}^1 T_i^2 = {M_{ET}}^{\alpha\alpha}{}_{ijk} T_k^2 S_{ij}^1 = {M_{ET}}^{\alpha\alpha}{}_{jki} T_i^2 S_{jk}^1$$

It gives that

$$ {M_{\Omega S}}^{\alpha\alpha}{}_{ijk} = {M_{ET}}^{\alpha\alpha}{}_{jki} \tag{B.70}$$

This can be generalized to many particles case:

$$ {M_{\Omega S}}^{\alpha\beta}{}_{ijk} = {M_{ET}}^{\beta\alpha}{}_{jki} \tag{B.71}$$

- strain-stresslet mobility tensor $\boldsymbol{M}_{ES}$.

$$(\boldsymbol{E}_1, \boldsymbol{S}_1), (\mathbf{u}_1, \boldsymbol{\sigma}_1 \cdot \hat{\mathbf{n}})|_{\mathbf{x}=S} = \left(E_{ij}^1 x_j, \frac{3}{4\pi a^3} S_{ij}^1 n_j \right)$$
$$(\boldsymbol{E}_2, \boldsymbol{S}_2), (\mathbf{u}_2, \boldsymbol{\sigma}_2 \cdot \hat{\mathbf{n}})|_{\mathbf{x}=S} = \left(E_{ij}^2 x_j, \frac{3}{4\pi a^3} S_{ij}^2 n_j \right)$$

By the LRT, $E_{ij}^1 S_{ij}^2 = E_{ij}^2 S_{ij}^1$. Also note the mobility relations, $E_{ij}^1 = {M_{ES}}^{\alpha\alpha}{}_{ijkl} S_{kl}^1, E_{ij}^2 = {M_{ES}}^{\alpha\alpha}{}_{ijkl} S_{kl}^2$. Therefore,

$${M_{ES}}^{\alpha\alpha}{}_{ijkl} S_{kl}^1 S_{ij}^2 = {M_{ES}}^{\alpha\alpha}{}_{ijkl} S_{kl}^2 S_{ij}^1 = {M_{ES}}^{\alpha\alpha}{}_{klij} S_{ij}^2 S_{kl}^1$$

It gives that

$$M_{ES}{}^{\alpha\alpha}{}_{ijkl} = M_{ES}{}^{\alpha\alpha}{}_{klij} \tag{B.72}$$

This can be generalized to many particles case:

$$M_{ES}{}^{\alpha\beta}{}_{ijkl} = M_{ES}{}^{\beta\alpha}{}_{klij} \tag{B.73}$$

B.4.4.4. Definition of the Faxén laws. There are also three additional symmetry relations of pair-mobility can be derived directly from its definitions:

$$\hat{M}_{\Omega F}{}^{\alpha\beta}{}_{ij} = \hat{M}_{UT}{}^{\alpha\beta}{}_{ij} \tag{B.74a}$$

$$\hat{M}_{EF}{}^{\alpha\beta}{}_{ijk} = -\hat{M}_{US}{}^{\alpha\beta}{}_{kij} \tag{B.74b}$$

$$\hat{M}_{ET}{}^{\alpha\beta}{}_{ijk} = \hat{M}_{\Omega S}{}^{\alpha\beta}{}_{kij} \tag{B.74c}$$

- rotation-force mobility tensor $\boldsymbol{M}_{\Omega F}$.

By the definition of the rotation-force mobility tensor [Eqn. 5.33], it gives that

$$\begin{aligned} M_{\Omega F}{}^{\alpha\beta}{}_{ij} &= \frac{1}{8\pi\mu}\frac{1}{2}\varepsilon_{ikl}\nabla_k\left(1+\frac{a^2}{6}\nabla^2\right)J_{lj}(\mathbf{x}^\alpha-\mathbf{x}^\beta) \\ &= \frac{1}{8\pi\mu}\left(1+\frac{a^2}{6}\nabla^2\right)\frac{1}{2}\varepsilon_{ikl}\nabla_k J_{lj}(\mathbf{x}^\alpha-\mathbf{x}^\beta) \\ &= \frac{1}{8\pi\mu}\left(1+\frac{a^2}{6}\nabla^2\right)R_{ij}(\mathbf{x}^\alpha-\mathbf{x}^\beta) \\ &= M_{UT}{}^{\alpha\beta}{}_{ij} \end{aligned} \tag{B.75}$$

- strain-force mobility tensor $\boldsymbol{M}_{EF}$.

  By the definition of the strain-force mobility tensor [Eqn. 5.33], it gives that

(B.76)
$$
\begin{aligned}
M_{EF}{}^{\alpha\beta}_{ijk} &= \frac{1}{8\pi\mu}\left(1+\frac{a^2}{10}\nabla^2\right)\frac{1}{2}\left[\nabla_j\left(1+\frac{a^2}{6}\nabla^2\right)J_{ik}(\mathbf{x}^\alpha-\mathbf{x}^\beta)+\nabla_i\left(1+\frac{a^2}{6}\nabla^2\right)J_{jk}(\mathbf{x}^\alpha-\mathbf{x}^\beta)\right] \\
&= \frac{1}{8\pi\mu}\left(1+\frac{a^2}{6}\nabla^2\right)\left(1+\frac{a^2}{10}\nabla^2\right)\frac{1}{2}\left[\nabla_j J_{ik}(\mathbf{x}^\alpha-\mathbf{x}^\beta)+\nabla_i J_{jk}(\mathbf{x}^\alpha-\mathbf{x}^\beta)\right] \\
&= \frac{1}{8\pi\mu}\left(1+\frac{a^2}{6}\nabla^2\right)\left(1+\frac{a^2}{10}\nabla^2\right)K_{kij}(\mathbf{x}^\alpha-\mathbf{x}^\beta) \\
&= -M_{US}{}^{\alpha\beta}_{kij}
\end{aligned}
$$

- strain-torque mobility tensor $\boldsymbol{M}_{ET}$.

  By the definition of the strain-torque mobility tensor [Eqn. 5.33], it gives that

(B.77)
$$
\begin{aligned}
M_{ET}{}^{\alpha\beta}_{ijk} &= \frac{1}{8\pi\mu}\left(1+\frac{a^2}{10}\nabla^2\right)\frac{1}{2}\left[\nabla_j R_{ik}(\mathbf{x}^\alpha-\mathbf{x}^\beta)+\nabla_i R_{jk}(\mathbf{x}^\alpha-\mathbf{x}^\beta)\right] \\
&= -\frac{1}{8\pi\mu}\left(1+\frac{a^2}{10}\nabla^2\right)\frac{1}{2}\left[\nabla_j R_{ki}(\mathbf{x}^\alpha-\mathbf{x}^\beta)+\nabla_i R_{kj}(\mathbf{x}^\alpha-\mathbf{x}^\beta)\right] \\
&= -\frac{1}{8\pi\mu}\left(1+\frac{a^2}{10}\nabla^2\right)\frac{1}{2}\left[\nabla_j \frac{1}{2}\varepsilon_{klm}\nabla_l J_{im}(\mathbf{x}^\alpha-\mathbf{x}^\beta)+\nabla_i \frac{1}{2}\varepsilon_{klm}\nabla_l J_{jm}(\mathbf{x}^\alpha-\mathbf{x}^\beta)\right] \\
&= -\frac{1}{8\pi\mu}\left(1+\frac{a^2}{10}\nabla^2\right)\frac{1}{2}\varepsilon_{klm}\nabla_l \frac{1}{2}\left[\nabla_j J_{im}(\mathbf{x}^\alpha-\mathbf{x}^\beta)+\nabla_i J_{jm}(\mathbf{x}^\alpha-\mathbf{x}^\beta)\right] \\
&= -\frac{1}{8\pi\mu}\left(1+\frac{a^2}{10}\nabla^2\right)\frac{1}{2}\varepsilon_{klm}\nabla_l K_{mij}(\mathbf{x}^\alpha-\mathbf{x}^\beta) \\
&= M_{\Omega S}{}^{\alpha\beta}_{kij}
\end{aligned}
$$

B.5. Explicit expressions of the odd mobility tensors

In this section, the explicit expressions of odd mobility tensors are documented for reference. All N particles are assumed to be equal size of radius a, i.e. $a^\alpha = a^\beta = a$. All

distance quantities are normalized by the particle radius, such as $r = \left|\mathbf{x}^\alpha - \mathbf{x}^\beta\right|/a$. All mobility expressions are normalized by $8\pi\mu a^n$, where the exponent n is chose to make the corresponding mobility tensor dimensionless, i.e. $\hat{M^o}_{XY}{}^{\alpha\beta}_{ij} = 8\pi\mu a^n {M^o}_{XY}{}^{\alpha\beta}_{ij}$. The hat symbol $\hat{}$ indicates the quantity is dimensionless and the additional superscript ^{o} means it's an odd viscosity related quantity; The subscript XY means the mobility tensor describes the coupling between kinetic motions X ($X = U$, Ω or E) and force moments Y ($Y = F$, T or S); The superscript $\alpha\beta$ specifies the mobility tensor describes the interaction between α-th and β-th particles ($\alpha, \beta = 1 \cdots N$); The subscript $ijkl$ indicates the Cartesian components of the mobility tensor ($i, j, k, l = 1, 2, 3$). δ_{ij} is the Kronecker delta and ε_{ijk} is the right-handed Levi-Civita symbol. Only six out of nine mobility tensors are given and the rest can be obtained by the symmetry relations of mobility tensors [Sec. B.5.4]. Only odd mobility tensors in the first order of the dimensionless viscosity ratio χ (odd viscosity μ_o over even viscosity μ_s) are derived. If necessary, higher order corrections can be computed in a similar manner [Sec. 6.3.3].

B.5.1. Self-mobility tensors

The dimensionless expressions of mobility tensors for a single isolated particle ($\alpha = \beta$) are shown below and its corresponding dimensional forms can be found at Eqn. 6.68 [Sec. 6.3.7].

(B.78a) $$\hat{M}^{o}{}_{UF}{}^{\alpha\alpha}{}_{ij} = \frac{2\chi}{3}\varepsilon_{ij3}$$

(B.78b) $$\hat{M}^{o}{}_{UT}{}^{\alpha\alpha}{}_{ij} = 0$$

(B.78c) $$\hat{M}^{o}{}_{US}{}^{\alpha\alpha}{}_{ijk} = 0$$

(B.78d) $$\hat{M}^{o}{}_{\Omega T}{}^{\alpha\alpha}{}_{ij} = \frac{\chi}{2}\varepsilon_{ij3}$$

(B.78e) $$\hat{M}^{o}{}_{\Omega S}{}^{\alpha\alpha}{}_{ijk} = \frac{3\chi}{5}\delta_{3ijk}$$

(B.78f) $$\hat{M}^{o}{}_{ES}{}^{\alpha\alpha}{}_{ijkl} = \frac{\chi}{10}\left[(\varepsilon_{ik3}\delta_{lj} + \varepsilon_{il3}\delta_{kj}) + (\varepsilon_{jk3}\delta_{li} + \varepsilon_{jl3}\delta_{ki})\right]$$

B.5.2. Pair-mobility tensors ($r > 2a$)

The definitions of far-field mobility tensors between two different non-overlapping particles ($\alpha \neq \beta$ and $r > 2a$) are given at Eqn. 6.72 [Sec. 6.3.8] and its corresponding dimensionless explicit expressions are shown below:

(B.79a) $$\hat{M^o}_{UF}{}^{\alpha\beta}_{ij} = \frac{\chi}{r}\left[\left(1-\frac{2}{3r^2}\right)\varepsilon_{ij3} - \left(1-\frac{2}{r}\right)\frac{\varepsilon_{ijk}r_k r_3}{r^2}\right]$$

(B.79b) $$\hat{M^o}_{UT}{}^{\alpha\beta}_{ij} = -\frac{\chi}{2r^2}\left[\left(1+\frac{8}{5}\frac{1}{r^2}\right)\delta_{ij}\frac{r_3}{r} - \left(1-\frac{8}{5}\frac{1}{r^2}\right)\delta_{i3}\frac{r_j}{r} - \left(1-\frac{8}{5}\frac{1}{r^2}\right)\delta_{j3}\frac{r_i}{r}\right]$$
$$- \frac{3\chi}{2r^2}\left(1-\frac{8}{3}\frac{1}{r^2}\right)\frac{r_i r_j r_3}{r^3}$$

(B.79c) $$\hat{M^o}_{US}{}^{\alpha\beta}_{ijk} = \frac{\chi}{2r^2}\left(1-\frac{8}{5}\frac{1}{r^2}\right)\left[\left(\varepsilon_{ij3}\frac{r_k}{r}+\varepsilon_{ik3}\frac{r_j}{r}\right)+\left(\varepsilon_{ijm}\delta_{k3}+\varepsilon_{ikm}\delta_{j3}\right)\frac{r_m}{r}\right]$$
$$- \frac{3\chi}{2r^2}\left(1-\frac{8}{3}\frac{1}{r^2}\right)\left(\varepsilon_{ijm}\frac{r_k}{r}+\varepsilon_{ikm}\frac{r_j}{r}\right)\frac{r_m r_3}{r^2}$$

(B.79d) $$\hat{M^o}_{\Omega T}{}^{\alpha\beta}_{ij} = \frac{\chi}{2r^3}\varepsilon_{ij3} - \frac{3\chi}{2r^5}\varepsilon_{ijl}r_l r_3$$

(B.79e) $$\hat{M^o}_{\Omega S}{}^{\alpha\beta}_{ijk} = -\frac{\chi}{2r^3}\left(1-\frac{6}{5}\frac{1}{r^2}\right)\delta_{i3}\delta_{jk} + \frac{3\chi}{5r^5}\left(\delta_{ij}\delta_{k3}+\delta_{ik}\delta_{j3}\right)$$
$$- \frac{\chi}{2r^3}\left(15-\frac{42}{r^2}\right)\frac{r_i r_j r_k r_3}{r^4} - \frac{3\chi}{r^5}\left(\delta_{ik}\frac{r_j}{r}+\delta_{ij}\frac{r_k}{r}\right)\frac{r_3}{r}$$
$$+ \frac{3\chi}{2r^3}\left(1-\frac{2}{r^2}\right)\left(\delta_{i3}\frac{r_j r_k}{r^2}+\delta_{j3}\frac{r_i r_k}{r^2}+\delta_{k3}\frac{r_i r_j}{r^2}+\delta_{jk}\frac{r_i r_3}{r^2}\right)$$

(B.79f) $$\hat{M^o}_{ES}{}^{\alpha\beta}_{ijkl} = \frac{\chi}{4r^3}\left(1-\frac{6}{5}\frac{1}{r^2}\right)\left[\left(\varepsilon_{ik3}\delta_{lj}+\varepsilon_{il3}\delta_{kj}\right)+\left(\varepsilon_{jk3}\delta_{li}+\varepsilon_{jl3}\delta_{ki}\right)\right]$$
$$\frac{15\chi}{4r^3}\left(1-\frac{14}{5r^2}\right)\left[\left(\varepsilon_{ikn}\frac{r_l}{r}+\varepsilon_{iln}\frac{r_k}{r}\right)\frac{r_j}{r}+\left(\varepsilon_{jkn}\frac{r_l}{r}+\varepsilon_{jln}\frac{r_k}{r}\right)\frac{r_i}{r}\right]\frac{r_n r_3}{r^2}$$
$$- \frac{3\chi}{4r^3}\left(1-\frac{2}{r^2}\right)\left[\left(\varepsilon_{ik3}\frac{r_l}{r}+\varepsilon_{il3}\frac{r_k}{r}\right)\frac{r_j}{r}+\left(\varepsilon_{jk3}\frac{r_l}{r}+\varepsilon_{jl3}\frac{r_k}{r}\right)\frac{r_i}{r}\right.$$
$$+ \varepsilon_{ikn}\frac{r_n}{r}\left(\delta_{l3}\frac{r_j}{r}+\delta_{lj}\frac{r_3}{r}+\delta_{j3}\frac{r_l}{r}\right)+\varepsilon_{iln}\frac{r_n}{r}\left(\delta_{k3}\frac{r_j}{r}+\delta_{kj}\frac{r_3}{r}+\delta_{j3}\frac{r_k}{r}\right)$$
$$\left.+ \varepsilon_{jkn}\frac{r_n}{r}\left(\delta_{l3}\frac{r_i}{r}+\delta_{li}\frac{r_3}{r}+\delta_{i3}\frac{r_l}{r}\right)+\varepsilon_{jln}\frac{r_n}{r}\left(\delta_{k3}\frac{r_i}{r}+\delta_{ki}\frac{r_3}{r}+\delta_{i3}\frac{r_k}{r}\right)\right]$$

B.5.3. Pair-mobility tensors ($r \leq 2a$)

The definitions of near-field mobility tensors between two different overlapping particles ($\alpha \neq \beta$ and $r \leq 2a$) are given at Eqn. 6.67 [Sec. 6.3.7] and its corresponding dimensionless explicit expressions are shown below:

$$\text{(B.80a)} \quad \hat{M}^o_{UF}{}^{\alpha\beta}_{ij} = \chi\left(\frac{2}{3} - \frac{1}{8}r\right)\varepsilon_{ij3} - \frac{\chi}{8}r\varepsilon_{ijk}\frac{r_k r_3}{r^2}$$

$$\text{(B.80b)} \quad \hat{M}^o_{UT}{}^{\alpha\beta}_{ij} = -\chi\left(\frac{2}{5} - \frac{5}{32}r\right)\delta_{ij}r_3 + \chi\left(\frac{1}{10} - \frac{1}{32}r\right)(\delta_{i3}r_j + r_i\delta_{j3}) - \frac{\chi}{32r}r_i r_j r_3$$

$$\text{(B.80c)} \quad \hat{M}^o_{US}{}^{\alpha\beta}_{ijk} = \chi\left(\frac{1}{10} - \frac{1}{32}r\right)\left[(\varepsilon_{ij3}r_k + \varepsilon_{ik3}r_j) + (\varepsilon_{ijm}\delta_{k3} + \varepsilon_{ikm}\delta_{j3})\,r_m\right] - \frac{\chi}{32r}(\varepsilon_{ijm}r_k + \varepsilon_{ikm}r_j)\,r_m r_3$$

$$\text{(B.80d)} \quad \hat{M}^o_{\Omega T}{}^{\alpha\beta}_{ij} = \frac{\chi}{2}\left(1 - \frac{9}{16}r + \frac{1}{32}r^3\right)\varepsilon_{ij3} - \frac{3\chi}{2}\left(\frac{3}{16}r - \frac{1}{32}r^3\right)\varepsilon_{ijl}\frac{r_l r_3}{r^2}$$

$$\begin{aligned}\text{(B.80e)} \quad \hat{M}^o_{\Omega S}{}^{\alpha\beta}_{ijk} &= -\chi\left(\frac{1}{5} - \frac{3}{32}r + \frac{1}{256}r^3\right)\delta_{i3}\delta_{kj} \\ &+ \frac{3\chi}{2}\left(\frac{1}{5} - \frac{1}{8}r + \frac{1}{128}r^3\right)(\delta_{ij}\delta_{k3} + \delta_{ik}\delta_{j3}) \\ &- \frac{3\chi}{256}\left(8r + r^3\right)\frac{r_i r_j r_k r_3}{r^4} - \frac{3\chi}{256}\left(16r - 3r^3\right)\left(\delta_{ik}\frac{r_j r_3}{r^2} + \delta_{ij}\frac{r_k r_3}{r^2}\right) \\ &+ \frac{3\chi}{256}\left(8r - r^3\right)\left(\delta_{i3}\frac{r_k r_j}{r^2} + \delta_{k3}\frac{r_i r_j}{r^2} + \delta_{j3}\frac{r_i r_k}{r^2} + \delta_{jk}\frac{r_i r_3}{r^2}\right)\end{aligned}$$

$$\begin{aligned}\text{(B.80f)} \quad \hat{M}^o_{ES}{}^{\alpha\beta}_{ijkl} &= -\chi\left(-\frac{1}{10} + \frac{3}{64}r - \frac{1}{512}r^3\right)\left[(\varepsilon_{ik3}\delta_{lj} + \varepsilon_{il3}\delta_{kj}) + (\varepsilon_{jk3}\delta_{li} + \varepsilon_{jl3}\delta_{ki})\right] \\ &+ \frac{3\chi}{512}\left(8r + r^3\right)\left[\left(\varepsilon_{ikn}\frac{r_l}{r} + \varepsilon_{iln}\frac{r_k}{r}\right)\frac{r_j}{r} + \left(\varepsilon_{jkn}\frac{r_l}{r} + \varepsilon_{jln}\frac{r_k}{r}\right)\frac{r_i}{r}\right]\frac{r_n r_3}{r^2} \\ &- \frac{3\chi}{512}\left(8r - r^3\right)\left[\left(\varepsilon_{ik3}\frac{r_l}{r} + \varepsilon_{il3}\frac{r_k}{r}\right)\frac{r_j}{r} + \left(\varepsilon_{jk3}\frac{r_l}{r} + \varepsilon_{jl3}\frac{r_k}{r}\right)\frac{r_i}{r}\right. \\ &+ \varepsilon_{ikn}\frac{r_n}{r}\left(\delta_{l3}\frac{r_j}{r} + \delta_{lj}\frac{r_3}{r} + \delta_{j3}\frac{r_l}{r}\right) + \varepsilon_{iln}\frac{r_n}{r}\left(\delta_{k3}\frac{r_j}{r} + \delta_{kj}\frac{r_3}{r} + \delta_{j3}\frac{r_k}{r}\right) \\ &+ \left.\varepsilon_{jkn}\frac{r_n}{r}\left(\delta_{l3}\frac{r_i}{r} + \delta_{li}\frac{r_3}{r} + \delta_{i3}\frac{r_l}{r}\right) + \varepsilon_{jln}\frac{r_n}{r}\left(\delta_{k3}\frac{r_i}{r} + \delta_{ki}\frac{r_3}{r} + \delta_{i3}\frac{r_k}{r}\right)\right]\end{aligned}$$

B.5.4. Symmetry relations

A complete list of symmetry relations of odd mobility tensors [Sec. 6.3.8.5] between component indices (i, j, k, l), pairs indices (α, β) and coupling indices (X, Y) ($X = U$, Ω or E and $Y = F$, T or S) is compiled below.

B.5.4.1. Components indices.

(B.81a) $$\hat{M}^o{}_{UF}{}^{\alpha\beta}{}_{ij} = -\hat{M}^o{}_{UF}{}^{\alpha\beta}{}_{ji}$$

(B.81b) $$\hat{M}^o{}_{UT}{}^{\alpha\beta}{}_{ij} = \hat{M}^o{}_{UT}{}^{\alpha\beta}{}_{ji}$$

(B.81c) $$\hat{M}^o{}_{US}{}^{\alpha\beta}{}_{ijk} = -\hat{M}^o{}_{US}{}^{\alpha\beta}{}_{ikj}$$

(B.81d) $$\hat{M}^o{}_{\Omega T}{}^{\alpha\beta}{}_{ij} = -\hat{M}^o{}_{\Omega T}{}^{\alpha\beta}{}_{ji}$$

(B.81e) $$\hat{M}^o{}_{\Omega S}{}^{\alpha\beta}{}_{ijk} = \hat{M}^o{}_{\Omega S}{}^{\alpha\beta}{}_{ikj}$$

(B.81f) $$\hat{M}^o{}_{ES}{}^{\alpha\beta}{}_{ijkl} = \hat{M}^o{}_{ES}{}^{\alpha\beta}{}_{ijlk} = \hat{M}^o{}_{ES}{}^{\alpha\beta}{}_{jikl}$$

B.5.4.2. Pairs indices.

(B.82a) $$\hat{M}^o{}_{UF}{}^{\alpha\beta}{}_{ij} = \hat{M}^o{}_{UF}{}^{\beta\alpha}{}_{ij}$$

(B.82b) $$\hat{M}^o{}_{UT}{}^{\alpha\beta}{}_{ij} = -\hat{M}^o{}_{UT}{}^{\beta\alpha}{}_{ij}$$

(B.82c) $$\hat{M}^o{}_{US}{}^{\alpha\beta}{}_{ijk} = -\hat{M}^o{}_{US}{}^{\beta\alpha}{}_{ijk}$$

(B.82d) $$\hat{M}^o{}_{\Omega T}{}^{\alpha\beta}{}_{ij} = \hat{M}^o{}_{\Omega T}{}^{\beta\alpha}{}_{ij}$$

(B.82e) $$\hat{M}^o{}_{\Omega S}{}^{\alpha\beta}{}_{ijk} = \hat{M}^o{}_{\Omega S}{}^{\beta\alpha}{}_{ijk}$$

(B.82f) $$\hat{M}^o{}_{ES}{}^{\alpha\beta}{}_{ijkl} = \hat{M}^o{}_{ES}{}^{\beta\alpha}{}_{ijkl}$$

B.5.4.3. generalized Lorentz reciprocal theorem. Based on the generalized Lorentz Reciprocal Theorem [Sec. 6.3.6.1], six symmetry relations can be derived by applying it to different motion modes. The proofs of these symmetry relations are highly similar to the case of even viscosity [Appx. B.4.4.3] and will be skipped here.

(B.83a) $$\hat{M}^o{}_{UF}{}^{\alpha\beta}_{ij} = -\hat{M}^o{}_{UF}{}^{\beta\alpha}_{ji}$$

(B.83b) $$\hat{M}^o{}_{\Omega T}{}^{\alpha\beta}_{ij} = -\hat{M}^o{}_{\Omega T}{}^{\beta\alpha}_{ji}$$

(B.83c) $$\hat{M}^o{}_{ES}{}^{\alpha\beta}_{ijkl} = -\hat{M}^o{}_{ES}{}^{\beta\alpha}_{klij}$$

(B.83d) $$\hat{M}^o{}_{\Omega F}{}^{\alpha\beta}_{ij} = -\hat{M}^o{}_{UT}{}^{\beta\alpha}_{ji}$$

(B.83e) $$\hat{M}^o{}_{EF}{}^{\alpha\beta}_{ijk} = -\hat{M}^o{}_{US}{}^{\beta\alpha}_{kij}$$

(B.83f) $$\hat{M}^o{}_{ET}{}^{\alpha\beta}_{ijk} = -\hat{M}^o{}_{\Omega S}{}^{\beta\alpha}_{kij}$$

B.5.4.4. Definition of the Faxén laws.

(B.84a) $$\hat{M}^o{}_{\Omega F}{}^{\alpha\beta}_{ij} = \hat{M}^o{}_{UT}{}^{\alpha\beta}_{ij}$$

(B.84b) $$\hat{M}^o{}_{EF}{}^{\alpha\beta}_{ijk} = -\hat{M}^o{}_{US}{}^{\alpha\beta}_{kij}$$

(B.84c) $$\hat{M}^o{}_{ET}{}^{\alpha\beta}_{ijk} = -\hat{M}^o{}_{\Omega S}{}^{\alpha\beta}_{kij}$$

APPENDIX C

Index